

Getting personal

The commercialization of personal genomics is moving with dizzying speed and scientists need to find innovative ways of discussing the implications with consumers.

As the first conference on personal genomes opened earlier this month at Cold Spring Harbor Laboratory in New York, some present were wondering whether the event was a little premature. After all, only four people's genomes have so far been fully sequenced and assembled, and it's still quite difficult to interpret the genetic variation found in them (see page 1014). But the participants soon began to realize that, in one sense, the meeting was overdue. Increasingly, private companies are offering personal genome scans and genetic tests for sale — and consumers are buying them. Meanwhile, some scientists earlier this week made public parts of their genetic and medical data through the Personal Genome Project, spearheaded by George Church, a geneticist at Harvard University. In this context, the ethical, legal and social issues usually sidelined at such gatherings kept intruding with uncommon urgency.

The day before the meeting began, for instance, deCODE Genetics of Reykjavik, Iceland, began selling a US\$1,625 risk-assessment test for breast cancer, which surveys seven of the single-point genetic variations known as single nucleotide polymorphisms (SNPs). The company says that the test will help identify women with a significantly elevated risk of the disease.

But the test is worrying some oncologists and geneticists. Mary-Claire King of the University of Washington in Seattle told the meeting that the SNPs included in the test are present at slightly different background frequencies in different populations across Europe. She raised the possibility that rather than predicting breast-cancer risk, the test might instead be detecting population differences between the control and test groups included in the studies that linked the SNPs to disease.

Regulation of such tests is patchy at best, so women have little official

guidance when it comes to balancing the potentially confusing scientific and medical facts about a product against their fear of breast cancer. But, as *New York Times* reporter Amy Harmon told the meeting, the public desperately wants help in making such decisions.

Part of the problem is the information overload provided by the Internet. Consumers can point their browsers to a slew of content, which can come from both trusted sources and charlatans. And in the age of e-mail whisper campaigns, lies can proliferate, opinions can replace facts, and experts are no longer trusted to know the truth.

"Scientists cannot put the genie back in the bottle."

Scientists can and should help the public sift through this information, interacting through blogs, newspaper articles or science cafes, for example. And if researchers are surprised at how quickly genome-wide association studies have become consumer products, they need to realize that things will only move faster in the future, with findings moving from the lab to Internet chat rooms and people's lives with astonishing rapidity.

The issue was articulated at the meeting by Robert Cook-Deegan, an ethicist at Duke University in Durham, North Carolina, who pointed out that scientists cannot put the genie back in the bottle. Anyone can now access his or her genome information through a personal genomics scan. And if people can get that information, they will — with or without the advice of genetic counsellors, doctors or expert scientists. It is impossible to guess what issues this will raise as the science matures, although new discoveries will no doubt trigger a fresh and more complicated set of societal discussions. Scientists need to get creative about how they participate in these discussions, because they won't have the luxury of opting out. ■

A look within

A series of Essays examines what science has to say about being human.

Some 2,500 years ago, legend has it, visitors to the Oracle at Delphi in Ancient Greece had to pass by an inscription bearing the words *gnothi seauton* — know thyself.

That advice is as wise today as it was then — and as hard to follow. Modern science can help, but using it to uncover truths about ourselves can also be fraught with difficulty. Consider, for example, that an important first step towards understanding contemporary human behaviour — establishing the evolutionary context in which it emerged — means piecing together odd scraps of evidence left by our hunter-gatherer ancestors tens of thousands of years ago. The paucity of data makes it all too easy to come up with untested,

and even untestable, Darwinian versions of Rudyard Kipling's *Just So Stories*.

Another major challenge for researchers is being objective about a topic as philosophically, politically and ethically charged as human nature. Take the sociobiology wars of the 1970s and 1980s. Left-wing scholars rejected biological explanations for phenomena such as gender roles, religion, homosexuality and xenophobia, largely because they feared such explanations would be used to justify a continuation of existing inequalities on genetic grounds. The resulting debates became hugely political.

The combustibility of the interface between science and society is one major reason for the extraordinary fragmentation of research that tackles human behaviour. In part because of the sociobiology battle, most social scientists still steer clear of using evolutionary hypotheses. And even researchers who do work under the unifying framework of evolution tend to fall into distinct camps such as gene-culture co-evolution or human behavioural ecology — their practitioners

divided by differences of opinion on, say, the relative importance of culture versus genes.

Given that humans are such a complicated species, it is no surprise that researchers from fields such as economics, political science, anthropology and biology are driven to pursue similar questions using their own distinct tools and approaches. But the lack of cross-talk between disciplines and subdisciplines means that efforts are too often duplicated, and opportunities to exchange insights lost. Much of the ethnographic data on hunter-gatherers collected by anthropologists, for instance, are largely unknown to modellers interested in the emergence of particular human traits. Similarly, evolutionary biologists constantly accuse social scientists of either ignoring evolution or invoking outdated versions of evolutionary theory.

It doesn't have to be this way. In other domains, such as the study of complex systems, scientists from biological, physical and social sciences are increasingly sharing information. Now is a particularly opportune moment for those studying human behaviour to follow suit. Genomics is beginning to provide a window onto many thousands of years of human history. Advances in mathematical analyses have greatly clarified our picture of the evolutionary process. And, because of the rapid assimilation of nomadic hunter-gatherer populations into modern societies, researchers have collected

most of the ethnographic data on these groups they are ever likely to obtain.

In the spirit of fostering dialogue between disparate fields of research, *Nature* has commissioned a series of Essays that asks how discoveries in psychology, anthropology, genetics, neuroscience, game theory and network engineering are altering our understanding of particular human characteristics, or of issues that are central to human life. Starting this week with religion (see page 1038), and appearing every two weeks for the next five months, these Essays move from human prehistory to look at how we operate within self-made highly interconnected cities and communication networks.

Cumulatively, the series indicates that the interface between science and society is no less thorny now than it's ever been; revelations about our appetite for warfare in an Essay on conflict, for example, will make for uncomfortable reading. But overall, practitioners from diverse areas of research deliver an optimistic message about how we may learn to manage ourselves more effectively as a result of knowing ourselves better. ■

"Now is a particularly opportune moment for those studying human behaviour to share their data."

Fair trade?

Europe needs to find a responsible way out of its climate-regulation impasse.

Is the worst financial storm in nearly 80 years having a deleterious effect on climate policy? It seemed that way last week, when European Union (EU) leaders failed to agree on a new set of market-based tools to cut the bloc's greenhouse-gas emissions by at least 20% from 1990 levels by 2020. Proponents could not overcome resistance from a group of countries, led by Poland, that argued that the plan would harm their national economies — an argument apparently given extra weight by the near-collapse of worldwide financial markets and the prospect of a deep economic downturn.

At issue was a set of amendments to the EU's mandatory carbon emissions trading system. In the first phase of this scheme, implemented in 2005, emissions allowances were given to industry for free — and, in retrospect, in far too great an abundance. The resulting oversupply led to a very low price, and a corresponding failure to deliver the desired emissions reductions. The proposed amendments would require large facilities to bid for 100% of their emissions allowances at auction.

Countries such as Poland, whose industries and energy systems are heavily based on coal, worry that this would put them at a serious competitive disadvantage. The proposed reforms do require nations such as Britain and Germany to contribute substantially more to the overall reduction target than economically less powerful countries. Nonetheless, Poland has threatened to block the amendments unless its energy-intensive heavy industries, such as cement and steel, can continue to use the free allowances.

The French government, which currently holds the EU presidency, is trying to broker a compromise before its term expires at the end of the year. But meeting that deadline will be difficult. Some concessions to eastern member countries may be inevitable, and even justifiable. Their overall emissions are comparatively low, so the system as a whole would not be greatly compromised by a temporary respite. But for the scheme to work in the long run, special provisions must be limited to industry sectors that would otherwise face intolerable competitive disadvantages. Moreover, those sectors should be identified by a thorough, data-driven analysis of their competitive situation, energy intensity and emissions-reduction potential — not on the basis of which country has the most political clout. And, perhaps most importantly, free allowances must be granted for only a limited time, and their allocation phased out quickly. Otherwise the worst polluters could be granted a free pass indefinitely.

Striking the right deal may take longer than the two months left to the French presidency. But a well-weighed set of rules is far preferable to a rushed political compromise that would substantially water down the EU's ambitious climate plan.

Meanwhile, the current economic turbulence cannot be allowed to serve as a pretext for lessening climate-protection efforts. And there are signs that governments are getting that message, both in Europe and elsewhere. The British commitment, announced last week, to cut domestic greenhouse-gas emissions by 80% of 1990 levels by 2050, is a courageous example. If the British plan sets the tone for the upcoming negotiations, then the EU's ambitious climate goals are not at risk, even if some eastern member states cannot quite keep pace. And if the next US administration puts into action what both leading presidential candidates are promising in terms of climate policies, this economically woeful time could mark the move into a greener future. ■

RESEARCH HIGHLIGHTS

T. J. BARKMAN



Growing flowers

Curr. Biol. **18**, 1508–1513 (2008)

The world's largest flowers, of the Southeast Asian *Rafflesia* genus, which mimic the smell and appearance of rotting flesh, evolved much more quickly and more often than botanists expected.

Todd Barkman of Western Michigan University in Kalamazoo and his team hypothesized that it would have taken a long time for the *Rafflesia* flowers to evolve from their smaller ancestors to their current maximum size of one metre in diameter because of the many structural and physiological changes required to support such large flowers. To their surprise, they found that the flowers of some *Rafflesia* species have more or less doubled in size during the past one million to two million years. As Barkman points out, it is hard to imagine a giraffe doubling the length of its neck in the same time frame. The scientists suggest that even bigger flowers could evolve in future.

GEOSCIENCES

Exporting ice

Geophys. Res. Lett. doi:10.1029/2008GL034813 (2008)

Ice export through the Fram Strait east of Greenland is a crucial determinant of recent Arctic sea-ice loss.

Lars Smetsrud and his colleagues evaluated three factors behind this spectacular ice loss. Since 1990, atmospheric heat transport to the Arctic has declined. More oceanic heat transport contributed to ice loss but, say the researchers, increased ice export was more important, especially in 2007–08.

If oceanic heat transport and ice export decrease, Arctic sea ice could remain robust. But if current patterns continue or strengthen, combined with increasing atmospheric carbon dioxide, a seasonally ice-free Arctic is possible within decades.

NANOMEDICINE

Disease nanosensors

Nano Lett. **8**, 3310–3314 (2008)

Yale University scientists have created a detection system that uses sensitive nanowire sensors to allow doctors to diagnose patients with infectious diseases non-invasively.

Unlike current detection techniques, the system does not rely on dyes or radioactivity. The sensors detect the activation of a particular type of immune cell by antigens — signatures of bacterial, viral or cancerous cells. Previously, Tarek Fahmy and his colleagues demonstrated that the sensors could detect a response by these cells, T cells, to many types of antigen. The new report shows that the sensors can now distinguish the specific antigen or antigens activating the immune system and so potentially detect disease.

Doctors could eventually use the sensors to

immediately diagnose patients' illnesses, or to test whether medication had successfully treated a disease, the researchers say.

CHEMISTRY

Selective separation

J. Am. Chem. Soc. doi:10.1021/ja804164y (2008)

Carbon nanotubes produced by the commonly used high-pressure carbon monoxide method are normally one-third metallic or semi-metallic and two-thirds semiconductor, and of various diameters. Now James Tour and his colleagues at Rice University in Houston, Texas, have developed what should be an easy way to separate these types in a reaction that may enable their use in a variety of micro-electronic components.

Their reaction uses ultraviolet light with a wavelength of 254 nanometres to add hydroxyl groups first to the semiconducting nanotubes in a mixture and then to metallic tubes of small diameters. This should mean that the larger metallic tubes could be easily separated from the mix.

NEUROLOGY

Contextual views

Neuron **60**, 162–173 (2008)

An animal's response to a stimulus depends on context, and it has now been shown that the connections between individual neurons depend on context as well. Marlene Cohen and William Newsome of Stanford University School of Medicine in California followed two direction-selective neurons in the middle temporal area of a monkey's brain as it looked at the same visual stimulus in two contexts.

The two cells were affiliated with the trajectories of two dots on a screen. The two neurons made the same direction judgement

when the monkey was asked to distinguish between northwards and southwards motion, but different judgements when asked to distinguish between eastwards and westwards.

The researchers found that, in general, the responses of the two neurons were more similar when they contributed to the same direction judgement. They presume that connection strength somewhere upstream of the target neurons changes depending on the task.

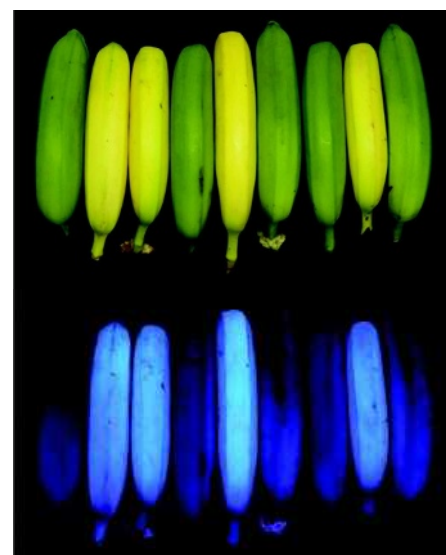
PLANT CHEMISTRY

Banana blues

Angew. Chem. Int. Edn doi:10.1002/anie.200803189 (2008)

Ripe bananas turn ... blue? Apparently so, when viewed under ultraviolet light (pictured in bottom panel, below).

Bernhard Kräutler of the University of Innsbruck in Austria and his co-workers



WILEY-VCH

have discovered hitherto unnoticed blue-fluorescent compounds in the peel of ripe bananas, which they attribute to the chemical degradation products of chlorophyll. These compounds, which have previously only been seen, fleetingly, in ageing leaves, are most abundant when the peels look the most yellow in daylight. They might have an important antioxidant role, delaying the decay of the ripe fruit.

BIOCHEMISTRY

Fungal facilitation

Ind. Eng. Chem. Res. **47**, 7476–7482 (2008)

A fungus has been found that can remove sulphur from crude oil more easily than conventional refining methods.

Jalal Shayegan and his colleagues at Sharif University of Technology in Tehran discovered the fungus *Stachybotrys sp.* while studying the microfauna of soil samples that were continuously being contaminated by oil. When they exposed the fungus to heavy crude oil samples, it removed up to 76% of the sulphur present.

Traditional sulphur-removal methods generally require temperatures above 400 °C and high pressures. The fungus, which functions perfectly well at 30 °C and atmospheric pressure, is expected to drastically improve the efficiency of oil refining methods.

ECOLOGY

Grunter gathering

Biol. Lett. doi:10.1098/rsbl.2008.0456 (2008); *PLoS ONE* **3**, e3472 (2008)

In the southeastern United States, some make their living by gathering worms for fishing bait through ‘worm grunting’. Worm grunTERS drive a wooden stake into the ground and then scrape it with a metal sheet; within minutes worms pop out of the ground and the grunTERS pick them up.

Two reports have recently been published on the phenomenon. Jayne Yack of Carleton University in Ontario, Canada, and her team found that the worms emerge in response to vibrations from the grunting — low-frequency pulsed vibrations at below 500 hertz that could be felt by researchers standing several metres away. They suggest that the vibrations mimic rain or the foraging of predators.

Kenneth Catania of Vanderbilt University in Nashville, Tennessee, compared the grunTERS’ vibrations with those made by rain and worm-devouring moles, and studied their relative effects on worms. He puts his chips on the vibrations mimicking the movement of the moles, causing the worms to flee.

ANIMAL BEHAVIOUR

Idle ants

Proc. R. Soc. B doi:10.1098/rspb.2008.1215 (2008)

The ant *Pristomyrmex punctatus* has no queens — female workers reproduce asexually. But that doesn’t mean that everyone is equal. Some nests harbour ‘cheaters’ that shirk their duties and concentrate on reproduction.

Shigeto Dobata of the University of Tokyo and his colleagues found that there are two morphologically distinct types of *P. punctatus* worker. One does the work; the other, which is larger (pictured below, right) and has more ovarioles, does hardly anything except lay eggs.

Genetic tests showed that cheaters, although closely related to their nest-mates, are genetically distinct. They also revealed the same cheater lineage in more than one nest, suggesting that it can spread between colonies, and leading the researchers to describe the cheats as a transmissible ‘social cancer’ that has evolved to exploit the cooperative behaviour of the majority.

S. DOBATA



DRUG DESIGN

Hitting the hinge

Cell **135**, 295–307 (2008)

Once a strain of bacteria has built up resistance to an antibiotic, a new antibiotic with a different mechanism is our next move in the arms race against pathogens such as tuberculosis. To this end, Eddy Arnold and Richard Ebright of Rutgers University in Piscataway, New Jersey, and their colleagues have found a new point of attack on an already popular target, bacterial RNA polymerase. This enzyme makes a good target because it is essential for making proteins from RNA and is highly conserved across bacteria.

The new target is at the hinge of a dynamic region of the enzyme that exposes or hides its active site. The researchers show that three natural products, myxopyronin, coralopyronin and ripostatin, all compounds certain bacteria use against one another, bind at the hinge and shut down RNA polymerase activity, crippling the bacterium.

JOURNAL CLUB

Lynne B. McCusker
Laboratory of Crystallography,
ETH Zurich, Switzerland

A crystallographer celebrates a method with niche applications.

In 2004, Oszlányi and Sütő introduced a new way to determine crystal structures from diffraction data. To many crystallographers, including myself, this was a remarkable development. Although most of us had assumed that the trend of incremental but significant improvements to existing methods would continue, we had not expected a completely different approach to be discovered. The algorithm is an elegant one, based on a very simple perturbation (called charge flipping) of electron-density maps that are generated during the structure solution process.

Initially, the algorithm was viewed as a curiosity. After all, existing methods for solving structures work very well about 95% of the time, so a new technique was not really needed. However, the algorithm caught the attention of some inquisitive crystallographers, who tested it on their favourite problem cases. The result is that, just 4 years after its development, the approach has found niches in areas in which traditional methods flounder (*Acta Cryst.* **A64**, 123–134; 2008).

Scientists studying aperiodic materials (modulated structures and quasicrystals, whose structures are best described in more than three dimensions) were among the first to recognize the possibilities offered by the algorithm, because it could be easily adapted to work in higher dimensions. Charge flipping has enjoyed great success with such structures, and is now considered the method of choice by this community.

The algorithm has also proved effective in solving the structures of polycrystalline materials, mainly because complementary information from other sources (such as chemical analysis and electron microscopy) can be easily included. Now small protein structures and neutron- and electron-diffraction data are being explored — no doubt further niches will be found.

Discuss this paper at <http://blogs.nature.com/nature/journalclub>

NEWS

Biosafety lab passes disaster test

GALVESTON, TEXAS

On 11 November, US officials will dedicate a new research complex containing high-containment labs for deadly pathogens: the \$175-million Galveston National Laboratory in Texas. Yet even as questions arise over the safety of other biosecurity research facilities, the cornerstone of the new complex survived its biggest test yet: Hurricane Ike, which devastated Galveston Island last month yet left the new biosafety level 4 (BSL-4) lab intact.

The Galveston lab is one of several BSL-4 facilities that have sprung up since the terrorist and anthrax attacks of 2001. Last week, the US Government Accountability Office released a scathing report on the security of the others. Two of the five current BSL-4 facilities, the report found, had security problems ranging from poor guard facilities to lax camera systems. Some members of Congress have called for the construction of new labs to be halted until such issues can be addressed. For now, the Galveston facility seems to be coming out the best — despite being located in a hurricane-prone zone.

Ike, which hit on 13 September, caused at least \$700 million worth of damage — including \$275 million in lost hospital revenues — to University of Texas facilities. That includes more than \$400 million for clinical facilities at the University of Texas Medical Branch (UTMB), and at least \$18 million for UTMB research labs. Lower-floor laboratories were flooded, and hundreds of animals had to be destroyed after auxiliary power systems failed.

But a sterling effort meant that staff moved dozens of freezers of samples to safety. No infectious agents were released, almost all frozen specimens were saved, and highly sensitive colonies of exotic animals were unharmed. For instance, the UTMB saved a colony of mosquitoes — *Culex taeniopus*, which transmits Venezuelan equine encephalitis to humans and horses — by rigging up a temporary fluctuating-light system to mimic sunrise and sunset for mating, says virologist Scott Weaver, the UTMB's vice chair of research.

Across Galveston Island, research facilities at Texas A&M University's marine centre also suffered after losing power. For example, the state laboratory that tests the popular Galveston Bay oysters for enteric pathogens lost a freezer of research samples. This is the final hurricane



Galveston National Laboratory was undamaged by the floods of Hurricane Ike.

season that the A&M centre will spend in the 70-year-old building; a new facility with better back-up power is under construction.

Flooding, not winds, caused most of the damage in Galveston — as did Tropical Storm Allison at research facilities in Houston, 75 kilometres north of Galveston, in 2001. Accordingly, at the new national laboratory in Galveston, the bottom two floors are built of sealed concrete, and a back-up power system — with a dedicated natural-gas line for fuel — is located 11 metres above sea level. The new BSL-4 labs are on the top floors. Indeed, the new facility came in handy as staff rushed to fill its -80°C freezers with research samples from elsewhere on campus before the storm hit. Other UTMB facilities, such as offices and wet labs, were built on lower, more vulnerable levels — mainly for cost reasons, says Stanley Lemon, director of the Institute for Human Infections and Immunity, the UTMB operation within the Galveston National Laboratory.

The university's current BSL-4 lab was safely positioned on the second floor of an older building. "We didn't lose the core," says Clarence Peters, the virologist who directs the UTMB's Center for Biodefense and Emerging Infectious Diseases. "If we had, it would be like

starting all over again." Still, he jokes: "I thought I was going to have to snorkel into my office." Located in the basement, it was waist-deep in water by the time he got there.

The vulnerability of BSL-4 labs is a hot topic in America these days. A second BSL-4 lab is under construction at Boston University in Massachusetts; its location, in South Boston, has triggered complaints from neighbourhood residents who worry about containment. Galveston, by comparison, is far less densely populated, and its history as a centre of tropical-disease research is more ingrained in the community.

The new lab at Galveston will be inaugurated with a lecture by Anthony Fauci, director of the National Institute of Allergy and Infectious Diseases in Bethesda, Maryland, which funded two-thirds of the facility's cost. It is meant to be certified and ready for operations this autumn.

Meanwhile, the federal government is to select by the end of the year a site for the \$450-million National Bio and Agro-Defense Facility, which will replace the Plum Island infectious-disease labs off New York. One of the five finalists is a low-rated site in Mississippi. It is inland, not immediately on the hurricane-prone Gulf Coast — but still is near the delta of the mighty Mississippi River.

Rex Dalton

J. KELLY

S. N. POOL/AP

**HAVE YOUR SAY**

Comment on any of our news stories, online.

www.nature.com/news

Cash row threatens Earth-monitoring system

An ambitious European proposal to launch an orbiting Earth-monitoring system called Kopernikus is facing possible delays to the launches of its component satellites after Italy and France demanded that costs be cut. A flurry of negotiations is under way to try to hammer out a compromise before a crucial meeting of the European Space Agency (ESA) from 25 to 26 November, at which the future of the project will be decided.

Kopernikus, formerly called the Global Monitoring for the Environment and Security (GMES) programme, is a joint venture of ESA and the European Commission. So far, it has secured €1.97 billion (US\$2.6 billion) in funding to carry it through to 2013 (see *Nature* 450, 778–779; 2008), which should cover the launching of the first members of the three Sentinel families of Kopernikus satellites (see ‘Meet the sentinels’).

Research satellites such as Envisat already provide data and images for Earth monitoring, but Kopernikus will operate its fleet of satellites over decades, and with regularly scheduled replacements. This means that it will generate continuous, cross-calibrated, long-term data sets on the state of the planet and its atmosphere. But the money for the operational system has yet to be approved, and the ESA ministerial meeting in November is crunch time.

Kopernikus enjoys strong political support. At a meeting in September, the European Space Council, a body made up of the ministers of the European Union's member states, rated it and the Galileo satellite navigation system as Europe's top immediate priorities in space.

Satellite shortfall

However, financial and political realities mean some member states are not showing the same support behind the scenes. Italy, for instance, is demanding that its initial contribution at least halve, which would cut more than €150 million from the budget. The shortfall is expected to be partly offset by the United Kingdom increasing its share from 1.5% to around 12% — a total contribution of about €120 million.

Italy and France also oppose ESA funding any satellites other than the first in each Sentinel family. They say that the costs of the subsequent satellites — the b-units essential to



The Sentinel-3 mission is scheduled for launch in 2012.

ensure long-term data continuity and adequate global coverage — should be borne by the European Union. Kopernikus's budget would therefore fall far short of what ESA needs to pursue its original proposal.

Germany, Spain and most of the smaller member states support funding the rapid deployment of the Sentinels, including the b-units. But decisions at ESA ministerial meetings must be unanimous. The goal now is to find a compromise that doesn't endanger Kopernikus's full operability.

The contours of that compromise were still

shifting as *Nature* went to press, but officials involved in the negotiations say that the option of cancelling any satellites is now off the table. Instead, the agency will probably ask the council of ministers for €857 million instead of €1 billion as initially planned. ESA would then still pay for all the satellites themselves, but would ask the European Commission to fund the launch and in-orbit validation of the b-units, a move that would delay the launch of these satellites until at least 2014.

Impending deadlock?

As the commission has no clear legal remit to procure future launches, it is highly unlikely to be able to commit to this before the ministerial meeting. This would trigger a deadlock and a probable postponement of any decision on funding of the b-units until the next ESA min-

isterial meeting in 2011. Moreover, although delaying the launches may initially save some member states money, it could make the programme more expensive in the long term.

Josef Aschbacher, head of the ESA branch of Kopernikus, is confident that the funding difficulties will be overcome, and says they are “typical of any major European programme” because of the diverging interests of member states. “By 2015 Kopernikus will be offering an operational monitoring system for everyone, similar to the systems in place today for meteorology, but for everything from air-quality and water-pollution monitoring and alerts, to city planning and emergency operations.”

Kopernikus isn't the only European space programme to face budget problems. ESA's ExoMars mission has been delayed until 2016, thanks to member states' reluctance to cover the higher costs of a proposed larger and more sophisticated rover (see *Nature* 455, 840–841; 2008). The delay could push costs up even higher, as the scientific and engineering teams working on the lander must be kept in place. But it should buy time for ESA to seek the greater international participation that will probably be needed to keep the mission alive.

The cuts to Italy's ESA contributions, announced since businessman Enrico Saggese was appointed as head of the Italian Space Agency in August (see *Nature* 454, 557; 2008), have affected both missions.

Declan Butler

Meet the sentinels

Sentinel 1: Carrying radar equipment for monitoring and mapping Earth's surface, these satellites will be useful for long-term environmental studies and to support deployment of humanitarian aid. They will build on the data set created by Envisat, the 8-tonne ESA research satellite.

Sentinel 2: A suite of imaging satellites with fine spectral resolution will continue the work of the US Landsat and French SPOT satellites.

Sentinel 3: These satellites will continue the ocean- and land-observing aspects of Envisat, and will be equipped with optical imaging and radar altimetry to measure topography and surface temperatures. An additional two Sentinels are planned for monitoring atmospheric chemistry.

D.B.

Accessible genomes move closer

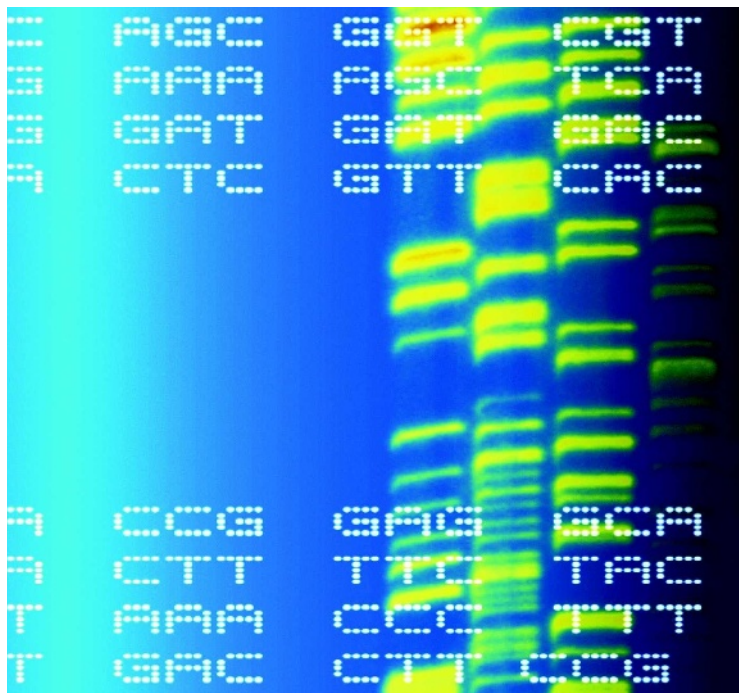
NEW YORK

Rarely do research subjects attend scientific meetings. Yet at the inaugural Cold Spring Harbor Personal Genomes meeting this month on Long Island in New York, the Nobel-prizewinning biologist James Watson sat in the front row as other researchers dissected his genetic vulnerabilities via a PowerPoint presentation. So far, Watson says, it has not been a particularly profound experience: "I haven't really learned anything, except that I'm lactose intolerant."

Other than Watson, only three people have had their genomes sequenced in full, but other sequencing efforts are under way, including the Personal Genome Project and the 1,000 Genomes Project. And researchers may soon be able to start linking this flood of personal genomic data to the biology of individual humans and the species.

The Cold Spring Harbor meeting marked the first steps in that direction. "It really feels like a new era is starting," says Martin Reese, a bioinformaticist at Omicia, which develops genome interpretation software in Emeryville, California. "People don't quite know how to apply these new techniques and technologies to human genomes, but very soon, they will."

One new approach tackles the human germline mutation rate — how much new genetic variation is born into each generation — which should inform theories of human evolution. At the Baylor College of Medicine in Houston, Texas, a group led by Richard Gibbs is sequencing and comparing thousands of genes of parents and their children. The preliminary data, reported at Cold Spring Harbor, suggest that the mutation rate is much higher than some estimates, but that has also been the case with direct measurements in other species, such as the fruitfly (*C. Haag-Liautard et al. Nature* 445, 82–85; 2007). Other scientists are using sequencing to look at the biological consequences of variation among individuals. Michael Snyder of Yale University in New Haven, Connecticut, is cataloguing the interactions between DNA



Information about what different gene variants do would aid genome interpretation.

and the enzyme RNA polymerase II — which helps to transcribe DNA into RNA — in cells containing human DNA. In each cell line, Snyder sequences the DNA wherever it binds to RNA polymerase II, thus obtaining a map of active transcription sites in each individual's genome. By comparing such maps, Snyder is discovering how human genetic differences are interpreted by the cell. "We're seeing some differences between individuals' DNA, and that will be the first translation of genetic differences to functional differences," Snyder says.

Ten-minute genomes

Snyder's work would not have been possible without the high-speed sequencing machines that he and many others at the conference are using (see *Nature* 448, 10–11; 2007). Pacific Biosciences, in Menlo Park, California, aims to build a machine that can sequence entire human genomes in ten minutes. The company said at the meeting that it is testing its technology on a bacteriophage, and it is now sequencing 550-base-pair segments of DNA. Researchers will soon see for themselves: the company begins an in-house early-access programme next year.

"People don't know how to apply these techniques to human genomes, but very soon, they will."

Exciting as it is, the prospect of multiple genomes per hour poses daunting data challenges, says Elaine Mardis, co-director of the Genome Sequencing Center at Washington University in St Louis. She is leading a project to catalogue all the mutations in one patient's cancer, an acute myeloid leukaemia. To interpret what these mutations mean, Mardis's group had to search numerous databases of variation — a job that will become more onerous, she says, as new projects contribute more data. She says that the field needs some kind of 'knowledgebase' to incorporate all that we already know and will soon learn about genomic variation and its links to biology and disease.

Reese is already trying to do that with Omicia, which is developing tools to analyse individual human-genome sequence data against scientific databases that link genetic variants to disease. The goal is to interpret how each of an individual's genetic variants influences his or her disease risk, then display that information in an accessible format that could, for instance, be used by a doctor interacting with a patient.

Reese was one of the few scientists at the Cold Spring Harbor meeting who spoke about how the public will use genomic data. Yet it is not too early to think so far ahead — and might indeed be too late. On 21 October, the participants in the Personal Genome Project — run by George Church, a geneticist at Harvard Medical School — posted their gene sequences on the Internet (see *Nature* doi:10.1038/news.2008.1182; 2008). They are also providing extensive medical and non-medical information about themselves so that anyone can interpret their data.

And already, anyone can buy a personal genomics test to analyse his or her own genetic variation. Indeed, the human desire for self-knowledge driving these ventures was embodied throughout the Cold Spring Harbor conference in the presence of Watson. Whether this desire is fulfilled or frustrated could now depend on the others who were in the room. ■

Erika Check Hayden

See Editorial, page 1007.

Eight-month delay for LHC

Details of last month's accident at the Large Hadron Collider (LHC), the world's premier particle accelerator, are emerging — and confirm that the machine will not restart before late May or early June 2009.

Officials at CERN, Europe's particle-physics laboratory near Geneva, Switzerland, say that the time is needed to overhaul a sector of the 27-kilometre-long machine, after an electrical failure on 19 September caused some 6 tonnes of ultra-cold liquid helium to leak into its tunnel. A preliminary report issued on 16 October says that as many as 29 of the nearly 10,000 magnets used to guide the accelerator's proton beam will need to be replaced. Further magnets may need to be removed and inspected, and modifications must also be made to prevent future accidents. "It's a serious incident," says James Gillies, a spokesman for the laboratory.

Still, CERN is confident it has the resources to make the repairs. No more than 24 dipole magnets and 5 quadrupole magnets were damaged; CERN has 30 dipole magnets — each weighing 35 tonnes — in reserve, as well as sufficient quadrupoles, says Gillies. Replacement magnets are already being tested in a facility above the buried accelerator tunnel. Nevertheless, Gillies says that the damage will take all of CERN's winter shutdown period to repair. Not including labour and the spares, the work will cost an estimated 100,000 Swiss francs (US\$90,000), he says.

The LHC's superconducting magnets generate enormous fields by circulating huge electrical currents with virtually no resistance. To work correctly, they must be immersed in liquid helium and kept at a temperature of just 1.9 kelvin. During the

19 September test, the accident report says, a weld in a superconducting wire connecting two magnets heated above its operating temperature. That in effect turned the wire into a resistor — causing a massive 8.7 kiloamps of power to arc through the liquid helium and puncture into the surrounding vacuum vessel.

In just milliseconds, the arc managed to vaporize a "significant fraction" of the nearly metre-long connection between the two magnets, says Jim Strait, an accelerator physicist at the Fermi National Accelerator Laboratory in Batavia, Illinois, who has been consulting on the accident

"The amount of helium released was larger than the valves were designed to handle."

investigation. The liquid helium flowed through the hole and into an insulating region of vacuum, which was meant to work as a thermos to keep the magnets cool. Relief valves

designed to allow the helium to escape were overwhelmed and, within seconds, the pressure in the machine became powerful enough to wrench magnets off their concrete supports.

Strait says that the relief valves' tolerances were based on "incorrect assumptions" about how much helium might escape in an accident. "The total amount of helium released was larger than the valves were designed to handle," he says. "You could call it a design error."

Gillies says that "clearly something was wrong" with the models of how much helium could be released, but he adds that it is difficult to foresee every possible scenario. "This thing is its own prototype," he says.

The electrical arc also penetrated the beam pipes, allowing soot from the accident to contaminate the pipes. "It's a mess in the affected spots," Strait says.

CERN is looking at adding extra relief valves and developing new diagnostics to catch such a failure before it occurs. A late May or early June start-up seems ambitious to Strait, but he has faith in the team at CERN. "It looks very difficult to me, but I would not count them out," he says.

Those awaiting the start of the machine remain stoic. "We are a bit disappointed," says Peter Jenni, a spokesman for the ATLAS detector, which employs more than 2,500 physicists. "But we all understand that in such an enterprise, things can go wrong." ■

Geoff Brumfiel



Broken magnets at CERN will need to be replaced.

M. BRICE/CERN



CRYING WOLF
Scientists clash over
wolves' endangered status
www.nature.com/news

PUNCHSTOCK

Pharma payment probe widens its net

US senator Charles Grassley (Republican, Iowa) is no Sigmund Freud, but since early this year he has succeeded in putting the psychiatric establishment on the couch. Grassley, the senior Republican on the Senate finance committee, has detailed how eight prominent academic researchers (see 'Show me the money') failed to obey rules and report to their universities payments from drug companies, some running into seven figures. Every one of those researchers is a psychiatrist.

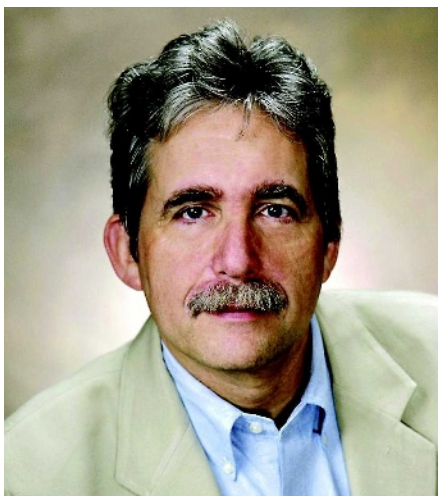
Grassley has denied singling out psychiatry, and is now demanding that Columbia University in New York produce financial-disclosure documentation for 22 cardiologists. But his revelations — along with his demand this summer that the American Psychiatric Association (APA), based in Arlington, Virginia, document its drug-company income — have created the impression, fair or otherwise, that academic psychiatry is permeated with often-undisclosed drug-company payments, biasing its findings, possibly harming patients and certainly eroding public trust.

As psychiatry has been reshaped by a wave of new medications during the past two decades, insurers have made it more lucrative for psychiatrists to prescribe drugs rather than conduct psychotherapy. Because those medications are often big money-makers for industry as well, "what you end up with is a very powerful and potentially corrupting relationship between pharmaceutical companies and psychiatrists," says Paul Root Wolpe, director of the Center for Ethics at Emory in Atlanta, Georgia.

Arguably, Grassley's biggest catch so far has been Charles Nemeroff, formerly chairman of psychiatry at Emory, who last week stepped aside as principal investigator or co-investigator on grants funded by the National Institutes of Health. According to documents released this month by Grassley, Nemeroff broke university and federal rules by failing to disclose at least \$1.2 million in drug-company income between 2000 and 2006 (see *Nature* 455, 835; 2008).

Nada Stotland, the president of the APA, suggests that Grassley's focus on psychiatry may reflect historical prejudice against the speciality. "There are conditions of similar magnitude, if not greater, in other specialties of medicine," she says. "It's a serious concern to me and the organization, the profession, why we are only hearing about psychiatrists."

Stotland, a professor of psychiatry at Rush Medical College in Chicago, who earns no money from companies, says that the APA receives 29% of its \$56-million annual budget



Charles Nemeroff failed to disclose more than US\$1 million in income from drug companies.

from drug companies, about half of which derives from advertising revenue for its three journals. The APA, she contends, is an exemplar of vigilant conflict policing — requiring, for example, that no one with a combined drug-company income of more than \$10,000 may sit on the committee that updates its standard-setting diagnostic manual.

A 2007 study by the *New York Times* looked at trends in payments to physicians in Minnesota, one of the few states requiring drug

companies to publicly post such payments. It found that, between 2000 and 2005, psychiatrists as a group collected more money from drug companies than doctors in any other speciality. It also found a striking relationship between drug-company payments and prescriptions made to children of a controversial but lucrative class of drugs called atypical antipsychotics. On average, psychiatrists who received at least \$5,000 from makers of these drugs wrote three times as many prescriptions for children as psychiatrists who received less or no money.

Experts say that a confluence of factors have made psychiatry vulnerable to drug-company influence. First, name-brand psychiatric drugs for a given disease may differ very little from each other, making the blessings of prominent specialists important in giving a particular drug the edge. Second, psychiatric drugs can be extremely lucrative. For instance, in 2007, Zyprexa (from Eli Lilly), Risperdal (from Johnson & Johnson) and Seroquel (from AstraZeneca), all leading atypical antipsychotics, earned \$4.8 billion, \$4.5 billion and \$4.0 billion, respectively.

But because specific psychiatric drugs don't work for every patient, and their performance in given cases is hard to predict, there's an element of judgment and even guesswork involved in prescribing them, says Charles Jennings, who directs the neurotechnology programme at the McGovern Institute for Brain Research at the Massachusetts Institute of Technology in Cambridge. "That may be one reason why drug companies invest so much in promoting these drugs," he says. "When the evidence is marginal, every little bit counts." (Jennings was editor of *Nature Neuroscience* in 2002 when the journal published a review by Nemeroff that brought him under fire for failing to disclose conflicts of interest (B. J. Carroll & R. T. Rubin *Nature Neurosci.* 6, 999–1000; 2003). Jennings was also involved in developing the *Nature* journals' disclosure policy for authors.)

Then there is the simple fact that psychiatrists earn considerably less than medics in many other specialist fields. In 2007, the median income for psychiatrists was \$199,000, according to the Medical Group Management Association. Anaesthesiologists, by contrast, made \$400,000, and dermatologists \$366,000. "I don't think that's irrelevant," says Wolpe. "I think low-paid specialties, especially in today's economic and medical climate, look for ways to increase their income."

Meredith Wadman

Show me the money

US Senator Charles Grassley's investigation has so far alleged that eight psychiatrists failed to declare payments from drug companies during the period 2000–07:

Joseph Biederman, Harvard University, Boston

Melissa DelBello, University of Cincinnati, Ohio

Charles Nemeroff, Emory University, Atlanta, Georgia

Augustus John Rush, University of Texas Southwestern Medical Center at Dallas

Alan Schatzberg, Stanford University, California

Thomas Spencer, Harvard University

Karen Wagner, University of Texas Medical Branch, Galveston

Timothy Wilens, Harvard University **M.W.**

Plumes of methane identified on Mars

ITHACA, NEW YORK

More than four years after researchers first said they had found methane gas on Mars, a scientist claims that he has “nailed” the controversial detection and identified key sources of the gas.

On Earth, methane is mostly biological in origin; on Mars, it could signal microbes living deep underground. The latest work suggests that martian methane is concentrated in both space and time — at a handful of hotspots hundreds of kilometres across, plumes of methane bloom and dissipate in less than a year.

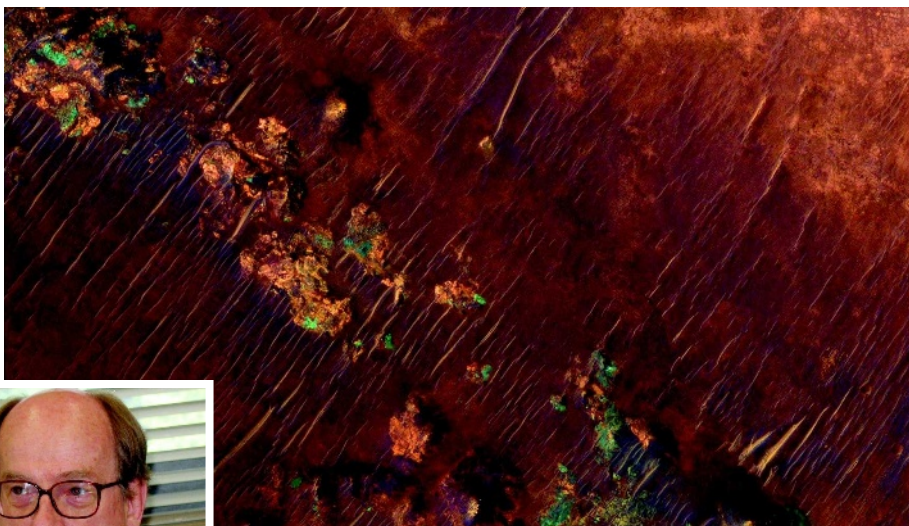
News of the detection is rippling through the Mars community just months before a destination is picked for the Mars Science Laboratory (MSL), the US\$2-billion rover that is due to launch in 2009. It will carry an instrument that could both detect trace amounts of methane and help discern whether it is of biological or geological origin. One of the proposed methane plumes blankets one of the seven possible landing sites: Nili Fossae, which was given a middling ranking by the science community after a September evaluation that did not consider the emerging methane results.

“Now we’ve got these little signposts saying: ‘Look, here I am. Come here!’” says Michael Mumma, a planetary scientist at NASA’s Goddard Space Flight Center in Greenbelt, Maryland. He presented his team’s work on 11 October at a meeting of the American Astronomical Society in Ithaca, New York.

Mumma has been arguing for methane on Mars since 2003, when other startling findings began to emerge. One group, using the Canada-France-Hawaii Telescope on Mauna Kea, Hawaii, found global trace methane levels of 10 parts per billion, but could see no more detail than that. A second group, using thousands of spectra taken by the European Space Agency’s Mars Express orbiter, found similar global levels, with hints of regional variability in concentration (V. Formisano *et al. Science* **306**, 1758–1761; 2004). But some of that paper’s impact was diluted when the lead investigator, Vittorio Formisano of the Institute of Physics and Interplanetary Space in Rome, made separate claims of ammonia and formaldehyde that have not been confirmed.

Mumma, a spectroscopy expert, obtained data from telescopes in Hawaii and Chile that supported the notion of methane hotspots.

Now he says he knows for sure and is ready



JPL-CALTECH/UNIV. ARIZONA/NASA

NASA



Nili Fossae is a hotspot for martian methane, says Michael Mumma (inset).

presence of methane by matching four lines in his infrared spectra of the planet’s atmosphere to the characteristic signature of methane — a more definite determination than previous analyses — and found more evidence that the methane is localized in discrete hotspots, which peak at levels of 60 parts per billion. “His numbers have changed a lot over time. But Mike has made a pretty compelling case,” says Steven Squyres, a planetary scientist at Cornell University in Ithaca, and principal investigator for the Mars rovers Spirit and Opportunity.

More important than the peak concentrations, Mumma says, are the short lifetimes of the plumes. Previously, methane was thought to be destroyed in the atmosphere by sunlight — a slow process that allows the gas to mix in the atmosphere and persist for about 300 years.

A global level of 10 parts per billion and a lifetime of hundreds of years means that a few hundred tonnes of methane are entering the

atmosphere each year: the work of a few thousand cows. But plumes of 60 parts per billion that live for less than a year imply a methane-production rate several orders of magnitude higher. “This is a big deal,” says Sushil Atreya of the University of Michigan in Ann Arbor, a co-author of the 2004 Mars Express paper.

Whether the methane plumes are biological or geological in origin is impossible to know

at the moment, says Atreya. For example, microbes could be living in deep groundwater below a permafrost zone, and their waste methane could percolate up and leak out. The methane could also come from chemical reactions in which buried volcanic rocks rich in the mineral olivine interact with water. A third possibility is that the methane is escaping from buried clathrates, deposits of methane ice formed long ago by one of the other two mechanisms.

But NASA’s next Mars rover will be able to analyse, at levels of parts per trillion, the fractional concentrations of the carbon isotopes in each methane molecule. Life on Earth prefers to process lighter carbon-12 atoms. And so, on Mars, methane freighted with carbon-12 could be a sign of a biological origin.

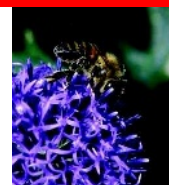
John Grotzinger, a geologist at the California Institute of Technology in Pasadena and project scientist for the MSL, says the methane detection could be important in deciding the MSL’s destination. “We’re going to take this very seriously,” he says. “We all need to sit back and evaluate the data and find out if Nili Fossae is the only place where this occurs.” The methane results could be considered at a meeting early next month, when the seven sites are evaluated from an engineering and safety standpoint.

A reshuffling of the sites’ rankings could be in order, Grotzinger adds, but he wants some hard data to consider. “Talks don’t count. The paper needs to be published,” he says.

A paper describing Mumma’s work is under review at *Science*.

Eric Hand

“Now we’ve got these little signposts saying: ‘Look, here I am. Come here!’”



BEE STING
Crop yields unaffected
by pollinator declines.
www.nature.com/news

PUNCHSTOCK

Iranian paper sparks sense of déjà vu

A review paper by Massoumeh Ebtekar, the former vice-president of Iran and an immunologist at Tarbiat Modares University in Tehran, is to be retracted from an Iranian journal following allegations that it was almost entirely stitched together from other scientists' papers.

The paper came to light after a *Nature* News article about the Deja Vu web database at the University of Texas Southwestern Medical Center at Dallas, which lists articles with potential plagiarisms (see *Nature* **455**, 715; 2008). Among the resulting spike in hits, Harold Garner's team, which runs the database, noticed many came from Farsi-language forums and blogs in Iran (see <http://alef.ir/content/view/32958>).

What triggered Iranians' interest was an entry about a paper on cytokines and air pollution, published in 2006 in the *Iranian Journal of Allergy, Asthma and Immunology* (M. Ebtekar Iran. *J. Allergy Asthma Immunol.*

5, 47–56; 2006). Deja Vu claims that about 85% of the text comes from five papers by other researchers, with the chunks ranging from 5% to 30% of their content.

The sole author of the paper was Ebtekar, who served as spokeswoman for the militant students holding 52 Americans hostage in the US Embassy in Tehran during 1979–81. She went on to become vice-president in 1997 under reformist president Mohammad Khatami, and was elected to Tehran City Council in 2007.

Ebtekar was unavailable for comment and did not respond to e-mail queries from *Nature*. But she admitted in a written response to Deja Vu, now posted on her own Farsi-language blog, that some paragraphs had been taken “without due reference to the authors which is a clear mistake”. She blamed this on a student whom she says helped her with the manuscript. “I have apologized for my

shortcomings and mistakes. I will take more care in writing my articles and preparing my manuscripts.” Publishing the entry on Deja Vu, she said, went “too far in condemning people and smearing their reputation before they have a chance to respond”.

Ian Mudway, a toxicologist at King's College London who authored an earlier paper cited

“The article is a veritable patchwork of other people's work, word for word.”

by Deja Vu in Ebtekar's work and extensively copied in her paper, isn't impressed. “The article is a veritable patchwork of other people's work, word for word, grammatical error for

grammatical error,” he says.

Mohammad Eslami, editor-in-chief of the *Iranian Journal of Allergy, Asthma and Immunology*, told *Nature* that the article will be retracted and that the journal will publish an editorial re-emphasizing its policy on the duplication of published material. ■

Declan Butler

Canada bans bisphenol A in baby products

The Canadian government announced on 17 October that it will prohibit the importation or sale of bisphenol A in bottles and food packaging for infants and newborns. The chemical is commonly used in polycarbonate plastic drinking bottles.

Animal studies have shown that

bisphenol A can disrupt hormone signalling, and last month a study linked the chemical to cardiovascular disease and diabetes in humans (I. A. Lang *et al.* *J. Am. Med. Assoc.* 300, 1303–1310; 2008).

Canada is the first country to take regulatory action, according to its health minister Tony Clement.

Adults “need not be concerned” about the chemical, according to a government press release. Nevertheless, the country plans to

spend Can\$1.7 million (US\$1.4 million) over the next three years for further studies of adverse health effects. The ban should come into effect in 2009.

US slashes acceptable limit for airborne lead

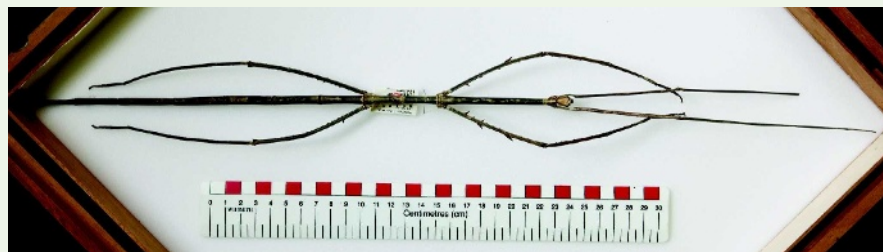
The US Environmental Protection Agency (EPA) has revised the airborne lead standard for the first time in 30 years, reducing the maximum permissible concentration by 90%.

The new standard of 0.15 micrograms per cubic metre is within the range recommended by a science advisory panel that evaluates air quality issues. By comparison the UK standard is 0.25 micrograms per cubic metre.

Environmentalists have generally praised the decision, although some say that the EPA missed a chance to curb emissions even more. A separate panel, focused on children's health, had recommended levels 7.5 times lower than the new standard; exposure to lead has been linked to negative effects on IQ and learning in children.

Lead emissions have dropped by 97% since 1980 in the United States, owing largely to the elimination of leaded petrol, according to the EPA.

A sticky situation hits the record books



This spindly creature is the new holder of the title ‘world’s longest insect’. The Chan’s megastick (*Phobaeticus chani*) was officially described in a paper last week and has a body that is 35.7 centimetres long. With limbs included, the Malaysian native stretches to 56.7 centimetres (F. H. Hennemann and O. V. Conle *Zootaxa* **1906**, 1–316; 2008).

Phobaeticus chani breaks the record for overall length by 1 centimetre and that for body length by 2.9 centimetres. Both previous record holders were discovered more than a century ago, according to George Beccaloni, an entomologist at the Natural History Museum in London. “It is extraordinary that an even bigger species has only just been discovered,” he says.

Initiative waives human life in favour of life on humans

Microbe experts from around the world are setting up a formal collaboration to study the organisms that live in and on humans.

The International Human Microbiome Consortium, announced on 16 October, involves geneticists and bacteriologists from more than a dozen countries. The researchers will look at the role of the microbiome — the microorganisms that dwell in and on the body and that vastly outnumber the body's own cells — in health and disease.

The consortium's two most prominent projects are a five-year initiative funded by the US National Institutes of Health (NIH) to genetically sequence microbes living in the mouth, skin, nose, vagina and faeces; and a four-year, European Commission scheme to analyse the gut flora of people living in Spain and Denmark to find microbial links to obesity and inflammatory bowel disease.

The NIH has pledged US\$115 million to the overall initiative and European collaborators have committed €20 million (US\$27 million). Other countries will provide smaller sums.



Hubble: currently comatose.

Computer failure leaves Hubble in limbo

Late last month, the main system for storing and transmitting data from the Hubble Telescope's science instruments failed. Operators can still send commands to the 18-year-old orbiting observatory, but they can no longer retrieve the images that have made it famous.

On 16 October, telescope engineers successfully booted up a backup for the faulty system. But as they were preparing to resume star-gazing, problems with the backup computer sent the entire spacecraft into safe-mode. NASA officials hope that Hubble will be healthy again by the end of this week, but are not certain when it will be

back in action. A shuttle mission to service the telescope has been delayed until at least February so that engineers can develop fixes for the computer problems.

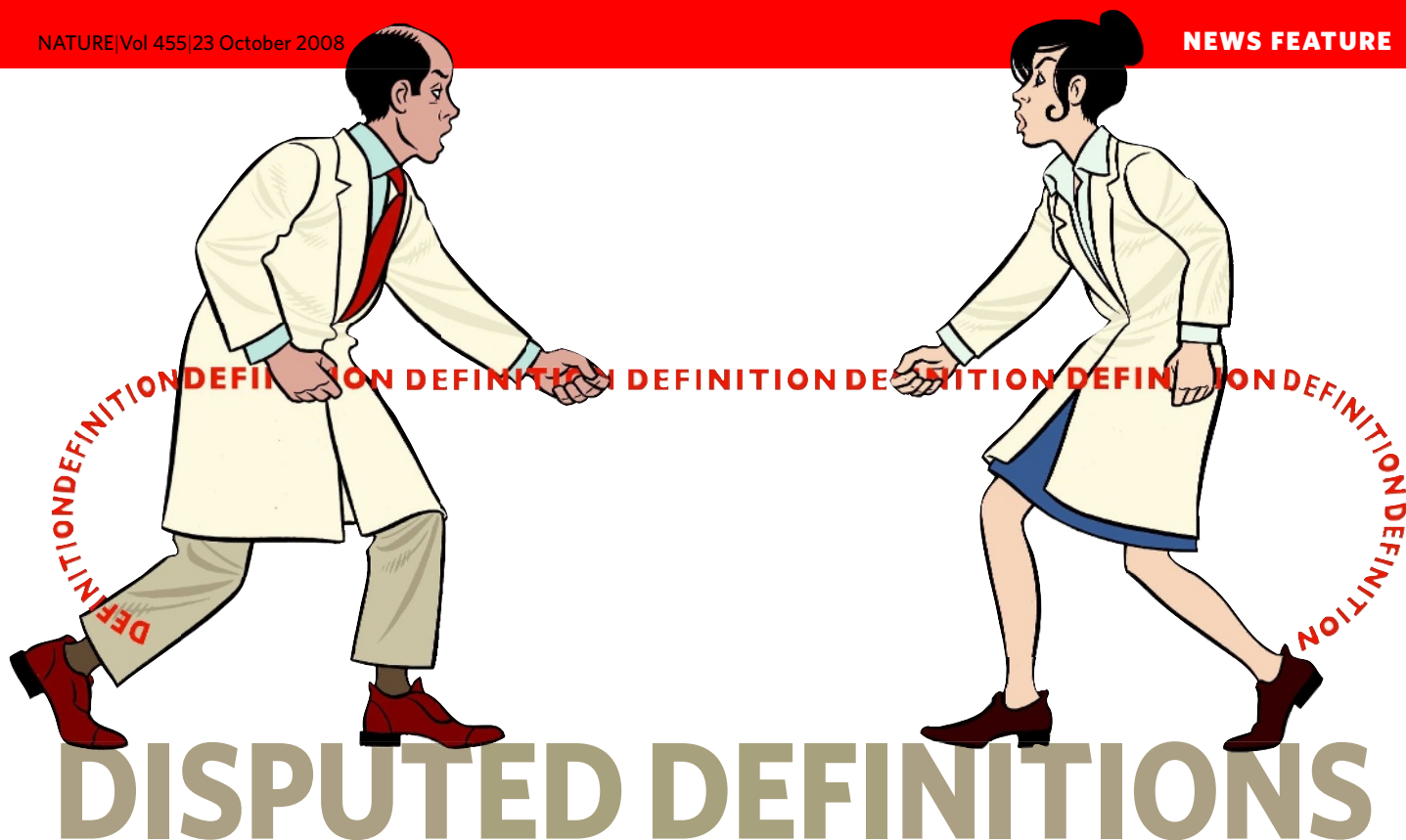
US agencies struggle over public relations

It is report-card season for US science agencies, and the grades are in on their media skills. The Union of Concerned Scientists, an advocacy group based in Cambridge, Massachusetts, has ranked the public-relations policies of 15 federal organizations.

It gave the highest marks to the Centers for Disease Control and Prevention in Atlanta, Georgia, whose written policy allows scientists to express their personal views. NASA also fared well, earning a "B" for its policy and a "satisfactory" for its practice. The Environmental Protection Agency (EPA) finished near the bottom of the class — its lack of an agency-wide policy earning it a "D".

The group says that the grades will help the next president to reduce the censorship of government scientists, but EPA spokesman Jonathan Schradar called the grades "nothing more than continued petty politics".

NASA



If you want to start an argument, ask the person who just said 'paradigm shift' what it really means. Or 'epigenetic'. *Nature* goes in search of the terms that get scientists most worked up.

To a great extent, science is about arriving at definitions. What is a man? What is a number? Questions such as these require substantial inquiry. But where science is supposed to be precise and measured, definitions can be frustratingly vague and variable.

Here, *Nature* looks at some of the most difficult definitions in science. Some are stipulative definitions, created by scientists for their convenience, but on which the community has not found consensus. Popular though they are, not everyone agrees on what is meant by 'paradigm shift' or 'tipping point'.

Essential definitions — those that get at the question of what makes a thing a thing — can be just as troublesome. What is race, or consciousness? And does it even matter if there is no agreed-on meaning?

The good news is that for every troublesome term there are thousands used every day with no problems. Scientists are competent, if unconscious wielders of definition, says Anil Gupta, a philosopher of science at the University of Pittsburgh in Pennsylvania, "just as one can walk quite happily without having a complete account of walking".

Paradigm shift

[ˈpærədɪm ʃɪft] *noun*.

Paradigm shift has a definite origin and originator: Thomas Kuhn, writing in his 1962 book *The Structure of Scientific Revolutions*, argued against the then prevalent view of science as an incremental endeavour marching ever truthwards. Instead, said Kuhn, most science is "normal science", which fills in the details of a generally accepted, shared conceptual framework. Troublesome anomalies build up, however, and eventually some new science

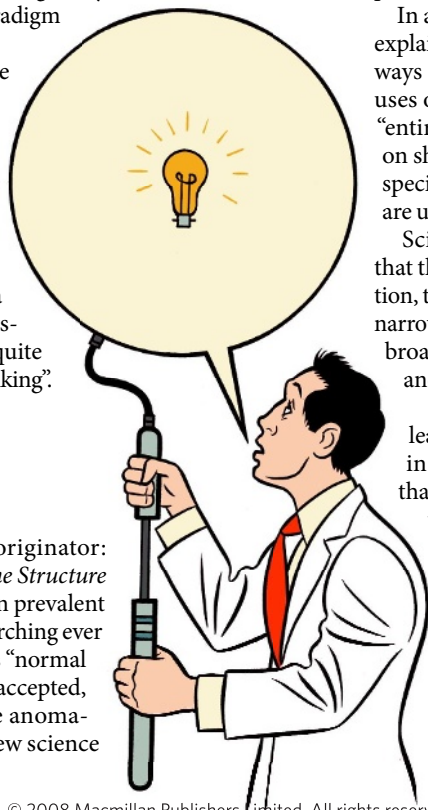
comes along and overturns the previous consensus. Voilà, a paradigm shift. The classic example, Kuhn said, is the Copernican revolution, in which Ptolemaic theory was swept away by putting the Sun at the centre of the Solar System. Post-shift, all previous observations had to be reinterpreted.

Kuhn's theory about how science works was arguably a paradigm shift of its own, by changing the way that academics think about science. And scientists have been using the phrase ever since.

In a postscript to the second edition of his book, Kuhn explained that he used the word 'paradigm' in at least two ways (noting that one "sympathetic reader" had found 22 uses of the term). In its broad form, it encompasses the "entire constellation of beliefs, values, techniques and so on shared by the members of a given community". More specifically it refers to "the concrete puzzle-solutions" that are used as models for normal science post-shift.

Scientists who use the term today don't usually mean that their field has undergone a Copernican-scale revolution, to the undying annoyance of many who hew to Kuhn's narrower definition. But their usage might qualify under his broader one. And so usage becomes a matter of opinion and, perhaps, vanity.

The use of the term in titles and abstracts of leading journals jumped from 30 papers in 1991 to 124 in 1998, yet very few of these papers garnered more than 10 citations apiece¹. Several scientists contacted for this article who had used paradigm shift said that, in retrospect, they were having second thoughts. In 2002, Stuart Calderwood, an oncologist at Harvard Medical School in Boston, Massachusetts, used it to describe the discovery that 'heat shock proteins', crucial to cell survival, could work outside the cell as well as in². "If you work in a field for a long time and everything changes, it does seem like a revolution," he says. But now he says he may have misused



ILLUSTRATIONS: N. DEWAR

the phrase because the discovery was adding to, rather than overturning, previous knowledge in the field.

Arvid Carlsson, of the University of Gothenburg in Sweden stands by his use of the phrase. "Until a certain time, the paradigm was that cells communicate almost entirely by electrical signals," says Carlsson. "In the 1960s and '70s, this changed. They do so predominantly by chemical signals. In my opinion, this is dramatic enough to deserve the term paradigm shift." Few would disagree: base assumptions were overturned in this case, and Carlsson's own work on the chemical neurotransmitter dopamine (which was instrumental in this particular shift) earned him the 2000 Nobel Prize in Physiology or Medicine.

Unless a Nobel prize is in the offing, it might be wise for scientists to adopt the caution of contemporary historians of science and think twice before using a phrase with a complex meaning and a whiff of self promotion. "Scientists all want to be the scientists that generate a new revolution," says Kuhn's biographer, Alexander Bird, a philosopher at the University of Bristol, UK. "But if Kuhn is right, most science is normal science and most people can't perform that role."

Emma Marris

Epigenetic

[ɛpɪdʒɪnɛtɪk] *adjective*.

No one denies that epigenetics is fashionable: its usage in PubMed papers increased by more than tenfold between 1997 and 2007. And few deny that epigenetics is important. What they do disagree on is what it is.

"The idea is that there is a clear meaning and that it's being violated by people like me who use it more loosely," says Adrian Bird at the University of Edinburgh, UK. Last year he suggested this as a definition: "the structural adaptation of chromosomal regions so as to register, signal or perpetuate altered activity states"³. But this wide-ranging proposal, which takes on-board pretty much every physical indicator of a gene's activity is "preposterously dumb," says Mark

'So big we don't know where to start' definitions

- Science
- Life
- Natural
- Intelligence
- Ethical
- Sustainability



NOAA GOES-7/NASA

Ptashne of Memorial Sloan-Kettering Cancer Center in New York, who has published his own take on the word's usage⁴. "I've grown to be very careful about using the term," says Bing Ren, who studies gene regulation at the University of California, San Diego.

According to the 'traditional' definition that Ptashne favours, epigenetics describes "a change in the state of expression of a gene that does not involve a mutation, but that is nevertheless inherited in the absence of the signal or event that initiated the change". The classic example is found in a bacteriophage called Lambda, which stays dormant in the genome of generations of cells through inheritance of a regulatory protein. These sort of processes are basic to some of the most pressing questions in biology today: such mechanisms are needed to explain how a single-celled embryo can generate cells that are genetically identical, but express a different array of genes and hence take on different jobs in blood, brain or muscle for generation after generation.

Over the past few years, however, all kinds of processes associated with gene control have been subsumed under the moniker. For example, 'epigenetic' is often used to refer to the chemical modification of histones — proteins that DNA winds around — which is involved in gene regulation. This infuriates those who learned the classical definition; they say it puts these modifications at the heart of development and disease despite scant evidence that they are inherited. "Why did histone marks become epigenetic?" says Kevin Struhl at Harvard Medical School in Boston. "People decided that if they call them that it makes them interesting." Others say that it is not about making things sound important, it is more the lack of any other phrase with which to collectively refer to this type of work.

The word had dual meanings long before the current debate. In the 1940s, Conrad Waddington used it to describe how the genetic information in a 'genotype' manifests itself as a set of characteristics, or 'phenotype'. In 1958, David Nanney at the University of Michigan, Ann Arbor, borrowed the term to describe "messy" inherited phenomena that could not be explained by conventional genetics⁵. "It was controversial in 1958 and everything died down and it has come alive again," says Nanney. "It took 40 years for epigenetics to become a major word in the vocabulary of modern biology."

A lot of money can ride on whether a researcher is, or is not, studying epigenetics: the US National Institutes of Health (NIH) this month started handing out US\$190 million as part of its epigenomics initiative and other countries are pouring funding into the area. (The NIH is careful to define the epigenetics it is paying for as including both heritable and non-heritable changes in gene activity, something that Ptashne describes as "a complete joke".) Bird says he remains in favour of a relaxed usage. "Epigenetics is a useful word if you don't know what's going on — if you do, you use something else," he says.

Helen Pearson

"Epigenetics is a useful word if you don't know what's going on — if you do, you use something else."

— Adrian Bird



Complexity

[kəm'pleksiti] noun.

In his book *Programming the Universe*, engineer Seth Lloyd of the Massachusetts Institute of Technology in Cambridge describes how he once compiled 42 definitions of complexity — none of which encompasses everything people mean by that word. Researchers in the many institutes and programmes formed to study 'complexity' are still searching for the right way to describe their discipline. "If we're a university centre, we should be able to say what we care about," says Carl Simon, director of the Center for the Study of Complex Systems at the University of Michigan.

The quest for a rigorous definition reached a particularly intense pitch in the early 1990s, when some of the more visionary researchers at the Santa Fe Institute in New Mexico held out the hope of a universal theory of complexity — a mathematically precise set of equations that would hold for all complex systems in much the same way that the second law of thermodynamics holds for all physical systems.

James Crutchfield, head of the Complexity Sciences Center at the University of California, Davis, says that this created a problem. "New people would come into the field and start using the word 'complexity' as if it was a unitary thing" — which, as became increasingly clear, it was not. No all-encompassing theory emerged. Even within the precise world of binary code and bit strings, there was computational complexity, which describes how much memory and processing is required to carry out a calculation; algorithmic complexity, which is related to how much a digital description of something can be compressed; and any number of combinations and variations. "So my bottom line is, add an adjective to 'complexity,'" Crutchfield says.

Researchers have found plenty of undeniably complex systems to study, such as economies, ecosystems, urban traffic and brains (see 'Consciousness'). And in a qualitative sense, at least, these systems do have certain features in common that might serve as a definition. They are, for instance, all composed of many independent 'agents' (consumers,



species, vehicles, neurons) that are constantly interacting with, and adapting to, one another. They all display a rich array of nonlinear feedback loops among the agents, which means that small changes can have a big effect. And they never quite settle down into static equilibrium.

The effort to understand complex systems has led researchers to develop new analytical tools such as network theory, agent-based modelling and genetic algorithms. These tools, combined with the exponential growth in computational power, have allowed researchers to build ever more complex models of complex systems — and study the subtle but powerful phenomenon of 'emergence,' in which multiple agents exhibit collective behaviour that is a great deal more than the sum of its parts.

So even though the field seems little closer to defining its subject, says Lloyd, "in places where people can apply these conceptual and computational tools, we've made huge progress in understanding complex systems". But in a world where we are constructing ever more complex artefacts — technologies, economies, organizations and societies — even better tools are needed to keep pace.

M. Mitchell Waldrop

Race

[reis] noun.

If biologists had a list of four-letter words to avoid, then 'race' would be higher up than anything more conventionally vulgar. It is controversial, it lacks a clear definition and the more that genetics reveals about race, the more biologically meaningless the term seems.

Race was long used to imply a shared, distinct ancestry, as in a 1936 definition of the term in *Nature*: "It has two main connotations, one being community of descent, the other distinctness from other races." But in 1972, Harvard geneticist Richard Lewontin showed that the concept of race starts to dissolve under genetic scrutiny. He found that the vast majority of human genetic variation, which he measured in 16 genes, is found within, not between, what he called the 'classical racial groupings'⁶. Since then, studies examining hundreds or even thousands of genetic markers have confirmed Lewontin's findings^{7,8}.

A consensus now exists across the social and biological sciences: regardless of appearance or heritage, groups of human beings are overwhelmingly more genetically similar to each other than different. This doesn't mean race does not exist or is meaningless in society — far from it. But it does mean that an individual's race is not a particularly useful or predictive indicator of biological traits or medical vulnerabilities. Race is "the social interpretation of how we look, in a race-conscious society", says Camara Phyllis Jones, the research director on the Social Determinants of Health and Equity programme at the US Centers for Disease



'There is a difference, honest' definitions

Molecular electronics versus	Molecule-based electronics
Thermohaline circulation versus	Meridional overturning circulation
Commensalism versus	Mutualism



G. HOLLAND/PHOTOLIBRARY.COM

Control and Prevention in Atlanta, Georgia. Lewontin says that assigned races are essentially arbitrary. "It means essentially a group of related people, and where you draw the line depends on where you are in history."

Some argue that severing biology from the definition of race risks jettisoning medically meaningful information. Patterns of genetic variation can be used to classify people from different geographical regions into clusters that sometimes mimic the classical racial groupings, and geneticists say that members of these groups seem to have distinctive disease prevalences and drug metabolism. So race could serve as a cheap, albeit imperfect, surrogate for defining groups for clinical trials or medical interventions.

But genetics is turning up ever more examples of how race obscures relevant information. A study published in April showed that a mutation found in 40% of African Americans acts like an endogenous beta blocker to protect patients with heart failure from death⁹. It also suggested why previous research had found conflicting evidence about the response of African Americans to beta blockers: those studies had lumped all African Americans into one group, obscuring the effects of mutations that confer protection or vulnerability.

A person's perception of his or her race can still serve to capture life experiences relevant to behavioural and clinical research, such as the stress of lifelong discrimination that may contribute to health disparities. But in other contexts researchers are abandoning the term in favour of other ways to group humans, by 'population,' genetic ancestry' or 'geographic ancestry'.

Erika Check Hayden

Tipping point

[ˈtɪpɪŋ poɪnt] *noun*.

In July 2006, scientists running the RealClimate blog ironically headlined one of their posts 'Runaway tipping points of no return'. The post laments that usage of the phrase 'tipping point' in climate-change and ecosystem discussions had reached, well — a tipping point.

It's not the frequency of the word that bothers researchers. It's the lack of one clear definition and the confusing way in which the concept is being used, among scientists and in the public discourse, often to imply that global warming-induced changes will propel Earth into irreversible and catastrophic climate change. "There is no convincing theoretical argument or model that at some point the planet as a whole will snap into a second state of system," says Timothy Lenton, an Earth scientist at the University of East Anglia, UK.

The term was originally coined in 1958 by sociologist Morton Grodzins in the context of studies on the racial makeup of US neighbourhoods. He found that when the migration of African-Americans into traditionally white neighbourhoods had reached a certain level, whites began to move out. In the 1970s, epidemiologists adopted tipping point to describe the threshold at which, mathematically,

Makeovers

Before

Nuclear magnetic resonance Magnetic resonance imaging
Clinical research Translational medicine
Cloning Somatic cell nuclear transfer
Genetic engineering Synthetic biology
Lots of [genes; transcriptions; citations; etc] [gen-; transcripto-; biblio-; etc]-omics

After



BLUESTONE/SPL

an infectious disease's 'reproductive rate' goes above one. This means that each infected person infects more than one other and the disease starts growing into an epidemic.

The phrase reached its own tipping point in 2000 when Malcolm Gladwell, a staff writer at *The New Yorker*, published his successful book *The Tipping Point: How Little Things Can Make a Big Difference*. It also acquired a worrisome — some say alarmist — flavour courtesy of its frequent usage in the context of climate change.

Regarding climate, the term is commonly defined as the critical threshold at which a slow gradual change qualitatively alters the state of an entire system. This is different to a 'point of no return' which is, by definition, irreversible. Only if internal forcing will cause a runaway effect is a tipping point also a point of no return.

The idea that positive feedbacks — such as the melting of polar ice reducing surface reflectivity, thereby causing yet more solar absorption, warming and melting — could amplify climate change to a point of fundamentally altering the global system has been around for decades. The debate now is about where those tipping points lie, and what will happen when they are crossed.

In a paper published in February, a team led by Lenton looked at 15 potential tipping 'elements' (things that could reach tipping points) in Earth's climate system¹⁰. Arctic sea-ice and the Greenland ice sheet were those most at risk from 'tipping' within the twenty-first century, the authors concluded.

But researchers accept that most known tipping points seem to be reversible on human timescales. Melting of the complete Arctic summer ice sheet, for example, could probably be reversed within a few years or so in a cooler world. Melting of the extremely thick Greenland and Antarctic ice sheets are a possible exception because, once melted, new ice would have to form at lower, warmer altitudes with less snowfall.

Claims that global warming could reach an irreversible tipping point by 2016, as made last year by James Hansen, director of NASA's Goddard Institute for Space Studies in New York, refer to the trajectory of greenhouse-gas emissions, not to changes in the climate system. Even if greenhouse-gas concentrations reach a point at which they cannot be restored to pre-industrial levels, it will not inevitably push the world's climate over a catastrophic tipping point.

Quirin Schiermeier





Stem cell

[stem sel] *noun*.

Ask a group of stem-cell biologists to define stem cell, and they'll say roughly the same thing: a cell that can, long term, divide to make more copies of itself as well as cells with more specialized identities. Ask the same scientists to list the most disputed terms in the field, however, and 'stem cell' will be top of that list.

The problem here is an operational one: reasonable people disagree on which cells qualify under the definition. "It's not unusual to pick up a paper and see someone call something a stem cell and the evidence that it is, is just not there," says Lawrence Goldstein, who directs the stem-cell research programme at the University of California, San Diego.

Alleged 'stem cells' can fail to meet the definition on many counts. Stem cells should persist long term, yet many 'stem cells' exist only in the fetus. Multipotency — the ability to generate multiple cell types — is a criterion for a haematopoietic, or blood-forming, stem cell, but spermatogonial stem cells only produce sperm. Stem cells specific to tissue such as cartilage, the kidney and the cornea have been reported, with varying degrees of acceptance. The quest for a 'stemness signature', a collection of markers common to all stem cells, has been met with frustration.

Debate erupts most commonly over whether a particular cell should be considered a stem cell, which can divide indefinitely, or a progenitor cell, which can differentiate into fewer cell types and is thought to burn itself out after a certain number of divisions.

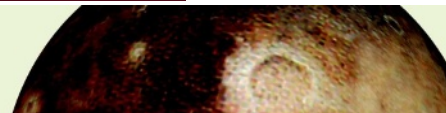
The only way to be really sure of what a cell can, and cannot do, is to observe it, but it is difficult to study cells *in vivo*, and putting them in a dish might change their behaviour. Haematopoietic stem cells were the first to be identified and have, to some extent, set default standards. Putative stem cells are isolated, then placed into animals whose own haematopoietic stem cells have been destroyed by radiation. If the blood-forming system is restored, the transplant is assumed to have contained stem cells. But such an assay is impossible when working with other cell types, such as neural stem cells, which are harder to transplant and assess in disease models. And it is difficult to pin the label to one cell type, when studies commonly involve a mixed population. "It is perhaps not realistic to come up with a generally applicable definition of an adult stem cell," says Thomas

"Some of this just breaks down. That's biology. It wasn't designed to fit the language."

— Lawrence Goldstein

Don't get us started

- Planet
- Species
- Fitness
- Nature



F. SAURER/SPL

Graf of the Centre for Genomic Regulation in Barcelona.

Some researchers are side-stepping the debate by referring in their papers to 'stem/progenitor cells'. Fully understanding what each cell can do is more important than knowing what to call them all, says Goldstein. "Some of this just breaks down," he says. "That's biology. It wasn't designed to fit the language."

Monya Baker

Significant

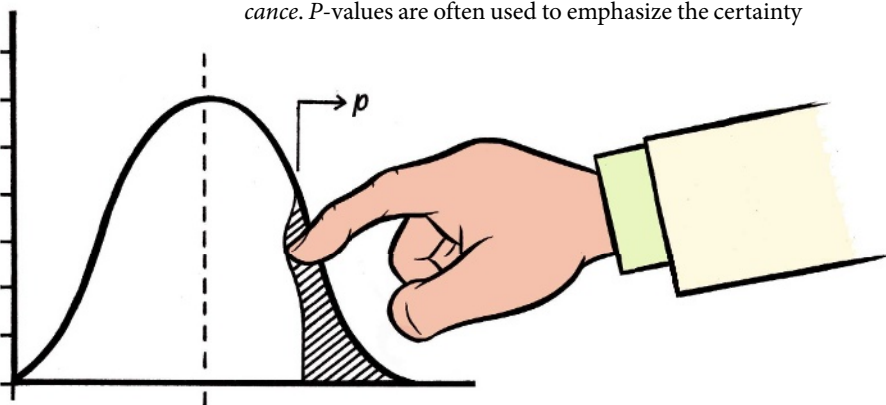
[sɪɡ'nɪfɪk(ə)nt] *adjective*.

Few words in the scientific lexicon are as confusing, or as loaded, as 'significant'. Statisticians wring their hands over its cavalier use to describe scientific validity. And backed by statistics or not, researchers commonly employ the word to illustrate the importance of their latest finding.

The very definition of statistical significance is misunderstood by most scientists, says Steven Goodman, a biostatistician at the Johns Hopkins School of Medicine in Baltimore, Maryland, and associate editor on *Annals of Internal Medicine*. Typically, researchers take a result to be statistically significant based on 'p-values'. This parameter is used, for example, to reveal whether a drug lowers cholesterol based on promising data collected in a clinical trial.

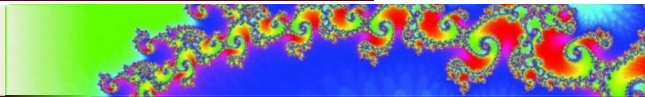
According to the common interpretation, a 'significant' result with a p-value of 0.05 or less means that there is a 5% or less chance that the drug is ineffective. According to the statistically accurate definition, there is a 5% or less chance of seeing the observed data even though the drug is, indeed, ineffective. Rhetorically, the difference may seem imperceptible; mathematically, say statisticians, it is crucial. In situations in which the data is somewhat ambiguous, there is a chance that results can be misinterpreted. "It's diabolically tricky," Goodman says.

Most statisticians resign themselves to abuse of the term's strict definition. But more grievous trespasses abound. "Statistical significance is neither a necessary nor a sufficient condition for proving a scientific result," says Stephen Ziliak, an economist at Roosevelt University in Chicago, Illinois, and co-author of *The Cult of Statistical Significance*. P-values are often used to emphasize the certainty



Yes, they do have scientific meanings:
no, we don't expect anyone to listen

- Quantum leap
- Organic
- Chaos



of data, but they are only a passive read-out of a statistical test and do not take into account how well an experiment was designed. A *p*-value would not reveal, for example, that everyone was taking different doses of that cholesterol drug. In many experiments, Ziliak says, “there are so many different errors that they tend to swamp the *p*-value errors”.

Even if a result is a genuinely statistically significant one, it can be virtually meaningless in the real world. A new cancer treatment may ‘significantly’ extend life by a month, but many terminally ill patients would not consider that outcome significant. A scientific finding may be ‘significant’ without having any major impact on a field; conversely, the significance of a discovery might not become apparent until years after it is made. “One has to reserve for history the judgement of whether something is significant with a capital S,” says Steven Block, a biophysicist at Stanford University in California.

In some situations other statistical methods can substitute, but Goodman believes that trying to use them in the scientific literature would be like “talking Swahili in Louisiana”. He says he and other editors do their best to keep the term out of *Annals* though. “We ask them to use words like ‘statistically detectable’ or ‘statistically discernable,’” he says.

Geoff Brumfiel

“You don’t waste your time defining the thing. You just go out there and study it.”

— Michael Gazzaniga

Consciousness

[ˈkɒnʃəsnɪs] noun.

Psychologists, philosophers, neurobiologists and doctors all grapple with the term consciousness. For clinicians, the definition is of life or death importance; for some others, it is a matter of determining how the brain’s interconnecting tissues collectively create a sense of self. “How can this three-pound piece of meat inside my head give rise to something like being me?” sums up Gerald Edelman, director of the Neurosciences Institute in La Jolla, California.

In 2006, neuroscientist Adrian Owen, at the Medical Research Council Cognition and Brain Sciences Unit in Cambridge, UK, reported that a woman who had been diagnosed as being in a vegetative state had shown signs of brain activity associated with consciousness¹¹. The activity was picked up with functional magnetic resonance imaging (fMRI), which can reveal changes in brain blood flow.

The finding rattled the clinical definition of consciousness, which is determined by using a series of behavioural tests to see if the patient can make voluntary movements in response to commands. The outcome can determine whether a patient needs pain medication, or whether it is time to

switch off life support, but clinicians readily acknowledge that the tests break down when patients are unable to move. Doctors now find themselves in an uncomfortable limbo, because it is not clear whether cortical activity measured on fMRI is enough to redefine those decision points. “What do we do as a community as long as this method is not yet validated?” asks Steven Laureys, a neurologist with the Coma Science Group at the University of Liège in Belgium.

The French philosopher René Descartes declared that consciousness was a fundamental property that fell beyond the rules of the physical world. Most scientists, says Edelman, are not satisfied with that answer. “There must be some physical basis for consciousness,” he says. “The difficulty is, how does that arise?”

Philosophers David Chalmers of the Australian National University in Canberra, explored what he called the “hard problem” of consciousness by pondering ‘qualia’, the subjective properties of experiences. Scientists and philosophers alike have struggled to explain how the physical properties of the world around us — such as colour and temperature — give rise to the experiences of ‘red’, or ‘warm’. Chalmers has argued that the functional organization of the brain rather than its chemical or molecular properties makes these experiences possible.

Many definitions of consciousness include the ability to sort through the relentless onslaught of incoming data to create and respond to an internal model of the external world. And some believe that simply gathering data about neurons and behaviours will not be enough. “What we need is a ‘theory of consciousness.’ Then we’ll be in a better position to define it,” says professor of biology and engineering Christof Koch of the California Institute of Technology in Pasadena. Koch thinks that information theory could provide the solution by determining whether consciousness might be an inherent by-product of a system as enormously complex as the brain (see ‘Complexity’).

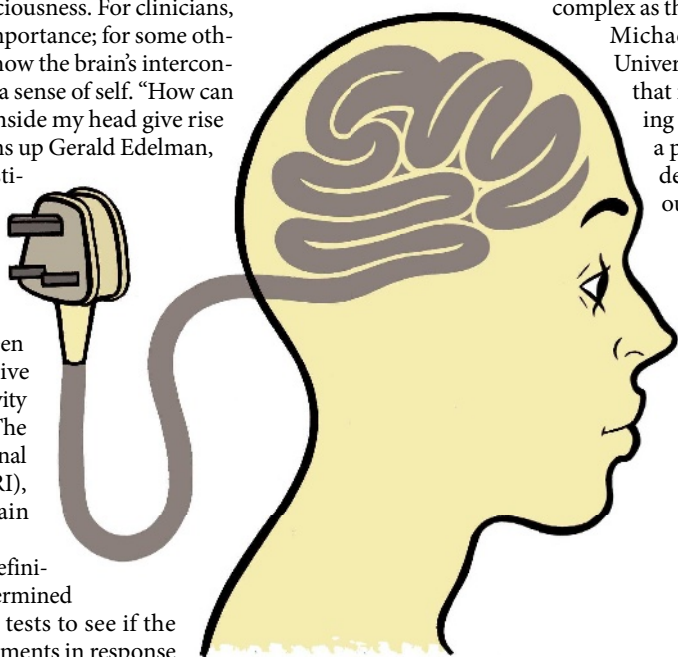
Michael Gazzaniga, a neuroscientist at the University of California, Santa Barbara, argues that researchers need only develop a working definition to explore consciousness, not a precise one. “You don’t waste your time defining the thing,” he says. “You just go out there and study it.”

Heidi Ledford

1. Cohen, J. *Science* **283**, 1998–1999 (1999).
2. Asea, A. et al. *J. Biol. Chem.* **277**, 15028–15034 (2002).
3. Bird, A. *Nature* **447**, 396–398 (2007).
4. Ptashne, M. *Curr. Biol.* **17**, R233–R236 (2007).
5. Nanney, D. L. *Proc. Natl Acad. Sci. USA* **44**, 712–717 (1958).
6. Lewontin, R. C. *Evol. Biol.* **6**, 381–398 (1972).
7. Li, J. Z. et al. *Science* **319**, 1100–1104 (2008).
8. Jakobsson, M. et al. *Nature* **451**, 998–1003 (2008).
9. Liggett, S. B. et al. *Nature Med.* **14**, 510–517 (2008).
10. Lenton, T. M. et al. *Proc. Natl Acad. Sci. USA* **105**, 1786–1793 (2008).
11. Owen, A. M. et al. *Science* **313**, 1402 (2006).

See Essay, page 1040.

Discuss definitions online at <http://tinyurl.com/4afapl>.



CORRESPONDENCE

Does risk to humans justify high cost of fighting bovine TB?

SIR — The UK government's strategy for controlling bovine tuberculosis (TB) is to work with stakeholders to reduce the economic impact of the disease and to maintain public-health protection, as well as animal health and welfare. In a nationwide programme, the Department for Environment, Food and Rural Affairs is investing between £74 million and £99 million a year on continuing cattle surveillance and control, slaughterhouse inspections, heat treatment of milk, occupational-health controls and monitoring for human cases (see <http://tinyurl.com/578s5x>).

The number of infected cattle herds increased from 88 in 1986 to 5,539 in 2005 (P. D. O. Davies *J. R. Soc. Med.* **99**, 539–540; 2006). However, this increase has not been mirrored by an increase in zoonotic TB in humans. Between 1993 and 2003, there were 315 cases of bovine TB confirmed in humans: a mean number of 28 cases per year. All 50 isolates of *Mycobacterium bovis*, the microorganism responsible, that were recovered from humans between 1997 and 2000 have been investigated (A. L. Gibson *et al. J. Clin. Microbiol.* **42**, 431–434; 2004), and of these, 15 had not been previously recorded in the UK cattle population.

Of the human cases of bovine TB, 72% of those infected were more than 50 years old (suggesting reactivation of an infection acquired before routine milk pasteurization was introduced), and many of the remaining cases were people born abroad. That leaves only a very small number of potential cases of transmission from present-day UK cattle, of which just two have been confirmed (R. M. M. Smith *et al. Emerg. Infect. Dis.* **10**, 539–541; 2004).

Since the introduction of milk pasteurization, TB in humans

caused by *M. bovis* has virtually disappeared in the United Kingdom. Consequently, the disease poses a negligible threat to public health.

Why then should a major intervention programme, proposed badger culling and vaccine research now be necessary to control it? The overwhelming societal cost of bovine TB is directly attributable to the costs of running the eradication programme and the associated research into control.

In the absence of significant transmission to humans, this question urgently needs to be addressed. Controlling bovine TB should be justified only in economic terms of reducing losses in animal productivity.
Paul Torgerson *Ross University, PO Box 334, St Kitts, West Indies and Institute for Parasitology, University of Zurich, Switzerland*
e-mail: ptorgerson@rossvet.edu.kn
David Torgerson *Department of Health Sciences, University of York, York YO10 5DD, UK*

Childcare not enough to make a science career family-friendly

SIR — Amanda Goh writes soberly in Naturejobs of her expectation that, as a postdoc, having a baby will almost certainly undermine her career prospects ('The coming challenge' *Nature* **455**, 704; 2008). She also acknowledges that being a mother while continuing to pursue a scientific career "may come at the cost of one's marriage".

Goh hits the nail on the head. In our experience, the predominant reason why women drop out of scientific careers is that it is virtually impossible to combine climbing the postdoctoral ladder with having children. Provision of better childcare facilities is helpful. But it is by no means sufficient, as most women who want children also want to play some part in bringing them up.

The career structure for young

scientists must be made more family-friendly. This means, for example, making part-time work a real possibility, emphasizing quality rather than quantity of output, and taking career breaks properly into account when judging candidates for appointments and promotions.

These changes would benefit male as well as female postdocs. Many young male scientists would like to have stable relationships and families, see their partners from time to time and help bring up their children.

If these quality-of-life issues are not addressed, then initiatives aimed at bringing more women into science are to a large extent pointless, and brave words about equal opportunities are mere window dressing. Indeed, it could be regarded as unethical to encourage young women to embark on a career that they are unlikely to wish to continue beyond the age of 30.

Timothy J. Roper, Larissa Conradt *Department of Biology and Environmental Sciences, John Maynard Smith Building, University of Sussex, Brighton BN1 9QG, UK*
e-mail: t.j.roper@sussex.ac.uk

Flags of convenience shield polluters in battle to protect seas

SIR — One of the most toxic substances ever deliberately put into the sea, the marine-paint additive tributyltin (TBT), has potentially entered its final chapter. An International Maritime Organization (IMO) convention aimed at phasing out its use on vessels came into effect in September, a year after the minimum requirements for ratification were reached. However, will this International Convention on the Control of Harmful Antifouling Systems on Ships see an end to the most efficient antifoulant ever produced?

Since the 1960s, TBT has been used as a biocide in antifouling

paints on the hulls of vessels. But the discovery of toxic effects in non-target species, especially molluscs, led to the global restriction of this chemical, in the late 1980s, to vessels that were more than 25 metres in length. These restrictions seemed to be successful, with molluscan populations returning to the levels they were before TBT usage began, in all but heavily polluted areas.

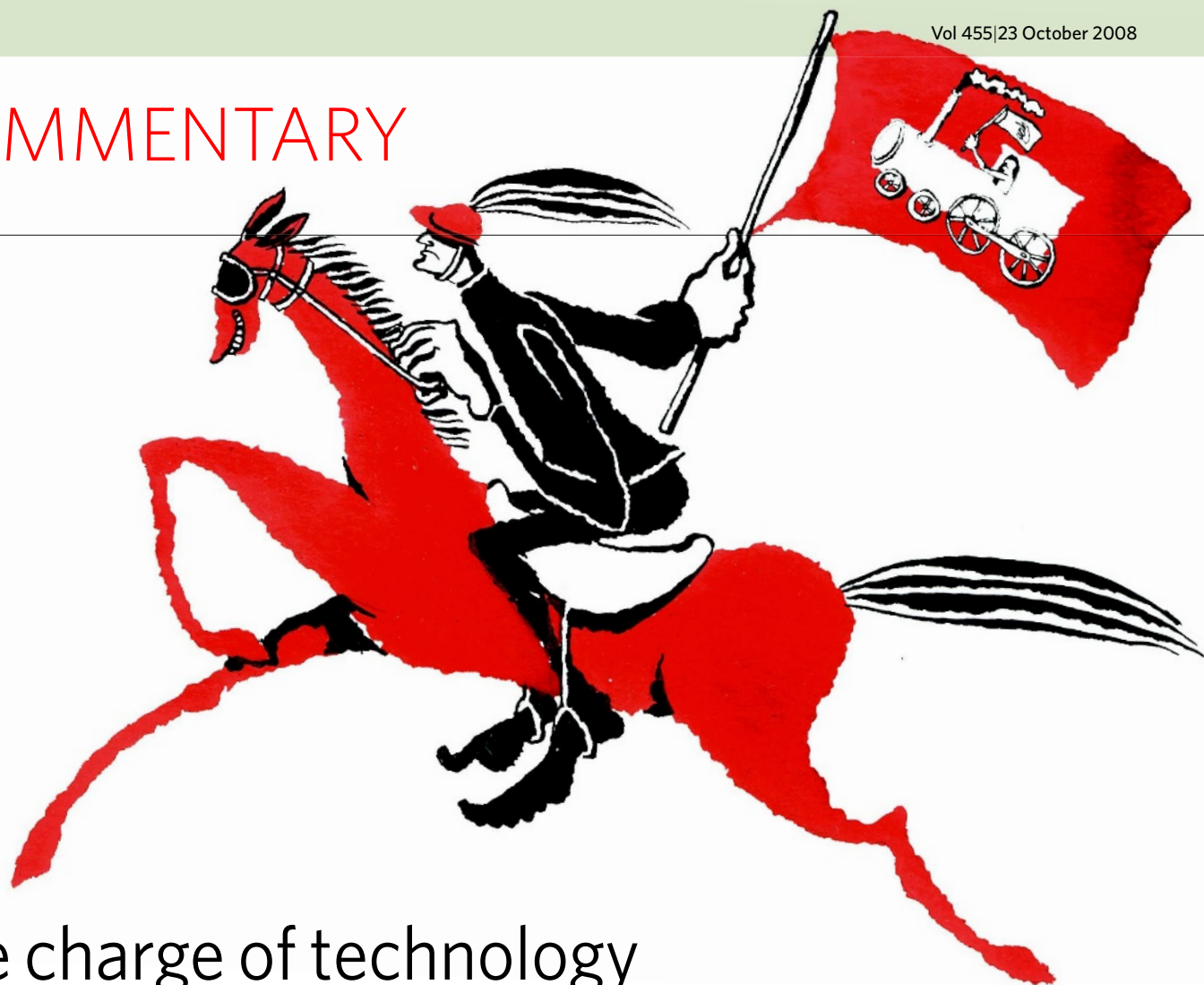
However, the IMO sought a complete ban on TBT. For this to be ratified, 25% of member states — representing 25% of the world's shipping tonnage — needed to be signatories. These double requirements were met when Panama signed in September last year, ending a quest that had lasted more than a decade.

Why was acceptance so slow and the signatory states so reluctant? For a start, there are no suitable alternatives to TBT. Copper, the next best realistic alternative, does not have the widespread biocidal properties of TBT and requires more frequent application, meaning more time spent by the vessel out of the water and greater expense.

Another reason is that most of the world's shipping sails under 'flags of convenience'. This Law of the Sea loophole means that shipping companies can register their vessels in countries where costs are lower and shipping laws, including restrictions on TBT, are only loosely policed. Motivation to sign the antifouling convention is limited in the case of countries providing these 'flags'. Now that the convention has finally come into effect, it may still prove difficult to get the signatory states to implement and enforce domestic legislation.

Regrettably, TBT's effects may continue to be felt for some time to come.
Scott P. Wilson *Centre for Environmental Management, CQUniversity Australia, PO Box 1319, Gladstone, Queensland 4680, Australia*
e-mail: s.wilson@cqu.edu.au

COMMENTARY



The charge of technology

Science policies based on techno-nationalist thinking and fantasies about the past technological revolutions will get us nowhere fast, says **David Edgerton**.

The steam engine changed the world. So too did electricity and the internal combustion engine, atomic power, and the Internet. Such stories are told with a hopeful eye to the future. They tell us that the next great revolution will be caused by technologies X, Y or Z, and that as nations we need to promote them. Such histories are given as evidence to support rational policies for national innovation today, bolstered by the assumption that national policies matter and that there is a clear link between national innovation and national success. We need, however, a much more critical understanding of this evidence base for science, technology and innovation policy.

That presents a formidable challenge. For all their seeming robustness, terms such as 'science', 'technology' and 'innovation' change meaning without warning. They come loaded with assumptions about their relation to society and the economy that don't hold under scrutiny. Moreover, the histories on which we base policies are clouded by propagandistic, romanticized accounts of single or a few (often

ill-chosen) technologies changing everything. The past, the present and the future of actual science and technology bears little relationship to what we are told it has been, is and will be.

Inadequate understanding of science policy and technology among scientific and political elites is a serious problem, and a much richer and better account is needed if we are to have evidence-based policy to meet the challenges of the future.

The world economy has both grown and changed radically, but assessing the contribution of science or innovation is difficult. It used to be suggested that the growth unexplained by increases in capital and labour (now dignified as 'total factor productivity' or 'multifactor productivity') was a measure of technical change, but the ironic reality was that, as Moses Abramovitz, the pioneering student of economic growth, put it, this growth was, "a measure of our ignorance"¹. To confound this ignorance by uncritically using terms such as innovation, technology, science, and research and development (R&D) is singularly inappropriate.

Yet we are remarkably confused about the relations of science, technology and the economy. The world economy now is not, and could not be, based on the same technologies as those of say 1900, or even 1950. Novelties from many sources, including R&D and academic laboratories, have been of fundamental importance, although which, when and how remains much more mysterious than most accounts allow. Inexcusably, a naive do-it-yourself economics of innovation (to adapt a phrase from the economist David Henderson) conflates the world economy with particular national economies.

Nationalistic naivety

This old-fashioned techno-nationalist way of thinking makes a category error — assuming that the part behaves in the same way as the whole — with serious consequences. Let us assume for the moment that 70% of global economic growth comes from technical change as might be (incorrectly) deduced from the simplest forms of growth economics. It simply does not follow that national science, innovation, technology or R&D leads to 70%



B. MELLOR

of national economic growth. Yet far too often such a connection is assumed in the expectation that there is, or should be, a positive correlation between national R&D expenditures and national rates of economic growth. For many decades the most straightforward inspection of the evidence has shown this is not the case. In the 1950s, Britain spent much more on R&D than Japan, and grew far more slowly; until more recently Japan spent far more than China (or Britain), and itself grows more slowly than it used to, and much slower than China^{2,3}. Only in techno-nationalist fantasies (and they have certainly infected policy studies in this area) does national invention drive national economic growth, and national investment in science, technology or R&D correlate positively with national economic growth. In the real world, global innovation leads to national growth, and national innovation leads to global growth.

Importing innovation

There is no mystery here. For most countries at most times, the importation of new techniques has been more important than their national development. This applies not just to China, but to, say, the United Kingdom and France too: most countries get their new technologies from abroad. France has the most nuclear-intensive electricity generation in the world, but the technology was developed in the United States; the laptop on which I write is not the product of only one country's R&D. Nowhere in the world do doctors prescribe only pharmaceuticals of national invention. As we are constantly reminded in other contexts, science and technology are global.

R&D activity, measured in dollars, euros and yen, and more often presented as a non-dimensional ratio of R&D to gross domestic product (GDP), has acquired a wholly inappropriate authority and significance. Everywhere government agencies and research scientists want to see this abstract number raised. From the European Union with its Lisbon target of spending 3% of GDP on R&D, to any number of individual nation states, one finds the belief that the national ratio of R&D spend to GDP needs to be raised in order to boost the growth rate of the national economy.

Raising R&D levels may be a good thing for the world economy, but not necessarily for the spending country. Of course, national R&D policies might not necessarily be good for the global economy either. There is a powerful tendency, everywhere in the world, to believe that national policies should be directed to the national development of a very small number of technologies, usually three, and usually the same three: nanotechnology, information technology and biotechnology. Replicating such

a limited portfolio around the world is not a sensible policy for global progress. There are, ironically and unfortunately, few things less innovative than innovation policies.

Current claims for the future effects of the three typical development fields are supported by analyses of past trinities of technologies that created the modern world. Sometimes in an echo of the prehistoric stone, bronze and iron ages, we are told that we have lived through eras characterized by one or a handful of technologies. The British prime minister Gordon Brown, who has a PhD in history, told us in a speech on the environment that he now looks forward to "no less than a fourth technological revolution", after the steam engine, the internal combustion engine and the microprocessor, which "transformed not just technology, but the way our society has been organized and the way people live"⁴.

Such analyses have a superficial plausibility that comes largely from repetition rather than serious analysis. To reduce whole historical periods, and extraordinary historical changes to one technology, or even three, is clearly absurd. And it encourages the kind of thinking that told us in the 1940s with supreme confidence that the future would be one of rockets, atomic power and automation. This was already called a 'fourth' revolution back then. The material basis of human life has been much more complex than, and very different to, that implied in these accounts. For example, until relatively recently, most humans have lived on the land, a place of extraordinary change, driven in part by increased animal power, mechanical power and chemical fertilisers. By any account, one of the most important changes in human history has been the increase in agricultural productivity after 1945. We might wonder too why, like agriculture, ships feature so marginally in histories of technology and science, when they carry massively more trade (in terms of value) than the information superhighway. And have not changes in machine tools transformed our capacity to make things from steam engines to microprocessors?

One hugely important problem in our thinking about science, technology and society, is that we take selected innovations and assume that their main effect comes soon after innovation. But the Wehrmacht had more horses per soldier for its march to Moscow in 1941 than did Napoleon's army in 1812. In this special but important case, the horse became more important with time, despite our image of a German army dominated by the

tank. We think of steam power as important around 1800, but the steam engine had a more radical impact in 1900 than in 1800; and today, it's arguably the steam turbines of coal-fired power stations that drive the Chinese economy and carbon emissions. The internal combustion engine drives the world's expanding fleet of ships. The Haber-Bosch process for creating synthetic ammonia was first used commercially in about 1913, but the massive application of synthetic nitrogen to the land came after 1945. The more one thinks about it, the more absurd the standard story becomes.

Understanding the material constitution of our world is an increasingly important task given the threat of climate change. Sensible policy needs to engage with a world in which production and consumption go up and up, an index of which is the increasing output of carbon dioxide, even in developed countries. We need to address the world as it is. To base policies on the fashionable idea that we live only in a networked, dematerialized information society, is to fail before starting. There is a great danger too that calling for new technologies to be developed, in the old-fashioned futuristic way, is a cover for inaction now. New technologies are necessary, but far from sufficient, to deal with the problem.

There are more than enough lessons from history to show us that we should reject the ignorant certainties of futuristic guru-talk. But we should take a positive message from debunking the standard arguments. New evidence and new thinking about science and technology could pay

off handsomely. There are many unexplored possibilities left out of consideration because of our over-commitment to narrow, crude, old-fashioned techno-nationalist thinking about where change is happening and what its effects are. There is plenty of evidence, necessarily from the past, that will help us think and act as experienced adults and not as children gawping at a future we cannot know. ■

David Edgerton is at the Centre for the History of Science, Technology and Medicine at Imperial College London, London SW7 2AZ, UK. He is the author of *The Shock of the Old: Technology and Global History since 1900*.

e-mail: d.edgerton@imperial.ac.uk

1. Abramovitz, M. *Am. Econ. Rev.* **46**, 5–23 (1956).
2. Edgerton, D. *Science, Technology and the British Industrial 'Decline', 1870–1970* (Cambridge Univ. Press, 1996).
3. National Science Board *Science and Engineering Indicators 2008* available at: www.nsf.gov/statistics/seind08/
4. www.number10.gov.uk/Page13791

To comment on this article and others in our innovation series, visit <http://tinyurl.com/Suolx2>.

BOOKS & ARTS

Deciphering vanished scripts

The origins of communication are explored in a landmark compilation that charts the disappearance of writing systems from ancient cuneiform to Turkish Arabic script, explains **Andrew Robinson**.

The Disappearance of Writing Systems: Perspectives on Literacy and Communication

Edited by John Baines, John Bennet and Stephen Houston

Equinox: 2008. 384 pp. £65.00

For more than 3,000 years, hieroglyphs were used to write the language of ancient Egypt. Then the script disappeared from use. The latest known hieroglyphic inscription was carved by a priest into the gate of Hadrian on the Egyptian island of Philae at Aswan on 24 August AD 394. Knowledge of how to read the hieroglyphs vanished in late antiquity and had to be recovered in the eighteenth and early nineteenth centuries, deciphered with the help of the newly discovered Rosetta Stone. By opening up the world of ancient Egypt before early Greek and Hebrew records, scholars doubled the time span of accessible history.

Archaeologists, epigraphists and linguists have for centuries puzzled over the origins of written communication, especially the alphabet. Less studied is the disappearance of long-established ancient writing systems, such as Egyptian hieroglyphs, Mesopotamian cuneiform and Mayan glyphs, an exception being the Chinese characters that continue to flourish after some 3,000 years. Yet, "writing systems that have been lost are often better understood than those for which we try to establish their process of formation", concludes Egyptologist John Baines in *The Disappearance of Writing Systems*, a landmark collection of articles by scholars. "Their loss may be just as revealing as their first appearance."

A modern example is Kemal Atatürk's 1928 abolition of the Arabic script from the Turkish language. He replaced it with the Latin script as part of his drive to bring Turkey closer to European culture. Today, few Turks can read Ottoman Turkish in Arabic script, and soon the ability will reside only with scholars. In centuries to come, Baines imagines, this combination of script and language may disappear too and need to be deciphered.

Although separated widely in time, these Egyptian and Turkish script disappearances share a common element: a seismic shift in political power and cultural prestige that caused the adoption of a new writing system. Pharaonic Egypt was conquered in the fourth



Hieroglyphs fell into obscurity because of political, religious and language changes in Egypt.

century BC by Alexander the Great and was ruled by the Greek-speaking Ptolemy dynasty, which used an alphabet — hence the inscription of the Greek alphabet on the Rosetta Stone in 196 BC along with the hieroglyphs. However, unlike in Turkey, the Egyptian script was not abolished. Instead, the hieroglyphs were slowly marginalized by a flux of politics, language, script and religion. After the death of Cleopatra in 30 BC, Egypt became a province of the Roman Empire, which wrote in Latin script. The spread of Christianity gave rise to the Egyptian Coptic Church, which wrote in Coptic script, and in the seventh century AD, Egypt was conquered by Arabs writing in the Arabic script of Islam. These changes together fossilized the hieroglyphs.

The book came out of the first major conference to focus on the disappearance of ancient writing systems, held in 2004 in Oxford, UK, and organized by the three editors. Baines is professor of Egyptology at the University of Oxford and well known for his work on literacy in ancient Egypt. John Bennet of the University of Sheffield, UK, is an expert on the Aegean scripts, notably Linear A and B, and Stephen Houston of Brown University in Rhode Island has been instrumental in the Maya decipherment revolution since the 1980s.

It is a pioneering, fascinating and authoritative book. The 17 contributors cover a surprising range of topics in detail and with comprehensive bibliographies. They discuss familiar lost scripts such as cuneiform, and more obscure examples, including the Kharosthi script of northwest India, the Meroitic script of Nubia in what is now northern Sudan, Aztec and Mexican pictography, the knotted-cord quipus of the Inca empire and its Andean successors, and the Manchu script of China, which fell out of favour with the end of the Qing dynasty in 1912 but was revived in the 1980s. Inevitably there are omissions, most regrettably the much-debated Rongorongo script of Easter Island in the southeastern Pacific, a script that probably flourished for less than 100 years until its rapid disappearance in the mid-nineteenth century.

David Brown's accessible essay on the increasing redundancy of cuneiform in Babylonia (now southern Iraq) after the Persian conquest of 539 BC offers a good case study of the multiple, often interdependent, causes of script obsolescence. Cuneiform, written in wedge-shaped signs on clay with a reed stylus, was used for three millennia before the first century AD to write many languages of the Middle East: Sumerian, Babylonian, Assyrian, Old Persian

and others, rather like today's use of the Latin script to write European languages. Brown advances economic, linguistic and administrative arguments for the gradual disappearance of cuneiform from its former heartland around Babylon, the capital of Babylonia.

Economically, Babylon declined in importance when Alexander's alleged plan to make the city the capital of Asia failed to transpire after his death in 323 BC. The city was also bypassed to the north by new desert trade routes from Asia to the Mediterranean, which opened up with the domestication of the camel as a pack animal. The use of Babylon's cuneiform script therefore diminished in commercial transactions.

Linguistically, Babylonian cuneiform was disadvantaged in comparison with alphabetic scripts. It was cumbersome, requiring hundreds of signs — a mixture of syllables and word symbols known as logograms — and used a clay medium. Unlike the alphabets used to write Greek, Phoenician and Aramaic, Babylonian cuneiform could not be written rapidly, cursively or conveniently with a brush on papyrus or other lightweight materials. Nevertheless, cuneiform was sometimes adapted to write alphabets. Such was its prestige that the Persian conquerors of Babylon invented a new cuneiform alphabet for their own language, now known as Old Persian.

Administratively, however, the Persian empire preferred the Aramaic script to any kind of cuneiform. Originally a Semitic language of ancient Syria, Aramaic had become the lingua franca of the Middle East by the sixth century BC. Later, it was the vernacular language of Jesus Christ and the Apostles and is used in the Dead Sea Scrolls. Aramaic eventually displaced cuneiform, which found its last refuge in astrology. Brown tells how scribes working in the collapsing temples of Babylon still, as late as the first century AD, "exploit[ed] a shrinking market for old-fashioned Babylonian astrology in cuneiform", even though they no longer wrote in an elegant hand.

The Aramaic script was itself extinguished in the seventh century AD by the Arabic script, which developed from Aramaic via the script of the Nabataeans, who ruled from Petra in Jordan. Arabic eliminated many pre-existing South Semitic alphabets that had been invented by literate but bored desert nomads in the Arabian peninsula before the arrival of Islam — a subtle process that is well explained

in Michael Macdonald's essay. The association of the Arabic script with the prestige of Islam and the Koran was the determining factor in its triumph.

In south Asia, by contrast, a unifying script has not been important. Most modern Indian scripts derive from one ancestor, Brahmi, first attested in the third century BC in the rock edicts of Ashoka at various sites in Pakistan and northern India. Yet Sanskrit, the language of the Hindu scriptures, has been written in many Indian scripts, including south Indian Grantha and Devanagari. Similarly, the Pali language of Buddhist scriptures is written in the Sinhala, Thai, Burmese and Khmer scripts, among others. This availability of alternatives, says Richard Salomon in his essay, explains why the early Kharosthi script — probably an Indian derivative of Aramaic — could be abandoned with the decline of the Kushan empire that used it, despite its use in Sanskrit and Buddhist texts between the third century BC and the third century AD. Perhaps because of the country's pluralistic traditions, India has chosen not to define its culture by a single script, unlike China and the Arab world.

One wonders whether China's enduring political unity may partly account for the

longevity of Chinese characters, a subject that is somewhat neglected by the book. The classical Chinese script enjoys high respect because of its antiquity — it is descended from the recognizable characters inscribed on 'oracle bones' of the Shang civilization from 1200 BC — and because of its imperial and artistic associations. When the former Chinese leader Mao Zedong, himself a calligrapher, proposed to romanize the Chinese script in the 1950s to educate the masses, he was forced by the literati to compromise with the introduction of a simplified character script and a parallel romanized phonetic system known as Pinyin. In Japan, several thousand Chinese characters were integrated with two sets of indigenous syllabic signs during the first five centuries AD to make one prestigious writing system. Despite the difficulties of writing Chinese and Japanese, neither script looks likely to disappear any time soon under the onslaught of alphabetic triumphalism.

The Disappearance of Writing Systems reveals that commerce, culture, language, medium, power, prestige and religion, in varying combinations, are all implicated in the disappearance of scripts. Each language-script combination raises issues that cannot be understood from linguistic considerations alone. We know more about script death than script birth, but no single theory can encompass why scripts flourish or vanish.

Andrew Robinson is a visiting fellow of Wolfson College, Cambridge CB3 9BB, UK, and author of *The Story of Writing and Lost Languages: The Enigma of the World's Undeciphered Scripts*. e-mail: ar471@cam.ac.uk



Cuneiform from 3000 BC records the beer rations given to workers in Mesopotamia.

TRUSTEES OF THE BRITISH MUSEUM

New look at cancer drugs

Durchleuchtet

Artpoint 222, Vienna, Austria

25 October until 27 November 2008

Margaret Oechsli goes on extraordinary journeys with her microscope. Peering at a smudge of a dried chemical, such as crystallized glutamic acid, she probes the refracted light looking for artistic inspiration. "I have no control over what I see in the microscope," she says in a rich Polish accent. But what she finds and photographs is stunning. She has created more than 3,000 images, shimmering geometries and colourful landscapes that look more like paintings than photos.

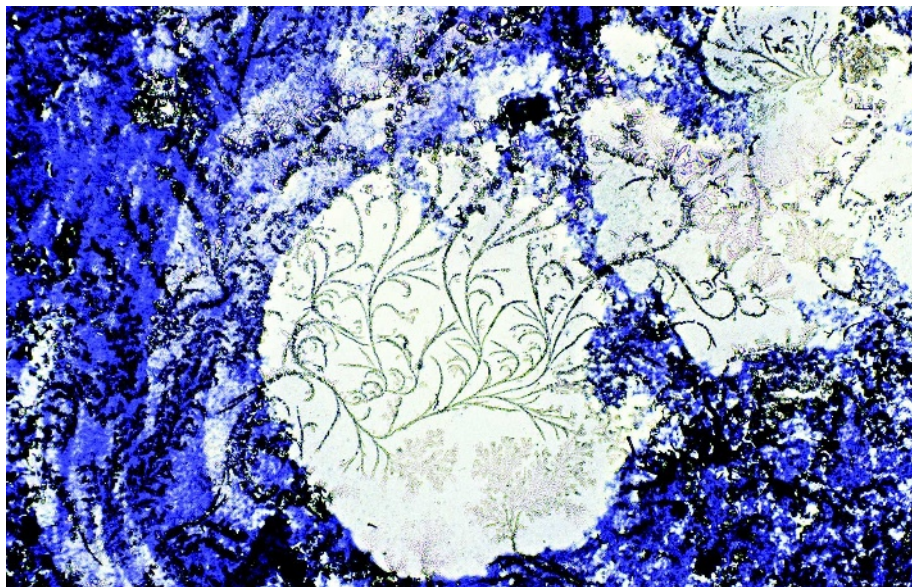
Oechsli's abstract studies of microscopic chemical structures will be shown in a new

exhibition called *Durchleuchtet*, starting this week at Artpoint 222 in Vienna. Each image explores a cancer drug — such as tamoxifen, oxaliplatin, herceptin and others — that Oechsli handles in her day job as a clinical research coordinator in the Heart and Lung Institute at Jewish Hospital in Louisville, Kentucky.

The medical theme complements the fund-raising goal of *Durchleuchtet* — which in German means both 'illuminated with light' and 'X-rayed'. Oechsli's photos will be auctioned alongside artistically rendered radiographs of Austrian athletes, and the proceeds will benefit the charity Médecins Sans Frontières (Doctors Without Borders).

Although her background in science has

M. OECHSLI



Oechsli's *Untested Beliefs* highlights the magnified fern-like branching of atropine, a muscle relaxant.

honed her techniques, Oechsli is drawn to the kaleidoscopic images for their own sake. An art lover, her most powerful photographs evoke familiar styles from famous abstract painters. "It pops to my mind that this style or this composition or this colour looks like [Robert] Motherwell or [Joan] Miró", she says. Some resemble still-life pictures — in *Dance Double*, magnified L-isoleucine morphs into ballet slippers dangling from their laces. Others are purely aesthetic. The technicolour

leopard-skin knives of L-glutamic acid pierce into black voids in a dramatic work she calls *Easter Island Fugue*.

Oechsli considers herself an artist, but embraces the parallels between her two worlds. "Science is art and art is science," she says. "In both areas you have to be very disciplined. And both of those disciplines have no finish line."

Brendan Maher is Features and Commentary editor for *Nature*.

He starts by introducing the reader to his theoretical approach, which hinges on finding common ground and then applying 'common-sense reasoning' to it. Lindsay considers the main schools of moral reasoning and their inherent problems, and goes on to consider the relationship between morals and the law. He concludes that we must take account of moral norms, but shows that we also need to consider whether these are or can be incorporated into law, and if so, how.

After noting that bioethics embraces a wide range of topics, Lindsay selects five areas for consideration. For a European reader, the selection is somewhat unusual, but nonetheless fascinating. The least surprising inclusion is assisted dying. Given Lindsay's concern with debunking myths, it is an obvious starting point because debate in this area is often bound by entrenched ideological positions. Lindsay provides a thorough and entertaining account of the arguments that are dusted off by opponents whenever someone builds a case for allowing assisted dying. When legalization is opposed using the argument for the sanctity of life, he asks whether adherence to that principle serves its intended goal in all cases. For example, whereas we all agree that taking a life is wrong on the face of it, we may adopt this view because we assume the life is wanted by the person living it. He suggests that by pronouncing it is always wrong to take a life, even when that life may no longer be desired, is to misunderstand the obligations derived from the principle of respecting, protecting and furthering the interests of others. Thus, in exceptional cases where great suffering is involved and death is inevitable, he concludes that "death is not necessarily prejudicial to that person's interests".

It is with the 'slippery slope' argument against legislation that Lindsay engages most convincingly. Challenging the argument's theoretical basis, he points to evidence showing that allowing assisted dying does not inevitably mean that 'vulnerable' groups, such as the elderly or people with disabilities, would find themselves driven to seek death

Bioethics laid bare

Future Bioethics: Overcoming Taboos, Myths, and Dogmas

by Ronald A. Lindsay

Prometheus Books: 2008. 291 pp.
\$28.95/£19.50

Bioethical debate has seldom been more vibrant, or more important. Although some people dispute whether it is even a discipline, bioethics claims the high ground by tackling some of the most complex and sensitive issues confronting modern society. From discussions about abortion to end of life, bioethicists are there. They carry the flag for informed and contentious argument, be it over assisted reproduction, cloning or stem-cell research. Ronald Lindsay, a lawyer with a doctorate in bioethics, is particularly well placed to bring his voice to the arena in his new book, *Future Bioethics*.

Given the range of topics that bioethicists cover, it is not surprising that emotions in the field run high. Discussions often begin from controversial positions that are entrenched in dogma. As the book's subtitle suggests, Lindsay's mission is to expose and debunk these myths. He does so in a book that is readable rather than obscure, and accessible to the interested lay person as well as to scholars in the field. Reckoning that progress is unlikely unless we can identify some common moral ground, he postulates that argument based on agreed norms can break the deadlock created by over-hyped language and untested dogma. What is needed, he argues, is "a well-reasoned, pragmatic approach to controversies in bioethics that avoids reliance on taboos, myths and dogma, whether these result from religious or ideological beliefs". These are fighting words, and Lindsay throws a number of powerful punches.



C. DHARAPAK/AP

or that it would become commonplace. The US state of Oregon has legalized physician-assisted dying, the practice of which is meticulously monitored, and no evidence of any slippery slope has emerged. This is Lindsay's trump card — but it only argues for dying assisted by a physician, which is a problem if autonomy is the underpinning rationale for legalization.

Other topics covered include an interesting discussion of conscientious objectors in health care, the often thoroughly misinformed debate about genetically modified food, and discourses about genetic enhancement and stem-cell research. Each chapter is richly informed by factual and theoretical discussion and approached in the common-sense way that

Lindsay recommends. His use of practical examples to point out inconsistencies in arguments is vivid and gives the non-expert reader insight into these issues.

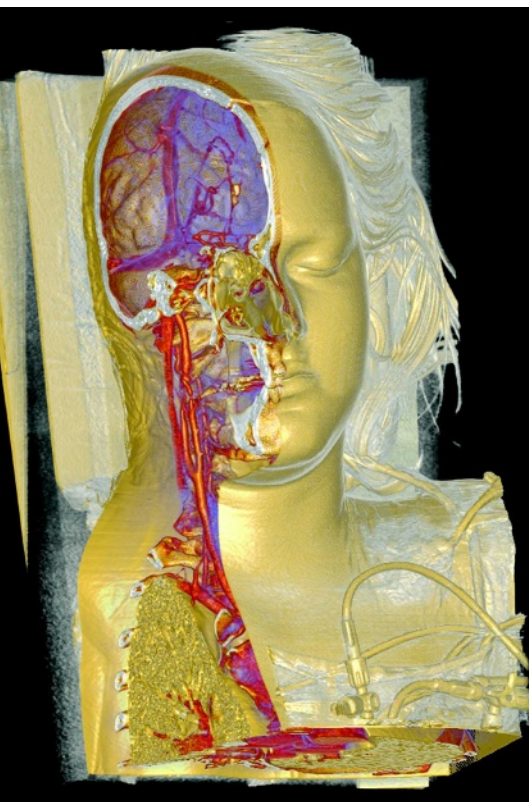
The book concludes by outlining a tentative theory of moral status. Perhaps the weakest part of the book, this reiterates how Lindsay thinks we should approach bioethical debate. We must, he argues, begin by identifying “the norms of the common morality”, then “engage in a very rough weighing of the projected harms and benefits of following a proposed course of action”. Then, we need to test the assumptions by examining their consequences, make them consistent and — of great importance — “understand the rationale for our norms”. Lindsay does not

pretend that this is easy, but he makes a good case that it is sensible and likely to be productive. Although I am less sure that such norms can be agreed, I endorse the need to think our positions through and to pay close attention to why we hold them, and the consequences of doing so. Overall, in his readable, reasoned and accessible book that challenges the taboos of bioethics, Lindsay achieves what he set out to do. ■

Sheila McLean is the International Bar Association Professor of Law and Ethics in Medicine at the School of Law, The University of Glasgow, Glasgow G12 8QQ, UK. She is author of *Assisted Dying: Reflections on the Need for Law Reform*.
e-mail: s.mclean@lbss.gla.ac.uk

Q&A: An insider's view of the body

Radiologist **Anders Persson** of Linköping University Hospital, Sweden, reveals the body's hidden structures to clinicians by applying new techniques in magnetic resonance imaging and computed tomography to produce stunning computer-enhanced three-dimensional images. The winner of the 2008 Lennart Nilsson Award for scientific photography, he tells *Nature* how visualization can revolutionize medicine.



Anders Persson (right) has pioneered computer-enhanced medical imaging to the benefit of patients and clinicians.

What drives your work?

Medical demand should lead technical research to the benefit of patients. I want to show the surgeon the real science, such as the true size, shape and colour of a vessel. Presenting precise and colourful details regarding the position, length and extent of aneurysms in arteries, for example, can save lives.

Why are these techniques also useful for post-mortem imaging?

Some forensic aspects, such as bone fractures, gas within wounds or metal under the skin are not visible in conventional autopsies. A virtual autopsy using three-dimensional (3D) medical imaging thus provides invaluable information about the crime scene, helping to determine the cause of death and saving time.

How did you become interested in medical photography?

As a young radiologist, I realized that 3D and four-dimensional X-ray visualization would rule the medical world in the future. Thirty years ago, I established a set of software functions for routine clinical use of 3D imaging, but it took many lectures to



A. PERSSON

convince colleagues and vendors that we needed better visual tools.

What are you working on today?

I'm building a new tool called synthetic MRI, in which magnetic resonance images can be collected much more quickly for each patient. And they provide realistic values for tissue characteristics that will give a more quantitative picture

of the development of pathology. I am also trying to sharpen techniques for visualizing the chemical constitution of the body, using multi-energy computed tomography.

What inspires you?

By providing beautiful images to benefit patients, I can give them vital information without scaring them. Also, the feedback I get from students stimulates me immensely to improve and explore new technical avenues. ■

Interview by **Marta Paterlini**, a writer based in Stockholm, Sweden.
e-mail: martapaterlini@nasw.org

See <http://tinyurl.com/3zscjl> for Anders Persson's 3D images.



is beginning to shed light on religious rituals. These behaviours include stereotyped, highly repetitive actions that participants feel they must do, even though most have no clear, observable results, such as striking the chest three times while repeating a set formula. Ritualized behaviour is also seen in patients with obsessive-compulsive disorders and in the routines of young children. In these contexts, rituals are generally associated with thoughts about pollution and purification, danger and protection, the required use of particular colours or numbers or the need to construct a safe and ordered environment.

We now know that human brains have a set of security and precaution networks dedicated to preventing potential hazards such as predation or contamination. These networks trigger specific behaviours such as washing and checking one's environment. When the systems go into overdrive they produce obsessive-compulsive pathology. Religious statements about purity, pollution, the hidden danger of lurking devils, may also activate these networks and make ritual precautions (cleansing, checking, delimiting a sacred space) intuitively appealing.

Finally, studies of social and evolutionary psychology demonstrate a specifically human coalitional capacity, which has an impact on religion. Humans are unique among animals in maintaining large, stable coalitions of unrelated individuals, strongly bonded by mutual trust. Humans evolved the cognitive tools to achieve this. They know how to gauge others' reliability. They can recall episodes of interaction and infer what people's characters are like. They can emit and detect costly, hard-to-fake signals of commitment.

This coalitional psychology is involved in the dynamics of public religious commitment. When people proclaim their adherence to a particular faith, they subscribe to claims for which there is no evidence, and

that would be taken as obviously wrong or ridiculous in other religious groups. This signals a willingness to embrace the group's particular norm for no other reason than that it is, precisely, the group's norm.

Cognitive cache

So is religion an adaptation or a by-product of our evolution? Perhaps one day we will find compelling evidence that a capacity for religious thoughts, rather than 'religion' in the modern form of socio-political institutions, contributed to fitness in ancestral times. For the time being, the data support a more modest conclusion: religious thoughts seem to be an emergent property of our standard cognitive capacities.

Religious concepts and activities hijack our cognitive resources, as do music, visual art, cuisine, politics, economic institutions and fashion. This hijacking occurs simply because religion provides some form of what psychologists would call super stimuli. Just as visual art is more symmetrical and its colours more saturated than what is generally found in nature, religious agents are highly simplified versions of absent human agents, and religious rituals are highly stylized versions of precautionary procedures. Hijacking also occurs because religions facilitate the expression of certain behaviours. This is the case for commitment to a group, which is made all the more credible when it is phrased as the acceptance of bizarre or non-obvious beliefs.

We should not try to pinpoint the unique origin of religious belief, because there is no unique domain for religion in human minds. Different cognitive systems handle representations of supernatural agents, of ritualized behaviours, of group commitment and so on, just as colour and shape are handled by different parts of the visual system. In other words, what makes a

god-concept convincing is not what makes a ritual intuitively compelling or what makes a moral norm self-evident. Most modern, organized religions present themselves as a package that integrates all these disparate elements (ritual, morality, metaphysics, social identity) into one consistent doctrine and practice. But this is pure advertising. These domains remain separated in human cognition. The evidence shows that the mind has no single belief network, but myriad distinct networks that contribute to making religious claims quite natural to many people.

The findings emerging from this cognitive-evolutionary approach challenge two central tenets of most established religions. First, the notion that their particular creed differs from all other (supposedly misguided) faiths; second, that it is only because of extraordinary events or the actual presence of supernatural agents that religious ideas have taken shape. On the contrary, we now know that all versions of religion are based on very similar tacit assumptions, and that all it takes to imagine supernatural agents are normal human minds processing information in the most natural way.

Knowing, even accepting these conclusions is unlikely to undermine religious commitment. Some form of religious thinking seems to be

the path of least resistance for our cognitive systems. By contrast, disbelief is generally the result of deliberate, effortful work against our natural cognitive dispositions — hardly the easiest ideology to propagate. ■

Pascal Boyer is in the Departments of Psychology and Anthropology, Washington University in St Louis, Missouri, USA, and is the author of *Religion Explained*.

e-mail: pboyer@wustl.edu

"The mind has myriad distinct belief networks that contribute to making religious claims quite natural to many people."

See <http://tinyurl.com/4f84wm> for further reading and Editorial, page 1007. For more on Being Human, see www.nature.com/nature/focus/beinghuman.

ESSAY

A question of class

Fundamental misunderstandings about classification can lead scientists down unproductive or dangerous paths, argue **Jeffrey Parsons** and **Yair Wand**.

Consider this list of scientific controversies: the decision by the International Astronomical Union to define 'planet' in such a way as to exclude Pluto; the ongoing debate over what 'species' means for bacteria; and the discovery, initially controversial, that the most common cause for peptic ulcers is an infection by the *Helicobacter pylori* bacterium. What do these diverse issues have in common? They are all examples of scientists disagreeing over how to classify phenomena 'correctly'.

Categorization is a fundamental skill learned in childhood. Yet the principles that guide it are sometime misunderstood and misused by scientists. Here, we analyse the concepts of 'category' and 'class', and reveal that some controversies over scientific classification, such as the case of planets, should not be controversial at all. Others, including the case of ulcers, can be explained as a consequence of wrong assumptions about categories.

Efforts to advance knowledge that is based on ill-conceived classifications can prove futile, and even harmful. At best, they might result in wasted time spent arguing over terminology. More seriously, they can misdirect research efforts and funding. And at worst, in cases such as the misclassification of medical conditions, the result can be serious harm, including misdiagnosis, improper treatment and even death.

To avoid such consequences, the scientific community should recognize that classification is a purposeful human activity that reflects observations about relationships among properties of phenomena. As a variety of relationships occur in nature, different classification schemes can coexist. On the other hand, classification that does not reflect true relationships can misguide scientific discourse.

Classification has long been a subject of research in cognitive psychology, and it is recognized as an evolved mechanism that supports survival. Being able to categorize actions and objects to anticipate possible 'good' or 'bad' outcomes is a critical skill for humans. At a basic level such predictions help us acquire food and shelter, or keep us from being eaten.

In science, classification is rarely related to survival so directly, yet the underlying principles are the same. Phenomena can be categorized in



many ways on the basis of the properties they share. However, categories are useful only if they make it possible to infer further information, and only if they do so consistently and over a reasonable time period. To distinguish a general category from a more useful one with inferences, we call the latter a 'class'.

Whereas a category simply reflects a repeating pattern of properties, a class additionally indicates that relationships exist between these properties, even if the mechanisms behind the relationships are unknown. For example, all the things in a room make up a category (they share the property of being in the room), but not necessarily a class; their presence in the room might not reflect some deeper underlying principle. In contrast, 'sea mammals' have the properties 'live in the sea', 'can regulate their body temperature within a narrow range', 'breathe air' and 'have blubber'. Having the first two properties is sufficient to recognize a creature as a sea mammal; the other properties can then be inferred reliably (indicating

some underlying relationships between the properties). Hence, 'sea mammals' is a class.

Many scientific discoveries begin with the identification of repeating patterns, leading to the formation of categories. If further discovery indicates that relationships exist between the properties of a category (that is, the group forms a class), this is often the first hint of some underlying law of nature. In structuring knowledge, scientists should aim to identify classes rather than categories, and controversies over classification should be understood and resolved in that context.

Planetary prowess

In 2006, the International Astronomical Union approved the following definition: "A 'planet' is a celestial body that: (a) is in orbit around the Sun, (b) has sufficient mass for its self-gravity to overcome rigid body forces so that it assumes a hydrostatic equilibrium (nearly round) shape, and (c) has cleared the neighborhood around its orbit." It turns out that all

D. PARKINS

celestial bodies that have these properties also have non-intersecting orbits and lie close to the ecliptic, giving this defined concept predictive power and making the definition a class. Pluto, however, does not have property (c) or the two additional predicted properties.

In our view, the fact that the International Astronomical Union definition of planet constitutes a class probably indicates a deep similarity between these bodies that is not shared by Pluto. Yet there are other ways of defining classes of bodies in the Solar System that will include the planets (according to the new definition) and Pluto, and might prove useful to scientists interested in other factors. A definition based on properties (a) and (b) alone, for example, includes Pluto, as well many other similar bodies (Plutinos). All these bodies share at least one other property — they are not large enough to have ever sustained thermonuclear reactions. Hence, this definition forms a distinct (but unnamed) class, the membership of which overlaps that of 'planet'.

Classes of bodies in our Solar System can be defined in many other ways, reflecting interrelationships associated with how the bodies were formed, their physical characteristics (size, composition, shape), their dynamic characteristics (orbit, rotation), or even whether they have an environment that can support life. Each of these definitions is useful for different reasons. As a result, supporting a multitude of definitions would be useful to the community and, in fact, this position has been taken by some astronomers. Thus, the controversy over a sole correct definition of 'planet', and whether Pluto falls within it, is unwarranted from a scientific perspective. Instead, it simply reflects historical and emotional associations with a specific term — 'planet'.

Although the Pluto controversy involves the classification of a specific object, in biology an entire classification system is in doubt — as evolutionary biologist Ernst Mayr wrote in his book *What Evolution Is* (Basic Books, 2001), "naturalists have had a terrible time trying to reach a consensus" on the notion of species. In particular, he added, "there is considerable uncertainty of how many 'species' of bacteria to recognize".

There are conflicting objectives in categorizing life forms. The more shared properties per category, the greater the potential predictive power, making highly specialized categories attractive. For example, knowing that an animal is a marsupial implies more than knowing it is a mammal, which implies more than knowing it is a vertebrate. But very specialized categories are not stable over time. Members of different subspecies, for example, can interbreed, such that a subspecies can lose

its predictable, distinct (from other subspecies) set of properties. Thus, an optimal level between predictive power and stability needs to be found.

For sexually reproducing organisms, the categorization level of 'species' delivers this compromise. But the case is much less clear for other organisms. For bacteria and archaea, extensive lateral gene transfer has placed in doubt even the idea of hierarchical classification. The rapid swapping of genes between these life forms means that their properties are not stable over time. When trying to construct a family tree, organisms that belong to different branches can share so many similarities that the tree turns into something more like a net. The identification of core genes has been helpful in categorizing certain microbes, but these organisms can easily acquire non-core genes that change their properties. Some researchers have controversially posited that the constant changeability of bacteria makes 'species' a meaningless label.

Much work in the microbiology community has been focused on these issues. Instead of asking 'what is a species?', biologists need to ask the more fundamental question 'what are the useful, stable, related properties that can be used to define a class?'. The answer for microbes is not clear. Perhaps it lies in finding maximal groups of coexisting sets of genes that persist within certain environments. Perhaps, as with planets, there are multiple solutions that allow for useful predictions, depending on the circumstances. The important thing is to avoid the trap of imposing a categorization solution that fits some organisms onto others that it does not fit.

Defining disease

In the case of disease, one of the most important classifications used in diagnosis is that of aetiology. Based on causation, diseases can be placed in one of three categories: genetic, environmental or pathogenic. These categories are also classes because they imply additional information, such as possible prognosis and effect of treatments.

In the 1950s, ulcers were placed quite firmly in the class of environmentally caused diseases rather than those caused by a pathogen. Variable delays between infection and onset of ulcers, and the difficulty of growing suspect bacteria *in vitro*, led to a widespread belief that bacteria could not live in the acidic environment of the stomach. Stress and diet were instead thought to be causes. Although

even in the 1940s there had been indications that peptic ulcers could be cured by antibiotics, the overriding assumption that the condition was environmental blinded scientists and doctors to the implications of those findings. This incorrect classification of a medical condition not only hindered the discovery of the causative factor, but also delayed its acceptance. Even though *H. pylori* was strongly implicated as a possible major cause of ulcers in 1982, it was not until 1994 that antibiotics were generally recommended for their treatment, and as late as 1995 only 5% of patients with ulcers were receiving antibiotic treatment.

When considering the reasons why the bacterial hypothesis was missed for such a long time (and then not readily accepted), the main problem was the misattribution of the property 'cannot grow in the acidity of the stomach' to the class of bacteria. Re-evaluating this fundamental property involved a major mind-shift that was difficult to accept.

Taking a classification perspective on scientific discourse suggests a sequence of questions to ask when studying a domain of phenomena. What are the properties of interest of these phenomena? Are there stable sets of properties common to these phenomena? Are there stable relationships in some of these sets? And finally, and most importantly, what is the evidence or rationale that these relationships reflect the true nature of the phenomena? This perspective has two important implications. First, scientists should make every effort to ensure that the assumed relationships among properties are indeed correct. Second, rather than arguing over which of several classification schemes is preferable, researchers should recognize that several correct and useful schemes can coexist. And overall, scientists should recognize that classification happens in the mind and, as a result, it can be influenced by beliefs and emotions. This is where science can go astray. ■

Jeffrey Parsons and **Yair Wand** are professors of information systems at, respectively, Memorial University of Newfoundland and the University of British Columbia.
e-mails: jeffreyp@mun.ca, yair.wand@ubc.ca

See <http://tinyurl.com/3lubso> for further reading.
See also News Feature, page 1023. Discuss definitions online at <http://tinyurl.com/4afapl>.

Correction

In the Essay "Beijing 1987: China's coming-out party" (*Nature* **455**, 598–599; 2008), we misspelt the name of Julia Marton-Lefèvre; this has been corrected in the online version.

"The controversy over a sole correct definition of 'planet', and whether Pluto falls within it, is unwarranted from a scientific perspective."

BIOCHEMISTRY

Cells enforce an ion curtain

Ben C. Berks

Metal cofactors are an essential part of many proteins. But how is the right choice of metal made? For bacteria, one answer is to change the cellular compartment where cofactor insertion occurs.

It has been estimated that a third of all proteins require the help of metal ions to carry out their biological functions¹. In most cases, these proteins obtain their metal cofactors directly from their surroundings, and so they need a mechanism to select the correct metal from the pool of metal ions to which they are exposed. On page 1138 of this issue, Tottey *et al.*² show that bacteria can optimize this process by undertaking metal insertion in a cellular compartment with a favourable metal-ion composition, rather than in the compartment in which the protein functions.

A critical chemical constraint on the selection of di-positive transition-metal ions by proteins is that the strength of the metal–protein interaction is dominated by the identity of the metal ion, rather than by the nature of the binding groups supplied by the protein. This is encapsulated in the Irving–Williams series³, in which the affinity of metal ions for binding groups increases in the order manganese, iron, cobalt, zinc, nickel and copper. The upshot of this binding chemistry is that a protein cannot select one transition-metal ion over another just by changing the metal-binding groups.

Proteins have, therefore, evolved alternative strategies that enable them to bind to specific metals⁴. Binding groups in proteins can be held in fixed positions that match the radius or preferred coordination geometry — the orientation in which a molecule binds a metal — of particular metal ions. Alternatively, specific helper proteins can increase the rate of loading of the desired metal ion into a protein as it folds, or use cellular energy sources to bias the selectivity of the process. More generally, cells can control the relative availabilities of competing metal ions. For example, a cell can insert the weakly binding manganese ion (Mn^{2+}) into a protein in the face of potential competition from strongly binding zinc (Zn^{2+})

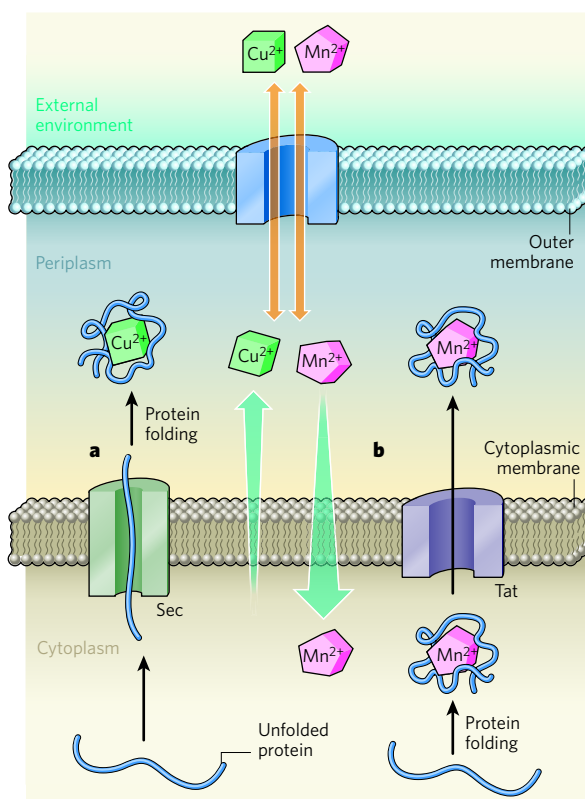


Figure 1 | Control of metal loading into bacterial periplasmic proteins. Manganese ions (Mn^{2+}) bind to the active sites of proteins less strongly than other di-positive metal ions. Nevertheless, certain periplasmic proteins in bacteria selectively bind to manganese ions, even though competing metal ions (such as copper, Cu^{2+}) pass freely into the periplasm through protein pores in the bacterial outer membrane. By contrast, bacteria control the metal-ion content of the cytoplasm, for example concentrating manganese and excluding copper. **a**, Copper-binding proteins are transported unfolded to the periplasm by the Sec pathway, where they then fold and preferentially bind copper ions. **b**, Tottey *et al.*² have identified a periplasmic, manganese-binding protein that folds in the cytoplasm, where copper does not compete with manganese for binding sites on the protein. The folded manganese-containing protein is then transported by the Tat pathway to the periplasm.

and copper (Cu^{2+}) ions, because the cell keeps the cytoplasmic concentrations of zinc and copper thousands of times lower than that of manganese.

Of interest to Tottey *et al.*² are those intracellular compartments in which metal-ion

concentrations cannot be easily manipulated. One such compartment is the bacterial periplasm, which lies between the bacterial cytoplasmic and outer membranes, and which is exposed to the metal-ion concentrations prevailing outside the cell. As the cell cannot dictate the levels of competing metal ions in the periplasm, it would be natural to assume that, when incorporating weakly binding metal ions into periplasmic proteins, selection by control of metal-ion concentration would be irrelevant. Tottey *et al.* force us to rethink this assumption.

The authors discovered that the main periplasmic manganese-containing and copper-containing proteins of a particular photosynthetic bacterium, *Synechocystis* PCC 6803, are structurally related. Indeed, the binding sites of the proteins are essentially identical, so the cell somehow selectively fills the two proteins with metal ions from opposite ends of the Irving–Williams series. The authors confirmed that this metal selectivity is not a property of the metal-binding sites by showing that the manganese-binding protein will bind copper in preference to manganese when both metal ions are present during protein folding. So how does the cell put different metals into the two proteins?

Tottey *et al.* noticed that the two proteins take different routes from their site of synthesis in the cytoplasm to their final location in the periplasm (Fig. 1). The copper protein uses the standard Sec export pathway, which transports proteins in an unfolded state. This suggests that the copper protein folds and receives its metal cofactor only after it has reached the periplasm. By contrast, the manganese protein uses the alternative Tat pathway, which has the dedicated role of transporting folded proteins⁵.

The authors realized that the Tat-targeted manganese protein must fold before export, and therefore must acquire its manganese cofactor in the cytoplasm, where there are low concentrations of competitor ions. In this way, the protein is protected from tightly binding

metals such as copper. Once the manganese protein has folded, the metal-binding sites are inaccessible to other metals, and the protein can be safely exposed to the periplasmic environment. In other words, the metal that binds to the protein is selected by the compartment in which the protein folds.

Tottey and colleagues suggest² that cytoplasmic metal insertion might be crucial not only for periplasmic proteins that bind individual metal ions, but also for the numerous Tat substrates that bind to other kinds of metal-containing cofactors, such as clusters of metal and sulphur atoms or complexes of metals with organic molecules. They propose that cytoplasmic insertion prevents the misincorporation of tightly binding metals into such cofactors; once ensconced within the folded protein, the cofactors are shielded from any interference by competing metals. For example, the authors note that iron–sulphur clusters are susceptible to the misincorporation of transition-metal ions such as cobalt and copper^{6,7}, and that periplasmic proteins that contain iron–sulphur clusters are always transported to their site of action by the Tat pathway. Strikingly, and consistent with the authors' proposal, the only periplasmic protein that has a copper–sulphur cofactor receives this cluster in the periplasm, rather than in the cytoplasm⁸.

Eukaryotic cells (such as those of animals, plants and fungi) might also control the metal loading of their secreted proteins by a variation of the protected-compartment strategy. In these cells, secreted proteins fold in the endoplasmic reticulum — an intracellular organelle that controls the concentrations of metal ions in its interior — before they reach the extracellular milieu. But in contrast to the mechanism described by Tottey *et al.*, these folded proteins are transferred to the outside world in vesicles that release their contents on fusion with the cell membrane; no physical transport of the protein across a membrane is required.

Some transport of folded proteins into organellar compartments does occur in eukaryotic cells — across the membranes of peroxisomes (ubiquitous organelles involved in metabolism) and across the photosynthetic thylakoid membranes of chloroplasts (which possess a Tat apparatus). It will be interesting to see whether these systems, like the bacterial Tat pathway, are exploited to control metal binding in organellar proteins. More generally, Tottey and colleagues' work² reminds us that different cellular compartments have their own distinct metal compositions, which are vital in determining which metals associate with their resident macromolecules. ■

Ben C. Berks is in the Department of Biochemistry, Oxford University, South Parks Road, Oxford OX13QU, UK.
e-mail: ben.berks@bioch.ox.ac.uk

- Irving, H. & Williams, R. J. P. *Nature* **162**, 746–747 (1948).
- Fraústo da Silva, J. J. R. & Williams, R. J. P. *The Biological Chemistry of the Elements* 2nd edn (Oxford Univ. Press, 2001).
- Berks, B. C., Palmer, T. & Sargent, F. *Adv. Microb. Physiol.* **47**, 187–254 (2003).
- Ranquet, C., Ollagnier-de-Choudens, S., Loiseau, L., Barras, F. & Fontecave, M. *J. Biol. Chem.* **282**, 30442–30451 (2007).
- Butt, J. N., Niles, J., Armstrong, F. A., Breton, J. & Thomson, A. J. *Nature Struct. Biol.* **1**, 427–433 (1994).
- Zumft, W. G. & Kroneck, P. M. *Adv. Microb. Physiol.* **52**, 107–227 (2007).

ECONOMICS

Sustainable fisheries

Geoffrey Heal and Wolfram Schlenker

Fishermen's aims of increasing their catch seem at odds with preserving fish stocks by limiting catch. A study of more than 11,000 fisheries shows that 'individual tradable quotas' can reconcile these goals.

The destruction of the world's major fisheries has been widely documented, with a general consensus that the biomass of top marine predators is now some 10% of what it was half a century ago¹. Many of these species — such as the bluefin tuna, Atlantic cod, and swordfish in the Atlantic and Indian oceans — are expected to be extinct within decades. There is therefore great interest in finding ways of managing fisheries that ensure their sustainable use, allowing a fish population to return to earlier levels and providing a secure basis for a healthy and profitable fishery. Writing in *Science*, Costello, Gaines and Lynham² present a convincing and thorough analysis of this issue. They suggest that a particular management approach,

the use of 'individual tradable quotas' (ITQs), has had dramatically beneficial impacts on many of the fisheries in which they have been implemented.

The destruction of the world's fisheries is a classic illustration of the 'tragedy of the commons'. With open access, all boats are competing for the same fish: the more fish one catches, the fewer there are for others. Everyone rushes to catch as many as possible. There is no point in leaving fish untouched so they can breed, as competitors will catch them. Economists have developed formal models showing that the outcome is a massive overuse relative to the policy that would generate the greatest economic value from the fishery.

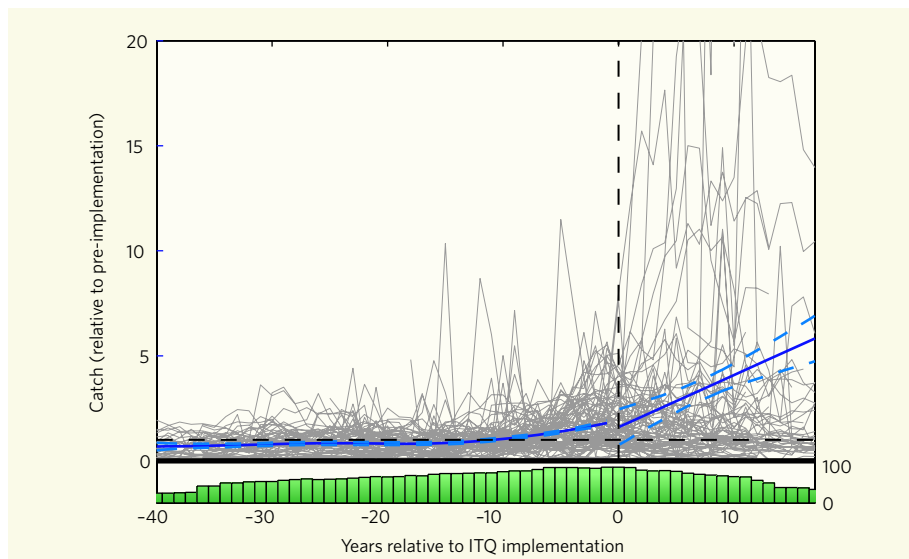


Figure 1 | Benefits of individual tradable quotas (ITQs). This figure uses catch data for all fisheries that had implemented ITQs by 2003, and for which there were at least five observations before ITQ implementation. (Two fisheries that had increases of more than a factor of 200 after ITQ implementation are excluded, as these could be outliers; the graph is thus a conservative estimate of the benefits of ITQs.) The x axis shows the time relative to ITQ implementation (time 0 is the year ITQs were implemented; time 1 is the first year after implementation). Upper panel, time series of individual fish species, shown as grey lines, where average catches before implementation are normalized to 1. The blue solid line shows the result from a non-parametric regression; blue dashed lines are the 95% confidence band. Lower panel, a histogram of how many fisheries had catch data available for each time period. (Catch data from refs 1 and 2, used to compile this figure, were kindly supplied by Costello *et al.*)

1. Holm, R. H., Kennepohl, P. & Solomon, E. I. *Chem. Rev.* **96**, 2239–2314 (1996).

2. Tottey, S. *et al. Nature* **455**, 1138–1142 (2008).

Introducing ITQs gives exclusive access to fishermen who work a fishery. A total allowable catch (TAC) is set and an ITQ entitles the owner to a fraction of this, so the TAC translates into a catch limit for each boat. ITQs can be traded, and their value of course depends on the productivity of the fishery: shares in a collapsed fishery are worth as little as shares in a collapsed bank. But shares in a thriving fishery command high prices and represent real wealth for their owners. Suddenly, fishermen have an incentive to preserve a fishery for the future, as preservation will be reflected in a higher value of which they 'own' a share. Each fisherman has an incentive to lobby for the optimal TAC. In theory, ITQs are a win-win solution: they align incentives for fishermen with the good of a fishery ecosystem, leading to reduced pressure on the fishery as well as higher profits for fishermen than under open access.

The innovation by Costello *et al.*² is a thorough statistical analysis of the impact of introducing ITQs on the status of a fishery, using a database covering 11,135 fisheries from between 1950 and 2003, of which 121 had instituted ITQs by 2003. Ecosystems with the largest number of ITQs include the New Zealand shelf (example species being squid, jack and blue mackerel); the Iceland shelf (capelin and her-ring, but also species with lower average catch, such as monkfish); and the Gulf of Alaska (for example, pollock and Pacific cod).

Costello and colleagues use the definition of collapse applied in an earlier paper by Worm *et al.*¹, and they show that introduction of an ITQ system reduces the probability of that outcome by about 14%. The fraction of ITQ fisheries that collapsed was about half that of the non-ITQ fisheries that collapsed. Because both Costello *et al.* and Worm *et al.* define a fishery as collapsed when the catch drops below 10% of the historic maximum to date, a policy that stabilizes catch by definition reduces the probability of collapse. (If catch is a random process with a constant mean, a one-time positive outlier equal to 10 times the mean would imply that, once catch reverts to the mean, it is now considered collapsed. Our Figure 1, which shows the win-win situation of ITQs, hence presents the entire catch series to emphasize that the results are not driven by outliers of the historic catch.)

The upper panel of Figure 1 displays the catch history for fish species for which ITQs were implemented. The *x* axis is the time from when the ITQ was implemented (ITQs are phased in over several years, and hence time 1 on the *x* axis corresponds to different years for each fish species; because we group together catches from different years for each time period, the results are less likely to be driven by year-specific environmental shocks). The *y* axis shows relative catches that are normalized to 1 before the ITQ was implemented. Grey lines display the time series of individual fish species. The blue line shows the results from a non-parametric regression (including

a 95% confidence band shown as dashed lines). Note how several fisheries (grey lines) show remarkable improvements above historic levels after the ITQ was implemented. Similarly, the smoothed overall line shows an upward trend. Sustained higher catches imply that the fishery is less likely to collapse and that the fishermen are reaping the benefits through higher catches.

In Figure 1, the 95% confidence band of the non-parametric regression starts to broaden towards either end, which is not surprising given the limited number of fisheries that have such long time series. The lower panel displays the number of observations we have for each time period. We truncated the graph after 17 years, as the number of observations drops sharply from 36 in time period 17 to 12 in time period 18. Continued monitoring and improved catch data for longer time periods will hence be crucial to assessing the continued sustainability of ITQs.

If ITQs work, why haven't they been more widely used? Undoubtedly, this is partly because, until Costello and colleagues' paper, we have not had unambiguous evidence that they do work. This study should give ITQ

implementation a boost. But there are also some political, ideological and regulatory issues in the way. Some environmental groups are opposed to anything based on market principles. Others feel that ocean fisheries are common property — that everyone should be free to use them, and that it is wrong to establish ownership rights in the sea. It is to be hoped that clear evidence of the effectiveness of ITQs will lead their opponents to think again. Finally, ITQs work best when a fish species resides exclusively within the waters of a particular country. Fish species in international waters, or migratory species, would require international agreements, with the complication that individual countries might have an incentive to cheat.

Geoffrey Heal is at Columbia Business School, and Wolfram Schlenker is at the School of International and Public Affairs and Department of Economics, Columbia University, New York, New York 10027, USA.

e-mails: gmh1@columbia.edu;
wolfram.schlenker@columbia.edu

1. Worm, B. *et al. Science* **314**, 787–790 (2006).
2. Costello, C., Gaines, S. D. & Lynham, J. *Science* **321**, 1678–1681 (2008).

INORGANIC CHEMISTRY

Confirmation of the improbable

Craig L. Hill

Certain transition-metal complexes are thought to exist only fleetingly, perhaps as intermediates in reactions. So the discovery of one such complex that is stable at room temperature is provocative.

During the past 40 years, few inorganic compounds have been more discussed or sought after than a curious class of transition-metal complexes. Known as late transition metal oxo (LTMO) complexes, these compounds are thought to be intermediates in all sorts of oxygen-dependent processes. For example, they could be involved in reactions promoted by copper-containing enzymes; in catalytic-converter processes; in reactions at the cathode of fuel cells; and in industrial oxidation reactions that use 'noble metal' catalysts (such as gold, platinum and silver) on solid supports. But for a long time, there was no evidence for their existence because LTMO complexes are intrinsically unstable. However, a few have recently been isolated and characterized^{1–4}. The surprising stability of these compounds might be due to the ligand molecules that bind to the metal, which lower the electron density in the metal–oxygen unit.

On page 1093 of this issue, Poverenov *et al.*⁵ report the first example of an LTMO complex in which the ligands are not electron-withdrawing. The complex undergoes reactions that provide insight into how the above-

mentioned catalytic processes might work.

LTMO complexes are characterized by a multiple bond between the metal and oxygen atoms (Fig. 1a, overleaf); in this context, the oxygen atom is known as a terminal oxo ligand. The metal–oxygen bond is destabilized by repulsion between the bonding electrons from the oxo ligand and the '*d* electrons' on the metal. The amount of repulsion depends on the number of *d* electrons. Those transition metals on the left-hand side of the periodic table (the early transition metals, such as vanadium and tungsten) have few or no *d* electrons, so terminal oxo complexes are stable and common for these elements. The transition metals in the middle of the periodic table (such as manganese and iron) have more *d* electrons, and their terminal oxo complexes are highly reactive. The late transition metals (such as platinum, silver and gold) are found towards the right-hand side of the periodic table, and have the most *d* electrons of all; their complexes are therefore generally so reactive that, for many years, none could be isolated.

But in 1993, the first LTMO complex¹ — an iridium complex — was isolated. Iridium,

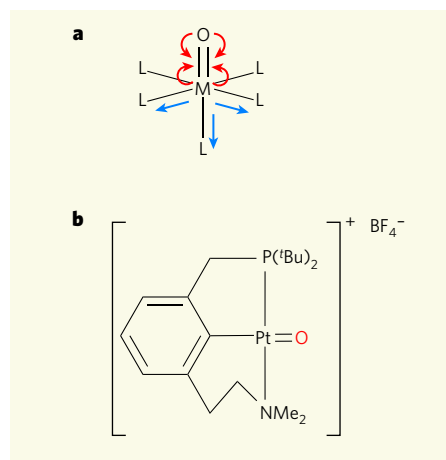


Figure 1 | Stability in metal oxo complexes.

Terminal transition-metal oxo complexes contain metal–oxygen multiple bonds ($M=O$). **a**, Electron density on the oxygen atom is repelled by d electrons on the metal (red arrows indicate clashing regions of high electron density). This destabilizes the complexes, especially for metals such as platinum that have many d electrons. Ligands that withdraw electron density (blue arrows indicate electron movement) from the $M=O$ unit stabilize the complexes. M can be any transition element, L represents general ligands. **b**, Poverenov *et al.*⁵ have made a stable terminal platinum oxo complex that lacks electron-withdrawing ligands, and propose the structure on the basis of computational predictions and analytical data. The oxo unit (red) projects above the plane defined by the platinum, phosphorus and nitrogen atoms, and by the carbon atom to which the platinum atom is attached. Me, methyl; t Bu, $C(Me)_3$; BF_4^- , tetrafluoroborate ion.

although technically a late transition metal, has fewer d electrons than platinum. The ligands in this complex adopt a tetrahedral arrangement around the metal, which permits iridium's d electrons to be accommodated without destabilizing the terminal oxo group. Subsequently isolated LTMO complexes incorporated electron-poor ligands, which probably withdraw electron density from the metal–oxo unit, thus reducing electron–electron repulsion. In this way, terminal oxo complexes of platinum², palladium³ and gold⁴ were made.

But Poverenov *et al.*⁵ have made a platinum terminal oxo complex that has non-electron-withdrawing ligands. The authors treated a conventional platinum complex that lacks oxygen ligands with a compound (dimethyl dioxirane) that acts as a potent oxygen-atom donor. The resulting product (Fig. 1b) is sufficiently stable, both as a powder and in solution, to be extensively characterized at room temperature. Remarkably, the ligand (an aromatic ring) opposite the oxo group on the metal is not an electron-withdrawing group — in fact, it actually donates electrons to the platinum. The authors used quantum-mechanical calculations to show that empty orbitals on this aryl ligand are too high in energy to receive electron density from the metal. Furthermore,

the other ligands in the complex are also more electron-donating than electron-accepting in character.

The stability of Poverenov and colleagues' complex is intriguing. The most widely used strategy for stabilizing reactive moieties — both in chemistry and biology — is to encapsulate them with other groups so that they can't interact and react with neighbouring molecules. But the authors show that such 'steric' protection doesn't happen in their compound: analytical data and structural predictions, along with the reactivity of the complex, all indicate that the platinum–oxygen bond is at least partly exposed. Thus, no convincing electronic or steric argument can be made to explain why the compound is stable.

Of course, extraordinary claims require extraordinary evidence. In this case, given that the reactivity of the authors' compound is lower than that expected for LTMO complexes, the proposed structure seems highly improbable — but it has been characterized by a commensurately extensive and convincing ensemble of techniques. Although the authors were not able to obtain an X-ray structure of the compound, several lines of evidence establish that their proposed structure, complete with a partly exposed terminal oxo ligand that lies out of the plane formed by the other ligands, is correct. Specifically, their X-ray spectroscopy data agree with predictions from computational modelling of the proposed structure; the infrared spectrum of the complex contains a signal characteristic of a multiple platinum–oxygen bond; and mass spectrometry data show that the molecular mass of the complex is the same as that of the proposed structure.

A similar battery of evidence strongly suggests that the oxidation state of the platinum atom in the complex is consistent with Poverenov and colleagues' suggested structure.

And as if all this weren't enough, the observed chemical reactions of the compound also support the authors' interpretation of the data: it transfers its oxo oxygen from the platinum atom to the adjacent phosphorus ligand, reacts with water, and takes part in other reactions that collectively are best explained by assuming a terminal oxo structure.

Poverenov and colleagues' findings⁵ go a long way to substantiating the previous reports of platinum², palladium³ and gold⁴ oxo complexes. This, in turn, makes it hard to argue that LTMO complexes don't exist, as might reasonably have been argued before on the basis of conventional wisdom about modes of chemical bonding. On the contrary, it seems that they might be fairly widespread. They can certainly now be regarded as realistic candidates for intermediates in many important catalytic reactions that involve oxygen.

The report of this remarkable platinum complex⁵ also raises many questions. What is it that stabilizes certain LTMO compounds, and how common are these stabilization mechanisms in other complexes that contain different ligands and/or different arrangements of ligands? Do terminal ligands other than oxo groups exist, in which atoms such as nitrogen or sulphur form multiple bonds to noble metals? And how might LTMO complexes take part in the widely used technologies that involve noble metals as catalysts? The answers to these questions will be of great fundamental and practical interest. ■ Craig L. Hill is in the Department of Chemistry, Emory University, Atlanta, Georgia 30322, USA. e-mail: chill@emory.edu

1. Hay-Motherwell, R. S., Wilkinson, G., Hussain-Bates, B. & Hursthouse, M. B. *Polyhedron* **12**, 2009–2012 (1993).
2. Anderson, T. M. *et al. Science* **306**, 2074–2077 (2004).
3. Anderson, T. M. *et al. J. Am. Chem. Soc.* **127**, 11948–11949 (2005).
4. Cao, R. *et al. J. Am. Chem. Soc.* **129**, 11118–11133 (2007).
5. Poverenov, E. *et al. Nature* **455**, 1093–1096 (2008).

APOPTOSIS

Stabbed in the BAX

Douglas R. Green and Jerry E. Chipuk

Apoptotic cell death is an intricate and highly regulated process. To initiate apoptosis, the protein BIM binds to a hitherto unrecognized site on the BAX protein to trigger permeabilization of the outer mitochondrial membrane.

Cell death in animals mainly proceeds through the programmed process of apoptosis. In vertebrates, this usually occurs by means of a pathway involving the mitochondrion, a cellular organelle¹. Following damaging cellular stress, the outer mitochondrial membrane becomes permeable, and factors are released into the cytoplasm that precipitate apoptosis. The pro-apoptotic effector proteins of the BCL-2 family — BAK and BAX — are responsible for permeabilizing the membrane, yet there

is little structural information on the main protein–protein interactions necessary to promote this mitochondrial event. On page 1076 of this issue, Walensky, Tjandra and colleagues² present an intriguing structural analysis of the interactions between BAX and one of its activators, revealing an unsuspected binding site.

Proteins of the BCL-2 family control the integrity of the outer mitochondrial membrane and are divided into three subfamilies: anti-apoptotic proteins, pro-apoptotic effectors

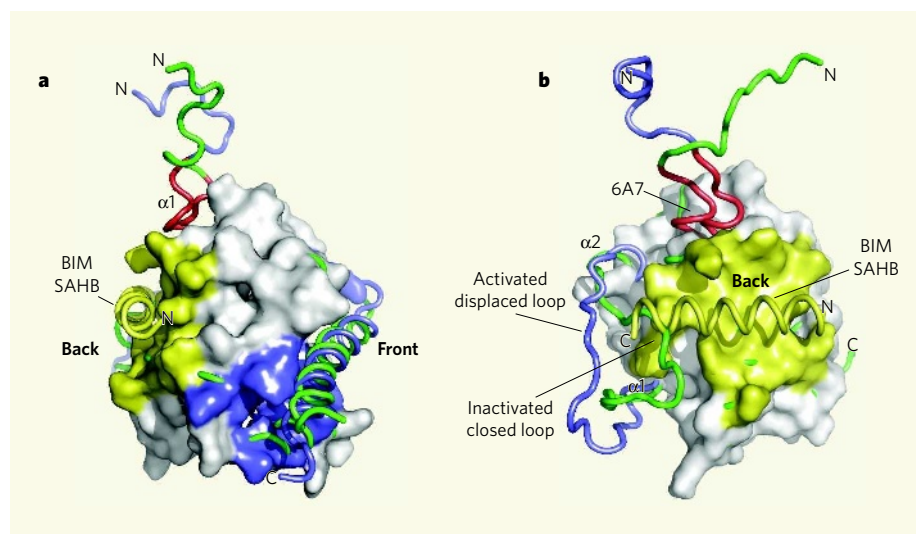


Figure 1 | Activation of the BAX protein by the BIM SAHB domain. **a**, The structure of BAX based on a previous study¹¹ is shown with BIM SAHB binding at a site on the 'back' of the molecule (yellow). This contrasts with the expected binding of a BH3-domain helix in the conventional (at least for anti-apoptotic proteins) hydrophobic BH pocket located at the 'front' of the molecule (blue). **b**, Walensky, Tjandra and colleagues² find that conformational changes accompany the binding of a BIM SAHB peptide to BAX. The chain containing α -helix 1 (α 1) and the loop between α 1 and α 2 is shown before (green) and after (blue) binding of BIM SAHB. The BAX amino-terminal region 6A7, which becomes exposed on association with BIM SAHB, is shown in red. (Images prepared by T. Moldoveanu, St Jude Children's Research Hospital.)

and BH3-only proteins (so called because, of the four evolutionarily conserved BCL-2-homology (BH) domains, only BH3 is present in these proteins)³. Anti-apoptotic BCL-2 proteins prevent apoptosis by inhibiting permeabilization of the membrane, whereas the BH3-only proteins promote it. When BAK and BAX are activated, they 'homo-oligomerize' — that is, they form complexes of either BAX-only or BAK-only molecules. These oligomers assemble in the outer mitochondrial membrane, causing its disruption. Proteins localized between the outer and inner membranes, such as cytochrome *c*, can then diffuse into the cytosol. Cytochrome *c* and other released proteins cooperate with cytosolic factors, leading to the activation of caspase enzymes that are responsible for the features of apoptosis. But even without caspase activation, permeabilized outer mitochondrial membranes can be sufficiently catastrophic to cause cell death.

The BH3-only proteins promote permeabilization of the outer mitochondrial membrane by regulating the other two subfamilies. These proteins bind to, and thereby inhibit, the anti-apoptotic BCL-2 proteins. Also, at least two BH3-only proteins — BID and BIM — directly activate BAK and/or BAX, allowing them to insert in the outer mitochondrial membrane, oligomerize there and permeabilize the membrane (BID and BIM are therefore referred to as direct activators). Although considerable structural and biochemical data⁴ have revealed how the BH3 domain of BH3-only proteins tightly binds to and inhibits the anti-apoptotic BCL-2 proteins, until now very little was understood about how the BH3 domains of BID or BIM induce the permeabilization activity of BAK and BAX.

Walensky and colleagues^{5,6} showed previously that BH3-domain peptides from BID and BIM can be 'stapled' into an α -helical conformation called SAHB (stabilized α -helices of BCL-2 domains), which can bind to and activate BAX. Now, using a combination of structural techniques, the authors² provide the first glimpse of how the SAHB peptide of BIM interacts with BAX.

If BAX behaved like the structurally similar anti-apoptotic proteins, such as BCL-x_L or MCL-1, then BIM SAHB would bind

to the conventional hydrophobic BH3-binding pocket at the 'front' of the BAX protein (Fig. 1a). However, unexpectedly, BIM SAHB stabs BAX in the 'back'. Consequently, the region of BAX adjacent to its amino-terminal α -helix (α 1) swings outwards (Fig. 1b). Other conformational changes not seen in this structure must also occur, as the authors find that an amino-terminal motif in α 1 (dubbed 6A7) becomes exposed when BAX monomers are activated by BIM SAHB.

In agreement with these results, a previous biochemical study⁷ suggested that cytosolic p53 — a direct activator that does not belong to the BCL-2 family — binds to a similar region in BAK to that described for the BIM-SAHB-BAX interaction. However, the findings contrast with another study⁸ showing that the BH3 domain of BID binds to BAK in the conventional hydrophobic BH3-binding pocket. As we will see, these observations are not necessarily incompatible.

A milestone in understanding proteins of the BCL-2 family will be to unravel how BAK and BAX form homo-oligomers, because this process seems to be essential for the permeabilization of the outer mitochondrial membrane. Earlier this year, researchers investigating BAK provided some notable clues. Using biochemical approaches, those authors showed⁹ that, during BID-induced BAK activation, BAK exposes its BH3 domain, probably revealing a groove corresponding to the hydrophobic BH pocket of the anti-apoptotic proteins at the front of the molecule. Two activated BAK molecules with their BH3 regions exposed then seem to interact with each other's grooves to form a BAK dimer.

Mutational analysis of BAX supports similar interactions in this molecule¹⁰. By inference, we propose that the binding of BIM SAHB to

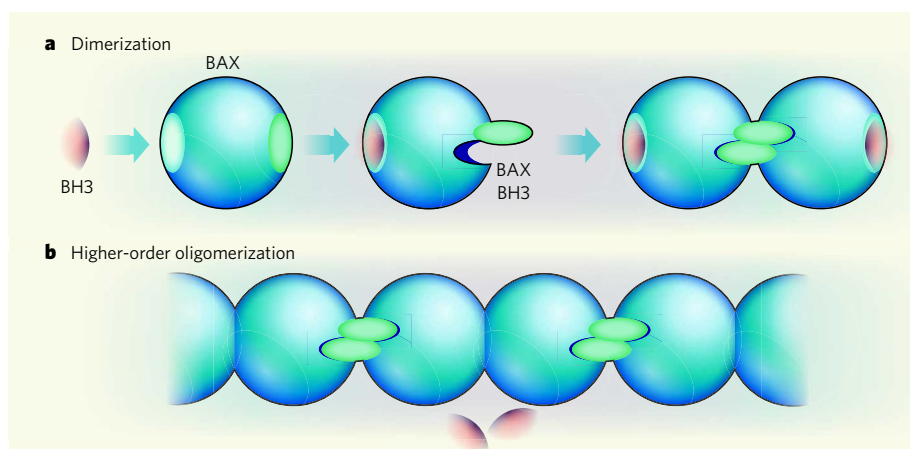


Figure 2 | Possible consequences of BIM SAHB binding to BAX. **a**, On the basis of the latest structural information², we speculate that the binding of BIM SAHB to the 'back' of BAX, and the ensuing conformational changes, constrain the 'front' of the molecule, including the hydrophobic BH pocket, causing the carboxy-terminal region (not shown) and α -helix 4 containing the BH3 domain (green) to move out of the BH pocket and create a groove. Two such BAX molecules could then dimerize 'nose-to-nose' through interactions between the BH3 domain and the hydrophobic BH groove. **b**, Interaction at an additional, undefined interface might result in the formation of BAX oligomers and so permeabilization of the outer mitochondrial membrane. On BAX activation, the inducer of activation — in this case BIM SAHB, but presumably any activator — might dissociate to allow higher-order oligomer formation.

BAX results in a conformational change that constrains the front of BAX. The carboxy-terminal tail of BAX, which normally resides in the front hydrophobic BH pocket, pops out, as, presumably, does the region containing the BH3 domain. Two such BAX molecules can then form 'nose-to-nose' dimers (Fig. 2a). If this model is correct, BAX with mutations in its BH3 region or in crucial residues in its hydrophobic groove would still bind to BIM SAHB but would not form oligomers or cause permeabilization of the outer mitochondrial membrane. Indeed, such mutations in BAX destroy its function¹⁰, but whether BIM SAHB would still bind remains unknown.

A problem with the idea of nose-to-nose dimer formation is that BAK and BAX form higher-order homo-oligomers that seem to be required for their apoptotic function. It is possible that there is at least one more interaction

surface on BAX and BAK that mediates homo-oligomerization; and it is tempting to speculate that this surface is exposed when $\alpha 1$ is displaced by BIM SAHB (and presumably by the full-length BIM protein, or any other direct activator). As BID and BIM are not found in oligomers of BAX or BAK, homo-oligomerization at this surface might then displace the direct-activator protein (Fig. 2b). Interactions of the BID or BIM BH3 domain with the revealed BH pocket might also help to stabilize this intermediate structure and facilitate oligomerization at the nose-to-nose interface. If so, there might actually be two interaction sites between BAX (or BAK) and their activators, one at the back and one at the front. We do not know the conformations of the activated (dimerized or oligomerized) forms of BAK or BAX, nor can we reasonably model the nose-to-nose dimers at this point. But the pieces are starting to come

together as we puzzle out how these killers do the dastardly deed of triggering apoptosis. ■

Douglas R. Green and Jerry E. Chipuk are in the Department of Immunology, St Jude Children's Research Hospital, 262 Danny Thomas Place, Memphis, Tennessee 38105, USA.
e-mail: douglas.green@stjude.org

1. Green, D. R. *Cell* **121**, 671–674 (2005).
2. Gavathiotis, E. *et al. Nature* **455**, 1076–1081 (2008).
3. Chipuk, J. E. & Green, D. R. *Trends Cell Biol.* **18**, 157–164 (2008).
4. Youle, R. J. & Strasser, A. *Nature Rev. Mol. Cell Biol.* **9**, 47–59 (2008).
5. Walensky, L. D. *et al. Science* **305**, 1466–1470 (2004).
6. Walensky, L. D. *et al. Mol. Cell* **24**, 199–210 (2006).
7. Pietsch, E. C. *et al. J. Biol. Chem.* **283**, 21294–21304 (2008).
8. Moldoveanu, T. *et al. Mol. Cell* **24**, 677–688 (2006).
9. Dewson, G. *et al. Mol. Cell* **30**, 369–380 (2008).
10. George, N. M., Evans, J. J. & Luo, X. *Genes Dev.* **21**, 1937–1948 (2007).
11. Suzuki, M., Youle, R. J. & Tjandra, N. *Cell* **103**, 645–654 (2000).

ASTROPHYSICS

How do galaxies form?

Sidney van den Bergh

A study of galaxies indicates that galaxy formation may be regulated by a single parameter. This unexpected finding shows that prevailing views on the process could need revision.

The current theory of galaxy formation holds that galaxies were assembled through the chaotic hierarchical merging of massive haloes of dark matter, in which star-forming matter was later embedded. One would therefore expect the properties of individual galaxies to be determined by numerous independent factors, such as star-forming history, merger history, mass, angular momentum, size and environment. It is thus surprising that galaxies seem to form an (almost) one-parameter family in which their mass is the dominant factor, as an investigation by Disney *et al.*¹ (on page 1082 of this issue) suggests.

New observations often provide a fresh perspective on the Universe, thus opening another window through which to view ancient problems. Disney *et al.*¹ provide a catalogue of roughly 200 galaxies — from giant spirals to extreme dwarfs — that were selected from a large, blind sky survey for neutral hydrogen (HI) emission using the hydrogen spectral line at a wavelength of 21 cm. For each galaxy in the catalogue, they measured a number of quantities: the total hydrogen mass; the width of the hydrogen spectral line; the redshift; the inclination with respect to the line of sight; two radii, containing 50% and 90% of the light, respectively; and the optical luminosity in four different colour bands. These various measurements provide a handle on the main properties of individual galaxies.

The HI-selected galaxies seem to have

colours comprising two components: a 'rogue' colour, which probably correlates with the recent star-forming history of the galaxy, and a systematic component that relates to the mean age of the stellar population in the galaxy. (Both rogue colour and galaxy morphology, according to Hubble's morphological classification scheme, are strongly correlated with galaxy environment.) Because the nature of a galaxy's colour is complex, Disney *et al.* initially neglect it and concentrate on the other factors that describe the galaxies in their sample.

From a principal-component analysis of their data, which basically reduces the dimensionality of the data by identifying directions — the principal components — along which the variation in the data is maximal, Disney and colleagues find that the six independent components that they use to describe the galaxies in their sample (including the systematic colour) are all correlated with each other and with a single principal component — the galaxy's mass. In other words, galaxies seem to constitute a single 'fundamental line' in parameter space.

The authors argue that such simplicity is difficult to understand within the framework of the theory of hierarchical galaxy merging. This is because it is expected that the evolution of individual galaxies depends on various factors: on the details of their chaotic-merger history (Fig. 1) — in particular the masses, spins and gas content of the individual merging galaxies, and on the density, temperature and



Figure 1 | Merger activity. Here, two spiral galaxies (NGC 6050 and IC 1179) are caught in the act of colliding. The prevailing theory of galaxy formation holds that the evolution of individual galaxies will depend on the details of their chaotic merger history — in particular the masses, spins and gas content of the individual merging galaxies — as well as on the environment in which a galaxy is assembled. But Disney *et al.*¹ find that galaxy formation seems to correlate most strongly with the present-day mass of the galaxy.

turbulence of the environment in which a galaxy is assembled.

Disney and colleagues' work follows closely in the footsteps of an earlier study by Gavazzi *et al.*² This showed that the radii of galaxies, measured at a blue-band surface brightness of 25 magnitudes per square arcsecond, are closely correlated with their luminosities, and that this correlation does not depend on galaxy environment. From this observation, Gavazzi *et al.* concluded that, to first order, the present colours and radii of galaxies can be linked to a

NASA/ESA/HUBBLE HERITAGE TEAM

single parameter — their present mass. In particular, they pointed out that the morphologies of galaxies exhibit little dependence on their structural properties. Therefore, such factors as environment and initial spin induce only second-order effects on the overall evolution of galaxies. Surprisingly, Gavazzi *et al.* note that the correlation between the radii and the luminosities of galaxies seems to differ little, if at all, between relatively isolated galaxies and galaxies that are located in rich clusters. They conclude from these results that gravitational interactions between galaxies may have played a lesser part than previously believed.

A similar result was obtained by Girardi *et al.*³, who divided observations of galaxies in the Virgo cluster into subregions: an inner region within a radius $R = 0.5$ megaparsec (Mpc); an intermediate shell with $0.5 < R < 1$ Mpc; and an outer zone with $R > 1$ Mpc from the cluster centre. In all three of these regions, Girardi *et al.* found that galaxies obeyed similar luminosity–radius relations. In other words, galaxy evolution does not seem to be strongly affected by environment.

To check whether the luminosity–radius relation of galaxies is indeed not strongly correlated with galaxy environment, I have compared⁴ the radii and the luminosities of the 80 brightest galaxies within a distance of 10 Mpc (33 million light years) from the Sun. These data show that nearby galaxies seem to exhibit the same luminosity–radius relation as do the galaxies in great clusters such as those of Virgo and Coma. Furthermore, these nearby galaxies seem to show no obvious correlations between their luminosity–radius relation and their current environment. In particular, no dependence is found on the mass density of the local neighbourhood as defined by Karachentsev and Makarov⁵.

The mounting volume of evidence discussed above suggests that galaxies constitute an (almost) one-parameter family based on their mass, with little or no indication of a major dependence on their environment. This conclusion poses several challenges to the prevailing theory of hierarchical galaxy merging. But this is not a theory that will crumble easily. One is reminded of the saying by the Danish poet Piet Hein: “Problems worthy of attack prove their worth by hitting back.”

Sidney van den Bergh is at the Dominion Astrophysical Observatory, Herzberg Institute of Astrophysics, National Research Council of Canada, Victoria, British Columbia V9E 2E7, Canada.

e-mail: sidney.vandenbergh@nrc-cnrc.gc.ca

1. Disney, M. J. *et al.* *Nature* **455**, 1082–1084 (2008).
2. Gavazzi, G., Pierini, D. & Boselli, A. *Astron. Astrophys.* **312**, 397–408 (1996).
3. Girardi, M., Biviano, A., Giuricin, G., Mardirossian, F. & Mezzetti, M. *Astrophys. J.* **366**, 393–404 (1991).
4. van den Bergh, S. *Astron. Astrophys.* (in the press); preprint at <http://arxiv.org/abs/0808.3601> (2008).
5. Karachentsev, I. D. & Makarov, D. I. in *Galaxy Interactions at High and Low Redshifts* (eds Barnes, J. E. & Sanders, D. B.) 109–116 (Kluwer, 1999).

BIOGEOCHEMISTRY

Life before the rise of oxygen

Woodward W. Fischer

The discovery of molecular fossils in 2.7-billion-year-old rocks prompted a re-evaluation of microbial evolution, and of the advent of photosynthesis and rise of atmospheric oxygen. That discovery now comes into question.

Go back to Archaean time, the interval of Earth's history between about 4 billion and 2.5 billion years ago, and we're in largely unknown biological territory. Attempts to identify a fossil record of life have produced meagre results¹, and controversy persists about whether certain microfossil-like structures are of biological origin².

Almost a decade ago, however, Archaean palaeontology received a big boost with the discovery by Brocks *et al.*³ of a diverse assemblage of lipid ‘biomarkers’ in 2.7-billion-year-old geological samples from Western Australia. Biomarkers, or molecular fossils, are natural products (often hydrocarbons) whose synthesis can be linked to a specific biological origin — and, by physiological proxy, to environmental conditions. Together, this report and a subsequent study⁴ hinted at a much richer biological diversity than had previously been recognized. On page 1101 of this issue, however, Rasmussen *et al.*⁵ provide a robust challenge to the age of these biomarkers, and the palaeontological and palaeoenvironmental insights that they offered.

The suite of lipid biomarkers reported by Brocks *et al.*^{3,4} included specific hopane and sterane compounds, respectively interpreted as the membrane remnants of cyanobacteria (a group of organisms characterized by oxygen-producing photosynthesis) and of eukaryotes (cells bearing a membrane-bound nucleus and a complex cytoskeleton). This discovery was so remarkable because it pushed back the minimum time for the origin of these groups by more than 700 million years (Fig. 1). The oldest unambiguous fossil cyanobacteria were found in tidal-flat sedimentary rocks, some 2 billion years old, from Canada's Belcher Islands⁶. It is probable that the evolution of cyanobacteria occurred much earlier; they must have existed by 2.4 billion years ago⁷, because their metabolism is required, at least in part, to explain the appearance and rise of environmental oxygen at that time. But this still leaves a gap of 300 million years.

The discordance between the sterane biomarkers and the oldest accepted eukaryotic fossils is even larger. The most convincing evidence for early eukaryotes comes from ornamented and ultrastructurally complex microfossils known as acritarchs in the Roper Group of Northern Australia⁸. These rocks are about 1.5 billion years old, leaving a gap of more than a billion years between unequivocal eukaryotic fossils and sterane biomarkers.

As well as creating a yawning palaeontological divide, the lipid biomarker data^{3,4} underscored an apparent paradox concerning the relative timing between the evolution of oxygenic photosynthesis and one of the most fundamental transitions in Earth history — the appearance and rise of atmospheric oxygen. Several lines of evidence indicate that a secular

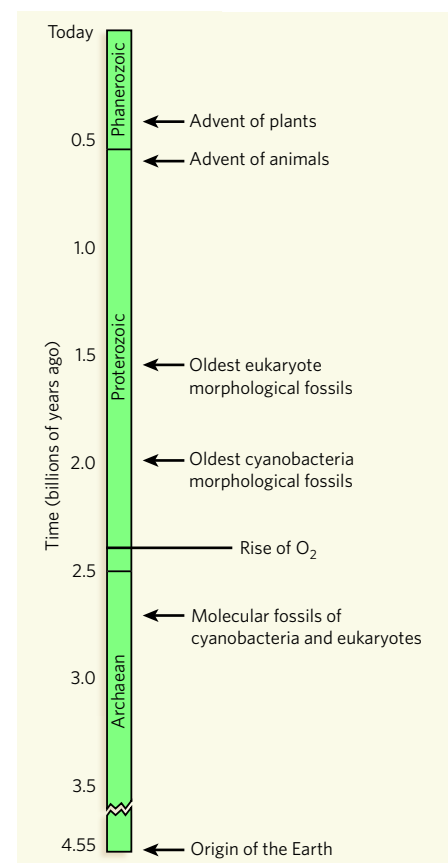


Figure 1 | The evolution of eukaryotes and cyanobacteria, and the rise of atmospheric oxygen. There are large gaps in time between the first morphological fossil evidence for cyanobacteria and eukaryotes, and the molecular-fossil occurrences inferred by Brocks *et al.*^{3,4} from lipid biomarkers. This discrepancy may disappear if the results of Rasmussen *et al.*⁵, showing that the biomarkers are younger than their host rocks, are confirmed — as may the 300-million-year delay before the later rise in atmospheric oxygen. Because oxygenic photosynthesis is the ultimate source of environmental oxygen, cyanobacteria must have evolved by a minimum of 2.4 billion years ago. This still leaves a gap of about 400 million years in the other direction, between the rise of oxygen and the first firm fossil evidence of cyanobacteria.



50 YEARS AGO

Current theory tends to emphasize the importance of interference in forgetting and to minimize the role of time lapse in the decay of the memory trace. Conrad, however, has recently shown that the immediate recall of eight-digit numbers is better when the numbers are presented and reproduced by subjects at a fast rate than when they are presented and reproduced at a slow rate ... I tested two groups of subjects for their ability to retain eight-digit numbers when presented and reproduced at different rates. Group A consisted of 26 teachers, aged 18–29, drawn from different regions of Canada. Group B consisted of 26 teachers, aged 30–55 ... [T]here is no significant difference between the two groups in the proportion of digits recalled at the fast rate, but there is a significant difference between the two groups ($P = 0.05$) in the proportion of digits recalled at the slower rate ... [I]t appears that the span of immediate memory is the same for the two age groups, but that the rate of decay of immediate memory tends to increase with age.

From *Nature* 25 October 1958.

100 YEARS AGO

Dr. F. A. Dixey pointed out that when Fritz Müller put forward, in 1879, his theory of common warning colours, or the assimilation of one distasteful form to another for the sake of mutual protection against insectivorous enemies, he recognised the probability, or even certainty, that the approach would not necessarily be one-sided, but might be convergent, each form in some respects advancing to meet the other. This suggestion, however, was never developed by Fritz Müller ... Dr. Dixey showed that there is much evidence that such reciprocal approach, or interchange of obvious characters ... does actually occur, and he exhibited some cases of mimicry the peculiar features of which are difficult to explain on any other hypothesis.

From *Nature* 22 October 1908.

change in the oxidation–reduction potential of the fluid Earth — the oceans and atmosphere — was captured in the geological record around 2.4 billion years ago⁷. The rise of oxygen can, in principle, be understood in terms of the proximal evolution of cyanobacterial oxygenic photosynthesis (and thus of oxygen production). But the molecular fossils called for an earlier origin of cyanobacteria, again some 300 million years before the rise of oxygen. This gap is approximately two orders of magnitude too large for standard geochemical thinking to accommodate, and much effort has been expended in developing models in which the time lag can be explained by first-order changes in chemical interactions between the solid and the fluid Earth⁹. But given Rasmussen and colleagues' results⁵, are such models required?

The biggest analytical challenge for those undertaking Archaean biomarker studies is contamination by younger hydrocarbons. Although Archaean rock samples may contain up to several per cent organic carbon by weight, biomarker compounds are present at only trace concentrations — parts per billion or less — and potential sources of contamination are ever-present in our petroleum-filled world. It was difficult for Brocks *et al.*^{3,4} to show with certainty that the extracted biomarkers were indigenous and syngenetic (that is, the timing of their synthesis corresponded to the age of the rock), but the biomarker abundance and distribution made a reasonable case against contamination.

However, one piece of evidence was at odds with an indigenous interpretation. The carbon isotope ratios ($^{13}\text{C}/^{12}\text{C}$) of the extracted lipid hydrocarbons did not match those of the solvent-resistant, macromolecular, residual organic carbon — termed kerogen — present in the rocks. Late Archaean kerogens are unique in the context of Earth history in that they commonly have carbon isotope ratios several per cent lower than those of organic carbon found in younger sedimentary deposits¹⁰. The kerogens analysed by Brocks *et al.*⁴ contained this unique isotopic signature, whereas the lipid biomarkers did not. Two hypotheses are compatible with this relationship. The first interprets the lipid biomarkers as younger contamination. The second posits that the biomarkers are indeed indigenous, but that the lipid hydrocarbons (oil) released during geological burial and heating of the sediments were derived from a different source from that which produces the bulk of the residual kerogen, and therefore would not share the same isotopic composition. This latter view was taken by Brocks *et al.*⁴.

The outstanding question, then, is whether the oil generated by these organic-rich sedimentary rocks was derived from a different isotopic source from the kerogen. Rasmussen *et al.*⁵ have addressed the problem by making use of new technology, the NanoSIMS ion microprobe (secondary ion mass spectrometry with 50-nanometre resolution). The advantage offered by NanoSIMS over standard, bulk-rock

analytical methods is the ability to assay, *in situ*, the carbon isotopic composition with a spatial resolution fine enough to resolve isotopic differences between micrometre-scale textures present in the rock.

Working on organic-rich samples from one of the Late Archaean sedimentary deposits in Western Australia from which the lipid biomarkers were first reported, the authors measured carbon isotope ratios of micrometre-sized particles of kerogen and pyrobitumen (residues of solidified petroleum). The pyrobitumen fraction, which represents indigenous petroleum, carries essentially the same unique carbon isotopic composition as the kerogen, not the heavier isotopic ratios of the extracted lipid hydrocarbons. This result reveals that the molecular fossils extracted from these samples probably came from contamination that was introduced some time after these rocks experienced their peak metamorphic temperatures about 2.15 billion years ago.

So does this study⁵ nullify the lipid-biomarker evidence for oxygenic photosynthesis some 300 million years before the rise of atmospheric oxygen, and does it close the gap between the morphological and molecular-fossil records of the evolution of eukaryotes? Not yet. Since the appearance of the papers by Brocks and colleagues^{3,4}, there have been other reports of lipid biomarkers — including hopanes and steranes — in sedimentary rocks deposited in other parts of the world before the rise of oxygen^{11–13}. The rocks concerned have very different geological histories, and there are insufficient data to say whether contamination also affected these studies.

The creative breakthrough offered by Rasmussen *et al.*⁵, however, is an analytical approach that seeks to link the isotopic composition of extracted lipid biomarkers with that of indigenous pyrobitumen. Perhaps by serendipity, the unique isotopic composition of Late Archaean sedimentary organic matter will provide an exceedingly useful screen for contamination in future investigations of ancient molecular fossils. ■

Woodward W. Fischer is in the Division of Geological and Planetary Sciences, California Institute of Technology, Pasadena, California 91125, USA.

e-mail: wfischer@caltech.edu

1. Schopf, J. W. *Phil. Trans. R. Soc. B* **361**, 869–885 (2006).
2. Brasier, M. D. *et al. Nature* **416**, 76–81 (2002).
3. Brocks, J. J. *et al. Science* **285**, 1033–1036 (1999).
4. Brocks, J. J., Buick, R., Summons, R. E. & Logan, G. A. *Geochim. Cosmochim. Acta* **67**, 4321–4335 (2003).
5. Rasmussen, B., Fletcher, I. R., Brocks, J. J. & Kilburn, M. R. *Nature* **455**, 1101–1104 (2008).
6. Hofmann, H. J. *J. Paleontol.* **50**, 1040–1073 (1976).
7. Bekker, A. *et al. Nature* **427**, 117–120 (2004).
8. Javaux, E. J., Knoll, A. H. & Walter, M. R. *Geobiology* **2**, 121–132 (2004).
9. Kump, L. R. & Barley, M. E. *Nature* **448**, 1033–1036 (2007).
10. Hayes, J. M. in *Early Life on Earth* (ed. Bengtson, S.) 220–236 (Columbia Univ. Press, 1994).
11. Dutkiewicz, A. *et al. Geology* **34**, 437–440 (2006).
12. Sherman, L. S., Waldbauer, J. R. & Summons, R. E. *Org. Geochem.* **38**, 1987–2000 (2007).
13. Ventura, G. T. *et al. Proc. Natl Acad. Sci. USA* **104**, 14260–14265 (2007).

OBITUARY

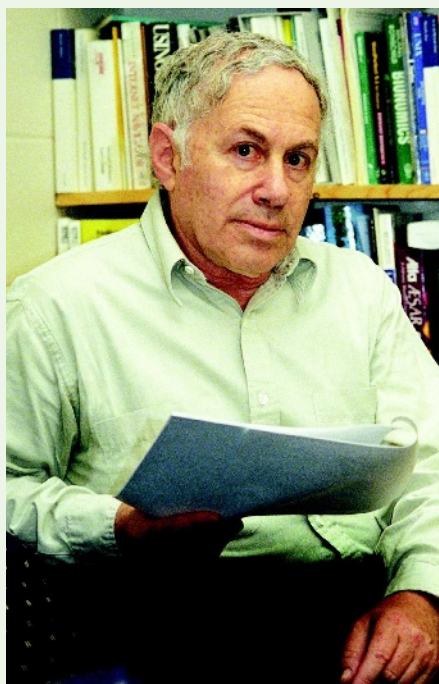
Anatol Zhabotinsky (1938–2008)

Pioneer of oscillating chemical reactions.

Anatol Zhabotinsky, the father of nonlinear chemical dynamics, passed away on 16 September after a brief illness. In many ways, his scientific career represents a microcosm of the history of Russia in the second half of the twentieth century. Born in Moscow at the height of the Stalinist purges, Zhabotinsky was able to enrol in the prestigious Moscow State University in 1955, during the brief window that opened for Jews in the years following Stalin's death in 1953. Although not a religious man, Zhabotinsky was proud of his Jewish heritage and refused to change his surname to "something more Russian", even when other members of his immediate family did so to improve their prospects in an anti-Semitic society.

It was as a graduate student at Moscow State that Zhabotinsky first learned of the phenomenon, now known as the Belousov–Zhabotinsky (BZ) reaction, for which he was to become famous. In the early 1950s, Boris Belousov, a military research chemist studying the effects of poison gases and radiation on humans, had stumbled upon the fact that a mixture of potassium bromate, citric acid and cerium ions exhibits periodic colour changes. These oscillations indicated that the chemical state of the system was changing in a rhythmic way, rather than proceeding monotonically from a starting point to an end point, as happens in most chemical reactions. Belousov tried to publish his results in peer-reviewed journals, but eventually gave up after referees and editors insisted that such behaviour contradicted the Second Law of Thermodynamics. He instead published a one-page description of his observations in an obscure conference proceedings on radiation medicine. He circulated a recipe for the reaction as a sort of samizdat among colleagues in Moscow, and then, apparently, returned to more applied studies.

A decade after Belousov's discovery, Zhabotinsky was starting his doctoral research under the direction of the biochemist Simon Schnoll. Zhabotinsky wanted to study rhythmic behaviour in glucose metabolism, but Schnoll told him that the materials required were in short supply and suggested that he take a look at Belousov's recipe (which two earlier graduate students had had little success with). Zhabotinsky, with his characteristic experimental skill and care, was soon observing chemical oscillations. He improved the recipe by substituting malonic acid for citric acid, and showed that the source of the colours was the ceric ions, rather than bromine as proposed by Belousov. He wrote up his results and sent them to Belousov for



comment, receiving a supportive note in return. Attempts to establish personal contact with Belousov proved unsuccessful, however, even after Zhabotinsky's work was published and Belousov's contributions were lauded. The two never met face to face, despite working only a few kilometres apart. Zhabotinsky always suspected that Belousov, who had lost many friends in the Stalinist purges and who was employed at a secret military establishment, was wary of establishing 'extracurricular' relationships. Belousov died in 1970.

The discovery of oscillating reactions revolutionized the way that scientists thought about chemical dynamics. Indeed, Ilya Prigogine — who received the 1977 Nobel Prize in Chemistry, in part for demonstrating that chemical systems far from equilibrium can exhibit periodic oscillations — regarded the BZ reaction as the most important scientific discovery of the twentieth century, surpassing quantum theory and relativity. Whether or not one accepts this assessment, it is clear that the discovery of a 'simple' chemical reaction that displays periodic temporal and spatial behaviour had far-reaching consequences, even leading to a greater understanding of the processes that underlie life itself, such as biological clocks and morphogenesis.

Zhabotinsky's role was to make the scientific world aware of the importance of a phenomenon that might have been relegated to an intriguing parlour trick or lecture

demonstration. He discovered early on that a thin, unstirred layer of BZ solution gives rise to beautiful spiral patterns of chemical concentration (see, for example, <http://heracles.chem.wvu.edu/gallery.html>), which were later observed to resemble those seen in aggregating slime moulds, newly fertilized frog egg cells and fibrillating hearts. At a conference on biological and biochemical oscillators held in Prague in 1968, only weeks before Soviet tanks rolled into the city, Zhabotinsky brought the BZ system to the attention of Western scientists, and the field of nonlinear chemical dynamics was born. Together with Belousov, Genrikh Ivanitsky, Valentin Krinsky and Albert Zaikin, he received the 1980 Lenin Prize, at that time the Soviet Union's highest scientific award, for his work.

Perhaps because of his Jewish heritage, or perhaps because of his tendency to make politically incorrect remarks, Zhabotinsky was not allowed to travel outside the Soviet bloc until the arrival of perestroika at the end of the 1980s. When I arranged a lecture tour of the United States for him, he was surprised to discover that a chemical ordered at the beginning of his 10-day visit could arrive by the end of that period. Impressed, he asked whether a longer stay at Brandeis University might be possible. A visit of one year was arranged, starting in July 1991, but he never returned to his home country.

At Brandeis, he pursued his interest in oscillatory chemical reactions, demonstrating, for example, that chemical waves in the BZ reaction obey the same laws of refraction at an interface as light waves, but that reflection of chemical waves is not perfectly mirror-like. He also returned to his initial fascination with biophysics, collaborating with neuroscientists such as John Lisman on models of synaptic transmission. With his vibrant intelligence and encyclopaedic knowledge, he was a major contributor to the education of a generation of students and postdocs, and was well known for his unwillingness to accept a vague response when a more exact answer could be dredged out by persistent questioning. When allegedly novel phenomena were described to him, he was frequently heard to remark "This was found in Russia by so-and-so thirty years ago", despite his alienation from his native land.

Like the complex chemical reactions that so intrigued him, Zhabotinsky's life — and that of his beloved and not-so-beloved Russia — underwent many ups and downs, occasionally becoming chaotic. The world of science is poorer today for his loss.

Irving R. Epstein

Irving R. Epstein is in the Department of Chemistry, Brandeis University, Waltham, Massachusetts 02454, USA.
e-mail: epstein@brandeis.edu

J. BROWN/BRANDEIS UNIV.

Q&A

SYSTEMS BIOLOGY

Metabonomics

Jeremy K. Nicholson and John C. Lindon

Organisms often respond in complex and unpredictable ways to stimuli that cause disease or injury. By measuring and mathematically modelling changes in the levels of products of metabolism found in biological fluids and tissues, metabonomics offers fresh insight into the effects of diet, drugs and disease.

What are the origins of the field?

The idea that changes in tissues and biological fluids are indicative of disease goes back at least as far as ancient Greece. Diagnostic 'urine charts' were widely used from the Middle Ages onwards (Fig. 1). These charts linked the colours, smells and tastes of urine to various medical conditions. Such features are, of course, metabolic in origin. Metabonomics, and the related field of metabolomics, uses modern techniques to analyse samples, but the basic principle of relating chemical patterns to biology is the same.

What's the difference between metabonomics and metabolomics?

The distinction is mainly philosophical, rather than technical. Metabonomics broadly aims to measure the global, dynamic metabolic response of living systems to biological stimuli or genetic manipulation. The focus is on understanding systemic change through time in complex multicellular systems. Metabolomics seeks an analytical description of complex biological samples, and aims to characterize and quantify all the small molecules in such a sample. In practice, the terms are often used interchangeably, and the analytical and modelling procedures are the same.

How did modern-day metabonomics begin?

There were two, largely independent, starting points. The first was metabolic-control analysis, a mathematical method developed in the 1960s for modelling metabolism in cells.

This required metabolite concentrations to be quantified, and so methods were developed to do this — often using gas chromatography (GC) or GC coupled to mass spectrometry (MS). The second contributing factor was the development of nuclear magnetic resonance (NMR) spectroscopy. By the mid-1980s, NMR was sensitive enough to identify metabolites in unmodified biological fluids. This led to the discovery that altered metabolite

profiles are caused by certain diseases or by adverse side effects to drugs. MS techniques were also developed for profiling biological fluids. But metabonomics really took off with the realization that pattern-recognition methods (also known as chemometrics or multivariate statistical analysis) could help to interpret the complex data sets that result from these studies.

How does this approach fit in with systems biology?

Metabonomics dovetails beautifully with the philosophy of systems biology, because it provides a 'top-down', integrated view of biochemistry in complex organisms, as opposed to the traditional 'bottom-up' approach that investigates the network of interactions between genes, proteins and metabolites in individual cell types. A problem with systems biology is that each level of biological organization and control — genomics, gene expression, protein expression and metabolism — operates on a markedly different timescale from the others, making it difficult to find causal linkages. Moreover, environmental and lifestyle factors greatly influence metabolism, making it difficult to disentangle their effects from gene-related outcomes. Environmental influences on gene expression also make it hard to interpret genomic data, for example to predict an individual's susceptibility to diseases. Metabonomics cuts through these problems by monitoring the global outcome of all the influencing factors, without making assumptions about the effect of any single contribution to that outcome. Yet in so doing, the individual contributions can be teased out.

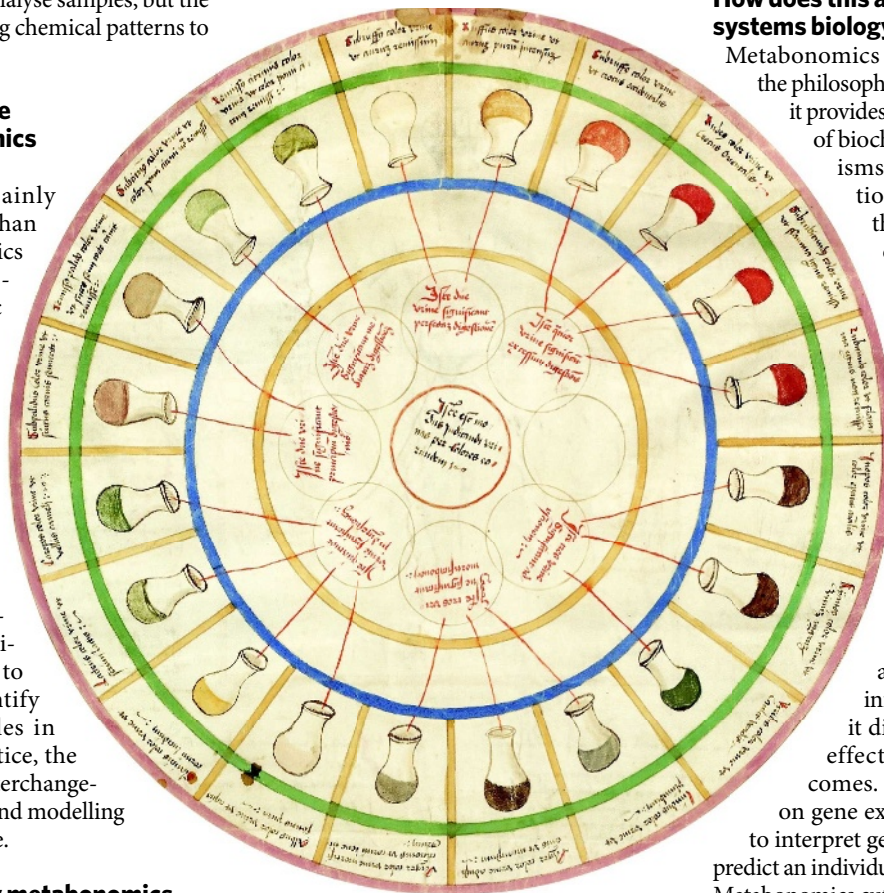


Figure 1 | Metabonomics of yore. This urine wheel was published in 1506 by Ullrich Pinder, in his book *Epiphania Medicorum*. It describes the possible colours, smells and tastes of urine, and uses them to diagnose disease.

What analytical techniques are used for metabonomics?

Usually NMR spectroscopy and MS. NMR is generally used to detect hydrogen atoms in metabolites. In a typical biological-fluid sample, all hydrogen-containing molecules in the sample — including nearly all metabolites — will give an ^1H NMR spectrum, as long as they are present in concentrations above the detection limit. The NMR spectrum of a biological fluid is therefore the superposition of the spectra of all of the metabolites in the fluid (Fig. 2). An advantage of NMR is that the biological fluid doesn't require any physical or chemical treatment prior to the analysis. MS studies, on the other hand, usually require the metabolites to be separated from the biological fluid before detection, typically by using high-performance liquid chromatography (or modern variants). Alternatively, the metabolites can be chemically modified to make them more volatile, so that GC-MS can be used.

What are the other pros and cons of these techniques?

Both methods yield information on a wide range of metabolites in a single measurement, without having to preselect which analytes to detect. Furthermore, both can be used to identify the metabolites' structures, and to measure the relative and absolute concentrations of the molecules (although NMR is more reliable for determining concentrations). MS is usually more sensitive than NMR, but many compounds in complex mixtures give variable responses in MS experiments, which can be highly misleading. Because NMR doesn't damage analytes, it is particularly useful for studying metabolite levels in intact tissues, such as biopsy samples, which can then be used in further experiments. The non-destructive nature of NMR also enables the dynamics and sequestration of metabolites in tissue samples to be observed; such information is lost in MS experiments, because this technique disrupts the structures and interactions of molecular complexes.

How are the resulting data interpreted?

The spectra of samples from organisms of interest (such as those with a specific disease) are compared with those from controls, so that the spectral features caused by the disease state can be determined. Precise metabolite concentrations are not always necessary to formulate hypotheses about the mechanism of the disease. But if only a few metabolites turn out to be important, then knowledge of their concentrations might be instructive, and these can subsequently be measured.

Doesn't the quantity and complexity of the data make interpretation impossible?

Not if you use multivariate statistical analysis — a collection of techniques in which the

intensities of peaks in a spectrum are used as coordinates in multidimensional plots of metabolic activity. This allows distinctive patterns in the data to be identified more easily than by looking at the original spectra. The multidimensional plots can even be reduced to two- or three-dimensional graphs, to help visualize any clustering of points that might be used to characterize the data (Fig. 2d).

What exactly do these analyses involve?

One frequently used technique, known as principal-components analysis, attempts to find a small set of variables that explain the original data set. Alternatively, in what are known as supervised methods, mathematical models are derived from a 'training' set of multiparametric data, so that individual biological samples can be classified (for example as being characteristic of a disease state). A widely used supervised method is called partial least squares (PLS) analysis. PLS is often combined with discriminant analysis — a method that finds a linear combination of features that can be used to classify data into sets. The combination of PLS with discriminant analysis defines a surface that can be placed in a multidimensional plot to separate data into classes.

How are metabolites associated with disease states identified?

There are various methods based on NMR and MS, but one exciting new approach is an NMR technique termed statistical total correlation spectroscopy (STOCSY). In this method, correlations are found between the intensities of spectral peaks across a cohort of samples. This enables all the peaks from a given metabolite to be identified, so that the structure of that molecule can be determined. The beauty of STOCSY is that additional information can be gleaned by examining lower correlations between peaks, or even negative correlations, as these indicate connections between two or more molecules that are involved in the same biochemical process. Statistical heterospectroscopy is a powerful extension of STOCSY that allows the co-analysis of data sets acquired using combinations of different spectroscopic techniques.

Once metabolites have been identified, what then?

They can be used as diagnostic biomarkers for biological events. Metabonomics thus allows real-world, medical observations to be related to data from all the other '-omics' technologies, which are less directly related to actual biological outcomes than metabolism is (Fig. 3, overleaf). And because samples of biological fluids (usually urine or blood) can be collected fairly easily, the time-dependent fluctuations of metabolites that occur in response to disease, drug effects or other stimuli can be easily studied in detail.

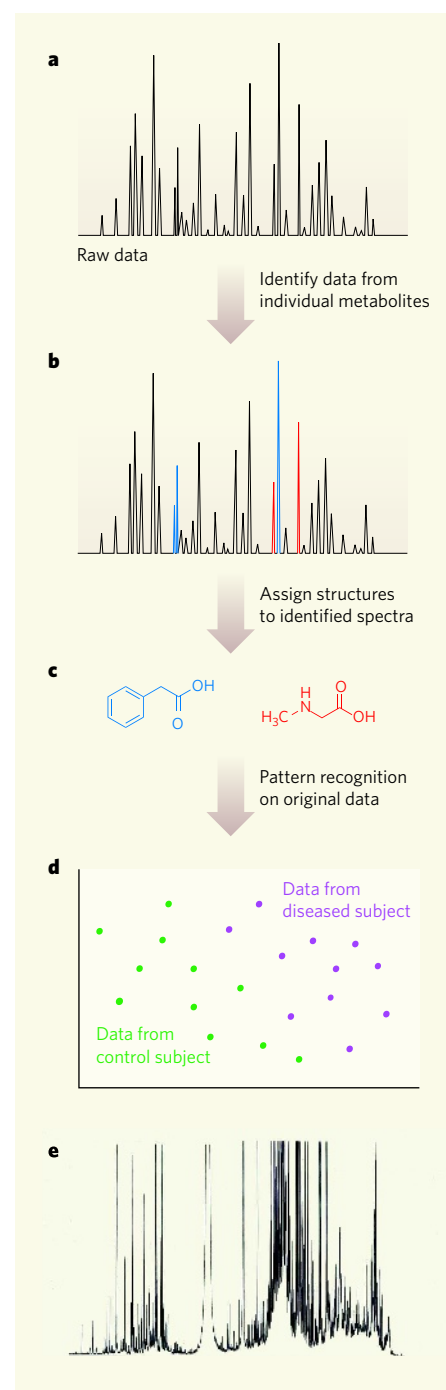


Figure 2 | The discovery process in metabonomics.

Metabonomics analyses the metabolites in biological fluids to determine the metabolic response of an organism to a physiological stimulus. **a**, A typical procedure might start with the NMR spectrum of a biological fluid, which contains signals from hundreds of metabolites. **b**, The individual spectra for each metabolite are identified. **c**, This enables the structure of the metabolites to be determined. **d**, Pattern-recognition techniques can be used to work out how the spectra of biological fluids from individuals who have a disease differ from those of healthy subjects. Here, 'principal-component analysis' has reduced multivariate data to a two-dimensional plot. **e**, Although the procedure above is conceptually simple, this NMR spectrum of human urine reveals how complicated the raw data can be.

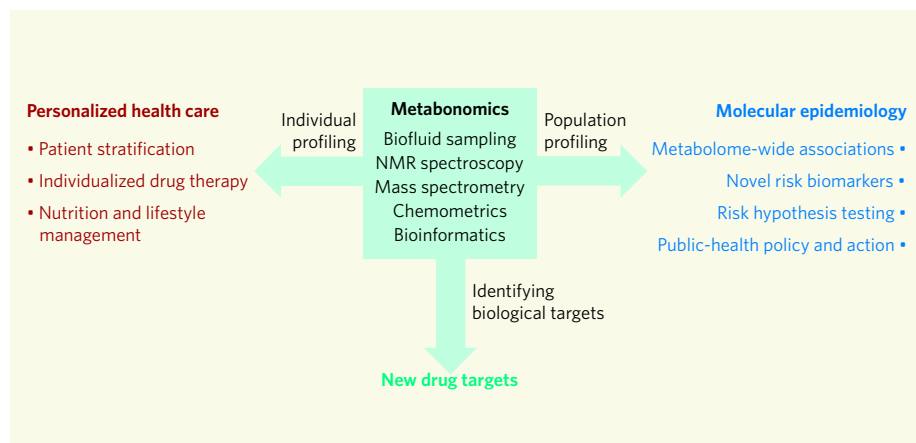


Figure 3 | Applications of metabolomics. There are three broad areas that might benefit from metabolomics. Metabolic profiling of individuals could be used in personalized health care to work out patients' susceptibilities to disease or their responses to medicines, and to tailor their lifestyles and drug therapies accordingly. Metabolic profiling of populations could allow the development of 'molecular epidemiology' — the ability to work out the susceptibilities of specific groups to disease. This might allow metabolites to be identified as risk identifiers (biomarkers) for diseases, with implications for health screening programmes. Finally, by identifying biochemical pathways for disease, metabolomics could uncover new targets for drug discovery.

Are there any drawbacks to metabolomics?

The need to use complex data-interpretation techniques and combinations of analytical methods isn't ideal. Another problem is that the number of metabolites produced by any given system cannot be predicted — compare this with genome sequencing, where the number of genes is known. But this problem isn't insurmountable, and is similar to that of other fields, such as epigenetics.

Is there an equivalent of the Human Genome Project?

Yes indeed. The Human Metabolome Project in Canada strives to provide a repository of all human metabolites. So far, it has collected a few thousand of these compounds and created an accompanying database of spectroscopic data. Both the repository and the database are publicly available as resources for metabolic research. Similarly, the LIPID Metabolites And Pathways Strategy (LIPID MAPS) consortium in the United States is attempting to characterize all the lipids in the human macrophage, and currently has a database of more than 10,000 characterized substances. Such resources are invaluable, but what they can't reveal are the all-important dynamic interactions of metabolites in space and time, or how metabolite profiles vary across human populations.

How has metabolomics been used for drug discovery?

Its use in evaluating drug toxicity has been comprehensively assessed by the Consortium for Metabonomic Toxicology (COMET), a collaboration between five pharmaceutical companies and Imperial College London. COMET produced a database of NMR spectra of rodent urine and blood serum, taken from

animals that had been dosed with a range of toxins. This database now forms the basis of a successful system for predicting the liver and kidney toxicity of drug candidates. A follow-up project, COMET-2, is currently investigating the detailed biochemical mechanisms of toxicity, and seeks a better understanding of inter-subject variation in metabolomic analyses. It has also been demonstrated in animals that the metabolic profile of an individual's urine can be used to predict both how that individual will metabolize a given drug and their susceptibility to the side effects of that drug. If this principle can be applied widely in humans, it will have enormous implications for personalized health care and in optimizing clinical trials.

What insights into diseases have emerged?

Many metabolites have been identified as flags for a variety of diseases. They include markers for schizophrenia found in cerebrospinal fluid; markers of coronary-artery occlusion found in plasma; and even indicators of spinal-trauma-induced infertility in men, found in seminal fluid. The concentrations of these metabolites often vary in response to therapy for the disease in question. Furthermore, the biomarkers carry information about the sites and mechanisms of disease. Metabolites have also been found that act as indicators for disease risk, individual susceptibility, or as markers of recovery from an illness.

What else has metabolomics taught us?

It has revealed much about humans' symbiotic relationship with their gut flora. Disruption of gut microbial activity seems to be central to certain diseases in the gut, liver, pancreas and even the brain. But there are thousands of

species of microorganism (the microbiome) in the human gut, and it is impossible to study each one in isolation to work out what they do. Large research programmes have therefore been devised to study the combined genetic structure of humans and their microbes — the metagenome. This genetic information is invaluable, but it says nothing about the actual activity of the microbial community, or its interactions with the host at a physiological level. Metabonomic modelling, statistically coupled to metagenomic analysis, has allowed possible communication networks between species to be identified, and has also shown which metabolic pathways are strongly influenced by which members of the microbiome.

What will be the next big thing in metabolomics?

We believe it will be metabolome-wide association (MWA) studies, which identify relationships between metabolic profiles and disease risks for both individuals and populations. In this approach, the metabolic profiles of thousands of people are captured spectroscopically, and are then statistically linked to disease risk factors such as obesity and diabetes. The beauty of MWA is that vast, well-curated collections of biological-fluid samples are available from epidemiological studies of many disease processes. These can be explored retrospectively for markers of disease risk. We need such indicators as part of a strategy for disease prevention, which is essential to drive down health costs as the world's population increases. Effective prevention requires knowledge of risk, which for most modern diseases involves unfavourable gene–environment interactions. Understanding how these interactions affect metabolic regulation and phenotype allows new testable hypotheses to be developed about future disease risk. It is in this field that metabolomics might prove to be strongest and of most value to humanity. ■

Jeremy K. Nicholson and John C. Lindon are in the Department of Biomolecular Medicine, Imperial College London, Sir Alexander Fleming Building, South Kensington, London SW7 2AZ, UK.
e-mails: j.nicholson@imperial.ac.uk;
j.lindon@imperial.ac.uk

FURTHER READING

- Nicholson, J. K. & Wilson, I. D. Understanding 'global' systems biology: Metabolomics and the continuum of metabolism. *Nature Rev. Drug Discov.* **2**, 668–676 (2003).
- Dethlefsen, L., McFall-Ngai, M. & Relman, D. A. An ecological and evolutionary perspective on human-microbe mutualism and disease. *Nature* **449**, 811–818 (2007).
- Lenz, E. M. & Wilson, I. D. Analytical strategies in metabolomics. *J. Proteome Res.* **6**, 443–458 (2007).
- Wishart, D. S. et al. HMDB: The Human Metabolome Database. *Nucleic Acids Res.* **35**, D521–D526 (2007).
- Holmes, E., Wilson, I. D. & Nicholson, J. K. Metabolic phenotyping in health and disease. *Cell* **134**, 714–717 (2008).
- Holmes, E. et al. Human metabolic phenotype diversity and its association with diet and blood pressure. *Nature* **453**, 396–400 (2008).

The mental wealth of nations

Countries must learn how to capitalize on their citizens' cognitive resources if they are to prosper, both economically and socially. Early interventions will be key.

John Beddington, Cary L. Cooper, John Field, Usha Goswami, Felicia A. Huppert, Rachel Jenkins, Hannah S. Jones, Tom B. L. Kirkwood, Barbara J. Sahakian and Sandy M. Thomas

To prosper and flourish in a rapidly changing world, we must make the most of all our resources — both mental and material. Globalization and its associated demands for competitiveness are increasing the pressures in our working lives. Added to this are the demands from evolving family structures and increased care responsibilities, both for children and for older relatives. And increased life expectancy in most industrialized nations means that ever greater numbers of people will be at risk of degenerative disorders in older age.

The UK Government Office for Science is this week announcing the findings of a peer-reviewed study: the Foresight Project on Mental Capital and Wellbeing. This used

state-of-the-art scientific and other evidence to investigate the challenges and opportunities that lie ahead in the next 20 years. The report provides an independent assessment that is intended to inform policy-makers both in the United Kingdom and around the world.

The project tracks the implications of future challenges to our mental development from cradle to grave. Taking two years to complete, it has involved more than 450 experts and stakeholders from many disciplines and from 16 countries. Eighty peer-reviewed papers summarize the latest evidence, and international workshops have brought together experts and policy-makers to discuss what could be done to address the challenges.

Although our project focused on the United Kingdom, the challenges of depression, dementia, learning difficulties and mental ill-health are evident worldwide. The project therefore has far-reaching implications for the course of an individual's life, for societies and for nations. Five reports synthesize the evidence base; and a final report sets out the overall findings and options for policy, which are summarized here. All reports are available at <http://tinyurl.com/49jonm>. Box 1 shows some of the key findings.

Defining mental capital

The project looked at two main aspects of mental development: mental capital and mental well-being. Mental capital encompasses both cognitive and emotional resources. It includes people's cognitive ability; their flexibility and efficiency at learning; and their 'emotional intelligence', or social skills and resilience in the face of stress. The term therefore captures a key dimension of the elements that establish how well an individual is able to contribute to society and to experience a high quality of life.

Mental well-being, on the other hand, is a dynamic state that refers to individuals' ability to develop their potential, work productively and creatively, build strong and positive relationships with others and contribute to their community.

However, the two concepts are intimately linked both throughout life and across different areas of the project. Positive emotional states or a generally positive approach to life are associated with greater curiosity, more flexible thinking and a greater openness to learning, and these qualities are particularly important

during the development of mental capital in childhood and adolescence. Early learning in children can increase their resilience to stress and common mental disorders. Later in life, this resilience helps to engender well-being at work and into old age. And older individuals who report higher levels of well-being also have better cognitive function, even when adjustment has been made for other possible explanatory factors, such as socio-demographic variables, health and lifestyle¹.

Thus, how a nation develops and uses its mental capital not only has a significant effect on its economic competitiveness and prosperity, it is also important for mental health and well-being and social cohesion and inclusion. Because they are so closely linked, mental health and well-being should both therefore be considered when developing policies and designing interventions.

The project comprised two key stages: understanding the evidence and identifying ways forward. Three particular areas of focus were: childhood development; mental health and well-being at work; and making the most of cognitive resources in older age.

Progression through life

Evidence on childhood learning difficulties shows that, left untreated, very small initial differences in the sensory processing systems used by the brain in learning can lead to significant problems later in life². Subtle impairments in auditory processing, for example, can give rise to developmental dyslexia, which can have significant negative effects on a person's passage through life. Moreover, the interactive nature of the developing brain means that a problem in one sensory area can affect development in other areas. By late childhood it can be hard to identify the core problem. The cognitive problems experienced by a child with a learning difficulty can lead to poor self-esteem, or to frustration that results in the child disengaging from learning and lacking the motivation to learn. If a problem is identified later in life, it is often harder for an individual to realize the full potential of their mental capital and well-being.

The brain undergoes significant structural and functional changes during adolescence³: the formation of new synapses peaks at around 9–12 years, followed by some 'pruning' of synapses that are surplus or underused. In

Box 1 | Key findings

● Boosting brain power in young and old

There is huge scope for improving mental capital through different types of intervention. The genetic contribution to mental capital is well below 50% in childhood, rising to more than 60% in adulthood and old age.

● What science could do in the early years

Cognitive neuroscience is already uncovering neural markers, or biomarkers, that can reveal learning difficulties as early as in infancy.

● Early detection of mental disorders

The challenge of tackling mental ill-health is considerable. There is great potential in improving diagnosis and treatment, and in addressing social risk factors such as debt.

● Learning must continue throughout life

This can have a direct effect on mental health and well-being across all age groups, and has particular promise in older people.

● Changing needs for a changing workplace

The workforce is changing both in demographics and in the demands placed on it. Workers' mental well-being is an important factor when attempting to improve the mental capital of economies and societies.

addition, adolescents go through significant emotional, hormonal and behavioural adjustment, and are particularly prone to risk-taking behaviour, such as drug and alcohol use. As the brain is still developing, such behaviour is particularly injurious to it at this stage³, with long-term effects. Neuroimaging and neuropsychological studies indicate that substance use during adolescence is associated with neural disadvantages, particularly in the networks involved in learning, attention and executive function.

To help address these issues, the report came up with three main recommendations. First, training should be available for parents and teachers about issues in child development and how to help children who have learning difficulties to flourish. In addition, a higher priority needs to be placed on supporting children with these difficulties, as well as their carers. Finally, more emphasis needs to be placed on early identification and treatment of intrinsic learning difficulties such as dyslexia and dyscalculia

— essentially dyslexia for numbers.

Much more can be done to improve mental well-being as children develop into adults. Occupational professionals should be closely integrated with primary-care givers, and workplaces can promote mental health through well-being audits and widespread availability of flexible working. In addition, demand should be stimulated for continued learning in both individuals and employers by raising awareness and providing incentives. New technologies are also available and constantly being developed to personalize learning. For adults who have problems with depression and alcohol use, for instance, use of best-practice treatments should become more widespread. Treatments for these and other problems should encompass social support (such as working with financial advisers to help reduce debt) and address the underlying social risk factors.

As people move into older age, learning should continue to be promoted and actively encouraged, as this can protect against

cognitive decline. In particular, information technology has an important role in helping people to overcome the memory effects of dementias. Governments should also be encouraged to enable and empower people to work longer if they so wish. Older people should also be involved in making these and other policy decisions. In addition, efforts should be made to tackle the negative social stereotypes associated with old age.

Biological basis

As in the case of learning difficulties, mental illnesses should also be a particular target for early identification and prompt action. Neural, genetic and cognitive biomarkers can play an important part in the early identification of many of these diseases.

Alzheimer's disease, for example, accounts for about 60% of all dementia cases. The plaques and neurofibrillary tangles that characterize the disease begin to form many years before any clinical signs start to appear⁴. A range

of biomarkers already exists. For instance, altered levels of proteins such as tau protein and A β 42 (a pathogenic form of amyloid) in cerebrospinal fluid can identify patients in the early stages of Alzheimer's disease⁵. Structural magnetic resonance imaging (MRI) can also be used to measure brain atrophy, particularly in regions that are affected in Alzheimer's, such as the entorhinal cortex and hippocampus^{6,7}. Genes have also been shown to play a part in the development of the disease, particularly the E4 variant of the apolipoprotein E (refs 8, 9). Furthermore, new insights into underlying mechanisms, coupled with the use of more selective cohorts in clinical trials (see below), will be essential in the development of effective drugs, including those to enhance cognition or for neuroprotection. This will also allow patients to be diagnosed earlier, allowing them to seek treatment and support, and plan for their futures.

Mechanistic studies coupled with novel biomarkers could also be important in the

treatment of depression. One effective way is to measure brain activity in the left amygdala and ventromedial prefrontal cortex using functional MRI. By monitoring brain activity in response to being shown happy or sad faces, researchers can differentiate between unipolar and bipolar depression¹⁰, disorders that require very different treatments.

Similarly, differences in the subgenual anterior cingulate identified by structural and functional neuroimaging can predict the likely responsiveness to treatment^{11,12}.

Implications for future research

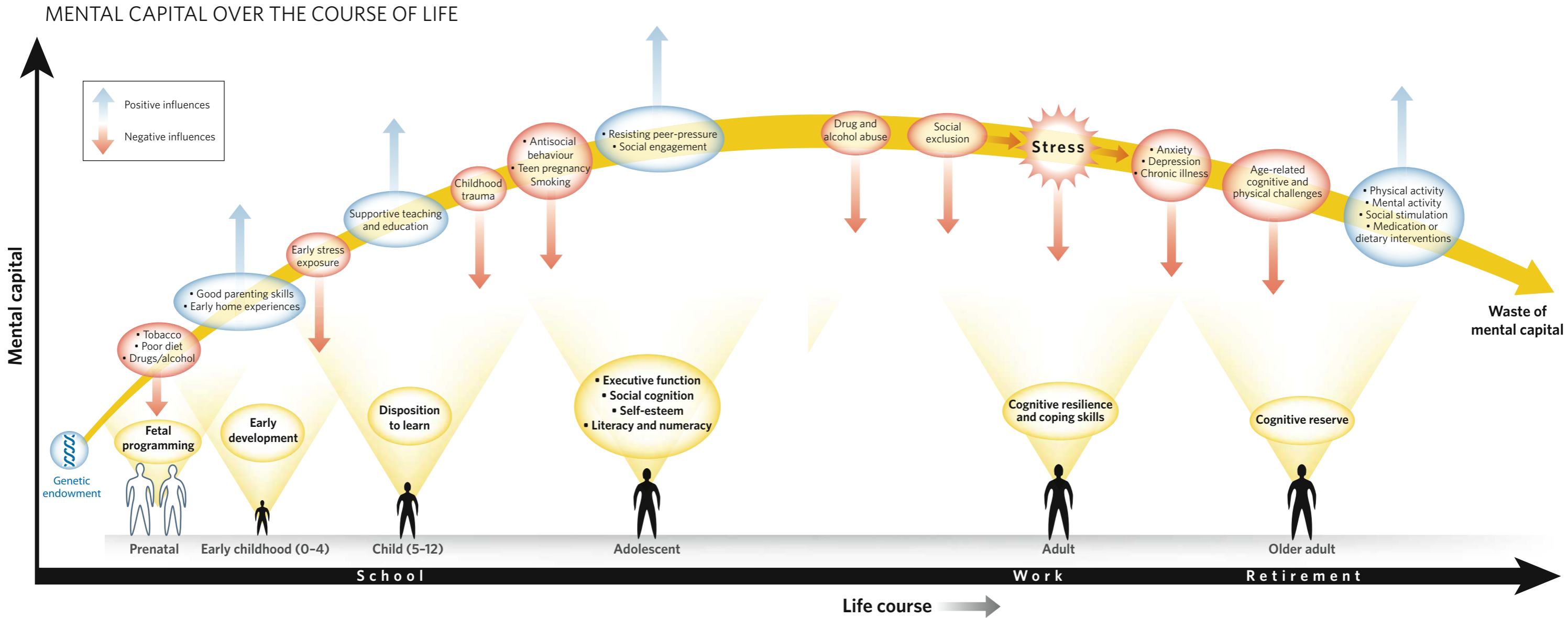
Future research will be key to improving both mental capital and mental well-being, as well as diagnosis and treatment of disease.

One strategy for identifying complex combinations of risk factors and for validating potential biomarkers of learning difficulties, dementia and depression is the development of large, publicly available cohorts. Cohorts containing tens of thousands of people have helped

to identify susceptibility genes in diseases such as type 2 diabetes. In much the same way, an international collaboration to generate similar cohorts for various mental illnesses could prove very valuable. Large public–privately funded consortia could play an important part here.

The challenge also extends to the research community. Research is needed to identify factors that directly affect our mental capital and well-being, as well as those that are merely associated with them. To deepen our understanding of causes and effects, multidisciplinary longitudinal studies involving genetics, neuroscience, social risk factors and behaviour will be required. For instance, we need to explore the underlying neuroscientific basis of the strong associations between mental disorders and lone parenting¹³, bullying¹⁴ and debt¹⁵.

Significant gaps also exist in medications for the treatment of mental disorders, particularly antipsychotics, antidepressants,



mood stabilizers, and neuroprotective agents for Alzheimer's. Improved techniques and longer-acting medications are needed to tackle addiction, and developing these will require innovative approaches. Furthermore, although many treatments are available for depression, most work by increasing levels of monoamine neurotransmitters. More effective therapies with different mechanisms of action and fewer side effects are urgently needed.

Behavioural and other non-pharmaceutical interventions for improving well-being also need to be developed. This would encompass the treatment of people affected and prevention of the disorders in high-risk groups, as well as the enhancement of mental capital and well-being for all members of the population.

A range of skills and behaviours is crucial in empowering people to develop and maintain their mental capital and well-being. These include executive function (self-regulation) skills; an eagerness to learn, train and retrain throughout life; the resilience to cope with stress and life events; and behaviours that can promote a healthy lifestyle and protect against decline in old age. Multidisciplinary research, in the natural and social sciences, will be needed to investigate the systematic relations between these skills, to determine how they can best be developed.

The costs of inaction

Our project shows that governments and others have tremendous opportunities to create environments in which mental capital and well-being flourish. However, failure to act could have severe consequences.

Already, we have found that learning difficulties such as dyslexia, which affects up to 10% of children, reduce the probability of achieving good grades at school¹⁶. In turn, disengagement with the educational system can lead to behavioural problems, social exclusion and crime and reduced employment prospects (which in turn make mental ill-health more likely). This in turn can have adverse consequences for cognitive function throughout life. In addition, developmental dyscalculia is currently the poor relation of dyslexia, with a much lower public profile². But the consequences of dyscalculia are at least as severe as those for dyslexia.

Mental ill-health is more widespread than many realize, with 16% of adults in Britain having a common mental disorder such as depression at any one time¹⁷. Worldwide, the prevalence of having any mental disorder in the year prior to assessment varies from 4% in Shanghai in China to 26% in the United States¹⁸.

Furthermore, depression is the leading global cause of years lived with disability¹⁹. The annual costs from mental ill-health in England alone are about £36 billion (US\$62 billion) for economic costs, rising to £77 billion when wider impacts are included, such as a reduction in quality of life²⁰. Measures to improve mental health would therefore yield benefits well in excess of costs.

Future demographic changes mean that this figure could rise substantially. The age profile of the population will change as life expectancy increases and fecundity levels fall. The UK Office of National Statistics²¹ estimates that, by 2071, the number of people older than 65 could double to nearly 21.3 million, and those aged 80 and over could more than treble to 9.5 million. This would probably lead to much more cognitive decline and dementia, and an expenditure time bomb: over the next 30 years, the number of people with dementia in the United Kingdom could double to 1.4 million, and costs to the UK economy could treble to more than £50 billion²². In addition, as the number of older people increases, there is a pressing case to take steps to prevent the wastage of their mental capital that occurs in part through marginalization.

The effects of mental capital and well-being on an individual's life course are profound, and governments have considerable scope to more fully realize a long-term and strategic perspective that spans the life course. As discussed earlier, this Foresight project has delivered some specific policy recommendations. It will now be for the UK government to consider how best to take these forward.

However, a cross-governmental approach is needed to realize the full benefits. Early intervention in education could provide benefits for reducing crime, improving productivity in work, and reducing pressure on health and care systems by preserving mental capital in older age. Departments will need to work together more closely. And interventions may have long timescales before they see any returns. Implementing these recommendations will require significant changes in the nature of governance, placing mental capital and well-being at the heart of policy-making.

John Beddington is the UK government chief scientific adviser and head of the Government Office for Science in London

Cary L. Cooper is pro-vice chancellor and professor of organizational psychology and health at Lancaster University

John Field is co-director of the Centre for Research in Lifelong Learning, Stirling Institute of Education, University of Stirling

Usha Goswami is director of the Centre for Neuroscience in Education, and professor of

education at the University of Cambridge
Felicia A. Huppert is professor of psychology in the Department of Psychiatry and director of the Well-being Institute at the University of Cambridge

Rachel Jenkins is professor of epidemiology and international mental health policy at the Institute of Psychiatry, King's College London, and director of the WHO Collaborating Centre on Research and Training

Hannah S. Jones is a member of the Foresight project team in the Government Office for Science

Tom B. L. Kirkwood is director of the Institute for Ageing and Health, Newcastle University

Barbara J. Sahakian is professor of clinical neuropsychology, University of Cambridge

Sandy M. Thomas is head of the Foresight programme at the Government Office for Science in London

1. Llewellyn, D. J., Lang, I. A., Langa, K. M., McWilliams, B. C. & Huppert, F. A. *Age Ageing* (in the press).
2. Goswami, U. *Foresight Mental Capital and Wellbeing Project. Learning Difficulties: Future Challenges* (Government Office for Science, 2008).
3. Kirkwood, T., Bond, J., May, C., McKeith, I. & Teh, M. *Foresight Mental Capital and Wellbeing Project. Mental Capital through Life: Future Challenges* (Government Office for Science, 2008).
4. Albert, M. S. & Blacker, D. *Annu. Rev. Clin. Psychol.* **2**, 379–388 (2006).
5. Blennow, K. & Hampel, H. *Lancet Neurol.* **2**, 605–613 (2003).
6. Chua, T. C., Wen, W., Slavin, M. J. & Sachdev, P. S. *Curr. Opin. Neurol.* **21**, 83–92 (2008).
7. Schott, J. M. *et al. Neurology* **65**, 119–124 (2005).
8. Papassotiropoulos, A. *et al. Science* **314**, 475–478 (2006).
9. Reiman, E. M. *et al. Neuron* **54**, 713–720 (2007).
10. Phillips, M. L. & Vieta, E. *Schizophr. Bull.* **33**, 893–904 (2007).
11. Mayberg, H. S. *et al. NeuroReport* **8**, 1057–1061 (1997).
12. Chen, C. H. *et al. Neuropsychopharmacology* **33**, 1909–1918 (2008).
13. Cooper, C. *et al. Psychol. Med.* **38**, 335–342 (2008).
14. Bebbington, P. E. *et al. Br. J. Psychiatr.* (in the press).
15. Jenkins, R. *et al. Psychol. Med.* **38**, 1485–1493 (2008).
16. Challen, A., King, D., Knapp, M. & McNally, S. *Foresight Mental Capital and Wellbeing Project. The Economic Consequences of Specific Learning Difficulties and the Cost-Effectiveness of Prevention Strategies* (Government Office for Science, 2008).
17. Jenkins, R. *et al. Foresight Mental Capital and Wellbeing Project. Mental Health: Future Challenges* (Government Office for Science, 2008).
18. The WHO World Mental Health Survey Consortium. *J. Am. Med. Assoc.* **291**, 2581–2590 (2004).
19. World Health Organization www.who.int/mental_health/management/depression/definition/en
20. Sainsbury Centre for Mental Health *Economic and Social Costs of Mental Illness in England* (2003).
21. Office for National Statistics *National Population Projections 2006-based* (ONS, 2008).
22. Knapp, M. *et al. Dementia UK* (Alzheimer's Society, 2007).

Author information

Reprints and permissions information is available at www.nature.com/reprints. The authors declare competing financial interests: details accompany the full-text HTML version of the paper at www.nature.com/nature. Correspondence should be addressed to S.M.T. (sandy.thomas@dius.gsi.gov.uk).

MicroRNA-10b and breast cancer metastasis

Arising from: L. Ma, J. Teruya-Feldstein & R. A. Weinberg *Nature* **449**, 682–688 (2007)

MicroRNAs regulate messenger RNA expression but are frequently dysregulated in tumours. Ma *et al.*¹ report that overexpression of microRNA-10b (miR-10b) initiates invasion and metastasis in models of breast cancer and that its expression in primary breast carcinomas correlates with clinical progression. We tested this in patients with primary breast cancer, of whom 92 had nodal metastases at diagnosis and 127 were node-negative. We found no significant association between miR-10b levels and metastasis or prognosis. Although we concede that miR-10b may have a biological effect in a few cells at the growing edge of a tumour, we believe that it is unlikely to correlate in whole tumour samples with clinical progression.

Ma *et al.*¹ found that miR-10b was upregulated in metastatic breast cancer cell lines compared with primary human mammary epithelial cells or spontaneously immortalized MCF-10A cells, and that its overexpression initiated invasion and metastasis in xenograft models of breast cancer. Their Fig. 6 (ref. 1) shows increased miR-10b in tumours of 9 out of 18 metastasis-positive patients, compared with none of 5 patients without metastasis—hence their conclusion that miR-10b is associated with metastasis outcome. However, their patient group was small, the type of metastasis not defined, and data on clinical variables, age and follow-up limited.

Ma *et al.*¹ converted the relative amount of miR-10b in tumour samples, a continuous variable, into a series of discrete variables and then applied a chi-squared test, applicable to categorical variables, instead of a non-parametric Mann–Whitney test.

We studied 219 consecutive patients with early breast cancer, for whom fresh frozen samples and long-term follow-up were available. We examined the population-based outcome, following the REporting recommendations for tumour MARKer prognostic studies (REMARK)², measuring expression of miR-10b by real-time PCR and normalizing our values to three controls—the small nucleolar RNAs RNU 43, RNU 44 and RNU 48—and to normal tissue.

We also found less miR-10b expression in patients without metastasis ($n = 114$) than in normal breast tissue ($n = 10$). However, unlike Ma *et al.*¹, we found lower miR-10b expression in patients with distant relapse ($n = 61$), regional relapse ($n = 11$) and local recurrence ($n = 33$). If miR-10b has a role in metastasis, we would expect a positive correlation with factors such as the presence or number of tumour-involved lymph nodes at the time of diagnosis; however, no significant correlation was found (Table 1). MiR-10b expression did not correlate with development of distant metastases, recurrence-free survival or distant-relapse-free survival³, or with recurrence-free survival and breast-cancer-specific survival⁴ (Fig. 1). Whereas Ma *et al.*¹ found that miR-10b overexpression increases tumour size and invasiveness, we find that its expression correlates inversely and significantly with tumour size and grade.

Table 1 | Relationship between miR-10b, miR-210 and clinico-pathological variables

	Correlation with clinico-pathological variables	
	miR-210	miR-10b
Categorical variable		
Nodal status* (node-positive = 92; node-negative = 127)	$Z = -1.13, P = 0.26$	$Z = -0.52, P = 0.61$
Grade†	$\chi^2 = 6.66, P = 0.04$	$\chi^2 = 9.40, P = 0.01$
Continuous variable‡		
ER ELISA	$\rho = -0.11, P = 0.11$	$\rho = 0.09, P = 0.19$
Tumour size (cm)	$\rho = 0.08, P = 0.22$	$\rho = -0.20, P = 0.003$

ER, oestrogen receptor.
* Mann–Whitney test.
† Chi-squared test.
‡ Spearman rank test.

In the same patient cohort, increased expression of hypoxia-induced microRNA miR-210 correlated with poor prognosis⁵. Our negative result for miR-10b is therefore unlikely to be due to problems of extraction, stability or analysis. Although the RNU6B control used by Ma *et al.*¹ is reported to vary more between tissues than RNU 44 or RNU 48 (ref. 6), we found that the four control genes had comparable stability in a subset of 48 samples and 5 pooled controls.

Our results are supported by microRNA array data. Downregulated miR-10b expression in breast carcinoma⁷ was found to be associated with vascular invasion but not with oestrogen-receptor status or nodal involvement. Expression profile comparison of microRNAs and mRNAs in primary breast cancers indicated that miR-10b is associated with the prognostically favourable ‘luminal A’ subtype⁸.

We conclude that miR-10b overexpression does not correlate with distant metastases or poor prognosis in breast cancer. Studies using many more patients with full clinicopathological information are needed before conclusions can be drawn about the function of miR-10b.

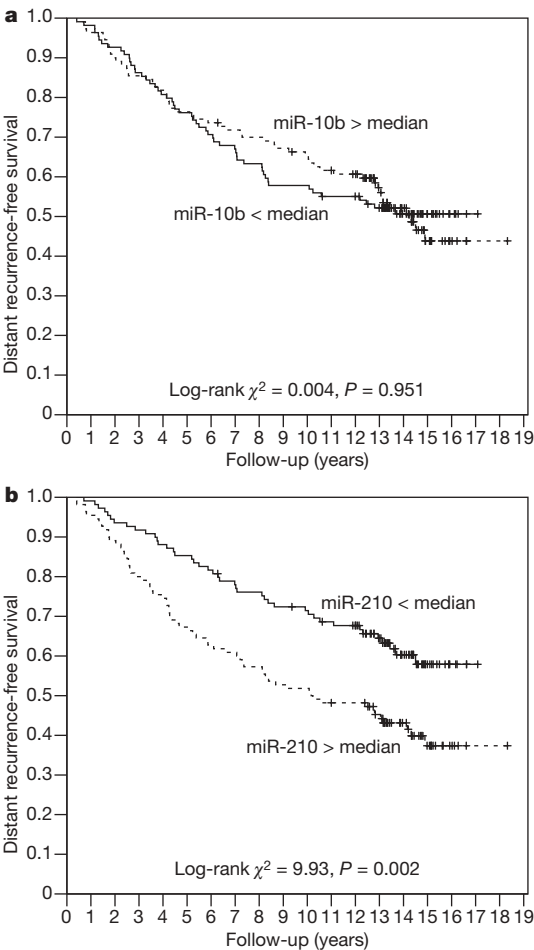


Figure 1 | miR-10b is not significantly associated with metastasis. Kaplan–Meier curves showing the relationship of miR-10b (a) and miR-210 (b) with distant recurrence-free survival (as defined by STEEP criteria³) of 219 patients with breast cancer. The results of a log-rank test are shown; miR-210 and miR-10b expression levels were stratified by median values. P values are computed by the use of log-rank test to miR-210 and miR-10b expression levels stratified by median values.

METHODS

A group of 219 patients with early first primary breast cancer, treated in Oxford from 1989 to 1992, were studied (ethical approval from the local Research Ethics Committee). RNA was extracted from liquid-nitrogen-frozen breast tumour samples or normal breast tissue using Tri-reagent (Sigma-Aldrich). MicroRNA expression was assessed by real-time PCR with TaqMan MicroRNA assay protocol (Applied Biosystems) using 5 ng total RNA per gene (for further details and methods, see ref. 5). Fold changes in microRNA expression were determined by the $2^{-\Delta\Delta C_t}$ method, normalizing the results to normal breast tissue and expression of RNU 43, RNU 44 and RNU 48.

Harriet E. Gee¹, Carme Camps², Francesca M. Buffa¹, Stefano Colella², Helen Sheldon¹, Jonathan M. Gleadle³, Jiannis Ragoussis² & Adrian L. Harris¹

¹Cancer Research UK Molecular Oncology Laboratories, Weatherall Institute of Molecular Medicine, University of Oxford, John Radcliffe Hospital, Oxford OX3 9DS, UK.

e-mail: adrian.harris@medonc.ox.ac.uk

²Genomics Group, Wellcome Trust Centre for Human Genetics, The Henry Wellcome Building for Genomic Medicine, University of Oxford, Oxford OX3 7BN, UK.

³Department of Medicine and Flinders University, Flinders Medical Centre, Bedford Park, South Australia, 5042, Australia.

Received 19 March; accepted 21 August 2008.

1. Ma, L., Teruya-Feldstein, J. & Weinberg, R. A. Tumour invasion and metastasis initiated by microRNA-10b in breast cancer. *Nature* **449**, 682–688 (2007).
2. McShane, L. M. *et al.* REporting recommendations for tumour MARKer prognostic studies (REMARK). *Br. J. Cancer* **93**, 387–391 (2005).
3. Hudis, C. A. *et al.* Proposal for standardized definitions for efficacy end points in adjuvant breast cancer trials: the STEEP system. *J. Clin. Oncol.* **25**, 2127–2132 (2007).
4. Tan, E. Y. *et al.* Cytoplasmic location of factor-inhibiting hypoxia-inducible factor is associated with an enhanced hypoxic response and a shorter survival in invasive breast cancer. *Breast Cancer Res.* **9**, R89 (2007).
5. Camps, C. *et al.* hsa-miR-210 is induced by hypoxia and is an independent prognostic factor in breast cancer. *Clin. Cancer Res.* **14**, 1340–1348 (2008).
6. Wong, L., Lee, K., Russell, I. & Chen, C. *Endogenous Controls for Real-Time Quantitation of miRNA Using TaqMan MicroRNA Assays* <<https://products.appliedbiosystems.com/ab/en/US/adirect/ab?cmd=catNavigate2&catID=604344&tab=Literature>> (2007).
7. Iorio, M. *et al.* MicroRNA gene expression deregulation in human breast cancer. *Cancer Res.* **65**, 7065–7070 (2005).
8. Blenkiron, C. *et al.* MicroRNA expression profiling of human breast cancer identifies new markers of tumour subtype. *Genome Biol.* **8**, R214 (2007).

doi:10.1038/nature07362

Ma et al. reply

Replying to: H. E. Gee *et al.* *Nature* **455**, doi:10.1038/nature07362 (2008)

Gee *et al.* contest that microRNA-10b is not a prognostic marker for metastasis risk in breast cancer¹. However, their observations do not bear on the pro-metastatic roles of microRNA-10b (miR-10b) as we described them², nor do they undermine our conclusions¹.

We used a variety of human metastatic cancer lines and tumours to discover which microRNA, if any, was correlated with metastatic behaviour, rather than to find a prognostic clinical marker. Our functional analysis of miR-10b suggested that it is mechanistically important², but we have no idea whether its expression in early-stage whole-tumour specimens can predict clinical progression. The discovery by Gee *et al.*¹ that miR-10b is not a useful prognostic marker is therefore not surprising.

Whereas Gee *et al.*¹ studied early-stage cancers, we analysed 23 primary tumour samples obtained at the time of mastectomy, when both lymph node and distant metastases had already developed. On the basis of these findings², we concluded that miR-10b expression increased in metastatic breast tumours—not that its expression in unfractionated bulk populations of tumours could predict metastatic relapse². MiR-10b is also significantly upregulated in human glioblastoma multiforme³ and in pancreatic adenocarcinomas⁴, two types of highly invasive and/or metastatic cancers.

Our results indicate that induction of miR-10b expression is probably not an early event during tumour progression, but occurs after activation of the Twist transcription factor at a later stage². We propose that expression of Twist and miR-10b in many primary tumours is likely to be only local and transient, occurring in a minority of cells such as those in the invasive front of a breast tumour that are responding to contextual signals from nearby stromal cells to undergo an epithelial–mesenchymal transition. However, it is technically difficult to capture this minority population of cancer cells. Almost all microRNA expression analyses performed so far have been

on bulk individual tumours consisting of neoplastic cells and recruited non-neoplastic stromal cells. These are therefore liable to underestimate or even misinterpret the range of messenger RNAs and microRNAs expressed by a small minority of the cells within such tumours.

Meaningful clinical data may eventually come from determination of which types of primary tumour cell do and do not express Twist and miR-10b when exposed to certain heterotypic contextual signals of stromal origin. Tumours that behave badly clinically might be those that upregulate Twist and miR-10b in response to such signals, but this is still years away from miR-10b as a prognostic marker. We agree with Gee *et al.*¹ that sufficient numbers of patients with long-term follow-up are needed for clinical correlative studies of molecular markers in breast cancer and other diseases.

Li Ma¹, Julie Teruya-Feldstein² & Robert A. Weinberg¹

¹Whitehead Institute for Biomedical Research and Department of Biology, Massachusetts Institute of Technology, Cambridge, Massachusetts 02142, USA.

e-mail: weinberg@wi.mit.edu

²Department of Pathology, Memorial Sloan-Kettering Cancer Center, New York, New York 10021, USA.

1. Gee, H. E. *et al.* MicroRNA-10b and breast cancer metastasis. *Nature* **455**, doi:10.1038/nature07362 (2008).
2. Ma, L., Teruya-Feldstein, J. & Weinberg, R. A. Tumour invasion and metastasis initiated by microRNA-10b in breast cancer. *Nature* **449**, 682–688 (2007).
3. Ciafre, S. A. *et al.* Extensive modulation of a set of microRNAs in primary glioblastoma. *Biochem. Biophys. Res. Commun.* **334**, 1351–1358 (2005).
4. Bloomston, M. *et al.* MicroRNA expression patterns to differentiate pancreatic adenocarcinoma from normal pancreas and chronic pancreatitis. *J. Am. Med. Assoc.* **297**, 1901–1908 (2007).

doi:10.1038/nature07363

Can light be stopped in realistic metamaterials?

Arising from: K. L. Tsakmakidis, A. D. Boardman & O. Hess *Nature* **450**, 397–401 (2007)

Tsakmakidis *et al.*¹ extend earlier work (for example, refs 2, 3) in proposing a novel metamaterial waveguide structure that can stop broadband light, producing so-called “trapped rainbows”. The authors make the bold assumption that metamaterial loss can be ignored: but material loss, with dispersion, is an inherent feature of negative-index metamaterials (for example, refs 4, 5); any realistic model must include loss and dispersion to satisfy the fundamental principle of causality⁶. Here we revisit the authors’ predictions¹ and show that even when an arbitrarily small metamaterial loss is introduced, it is impossible to stop the light; moreover, we find that all slow-light modes in such structures give impractically large propagation losses.

We investigate the TM₂ (where TM is transverse-magnetic) mode, analysed by Tsakmakidis *et al.*¹, and calculate the complex waveguide dispersion curves in the presence of metamaterial loss and dispersion. This mode arises from the complex solution to the transcendental equation derived from Maxwell’s equations and guidance conditions⁷. Figure 1a shows the computed TM₂ dispersion using three

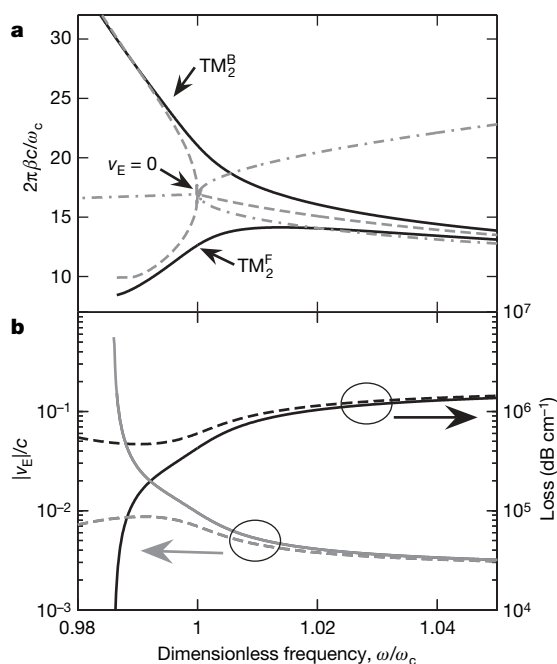


Figure 1 | Dispersion, energy velocity and propagation loss. **a**, Dispersion curves for the TM₂ modes of the waveguide structure of ref. 1. We plot the dispersion for three different models: the lossless and dispersionless model of ref. 1 (dot-dashed grey line), and models including metamaterial dispersion with $\tilde{\Gamma}=0$ (dashed grey line) and $\tilde{\Gamma}\equiv\Gamma/\omega_c=0.01$ (solid black line). A loss parameter of $\tilde{\Gamma}=0.01$ yields a figure-of-merit roughly 30 times better than has been experimentally achieved at optical frequencies and comparable to the state-of-the-art at GHz frequencies^{4,5}. **b**, The energy velocity (defined by the ratio of the spatial average of the time-averaged Poynting vector to the spatial average of the time-averaged energy density¹²) and propagation loss versus frequency for the loss model with $\tilde{\Gamma}=0.01$ for TM₂^F (solid line) and TM₂^B (dashed) modes. Clearly, the energy velocity is never zero and the propagation losses are extremely high whenever the energy velocity is below 0.1c. To better connect to the highlighted optical applications in ref. 1, the propagation loss is calculated for a critical frequency in the optical ($\omega_c/2\pi=385$ THz). However, our general findings and conclusions scale to GHz and THz. For example, at a frequency of 1 THz, the loss is approximately 1,000 dB cm^{−1} or greater; this is completely impractical as a delay element, given the corresponding energy velocity.

different models: (1) neglecting dispersion and loss (dot-dashed grey lines); (2) including dispersion but not loss (dashed grey lines); and (3) including both dispersion and loss (solid black lines). Using the unrealistic (idealized) models (1) or (2), we naturally recover the key result of ref. 1 and obtain a point of zero group velocity at a critical frequency, ω_c , where the group velocity is given by $v_g \equiv d\omega/d\beta$ (here ω is the frequency and β is the propagation constant). In model (2), in addition to the normal mode, there is also a complex mode that was neglected by Tsakmakidis *et al.*¹: it is bound to the slab but has zero total power flux and a complex propagation constant, $k \equiv \beta + i\alpha$. In model (3), we include the metamaterial loss, which is characterized through the normalized loss parameter, $\tilde{\Gamma} \equiv \Gamma/\omega_c = 0.01$ (see Methods). For this realistic case, the mode dispersion near ω_c changes dramatically: the complex mode splits in two and the normal mode pulls away from its lossless counterpart—rather than having a normal mode and a complex mode, one obtains complex forward-and-backward propagating modes, TM₂^F and TM₂^B, respectively. Evidently, the influence of material loss on mode structure is highly non-perturbative near ω_c , where even a tiny amount of loss produces large changes in the dispersion, such that the group velocity is never zero.

Group velocity and energy flux have been investigated for light propagation in lossy metamaterial waveguides^{3,8}; however, as the dispersion relation is complex in lossy systems, the meaning of the group velocity is unclear and the energy velocity (v_E), computed from modes with complex k and real ω , is a better measure of the speed of transport than either v_g or energy flux. We find that, even for arbitrarily small metamaterial loss, the energy velocity is not zero for either mode at any frequency. In Fig. 1b, we plot v_E for $\tilde{\Gamma}=0.01$; although v_E goes as low as 0.003c (where c is the speed of light in vacuum), it is never zero and the imaginary part of the propagation constant, α , is impractically large. Figure 1b shows the propagation loss for a range of optical frequencies ($\omega_c/2\pi=385$ THz), which demonstrates a propagation loss $>300,000$ dB cm^{−1} whenever $v_E < 0.01c$. To put this in context, such losses would result in 200 dB of loss for a pulse delay of only 2.6 ps at optical frequencies. Even if metamaterial losses were reduced by over two orders of magnitude from the state-of-the-art, the losses would be unacceptably high and the slowing of the light would remain unimpressive. Similar calculations for the various modes of this proposed structure and similar structures show comparable—or worse—results for all TM and TE modes.

To ensure a positive energy density, any real metamaterial must have dispersion and thus finite loss at some frequencies. Theoretically, metamaterials are never lossless, even in the presence of gain, except, perhaps, at discrete frequencies⁶. To date, no lossless metamaterial has been found, even at a single frequency.

We have shown that it is impossible to achieve zero-velocity or even practical slow-light modes in metamaterial waveguides over any appreciable bandwidth, so it is impossible to produce “trapped rainbows”¹. Also, as our findings are important even for arbitrarily small amounts of material loss, attempts to stop light in metallic structures will also fail⁹. Massive losses are also evident in slow-light propagation modes in photonic-crystal waveguides when there is even a tiny amount of unavoidable surface roughness¹⁰. Surface roughness will also result in additional loss in the metamaterial structure of Tsakmakidis *et al.*¹ and in recently proposed hybrid metamaterial–photonic-crystal structures¹¹. In all these cases, the enormous propagation loss and non-zero energy velocity is a direct consequence of the long time that the slow light ultimately spends near the potential absorbers and/or scatterers.

Methods

The permittivity and permeability of the three waveguide layers (top to bottom) are $\epsilon_i(\omega)$ and $\mu_i(\omega)$ respectively, where $i = \{1, 2, 3\}$. As in ref. 1, the permittivity and permeability of the cladding layers ($i = \{1, 3\}$) are lossless, while for the (realistic) lossy metamaterial we use the standard Drude and Lorentz medium models, respectively, with loss parameter Γ . In all calculations, we use $F = 0.6$, $\omega_p = \sqrt{6}\omega_c$, $\omega_o = \sqrt{0.9}\omega_c$ and (as in ref. 1) we take the metamaterial slab thickness to be $d/2 = 0.55c/\omega_c$; these parameters (defined in ref. 12) have been chosen so as to yield identical results to those presented in ref. 1 for $\omega = \omega_c$ when $\Gamma = 0$. In our loss model, we take $\Gamma = 0.01$ (refs 4, 5).

A. Reza¹, M. M. Dignam¹ & S. Hughes¹

¹Department of Physics, Engineering Physics and Astronomy, Queen's University, Kingston, Ontario K7L 4J1, Canada.

e-mail: dignam@physics.queensu.ca

Received 3 June; accepted 31 July 2008.

1. Tsakmakidis, K. L., Boardman, A. D. & Hess, O. 'Trapped rainbow' storage of light in metamaterials. *Nature* **450**, 397–401 (2007).
2. Shadrivov, I. V., Sukhorukov, A. A. & Kivshar, Y. S. Guided modes in negative-refractive-index waveguides. *Phys. Rev. E* **67**, 057602 (2003).

3. He, J. & He, S. Slow propagation of electromagnetic waves in a dielectric slab waveguide with a left-handed material substrate. *IEEE Microw. Wirel. Compon. Lett.* **16**, 96–98 (2005).
4. Dolling, G., Wegener, M., Soukoulis, C. M. & Linden, S. Negative-index metamaterial at 780 nm wavelength. *Opt. Lett.* **32**, 53–55 (2007).
5. Shalaev, V. M. Optical negative-index metamaterials. *Nature Photon.* **1**, 41–48 (2007).
6. Stockman, M. I. Criterion for negative refraction with low losses from a fundamental principle of causality. *Phys. Rev. Lett.* **98**, 177404 (2007).
7. Collin, R. E. *Field Theory of Guided Waves* 2nd edn (IEEE Press, 1991).
8. Alekseyev, L. V. & Narimanov, E. Slow light and 3D imaging with non-magnetic negative index systems. *Opt. Express* **14**, 11184–11193 (2006).
9. Gan, Q., Fu, Z., Ding, Y. J. & Bartoli, F. J. Ultrawide-bandwidth slow-light system based on THz plasmonic graded metallic grating structures. *Phys. Rev. Lett.* **100**, 256803 (2008).
10. Hughes, S., Ramunno, L., Young, J. F. & Sipe, J. E. Extrinsic optical scattering loss in photonic crystal waveguides: Role of fabrication disorder and photon group velocity. *Phys. Rev. Lett.* **94**, 033903 (2005).
11. He, J., Jin, Y., Hong, Z. & He, S. Slow light in a dielectric waveguide with negative-refractive-index photonic crystal cladding. *Opt. Express* **16**, 11077–11082 (2008).
12. Boardman, A. D. & Marinov, K. Electromagnetic energy in a dispersive metamaterial. *Phys. Rev. B* **73**, 165110 (2006).

doi:10.1038/nature07359

Tsakmakidis et al. reply

Replying to: A. Reza, M. M. Dignam & S. Hughes *Nature* **455**, doi:10.1038/nature07359 (2008)

Reza *et al.*¹ have confirmed our calculations and results on storing light inside metamaterial waveguides². But they claim that losses constitute an “inherent” feature of any “realistic” negative-refraction metamaterial (NR-MM), and that light can never be stopped inside such a material in a practical way. We argue that both of these assertions are incorrect.

We used a lossless NR-MM core layer, in line with ‘perfect’ lens and invisibility cloak concepts. Reza *et al.* posit that losses are always present in an NR-MM³, but this does not imply that a zero-loss NR-MM cannot be designed^{4,5}. Those conclusions³ were based on specific assumptions for the variation of the refractive index imaginary part (n_i) with frequency. Assuming a realistic frequency variation for n_i (but different to the one in ref. 3), based on adjacent absorptive and gain resonances and obeying causality and Kramers-Kronig relations⁴, leads to just such a design of a lossless metallic NR-MM, giving a refractive index of $n = -1$. One can also deploy a broadband photonic crystal in its negative-refraction regime, with vanishing losses for a chosen frequency window. Moreover, when electromagnetically induced chirality or some other gain mechanism is deployed it leads to a specific zero-loss frequency window (see ref. 5, for example). Hence the suggestion by Reza *et al.* that the conclusions of ref. 3 are general and applicable to all NR-MM designs, as well as their statements that NR-MMs are never lossless and that no lossless metamaterial has ever been found are, at least, a bit misleading.

We also disagree that light cannot be stopped inside realistic NR-MMs. The mechanism we described for trapping light in NR-MMs relies critically on the presence of negative Goos-Hänchen phase shifts², which are also realizable using materials with no negative effective refractive index; our use of a negative-index material in storing THz light shows how this general scheme works. It has been recently shown independently that light can be ‘trapped rainbow’-stopped inside realistic NR-MMs, either by using ‘spoof’ surface plasmons in graded metallic structures—practically lossless in the THz regime^{6,7}—or simply by deploying (lossless) photonic crystals in their negative-refraction regime⁸. The former may serve as a way to stop light in metamaterials, by analogy with negative-refraction-enabled subwavelength imaging using plasmonic lenses. Such numerical studies unavoidably model—via the inherent staircase

approximations in the representation of the material structure—the influence of surface roughness.

Light does not need to assume precisely zero group (or energy) velocity before it can be practically deployed for slow-light applications and/or regarded as “stored light”⁹. It can be ‘trapped rainbow’-stopped inside NR-MMs even in the presence of losses^{10,11}. The 30 dB μm^{-1} losses that Reza *et al.* calculate¹ are not at all unusual for slow-light waveguides; ways to drastically reduce higher optical losses, such as 72 dB μm^{-1} (ref. 12) or 50 dB μm^{-1} (ref. 10), which are typical for slow-light plasmonic waveguides, have been reported^{12,13}. Also, splitting of the mode band diagram and the loss of the mode degeneracy point² in lossy waveguides with negative optical parameters is well-known¹⁴ and has been noted for NR-MM waveguides¹⁵.

The ‘trapped rainbow’ technique is a powerful method for storing light inside engineered waveguides and is the only way to do so. It should lead to the first experimental demonstration of ‘true’—that is, not via atomic or acoustic coherences—storage of photons inside solid-state structures, at room temperature.

Kosmas L. Tsakmakidis¹, Alan D. Boardman² & Ortwin Hess¹

¹Advanced Technology Institute and Department of Physics, Faculty of Engineering and Physical Sciences, University of Surrey, Guildford GU2 7XH, UK.

²Photonics and Nonlinear Science Group, Joule Laboratory, Department of Physics, University of Salford, Salford M5 4WT, UK.

e-mail: O.Hess@surrey.ac.uk

1. Reza, A., Dignam, M. M. & Hughes, S. Can light be stopped in realistic metamaterials? *Nature* **455**, doi:10.1038/nature07359 (2008).
2. Tsakmakidis, K. L., Boardman, A. D. & Hess, O. 'Trapped rainbow' storage of light in metamaterials. *Nature* **450**, 397–401 (2007).
3. Stockman, M. I. Criterion for negative refraction with low optical losses from a fundamental principle of causality. *Phys. Rev. Lett.* **98**, 177404 (2007).
4. Webb, K. J. & Thylén, L. Perfect-lens-material condition from adjacent absorptive and gain resonances. *Opt. Lett.* **33**, 747–749 (2008).
5. Kästel, J., Fleischhauer, M., Yelin, S. F. & Walsworth, R. L. Tunable negative refraction without absorption via electromagnetically induced chirality. *Phys. Rev. Lett.* **99**, 073602 (2007).
6. Gan, Q., Fu, Z., Ding, Y. J. & Bartoli, F. J. Ultrawide-bandwidth slow-light system based on THz plasmonic graded metallic grating structures. *Phys. Rev. Lett.* **100**, 256803 (2008).

7. Fu, Z., Gan, Q., Ding, Y. J. & Bartoli, F. J. From waveguiding to spatial localization of THz waves within a plasmonic metallic grating. *IEEE J. Select. Top. Quantum Electron.* **14**, 486–490 (2008).
8. He, J., Hong, Z. & He, S. Slow light in a dielectric waveguide with negative-refractive-index photonic crystal cladding. *Opt. Express* **16**, 11077–11082 (2008).
9. Zhu, Z., Gauthier, D. J. & Boyd, R. W. Stored light in an optical fiber via stimulated Brillouin scattering. *Science* **318**, 1748–1750 (2007).
10. Wang, Y., Islam, R. & Eleftheriades, G. V. An ultra-short contra-directional coupler utilizing surface plasmon-polaritons at optical frequencies. *Opt. Express* **14**, 7279–7290 (2006).
11. Zhao, L. & Yelin, S. F. 'Trapped rainbow' in graphene. Preprint at (<http://arXiv.org/abs/0804.2225v1>) (2008).
12. Karalis, A., Lidorikis, E., Ibanescu, M., Joannopoulos, J. D. & Soljačić, M. Surface-plasmon-assisted guiding of broadband slow and subwavelength light in air. *Phys. Rev. Lett.* **95**, 063901 (2005).
13. Karalis, A. *et al.* Surface-plasmon index guided (SPIG) waveguides and surface-plasmon effective index guided (SPEIG) waveguides. US Patent 20050259936 (2005).
14. Burke, J. J., Stegeman, G. I. & Tamir, T. Surface-polariton-like waves guided by thin, lossy metal films. *Phys. Rev. B* **33**, 5186–5201 (1986).
15. He, J. & He, S. Slow propagation of electromagnetic waves in a dielectric slab waveguide with a left-handed material substrate. *IEEE Microw. Wirel. Compon. Lett.* **16**, 96–98 (2006).

doi:10.1038/nature07360

Comprehensive genomic characterization defines human glioblastoma genes and core pathways

The Cancer Genome Atlas Research Network*

Human cancer cells typically harbour multiple chromosomal aberrations, nucleotide substitutions and epigenetic modifications that drive malignant transformation. The Cancer Genome Atlas (TCGA) pilot project aims to assess the value of large-scale multi-dimensional analysis of these molecular characteristics in human cancer and to provide the data rapidly to the research community. Here we report the interim integrative analysis of DNA copy number, gene expression and DNA methylation aberrations in 206 glioblastomas—the most common type of primary adult brain cancer—and nucleotide sequence aberrations in 91 of the 206 glioblastomas. This analysis provides new insights into the roles of *ERBB2*, *NF1* and *TP53*, uncovers frequent mutations of the phosphatidylinositol-3-OH kinase regulatory subunit gene *PIK3R1*, and provides a network view of the pathways altered in the development of glioblastoma. Furthermore, integration of mutation, DNA methylation and clinical treatment data reveals a link between *MGMT* promoter methylation and a hypermutator phenotype consequent to mismatch repair deficiency in treated glioblastomas, an observation with potential clinical implications. Together, these findings establish the feasibility and power of TCGA, demonstrating that it can rapidly expand knowledge of the molecular basis of cancer.

Cancer is a disease of genome alterations: DNA sequence changes, copy number aberrations, chromosomal rearrangements and modification in DNA methylation together drive the development and progression of human malignancies. With the complete sequencing of the human genome and continuing improvement of high-throughput genomic technologies, it is now feasible to contemplate comprehensive surveys of human cancer genomes. The Cancer Genome Atlas aims to catalogue and discover major cancer-causing genome alterations in large cohorts of human tumours through integrated multi-dimensional analyses.

The first cancer studied by TCGA is glioblastoma (World Health Organization grade IV), the most common primary brain tumour in adults¹. Primary glioblastoma, which comprises more than 90% of biopsied or resected cases, arises *de novo* without antecedent history of low-grade disease, whereas secondary glioblastoma progresses from previously diagnosed low-grade gliomas¹. Patients with newly diagnosed glioblastoma have a median survival of approximately 1 year with generally poor responses to all therapeutic modalities². Two decades of molecular studies have identified important genetic events in human glioblastomas, including the following: (1) dysregulation of growth factor signalling via amplification and mutational activation of receptor tyrosine kinase (RTK) genes; (2) activation of the phosphatidylinositol-3-OH kinase (PI(3)K) pathway; and (3) inactivation of the p53 and retinoblastoma tumour suppressor pathways¹. Recent genome-wide profiling studies have also shown remarkable genomic heterogeneity among glioblastoma and the existence of molecular subclasses within glioblastoma that may, when fully defined, allow stratification of treatment^{3–8}. Albeit fragmentary, such baseline knowledge of glioblastoma genetics sets the stage to explore whether novel insights can be gained from a more systematic examination of the glioblastoma genome.

Results

Data release. As a public resource, all TCGA data are deposited at the Data Coordinating Center (DCC) for public access (<http://cancergenome.nih.gov/>). TCGA data are classified by data type (for example, clinical, mutations, gene expression) and data level to allow structured access to this resource with appropriate patient privacy protection. An overview of the data organization is provided in the Supplementary Methods, and a detailed description is available in the TCGA Data Primer (http://tcga-data.nci.nih.gov/docs/TCGA_Data_Primer.pdf).

Biospecimen collection

Retrospective biospecimen repositories were screened for newly diagnosed glioblastoma based on surgical pathology reports and clinical records (Supplementary Fig. 1). Samples were further selected for having matched normal tissues as well as associated demographic, clinical and pathological data (Supplementary Table 1). Corresponding frozen tissues were reviewed at the Biospecimen Core Resource (BCR) to ensure a minimum of 80% tumour nuclei and a maximum of 50% necrosis (Supplementary Fig. 1). DNA and RNA extracted from qualified biospecimens were subjected to additional quality control measurements (Supplementary Methods) before distribution to TCGA centres for analyses (Supplementary Fig. 2).

After exclusion based on insufficient tumour content ($n = 234$) and suboptimal nucleic acid quality or quantity ($n = 147$), 206 of the 587 biospecimens screened (35%) were qualified for copy number, expression and DNA methylation analyses. Of these, 143 cases had matched normal peripheral blood or normal tissue DNAs and were therefore appropriate for re-sequencing. This cohort also included 21 post-treatment glioblastoma cases used for exploratory comparisons

*Lists of participants and their affiliations appear at the end of the paper.

(Supplementary Table 1). Although it is possible that a small number of progressive secondary glioblastomas were among the remaining 185 cases of newly diagnosed glioblastomas, this cohort represents predominantly primary glioblastoma. Indeed, when compared with published cohorts, overall survival of the newly diagnosed glioblastoma cases in TCGA is similar to that of primary glioblastomas reported in the literature (Supplementary Fig. 3, $P = 0.2$)^{9–12}.

Genomic and transcriptional aberrations

Genomic copy number alterations (CNAs) were measured on three microarray platforms (Supplementary Methods) and analysed with multiple analytical algorithms^{13–15} (Supplementary Fig. 4 and Supplementary Tables 2–4). In addition to the well-known alterations^{3,13,14}, we detected significantly recurrent focal alterations not previously reported in glioblastomas, such as homozygous deletions involving *NF1* and *PARK2*, and amplifications of *AKT3* (Fig. 1a and Supplementary Tables 2–4). Search for informative but infrequent CNAs also uncovered rare focal events, such as amplifications of *FGFR2* and *IRS2*, and deletion of *PTPRD* (Supplementary Table 4). Abundance of protein-coding genes and non-coding microRNA was also measured by transcript-specific and exon-specific probes on multiple platforms (Supplementary Methods). The resulting integrated gene expression data set showed that ~76% of genes within recurrent CNAs have expression patterns that correlate with copy number (Supplementary Table 2). In addition, single-nucleotide-polymorphism (SNP)-based analyses also catalogued copy-neutral loss of heterozygosity (LOH), with the most significant region being 17p, which contains *TP53* (Supplementary Methods).

Patterns of somatic nucleotide alterations in glioblastoma

A total of 91 matched tumour–normal pairs (72 untreated and 19 treated cases) were selected from the 143 cases for detection of

somatic mutations in 601 selected genes (Supplementary Table 5). The resulting sequences, totalling 97 million base pairs (1.1 ± 0.1 million bases per sample), uncovered 453 validated non-silent somatic mutations in 223 unique genes, 79 of which contained two or more events (Supplementary Table 6; see also http://tcga-data.nci.nih.gov/docs/somatic_mutations/tcga_mutations.htm). The background mutation rates differed markedly between untreated and treated glioblastomas, averaging 1.4 versus 5.8 somatic silent mutations per sample (98 events among 72 untreated cases versus 111 among 19 treated, $P < 10^{-21}$), respectively. This difference was predominantly driven by seven hypermutated samples, as determined by frequencies of both silent and non-silent mutations (Fig. 1b, c). Four of the seven hypermutated tumours were from patients previously treated with temozolomide and three were from patients treated with CCNU (lomustine) alone or in combination (Supplementary Table 1b). A hypermutator phenotype in glioblastoma has been described in three glioblastoma specimens with *MSH6* mutations^{16,17}, prompting us to perform a systematic analysis of the genes involved in mismatch repair (MMR). Indeed, six of the seven hypermutated samples harboured mutations in at least one of the MMR genes *MLH1*, *MSH2*, *MSH6* or *PMS2*, as compared with only one sample among the eighty-four non-hypermutated samples ($P = 7 \times 10^{-8}$), suggesting a role of decreased DNA repair competency in these highly mutated samples derived from treated patients.

By applying a statistical analysis of mutation significance¹⁸, we identified eight genes as significantly mutated (false discovery rate $< 10^{-3}$) (Fig. 2d and Supplementary Table 6). Interestingly, 27 *TP53* mutations were detected in the 72 untreated glioblastomas (37.5%) and 11 mutations in the 19 treated samples (58%). All of those mutations clustered in the DNA binding domain, a well-known hotspot for p53 mutations in human cancers (Supplementary Fig. 5 and Supplementary Table 6). Given the predominance of primary

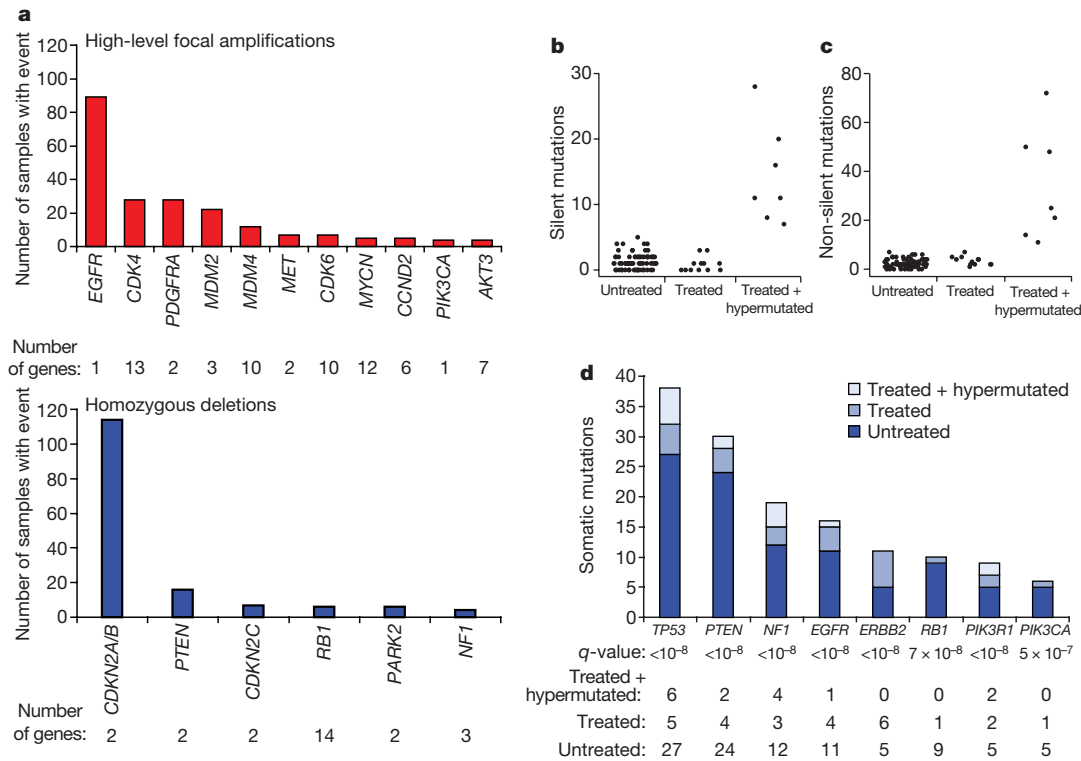


Figure 1 | Significant copy number aberrations and pattern of somatic mutations. **a**, Frequency and significance of focal high-level CNAs. Known and putative target genes are listed for each significant CNA, with ‘Number of genes’ denoting the total number of genes within each focal CNA boundary. **b**, **c**, Distribution of the number of silent (**b**) and non-silent (**c**) mutations across the 91 glioblastoma samples separated according to their treatment

status, showing hypermutation in 7 out of the 19 treated samples. **d**, Significantly mutated genes in 91 glioblastomas. The eight genes attaining a false discovery rate < 0.1 are displayed here. Somatic mutations occurring in untreated samples are in dark blue; those found in statistically non-hypermutated and hypermutated samples among the treated cohort are in respectively lighter shades of blue. Numbers of events in each group are noted.

glioblastoma among this newly diagnosed collection, that result unequivocally proves that p53 mutation is a common event in primary glioblastoma.

***NF1* is a human glioblastoma suppressor gene.** Although somatic mutations in *NF1* have been reported in a small series of human glioblastoma tumours¹⁹, their role remains controversial²⁰, despite strong genetic data in mouse model systems^{20–22}. Here, 19 *NF1* somatic mutations were identified in 13 samples (14% of 91), including 6 nonsense mutations, 4 splice site mutations, 5 missense changes and 4 frameshift insertions/deletions (indels) (Fig. 2a). Five of these mutations—R1391S (ref. 23), R1513* (ref. 24), e25–1 and e29+1 (ref. 25) and Q1966* (ref. 26)—have been reported as germline alterations in neurofibromatosis patients, and thus are probably inactivating. In addition, 30 heterozygous deletions in *NF1* were observed among the entire interim sample set of 206 cases, 6 of which also harbour point mutation (Supplementary Tables 8 and 9). Some samples also exhibited loss of expression without evidence of genomic alteration (Fig. 2b). Overall, at least 47 of these 206 patient samples (23%) harboured somatic *NF1* inactivating mutations or deletions, definitively addressing *NF1*'s relevance to sporadic human glioblastoma.

Prevalence of *EGFR* family activation. *EGFR* is frequently activated in primary glioblastomas. Variant III deletion of the extracellular domain ('vIII mutant')²⁷ has been the most commonly described event, in addition to extracellular domain point mutations and cytoplasmic domain deletions^{28,29}. Here, high-resolution genomic and exon-specific transcriptomic profiling readily detected vIII and carboxy-terminal deletions with correspondingly altered transcripts (Fig. 2c). Among the 91 glioblastoma cases with somatic mutation

data, 22 harboured focal amplification of wild-type *EGFR* with no point mutation, 16 had point mutations in addition to focal amplification, and 3 had *EGFR* point mutations but no amplification (Supplementary Fig. 6 and Supplementary Table 9). Collectively, *EGFR* alterations were observed in 41 of the 91 sequenced samples.

***ERBB2* mutation** has previously been reported in only one glioblastoma tumour³⁰. In the TCGA cohort, 11 somatic *ERBB2* mutations in 7 of 91 samples were validated, including 3 in the kinase domain and 2 involving V777A, a site of recurrent missense and in-frame insertion mutations in lung, gastric and colon cancers³¹. The remaining eight mutations (including seven missense and one splice-site mutation) occurred in the extracellular domain of the protein, similar to somatic *EGFR* substitutions in glioblastoma (Fig. 2d). Unlike in breast cancers, focal amplifications of *ERBB2* were not observed in glioblastomas.

Somatic mutations of the PI(3)K complex in human glioblastoma. The PI(3)K complex consists of a catalytically active protein, p110 α , encoded by *PIK3CA*, and a regulatory protein, p85 α , encoded by *PIK3R1*. Frequent activating missense mutations of *PIK3CA* have been reported in multiple tumour types, including glioblastoma^{32,33}. These mutations occur primarily in the adaptor binding domain (ABD) as well as the C2 helical and kinase domains^{34–36}. Indeed, *PIK3CA* somatic nucleotide substitutions were detected in 6 of the 91 sequenced samples (Supplementary Table 6). Apart from the four mutations already reported in the COSMIC database (<http://www.sanger.ac.uk/genetics/CGP/cosmic/>), two novel in-frame deletions were detected in the adaptor binding domain of *PIK3CA* ('L10del' and 'P17del'). Those deletions may disrupt interactions between p110 α and its regulatory subunit, p85 α (ref. 37).

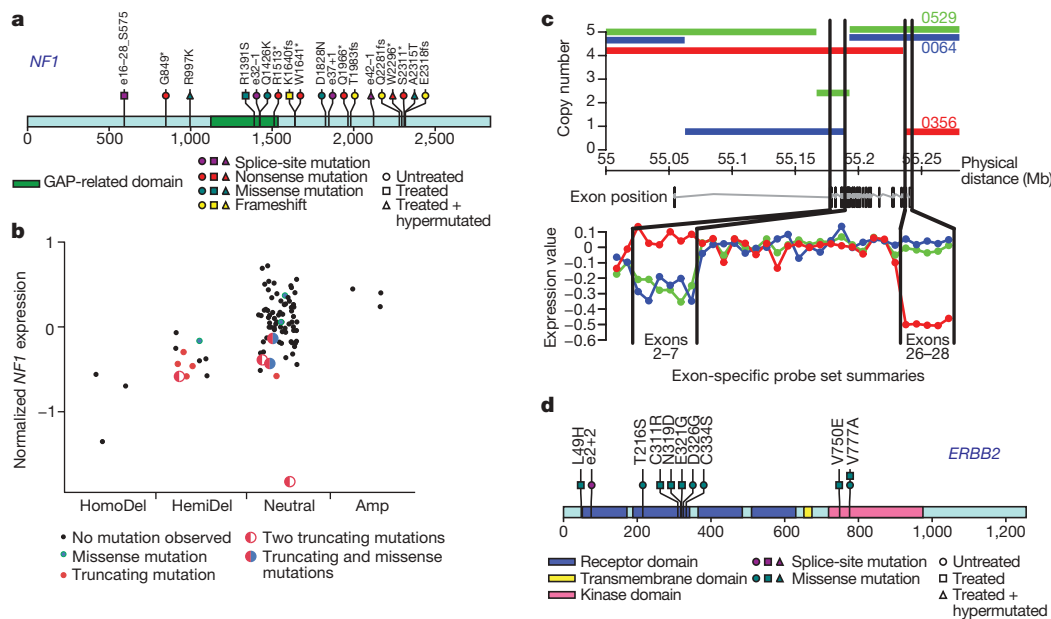


Figure 2 | Mutations in *NF1* tumour suppressor gene and *EGFR* family members. **a**, *NF1* somatic mutations in 91 glioblastoma tumours. Both missense mutations and truncating nonsense, frameshift and splice site mutations were observed. Splice positions are given in number of bases to the closest exon (e#) numbered according to the *NF1* reference transcript in the Human Gene Mutation Database; positive indicates 3' of exon, negative indicates 5' of exon. Asterisk indicates a stop codon. fs, frameshift. **b**, Correlation of copy number and mutation status at the *NF1* locus with level of expression (y axis). Mutation events predicted to result in fewer expressed copies (including deletion, nonsense, splice site and frameshift mutations) generally have lower observed expression. HomoDel, homozygous deletion; HemiDel, single-copy loss; Neutral, no change in copy number (presumed diploid); Amp, increased copy number. Copy number status of the *NF1* locus in each sample was determined as described in the Supplementary Information. **c**, DNA copy number and mRNA

expression profiles for TCGA samples TCGA-08-0356 (red), TCGA-02-0064 (blue) and TCGA-02-0529 (green) at the *EGFR* locus. The upper panel shows the segmented DNA copy number (based on Affymetrix SNP6.0 data) versus genomic coordinates on chromosome 7. The lower panel shows relative exon expression levels across the known *EGFR* exons from the Affymetrix Exon array ordered by genomic position, where relative expression is the median-centred difference in exon intensity and gene intensity. The *EGFR* gene model lies between the two plots. Black lines map the genomic positions of exons 2 through to 7 and 26 through to 28. Note that structural deletions cause the relatively lower expression of exons 2–7 in the green and blue samples and exons 26–28 in the red sample. **d**, *ERBB2* somatic mutations in 91 glioblastoma tumours. Mutations cluster in the extracellular domain as seen in *EGFR* in glioblastoma. Splice site mutation position is given in number of bases to the closest exon (e#); positive indicates 3' of exon.

Unlike *PIK3CA*, *PIK3R1* has rarely been reported as mutated in cancers. Among the five reported *PIK3R1* nucleotide substitutions in cancers^{38,39}, one was in a glioblastoma³⁹. In our TCGA cohort, 9 *PIK3R1* somatic mutations were detected among the 91 sequenced glioblastomas. None of them was in samples with *PIK3CA* mutations. Of the nine mutations, eight lay within the intervening SH2 (or iSH2) domain and four are 3-bp in-frame deletions (Fig. 3a and Supplementary Table 6). In accord with the crystal structure of PI(3)K, which identifies the D560 and N564 amino acid residues in p85 α as contact points with the N345 amino acid residue in the C2 domain of p110 α (ref. 37), the mutations detected in glioblastoma cluster around those three amino acid residues (Fig. 3b), including a N345K mutation in *PIK3CA* (previously reported in colon and breast cancers⁴⁰) and D560Y and N564K mutations in *PIK3R1*. We also identified an 18-bp deletion spanning residues D560 to S565 (DKRMNS) in *PIK3R1* (Fig. 3b) in addition to three other novel deletions (R574del, T576del and W583del) in proximity to the two key residues. We speculate that spatial constraints due to these deletions might prevent inhibitory contact of the p85 α N-terminal SH2 (nSH2) domain with the helical domain of p110 α , causing constitutive PI(3)K activity. Taken together, the pattern of clustering of the

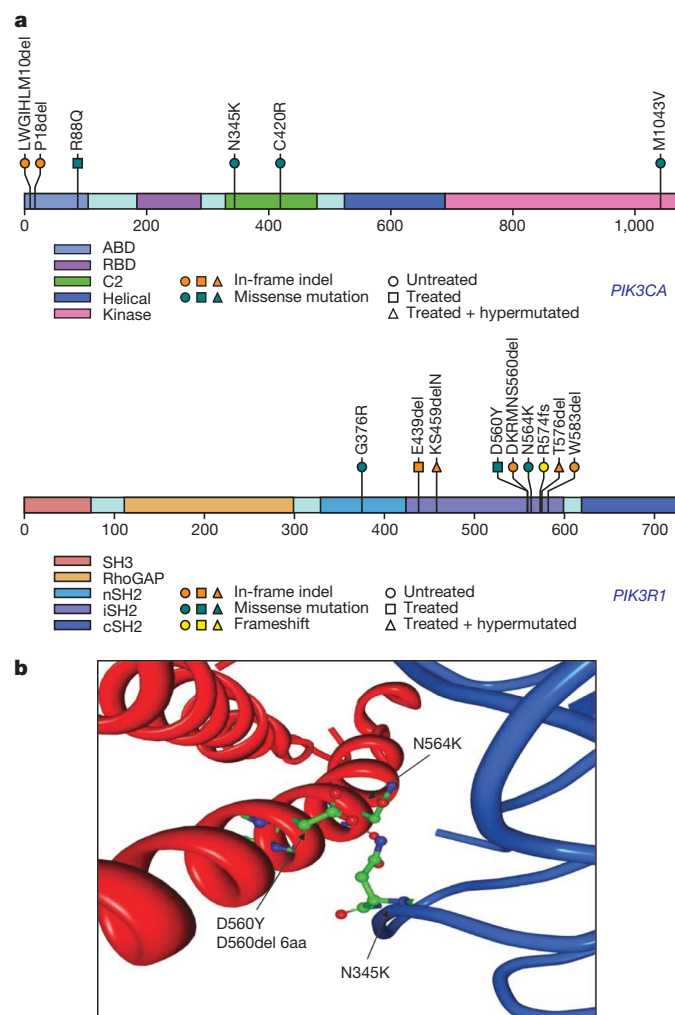


Figure 3 | *PIK3R1* and *PIK3CA* mutations in glioblastoma. **a**, The locations of mutations found in TCGA tumours are indicated above the backbone. ABD, adaptor binding domain; RBD, Ras binding domain; C2, membrane-binding domain; nSH2, N-terminal SH2 domain; iSH2, inter-SH2 domain; cSH2, C-terminal SH2 domain. **b**, Three mutations found in the interaction interface of the C2 domain of p110 α with iSH2 of p85 α . Two residues of p85 α , D560 and N564, are within hydrogen-bonding distance of the C2 residue of p110 α , N345.

mutations around key residues defined by the crystal structure of PI(3)K strongly suggests that these novel *PIK3R1* point mutations and indels disrupt the important C2–iSH2 interaction, relieving the inhibitory effect of p85 α on p110 α .

MGMT methylation and MMR in treated glioblastomas

Cancer-specific DNA methylation of CpG dinucleotides located in CpG islands within the promoters of 2,305 genes was measured relative to normal brain DNA (Supplementary Table 7 and Supplementary Methods). The promoter methylation status of *MGMT*, a DNA repair enzyme that removes alkyl groups from guanine residues⁴¹, is associated with glioblastoma sensitivity to alkylating agents^{42,43}. Among the 91 sequenced cases, 19 samples were found to contain *MGMT* promoter methylation (including 13 of the 72 untreated cases and 6 of the 19 treated cases). When juxtaposed with somatic mutation data, an

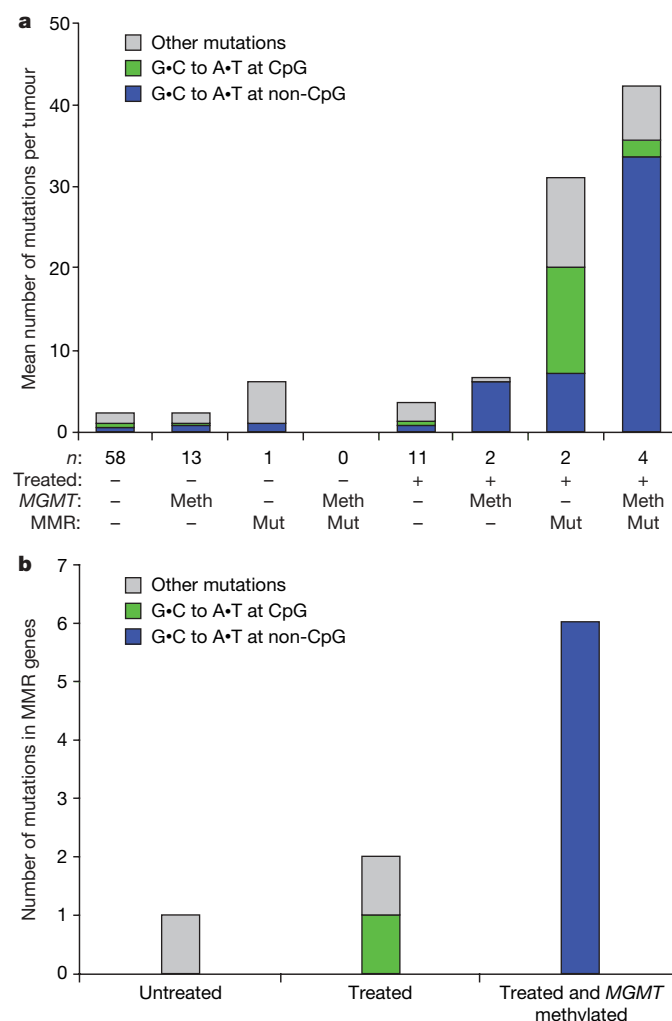


Figure 4 | Pattern of somatic mutations, *MGMT* DNA methylation and MMR gene mutations in treated glioblastomas. **a**, The mean number of validated somatic nucleotide substitutions per tumour for key sample groups is indicated on the y axis and denoted by the height of the bar histograms. Samples are grouped along the x axis according to treatment status of the patient (minus indicates untreated; plus indicates treated), DNA methylation status of *MGMT* (Meth, DNA methylated; minus, not methylated), and genetic status of MMR genes (minus, no genes mutated; Mut, one or more of the *MLH1*, *MSH2*, *MSH6* or *PMS2* genes mutated); the number below each bar indicates the number of samples in the group. Bars are colour-coded for types of nucleotide substitutions including G-to-A transitions at non-CpG sites (blue), G-to-A transitions at CpG sites (green), and other mutation types (grey). **b**, Bar histogram for mutation spectrum in the MMR genes as a function of treatment status and methylation status of *MGMT*. The colour code for substitution types is the same as in **a**.

intriguing relationship between the hypermutator phenotype and *MGMT* methylation status emerged in the treated samples. Specifically, *MGMT* methylation was associated with a profound shift in the nucleotide substitution spectrum of treated glioblastomas (Fig. 4a). Among the 13 treated samples without *MGMT* methylation, 29% (29 out of 99) of the validated somatic mutations occurred as G•C to A•T transitions in CpG dinucleotides (characteristic of spontaneous deamination of methylated cytosines), and a comparable 23% (23 out of 99) of all mutations occurred as G•C to A•T transitions in non-CpG dinucleotides. In contrast, in the six treated samples with *MGMT* methylation, 81% of all mutations (146 out of 181) turned out to be of the G•C to A•T transition type in non-CpG dinucleotides, whereas only 4% (8 out of 181) of all mutations were G•C to A•T transition mutations within CpGs. That pattern is consistent with a failure to repair alkylated guanine residues caused by treatment. In other words, *MGMT* methylation shifted the mutation spectrum of treated samples to a preponderance of G•C to A•T transition at non-CpG sites.

Notably, the mutational spectra in the MMR genes themselves reflected *MGMT* methylation status and treatment consequences. All seven mutations in MMR genes found in six *MGMT* methylated, hypermutated (treated) tumours occurred as G•C to A•T mutations at non-CpG sites (Fig. 4b and Supplementary Table 6), whereas neither MMR mutation in non-methylated, hypermutated tumours was of this characteristic. Hence, these data show that MMR deficiency and *MGMT* methylation together, in the context of treatment, exert a powerful influence on the overall frequency and pattern of somatic point mutations in glioblastoma tumours, an observation of potential clinical importance.

Integrative analyses define glioblastoma core pathways

To begin to construct an integrated view of common genetic alterations in the glioblastoma genome, we mapped the unequivocal genetic

alterations—validated somatic nucleotide substitutions, homozygous deletions and focal amplifications—onto major pathways implicated in glioblastoma¹. That analysis identified a highly interconnected network of aberrations (Supplementary Figs 7 and 8), including three major pathways: RTK signalling, and the p53 and RB tumour suppressor pathways (Fig. 5).

By copy number data alone, 66%, 70% and 59% of the 206 samples harboured somatic alterations in core components of the RB, TP53 and RTK pathways, respectively (Supplementary Table 8). In the 91 samples for which there was also sequencing data, the frequencies of somatic alterations increased to 87%, 78% and 88%, respectively (Supplementary Table 9). There was a statistical tendency towards mutual exclusivity of alterations of components within each pathway (*P*-values of 9.3×10^{-10} , 2.5×10^{-13} and 0.022, respectively, for the p53, RB and RTK pathways; Supplementary Table 10), consistent with the thesis that deregulation of one component in the pathway relieves the selective pressure for additional ones. However, we observed a greater than random chance (one-tailed, *P* = 0.0018) that a given sample harbours at least one aberrant gene from each of the three pathways (Supplementary Table 10). In fact, 74% harboured aberrations in all three pathways, a pattern suggesting that deregulation of the three pathways is a core requirement for glioblastoma pathogenesis.

As well as frequent deletions and mutations of the *PTEN* lipid phosphatase tumour suppressor gene, 86% of the glioblastoma samples harboured at least one genetic event in the core RTK/PI3K pathway (Fig. 5a). In addition to *EGFR* and *ERBB2*, *PDGFRA* (13%) and *MET* (4%) showed frequent aberrations (Supplementary Table 9). A total of 10 of the 91 sequenced samples have amplifications or point mutations in at least 2 of the 4 RTKs catalogued (*EGFR*, *ERBB2*, *PDGFRA* and *MET*; Supplementary Table 9), suggesting that genomic activation can be a mechanism for co-activated RTKs⁴⁴.

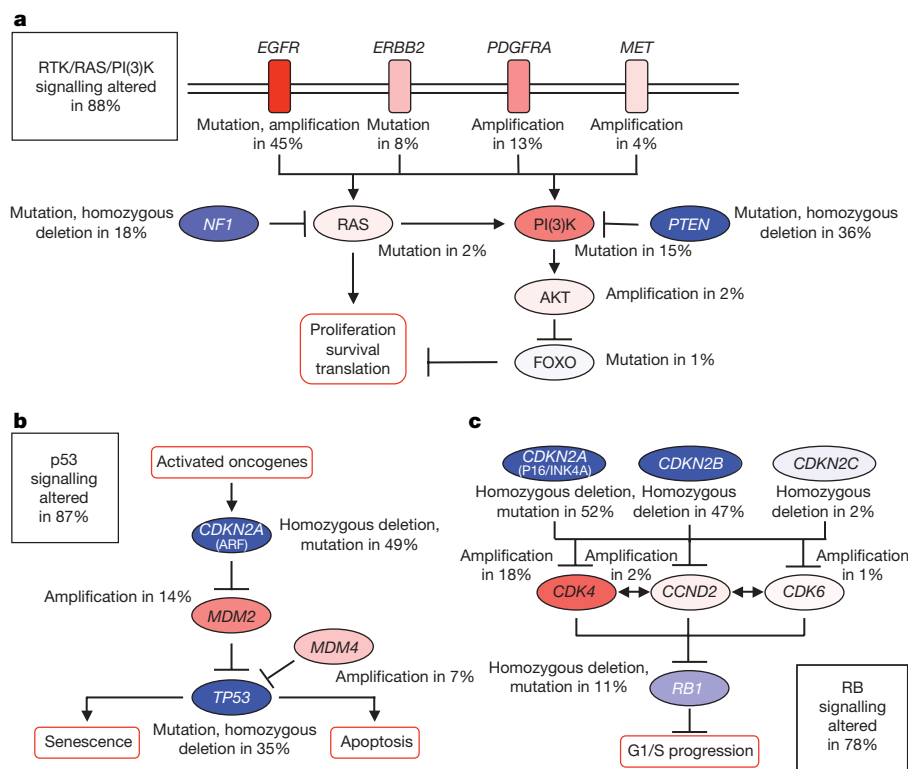


Figure 5 | Frequent genetic alterations in three critical signalling pathways. **a–c**, Primary sequence alterations and significant copy number changes for components of the RTK/RAS/PI(3)K (**a**), p53 (**b**) and RB (**c**) signalling pathways are shown. Red indicates activating genetic alterations, with frequently altered genes showing deeper shades of red. Conversely, blue indicates inactivating alterations, with darker shades

corresponding to a higher percentage of alteration. For each altered component of a particular pathway, the nature of the alteration and the percentage of tumours affected are indicated. Boxes contain the final percentages of glioblastomas with alterations in at least one known component gene of the designated pathway.

Inactivation of the p53 pathway occurred in the form of *ARF* deletions (55%), amplifications of *MDM2* (11%) and *MDM4* (4%), in addition to mutations of p53 itself (Fig. 5b and Supplementary Table 8). Among 91 sequenced samples (Supplementary Table 9), genetic lesions in *TP53* were mutually exclusive of those in *MDM2* or *MDM4* (odds ratios of 0.00 for both; $P = 0.02$ and 0.068 , respectively; Supplementary Table 10), but not of those in *ARF*. In fact, 10 of the 32 tumours with *TP53* mutations also had deleted *ARF*, suggesting that homozygous deletion of the *CDKN2A* locus (which encodes both p16^{INK4A} and *ARF*) was at least in part driven by p16^{INK4A}.

Among the 77% samples harbouring RB pathway aberrations (Fig. 5c), the most common event was deletion of the *CDKN2A/CDKN2B* locus on chromosome 9p21 (55% and 53%), followed by amplification of the *CDK4* locus (14%) (Fig. 5c and Supplementary Tables 8 and 9). Although CNAs in the CDK/RB pathway members can co-occur in the same tumour¹⁴, all nine samples with *RB1* nucleotide substitutions (Supplementary Table 9) lacked *CDKN2A/CDKN2B* deletion or other CNAs in the pathway, suggesting that inactivation of *RB1* by nucleotide substitution, in contrast to copy number loss, obviates the genetic pressure for activation of upstream cyclin/cyclin-dependent kinases.

Discussion

In establishing this pilot programme, TCGA has developed important principles in biospecimen banking and collection, and established the infrastructure that will serve similar efforts in the future. Although it ensured high-quality data, the stringent biospecimen selection criteria may have introduced a degree of bias because small samples and samples with high levels of necrosis were excluded. Nonetheless, the clinical parameters of this cohort are similar to other published cohorts (Supplementary Fig. 3 and Supplementary Table 1).

The integrated analyses of multi-dimensional genomic data from complementary technology platforms have proved informative. In addition to pinpointing deregulation of RB, p53 and RTK/RAS/PI(3)K pathways as obligatory events in most, and perhaps all, glioblastoma tumours, the patterns of mutations may also inform future therapeutic decisions. It would be reasonable to speculate that patients with deletions or inactivating mutations in *CDKN2A* or *CDKN2C* or patients with amplifications of *CDK4/CDK6* would be candidates for treatment with CDK inhibitors, a strategy not likely to be effective in patients with *RB1* mutation. Similarly, patients with *PTEN* deletions or activating mutations in *PIK3CA* or *PIK3R1* might be expected to benefit from a PI(3)K or PDK1 inhibitor, whereas tumours in which the PI(3)K pathway is altered by *AKT3* amplification might prove refractory to those modalities. The presence of genomic co-amplification reinforces the recent report of multiple phosphorylated (activated) RTKs in individual glioblastoma specimens⁴⁴, suggesting a way to tailor anti-RTK therapeutic cocktails to specific patterns of RTK mutation. In addition, combination anti-RTK therapy might synergize with downstream inhibition of PI(3)K or cell cycle mediators. In contrast, glioblastomas with *NF1* mutations might benefit from a RAF or MEK inhibitor as part of a combination, as shown for *BRAF* mutant cancers⁴⁵.

One of the most important biomarkers for glioblastomas is the methylation status of *MGMT*, which predicts sensitivity to temozolomide^{42,43}, an alkylating agent that is the current standard of care for glioblastoma patients. Integrative analysis of mutation, DNA methylation and clinical (treatment) data, albeit with small sample numbers, suggests a series of inter-related events that may have an impact on clinical response and outcome. Newly diagnosed glioblastomas with *MGMT* methylation respond well to treatment with alkylating agents, in part as a consequence of unrepaired alkylated guanine residues initiating cycles of futile mismatch repair, which can lead to cell death^{46–48}. Therefore, treatment of *MGMT*-deficient glioblastomas with alkylating therapy introduces a strong selective pressure to lose mismatch repair function⁴⁹. That conclusion is consistent with

our observation that the mismatch repair genes themselves are mutated with characteristic C•G to A•T transitions at non-CpG sites resulting from unrepaired alkylated guanine residues. Thus, initial methylation of *MGMT*, in conjunction with treatment, may lead to both a shift in mutation spectrum affecting mutations at mismatch repair genes and selective pressure to lose mismatch repair function. In other words, our finding raises the possibility that patients who initially respond to the frontline therapy in use today may evolve not only treatment resistance, but also an MMR-defective hypermutator phenotype. If such a hypothesis is validated, one may speculate that selective strategies designed to target mismatch-repair-deficient cells⁵⁰ would represent a rational upfront combination with alkylating agent that together may prevent or minimize emergence of such resistance. Conversely, such a treatment-mediated mutator phenotype may enhance pathway mutations that can confer resistance to targeted therapies, thereby cautioning the combination of alkylating agents with targeted agents, as this may substantially increase the probability of developing resistance to such targeted drugs.

The power of TCGA to produce unprecedented multi-dimensional data sets using statistically robust numbers of samples sets the stage for a new era in the discovery of new cancer interventions. The integrative analyses leading to the formulation of an unanticipated hypothesis on a potential mechanism of resistance highlights precisely the value and power of such project design, demonstrating how unbiased and systematic cancer genome analyses of large sample cohorts can lead to important discoveries.

METHODS SUMMARY

Biospecimens were screened from retrospective banks of tissue source sites under appropriate Institutional Review Board approvals for newly diagnosed glioblastoma with minimal 80% tumour cell percentage. RNA and DNA extracted from qualified specimens were distributed to TCGA centres for analysis. Whole-genome-amplified genomic DNA samples from tumours and normal samples were sequenced by the Sanger method. Mutations were called, verified using a second genotyping platform, and systematically analysed to identify significantly mutated genes after correcting for the background mutation rate for nucleotide type and the sequence coverage of each gene. DNA copy number analyses were performed using the Agilent 244K, Affymetrix SNP6.0 and Illumina 550K DNA copy number platforms. Sample-specific and recurrent copy number changes were identified using various algorithms (GISTIC, GTS, RAE). Messenger RNA and microRNA (miRNA) expression profiles were generated using Affymetrix U133A, Affymetrix Exon 1.0 ST, custom Agilent 244K, and Agilent miRNA array platforms. mRNA expression profiles were integrated into a single estimate of relative gene expression for each gene in each sample. Methylation at CpG dinucleotides was measured using the Illumina GoldenGate assay. All data for DNA sequence alterations, copy number, mRNA expression, miRNA expression and CpG methylation were deposited in standard common formats in the TCGA DCC at <http://cancergenome.nih.gov/dataportal/>. All archives submitted to DCC were validated to ensure a common document structure and to ensure proper use of identifying information.

Received 28 July; accepted 1 September 2008.

Published online 4 September 2008, corrected online 17 September 2008.

1. Furnari, F. B. *et al.* Malignant astrocytic glioma: genetics, biology, and paths to treatment. *Genes Dev.* **21**, 2683–2710 (2007).
2. Mischel, P. S. & Cloughesy, T. F. Targeted molecular therapy of GBM. *Brain Pathol.* **13**, 52–61 (2003).
3. Mischel, P. S., Nelson, S. F. & Cloughesy, T. F. Molecular analysis of glioblastoma: pathway profiling and its implications for patient therapy. *Cancer Biol. Ther.* **2**, 242–247 (2003).
4. Phillips, H. S. *et al.* Molecular subclasses of high-grade glioma predict prognosis, delineate a pattern of disease progression, and resemble stages in neurogenesis. *Cancer Cell* **9**, 157–173 (2006).
5. Maher, E. A. *et al.* Marked genomic differences characterize primary and secondary glioblastoma subtypes and identify two distinct molecular and clinical secondary glioblastoma entities. *Cancer Res.* **66**, 11502–11513 (2006).
6. Lee, J. *et al.* Tumor stem cells derived from glioblastomas cultured in bFGF and EGF more closely mirror the phenotype and genotype of primary tumors than do serum-cultured cell lines. *Cancer Cell* **9**, 391–403 (2006).
7. Diehn, M. *et al.* Identification of noninvasive imaging surrogates for brain tumor gene-expression modules. *Proc. Natl Acad. Sci. USA* **105**, 5213–5218 (2008).

8. Liang, Y. *et al.* Gene expression profiling reveals molecularly and clinically distinct subtypes of glioblastoma multiforme. *Proc. Natl Acad. Sci. USA* **102**, 5814–5819 (2005).
9. Freije, W. A. *et al.* Gene expression profiling of gliomas strongly predicts survival. *Cancer Res.* **64**, 6503–6510 (2004).
10. Murat, A. *et al.* Stem cell-related “self-renewal” signature and high epidermal growth factor receptor expression associated with resistance to concomitant chemoradiotherapy in glioblastoma. *J. Clin. Oncol.* **26**, 3015–3024 (2008).
11. Nutt, C. L. *et al.* Gene expression-based classification of malignant gliomas correlates better with survival than histological classification. *Cancer Res.* **63**, 1602–1607 (2003).
12. Sun, L. *et al.* Neuronal and glioma-derived stem cell factor induces angiogenesis within the brain. *Cancer Cell* **9**, 287–300 (2006).
13. Beroukhi, R. *et al.* Assessing the significance of chromosomal aberrations in cancer: methodology and application to glioma. *Proc. Natl Acad. Sci. USA* **104**, 20007–20012 (2007).
14. Wiedemeyer, R. *et al.* Feedback circuit among INK4 tumor suppressors constrains human glioblastoma development. *Cancer Cell* **13**, 355–364 (2008).
15. Taylor, B. S. *et al.* Functional copy-number alterations in cancer. *PLoS ONE* (in the press).
16. Hunter, C. *et al.* A hypermutation phenotype and somatic MSH6 mutations in recurrent human malignant gliomas after alkylator chemotherapy. *Cancer Res.* **66**, 3987–3991 (2006).
17. Cahill, D. P. *et al.* Loss of the mismatch repair protein MSH6 in human glioblastomas is associated with tumor progression during temozolomide treatment. *Clin. Cancer Res.* **13**, 2038–2045 (2007).
18. Getz, G. *et al.* Comment on “The consensus coding sequences of human breast and colorectal cancers”. *Science* **317**, 1500 (2007).
19. Thiel, G. *et al.* Somatic mutations in the neurofibromatosis 1 gene in gliomas and primitive neuroectodermal tumours. *Anticancer Res.* **15**, 2495–2499 (1995).
20. Zhu, Y. *et al.* Early inactivation of p53 tumor suppressor gene cooperating with NF1 loss induces malignant astrocytoma. *Cancer Cell* **8**, 119–130 (2005).
21. Reilly, K. M., Loisel, D. A., Bronson, R. T., McLaughlin, M. E. & Jacks, T. Nf1;Trp53 mutant mice develop glioblastoma with evidence of strain-specific effects. *Nature Genet.* **26**, 109–113 (2000).
22. Kwon, C. H. *et al.* Pten haploinsufficiency accelerates formation of high-grade astrocytomas. *Cancer Res.* **68**, 3286–3294 (2008).
23. Upadhyaya, M. *et al.* Mutational and functional analysis of the neurofibromatosis type 1 (NF1) gene. *Hum. Genet.* **99**, 88–92 (1996).
24. Side, L. *et al.* Homozygous inactivation of the NF1 gene in bone marrow cells from children with neurofibromatosis type 1 and malignant myeloid disorders. *N. Engl. J. Med.* **336**, 1713–1720 (1997).
25. Fahsold, R. *et al.* Minor lesion mutational spectrum of the entire NF1 gene does not explain its high mutability but points to a functional domain upstream of the GAP-related domain. *Am. J. Hum. Genet.* **66**, 790–818 (2000).
26. Messiaen, L. M. *et al.* Exhaustive mutation analysis of the NF1 gene allows identification of 95% of mutations and reveals a high frequency of unusual splicing defects. *Hum. Mutat.* **15**, 541–555 (2000).
27. Humphrey, P. A. *et al.* Anti-synthetic peptide antibody reacting at the fusion junction of deletion-mutant epidermal growth factor receptors in human glioblastoma. *Proc. Natl Acad. Sci. USA* **87**, 4207–4211 (1990).
28. Lee, J. C. *et al.* Epidermal growth factor receptor activation in glioblastoma through novel missense mutations in the extracellular domain. *PLoS Med.* **3**, e485 (2006).
29. Ekstrand, A. J., Sugawa, N., James, C. D. & Collins, V. P. Amplified and rearranged epidermal growth factor receptor genes in human glioblastomas reveal deletions of sequences encoding portions of the N- and/or C-terminal tails. *Proc. Natl Acad. Sci. USA* **89**, 4309–4313 (1992).
30. Stephens, P. *et al.* Lung cancer: intragenic ERBB2 kinase mutations in tumours. *Nature* **431**, 525–526 (2004).
31. Bamford, S. *et al.* The COSMIC (Catalogue of Somatic Mutations in Cancer) database and website. *Br. J. Cancer* **91**, 355–358 (2004).
32. Samuels, Y. *et al.* High frequency of mutations of the PIK3CA gene in human cancers. *Science* **304**, 554 (2004).
33. Gallia, G. L. *et al.* PIK3CA gene mutations in pediatric and adult glioblastoma multiforme. *Mol. Cancer Res.* **4**, 709–714 (2006).
34. Bader, A. G., Kang, S., Zhao, L. & Vogt, P. K. Oncogenic PI3K deregulates transcription and translation. *Nature Rev. Cancer* **5**, 921–929 (2005).
35. Bader, A. G., Kang, S. & Vogt, P. K. Cancer-specific mutations in PIK3CA are oncogenic *in vivo*. *Proc. Natl Acad. Sci. USA* **103**, 1475–1479 (2006).
36. Liu, Z. & Roberts, T. M. Human tumor mutants in the p110 α subunit of PI3K. *Cell Cycle* **5**, 675–677 (2006).
37. Huang, C. H. *et al.* The structure of a human p110 α /p85 α complex elucidates the effects of oncogenic PI3K α mutations. *Science* **318**, 1744–1748 (2007).
38. Philp, A. J. *et al.* The phosphatidylinositol 3'-kinase p85 α gene is an oncogene in human ovarian and colon tumors. *Cancer Res.* **61**, 7426–7429 (2001).
39. Mizoguchi, M., Nutt, C. L., Mohapatra, G. & Louis, D. N. Genetic alterations of phosphoinositide 3-kinase subunit genes in human glioblastomas. *Brain Pathol.* **14**, 372–377 (2004).
40. Zhang, H. *et al.* Comprehensive analysis of oncogenic effects of PIK3CA mutations in human mammary epithelial cells. *Breast Cancer Res. Treat.* doi:10.1007/s10549-007-9847-6 (2007).
41. Pegg, A. E., Dolan, M. E. & Moschel, R. C. Structure, function, and inhibition of O6-alkylguanine-DNA alkyltransferase. *Prog. Nucleic Acid Res. Mol. Biol.* **51**, 167–223 (1995).
42. Esteller, M. *et al.* Inactivation of the DNA-repair gene MGMT and the clinical response of gliomas to alkylating agents. *N. Engl. J. Med.* **343**, 1350–1354 (2000).
43. Hegi, M. E. *et al.* MGMT gene silencing and benefit from temozolomide in glioblastoma. *N. Engl. J. Med.* **352**, 997–1003 (2005).
44. Stommel, J. M. *et al.* Coactivation of receptor tyrosine kinases affects the response of tumor cells to targeted therapies. *Science* **318**, 287–290 (2007).
45. Solit, D. B. *et al.* BRAF mutation predicts sensitivity to MEK inhibition. *Nature* **439**, 358–362 (2006).
46. Drablos, F. *et al.* Alkylation damage in DNA and RNA-repair mechanisms and medical significance. *DNA Repair* **3**, 1389–1407 (2004).
47. Hirose, Y., Kreklau, E. L., Erickson, L. C., Berger, M. S. & Pieper, R. O. Delayed repletion of O6-methylguanine-DNA methyltransferase resulting in failure to protect the human glioblastoma cell line SF767 from temozolomide-induced cytotoxicity. *J. Neurosurg.* **98**, 591–598 (2003).
48. Kaina, B., Christmann, M., Naumann, S. & Roos, W. P. MGMT: key node in the battle against genotoxicity, carcinogenicity and apoptosis induced by alkylating agents. *DNA Repair* **6**, 1079–1099 (2007).
49. Casorelli, I., Russo, M. T. & Bignami, M. Role of mismatch repair and MGMT in response to anticancer therapies. *Anticancer Agents Med. Chem.* **8**, 368–380 (2008).
50. Yang, J. L., Qu, X. J., Yu, Y., Kohn, E. C. & Friedlander, M. L. Selective sensitivity to carboxyamidotriazole by human tumor cell lines with DNA mismatch repair deficiency. *Int. J. Cancer* **123**, 258–263 (2008).

Supplementary Information is linked to the online version of the paper at www.nature.com/nature.

Acknowledgements We thank the members of TCGA's External Scientific Committee, the Glioblastoma Disease Working Group (<http://cancergenome.nih.gov/components>) and D. N. Louis for discussions; A. Mirick, J. Melone and C. Collins for administrative coordination of TCGA activities; and L. Gaffney for graphic art. This work was supported by the following grants from the United States National Institutes of Health: U54HG003067, U54HG003079, U54HG003273, U24CA126543, U24CA126544, U24CA126546, U24CA126551, U24CA126554, U24CA126561 and U24CA126563.

Author Contributions The TCGA research network contributed collectively to this study. Biospecimens were provided by the tissue source sites and processed by the Biospecimen Core Resource. Data generation and analyses were performed by the genome sequencing centres and cancer genome characterization centres. All data were released through the Data Coordinating Center. Project activities were coordinated by the NCI and NHGRI project teams. The following TCGA investigators contributed substantively to the writing of this manuscript. **Leaders:** L. Chin and M. Meyerson. **Neuropathology:** K. Aldape, D. Bigner, T. Mikkelsen and S. VandenBerg. **Databases:** A. Kahn. **Biospecimen analysis:** R. Penny, M. L. Ferguson and D. S. Gerhard. **Copy number:** G. Getz, C. Brennan, B. S. Taylor, W. Winckler, P. Park and M. Ladanyi. **Gene expression:** K. A. Hoadley, R. G. W. Verhaak, D. N. Hayes and P. Spellman. **LOH:** D. Absher and B. A. Weir. **Sequencing:** G. Getz, L. Ding, D. Wheeler, M. S. Lawrence, K. Cibulskis, E. Mardis, Jinghui Zhang and R. K. Wilson. **TP53:** L. Donehower and D. A. Wheeler. **NF1:** W. Winckler, L. Ding and Jinghui Zhang. **EGFR:** E. Purdom and W. Winckler. **ERBB2:** W. Winckler. **PIK3R1:** L. Ding, J. Wallis and E. Mardis. **DNA methylation:** P. W. Laird, J. G. Herman, L. Ding, K. E. Schuebel, D. J. Weisenberger and S. B. Baylin. **Pathway analysis:** N. Schultz, L. Donehower, D. A. Wheeler, Jun Yao, R. Wiedemeyer, J. Weinstein and C. Sander. **General:** S. B. Baylin, R. A. Gibbs, J. Gray, R. Kucherlapati, M. Ladanyi, E. S. Lander, R. M. Myers, C. M. Perou, J. Weinstein and R. K. Wilson.

Author Information Reprints and permissions information is available at www.nature.com/reprints. Correspondence and requests for materials should be addressed to L.C. (lynda_chin@dfci.harvard.edu) or M.M. (matthew_meyerson@dfci.harvard.edu).

The Cancer Genome Atlas Research Network

Tissue source sites: Duke University Medical School Roger McLendon¹, Allan Friedman², Darrell Bigner¹, Emory University Erwin G. Van Meir^{3,4,5}, Daniel J. Brat^{5,6}, Gena M. Mastrogianakis³, Jeffrey J. Olson^{3,4,5}, Henry Ford Hospital Tom Mikkelsen⁷, Norman Lehman⁸, MD Anderson Cancer Center Ken Aldape⁹, W. K. Alfred Yung¹⁰, Oliver Bogler¹¹, John N. Weinstein^{5,7}, University of California San Francisco Scott VandenBerg¹², Mitchell Berger¹³, Michael Prados¹³

Genome sequencing centres: Baylor College of Medicine Donna Muzny¹⁴, Margaret Morgan¹⁴, Steve Scherer¹⁴, Aniko Sabo¹⁴, Lynn Nazareth¹⁴, Lora Lewis¹⁴, Otis Hall¹⁴, Yiming Zhu¹⁴, Yanru Ren¹⁴, Omar Alvi¹⁴, Jiqiang Yao¹⁴, Alicia Hawes¹⁴, Shalini Jhangiani¹⁴, Gerald Fowler¹⁴, Anthony San Lucas¹⁴, Christie Kover¹⁴, Andrew Cree¹⁴, Huyen Dinh¹⁴, Jireh Santibanez¹⁴, Vandita Joshi¹⁴, Manuel L. Gonzalez-Garay¹⁴, Christopher A. Miller^{14,15}, Aleksandar Milosavljevic^{14,15,16}, Larry Donehower¹⁷, David A. Wheeler¹⁴, Richard A. Gibbs¹⁴, Broad Institute of MIT and Harvard Kristian

Cibulskis¹⁸, Carrie Sougnez¹⁸, Tim Fennell¹⁸, Scott Mahan¹⁸, Jane Wilkinson¹⁸, Liuda Ziaugra¹⁸, Robert Onofrio¹⁸, Toby Bloom¹⁸, Rob Nicol¹⁸, Kristin Ardlie¹⁸, Jennifer Baldwin¹⁸, Stacey Gabriel¹⁸, Eric S. Lander^{18,19,20}, **Washington University in St Louis** Li Ding²¹, Robert S. Fulton²¹, Michael D. McLellan²¹, John Wallis²¹, David E. Larson²¹, Xiaoqi Shi²¹, Rachel Abbott²¹, Lucinda Fulton²¹, Ken Chen²¹, Daniel C. Koboldt²¹, Michael C. Wendt²¹, Rick Meyer²¹, Yuzhu Tang²¹, Ling Lin²¹, John R. Osborne²¹, Brian H. Dunford-Shore²¹, Tracie L. Miner²¹, Kim Delehaunty²¹, Chris Markovic²¹, Gary Swift²¹, William Courtney²¹, Craig Pohl²¹, Scott Abbott²¹, Amy Hawkins²¹, Shin Leong²¹, Carrie Haipek²¹, Heather Schmidt²¹, Maddy Wiechert²¹, Tammi Vickery²¹, Sacha Scott²¹, David J. Dooling²¹, Asif Chinwalla²¹, George M. Weinstock²¹, Elaine R. Mardis²¹, Richard K. Wilson²¹

Cancer genome characterization centres: Broad Institute/Dana-Farber Cancer Institute Gad Getz¹⁸, Wendy Winckler^{18,22,23}, Roel G. W. Verhaak^{18,22,23}, Michael S. Lawrence¹⁸, Michael O'Kelly¹⁸, Jim Robinson¹⁸, Gabriele Alexe¹⁸, Rameen Beroukhi^{18,22,23}, Scott Carter¹⁸, Derek Chiang^{18,22}, Josh Gould¹⁸, Supriya Gupta¹⁸, Josh Korn¹⁸, Craig Mermel^{18,22}, Jill Mesirov¹⁸, Stefano Monti¹⁸, Huy Nguyen¹⁸, Melissa Parkin¹⁸, Michael Reich¹⁸, Nicolas Stransky¹⁸, Barbara A. Weir^{18,22,23}, Levi Garraway^{18,22,23}, Todd Golub^{18,22,23}, Matthew Meyerson^{18,22,23}, **Harvard Medical School/Dana-Farber Cancer Institute** Lynda Chin^{22,24,25}, Alexei Protopopov²⁴, Jianhua Zhang²⁴, Ilana Perna²⁴, Sandy Aronson²⁶, Narayanan Sathiamoorthy²⁶, Georgia Ren²⁴, Jun Yao²⁴, W. Ruprecht Wiedemeyer²², Hyunsoo Kim²⁶, Sek Won Kong^{27,28}, Yonghong Xiao²⁴, Isaac S. Kohane^{26,27,29}, Jon Seidman³⁰, Peter J. Park^{26,27,29}, Raju Kucherlapati²⁶, **Johns Hopkins/University of Southern California** Peter W. Laird³¹, Leslie Cope³², James G. Herman³³, Daniel J. Weisenberger³¹, Fei Pan³¹, David Van Den Berg³¹, Leander Van Neste³⁴, Joo Mi Yi³³, Kornel E. Schuebel³³, Stephen B. Baylin³³, **HudsonAlpha Institute/Stanford University** Devin M. Absher³⁵, Jun Z. Li³⁶, Audrey Southwick³⁷, Shannon Brady³⁷, Amita Aggarwal³⁷, Tisha Chung³⁷, Gavin Sherlock³⁷, James D. Brooks³⁸, Richard M. Myers³⁵, **Lawrence Berkeley National Laboratory** Paul T. Spellman³⁹, Elizabeth Purdom⁴⁰, Lakshmi R. Jakkula³⁹, Anna V. Lapuk³⁹, Henry Marr³⁹, Shannon Dorton³⁹, Yoon Gi Choi⁴¹, Ju Han³⁹, Amrita Ray³⁹, Victoria Wang⁴⁰, Steffen Durinck³⁹, Mark Robinson⁴², Nicholas J. Wang³⁹, Karen Vranizan⁴¹, Vivian Peng⁴¹, Eric Van Name⁴¹, Gerald V. Fontenay³⁹, John Ngai⁴¹, John G. Conboy³⁹, Bahram Parvin³⁹, Heidi S. Feiler³⁹, Terence P. Speed^{40,42}, Joe W. Gray³⁹, **Memorial Sloan-Kettering Cancer Center** Cameron Brennan⁴³, Nicholas D. Succi⁴⁴, Adam Olshen⁴⁵, Barry S. Taylor^{44,46}, Alex Lash⁴⁴, Nikolaus Schultz⁴⁴, Boris Reva⁴⁴, Yevgeniy Antipin⁴⁴, Alexey Stukalov⁴⁴, Benjamin Gross⁴⁴, Ethan Cerami⁴⁴, Wei Qing Wang⁴⁴, Li-Xuan Qin⁴⁵, Venkatraman E. Seshan⁴⁵, Liliana Villafania⁴⁷, Magali Cavatore⁴⁷, Laetitia Borsu⁴⁸, Agnes Viale⁴⁷, William Gerald⁴⁸, Chris Sander⁴⁴, Marc Ladanyi⁴⁸, **University of North Carolina, Chapel Hill** Charles M. Perou^{49,50}, D. Neil Hayes⁵¹, Michael D. Topal^{50,52}, Katherine A. Hoadley⁴⁹, Yuan Qi⁵¹, Sai Balu⁵², Yan Shi⁵², Junyuan Wu⁵²

Biospecimen Core Resource: Robert Penny⁵³, Michael Bittner⁵⁴, Troy Shelton⁵³, Elizabeth Lenkiewicz⁵³, Scott Morris⁵³, Debbie Beasley⁵³, Sheri Sanders⁵³

Data Coordinating Center: Ari Kahn⁵⁵, Robert Sfeir⁵⁵, Jessica Chen⁵⁵, David Nassau⁵⁵, Larry Feng⁵⁵, Erin Hickey⁵⁵

Project teams: National Cancer Institute Anna Barker⁵⁸, Daniela S. Gerhard⁵⁸, Joseph Vockley⁵⁸, Carolyn Compton⁵⁸, Jim Vaught⁵⁸, Peter Fielding⁵⁸, Martin L. Ferguson⁵⁹, Carl Schaefer⁵⁶, Jinghui Zhang⁵⁶, Subhashree Madhavan⁵⁶, Kenneth H. Buetow⁵⁶, **National Human Genome Research Institute** Francis Collins⁶⁰, Peter Good⁶⁰, Mark Guyer⁶⁰, Brad Ozenberger⁶⁰, Jane Peterson⁶⁰ & Elizabeth Thomson⁶⁰

¹Department of Pathology, ²Department of Surgery, Duke University Medical Center, Durham, North Carolina 27710, USA. ³Department of Neurosurgery, ⁴Department of Hematology and Medical Oncology, ⁵Winship Cancer Institute, ⁶Department of Pathology and Laboratory Medicine, Emory University School of Medicine, Atlanta,

Georgia 30322, USA. ⁷Department of Neurological Surgery, ⁸Department of Pathology, Henry Ford Hospital, Detroit, Michigan 48202, USA. ⁹Department of Pathology, ¹⁰Department of Neuro-Oncology, ¹¹Department of Neurosurgery, University of Texas M.D. Anderson Cancer Center, Houston, Texas 77030, USA. ¹²Department of Pathology, ¹³Department of Neurosurgery, University of California San Francisco, San Francisco, California 94143, USA. ¹⁴Human Genome Sequencing Center, Baylor College of Medicine, Houston, Texas 77030, USA. ¹⁵Graduate Program in Structural and Computational Biology and Molecular Biophysics, ¹⁶Department of Molecular and Human Genetics, Baylor College of Medicine, Houston, Texas 77030, USA. ¹⁷Department of Molecular Virology and Microbiology, Human Genome Sequencing Center, Baylor College of Medicine, Houston, Texas 77030, USA. ¹⁸The Eli and Edythe L. Broad Institute of Massachusetts Institute of Technology and Harvard University, Cambridge, Massachusetts 02142, USA. ¹⁹Department of Biology, Institute of Massachusetts Institute of Technology, Cambridge, Massachusetts 02142, USA. ²⁰Department of Systems Biology, Harvard University, Boston, Massachusetts 02115, USA. ²¹The Genome Center at Washington University, Department of Genetics, Washington University School of Medicine, St Louis, Missouri 63108, USA. ²²Department of Medical Oncology, ²³Center for Cancer Genome Discovery, ²⁴Center for Applied Cancer Science of the Belfer Institute for Innovative Cancer Science, Dana-Farber Cancer Institute, Boston, Massachusetts 02115, USA. ²⁵Department of Dermatology, Harvard Medical School, Boston, Massachusetts 02115, USA. ²⁶Harvard Medical School-Partners HealthCare Center for Genetics and Genomics, Boston, Massachusetts 02115, USA. ²⁷Informatics Program, ²⁸Department of Cardiology, Children's Hospital, Boston, Massachusetts 02115, USA. ²⁹Center for Biomedical Informatics, ³⁰Department of Genetics, Harvard Medical School, Boston, Massachusetts 02115, USA. ³¹USC Epigenome Center, University of Southern California, Los Angeles, California 90089, USA. ³²Biometry and Clinical Trials Division, ³³Cancer Biology Division, The Sidney Kimmel Comprehensive Cancer Center at Johns Hopkins University, Baltimore, Maryland 21231, USA. ³⁴Department of Molecular Biotechnology, Faculty of Bioscience and Engineering, Ghent University, Ghent B-9000, Belgium. ³⁵HudsonAlpha Institute for Biotechnology, Huntsville, Alabama 35806, USA. ³⁶Department of Human Genetics, University of Michigan, Ann Arbor, Michigan 48109, USA. ³⁷Department of Genetics, ³⁸Department of Urology, Stanford University School of Medicine, Stanford, California 94305, USA. ³⁹Life Sciences Division, Lawrence Berkeley National Laboratory, Berkeley, California 94720, USA. ⁴⁰Department of Statistics, ⁴¹Functional Genomics Laboratory, University of California at Berkeley, Berkeley, California 94720, USA. ⁴²Walter and Eliza Hall Institute, Parkville, Victoria 3052, Australia. ⁴³Department of Neurosurgery, ⁴⁴Computational Biology Center, ⁴⁵Department of Epidemiology and Biostatistics, Memorial Sloan-Kettering Cancer Center, New York, New York 10065, USA. ⁴⁶Department of Physiology and Biophysics, Weill Cornell Graduate School of Medical Sciences, New York, New York 10065, USA. ⁴⁷Genomics Core Laboratory, Memorial Sloan-Kettering Cancer Center, New York, New York 10065, USA. ⁴⁸Department of Pathology, Human Oncology and Pathogenesis Program, Memorial Sloan-Kettering Cancer Center, New York, New York 10065, USA. ⁴⁹Department of Genetics, ⁵⁰Department of Pathology and Laboratory Medicine, ⁵¹Department of Internal Medicine, Division of Medical Oncology, Lineberger Comprehensive Cancer Center, University of North Carolina at Chapel Hill, Chapel Hill, North Carolina 27599, USA. ⁵²Lineberger Comprehensive Cancer Center, University of North Carolina at Chapel Hill, Chapel Hill, North Carolina 27599, USA. ⁵³International Genomics Consortium, Phoenix, Arizona 85004, USA. ⁵⁴Computational Biology Division, Translational Genomics Research Institute, Phoenix, Arizona 85004, USA. ⁵⁵SRA International, Fairfax, Virginia 22033, USA. ⁵⁶Center For Biomedical Informatics and Information Technology, National Cancer Institute, Rockville, Maryland 20852, USA. ⁵⁷Department of Bioinformatics and Computational Biology, M.D. Anderson Cancer Center, Houston, Texas 77030, USA. ⁵⁸National Cancer Institute, National Institutes of Health, Bethesda, Maryland 20892, USA. ⁵⁹MLF Consulting, Arlington, Massachusetts 02474, USA. ⁶⁰National Human Genome Research Institute, National Institutes of Health, Bethesda, Maryland 20892, USA.

Somatic mutations affect key pathways in lung adenocarcinoma

Li Ding^{1*}, Gad Getz^{2*}, David A. Wheeler^{3*}, Elaine R. Mardis¹, Michael D. McLellan¹, Kristian Cibulskis², Carrie Sougnez², Heidi Greulich^{2,4}, Donna M. Muzny³, Margaret B. Morgan³, Lucinda Fulton¹, Robert S. Fulton¹, Qunyan Zhang⁵, Michael C. Wendl¹, Michael S. Lawrence², David E. Larson¹, Ken Chen¹, David J. Dooling¹, Aniko Sabo³, Alicia C. Hawes³, Hua Shen³, Shalini N. Jhangiani³, Lora R. Lewis³, Otis Hall³, Yiming Zhu³, Tittu Mathew³, Yanru Ren³, Jiqiang Yao³, Steven E. Scherer³, Kerstin Clerc³, Ginger A. Metcalf³, Brian Ng³, Aleksandar Milosavljevic³, Manuel L. Gonzalez-Garay³, John R. Osborne¹, Rick Meyer¹, Xiaoqi Shi¹, Yuzhu Tang¹, Daniel C. Koboldt¹, Ling Lin¹, Rachel Abbott¹, Tracie L. Miner¹, Craig Pohl¹, Ginger Fewell¹, Carrie Haipek¹, Heather Schmidt¹, Brian H. Dunford-Shore¹, Aldi Kraja⁵, Seth D. Crosby¹, Christopher S. Sawyer¹, Tammi Vickery¹, Sacha Sander¹, Jody Robinson¹, Wendy Winckler^{2,4}, Jennifer Baldwin², Lucian R. Chirieac^{6,7}, Amit Dutt^{2,4}, Tim Fennell², Megan Hanna^{2,4}, Bruce E. Johnson⁴, Robert C. Onofrio², Roman K. Thomas^{8,9}, Giovanni Tonon⁴, Barbara A. Weir^{2,4}, Xiaojun Zhao^{2,4}, Liuda Ziaugra², Michael C. Zody², Thomas Giordano¹⁰, Mark B. Orringer¹¹, Jack A. Roth¹², Margaret R. Spitz¹³, Ignacio I. Wistuba^{12,14}, Bradley Ozenberger¹⁵, Peter J. Good¹⁵, Andrew C. Chang¹¹, David G. Beer¹¹, Mark A. Watson¹⁶, Marc Ladanyi^{17,18}, Stephen Broderick¹⁷, Akihiko Yoshizawa¹⁷, William D. Travis¹⁷, William Pao^{17,18}, Michael A. Province⁵, George M. Weinstock¹, Harold E. Varmus¹⁹, Stacey B. Gabriel², Eric S. Lander², Richard A. Gibbs³, Matthew Meyerson^{2,4} & Richard K. Wilson¹

Determining the genetic basis of cancer requires comprehensive analyses of large collections of histopathologically well-classified primary tumours. Here we report the results of a collaborative study to discover somatic mutations in 188 human lung adenocarcinomas. DNA sequencing of 623 genes with known or potential relationships to cancer revealed more than 1,000 somatic mutations across the samples. Our analysis identified 26 genes that are mutated at significantly high frequencies and thus are probably involved in carcinogenesis. The frequently mutated genes include tyrosine kinases, among them the *EGFR* homologue *ERBB4*; multiple ephrin receptor genes, notably *EPHA3*; vascular endothelial growth factor receptor *KDR*; and *NTRK* genes. These data provide evidence of somatic mutations in primary lung adenocarcinoma for several tumour suppressor genes involved in other cancers—including *NF1*, *APC*, *RB1* and *ATM*—and for sequence changes in *PTPRD* as well as the frequently deleted gene *LRP1B*. The observed mutational profiles correlate with clinical features, smoking status and DNA repair defects. These results are reinforced by data integration including single nucleotide polymorphism array and gene expression array. Our findings shed further light on several important signalling pathways involved in lung adenocarcinoma, and suggest new molecular targets for treatment.

Lung cancer is the leading cause of cancer death, annually resulting in more than one million deaths worldwide. About 1.2 million new cases are diagnosed each year¹ and prognoses are poor. Lung adenocarcinoma is the most common form of lung cancer and has an average 5-yr survival rate of 15%², mainly because of late-stage detection and a paucity of late-stage treatments.

Although smoking is unquestionably the leading cause of lung cancer, approximately 10% of cases occur in patients who have never smoked³.

Environmental exposures and genetic susceptibility are also thought to contribute to cancer risk^{4–7}. Adenocarcinomas in patients who have never smoked frequently contain mutations within the tyrosine kinase domain of the epidermal growth factor receptor (*EGFR*) gene; those patients often respond to tyrosine kinase inhibitor drugs such as gefitinib and erlotinib^{8–10}, but usually develop drug resistance^{11,12}. Conversely, *KRAS* mutations are more common in individuals with a history of cigarette use and are associated with resistance to *EGFR*-tyrosine-kinase inhibitors^{13,14}.

¹The Genome Center at Washington University, Department of Genetics, Washington University School of Medicine, St Louis, Missouri 63108, USA. ²Cancer Program, Genetic Analysis Platform, and Genome Biology Program, Broad Institute of Harvard and MIT, Cambridge, Massachusetts 02142, USA. ³Human Genome Sequencing Center, Baylor College of Medicine, Houston, Texas 77030, USA. ⁴Department of Medical Oncology and Center for Cancer Genome Discovery, Dana-Farber Cancer Institute, Boston, Massachusetts 02115, USA. ⁵Division of Statistical Genomics, Department of Genetics, Washington University School of Medicine, St Louis, Missouri 63108, USA. ⁶Department of Pathology, Brigham and Women's Hospital, Boston, Massachusetts 02115, USA. ⁷Department of Pathology and Department of Systems Biology, Harvard Medical School, Boston, Massachusetts 02115, USA. ⁸Max-Planck Institute for Neurological Research with Klaus-Joachim Zülch Laboratories of the Max-Planck Society and the Medical Faculty of the University of Cologne, Cologne 50931, Germany. ⁹Center for Integrated Oncology and Department I for Internal Medicine, University of Cologne, Cologne 50931, Germany. ¹⁰Department of Pathology, ¹¹Section of Thoracic Surgery, Department of Surgery, University of Michigan, Ann Arbor, Michigan 48109, USA. ¹²Department of Thoracic and Cardiovascular Surgery, ¹³Department of Epidemiology, and ¹⁴Department of Pathology, The University of Texas M.D. Anderson Cancer Center, Houston, Texas 77030, USA. ¹⁵National Human Genome Research Institute, National Institutes of Health, Bethesda, Maryland 20892, USA. ¹⁶Department of Pathology and Immunology, Washington University in St Louis, St Louis, Missouri 63108, USA. ¹⁷Departments of Medicine, Surgery, Pathology, and Computational Biology. ¹⁸Human Oncology and Pathogenesis Program, and ¹⁹Cancer Biology and Genetics Program, Memorial Sloan-Kettering Cancer Center, New York, New York 10065, USA.

*These authors contributed equally to this work.

Previous gene resequencing efforts have identified several key mutations associated with human cancers^{15–18}. The Tumour Sequencing Project (TSP) is a pilot project to characterize cancer genomes, and has allowed the discovery of somatic mutations in the coding exons of 623 candidate cancer genes in 188 lung adenocarcinomas. Here we identify significantly mutated genes not previously associated with lung adenocarcinoma, describe relationships between different genetic alterations, and report correlations between genetic alterations and clinical features. Moreover, our integration of single nucleotide polymorphism (SNP) array, gene expression array and mutation data provides a broader view of genomic alterations in lung adenocarcinomas. These findings further our understanding of lung cancer and provide clues to new therapeutic targets.

Overview of samples, genes and mutations discovered

We selected 188 primary lung adenocarcinomas, each containing a minimum of 70% tumour cells as determined by study pathologists. We screened for somatic mutations in 623 candidate genes comprising known oncogenes and tumour suppressor genes, protein kinase families, and genes in regions of copy number alteration, focusing on coding exons and splice sites (Supplementary Table 1). A total of 247 megabases of tumour DNA sequence was analysed to identify putative mutations, and non-synonymous mutations were validated by orthogonal methods or confirmed by independent polymerase chain reaction (PCR) amplification and sequencing (Supplementary Methods and Supplementary Fig. 1).

We have identified 1,013 non-synonymous somatic mutations in 163 of the 188 tumours, including 915 point mutations, 12 dinucleotide mutations (mutations affecting two consecutive bases on the same allele), 29 insertions and 57 deletions, with insertions/deletions (indels) ranging from 1 to 23 nucleotides. The point mutations include 802 missense, 75 nonsense, 1 read-through and 37 splice-site mutations (Supplementary Table 2).

A set of 12 genes was found with significantly higher frequencies of nonsense, splice-site and frameshift mutations ($P < 0.1$), suggesting that they were candidate tumour suppressor genes (Supplementary Table 3a). Recurrent somatic mutations were observed at 28 sites across seven genes; these included five previously unknown sites in five genes (Supplementary Table 3b). *In silico* predictions suggest that 580 of the missense mutations have potential functional relevance. A comparison of the mutations to the COSMIC¹⁹ and OMIM²⁰ databases identified 823 somatic mutations and 818 mutation sites that were not present in these databases, respectively (Supplementary Methods and Supplementary Table 2).

Significantly mutated genes in lung adenocarcinoma

The large size of our sample set enabled the identification of mutated genes that show evidence for positive selection in lung adenocarcinoma. We used three different methods (Supplementary Methods and Supplementary Tables 4 and 5) to determine the significance of the difference between the observed versus expected numbers of mutations in 188 tumours. We identified a total of 26 significantly mutated genes, among them 17 genes are designated as significant by at least two approaches (Fig. 1 and Supplementary Table 6a). Note that *LRP1B*, despite its large number of mutations, was found to be significant by only one method, mostly owing to its long coding sequence.

The study identified many genes previously known to be mutated in lung adenocarcinoma, including several tumour suppressor genes (*TP53* (ref. 21), *CDKN2A* (ref. 22) and *STK11* (ref. 23)) and oncogenes (*KRAS*²⁴, *EGFR*⁸ and *NRAS*²⁵). In addition, we found several new genes that were significantly mutated in this disease.

Bona fide and putative tumour suppressor genes. The most prominent case for a tumour suppressor gene is *NF1*, for which inactivating mutations are found in neurofibromatosis type I patients²⁶. In this study, 16 *NF1* mutations (4 nonsense, 5 splice-site and 1 frameshift mutations) were identified in 13 patients (Supplementary Table

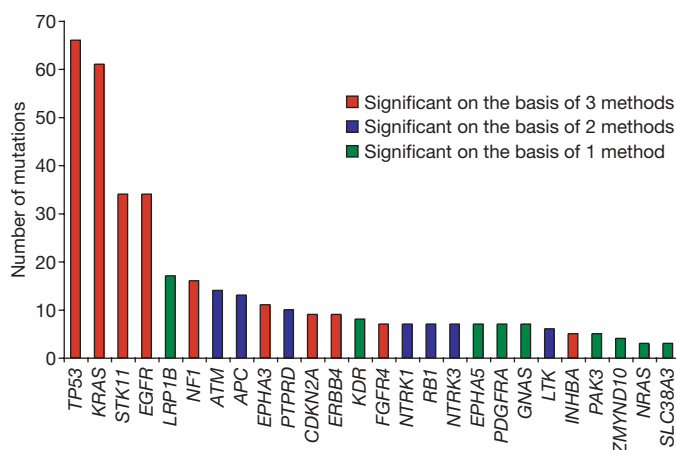


Figure 1 | Significantly mutated genes in lung adenocarcinomas. The height of the bars represents the number of somatic mutations in each indicated gene in 188 tumour and normal pairs. Standard, gene-specific and category-based tests were used for this analysis (Supplementary Information). Ten genes were found to be significantly mutated by all three statistical methods (red bars), 7 genes by at least two methods (blue bars) and 9 genes by one of the three methods (green bars), for up to 26 significantly mutated genes in total.

2). Three tumours harboured two mutations each, although it is not known whether these mutations are *in cis* or *in trans*. This suggests potential bi-allelic inactivation of *NF1* in these three patients.

Another previously unknown mutated tumour suppressor gene in lung adenocarcinoma is *ATM*, encoding a cell-cycle checkpoint kinase that functions as a regulator of p53 (ref. 27). Genetic polymorphisms of *ATM* are known to affect lung cancer risk²⁸, but only isolated instances of *ATM* somatic mutation have been reported in lung adenocarcinoma¹⁵. We found 14 *ATM* mutations in 13 tumours, including 1 nonsense, 1 splice-site and 2 frameshift mutations (Supplementary Table 2).

Another tumour suppressor gene harbouring frequent mutations is *RBI*, which was first identified as the susceptibility gene for retinoblastoma²⁹. Given that DNA tumour viruses such as papillomaviruses typically target *RBI* and *TP53* simultaneously³⁰, it is interesting to note that five of the seven *RBI* mutations occur in tumours with *TP53* mutations, and two occur in tumours with *ATM* mutations, suggesting that an *ATM* mutation may substitute functionally for a *TP53* mutation.

APC mutations have been reported in lung squamous cell carcinoma and small-cell lung carcinoma³¹, but not in lung adenocarcinoma. We observed 13 mutations in 11 tumours confirmed by pathology evaluation to be lung tumour samples and not metastatic colorectal carcinomas. Mutations (G34E and S37F) of the *CTNNB1* gene were observed in two other tumours.

Deletion and epigenetic silencing of *LRP1B* have been previously observed in lung cancer cell lines and oesophageal tumours^{32,33}. Our finding of 17 mutations in *LRP1B* further supports the notion that *LRP1B* genomic alterations are significant in lung cancer pathogenesis (Fig. 1). *PTPRD*, previously shown to be deleted in lung adenocarcinoma^{34,35}, is also found to be frequently mutated³⁴. Owing to the absence of nonsense, splice-site or frameshift mutations in both of these genes in our tumour set, further evidence is required to determine whether they are tumour suppressors or another category of genes.

Possible proto-oncogenes. Although the involvement of *EGFR* and *ERBB2* mutations in lung cancer has been reported previously, we also found mutations at a significant frequency in *ERBB4* (Fig. 1). The discovery of nine mutations in *ERBB4*, two of which are putatively deleterious with respect to the protein tyrosine kinase domain and five of which are clustered in the receptor ligand binding domain, indicates its involvement in lung cancer (Fig. 2). We also discovered four mutations in *ERBB2* and three in *ERBB3*.

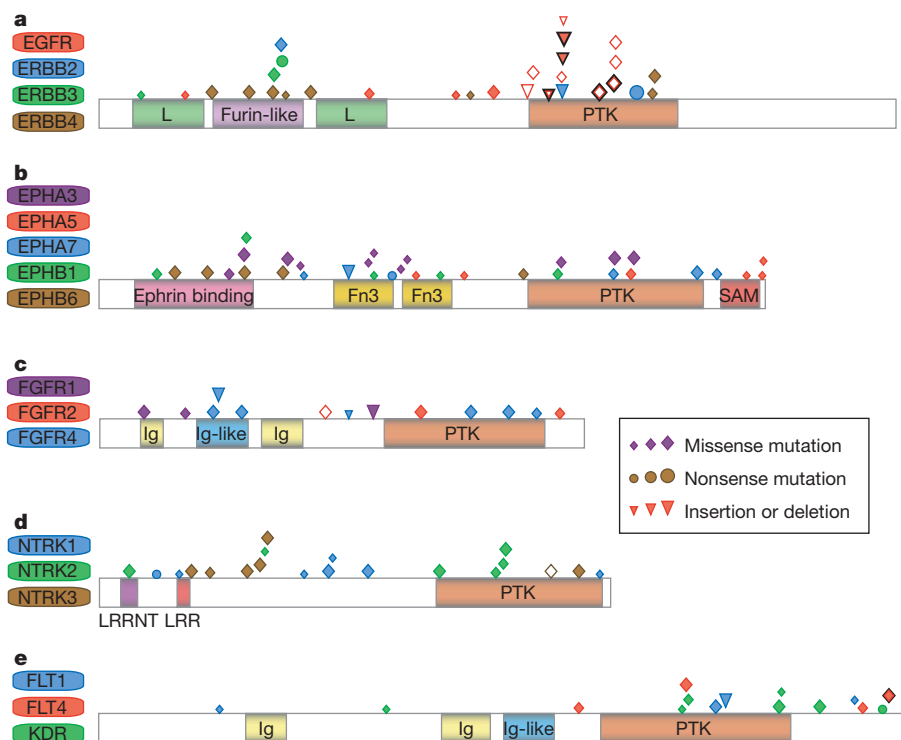


Figure 2 | Diagrams of mutations found in the members of several receptor families in lung adenocarcinomas. **a–e**, Mutations in members of the EGF (**a**), EPH (**b**), FGF (**c**), NTRK (**d**) and VEGF (**e**) receptor families are shown. Protein domains are determined by using HMMFAM. The PFAM domains include 'L' (receptor ligand binding domain), Fn3 (fibronectin type III domain), Ig (immunoglobulin domain), LRR (leucine rich repeat domain), LRRNT (leucine rich repeat amino-terminal domain), PTK (protein

tyrosine kinase domain) and SAM (sterile α -motif). The locations of mutations are indicated by diamonds, circles and triangles, with filled shapes representing new mutations and open shapes denoting known mutations. The size of the shapes is positively proportional to the degree of conservation at the mutated residue. Representative scheme for each family is constructed based on the ClustalW2 alignment. Recurrent mutations are outlined in black.

The most significantly mutated gene in the ephrin family is *EPHA3* (Fig. 1). Although isolated mutations in this gene have been reported^{15,17}, this is to our knowledge the first demonstration of statistical significance of *EPHA3* mutations in lung adenocarcinoma. The 11 mutations in *EPHA3* are distributed along the length of the gene, with 8 mutations in the extracellular domain and 3 in the kinase

domain, but no hotspot positions in which mutations cluster. One observed mutation in *EPHA3*, K761N, is located in the kinase domain at a highly conserved position analogous to *FGFR2*(K641)—part of a newly described “molecular brake”³⁶. In total, we identified 37 mutations in 10 of the 13 ephrin receptors sequenced, finding high mutation rates in several family members (Figs 1 and 2).

Previous mutational screening of the tyrosine kinase domain of NTRKs identified 9 mutations in 29 large-cell neuroendocrine carcinomas, but found no mutations in 443 non-small-cell lung cancers³⁷. In contrast we discovered 20 mutations in NTRKs (Fig. 1) of which 7 mutations occur within their tyrosine kinase domains, suggesting that the role of NTRKs is not restricted to large-cell neuroendocrine carcinomas. A significant number of mutations have also been identified in VEGFR and FGFR family members. In particular, four and three kinase domain mutations were found in *KDR* and *FGFR4* (ref. 38), respectively (Fig. 2 and Supplementary Table 2).

Notably, several known oncogenes and tumour suppressor genes fell below the borderline of significance in our study. These genes include the proto-oncogenes *AKT1* (in which we found two mutations, including one (E17K) described as a transforming mutation in other cancers³⁹), *CTNNB1*, *ERBB2* (ref. 40) and *BRAF*⁴¹, as well as the *PTEN* tumour suppressor gene⁴². These results offer enriched data for investigating mutated functional domains (Supplementary Methods and Supplementary Table 6b) and for analysing interactions among mutations and pathways.

Concurrent and mutually exclusive mutations

We searched for correlations among mutations in 29 genes with at least 6 mutations each. The strongest positive correlations were for mutations in *PIK3C3* and *PTPRD*, *NTRK2* and *PDGFRA*, *FGFR4* and

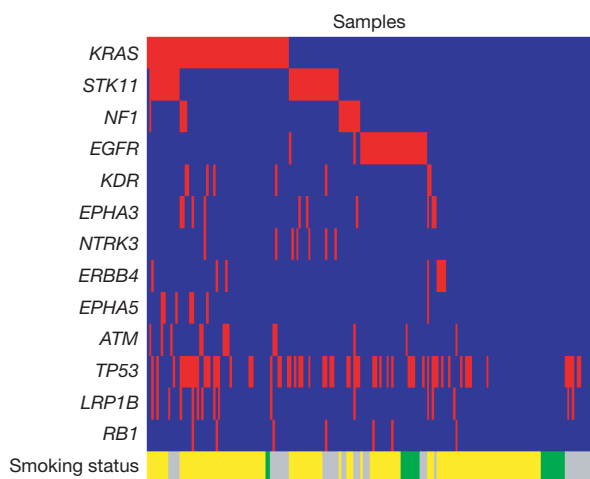


Figure 3 | Concurrent and mutual exclusion of mutations observed across genes in lung adenocarcinomas. Tumours with and without mutations in the indicated genes are labelled in red and blue in the corresponding columns, respectively. Tumours from smokers (former and current) and from individuals who have never smoked are labelled in yellow and green, respectively. Tumours without smoking status are labelled in grey.

NTRK2, and *FGFR4* and *PDGFRA* ($P \leq 0.01$; Supplementary Table 7a, c). The well-known example of negative correlation of mutations in *EGFR* and *KRAS*¹⁴ was confirmed in this study ($P < 1 \times 10^{-07}$), with no sample having mutations in both genes (Fig. 3). We also found negative correlation between mutations in *EGFR* and *STK11* ($P = 7 \times 10^{-06}$), consistent with a previous report⁴³. Notably, samples with mutations in several receptor tyrosine kinase genes do not harbour any mutations in *EGFR* (Fig. 3). We also detected a strong negative correlation between mutations in *ATM* and *TP53* ($P = 9.5 \times 10^{-05}$; Fig. 3), suggesting that mutations in *ATM* and *TP53* may be independently sufficient for the loss of cell-cycle checkpoint control.

Distributions of mutations in individual cancer genomes

We studied the spectrum of mutations observed across tumours, in relation to the overall mutation rate and to clinical phenotypes. We found that mutations in *TP53*, *PRKDC*, *SMG1* and a set of other genes (Supplementary Table 8) are positively correlated with higher mutation rates. Of particular interest, four of the six most highly mutated tumours have mutations in *PRKDC*, which encodes a protein involved in the repair of double-stranded DNA breaks⁴⁴ (Fig. 4a). The average of 24.3 mutations in tumours having *PRKDC* mutations is significantly higher than the average of 4.7 mutations in tumours without *PRKDC* mutations ($P = 3.52 \times 10^{-59}$).

We also determined that a set of genes including *EGFR* ($P = 0.05$) and *PTEN* ($P = 0.03$) tended to be mutated in tumours with lower-than-average mutation rates. Mutations in *EGFR* and *PTEN* may have strong tumour-growth-promoting capability and thereby reduce the selection pressure for acquiring further mutations.

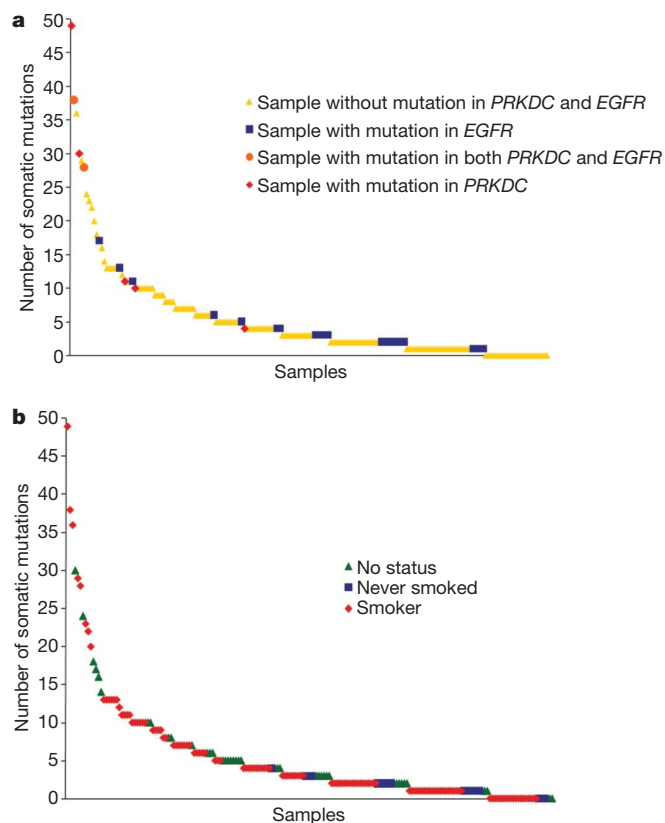


Figure 4 | Mutation distributions in individual lung adenocarcinoma genomes. **a**, Tumours with mutations in *PRKDC* showed higher than average mutation rates, and conversely tumours with mutations in *EGFR* had lower than average mutation rates. **b**, Smokers have on average threefold higher mutation rates compared to individuals who have never smoked.

Integration with copy number and gene expression data

Subsets of the TSP tumour collection were analysed using SNP array ($n = 383$), re-sequencing ($n = 188$) and gene expression array ($n = 75$). All tumours used for sequencing and expression studies have been analysed using SNP array. Significant correlation (false discovery rate < 0.05) between copy number and expression level in 75 tumours was observed, similar to the trend seen in a previous study⁴⁵ (Supplementary Information and Supplementary Table 9).

Comparison of mutation data with copy number analysis³⁴ shows that several significantly mutated genes are present in peaks of copy number gain (*EGFR* and *KRAS*) or loss (*CDKN2A*, *PTPRD* and *RB1*). Other amplified genes are subject to recurrent mutations (for example *ERBB2*, *MDM2* and *TERT*) although the mutation frequency does not reach statistical significance. In parallel, several significantly mutated genes show rare amplifications or deletions. The *NRAS* oncogene is subject to rare amplification in lung adenocarcinoma (Supplementary Fig. 4). The amplification of *EPHA3* and *KDR* (Supplementary Figs 4 and 5) seen in two tumours each, indicates that these genes are probably proto-oncogenes. Conversely, we found *NF1* to be homozygously deleted in one tumour (Supplementary Fig. 4).

Furthermore, we found that mutations in *PTEN*, *APC* and *TP53* were correlated with copy number loss (Supplementary Table 10a), suggesting that these three genes might each undergo homozygous loss of function. Conversely, mutations in *EGFR*, *HCK*, *KRAS* and *EPHB1* were associated with copy number gain (Supplementary Table 10a), consistent with a proto-oncogene function. Notably, three of the six tumours with the highest *EGFR* amplification also have mutations in *EGFR*, and five of the six tumours with the highest *KRAS* amplification also harbour *KRAS* mutations (Supplementary Table 11). In many cases, the mutant allele is preferentially amplified (Supplementary Fig. 6) but larger sample sets are required to determine the statistical significance.

We investigated the correlation among mutations, copy number and gene expression in 41 lung adenocarcinomas with all three types of data. Mutations in *TP53* (Fig. 5a) and *APC* (Fig. 5b) are correlated with lower copy number and lower messenger RNA expression levels. Correlations with lower gene expression are also seen for *STK11* and *ATM* mutations (Supplementary Table 10b). Mutations in these tumour suppressor genes could cause instability of their cognate mRNAs. Conversely, mutations in *EGFR* (Fig. 5c) and *KRAS* (Fig. 5d) are associated with higher mRNA expression levels as well as higher copy number, as are *EPHB1* mutations (Supplementary Table 10b).

Integrated analysis of significantly mutated pathways

Further insight into the role of genomic alterations underlying lung adenocarcinoma was gained by examining the distribution of mutations across Kyoto Encyclopedia of Genes and Genomes (KEGG) pathways (Fig. 6, Supplementary Methods and Supplementary Tables 11–13).

In the MAPK pathway we found 289 mutations in 56 genes, including members of EGF, FGF and NTRK receptor families, and *KRAS* and *NF1* (Fig. 6). Notably, 132 of the 188 tumours sequenced have at least one mutation in the MAPK pathway, underscoring its pivotal role in lung cancer.

We identified mutations in multiple components of the Wnt pathway, including *APC*, *CTNNB1*, *SMAD2*, *SMAD4* and *GSK3B*. Of the 188 lung adenocarcinomas 29 showed mutations in this pathway (not including mutations in *TP53*, which is included in the Wnt pathway in KEGG), which is to our knowledge the first demonstration of Wnt alteration in lung adenocarcinoma. At least one mutation in the p53 pathway was seen in 85 tumours. In addition to the 66 *TP53* mutations, frequent mutations were found in *ATM* and amplifications were identified in *MDM2* (Fig. 6).

We have found an array of mutations in *PTEN*, PI3K genes and AKT genes—all members of the insulin/PI3K/AKT signalling arm of this pathway (Fig. 6). In addition, 13 tumours were found to carry 16

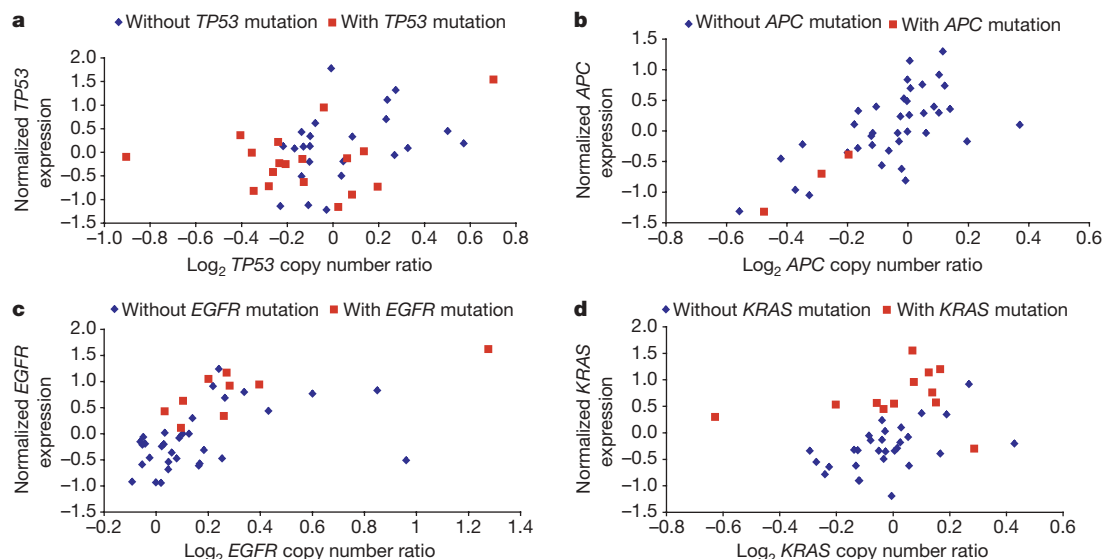


Figure 5 | DNA copy number, gene expression, and mutation distributions in lung adenocarcinomas. **a–d**, Copy number, gene expression and mutation status at *TP53* (**a**), *APC* (**b**), *EGFR* (**c**) and *KRAS* (**d**) loci in 41 lung

NF1 mutations, the deficiency of which has been implicated in RAS- and PI3K-dependent hyperactivation of the mTOR pathway⁴⁶. More than 30 mutations were also discovered in *STK11*, a member of the AMP-dependent protein kinase signalling pathway. By sequencing 70 polymorphic *STK11* SNP sites, we identified 17 tumours with loss of heterozygosity (LOH) (as defined by at least three consecutive heterozygous loci that reduced to homozygosity in the tumour; Supplementary Table 14). Two tumours having clear regions of LOH at *STK11* also harboured one nonsense mutation and one deletion, suggesting possible homozygous loss of function. Six tumours

adenocarcinomas. Normalized gene expression and \log_2 DNA copy number ratio in each sample were determined as described in Supplementary Information.

have mutations in the tuberous sclerosis complex 1 and 2 (TSC1 and TSC2). In summary, mTOR pathway components are mutated in 17 genes and in more than 30% of tumours sequenced, not including tumours with *KRAS* mutations. Our finding suggests that dysregulation of mTOR is important for lung carcinogenesis and hence is a potential therapeutic target. The effectiveness of rapamycin and its analogues in the treatment of lung adenocarcinoma should be further tested.

There are nine mutations in *CDKN2A* and one each in *CDKN2B* and *CDKN2C*, as well as seven mutations in *RB1*. Furthermore, as described there are frequent focal amplifications of *CDK4* and *CDK6* as well as *CCND1* and *CCNE1*, and frequent deletions of *RB1*, *CDKN2A* and *CDKN2B* (ref. 34; Fig. 6).

Mutations correlated with clinical features

We investigated the distribution of mutations across different clinical subgroups, including smoking status, tumour grade, tumour stage and histological subtype (Fig. 4, Supplementary Fig. 7 and Supplementary Table 15).

The average number of mutations in smokers is significantly higher than in individuals who have never smoked ($P = 0.021$, t -test), and notably none of the tumours from those who have never smoked had more than five mutations in the resequenced genes, whereas smokers had as many as 49 mutations (Fig. 4b). Consistent with previous findings⁴⁷, we observed that *EGFR* mutations correlate with the status of patients who have never smoked ($P = 0.0046$, Fisher's exact test), whereas *KRAS* mutations correlate with smoker status ($P = 0.021$). We also have observed correlation between mutations in *STK11* and smokers ($P = 0.044$), consistent with a previous report⁴³.

As expected, tumours with higher grade had accumulated more mutations than tumours of lower grade ($P = 0.001$; Supplementary Fig. 7a). Some genes showed a clear increase in the frequency of somatic mutation with tumour grade, suggesting that these genes may have a role in transformation or progression. A clear example is *TP53*, with somatic mutations in 13%, 24% and 52% of tumours of grade 1, 2 and 3, respectively (correlation $P = 7.8 \times 10^{-06}$), consistent with a previous report⁴⁸. Other genes in which the mutation frequency positively correlated with tumour grade were *LRP1B* ($P = 0.013$), *INHBA* ($P = 0.013$) and *PRKDC* ($P = 0.018$). Conversely, other genes showed no significant correlation with tumour grade, which could indicate that mutations in this group

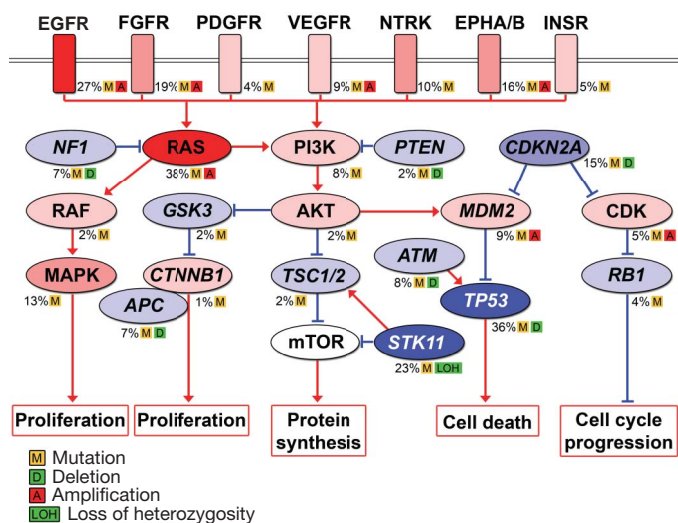


Figure 6 | Significantly mutated pathways in lung adenocarcinomas. Genetic alterations in lung adenocarcinoma frequently occur in genes of the MAPK signalling, p53 signalling, Wnt signalling, cell cycle and mTOR pathways. Oncoproteins are indicated in pink to red and tumour suppressor proteins are shown in light to dark blue. The darkness of the colours is positively correlated to the percentage of tumours with genetic alterations. Frequency of genetic alterations for each of these pathway members in 188 tumours is indicated. Genes (*EGFR*, *FGFR1*, *FGFR4*, *KDR*, *EPHA3*, *KRAS*, *NRAS*, *MDM2* and *CDK6*) lying in regions of focal amplification were analysed for the percentage of samples with copy number amplification. Samples with greater than 2.5 and fewer than 1.5 DNA copies were considered as amplified and deleted, respectively. Selected components of each pathway are shown in the figure.

of genes are critical early in tumorigenesis. A clear example is *KRAS*, with somatic mutations in 38%, 32% and 32% of tumours of grades 1, 2 and 3, respectively.

Our analysis shows that tumours of higher stage had accumulated more mutations than tumours of lower stage ($P = 0.006$; Supplementary Fig. 7b), although this rate varies widely among individual tumours. We found significant correlations between tumour stage and mutations in *NTRK2* ($P = 0.003$), *EPHA7* ($P = 0.003$), *PRKCG* ($P = 0.0087$) and *FLT4* ($P = 0.0093$).

There are several subclasses of lung adenocarcinoma, including acinar, papillary, BAC (bronchioloalveolar carcinoma) and solid, on the basis of World Health Organization standards^{49,50}. Our most notable finding was that mutations in *LRP1B*, *TP53* and *INHBA* show various levels of negative correlation with acinar, papillary and BAC subtypes, but significant positive correlation with solid subtype (*LRP1B*, $P = 2.29 \times 10^{-05}$; *TP53*, $P = 0.002$; *INHBA*, $P = 0.0023$) in 152 tumours with subtype information. On the other hand mutations in *EGFR* showed moderate negative correlation with the solid subtype ($P = 0.13$) and significant positive correlation with the papillary subtype ($P = 0.041$), consistent with a previous report⁵⁰.

Furthermore, our analysis shows that the 25 patients in which no mutations were found have diverse clinical features and some show a comparable extent of copy number alterations compared to samples having mutations (Supplementary Table 16). Of note, 16 of 25 tumours without discovered mutations in the 623 genes are from the group with higher stromal contamination rate (Supplementary Table 17), suggesting that stromal contamination might reduce the sensitivity in discovering mutations.

Discussion

Our study represents to our knowledge the largest effort so far to characterize genomic alterations in lung adenocarcinoma. Before this study, there were five genes known to be mutated at high frequency in lung adenocarcinoma—*TP53*, *KRAS*, *STK11*, *EGFR* and *CDKN2A*—as well as several known genes with lower mutation frequencies—*PTEN*, *NRAS*, *ERBB2*, *BRAF* and *PIK3CA*. After sequencing 623 genes in 188 tumours, we have identified further significantly mutated genes, more than doubling the list. The newly identified genes include tumour suppressor genes (*NF1*, *RB1*, *ATM* and *APC*) along with tyrosine kinase genes (ephrin receptor genes, *ERBB4*, *KDR*, *FGFR4* and *NTRK* genes) that may function as proto-oncogenes. We have demonstrated that many of these genes are also targeted by copy number alterations and/or gene expression changes. Additionally, there is a significant excess of mutations and copy number alterations in genes from the MAPK, p53, Wnt, cell cycle and mTOR signalling pathways, suggesting links to the disease. Our results also demonstrate that lung adenocarcinomas are heterogeneous, with diverse combinations of mutations yet commonality in the main pathways affected by these mutations. The mutation rate varies across tumour samples and is probably influenced by DNA mismatch repair defects and clinical features. The newly discovered genes and pathways may expand the range of potential therapeutic options for treatment of lung adenocarcinoma. For example, inhibitors of the MEK kinase could be tested in tumours with *NF1* mutations, whereas inhibitors of KDR, such as sorafenib and sunitinib, might be tested in tumours with *KDR* mutations.

Although the analysis of the 188 TSP tumours is the largest tumour-type-specific screen for mutations to date, it does not have complete power to detect some genes known to be associated with lung cancer. Thus, larger sample sizes will be desirable. Moreover, these approaches should be extended to other types of lung cancer, metastatic lung cancer, and other cancers to determine the underlying genetic basis of those diseases and to highlight potential approaches for diagnosis and therapy. These studies can also be extended by comprehensive resequencing of the entire transcriptome, the entire collection of exons or the entire genome in large collections of cancers. Such studies

should be feasible with next-generation sequencing technologies and at present are being prototyped within this programme.

METHODS SUMMARY

Source DNAs were extracted from primary lung adenocarcinoma tumours and adjacent normal tissue (or peripheral blood lymphocytes). Collection and use of all tissue samples were approved by the human subjects Institutional Review Boards of participating institutions. These samples were snap-frozen, anonymized and contributed along with matched normal samples by the Dana-Farber Cancer Institute, MD Anderson Cancer Center, Memorial Sloan-Kettering Cancer Center, University of Michigan, and Washington University in St Louis. Affymetrix 250K StyI Array data were used to estimate the level of stromal contamination and thereby to select 188 tumours and matched normals for the resequencing study. Whole-genome amplification was performed using Qiagen REPLI-g Service before sequencing. All coding exons and splice-site sequences of 623 target genes were PCR amplified and sequenced on both strands for all of the tumours. Additional data were generated until more than 90% of targeted exonic and splice-site bases were covered by at least one sequence read. Traces were automatically processed to identify SNPs and indels. Sequence data were obtained for the matched normals from a variety of platforms to determine the somatic status of new variants and unvalidated dbSNPs. Further data were generated using orthogonal technologies to validate the candidate somatic mutations. Synonymous somatic mutations identified in 250 genes were used to estimate the background mutation rate, which was used in statistical calculations to identify significantly mutated genes. Statistical approaches were used to identify significantly mutated pathways. Expression profiles were determined for 75 TSP tumours using the Affymetrix U133Plus2 GeneChip. Further analyses were performed to determine correlation between mutation and copy number variation, mutation and gene expression, copy number variation and gene expression, as well as mutation and clinical attributes.

Received 9 June; accepted 10 September 2008.

- Juergens, R. A. & Brahmer, J. R. Adjuvant treatment in non-small cell lung cancer: Where are we now? *J. Natl Compr. Canc. Netw.* **4**, 595–600 (2006).
- Parkin, D. M., Bray, F., Ferlay, J. & Pisani, P. Global cancer statistics, 2002. *CA Cancer J. Clin.* **55**, 74–108 (2005).
- Hecht, S. S. Tobacco smoke carcinogens and lung cancer. *J. Natl Cancer Inst.* **91**, 1194–1210 (1999).
- Hung, R. J. *et al.* A susceptibility locus for lung cancer maps to nicotinic acetylcholine receptor subunit genes on 15q25. *Nature* **452**, 633–637 (2008).
- Sellers, T. A. *et al.* Evidence for mendelian inheritance in the pathogenesis of lung cancer. *J. Natl Cancer Inst.* **82**, 1272–1279 (1990).
- Sellers, T. A., Weaver, T. W., Phillips, B., Altmann, M. & Rich, S. S. Environmental factors can confound identification of a major gene effect: results from a segregation analysis of a simulated population of lung cancer families. *Genet. Epidemiol.* **15**, 251–262 (1998).
- Thorgeirsson, T. E. *et al.* A variant associated with nicotine dependence, lung cancer and peripheral arterial disease. *Nature* **452**, 638–642 (2008).
- Pao, W. *et al.* EGF receptor gene mutations are common in lung cancers from “never smokers” and are associated with sensitivity of tumors to gefitinib and erlotinib. *Proc. Natl Acad. Sci. USA* **101**, 13306–13311 (2004).
- Lynch, T. J. *et al.* Activating mutations in the epidermal growth factor receptor underlying responsiveness of non-small-cell lung cancer to gefitinib. *N. Engl. J. Med.* **350**, 2129–2139 (2004).
- Paez, J. G. *et al.* EGFR mutations in lung cancer: correlation with clinical response to gefitinib therapy. *Science* **304**, 1497–1500 (2004).
- Kobayashi, S. *et al.* EGFR mutation and resistance of non-small-cell lung cancer to gefitinib. *N. Engl. J. Med.* **352**, 786–792 (2005).
- Pao, W. *et al.* Acquired resistance of lung adenocarcinomas to gefitinib or erlotinib is associated with a second mutation in the EGFR kinase domain. *PLoS Med.* **2**, e73 (2005).
- Le Calvez, F. *et al.* TP53 and KRAS mutation load and types in lung cancers in relation to tobacco smoke: distinct patterns in never, former, and current smokers. *Cancer Res.* **65**, 5076–5083 (2005).
- Pao, W. *et al.* KRAS mutations and primary resistance of lung adenocarcinomas to gefitinib or erlotinib. *PLoS Med.* **2**, e17 (2005).
- Davies, H. *et al.* Somatic mutations of the protein kinase gene family in human lung cancer. *Cancer Res.* **65**, 7591–7595 (2005).
- Greenman, C. *et al.* Patterns of somatic mutation in human cancer genomes. *Nature* **446**, 153–158 (2007).
- Sjoberg, T. *et al.* The consensus coding sequences of human breast and colorectal cancers. *Science* **314**, 268–274 (2006).
- Wood, L. D. *et al.* The genomic landscapes of human breast and colorectal cancers. *Science* **318**, 1108–1113 (2007).
- Forbes, S. *et al.* Cosmic 2005. *Br. J. Cancer* **94**, 318–322 (2006).
- McKusick, V. A. Mendelian inheritance in man and its online version, OMIM. *Am. J. Hum. Genet.* **80**, 588–604 (2007).

21. Takahashi, T. *et al.* p53: a frequent target for genetic abnormalities in lung cancer. *Science* **246**, 491–494 (1989).
22. Packenham, J. P. *et al.* Homozygous deletions at chromosome 9p21 and mutation analysis of p16 and p15 in microdissected primary non-small cell lung cancers. *Clin. Cancer Res.* **1**, 687–690 (1995).
23. Sanchez-Cespedes, M. *et al.* Inactivation of LKB1/STK11 is a common event in adenocarcinomas of the lung. *Cancer Res.* **62**, 3659–3662 (2002).
24. Rodenhuis, S. *et al.* Incidence and possible clinical significance of K-ras oncogene activation in adenocarcinoma of the human lung. *Cancer Res.* **48**, 5738–5741 (1988).
25. Sasaki, H. *et al.* Nras and Kras mutation in Japanese lung cancer patients: Genotyping analysis using LightCycler. *Oncol. Rep.* **18**, 623–628 (2007).
26. Cawthon, R. M. *et al.* A major segment of the neurofibromatosis type 1 gene: cDNA sequence, genomic structure, and point mutations. *Cell* **62**, 193–201 (1990).
27. Chehab, N. H., Malikzay, A., Appel, M. & Halazonetis, T. D. Chk2/hCds1 functions as a DNA damage checkpoint in G₁ by stabilizing p53. *Genes Dev.* **14**, 278–288 (2000).
28. Kim, J. H. *et al.* Genetic polymorphisms of ataxia telangiectasia mutated affect lung cancer risk. *Hum. Mol. Genet.* **15**, 1181–1186 (2006).
29. Friend, S. H. *et al.* Deletions of a DNA sequence in retinoblastomas and mesenchymal tumors: organization of the sequence and its encoded protein. *Proc. Natl Acad. Sci. USA* **84**, 9059–9063 (1987).
30. Howley, P. M., Scheffner, M., Huibregtse, J. & Munger, K. Oncoproteins encoded by the cancer-associated human papillomaviruses target the products of the retinoblastoma and p53 tumor suppressor genes. *Cold Spring Harb. Symp. Quant. Biol.* **56**, 149–155 (1991).
31. Ohgaki, H. *et al.* APC mutations are infrequent but present in human lung cancer. *Cancer Lett.* **207**, 197–203 (2004).
32. Liu, C. X. *et al.* LRP-DIT, a putative endocytic receptor gene, is frequently inactivated in non-small cell lung cancer cell lines. *Cancer Res.* **60**, 1961–1967 (2000).
33. Sonoda, I. *et al.* Frequent silencing of low density lipoprotein receptor-related protein 1B (LRP1B) expression by genetic and epigenetic mechanisms in esophageal squamous cell carcinoma. *Cancer Res.* **64**, 3741–3747 (2004).
34. Weir, B. A. *et al.* Characterizing the cancer genome in lung adenocarcinoma. *Nature* **450**, 893–898 (2007).
35. Zhao, X. *et al.* Homozygous deletions and chromosome amplifications in human lung carcinomas revealed by single nucleotide polymorphism array analysis. *Cancer Res.* **65**, 5561–5570 (2005).
36. Chen, H. *et al.* A molecular brake in the kinase hinge region regulates the activity of receptor tyrosine kinases. *Mol. Cell* **27**, 717–730 (2007).
37. Marchetti, A. *et al.* Frequent mutations in the neurotrophic tyrosine receptor kinase gene family in large cell neuroendocrine carcinoma of the lung. *Hum. Mutat.* **29**, 609–616 (2008).
38. Marks, J. L. *et al.* Mutational analysis of EGFR and related signaling pathway genes in lung adenocarcinomas identifies a novel somatic kinase domain mutation in FGFR4. *PLoS One* **2**, e426 (2007).
39. Carpten, J. D. *et al.* A transforming mutation in the pleckstrin homology domain of AKT1 in cancer. *Nature* **448**, 439–444 (2007).
40. Stephens, P. *et al.* Lung cancer: intragenic ERBB2 kinase mutations in tumours. *Nature* **431**, 525–526 (2004).
41. Davies, H. *et al.* Mutations of the BRAF gene in human cancer. *Nature* **417**, 949–954 (2002).
42. Forgacs, E. *et al.* Mutation analysis of the PTEN/MMAC1 gene in lung cancer. *Oncogene* **17**, 1557–1565 (1998).
43. Koivunen, J. P. *et al.* Mutations in the LKB1 tumour suppressor are frequently detected in tumours from Caucasian but not Asian lung cancer patients. *Br. J. Cancer* **99**, 245–252 (2008).
44. Burma, S. & Chen, D. J. Role of DNA-PK in the cellular response to DNA double-strand breaks. *DNA Repair (Amst.)* **3**, 909–918 (2004).
45. Pollack, J. R. *et al.* Microarray analysis reveals a major direct role of DNA copy number alteration in the transcriptional program of human breast tumors. *Proc. Natl Acad. Sci. USA* **99**, 12963–12968 (2002).
46. Sandsmark, D. K. *et al.* Nucleophosmin mediates mammalian target of rapamycin-dependent actin cytoskeleton dynamics and proliferation in neurofibromin-deficient astrocytes. *Cancer Res.* **67**, 4790–4799 (2007).
47. Subramanian, J. & Govindan, R. Lung cancer in never smokers: a review. *J. Clin. Oncol.* **25**, 561–570 (2007).
48. Ahrendt, S. A. *et al.* p53 mutations and survival in stage I non-small-cell lung cancer: results of a prospective study. *J. Natl Cancer Inst.* **95**, 961–970 (2003).
49. Beasley, M. B., Brambilla, E. & Travis, W. D. The 2004 World Health Organization classification of lung tumors. *Semin. Roentgenol.* **40**, 90–97 (2005).
50. Motoi, N. *et al.* Lung adenocarcinoma: modification of the 2004 WHO mixed subtype to include the major histologic subtype suggests correlations between papillary and micropapillary adenocarcinoma subtypes, EGFR mutations and gene expression analysis. *Am. J. Surg. Pathol.* **32**, 810–827 (2008).

Supplementary Information is linked to the online version of the paper at www.nature.com/nature.

Acknowledgements We thank A. Lash, M. F. Zakowski, M. G. Kris and V. Rusch for intellectual contributions, and many members of the Baylor Human Genome Sequencing Center, the Broad Institute of Harvard and MIT, and the Genome Center at Washington University for support. This work was funded by grants from the National Human Genome Research Institute to E.S.L., R.A.G. and R.K.W.

Author Information The TSP study accession number in the database of Genotype and Phenotype (dbGaP) is phs000144.v1.p1. The gene expression omnibus (GEO) accession number for TSP expression data is GSE12667. Reprints and permissions information is available at www.nature.com/reprints. Correspondence and requests for materials should be addressed to R.K.W. (rwilson@wustl.edu) or M.M. (matthew_meyerson@dfci.harvard.edu).

ARTICLES

BAX activation is initiated at a novel interaction site

Evripidis Gavathiotis^{1,2,3*}, Motoshi Suzuki^{4*}, Marguerite L. Davis^{1,2,3}, Kenneth Pitter^{1,2,3}, Gregory H. Bird^{1,2,3}, Samuel G. Katz^{1,2,3}, Ho-Chou Tu⁵, Hyungjin Kim⁵, Emily H.-Y. Cheng⁵, Nico Tjandra⁴ & Loren D. Walensky^{1,2,3}

BAX is a pro-apoptotic protein of the BCL-2 family that is stationed in the cytosol until activated by a diversity of stress stimuli to induce cell death. Anti-apoptotic proteins such as BCL-2 counteract BAX-mediated cell death. Although an interaction site that confers survival functionality has been defined for anti-apoptotic proteins, an activation site has not been identified for BAX, rendering its explicit trigger mechanism unknown. We previously developed stabilized α -helix of BCL-2 domains (SAHBs) that directly initiate BAX-mediated mitochondrial apoptosis. Here we demonstrate by NMR analysis that BIM SAHB binds BAX at an interaction site that is distinct from the canonical binding groove characterized for anti-apoptotic proteins. The specificity of the human BIM-SAHB-BAX interaction is highlighted by point mutagenesis that disrupts functional activity, confirming that BAX activation is initiated at this novel structural location. Thus, we have now defined a BAX interaction site for direct activation, establishing a new target for therapeutic modulation of apoptosis.

The BCL-2 family comprises a network of pro- and anti-apoptotic proteins whose interactions regulate the critical balance between cellular life and death^{1–3}. The family is structurally defined by the presence of up to four conserved ‘BCL-2 homology’ (BH) domains, all of which include α -helical segments⁴. Anti-apoptotic proteins such as BCL-2 and BCL-X_L (also known as BCL2 and BCL2L1, respectively) show sequence conservation in three to four BCL-2 homology domains (BH1–4), whereas pro-apoptotic proteins are divided into multi-BCL-2 homology domain members such as BAX and BAK that contain three conserved domains (BH1–3) and ‘BH3-only’ members such as BIM (also known as BCL2L11) and BID that only show homology to the α -helical BH3 domain. The BH3-only subgroup is diverse and transmits pro-death signals arising from disparate stimuli to the core apoptotic machinery located at the mitochondrion^{5,6}. Once deployed, the BH3 death signal is either neutralized by anti-apoptotic proteins or delivered to the mitochondrial executioners BAX and BAK, which on activation permeabilize the outer mitochondrial membrane^{7,8}. Released mitochondrial factors activate caspases that then implement the death program⁹.

Structural studies have established a survival mechanism for BCL-2 family interactions on the basis of sequestration of the α -helical BH3 death domain by a hydrophobic groove formed by the juxtaposition of the BH1–3 domains (BH1: portions of helices α 4– α 5; BH2: α 7– α 8; BH3: α 2) of anti-apoptotic members¹⁰. The selective binding interactions of pro-apoptotic BH3 peptides and pro-apoptotic multi-BCL-2 homology domain proteins with anti-apoptotic BCL-2 family members have been well documented^{11–16}. The small molecules ABT-737 and ABT-263, constructed to selectively inhibit the anti-apoptotic proteins BCL-2 and BCL-X_L by targeting the hydrophobic groove, reactivate apoptosis in select tumours^{17,18}. Thus, there is general agreement that one level of apoptosis regulation is mediated by the competitive interactions between pro- and anti-apoptotic members at the structurally-defined anti-apoptotic groove. However, what directly triggers BAX and BAK activation during apoptotic stress remains a matter of active

debate^{11,13,19}. Indeed, this lingering question concerning the biochemical mechanism that initiates BAX and BAK activation has recently been characterized as the ‘holy grail of apoptosis research’²³.

BAX activation is believed to be a highly regulated, multi-step process involving an interaction-triggered conformational change, mitochondrial translocation and oligomerization that ultimately leads to mitochondrial dysfunction and apoptosis^{20–23}. A diversity of stimuli have been implicated in initiating BAX and BAK activation^{24–26}, including direct involvement by select BH3 domains and BH3-only proteins^{13,27–34}. To investigate the elusive initiating event for BAX activation, we studied the interaction of BAX with the BH3 ligand BIM SAHB, which we previously demonstrated recapitulates the α -helical character of native death domains and binds directly to BAX³³. We report to our knowledge the first structural analysis of a BH3 α -helix bound to a full-length pro-apoptotic multi-BCL-2 homology domain protein, unveiling a previously unknown site of protein interaction for functional activation and pharmacological modulation of BAX (Supplementary Fig. 1).

Identification of a BH3 interaction site on BAX

BIM SAHB binding to BAX was monitored using NMR spectroscopy. Compared to the ¹H-¹⁵N heteronuclear single quantum coherence (HSQC) spectrum of BAX, the addition of BIM SAHB broadened and shifted select NMR cross-peaks, indicating fast exchange between the bound and unbound conformations of BAX. The overall features of the NMR spectra are quite similar except for significant changes in the loop residues between α 1 and α 2 on BIM SAHB binding. Chemical shift perturbation mapping of BAX with BIM SAHB titration revealed interactions at a discrete subset of BAX residues. The degree of change in the ¹H-¹⁵N cross-peak positions for backbone amides is shown in Fig. 1a. The largest changes were observed for residues located in the α 1 and α 6 helices, as well as residues in the flexible loop between α 1 and α 2. Significant changes were also observed for the side-chain NH₂ of Q28, Q32 and Q52 (Supplementary Fig. 2). In the BAX structure³⁵, the α 1 and α 6 helices are positioned adjacent to one another, and the

¹Department of Pediatric Oncology and the Program in Cancer Chemical Biology, Dana-Farber Cancer Institute, 44 Binney Street, Boston, Massachusetts 02115, USA. ²Division of Hematology/Oncology, Children’s Hospital Boston, 300 Longwood Avenue, Boston, Massachusetts 02115, USA. ³Department of Pediatrics, Harvard Medical School, Boston, Massachusetts 02115, USA. ⁴Laboratory of Molecular Biophysics, National Heart, Lung and Blood Institute, National Institutes of Health, Bethesda, Maryland 20892, USA.

⁵Departments of Internal Medicine and Pathology and Immunology, Washington University School of Medicine, Saint Louis, Missouri 63110, USA.

*These authors contributed equally to this work.

residues affected by BIM SAHB binding localize to a discrete site at the juxtaposition of these α -helices on one side of the protein structure (Fig. 1b). Of note, no residues on the carboxy-terminal side of the protein are affected by BIM SAHB titration under these conditions, thus placing the novel binding site on the completely opposite face of the protein from the canonical BH3 binding site of anti-apoptotic proteins (Supplementary Fig. 1). The binding site of BIM SAHB on BAX is thus defined by the two helices $\alpha 1$ and $\alpha 6$, with the interhelical junction forming a hydrophobic cleft surrounded by a perimeter of hydrophilic and charged residues (Fig. 1c).

Orientation of BIM SAHB at the BAX site

One of the challenges of capturing a BAX-activating interaction by NMR is time- and dose-dependent BAX aggregation due to BIM

SAHB addition to the NMR sample. With time, the size of the protein aggregate formed leads to line broadening of the NMR resonances beyond detection, thereby precluding acquisitions of data for the duration required to resolve the initial complex by conventional NMR. Nevertheless, to orient BIM SAHB at the BAX interaction site, we conducted paramagnetic relaxation enhancement (PRE) NMR experiments, which can be performed on a timescale that is compatible with the lifespan of the complex under NMR conditions. ^1H - ^{15}N HSQC spectra of BAX, were acquired with methane thiosulphonate (MTSL)-derivatized BIM SAHBs (Fig. 2a) in the oxidized state and then repeated after nitroxide reduction. Of note, the chemical shift perturbation maps of BAX in complex with BIM SAHB and the

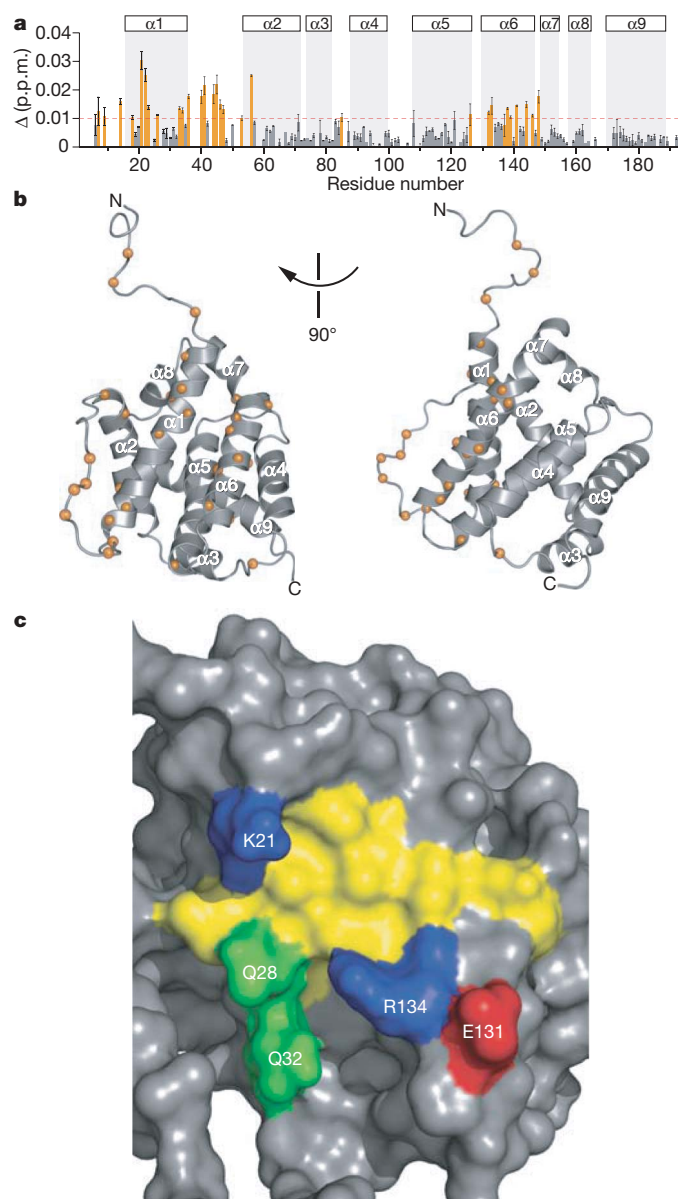


Figure 1 | NMR analysis of BAX on BIM SAHB titration. **a**, Chemical shift changes (Δ) are plotted as a function of the residue number of BAX. Residues with significant backbone amide chemical shift change (>0.01 p.p.m., horizontal dashed line) are coloured orange. The absence of a bar indicates the presence of a proline or a residue that is overlapped. Data are mean \pm s.d. **b**, The C α atoms of BAX residues affected by BIM SAHB binding are shown as orange spheres. **c**, Surface diagram illustrating the BAX binding site. The side chains of hydrophobic, positively charged, negatively charged and hydrophilic residues are coloured yellow, blue, red and green, respectively.

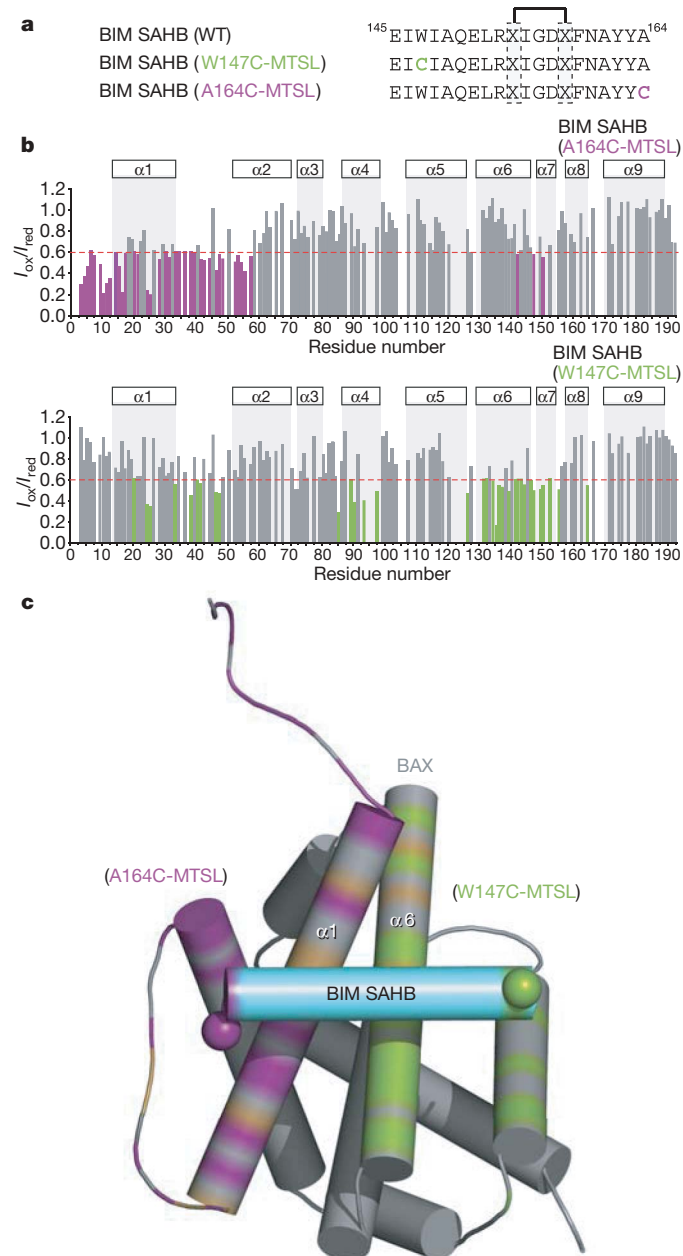


Figure 2 | Orientation of BIM SAHB at the BAX binding site.

a, Paramagnetically-labelled derivatives of BIM SAHB. **b**, Ratios of BAX cross-peak intensities in the presence of oxidized or reduced ($I_{\text{ox}}/I_{\text{red}}$) BIM SAHB(A164C-MTSL) (top) and BIM SAHB(W147C-MTSL) (bottom) versus residue number. BAX residue intensities reduced below 0.6 are coloured (dashed horizontal line). **c**, Orientation of BIM SAHB at the BAX site. On the basis of an $I_{\text{ox}}/I_{\text{red}}$ threshold of 0.6, BAX residues affected by BIM SAHB(A164C-MTSL), BIM SAHB(W147C-MTSL) or both are coloured in purple, green or brown, respectively.

MTSL-labelled derivatives demonstrate consistent changes in BAX helices $\alpha 1$ and $\alpha 6$, and in the $\alpha 1$ – $\alpha 2$ loop (Supplementary Fig. 3). Whereas the intensity of BAX $\alpha 1$ residues are predominantly reduced in the presence of an oxidized C-terminal label, the intensity of BAX $\alpha 6$ residues are predominantly decreased by the presence of an oxidized amino-terminal label (Fig. 2b). As an example, BIM SAHB(A164C-MTSL) caused marked signal suppression of S16 ($\alpha 1$) but had essentially no effect on D142 ($\alpha 6$) (Supplementary Fig. 4a), whereas BIM SAHB(W147C-MTSL) had no effect on S16 ($\alpha 1$) but reduced the D142 ($\alpha 6$) signal (Supplementary Fig. 4b). Because the degree of PRE correlates with the distance between the nitroxide label and the affected BAX residues³⁶, structure calculations using restraints derived from PRE and chemical shift perturbation data were performed to define the orientation of BIM SAHB at the new BAX site. The calculated model structures converged to place BIM SAHB perpendicular to BAX helices $\alpha 1$ and $\alpha 6$, with the N to C terminus directionality of the peptide disposed right to left (Fig. 2c and Supplementary Table 1). Whereas the location of the BAX binding site is geographically distinct, the calculated model structure of the BIM-BH3–BAX complex shows an interaction topography that is notably similar to that of BIM BH3 with anti-apoptotic BCL-X_L, MCL1 and BFL1/A1 (also known as BCL2A1), as previously determined by X-ray crystallography (Supplementary Fig. 5).

Initiation of BAX activation by BIM SAHB

In contrast to the stable inhibitory interactions of BIM BH3 with anti-apoptotic proteins, the BAX-activating interaction triggers a dynamic continuum of events that includes BAX conformational change and oligomerization (Supplementary Fig. 6). Of particular interest, NMR resonances of residues in the $\alpha 1$ – $\alpha 2$ loop of BAX shifted significantly on BIM SAHB binding (Fig. 1a and Supplementary Fig. 3). In monomeric BAX, the centre of the loop

weakly associates with residues I133 and M137 of the $\alpha 6$ helix³⁵. Changes observed in the loop residues can readily be explained by the shift of the loop conformation into an open form on BIM SAHB binding. Because loop displacement on ligand engagement may initiate a conformational change of BAX, we investigated whether BIM SAHB binding could directly activate BAX in solution. We monitored both the conversion of BAX from monomer to oligomer by size-exclusion chromatography (SEC) and the exposure of its buried N-terminal residues using the 6A7 antibody, which selectively detects the conformational change associated with BAX activation³⁷. Indeed, BIM SAHB triggered dose-dependent oligomerization of BAX (Fig. 3a). This BIM-SAHB-induced oligomerization correlated with exposure of the N-terminal epitope of BAX as recognized by the 6A7 antibody (Fig. 3b). Thus, the transient stability of the BIM-SAHB–BAX complex we observe by NMR correlates with the interaction-triggered BAX conformational change and oligomerization that we detect biochemically.

To confirm that the SEC-based detection of BIM-SAHB-induced BAX oligomerization reflects functional activation of BAX for its release activity, we performed correlative liposomal and mitochondrial assays. In liposomal assays that explicitly explore the capacity of BIM SAHB to directly trigger functional BAX activation in the absence of other factors, the combination of BIM SAHB and BAX yielded dose-responsive liposomal release of entrapped fluorescein isothiocyanate (FITC)-dextran (Fig. 3c). Similarly, in mitochondrial release assays that used BAX- and BAK-deficient mouse liver mitochondria prepared from *Alb-cre^{pos} Bax^{fllox/-} Bak^{-/-}* mice, BIM SAHB induced dose-responsive BAX-mediated cytochrome *c* release (Fig. 3d). Thus, in four distinct *in vitro* assays that measure ligand-induced BAX activation, BIM SAHB directly and dose-responsively activated BAX.

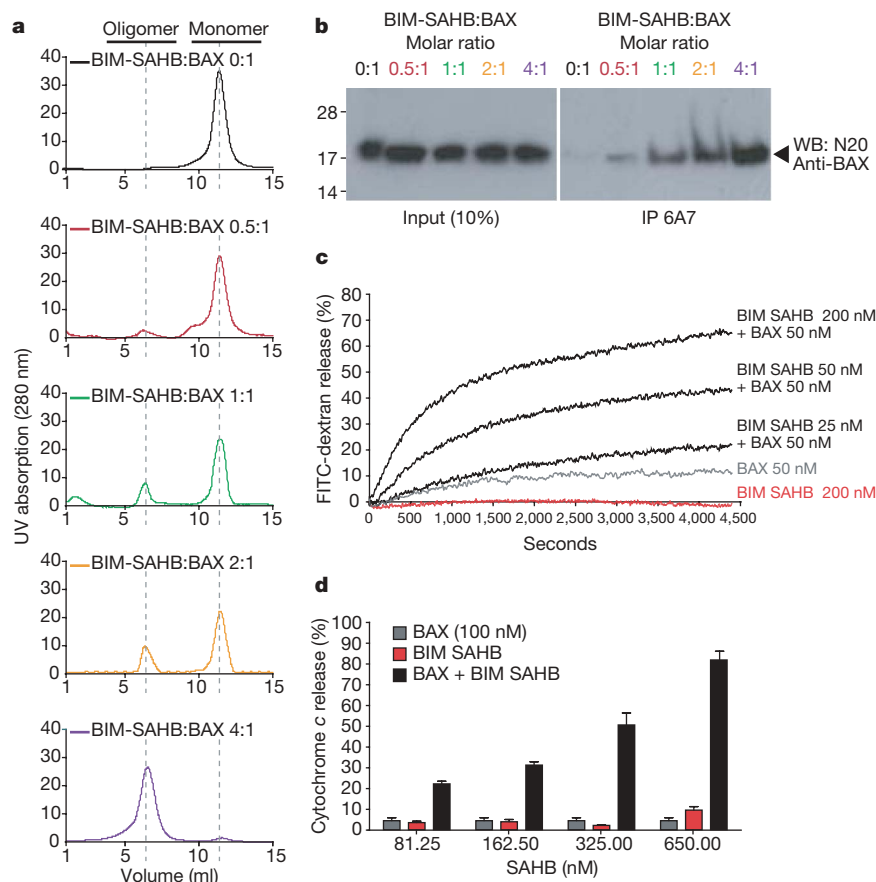


Figure 3 | BIM SAHB directly initiates BAX activation *in vitro*.

a, b, Oligomerization (**a**) and 6A7 immunoprecipitation (IP) (**b**) of BAX after BIM SAHB treatment. UV, ultraviolet; WB, western blot. **c**, Liposomal

FITC-dextran release in the presence of BAX and BIM SAHB. **d**, Cytochrome *c* release from BAX- and BAK-deficient mitochondria on incubation with BAX and BIM SAHB. Data are mean and s.d.

Specificity of BIM-SAHB-induced BAX activation

We next performed a 'staple scan' and mutagenesis studies to demonstrate and link the specificity of BIM-SAHB-induced BAX activation to interaction at the new site. By performing a staple scan that effectively replaces pairs of amino acid residues within the core BH3 sequence with crosslinked norleucine-like side chains, we simultaneously addressed which residues are essential to the functional interaction between BIM BH3 and BAX, and further confirm which surface along the BIM BH3 α -helix is essential to BAX engagement (Fig. 4a). Substituting the non-natural amino acid at positions W147, A149, E151, R153, R154, E158 or Y162 did not disrupt BIM-SAHB-induced BAX oligomerization (Fig. 4b) or BAX-mediated cytochrome *c* release (Fig. 4c and Supplementary Fig. 7a). Indeed, hydrocarbon staples located along the length of the α -helix at surfaces that do not face the hydrophobic contact site on BAX did not disrupt the functional interactions between the BIM SAHB analogues and BAX. However, a staple position that replaced I148 and the highly conserved L152, and localizes to the hydrophobic contact surface for BAX on the BIM BH3 α -helix (Fig. 4a), markedly decreased both BAX oligomerization (Fig. 4b) and BAX-mediated cytochrome *c* release (Fig. 4c and Supplementary Fig. 7a), findings which are consistent with the near abrogation of BIM-SAHB-induced chemical shift perturbations of ^{15}N -BAX by BIM SAHB_C (Supplementary Fig. 8a). In addition, BAD SAHB_A (ref. 33), which has the identical staple position as BIM SAHB_A but otherwise contains a distinct amino acid sequence, did not bind (Supplementary Fig. 8b) or oligomerize (Fig. 4b) BAX, or induce BAX-mediated cytochrome *c* release (Fig. 4c and Supplementary Fig. 7a).

To further examine ligand specificity, we generated and screened a panel of BIM SAHBs bearing single amino acid mutations within the

core BH3 consensus sequence, including I155E, R153D and D157R (Fig. 4d and Supplementary Fig. 5a). In each case, point mutagenesis abolished BIM-SAHB-induced BAX oligomerization (Fig. 4e) and BAX-mediated cytochrome *c* release (Fig. 4f and Supplementary Fig. 7b), indicating that interference with principal hydrophobic or charge interactions specifically disrupts BIM SAHB engagement of the new BAX site.

Mutagenesis of the BAX site impairs activation

To examine the effect of BAX mutagenesis at the $\alpha 1$ – $\alpha 6$ interaction site, we mutated residue K21, which exhibited the most pronounced chemical shift on BIM SAHB binding (Fig. 1a). We generated recombinant BAX bearing a K21E point mutation (Supplementary Fig. 9) and observed that BIM-SAHB-induced BAX(K21E) activation was significantly reduced compared to wild-type BAX as measured by the oligomerization assay (Fig. 5a). BAX(K21E)-mediated cytochrome *c* release in response to BIM SAHB was likewise blunted (Fig. 5b). To determine whether this single amino acid mutation within the BAX binding site affected the capacity to activate BAX in a cellular context, we retrovirally reconstituted *Bax*^{-/-} *Bak*^{-/-} mouse embryonic fibroblasts (DKO MEFs) with either wild type or BAX(K21E) and monitored apoptosis induction in response to BIM SAHB. Whereas BIM SAHB induced time-dependent apoptosis of BAX-reconstituted MEFs, as quantified by annexin V binding, a single K21E point mutation within the BAX binding site reduced BIM-SAHB-triggered apoptosis (Fig. 5c). This decrease in BAX(K21E)-mediated apoptosis correlates with impaired activation of BAX(K21E) by BIM SAHB in both oligomerization and cytochrome *c* release assays (Fig. 5a, b). As a further measure of specificity, we

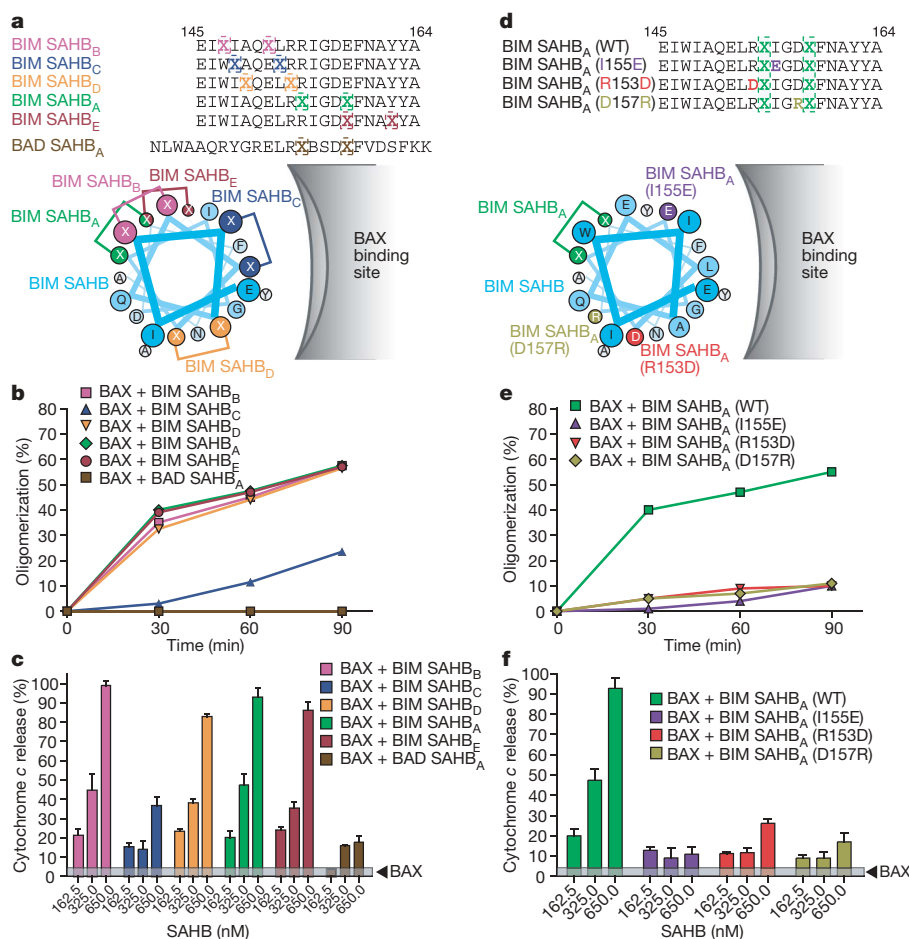


Figure 4 | Sequence specificity of BIM-SAHB-induced BAX activation. **a–c**, BIM SAHBs with differential staple positions (**a**) and their activities in BAX oligomerization (**b**) and BAX-mediated cytochrome *c* release assays

(**c**). In the sequence in **a**, X is a stapling amino acid, B is norleucine. **d–f**, BIM SAHB_A point mutants (**d**) and their activities in BAX oligomerization (**e**) and BAX-mediated cytochrome *c* release assays (**f**). Data are mean and s.d.

found that R153D mutagenesis of BIM SAHB, which eliminated its BAX activating capacity in the oligomerization and cytochrome *c* release assays (Fig. 4e, f), similarly abolished BIM-SAHB-induced activation of BAX and BAX(K21E) in a cellular context (Fig. 5c).

To probe the broader physiological effect of the new BAX activation site, we examined the apoptotic response of DKO MEFs reconstituted with BAX or BAX(K21E) to staurosporine (STS), a general stimulus known to operate through endogenous BH3-only proteins^{13,38}, including BIM³⁹. K21E mutagenesis impaired STS-induced apoptosis, as monitored by annexin V binding over time (Fig. 5d). The reduced activity of BAX(K21E) was also reflected by impaired cytochrome *c* release, as detected by subcellular fractionation western analysis and indirect immunofluorescence (Supplementary Fig. 10). The blunted response of BAX(K21E)-reconstituted DKO MEFs to STS is uniformly consistent with impaired activation of BAX(K21E) by BIM SAHB in oligomerization (Fig. 5a), cytochrome *c* release (Fig. 5b) and cell-based apoptosis assays (Fig. 5c). Thus, the MEF studies extend the mechanistic

relevance of direct BAX activation to a cellular context in which BAX-mediated apoptosis is impaired by single amino acid mutagenesis at the previously unknown BH3 interaction site. Taken together, the *in vitro* and cell-based mutagenesis experiments highlight the exquisite specificity of the BIM-BH3-BAX interaction and implicate engagement of the novel binding site as a trigger mechanism for initiating BAX activation.

Discussion

Our data now define an explicit binding site on BAX for BH3 engagement that directly initiates BAX activation. In contrast to the constitutive mitochondrial localization of pro-apoptotic BAK, BAX is predominantly cytosolic, thereby necessitating a trigger mechanism for its activation and translocation to the mitochondria to induce mitochondrial outer membrane permeabilization⁴⁰. The C-terminal α -helix of BAX folds back into its hydrophobic cleft³⁵, which is homologous to the BH3-binding anti-apoptotic groove^{10,41} (Supplementary Fig. 1). The amphipathic nature of the C-terminal α -helix of BAX enables the hydrophobic face to closely interact with the canonical hydrophobic groove, whereas the hydrophilic face promotes solubility by readily engaging the aqueous environment. In order for BAX to insert into the outer mitochondrial membrane during targeting, the C-terminal α -helix must be dislodged, presumably coinciding with an induced global protein conformational change³⁵ (Supplementary Fig. 6). Although the structural characteristics of this conformational change are unknown, the N and C termini of BAX have been implicated in locking down cytosolic BAX until structural reorganization and mitochondrial targeting are initiated^{21,37,42–44}. Here we report, to our knowledge, the first structural identification of a distinct BH3 binding site on BAX comprised of helices $\alpha 1$ and $\alpha 6$. Indeed, our findings support a previous observation that the first α -helix of BAX participates in an interaction with the BH3 domains of BID and PUMA (also known as BBC3), as demonstrated by yeast two-hybrid and co-immunoprecipitation analyses²⁷. We find that BIM SAHB engagement directly triggers the functional activation of BAX. Furthermore, BAX activation is specifically disrupted by mutagenesis of the new interface. These data indicate that BAX can be directly targeted by a BH3 domain at a site that is geographically distinct from but markedly similar in topography to the canonical anti-apoptotic groove, and can thereby unleash the pro-apoptotic activity of BAX.

Structural reorganization to achieve functional activity is a unifying feature of BCL-2 family proteins, and for a subset of pro- and anti-apoptotic members, translocation from the cytosol to organelle compartments is also essential^{21,23,35,40,45}. Our identification of a BH3 ligand binding site on BAX suggests that engagement of alternative BCL-2 family binding sites may have important roles in regulating apoptotic protein structure, intracellular localization and functional activation. Whereas blockade of the new site may effectively repress BAX-induced cell death, ligand engagement may trigger BAX-mediated apoptosis. Thus, our identification of a previously unknown BAX activation site has important implications for the development of pharmacological agents to respectively activate or inhibit apoptosis in human diseases characterized by unrestrained cell survival or pathological cell death.

METHODS SUMMARY

SAHBs were synthesized using our established method^{46,47} and recombinant BAX for NMR and biochemical analyses was generated as previously described^{33,35}. Samples for HSQC and PRE NMR contained uniformly ¹⁵N-labelled BAX at 0.2 mM prepared in 10 mM sodium acetate solution at pH 6.0 with up to a 1:1 molar ratio of SAHB. NMR spectra were acquired at 32 °C on Bruker 600 and 800 MHz spectrometers, and then processed and analysed as described in the Methods. To evaluate BIM-SAHB-induced BAX activation, four *in vitro* assays were performed. The oligomerization assay used freshly purified monomeric BAX in combination with BIM SAHB at the indicated ratios and incubation durations followed by size-exclusion chromatography to quantify monomeric versus oligomeric BAX. The BAX conformational change assay also used the indicated BIM-SAHB:BAX mixtures, which were exposed to the conformation-specific 6A7 anti-BAX antibody, followed by immunoprecipitation and BAX western analysis to monitor the proportion of activated conformer of

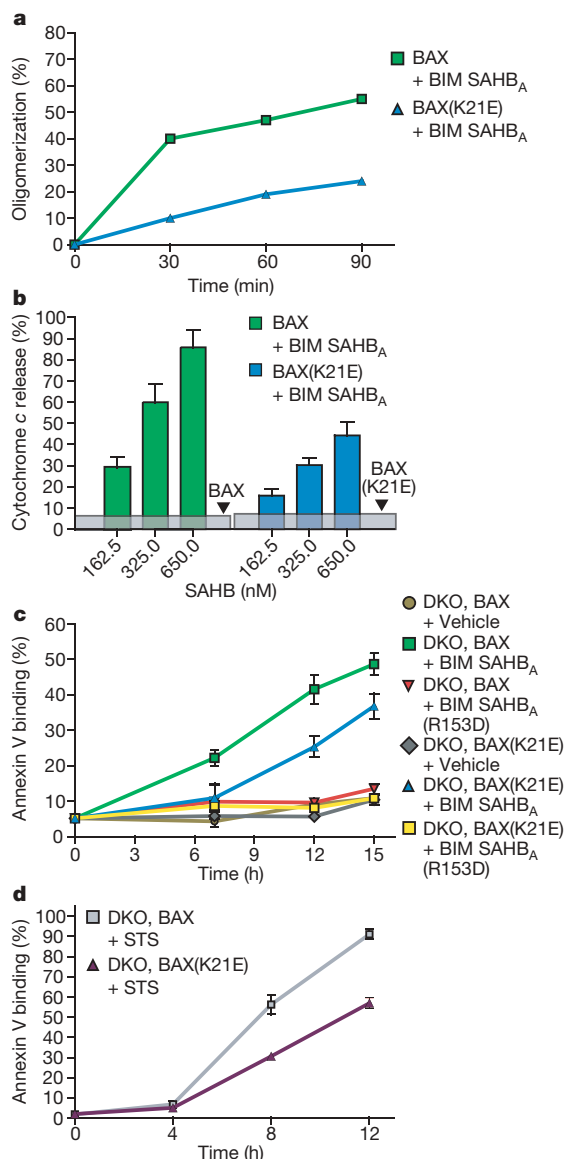


Figure 5 | Mutagenesis of the BAX interaction site impairs activation and BAX-mediated apoptosis. **a**, **b**, Effect of BAX K21E mutagenesis in oligomerization (**a**) and cytochrome *c* release assays (**b**). **c**, Apoptotic response of *Bax*^{-/-} *Bak*^{-/-} MEFs reconstituted with BAX or BAX(K21E) to treatment with BIM SAHB_A or BIM SAHB_A(R153D). **d**, Effect of BAX K21E mutagenesis on STS-induced apoptosis of BAX-reconstituted DKO MEFs. Data are mean \pm s.d.

BAX on BIM SAHB exposure. To determine whether the BIM-SAHB-induced BAX conformational change reflected functional activation of its release activity, we conducted liposomal and mitochondrial release assays as previously described^{33,48} and using the indicated doses and constructs of BIM SAHB and BAX. For cellular studies, DKO MEFs were reconstituted with BAX by retroviral transduction of BAX-IRES-GFP as previously reported^{7,13} and as described in the Methods. BAX or BAX(K21E)-reconstituted DKO MEFs were exposed to either BIM SAHBs or staurosporine, and cell death was quantified over time by annexin-V-Cy3 binding followed by flow cytometric analysis.

Full Methods and any associated references are available in the online version of the paper at www.nature.com/nature.

Received 11 April; accepted 1 September 2008.

- Danial, N. N. & Korsmeyer, S. J. Cell death: critical control points. *Cell* **116**, 205–219 (2004).
- Leber, B., Lin, J. & Andrews, D. W. Embedded together: the life and death consequences of interaction of the Bcl-2 family with membranes. *Apoptosis* **12**, 897–911 (2007).
- Youle, R. J. & Strasser, A. The BCL-2 protein family: opposing activities that mediate cell death. *Nature Rev. Mol. Cell Biol.* **9**, 47–59 (2008).
- Petros, A. M., Olejniczak, E. T. & Fesik, S. W. Structural biology of the Bcl-2 family of proteins. *Biochim. Biophys. Acta* **1644**, 83–94 (2004).
- Huang, D. C. & Strasser, A. BH3-only proteins—essential initiators of apoptotic cell death. *Cell* **103**, 839–842 (2000).
- Walensky, L. D. BCL-2 in the crosshairs: tipping the balance of life and death. *Cell Death Differ.* **13**, 1339–1350 (2006).
- Cheng, E. H. *et al.* BCL-2, BCL-X(L) sequester BH3 domain-only molecules preventing BAX- and BAK-mediated mitochondrial apoptosis. *Mol. Cell* **8**, 705–711 (2001).
- Wei, M. C. *et al.* Proapoptotic BAX and BAK: a requisite gateway to mitochondrial dysfunction and death. *Science* **292**, 727–730 (2001).
- Li, P. *et al.* Cytochrome c and dATP-dependent formation of Apaf-1/caspase-9 complex initiates an apoptotic protease cascade. *Cell* **91**, 479–489 (1997).
- Sattler, M. *et al.* Structure of Bcl-x_L-Bak peptide complex: recognition between regulators of apoptosis. *Science* **275**, 983–986 (1997).
- Certo, M. *et al.* Mitochondria primed by death signals determine cellular addiction to antiapoptotic BCL-2 family members. *Cancer Cell* **9**, 351–365 (2006).
- Chen, L. *et al.* Differential targeting of prosurvival Bcl-2 proteins by their BH3-only ligands allows complementary apoptotic function. *Mol. Cell* **17**, 393–403 (2005).
- Kim, H. *et al.* Hierarchical regulation of mitochondrion-dependent apoptosis by BCL-2 subfamilies. *Nature Cell Biol.* **8**, 1348–1358 (2006).
- Olvtal, Z. N., Milliman, C. L. & Korsmeyer, S. J. Bcl-2 heterodimerizes *in vivo* with a conserved homolog, Bax, that accelerates programmed cell death. *Cell* **74**, 609–619 (1993).
- Willis, S. N. *et al.* Proapoptotic Bak is sequestered by Mcl-1 and Bcl-x_L, but not Bcl-2, until displaced by BH3-only proteins. *Genes Dev.* **19**, 1294–1305 (2005).
- Zhai, D., Jin, C., Huang, Z., Satterthwait, A. C. & Reed, J. C. Differential regulation of Bax and Bak by anti-apoptotic Bcl-2 family proteins Bcl-B and Mcl-1. *J. Biol. Chem.* **283**, 9580–9586 (2008).
- Oltersdorf, T. *et al.* An inhibitor of Bcl-2 family proteins induces regression of solid tumours. *Nature* **435**, 677–681 (2005).
- Tse, C. *et al.* ABT-263: a potent and orally bioavailable Bcl-2 family inhibitor. *Cancer Res.* **68**, 3421–3428 (2008).
- Willis, S. N. *et al.* Apoptosis initiated when BH3 ligands engage multiple Bcl-2 homologs, not Bax or Bak. *Science* **315**, 856–859 (2007).
- Annis, M. G. *et al.* Bax forms multispanning monomers that oligomerize to permeabilize membranes during apoptosis. *EMBO J.* **24**, 2096–2103 (2005).
- Goping, I. S. *et al.* Regulated targeting of BAX to mitochondria. *J. Cell Biol.* **143**, 207–215 (1998).
- Gross, A., Jockel, J., Wei, M. C. & Korsmeyer, S. J. Enforced dimerization of BAX results in its translocation, mitochondrial dysfunction and apoptosis. *EMBO J.* **17**, 3878–3885 (1998).
- Wolter, K. G. *et al.* Movement of Bax from the cytosol to mitochondria during apoptosis. *J. Cell Biol.* **139**, 1281–1292 (1997).
- Chipuk, J. E. *et al.* Direct activation of Bax by p53 mediates mitochondrial membrane permeabilization and apoptosis. *Science* **303**, 1010–1014 (2004).
- Nie, C. *et al.* Cysteine 62 of Bax is critical for its conformational activation and its proapoptotic activity in response to H₂O₂-induced apoptosis. *J. Biol. Chem.* **283**, 15359–15369 (2008).
- Pagliari, L. J. *et al.* The multidomain proapoptotic molecules Bax and Bak are directly activated by heat. *Proc. Natl Acad. Sci. USA* **102**, 17975–17980 (2005).
- Cartron, P. F. *et al.* The first α helix of Bax plays a necessary role in its ligand-induced activation by the BH3-only proteins Bid and PUMA. *Mol. Cell* **16**, 807–818 (2004).
- Harada, H., Quearry, B., Ruiz-Vela, A. & Korsmeyer, S. J. Survival factor-induced extracellular signal-regulated kinase phosphorylates BIM, inhibiting its association with BAX and proapoptotic activity. *Proc. Natl Acad. Sci. USA* **101**, 15313–15317 (2004).
- Kuwana, T. *et al.* BH3 domains of BH3-only proteins differentially regulate Bax-mediated mitochondrial membrane permeabilization both directly and indirectly. *Mol. Cell* **17**, 525–535 (2005).
- Kuwana, T. *et al.* Bid, Bax, and lipids cooperate to form supramolecular openings in the outer mitochondrial membrane. *Cell* **111**, 331–342 (2002).
- Letai, A. *et al.* Distinct BH3 domains either sensitize or activate mitochondrial apoptosis, serving as prototype cancer therapeutics. *Cancer Cell* **2**, 183–192 (2002).
- Marani, M., Tenev, T., Hancock, D., Downward, J. & Lemoine, N. R. Identification of novel isoforms of the BH3 domain protein Bim which directly activate Bax to trigger apoptosis. *Mol. Cell Biol.* **22**, 3577–3589 (2002).
- Walensky, L. D. *et al.* A stapled BID BH3 helix directly binds and activates BAX. *Mol. Cell* **24**, 199–210 (2006).
- Wang, K., Yin, X. M., Chao, D. T., Milliman, C. L. & Korsmeyer, S. J. BID: a novel BH3 domain-only death agonist. *Genes Dev.* **10**, 2859–2869 (1996).
- Suzuki, M., Youle, R. J. & Tjandra, N. Structure of Bax: coregulation of dimer formation and intracellular localization. *Cell* **103**, 645–654 (2000).
- Battiste, J. L. & Wagner, G. Utilization of site-directed spin labeling and high-resolution heteronuclear nuclear magnetic resonance for global fold determination of large proteins with limited nuclear Overhauser effect data. *Biochemistry* **39**, 5355–5365 (2000).
- Hsu, Y. T. & Youle, R. J. Nonionic detergents induce dimerization among members of the Bcl-2 family. *J. Biol. Chem.* **272**, 13829–13834 (1997).
- Villunger, A. *et al.* p53- and drug-induced apoptotic responses mediated by BH3-only proteins Puma and Noxa. *Science* **302**, 1036–1038 (2003).
- Chen, D. & Zhou, Q. Caspase cleavage of BimEL triggers a positive feedback amplification of apoptotic signaling. *Proc. Natl Acad. Sci. USA* **101**, 1235–1240 (2004).
- Hsu, Y. T., Wolter, K. G. & Youle, R. J. Cytosol-to-membrane redistribution of Bax and Bcl-x_L during apoptosis. *Proc. Natl Acad. Sci. USA* **94**, 3668–3672 (1997).
- Muchmore, S. W. *et al.* X-ray and NMR structure of human Bcl-x_L, an inhibitor of programmed cell death. *Nature* **381**, 335–341 (1996).
- Cartron, P. F. *et al.* Involvement of the N-terminus of Bax in its intracellular localization and function. *FEBS Lett.* **512**, 95–100 (2002).
- Nechushtan, A., Smith, C. L., Hsu, Y. T. & Youle, R. J. Conformation of the Bax C-terminus regulates subcellular location and cell death. *EMBO J.* **18**, 2330–2341 (1999).
- Schinkel, A. *et al.* Conformational control of Bax localization and apoptotic activity by Pro168. *J. Cell Biol.* **164**, 1021–1032 (2004).
- Drugosz, P. J. *et al.* Bcl-2 changes conformation to inhibit Bax oligomerization. *EMBO J.* **25**, 2287–2296 (2006).
- Bird, G. H., Bernal, F., Pitter, K. & Walensky, L. D. Synthesis and biophysical characterization of stabilized α -helices of BCL-2 domains. *Methods Enzymol.* **446**, 369–386 (2008).
- Walensky, L. D. *et al.* Activation of apoptosis *in vivo* by a hydrocarbon-stapled BH3 helix. *Science* **305**, 1466–1470 (2004).
- Pitter, K., Bernal, F., Labelle, J. & Walensky, L. D. Dissection of the BCL-2 family signaling network with stabilized α -helices of BCL-2 domains. *Methods Enzymol.* **446**, 387–408 (2008).

Supplementary Information is linked to the online version of the paper at www.nature.com/nature.

Acknowledgements We thank E. Smith for editorial and graphics assistance, W. Beavers for amino acid analyses, A. Perry for technical assistance, C. Turner and A. Bielecki of the MIT/Harvard Center for Magnetic Resonance for NMR technical advice, and R. Youle for feedback on the manuscript. We acknowledge the indelible contributions of the late S. J. Korsmeyer, who inspired this work. L.D.W. is supported by National Cancer Institute (NCI) grant 5P01CA92625, a Burroughs Wellcome Fund Career Award in the Biomedical Sciences, a Culpeper Scholarship in Medical Science from the Goldman Philanthropic Partnerships, an American Society of Hematology Junior Faculty Scholar Award, and a grant from the William Lawrence Children's Foundation. This research was also supported by NCI grant 5R01CA50239. N.T. is supported by the Intramural Research Program of the National Heart, Lung and Blood Institute, NIH. E.H.-Y.C. is supported by the Searle Scholars Program and NCI grant 5R01CA125562.

Author Contributions G.H.B. and L.D.W. designed, synthesized and characterized the SAHBs for structural and biological studies. M.S. and N.T. performed the NMR analysis of BAX and BIM SAHB, and E.G. and L.D.W. conducted the PRE NMR analysis of BAX using MTSL-derivatized SAHBs and performed the structure calculations. E.G., M.L.D. and K.P. executed the *in vitro* BAX activation studies. H.-C.T., H.K. and E.H.-Y.C. generated the BAX-reconstituted DKO MEFs and analysed their response to staurosporine, and S.G.K. examined the cellular response to BIM SAHB treatment.

Author Information The authors declare competing financial interests: details accompany the full-text HTML version of the paper at www.nature.com/nature. The structural coordinates have been submitted to the Protein Data Bank under accession number 2K7W. Reprints and permissions information is available at www.nature.com/reprints. Correspondence and requests for materials should be addressed to N.T. (tjandran@nhlbi.nih.gov) or L.D.W. (loren_walensky@dfci.harvard.edu).

METHODS

SAHB synthesis and characterization. Hydrocarbon-stapled peptides corresponding to the BH3 domain of BIM and its point mutants were synthesized, purified and characterized using methodologies previously described^{33,46,47}. BIM SAHB_A used in the NMR and *in vitro* studies is an *N*-acetylated, C-amidated 20-amino-acid peptide Ac-¹⁴⁵EIWIAQELRXIGDXFNAYYA¹⁶⁴-CONH₂, in which X represents the non-natural amino acid inserted for olefin metathesis. To generate paramagnetically-labelled BIM SAHBs for PRE NMR studies, cysteine was substituted at position 147 or 164 and then reacted with five molar excess MTSL reagent in dimethylsulphoxide for 30 min at room temperature. Once the reaction reached completion, as confirmed by liquid chromatography-mass spectrometry (LC-MS), excess MTSL was removed by lyophilization, the residual powder was resuspended in methanol and then pure MTSL-labelled SAHB was precipitated with ether/hexanes. For MEF studies, the cell-permeable *N*-acetylated, C-amidated 21-amino-acid peptide Ac-¹⁴⁶EWIAQELRXIGDXFNAYYARR¹⁶⁶-CONH₂ (ref. 33) and its R153D mutant were used.

BAX preparation. Recombinant BAX was produced as previously described^{33,35}. Mutant BAX was generated by PCR-based site-directed mutagenesis followed by DNA sequencing to verify the construct.

NMR sample and spectroscopy. Uniformly ¹⁵N-labelled or ¹³C/¹⁵N-labelled full-length human BAX was generated as previously described³⁵. SAHB (1 mM stock) was added to a solution of 0.2 mM BAX to achieve a 1:1 molar ratio. Both peptide stock and protein samples were prepared in 10 mM sodium acetate solution at pH 6.0. Spectra were acquired at 32 °C on a Bruker 800 MHz NMR spectrometer, processed using NMRPipe and analysed with PIPP (see Supplementary Information for software references). Two independent NMR titrations were performed. The pulse program used to acquire the correlation spectra was ¹H-¹⁵N HSQC⁴⁹. The weighted average chemical shift difference (Δ) at the molar ratio of 1:1 was calculated as $\sqrt{\{(\Delta H)^2 + (\Delta N/5)^2\}}/2$ in p.p.m. Ribbon diagrams and molecular models were depicted using PYMOL⁵⁰.

Paramagnetic relaxation enhancement. Samples for PRE NMR contained uniformly ¹⁵N-labelled human BAX at 0.2 mM prepared in 10 mM sodium acetate solution at pH 6.0. NMR spectra were acquired at 32 °C on a Bruker 600 MHz NMR spectrometer, processed using NMRPipe and analysed with NMRView (see Supplementary Information for software references). Two ¹H-¹⁵N HSQC⁴⁹ spectra for PRE NMR were acquired using a 1:1 ratio of BAX to MTSL-labelled SAHB in the oxidized and reduced state. The reduced compound was generated by exposure to five molar excess ascorbic acid for 1 h. PRE effects were measured from the ratio of integrated peak intensities of the oxidized and reduced HSQC spectra. Peak intensities were normalized to account for small differences between the paramagnetic and the diamagnetic BAX samples using cross-peaks arising from unaffected BAX residues that are distant from the SAHB binding site. To evaluate the paramagnetic broadening effects of each BIM SAHB(MTSL), the calculated ratios from the peak intensities of the oxidized and reduced spectra (I_{ox}/I_{red}) were determined. BAX residues closest to a paramagnetic label have calculated values of $I_{ox}/I_{red} < 0.6$. Measurements for proline or overlapped residues are absent from the intensity ratio plot.

Structure calculations. Structure calculations using restraints derived from the chemical shift perturbation and PRE data were performed as described in the Supplementary Methods.

Oligomerization assay. BIM SAHB was added to a 200 µl solution (20 mM HEPES/KOH, pH 7.2–7.4, 150 mM KCl) containing monomeric BAX (38 µM) at a ratio of 0.5:1, 1:1, 2:1 and 4:1 BIM-SAHB:BAX. The mixtures and a sample of BAX monomer alone were incubated at 22 °C for 15 min and then subjected to analysis by size exclusion chromatography (SEC) using an SD75 column. The chromatogram demonstrates the monomeric and oligomeric peaks at ~11.5 and

~6.5 min, respectively. Protein standards (GE Healthcare) were used to calibrate the molecular mass of gel filtration peaks. For time-dependent analysis, BIM SAHB was added to monomeric BAX at a ratio of 1:1, and the mixtures were analysed by SEC after incubation for 30, 60 and 90 min at 22 °C. As a baseline for comparison, BAX monomer alone was analysed at time 0 and the previously mentioned time points. Replicates were performed using at least two independent preparations of freshly SEC-purified monomeric BAX.

Conformational change assay. BIM SAHB was added to a 20 µl PBS solution containing monomeric BAX (9 µM) at a ratio of 0.5:1, 1:1, 2:1 and 4:1 BIM-SAHB:BAX. The mixtures (10 µl) and a BAX monomer sample (10 µl) were incubated at 22 °C for 15 min and then added to a 3% BSA in PBS solution (250 µl) containing 15 µl of 6A7 anti-BAX antibody for 1 h at 4 °C. Additionally, 1 µl of each input sample (10%) was mixed with 50 µl of SDS-sample buffer to measure baseline BAX levels across specimens. Preclarified sepharose beads (50 µl) were added to the BIM-SAHB:BAX and BAX monomer solutions for a further 2 h incubation at 4 °C. The sepharose beads were spun down, washed three times with 1 ml of 3% BSA in PBS solution, resuspended in 50 µl of SDS-sample buffer and boiled at 95 °C for 2 min. Ten microlitres each of inputs and immunoprecipitation samples were used for analysis. Samples were separated on 12% SDS-PAGE Bis-Tris gel, blotted on a PVDF membrane, and western analysis was performed using the rabbit polyclonal N20 anti-BAX antibody (Santa Cruz Biotechnology) and chemiluminescence-based detection (PerkinElmer).

Release assays. Mitochondrial cytochrome *c* release assays^{33,48} were performed in triplicate on *Alb-cre^{pos} Bax^{flox/flox} Bak^{-/-}* mitochondria, treated with BAX and BIM SAHBs at the indicated doses. Analogous treatments were used in liposomal assays, in which BAX-induced release of FITC-labelled dextran (10 kDa) from large unilamellar vesicles was monitored using a FluoroMax-2 spectrofluorometer (SPX) as previously reported^{33,48}.

Plasmid construction and retrovirus production. BAX was cloned into the retroviral expression vector MSCV-IRES-GFP (pMIG)¹³. The mutant BAX(K21E) construct was generated by PCR-based site-directed mutagenesis and confirmed by DNA sequencing. The production of retroviruses was performed as described previously¹³. Retroviral transduction of BAX constructs was confirmed by western analysis.

Cell culture, cell transfection and apoptosis assay. *Bax^{-/-} Bak^{-/-}* MEFs are SV40-transformed and were maintained in DMEM supplemented with 10% fetal bovine serum following standard culture conditions and procedures. Reconstitution of BAX and the indicated mutant into DKO cells was achieved by retroviral transduction of BAX-IRES-GFP or BAX(K21E)-IRES-GFP, followed by MoFlo sorting for GFP-positive cells. Comparable expression of wild-type or mutant BAX protein was confirmed by anti-BAX western analysis. For BIM SAHB treatment, MEFs were trypsinized, collected and then washed twice in serum-free media followed by plating of cells ($3\text{--}5 \times 10^4$ /well) in 50 µl, exposure to BIM SAHB (20 µM) or vehicle in serum-free media for 2 h, and serum replacement (2× serum in 50 µl media) for an overall treatment duration as indicated. Cell death of triplicate samples was quantified by annexin-V-Cy3 (BioVision) binding according to the manufacturer's protocol, followed by flow cytometric analysis using a FACS Caliber (BD Bioscience) and CellQuest software. For staurosporine treatment, plated MEFs in serum-containing media were exposed to drug (1 µM) and the cell death of triplicate samples was quantified at the indicated time points by annexin V binding as described earlier.

49. Grzesiek, S. & Bax, A. The importance of not saturating water in protein NMR. Application to sensitivity enhancement and NOE measurements. *J. Am. Chem. Soc.* **115**, 12593–12594 (1993).

50. DeLano, W. L. The PyMOL Molecular Graphics System. <<http://www.pymol.org>> (DeLano Scientific, 2002).

LETTERS

Galaxies appear simpler than expected

M. J. Disney¹, J. D. Romano^{1,2}, D. A. Garcia-Appadoo^{3,1}, A. A. West^{4,5}, J. J. Dalcanton⁵ & L. Cortese¹

Galaxies are complex systems the evolution of which apparently results from the interplay of dynamics, star formation, chemical enrichment and feedback from supernova explosions and super-massive black holes¹. The hierarchical theory of galaxy formation holds that galaxies are assembled from smaller pieces, through numerous mergers of cold dark matter^{2–4}. The properties of an individual galaxy should be controlled by six independent parameters including mass, angular momentum, baryon fraction, age and size, as well as by the accidents of its recent haphazard merger history. Here we report that a sample of galaxies that were first detected through their neutral hydrogen radio-frequency emission, and are thus free from optical selection effects⁵, shows five independent correlations among six independent observables, despite having a wide range of properties. This implies that the structure of these galaxies must be controlled by a single parameter, although we cannot identify this parameter from our data set. Such a degree of organization appears to be at odds with hierarchical galaxy formation, a central tenet of the cold dark matter model in cosmology⁶.

About 300 sources, from part of the much larger, blind 21-cm survey for neutral hydrogen made with the Parkes radio telescope^{7–9}, overlap a region surveyed by the Sloan Digital Sky Survey (SDSS) in the optical spectral region¹⁰. Two hundred were unambiguously identified as individual galaxies¹¹, and are representative of the whole range of galaxies between giant spirals and extreme dwarfs, missing only the ~10% of largely neutral-gas-free galaxies found mainly in big clusters. For each object, we measured the H I (neutral hydrogen) mass and line width ΔV , redshift, inclination, two radii (R_{50} and R_{90}) respectively containing 50 and 90% of the emitted light, the luminosity L_g and four colours. Three of the colours are degenerate^{11,12}, leaving dynamical mass ($M_d \equiv (\Delta V)^2 R_{90}/G$; ref. 13), H I mass ($M_{H\,I}$), luminosity, radius, concentration (R_{50}/R_{90}) and colour (SDSS $(g-r)$). For comparison, we can imagine galaxies being controlled by seven physical quantities, namely total mass, baryon fraction, age, specific angular momentum, specific heat energy (random motion), radius and concentration, only six of which can be independent, owing to the Virial theorem. We thus have as many independent observables as we do controlling physical parameters, making an examination of the correlation structure potentially very interesting. Each discovered correlation, if independent of the rest, will set a further constraint on galaxy physics.

We find five correlations, four of which were already known: that between dynamical mass and luminosity ($M_d \propto L_g$)¹⁴, that between luminosity and colour (luminous galaxies are redder)¹⁵, that between R_{50} and R_{90} (H I galaxies have exponential profiles)¹⁶, and that between $M_{H\,I}$ and R_{50} (all the galaxies have the same H I surface density, $M_{H\,I}/R_{50}^2$)^{11,17,18}. The new correlation, namely that surface brightness $\Sigma \equiv L_g/R_{50}^2$ is proportional to R_{50} (ref. 11), required a blind H I survey to clearly separate it from the pronounced selection effects in the optical. All the data and the correlations appear in ref. 11.

Here we examine the correlation structure by means of a principal component analysis (PCA)^{19,20} based on the correlation matrix of the measured data. Being normalized (unlike the covariance matrix), a correlation-based analysis is immune to the influence of scaling. PCA can be thought of as a search in the six-dimensional space of observables for a smaller number of coordinates that describe nearly all the variance. For instance, PCA has been used to show that elliptical galaxies lie on a ‘fundamental plane’^{21,22}, that is, in a two-dimensional space. Because such a correlation analysis relies on linear relations between variables, we use logarithmic quantities (the colour, being a magnitude, is also logarithmic)²³.

Colour turns out to be more complex than the other observables, so we omit it at first and reintroduce it later. Figure 1 demonstrates the strong correlations that exist between the five other variables. This is emphasized in Fig. 2, where all are seen to be strongly correlated with the first principal component, PC1, and scattered with respect to the other principal components. A high degree of organization is already evident. The eigenvalue of PC1 is 4.1, in comparison with a maximum

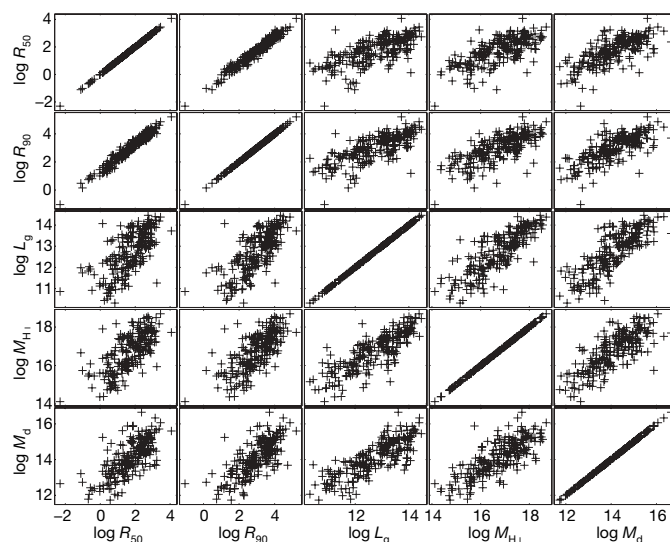


Figure 1 | Scatter plots showing correlations between five measured variables, not including colour. The variables are two optical radii, R_{50} and R_{90} (in parsecs), respectively containing 50 and 90% of the emitted light; and luminosity, L_g ; neutral hydrogen mass, $M_{H\,I}$; and dynamical mass, M_d (inferred from the 21-cm linewidth, the radius and the inclination in the usual way; see main text), all in solar units. In this normalized, logarithmic representation, the slopes are irrelevant; only the scatters are significant. We find that (see ref. 11) $R_{90} \propto R_{50}$, $L_g \propto R_{50}^2$, $M_{H\,I} \propto R_{50}^2$ and $M_d \propto L_g$. Alternatively, the surface brightness $\Sigma \equiv L_g/R_{50}^2 \propto L_g^{1/3} \propto R_{50}$, whereas the luminosity density (defined as L_g/R_{50}^3) and mass density (defined as M_d/R_{50}^3) are independent of size. Colour is included in Fig. 3.

¹School of Physics & Astronomy, Cardiff University, 5 The Parade, Cardiff CF24 3AA, UK. ²Department of Physics and Astronomy, The University of Texas at Brownsville, 80 Fort Brown, Brownsville, Texas 78520, USA. ³European Southern Observatory, Alonso de Cordova 3107, Casilla 19001, Vitacura, Santiago 19, Chile. ⁴Astronomy Department, University of California, 601 Campbell Hall, Berkeley, California 94720-3411, USA. ⁵Department of Astronomy, Physics-Astronomy Building C309, University of Washington, Box 351580, Seattle, Washington 98195, USA.

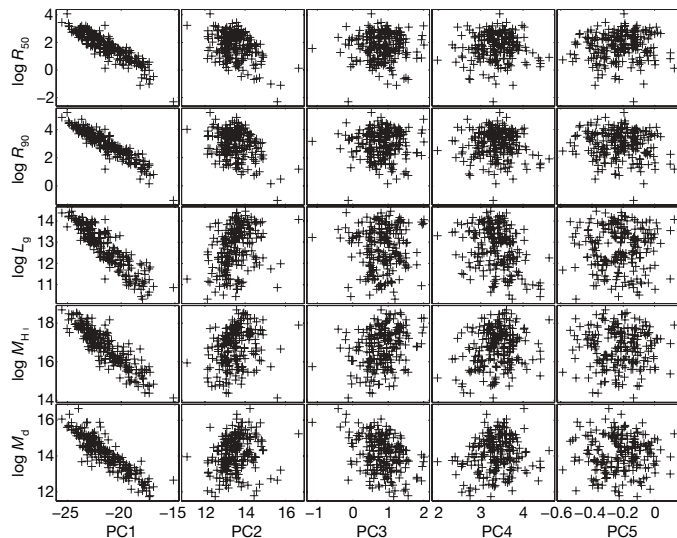


Figure 2 | Scatter plots showing correlations between the five measured variables and the principal components. The five physical quantities are tightly correlated with a single principal component, PC1, which accounts for their correlations with one another. The principal components are labelled from the strongest, PC1, to the weakest, PC5, with eigenvalues 4.1, 0.53, 0.23, 0.17 and 0.02, respectively. Eigenvalues less than 1 are normally thought to represent scatter only—but see main text. The direction cosines for PC1 relative to the physical variables in order plotted (top to bottom) are -0.45 , -0.46 , -0.44 , -0.44 and -0.44 (that is, approximately $-1/\sqrt{5}$). This is expected for such a strong principal component and makes it impossible to single out any one observable as the ‘driving force’. In any case, correlations alone should not be used to infer causation.

possible of 5.0 (1 for each variable; they should sum to 5), whereas the next principal component has an eigenvalue of only 0.53. We note that all five correlations are independent because each introduces at least one a priori independent observable not present in any preceding correlation. We note further that each implies some new intrinsic (not merely scaling) property that calls for a physical explanation. For instance, the correlation between surface brightness and R_{50} implies that $L_g/R_{50}^2 \propto R_{50}$, or that the luminosity density (defined as L_g/R_{50}^3) is independent of either luminosity or dynamical mass.

Figure 3 shows the correlations when the colour is included. Colour is evidently correlated with all the remaining variables, but more weakly so. (The least significant such correlation (0.39) is nevertheless significant at the 0.01% level). Figure 4 clarifies the situation by exhibiting the principal component structure. Like all the other variables, colour is definitely correlated with PC1, which now has an eigenvalue of 4.4 out of a maximum possible of 6.0 (that is, explains 73% of the variance). The next highest eigenvalue is 0.75, for PC2 (Fig. 4, column two). Statisticians normally ignore, as insignificant, principal components with eigenvalues of less than 1.0, except in the special case in which one observable is scattered mostly independently of the rest, when values as low as 0.7 may be considered significant¹⁹. This turns out to be the situation here (0.75). There is a component of the colour that is correlated with nothing but itself, and this ‘rogue’ component constitutes a weak, but nevertheless significant, principal component, PC2, as is clear from column two. The strong correlation in the colour plot of column two is notable. Beyond the fact that PC2 is strongly aligned with colour (direction cosine, 0.83), what does this mean? Simulations (Supplementary Information) show that if colour were perfectly uncorrelated with everything else (that is, were randomly scattered), then the colour plot of column two would be a sharp, straight line at a slope of 45° . This is because even if an observable (for example colour) is correlated with nothing else it is nevertheless correlated perfectly with itself, and the PCA seeks out a principal component aligned perfectly with that observable (in this case colour).

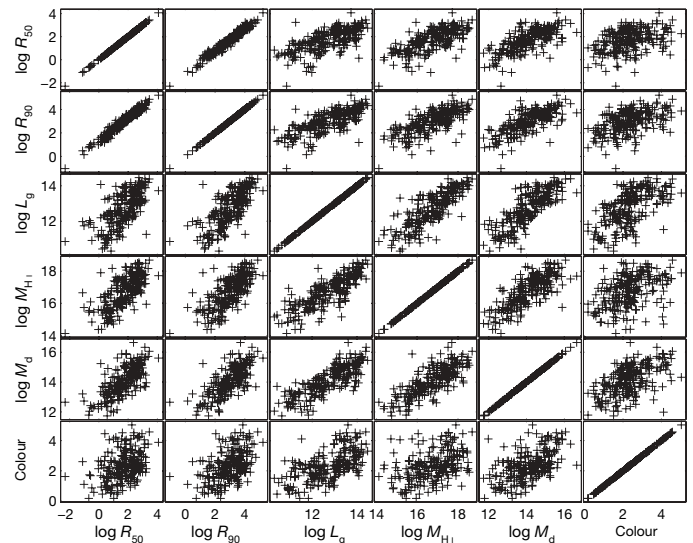


Figure 3 | Scatter plots showing correlations between the previous five measured variables (Fig. 1), but now including colour. The colour is $(g-r)$, that is, ‘green minus red’, and is also logarithmic. Colour (measured within R_{90}) is correlated with the five other observables in the sense that more luminous galaxies are redder, which is usually taken to mean that their output is dominated by older stars. However, the colour correlations are much weaker, though still highly significant (at the 0.01% level).

We can summarize the PCA as follows. H I-selected galaxies appear to have colours made up of two components, which we label the ‘systematic’ component and the ‘rogue’ component. The rogue colour

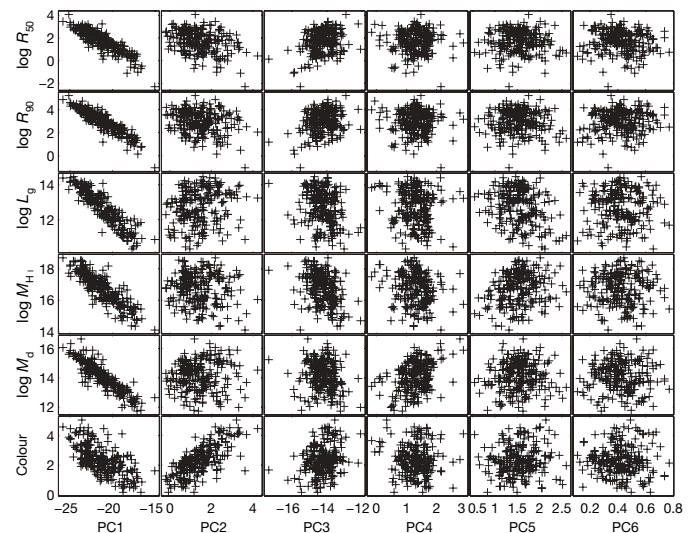


Figure 4 | Scatter plots showing correlations between all the six measured variables (including colour) and the principal components. The principal components are labelled from the strongest, PC1, to the weakest, PC6, with eigenvalues 4.4, 0.75, 0.48, 0.22, 0.14 and 0.02, respectively. The bottom plot of column one shows that colour is well correlated with the other five observables and with PC1. However, the bottom plot in column two shows that colour is even more strongly correlated with a new principal component, PC2, which is correlated with nothing else. If colour were entirely independent of all the other variables, it would have its own principal component with an eigenvalue of 1.0, instead of 0.75 as observed, and the data plotted against PC2 would lie on a sharp, straight line, because they would be correlated perfectly with themselves. The colour of a galaxy is evidently composed of two components: a ‘systematic’ component correlated with all the other observables, and a ‘random’ or ‘rogue’ component correlated with nothing but itself. Appreciation of this non-intuitive point was greatly assisted by examining a PCA of simulated data (see Supplementary Information).

is scattered more or less randomly, and is correlated with none of the other observables. (It would be natural, although not compelling, to identify the systematic colour with the old population of stars, and the rogue component with recent and transitory bursts of star formation—very luminous young stars being far bluer and shorter lived than older ones.) The remaining six variables, including the systematic colour, are all correlated with one another and with a single principal component. In other words, they form a one-parameter set lying on a single fundamental line. Such simplicity was unpredicted and is noteworthy when galaxies might have been controlled by any six of the seven potentially independent physical parameters listed earlier. It is even more significant considering the enormous variety among the galaxies in the sample¹¹.

If, as we have argued, galaxies come from at most a six-parameter set, then for gaseous galaxies to appear as a one-parameter set, as observed here, the theory of galaxy formation and evolution must supply five independent constraint equations to constrain the observations. This is such a stringent set of requirements that it is hard to imagine any theory, apart from the correct one, fulfilling them all. For instance, consider hierarchical galaxy formation in the dark matter model, which has been widely discussed in the literature^{3,4}. Even after extensive simplification, it still contains four parameters per galaxy: mass, spin, halo-concentration index and epoch of formation. Consider spin alone, which is thought to be the result of early tidal torquing. Simulations produce spins, independent of mass, with a log-normal distribution. Higher-spin discs naturally cannot contract as far; thus, to a much greater extent than for low-spin discs, their dynamics is controlled by their dark haloes, so it is unexpected to see the nearly constant dynamical-mass/luminosity ratio that we and others¹⁴ actually observe. Hierarchical galaxy formation simply does not fit the constraints set by the correlation structure in the Equatorial Survey.

More generally, a process of hierarchical merging, in which the present properties of any galaxy are determined by the necessarily haphazard details of its last major mergers, hardly seems consistent with the very high degree of organization revealed in this analysis. Hierarchical galaxy formation does not explain the commonplace gaseous galaxies we observe. So much organization, and a single controlling parameter—which cannot be identified for now—argue for some simpler model of formation. It would be illuminating to identify the single controlling galaxy parameter, but this cannot be attempted from the present data. To confuse correlation with cause is the critical mistake that can be made in this kind of analysis.

It is natural to ask why this fundamental line was not discovered before. To some extent it was because even the pioneers^{24,25} and others^{26–28} working with small numbers of optically selected spirals could reduce six observables to two; one relating to size, one to morphology. The strong optical selection effects, which hamper optical astronomers in detecting and measuring objects whose surface brightnesses are barely brighter than the sky^{5,29}, probably disguised galaxies' simplicity.

Received 27 March; accepted 26 August 2008.

1. de Jong, R. S. (ed.) *Island Universes: Structure and Evolution of Disk Galaxies* (Astrophys. Space Sci. Proc., Springer, 2007).
2. Baugh, C. M. A primer on hierarchical galaxy formation: the semi-analytical approach. *Rep. Prog. Phys.* **69**, 3101–3156 (2006).

3. Dalcanton, J. J., Spergel, D. N. & Summers, I. J. The formation of disk galaxies. *Astrophys. J.* **482**, 659–676 (1997).
4. Mo, H. J., Mao, S. & White, S. D. M. The formation of galactic discs. *Mon. Not. R. Astron. Soc.* **295**, 319–336 (1998).
5. Disney, M. J. in *The Low Surface Brightness Universe* (eds Davies, J. I., Impey, C. & Phillipps, S.) 9–18 (IAU Symp. 171, Astron. Soc. Pacif. Conf. Ser. 170, Astronomical Society of the Pacific, 1999).
6. Blumenthal, G. R., Faber, S. M., Primack, J. R. & Rees, M. J. Formation of galaxies and large-scale structure with cold dark matter. *Nature* **311**, 517–525 (1984).
7. Staveley-Smith, L. et al. The Parkes 21-cm multibeam receiver. *Publ. Astron. Soc. Austral.* **13**, 243–248 (1996).
8. Zwaan, M. A. et al. The HIPASS catalogue – II. Completeness, reliability, and parameter accuracy. *Mon. Not. R. Astron. Soc.* **350**, 1210–1219 (2004).
9. Meyer, M. J. et al. The HIPASS catalogue – I. Data presentation. *Mon. Not. R. Astron. Soc.* **350**, 1195–1209 (2004).
10. Adelman-McCarthy, J. K. et al. The fifth data release of the Sloan Digital Sky Survey. *Astrophys. J. Suppl. Ser.* **172**, 634–644 (2007).
11. Garcia-Appadoo, D. A., West, A. A., Dalcanton, J. J., Cortese, L. & Disney, M. J. Correlations among the properties of galaxies found in a blind HI survey. *Mon. Not. R. Astron. Soc.* (submitted); preprint at (<http://arxiv.org/abs/0809.1434>) (2008).
12. Strateva, I. et al. Color separation of galaxy types in the Sloan Digital Sky Survey imaging data. *Astron. J.* **122**, 1861–1874 (2001).
13. Kulkarni, S. R. & Heiles, C. in *Galactic and Extra-Galactic Radio Astronomy* 2nd edn (eds Kellerman, K. I. & Verschuur, G. L.) 95–153 (Springer, 1988).
14. Gavazzi, G., Pierini, D. & Boselli, A. The phenomenology of disk galaxies. *Astron. Astrophys.* **312**, 397–408 (1996).
15. Blanton, M. R. et al. The galaxy luminosity function and luminosity density at redshift $z = 0.1$. *Astrophys. J.* **592**, 819–838 (2003).
16. van der Kruit, P. The three-dimensional distribution of light and mass in disks of spiral galaxies. *Astron. Astrophys.* **192**, 117–127 (1988).
17. Haynes, M. P. & Giovanelli, R. Neutral hydrogen in isolated galaxies. IV – Results for the Arecibo sample. *Astron. J.* **89**, 758–800 (1984).
18. Rosenberg, J. L., Schneider, S. E. & Posson-Brown, J. Gas and stars in an HI-selected galaxy sample. *Astrophys. J.* **129**, 1311–1330 (2005).
19. Jolliffe, I. T. *Principal Component Analysis* (Springer, 1986).
20. Chatfield, C. & Collins, A. J. *Introduction to Multivariate Analysis* (Chapman & Hall, 1980).
21. Kormendy, J. & Kennicutt, R. C. Jr. Secular evolution and the formation of pseudobulges in disk galaxies. *Annu. Rev. Astron. Astrophys.* **42**, 603–683 (2004).
22. Zibetti, S. et al. 1.65 micron (H band) surface photometry of galaxies. I. Structural and dynamical properties of elliptical galaxies. *Astrophys. J.* **579**, 261–269 (2002).
23. Conselice, C. J. The fundamental properties of galaxies and a new galaxy classification system. *Mon. Not. R. Astron. Soc.* **373**, 1389–1408 (2006).
24. Brosche, P. The manifold of galaxies. Galaxies with known dynamical parameters. *Astron. Astrophys.* **23**, 259–268 (1973).
25. Balkowski, C. Statistical study of integral properties of galaxies measured in the 21-cm line. *Astron. Astrophys.* **29**, 43–55 (1973).
26. Bujarrabal, V., Guibert, J. & Balkowski, C. Multidimensional statistical analysis of normal galaxies. *Astron. Astrophys.* **104**, 1–9 (1981).
27. Shostak, G. S. Integral properties of late-type galaxies derived from HI observations. *Astron. Astrophys.* **68**, 321–341 (1978).
28. Whitmore, B. C. An objective classification system for spiral galaxies. I. The two dominant dimensions. *Astrophys. J.* **278**, 61–80 (1984).
29. Dalcanton, J. J., Spergel, D. N., Gunn, J. E., Schmidt, M. & Schneider, D. P. The number density of low-surface brightness galaxies with $23 < \mu_0 < 25$ V Mag/arcsec². *Astron. J.* **114**, 635–654 (1997).

Supplementary Information is linked to the online version of the paper at www.nature.com/nature.

Acknowledgements We would like to thank the HIPASS team, and especially R. Ekers, A. Wright and L. Staveley-Smith of the Australian National Telescope at CSIRO Radiophysics in Sydney for their foresight and enterprise in getting the Multibeam project started. M.J.D. would like to thank M. Disney of the Geography Department at University College London for first pointing out the one-dimensional nature of this data.

Author Information Reprints and permissions information is available at www.nature.com/reprints. Correspondence and requests for materials should be addressed to M.J.D. (mjd@astro.cf.ac.uk).

Solid-state quantum memory using the ^{31}P nuclear spin

John J. L. Morton^{1,2}, Alexei M. Tyryshkin³, Richard M. Brown¹, Shyam Shankar³, Brendon W. Lovett¹, Arzhang Ardavan², Thomas Schenkel⁴, Eugene E. Haller^{4,5}, Joel W. Ager⁴ & S. A. Lyon³

The transfer of information between different physical forms—for example processing entities and memory—is a central theme in communication and computation. This is crucial in quantum computation¹, where great effort² must be taken to protect the integrity of a fragile quantum bit (qubit). However, transfer of quantum information is particularly challenging, as the process must remain coherent at all times to preserve the quantum nature of the information³. Here we demonstrate the coherent transfer of a superposition state in an electron-spin ‘processing’ qubit to a nuclear-spin ‘memory’ qubit, using a combination of microwave and radio-frequency pulses applied to ^{31}P donors in an isotopically pure ^{28}Si crystal^{4,5}. The state is left in the nuclear spin on a time-scale that is long compared with the electron decoherence time, and is then coherently transferred back to the electron spin, thus demonstrating the ^{31}P nuclear spin as a solid-state quantum memory. The overall store–readout fidelity is about 90 per cent, with the loss attributed to imperfect rotations, and can be improved through the use of composite pulses⁶. The coherence lifetime of the quantum memory element at 5.5 K exceeds 1 s.

Classically, transfer of information can include a copying step, facilitating the identification and correction of errors. However, the no-cloning theorem limits the ability to faithfully copy quantum states across different degrees of freedom⁷; thus, error correction becomes more challenging for quantum information than for classical, and the transfer of information must take place directly. Experimental demonstrations of such transfer include moving a trapped ion qubit in and out of a decoherence-free subspace for storage purposes⁸ and optical measurements of nitrogen-vacancy centres in diamond⁹.

Nuclear spins are known to benefit from coherence times long in comparison with those of electron spins, but are slow to manipulate and suffer from weak thermal polarization. A powerful model for quantum computation is thus one in which electron spins are used for processing and readout and nuclear spins are used for storage. The storage element can be a single, well-defined nuclear spin, or perhaps a bath of nearby nuclear spins¹⁰. ^{31}P donors in silicon provide an ideal combination of long-lived spin-1/2 electron¹¹ and nuclear spins¹², with the additional advantage of integration with existing technologies⁴ and the possibility of single-spin detection by electrical measurement^{13–15}. Direct measurement of the ^{31}P nuclear spin by NMR has only been possible at very high doping levels (for example near the metal–insulator transition¹⁶). Instead, electron–nuclear double resonance can be used to excite both the electron and nuclear spins associated with the donor site, and measure the nuclear spin by means of the electron¹⁷. This was recently used to measure the nuclear spin-lattice relaxation time, T_{1n} , which was

found to follow the electron relaxation time, T_{1e} , over the range 6–12 K with the relationship $T_{1n} \approx 250 T_{1e}$ (refs 5, 12). The suitability of the nuclear spin as a quantum memory element depends more critically on the nuclear coherence time, T_{2n} , the measurement of which has now been made possible through the storage procedure described here: varying the storage time and observing the amplitude of the recovered electron coherence.

Figure 1b shows the coherence transfer scheme used for the write process from a processing qubit represented by an electron-spin degree of freedom to a memory qubit residing in a nuclear-spin degree of freedom. Each π pulse is equivalent to a controlled-NOT gate¹⁸ (with some additional phase that can be ignored) such that the pair of π pulses constitute a SWAP gate.

The scheme assumes that all pulses are on-resonance and have sufficient bandwidth to completely excite an individual transition. A read operation is performed by applying the reverse sequence, to bring the coherent state back to the electron-spin qubit. Although the phase relationship between the microwave and radio-frequency

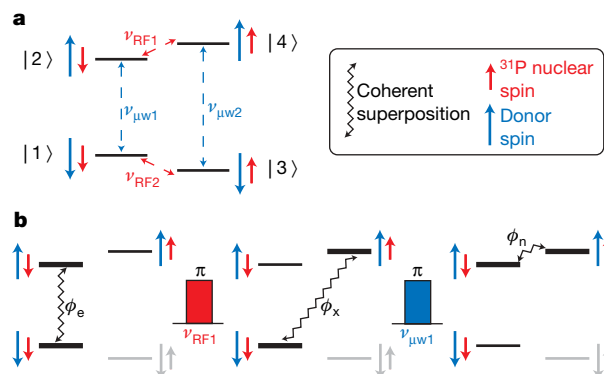


Figure 1 | The level structure of the coupled electron and nuclear spins and scheme for the transfer of a logical qubit within the two physical spin qubits. a, The four-level system may be manipulated by resonant microwave ($\nu_{\mu w1}$, $\nu_{\mu w2}$) and radio-frequency (ν_{RF1} , ν_{RF2}) radiation. In our experiments, the logical electron-spin ‘processing’ qubit is represented by states $|1\rangle$ and $|2\rangle$, whose state can be transferred to a nuclear-spin ‘memory’ qubit represented by states $|2\rangle$ and $|4\rangle$. State $|3\rangle$ is never addressed at any point and can be ignored. **b**, An electron-spin coherence ϕ_e between states $|1\rangle$ and $|2\rangle$ is transferred to the nuclear-spin qubit by a radio-frequency π pulse followed by a microwave π pulse. Both pulses must fully excite the transition, and be short in comparison with the electron and nuclear coherence times. The reverse process is used to transfer the nuclear coherence ϕ_n back to the electron. The intermediate state ϕ_x is a double quantum coherence representing an entangled electron–nuclear spin state.

¹Department of Materials, Oxford University, Oxford OX1 3PH, UK. ²CAESR, Clarendon Laboratory, Department of Physics, Oxford University, Oxford OX1 3PU, UK. ³Department of Electrical Engineering, Princeton University, Princeton, New Jersey 08544, USA. ⁴Lawrence Berkeley National Laboratory, 1 Cyclotron Road, Berkeley, California 94720, USA.

⁵Department of Materials Science and Engineering, University of California, Berkeley, California 94720, USA.

pulses must be constant throughout this process, any phase difference is cancelled out over the course of the write–read process. In practice, this means that the microwave and radio-frequency sources need not be phase locked, but must have high phase stability. This is illustrated in calculations following the evolution of the density matrix, provided in the Supplementary Information.

Although the electron-spin qubit can be prepared in a state of high purity using experimentally accessible magnetic fields and temperatures, the small nuclear Zeeman energy results in the nuclear spin being initially in a highly mixed thermal state. However, for the purposes of this quantum memory scheme it is not necessary to perform any pre-cooling of the nuclear-spin resource.

This model is sufficient given a single electron–nuclear spin pair or a homogenous ensemble. However, in the experiment described here we must consider the effects of inhomogeneous broadening across the ensemble of spins being manipulated. The effect of inhomogeneous broadening is to leave some electron spins detuned from the applied microwave radiation, by δ_e , and some nuclear spins detuned from the applied radio-frequency radiation, by δ_n . In a suitable rotating reference frame, electron- and nuclear-spin coherences will thus acquire additional phases at the respective rates δ_e and δ_n , whereas double quantum coherences will acquire a phase at a rate $\delta_e + \delta_n$. Hence, inhomogeneous broadening requires the application of carefully placed refocusing pulses to bring all spin packets into focus at key points during the transfer process. In the experiment described here, $\pi/\delta_e \approx 2 \mu\text{s}$ and $\pi/\delta_n \approx 100 \mu\text{s}$.

Figure 2 shows the practical implementation of a protocol that generates a coherent electron-spin state, stores it in a state of the nuclear spin for some time, and then returns it to the electron state for readout again. The coherence is first generated by a microwave $\pi/2$ pulse of a chosen phase ϕ , representing our bit of quantum information. A free induction decay (that is, the reversible dephasing of the ensemble) follows this pulse. We apply a refocusing microwave

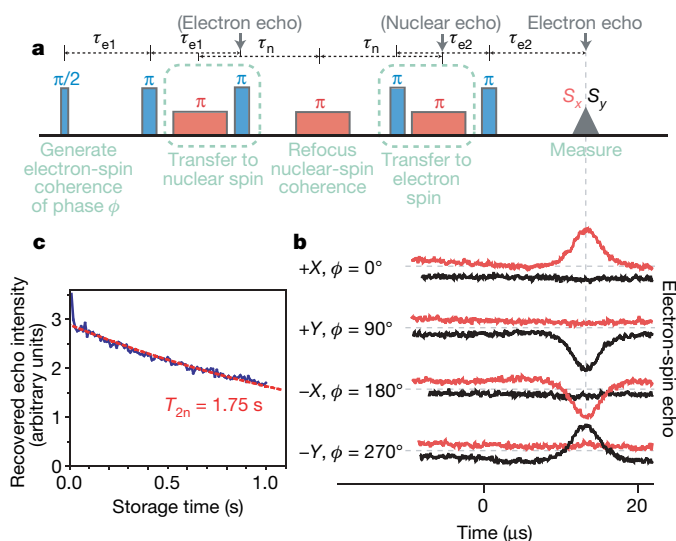


Figure 2 | Coherent storage of an electron-spin state in a nuclear-spin state, using a ^{31}P -doped ^{28}Si -enriched silicon single crystal. **a**, The general sequence for the storage and revival of the electron-spin state comprises microwave and RF pulses applied at certain times, defined by τ_{e1} , τ_{e2} and τ_n . **b**, An electron-spin coherence is stored in the nuclear spin for $2\tau_n \approx 50 \text{ ms}$, at 7.2 K. Real (red) and imaginary (black) parts of the recovered electron-spin echo are shown for different initial phases ϕ . The echo is of comparable intensity to that obtained at the beginning of the sequence, even though the electron-spin coherence time, T_{2e} , is about 5 ms here. The lifetime of the stored state is limited instead by the nuclear decoherence time, T_{2n} , which can be measured directly by varying τ_n . **c**, The recovered echo intensity was measured as a function of the storage time at 5.5 K while a dynamic (Carr–Purcell–Meiboom–Gill) decoupling sequence was applied to the nuclear spin, yielding a T_{2n} exceeding 1 s.

π pulse at time τ_e to initiate a revival in the electron-spin coherence. The subsequent radio-frequency π pulse transfers the coherence from the electron to a double quantum coherence of entangled electron–nuclear spin states. During this period, the phase $\delta_e\tau_e$, acquired before application of the microwave refocusing pulse, continues to reverse in such a way that when the final step of the transfer, a microwave π pulse, is applied, the effect of the inhomogeneous electron-spin packets has been completely refocused. The quantum information that was generated by the first microwave $\pi/2$ pulse now resides entirely in the state of the nucleus.

This information may be stored in the nuclear state for some extended period, so the effects of inhomogeneities on the phase of the nuclear state become appreciable and a preparatory radio-frequency refocusing pulse must be applied before the information can be recovered. During the nuclear-spin echo, the coherence is transferred back to the electron state with a microwave π pulse followed by a radio-frequency π pulse. We apply one further microwave π pulse to stimulate an electron-spin echo representing the readout event. Figure 2b shows the real (red) and imaginary (black) parts of this echo for different initial phases ϕ , demonstrating that the encoded phase is recovered through the storage–recovery process, as required for an effective quantum memory element.

The storage time is limited only by the nuclear decoherence time, T_{2n} , which is in turn limited to $2T_{1e}$ when there is a significant hyperfine interaction ($A \gg 1/T_{1e}$) between the electron and nuclear spins and in the limit where the thermal energy exceeds the magnetic field splitting ($k_B T \gg g\mu_B B$; see Supplementary Information); T_{1e} becomes very long (for example hours) at low temperatures¹⁷. A direct measurement of T_{2n} in anything other than highly doped Si:P has been impossible by traditional NMR means, but our write–read procedure provides a method of performing this measurement by increasing the storage time, T_{store} , and observing the resulting decay in the recovered electron coherence. The T_{2n} obtained in this way follows $2T_{1e}$ approximately over the range 9–12 K as expected, though at lower temperatures an additional nuclear decoherence mechanism appears to have a role, yielding a limit of about 65 ms for T_{2n} . A leading candidate for this additional process is slowly fluctuating fields, the effect of which may be mitigated by dynamically decoupling the system^{19,20}. By applying a Carr–Purcell–Meiboom–Gill decoupling sequence at a 1-kHz repetition rate to the nuclear spin during the storage period, we were able to obtain much longer decoherence times than for a simple Hahn echo measurement, rising to 1.75 s at 5.5 K, as shown in Fig. 2c.

Under optimized conditions, the electron-spin decoherence time, T_{2e} , is limited only by magnetic dipole–dipole interactions, and values between 4 and 6.5 ms have been measured in the samples used here, varying according to the donor-spin concentration¹¹. Using the nuclear degree of freedom, we have achieved storage times several orders of magnitude longer than T_{2e} .

The removal, or substantial detuning, of any of the radio-frequency pulses in the sequence destroys the recovered echo, confirming the importance of the transfer to the nuclear spin and providing evidence that the stored quantum information does reside in the nuclear state. For a more direct proof, we require a tool permitting inspection of the state of the nuclear spin during the storage period. We therefore applied a sequence to probe (destructively) the nuclear coherence through the electron state, as shown in Fig. 3a. The early part of the sequence is as described above: an electron-spin coherence is stored in the state of the nucleus. When we decide to observe the state of the nucleus, we apply a radio-frequency $\pi/2$ pulse to convert the nuclear coherence into a nuclear polarization (in the spirit of a Ramsey fringe experiment). A short electron-spin echo sequence, selective in one nuclear subspace, then reveals the population of the nuclear level.

This sequence can be performed at any time; Fig. 3b shows the result of observing the state of the nucleus at a range of times for different starting phases ϕ , revealing the nuclear-spin echo following

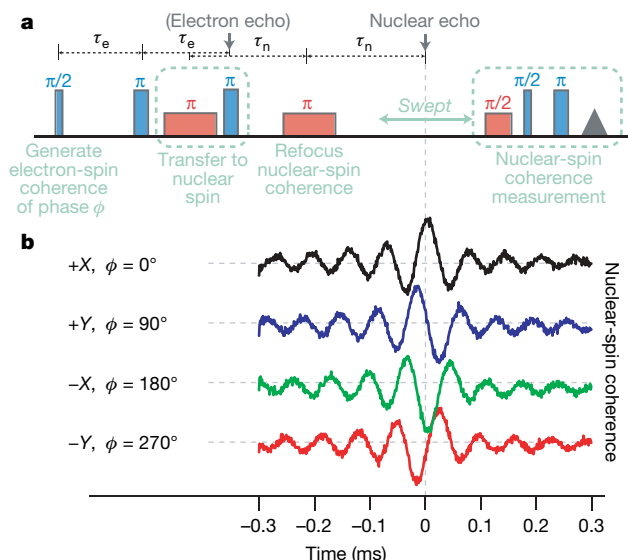


Figure 3 | Observing the nuclear-spin coherence during the storage process. **a**, The phase of the initial electron superposition state is determined by the phase of initial microwave $\pi/2$ excitation pulse, which we can control. This state is then transferred to the nuclear spin using the scheme outlined in Fig. 1. The nuclear-spin coherence is read using a process similar to a Ramsey fringe measurement: a radio-frequency $\pi/2$ pulse converts nuclear coherence to nuclear polarization, which is then detected by means of an electron spin echo measurement selective of one nuclear-spin state. **b**, The correlation of the phase of the nuclear-spin echo and the phase of the original electron-spin superposition confirms the coherent nature of the transfer from electron to nuclear spin.

the radio-frequency refocusing pulse. The centre of the radio frequency was intentionally moved off-resonance to produce oscillations in the nuclear echo and, hence, aid the identification of the phase of the nuclear coherence. The fact that the phase of the nuclear-spin echo follows the phase of the original microwave $\pi/2$ pulse confirms that the information transfer process has remained coherent. In contrast to other nuclear-spin echoes observed by means of electron–nuclear double resonance^{21,22}, in which an electron-spin polarization is used to create a nuclear-spin polarization and then a nuclear coherence, this echo represents a coherent state of the electron that has been directly transferred to the nuclear spin.

To demonstrate the generality of the storage sequence described here, we applied it to a wider set of initial states, in particular the $\pm X$, $\pm Y$, $\pm Z$ (spin component direction) and identity basis states, and performed density matrix tomography by comparing the original states with those recovered after the write–read process (see Supplementary Information for full details). The results are summarized in Fig. 4 and show fidelities of approximately 0.90, where the fidelity between the initial (pseudo)pure state, ρ_0 , and the recovered state, ρ_1 , is defined as $F = \langle \psi | \rho_1 | \psi \rangle$, where $\rho_0 = |\psi\rangle\langle\psi|$. We attribute the reduced fidelity to a $\sim 5\%$ error in each of the seven microwave and radio-frequency pulses applied over the course of the sequence, which is entirely consistent with previous measurements of pulse fidelities²³. Such errors are mostly systematic and may be corrected through the application of composite pulses, as previously demonstrated in both electron paramagnetic resonance (EPR) and NMR^{6,24}. By replacing some of the microwave pulses with BB1 composite pulses, we were able to improve the overall fidelity to approximately 0.97, and further improvements are to be expected with greater control of the radio-frequency pulse phases.

As the experimental challenges of quantum information processing have become better understood, the importance of hybrid quantum systems in models of quantum information has emerged^{25–27}. The approach described here demonstrates the advantages of such hierarchical models and has a broad applicability in

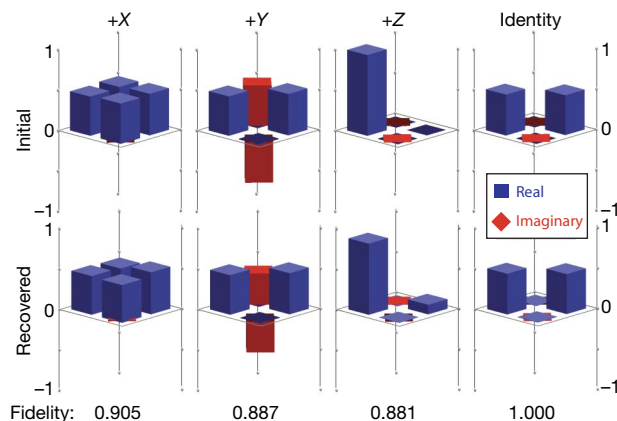


Figure 4 | Density matrix tomography for original and recovered states. Pseudopure states $+X$, $+Y$ and $+Z$ and the identity were prepared in the electron-spin qubit and measured (first row, initial). These states were then stored in the nuclear-spin degree of freedom and then returned to the electron spin and measured (second row, recovered). Tomography was performed by measuring the qubit in the $(\sigma_x, \sigma_y, \sigma_z)$ basis. The fidelity of the quantum memory was obtained by comparing the initial and recovered density matrices.

systems where there is a substantial asymmetry in relaxation times. Storage can be driven globally, as shown here, or locally, using EPR gates²⁸ or Stark tuning⁴. Furthermore, our protocol for faithfully transferring a coherent electron-spin state to the nuclear spin offers a route to projective measurements of the qubit state through proposed spectrally sensitive single-spin-detection methodologies such as EPR detected either using scanning tunnelling microscopy or electrically²⁹.

METHODS SUMMARY

Si:P consists of an electron spin, $S = 1/2$ ($g = 1.9987$), coupled to the nuclear spin, $I = 1/2$, of ^{31}P through a hyperfine coupling $A = 117$ MHz (ref. 17), and is described by an isotropic spin Hamiltonian $H_0 = \omega_e S_z - \omega_I I_z + ASI$ (in angular frequency units), where, respectively, S and I are the electron and nuclear spin tensors, $\omega_e = g\beta B_0/\hbar$ and $\omega_I = g_I\beta_n B_0/\hbar$ are the electron and nuclear Zeeman frequencies, g and g_I are the electron and nuclear g -factors, β and β_n are the Bohr and nuclear magnetons, \hbar is Planck's constant divided by 2π and B_0 is the magnetic field applied along z axis in the laboratory frame. The X-band EPR signal comprises two lines (one for each nuclear-spin projection $M_I = \pm 1/2$). Our experiments were performed on the high-field line of the EPR doublet corresponding to $M_I = -1/2$.

Single-crystal samples were used, as epilayers of ^{28}Si have a biaxial residual stress that broadens the ^{31}P electron–nuclear double resonance line and makes it difficult to fully excite. ^{28}Si -enriched single crystals with a residual ^{29}Si concentration of 800 p.p.m. were produced by decomposing isotopically enriched silane (SiH_4) in a recirculating reactor to produce poly-Si rods, followed by floating-zone crystallization³⁰. To reduce spin–spin coupling effects, the P concentration was reduced from an initial value of near $1 \times 10^{15} \text{ cm}^{-3}$ to $2 \times 10^{14} - 5 \times 10^{14} \text{ cm}^{-3}$ by five passes of zone refining followed by floating-zone crystallization.

Pulsed EPR experiments were performed using an X-band (9–10 GHz) Bruker EPR spectrometer (Elexsys 580) equipped with a low-temperature helium-flow cryostat (Oxford CF935). An Amplifier Research 20W solid-state continuous-wave amplifier was used, with $\pi/2$ and π pulses of 80 and 160 ns, respectively. Radio-frequency pulses of $20 \mu\text{s}$ were used for π rotations of the ^{31}P nuclear spins. During Carr–Purcell–Meiboom–Gill decoupling, up to 1,000 refocusing pulses were applied during a single sequence.

Received 27 June; accepted 29 July 2008.

- Deutsch, D. Quantum theory, the Church-Turing principle and the universal quantum computer. *Phil. Trans. R. Soc. Lond. A* **400**, 97–117 (1985).
- Steane, A. M. Efficient fault-tolerant quantum computing. *Nature* **399**, 124–126 (1999).
- Julsgaard, B., Sherson, J., Cirac, J. I., Fiurák, J. & Polzik, E. S. Experimental demonstration of quantum memory for light. *Nature* **432**, 482–486 (2004).
- Kane, B. E. A silicon-based nuclear spin quantum computer. *Nature* **393**, 133–137 (1998).

5. Tyryshkin, A. M. *et al.* Coherence of spin qubits in silicon. *J. Phys. Condens. Matter* **18**, S783–S794 (2006).
6. Morton, J. J. L. *et al.* High fidelity single qubit operations using pulsed electron paramagnetic resonance. *Phys. Rev. Lett.* **95**, 200501 (2005).
7. Wootters, W. K. & Zurek, W. H. A single quantum cannot be cloned. *Nature* **299**, 802–803 (1982).
8. Kielpinski, D. *et al.* A decoherence-free quantum memory using trapped ions. *Science* **291**, 1013–1015 (2001).
9. Dutt, M. V. G. *et al.* Quantum register based on individual electronic and nuclear spin qubits in diamond. *Science* **316**, 1312–1316 (2007).
10. Dobrovitski, V. V., Taylor, J. M. & Lukin, M. D. Long-lived memory for electronic spin in a quantum dot: Numerical analysis. *Phys. Rev. B* **73**, 245318 (2006).
11. Tyryshkin, A. M., Lyon, S. A., Astashkin, A. V. & Raitsimring, A. M. Electron spin relaxation times of phosphorus donors in silicon. *Phys. Rev. B* **68**, 193207 (2003).
12. Tyryshkin, A. M., Morton, J. J. L., Ardavan, A. & Lyon, S. A. Davies electron-nuclear double resonance revisited: Enhanced sensitivity and nuclear spin relaxation. *J. Chem. Phys.* **124**, 234508 (2006).
13. Stegner, A. R. *et al.* Electrical detection of coherent ^{31}P spin quantum states. *Nature Phys.* **2**, 835–838 (2006).
14. McCamey, D. R. *et al.* Electrically detected magnetic resonance in ion-implanted Si:P nanostructures. *Appl. Phys. Lett.* **89**, 182115 (2006).
15. Lo, C. C. *et al.* Spin-dependent scattering off neutral antimony donors in ^{28}Si field-effect transistors. *Appl. Phys. Lett.* **91**, 242106 (2007); *Appl. Phys. Lett.* **92**, 109908 (2008).
16. Hirsch, M. J. & Holcomb, D. F. NMR study of Si:As and Si:P near the metal-insulator transition. *Phys. Rev. B* **33**, 2520–2529 (1986).
17. Feher, G. Electron spin resonance experiments on donors in silicon I: Electronic structure of donors by the electron nuclear double resonance technique. *Phys. Rev.* **114**, 1219–1244 (1959).
18. Mehring, M., Mende, J. & Scherer, W. Entanglement between an electron and a nuclear spin 1/2. *Phys. Rev. Lett.* **90**, 153001 (2003).
19. Viola, L. & Lloyd, S. Dynamical suppression of decoherence in two-state quantum systems. *Phys. Rev. A* **58**, 2733–2744 (1998).
20. Morton, J. J. L. *et al.* Bang-bang control of fullerene qubits using ultra-fast phase gates. *Nature Phys.* **2**, 40–43 (2006).
21. Höfer, P., Grupp, A. & Mehring, M. High-resolution time-domain electron-nuclear-sublevel spectroscopy by pulsed coherence transfer. *Phys. Rev. A* **33**, 3519–3522 (1986).
22. Morton, J. J. L. *et al.* The N@C60 nuclear spin qubit: Bang-bang decoupling and ultrafast phase gates. *Phys. Status Solidi B* **243**, 3028–3031 (2006).
23. Morton, J. J. L. *et al.* Measuring errors in single-qubit rotations by pulsed electron paramagnetic resonance. *Phys. Rev. A* **71**, 012332 (2005).
24. Cummins, H. K., Llewellyn, G. & Jones, J. A. Tackling systematic errors in quantum logic gates with composite rotations. *Phys. Rev. A* **67**, 042308 (2003).
25. Taylor, J. M. *et al.* Fault-tolerant architecture for quantum computation using electrically controlled semiconductor spins. *Nature Phys.* **1**, 177–183 (2005).
26. Thaker, D. D., Metodi, T. S., Cross, A. W., Chuang, I. L. & Chong, F. T. in *ISCA '06* 378–390 (Proc. 33rd Internat. Symp. Computer Architecture, IEEE, 2006).
27. Rabl, P. *et al.* Hybrid quantum processors: Molecular ensembles as quantum memory for solid state circuits. *Phys. Rev. Lett.* **97**, 033003 (2006).
28. Nowack, K. C., Koppens, F. H. L., Nazarov, Y. V. & Vandersypen, L. M. K. Coherent control of a single electron spin with electric fields. *Science* **318**, 1430–1433 (2007).
29. Sarovar, M., Young, K. C., Schenkel, T. & Whaley, K. B. Quantum non-demolition measurements of single spins in semiconductors. Preprint at <http://arxiv.org/abs/0711.2343v1> (2007).
30. Ager, J. W. *et al.* High-purity, isotopically enriched bulk silicon. *J. Electrochem. Soc.* **152**, G448–G451 (2005).

Supplementary Information is linked to the online version of the paper at www.nature.com/nature.

Acknowledgements We thank G. A. D. Briggs for comments and support and R. Weber, P. Höfer and Bruker Biospin for support with instrumentation. We thank P. Weaver of Advanced Silicon Materials, Inc. for zone-refining and H. Riemann of the Institut für Kristallzüchtung for float-zone processing of the ^{28}Si crystals used in this work. This research is supported by the National Security Agency (MOD 713106A) and the EPSRC through the Quantum Information Processing Interdisciplinary Research Collaboration (GR/S82176/01) and CAESR (EP/D048559/1). J.J.L.M. is supported by St John's College, Oxford. A.A. and B.W.L. are supported by the Royal Society. Work at Princeton received support from the US National Science Foundation through the Princeton MRSEC (DMR-0213706). Work at Lawrence Berkeley National Laboratory was supported by the Director, Office of Science, Office of Basic Energy Sciences, Materials Sciences and Engineering Division of the US Department of Energy (DE-AC02-05CH11231).

Author Information Reprints and permissions information is available at www.nature.com/reprints. Correspondence and requests for materials should be addressed to J.J.L.M. (john.morton@materials.ox.ac.uk).

Correlation between nanosecond X-ray flashes and stick–slip friction in peeling tape

Carlos G. Camara^{1*}, Juan V. Escobar^{1*}, Jonathan R. Hird¹ & Seth J. Putterman¹

Relative motion between two contacting surfaces can produce visible light, called triboluminescence¹. This concentration of diffuse mechanical energy into electromagnetic radiation has previously been observed to extend even to X-ray energies². Here we report that peeling common adhesive tape in a moderate vacuum produces radio and visible emission^{3,4}, along with nanosecond, 100-mW X-ray pulses that are correlated with stick–slip peeling events. For the observed 15-keV peak in X-ray energy, various models^{5,6} give a competing picture of the discharge process, with the length of the gap between the separating faces of the tape being 30 or 300 μm at the moment of emission. The intensity of X-ray triboluminescence allowed us to use it as a source for X-ray imaging. The limits on energies and flash widths that can be achieved are beyond current theories of tribology.

When a continuous medium is driven far from equilibrium, non-linear processes can lead to strong concentrations in the energy density. Sonoluminescence⁷ provides an example in which acoustic energy concentrates by 12 orders of magnitude to generate subnanosecond flashes of ultraviolet radiation. Charge separation at contacting surfaces^{8,9} is another example of a process that funnels diffuse mechanical energy into high-energy emission. Lightning¹⁰, for instance, has been shown to generate X-rays with energies of more than 10 keV (ref. 11). Although triboelectrification is important in many natural and industrial processes, its physical explanation is still debated^{10,12}.

By peeling pressure-sensitive adhesive tape one realizes an everyday example of tribocharging and triboluminescence¹: the emission of visible light. Tape provides a particularly interesting example of these phenomena because it has been claimed that the fundamental energy that holds tape to a surface is provided by the van der Waals interaction¹³. This energy—the weakest in chemistry—is almost 100-fold smaller than the energy required for generating a visible photon, yet, as demonstrated in 1939 (ref. 3), light emission from peeling tape can be seen with the unaided eye. That even more energetic processes were at play had already been suggested in 1930 (ref. 14); it was observed that when mica is split under vacuum “the glass of the vessel fluoresces like an X-ray bulb”. This insight led to the discovery in 1953 (ref. 2) that peeling tape is a source of X-rays. The simultaneous emission of visible and X-ray photons from peeling tape is shown in Fig. 1a, in which the blue glow is due to a scintillator responsive to X-ray energies and the red patch near the peel point is neon-enhanced triboluminescence³. Figure 1b shows that when the vacuum pressure is 10^{-3} torr the high-energy emission is so strong that the photo is illuminated entirely with scintillations.

Motivated by these photos, we interpret triboluminescence¹, a phenomenon known for centuries, as being part of an energy-density-focusing process that can extend four orders of magnitude beyond visible light to X-ray photons. To learn about the processes occurring

in peeling tape, we employed efficient high-speed X-ray detection equipment. Our measurements indicated that the scintillations in

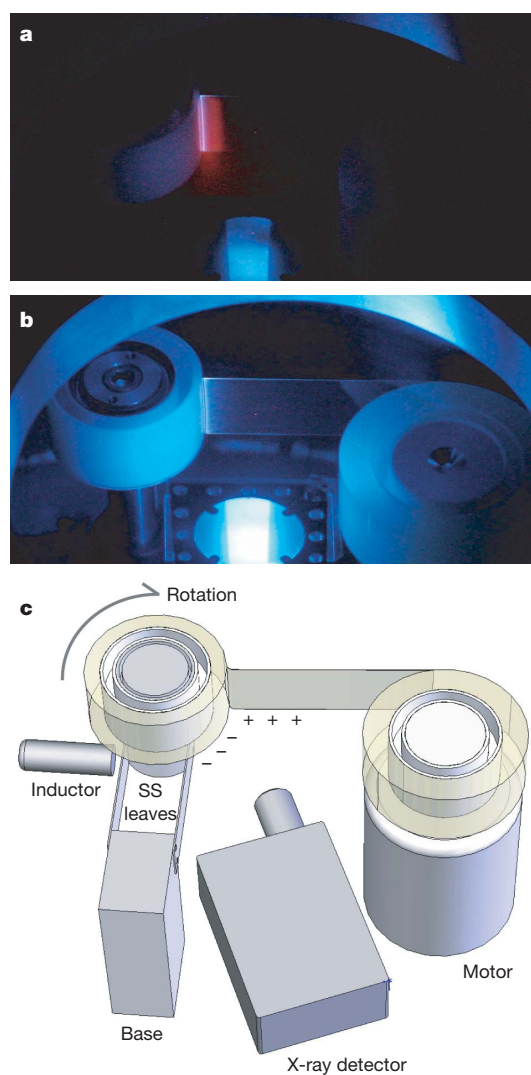


Figure 1 | Apparatus for studying high-energy emission from peeling tape. **a**, Photograph of the simultaneous emission of triboluminescence (red line) and scintillations of a phosphor screen sensitive to electron impacts with energies in excess of 500 eV (under neon at a pressure of 150 mtorr). **b**, Photograph of the apparatus (under a pressure of 10^{-3} torr) illuminated entirely by scintillations. **c**, Diagram of the apparatus used to measure peeling force; SS, spring steel (Methods).

¹Department of Physics and Astronomy, University of California, Los Angeles, Los Angeles, California 90095, USA.

*These authors contributed equally to this work.

Fig. 1b contain nanosecond X-ray pulses whose emission is correlated with radiofrequency (r.f.) pulses and slips in the force required to peel the pressure-sensitive adhesive tape. Furthermore, the short duration of these X-ray pulses indicated that the emission originates from a submillimetre region near the vertex of peeling, with a transient charge density ($\sim 10^{12}$ electrons cm^{-2}); that is, more than an order of magnitude greater than is measured in typical tribocharging systems.

The correlation between X-ray emission and peeling force in a 10^{-3} torr vacuum is displayed in Fig. 2a. As the force (black trace) increases above its value under an applied pressure of 1 atm (ref. 15) (dashed green trace), emissions with X-ray energies are recorded (blue trace). No X-ray emission has been observed at 1 atm. The slips are also correlated with a signal detected by an r.f. antenna¹⁶ (red trace). Figure 2b shows subnanosecond-resolved data used to correlate r.f. emission from peeling tape with liquid-scintillator signals (blue trace). The solid red and dashed red traces are the response of the antenna to signals generated, respectively, by peeling tape and by the relative motion of mercury and glass, in which r.f. discharges due to tribocharging are known to occur¹⁶.

The data in Fig. 2a were acquired with tantalum foil shielding the window of a solid-state X-ray detector. This attenuates X-rays with energies below about 20 keV in favour of larger events synchronized to the slips. The spectrum¹⁷ of all X-ray photons emitted from the peeling tape as recorded by an unshielded solid-state detector is shown in Fig. 3 and in Supplementary Fig. 1. To minimize the pile-up of photons the detector was placed 69 cm from the peeling vertex of the tape, so the plotted data have a solid angle correction of 120,000 relative to the raw data (see Methods). The total energy in the bursts that accompany the slips was obtained from events that

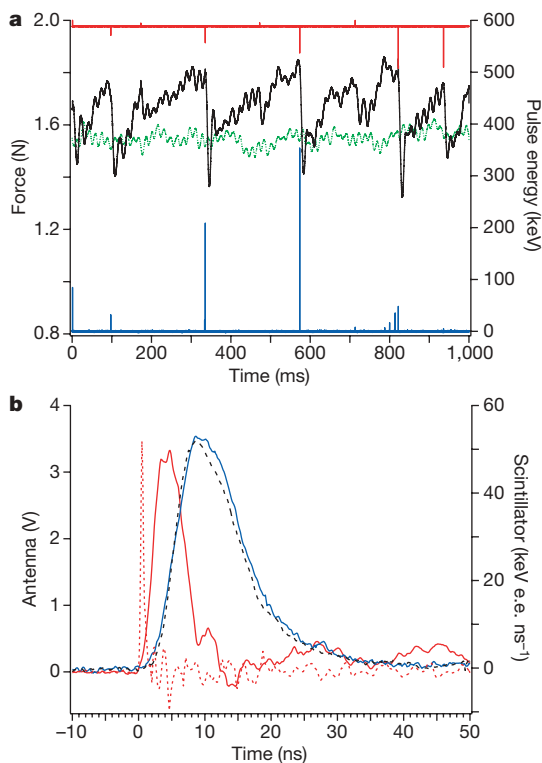


Figure 2 | Correlation between X-rays, force and radio frequency. **a**, The left axis shows the force for peeling tape at 3 cm s^{-1} in a 10^{-3} torr vacuum (black line) and at 1 atm (dashed green line). The right axis shows the X-ray signal (blue trace) from an Amptek detector with tantalum foil shield. The red upper trace is the r.f. antenna signal. **b**, Correlation of liquid scintillator (blue line) with radio frequency (red line) from peeling tape. The rise time of the scintillator is about 5 ns for the tape signal (blue line) and cosmic-ray calibration (dashed blue line). The dashed red line is an antenna calibration signal (Methods); keV e.e. ns^{-1} is the electron equivalent energy per

were three-way coincident between a solid-state detector, the liquid scintillator and the characteristic r.f. pulse (Fig. 2b). The inset to Fig. 3 shows the spectrum of X-ray burst energies that accompany slip events out to 10 GeV. These pulses occur at a rate in excess of 1 Hz and their time traces fall within the 5-ns resolution of the liquid-scintillator detectors. The spectrum did not change significantly during ten rewindings of a given roll of tape.

According to studies of controlled vacuum discharges¹⁸, the rise time of the current is the width of the X-ray flash. From the red trace in Fig. 2b this implies that the width of the coincident X-ray pulses is $\sim 1\text{--}2$ ns. Thus a typical 2-ns burst with an energy of 2 GeV has a peak power of more than 100 mW. These bursts, which occur more than once per second, contain more than 50% of the total energy radiated as X-ray photons above 10 keV. This includes X-ray photons synchronized to slip events as well as ‘precursor’ X-rays emitted between slips. According to Fig. 3 the total emission is $1.2 \times 10^{10} \text{ eV s}^{-1}$ or 2 nW average X-ray power.

On the basis of the long-standing phenomenology of tribocharging^{8,12}, we propose the following sequence of events: as the tape peels, the sticky acrylic adhesive becomes positively charged and the polyethylene roll becomes negatively charged, so that electric fields build up to values that trigger discharges. At a reduced pressure, the discharges accelerate electrons to energies that generate Bremsstrahlung X-rays when they strike the positive side of the tape. To determine the current of high-energy electrons that drive this process we compared Fig. 3 with published scattering data¹⁹. A strand of adhesive tape is thick in comparison with an electron absorption length (the Kramers limit¹⁹) but not so thick as to absorb all the X-rays. Given that the difference is not significant¹⁹, here we take the thick target limit. The peak near 15 keV with 3×10^5 X-rays per second is therefore due to electrons with energies of about 30 keV, which then create an integrated Bremsstrahlung X-ray spectrum with an efficiency of 10^{-4} . Only 5% of these X-rays are above 15 keV. These factors imply a discharge current of 6×10^{10} electrons per second, which corresponds to an average electric power of 0.2 mW; this is five orders of magnitude higher than the integrated X-ray spectra displayed in Fig. 3. As the 2-cm-wide tape peels at 3 cm s^{-1} , the average density of charge separated and discharged is 10^{10} electrons cm^{-2} , which is consistent with known tribocharging processes¹².

The X-ray bursts require charge densities that are substantially larger than those that characterize the average tribocharging discussed above. For a Townsend discharge⁶, the bottleneck is the time it takes an ion to cross a gap of length l times the number of round trips (about ten) needed to build up an avalanche. For a hydrogen ion

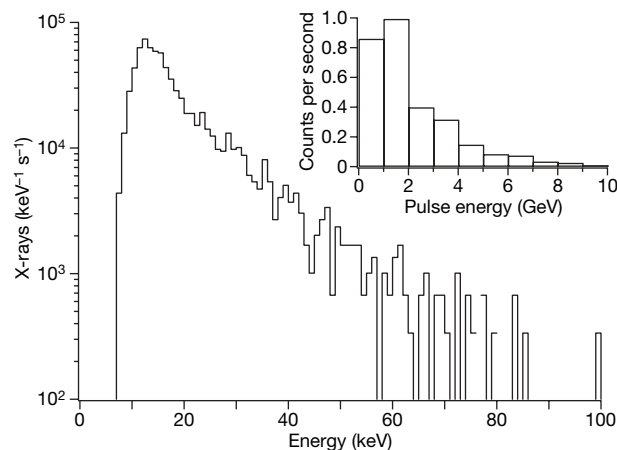


Figure 3 | Spectrum of X-ray energies from peeling one roll of tape. The peel speed was between 3 and 3.6 cm s^{-1} at 10^{-3} torr of air. Data were acquired with the Amptek CdTe detector. Inset: energies for nanosecond pulses out to 10 GeV for the same run taken with the Amptek 3-Stack detector (Methods).

moving with a velocity $v = \sqrt{(2eV/m)}$ in a potential $V = 30$ kV, a pulse width $\Delta t = 10/v$ of ~ 1 ns implies a characteristic length l of ~ 300 μm , which in turn implies an accelerating field $E \sim V/l$ of $\sim 10^6$ V cm^{-1} and a charge density $\sigma \approx \epsilon_0 E$ of 7×10^{11} electrons cm^{-2} (ref. 20). According to an alternative theory, the discharge consists of an explosive plasma emission⁵. The characteristic time for the current to flow is determined by the time it takes the plasma moving at 2×10^6 cm s^{-1} to expand across the gap^{5,18}. It has been established experimentally that the duration of the pulse increases linearly with the gap size with proportionality factor of 5 ns/100 μm (refs 5, 18). This implies a gap l of the order of tens of micrometres, and the corresponding field of 10^7 V cm^{-1} requires a charge density of 7×10^{12} electrons cm^{-2} . An image of the X-ray emission region could distinguish between the various theories.

When the tape is peeled, part of the energy supplied is converted to elastic deformation of the tape²¹, cavitation²² and filamentation²³ of the adhesive, acoustic emission²⁴, visible light^{3,25} and high-energy electron emission². According to Fig. 2 the power required to peel the tape at a speed of 3 cm s^{-1} is 50 mW under ambient conditions of 1 atm. Under vacuum, an additional power of 3 mW must be supplied to overcome the observed stick-slip friction. Of this 3 mW at least 0.2 mW goes into accelerating electrons to 30 keV so as to generate an average X-ray power of 2 nW. The power going into visible triboluminescence is 10 nW, as shown by the spectrum (Fig. 4).

Although tribocharging has substantial technological applications¹², its physical origin is still in dispute. In one view, tribocharging of insulators involves the statistical mechanical transfer of mobile ions between surfaces as they are separated adiabatically⁸. A competing theory⁹ proposes that a charged double layer is formed by electron transfer across the interface of dissimilar surfaces in contact. When these surfaces are suddenly pulled apart, the net charge of each layer is exposed. We have observed two timescales in dynamic tribocharging. One is the long timescale over which average charge densities of about 10^{10} electrons cm^{-2} are maintained on the tape. In addition, there exists a process that concentrates charge on a transient timescale of the order of 1 ns to reach densities that are about 100-fold larger than the average value. The physical process whereby such a large concentration of charge is attained involves the surface conductivity of the tape. This conductivity could be provided by mobile ions¹² or perhaps by means of precursor discharges stirring up the surface of the peeling tape. We propose that X-ray emission should yield insight into this and other fundamental aspects of tribology.

The intensity of emission is sufficiently strong (see Supplementary Fig. 2) to make peeling tape useful as a source for X-ray photography.

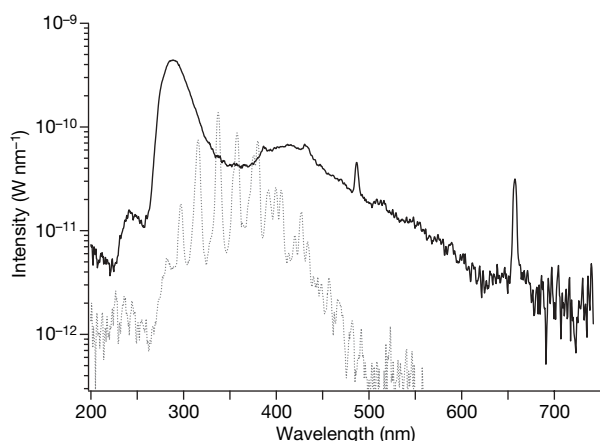


Figure 4 | Light spectra from peeling tape. The black trace was taken at 10^{-4} torr of air, and the grey dashed trace was taken at 1 atm. The nitrogen lines, which are prominent in air at 1 atm, are indicative of a gas discharge, which is typical of other processes such as fractoluminescence²⁷ and lightning. At low pressure the nitrogen lines are overshadowed by a process that leads to broadband emission with hydrogen lines.

Examples of X-ray photos are provided in Supplementary Fig. 3 and Supplementary Fig. 4. The correlation displayed in Fig. 2 has a resemblance to the geophysical effect called earthquake lights²⁶, in which the liberation of stress-induced charge during earthquakes generates electromagnetic radiation. The macroscopic physical processes that spontaneously organize an off-equilibrium throughput of low-energy density into X-ray emission suggest that it will be worth while to look for this phenomenon in systems that show fractoluminescence²⁷, stick-slip friction^{16,28}, triboluminescence¹ and gecko adhesion²⁹. The charge density realized in these experiments is about the same as the effective charge that accumulates on the surface of pyroelectric crystals used to generate table-top nuclear fusion³⁰.

METHODS SUMMARY

All experiments were performed with off-the-shelf rolls of Photo Safe 3M Scotch Tape (19 mm \times 25.4 m) that were secured to a precision ball-bearing mounted on a stage supported by two very stiff steel spring leaves (with spring constant $6.6 \times 10^3 \pm 3 \times 10^2$ N m^{-1} ; Fig. 1c). The displacement of the leaves from their equilibrium position was measured with a commercial inductor position detector (Baumer Electric) with a resolution of 505 nm V^{-1} . A free portion of the tape was stuck to a cylinder connected to a rotating motor, and the whole setup was placed in a vacuum chamber. All X-ray data were acquired at a pressure of $\sim 10^{-3}$ torr and at a peel speed of $\sim 3 \text{ cm s}^{-1}$. X-ray energy emissions were recorded with Amptek (XR-100T 3-stack and XR-100 CdTe) X-ray detectors and with Bicon 501A liquid scintillators 12.7 cm in diameter and 12.7 cm long, coupled to Hamamatsu 12.7-cm photomultiplier tubes (R1250)³⁰. Radiofrequency signals were recorded with antennas made of the exposed inside conductor of BNC cables placed within millimetres of the peeling point. All data were digitized and saved to disk for offline analysis as detailed in the Methods section. The spectrum of visible photons (Fig. 4) was taken with a grating spectrometer (300i; Acton Research) coupled to an intensified camera (Princeton Instruments) and is corrected for the response function of the instrument.

Full Methods and any associated references are available in the online version of the paper at www.nature.com/nature.

Received 30 December 2007; accepted 27 August 2008.

- Walton, A. J. Triboluminescence. *Adv. Phys.* **26**, 887–948 (1977).
- Karasev, V. V., Krotova, N. A. & Deryagin, B. V. Study of electronic emission during the stripping of a layer of high polymer from glass in a vacuum. [in Russian] *Dokl. Akad. Nauk. SSR* **88**, 777–780 (1953).
- Harvey, N. E. The luminescence of adhesive tape. *Science* **89**, 460–461 (1939).
- Zhenyi, M., Fan, J. & Dickinson, J. T. Properties of the photon emission accompanying the peeling of a pressure-sensitive adhesive. *J. Adhesion* **25**, 63–77 (1988).
- Mesyats, G. A. Ectons and their role in plasma processes. *Plasma Phys. Contr. Fusion* **47**, A109–A151 (2005).
- Raizer, Y. *Gas Discharge Physics* (Springer, 1991).
- Putterman, S. J. & Weninger, K. R. Sonoluminescence: how bubbles turn sound into light. *Annu. Rev. Fluid Mech.* **32**, 445–476 (2000).
- Harper, W. R. *Contact and Frictional Electrification* (Laplacian Press, 1998).
- Deryagin, B. V., Krotova, N. A. & Smilga, V. P. *Adhesion of Solids* (Consultants Bureau, 1978).
- Black, R. A. Hallett, J. The mystery of cloud electrification. *Am. Sci.* **86**, 526–534 (1998).
- Dwyer, J. R. et al. Energetic radiation produced during rocket-triggered lightning. *Science* **299**, 694–697 (2003).
- McCarty, L. & Whitesides, G. M. Electrostatic charging due to separation of ions at interfaces: contact electrification of ionic electrets. *Angew. Chem. Int. Ed.* **47**, 2188–2207 (2008).
- Gay, C. & Leibler, L. Theory of tackiness. *Phys. Rev. Lett.* **82**, 936–939 (1999).
- Obreimoff, J. W. The splitting strength of mica. *Proc. R. Soc. A* **127**, 290–297 (1930).
- Zosel, A. Adhesive failure and deformation behavior of polymers. *J. Adhesion* **30**, 135–149 (1989).
- Budakian, R., Weninger, K., Hiller, R. A. & Putterman, S. J. Picosecond discharges and stick-slip friction at a moving meniscus of mercury on glass. *Nature* **391**, 266–268 (1997).
- Klyuev, V. A., Toporov, Yu P., Aliev, A. D., Chalykh, A. E. & Lipson, A. G. The effect of air pressure on the parameters of x-ray emission accompanying adhesive and cohesive breaking of solids. *Sov. Phys. Tech. Phys.* **34**, 361–364 (1989).
- Baksht, R. B., Vavilov, S. P. & Urbayev, M. N. Duration of the x-ray emission arising in a vacuum discharge. *Izv. Ucheb. Zaved. Fiz.* **2**, 140–141 (1973).
- Chervenak, J. G. & Liuzzi, A. Experimental thick target Bremsstrahlung spectra from electrons in the range 10–30 keV. *Phys. Rev. A* **12**, 26–33 (1975).
- Graf von Harrach, H. & Chapman, B. N. Charge effects in thin film adhesion. *Thin Solid Films* **12**, 157–161 (1972).

21. Kendall, K. Thin-film peeling—the elastic term. *J. Phys. D* **8**, 1449–1453 (1975).
22. Chikina, I. & Gay, C. Cavitation in adhesives. *Phys. Rev. Lett.* **85**, 4546–4549 (2000).
23. Urahama, Y. Effect of peel load on stringiness phenomena and peel speed of pressure-sensitive adhesive tape. *J. Adhesion* **31**, 47–58 (1989).
24. De, R. & Ananthakrishna, G. Dynamics of the peel front and the nature of acoustic emission during peeling of an adhesive tape. *Phys. Rev. Lett.* **97**, 165503–165506 (2006).
25. Miura, T., Chini, M. & Bennewitz, R. Forces, charges, and light emission during the rupture of adhesive contacts. *J. Appl. Phys.* **102**, 103509 (2007).
26. Freund, F. & Sornette, D. Electro-magnetic earthquake bursts and critical rupture of peroxy bond networks in rocks. *Tectonophysics* **431**, 33–47 (2007).
27. Eddingsaas, N. C. & Suslick, K. S. Light from sonication of crystal slurries. *Nature* **444**, 163 (2006).
28. Dickinson, J. T. *et al.* Dynamical tribological probes: particle emission and transient electrical measurements. *Tribology Lett.* **3**, 53–67 (1997).
29. Autumn, K. *et al.* Adhesive force of a single gecko foot-hair. *Nature* **405**, 681–685 (2000).
30. Naranjo, B., Gimzewski, J. K. & Putterman, S. Observation of nuclear fusion driven by a pyroelectric crystal. *Nature* **434**, 1115–1117 (2005).

Supplementary Information is linked to the online version of the paper at www.nature.com/nature.

Acknowledgements We thank R. Lofstedt for bringing to our attention the importance of ref. 14; C. Regan for advice; B. Naranjo for many insights and for use of his uniquely designed liquid scintillator detection system; B. Kappus and S. Khalid for experimental assistance; J. Cambier for valuable discussions, E. Adams for archival assistance; and A. Bass for an independent translation of ref. 2. We thank Hamamatsu Corporation for lending us X-ray cameras. Various stages of this research were supported by the Office of Naval Research and the Defense Advanced Research Projects Agency (Microsystems Technologies Office and Defense Sciences Office). J.E. thanks the Fulbright–Garcia Robles Scholarship Program and UC-MEXUS-CONACYT for support.

Author Contributions J.H. was instrumental in motivating this research. J.E. pinned down the correlation between the force and X-ray emission. C.C. obtained the GeV pulses, and S.P. is the principal investigator.

Author Information Reprints and permissions information is available at www.nature.com/reprints. Correspondence and requests for materials should be addressed to C.C. (camara@physics.ucla.edu) or J.E. (escobar@physics.ucla.edu).

METHODS

Figure 1a and Fig. 1b are 15-s exposures on a Canon EOS 10D camera. The electron scintillator visible in the forefront of these images is a Kimball Physics C5X5-R1000. The data shown in Fig. 2a were obtained with a National Instruments PXI-5122 14-bit digitizer at ten points μs^{-1} . The ~ 80 -Hz oscillations on the force measurement correspond to the resonance frequency of the loaded spring. We note that although our data clearly show stick-slip motion, our peel speed of 3 cm s^{-1} is much lower than that referred to in the literature as the stick-slip regime for peeling pressure-sensitive adhesive tape³¹. The r.f. emission was recorded with a BNC chassis mount placed about 1 cm from the peel line terminated with $500\ \Omega$ (red upper trace) displayed in arbitrary units. For this figure the Amptek X-ray detector (XR-100T 3-stack) was placed about 5 cm from the peeling interface and its beryllium window was shielded with tantalum foil 25 mm thick, to prevent saturation. This detector has a background of about one count every 3 s from 5 to 400 keV (Supplementary Fig. 1), and pileup cannot be discriminated for events shorter than 600 ns. The possibility of pileup affecting spectral data also challenges efforts to resolve X-ray energy emission from lightning bolts in which similar energy scales are detected¹¹. The X-ray data in Fig. 2b were acquired with a Hamamatsu 5-inch photomultiplier (R1250) looking at Bicron 501A liquid scintillator (5 inches in diameter by 5 inches long)³⁰ and recorded with an Infinium oscilloscope at $8 \times 10^9\text{ samples s}^{-1}$ (1.5 GHz bandwidth). The units in the scintillator axis are kiloelectronvolt electron equivalent per nanosecond, and are with reference to the calibration performed with several Compton edges from different radioactive sources³⁰. The centre of the scintillator was placed 15 cm from the peeling tape outside the vacuum chamber looking through a 2-cm quartz window. In this figure the antenna is 5 mm of exposed inside wire of a BNC cable terminated with $50\ \Omega$. The relative timing of the signal has been corrected for the 54-ns transit time of the photomultiplier and the 3-ns length of the antenna. The characteristic rise time of the scintillator-photomultiplier arrangement can be determined by capturing a high-energy cosmic ray (dashed blue trace) and is seen to be about 5 ns, the same as for the X-ray pulse. The subnanosecond pulse (dashed red line) used to calibrate the antenna is generated by charge transfer between mercury and glass in relative

motion¹⁶. Further studies of the timescales for discharge^{18,32} could yield insight into the mechanisms involved.

The X-ray spectrum shown in Fig. 3 was obtained by unwinding an entire roll of tape at between 3 and 3.6 cm s^{-1} , which took about 700 s. The data were acquired with a solid-state X-ray detector (100-XR CdTe; Amptek), unshielded, placed outside the vacuum chamber at 69 cm from the peeling tape and looking through a $\frac{1}{4}$ -inch plastic window. This detector has an active area of 25 mm^2 , is 100% efficient from 10 to 50 keV, and has a background count rate of ~ 1 count per 100 s. The data were digitized with a National Instruments PXI-5122 board at a rate of 1 s every 1.9 s for a total of 364 s. The inset in Fig. 3 is the frequency of emission of nanosecond-long X-ray pulses as a function of the total pulse energy generated during the same unwinding. An X-ray pulse was deemed valid if a coincidence within 10 ns was recorded between the r.f. antenna and the liquid scintillator (501A; Bicron), and within $2\ \mu\text{s}$ of a signal on an unshielded solid-state detector (XR-100 3-stack; Amptek) with more than 10 keV. All the Amptek coincidences are, however, found within a 400-ns window, which we believe is the limit of the internal electronics of the device. The antenna was 5 mm of exposed inside conductor of a standard BNC cable terminated with $50\ \Omega$, placed 5 mm from the peel line. The X-ray detectors were placed outside the chamber looking through a $\frac{1}{4}$ -inch plastic window, the 3-stack solid-state detector at 40 cm from the tape and the scintillator at 76 cm. Coincidence data were digitized at $10^9\text{ samples s}^{-1}$ with an Acqiris DC270 board³⁰ triggered on the antenna signal. The dead time of these acquisitions was less than 20 s for the 700-s run, and the background coincidences were found to be 0 for a 1,000-s wait.

The visible spectrum at 1 atm in Fig. 4 shows lines that are indicative of gas discharge, also observed in fractoluminescence²⁷ and lighting³³. At low pressure the nitrogen lines are overshadowed by a process that leads to broadband emission with hydrogen lines.

31. Cortet, P. P., Ciccotti, M. & Vanel, L. Imaging the stick-slip peeling of an adhesive tape under a constant load. *J. Statist. Mech.* **3**, P03005 (2007).
32. Mesyats, G. A. Nanosecond x-ray pulses. *Sov. Phys. Tech. Phys.* **19**, 948–951 (1975).
33. Orville, R. E. & Henderson, R. W. Absolute spectral measurements of lightning from 375 to 880 nm. *J. Atmos. Sci.* **41**, 3180–3187 (1984).

Evidence for a terminal Pt(IV)-oxo complex exhibiting diverse reactivity

Elena Poverenov¹, Irena Efremenko¹, Anatoly I. Frenkel³, Yehoshua Ben-David¹, Linda J. W. Shimon², Gregory Leitus², Leonid Konstantinovski², Jan M. L. Martin¹ & David Milstein¹

Terminal oxo complexes of transition metals have critical roles in various biological and chemical processes^{1,2}. For example, the catalytic oxidation of organic molecules^{3,4}, some oxidative enzymatic transformations^{5–7}, and the activation of dioxygen on metal surfaces⁸ are all thought to involve oxo complexes. Moreover, they are believed to be key intermediates in the photocatalytic oxidation of water to give molecular oxygen, a topic of intensive global research aimed at artificial photosynthesis and water splitting^{9–13}. The terminal oxo ligand is a strong π -electron donor, so it readily forms stable complexes with high-valent early transition metals. As the d orbitals are filled up with valence electrons, the terminal oxo ligand becomes destabilized². Here we present evidence for a d^n ($n > 5$) terminal oxo complex that is not stabilized by an electron withdrawing ligand framework. This d^6 Pt(IV) complex exhibits reactivity as an inter- and intramolecular oxygen donor and as an electrophile. In addition, it undergoes a water activation process leading to a terminal dihydroxo complex, which may be relevant to the mechanism of catalytic reactions such as water oxidation.

To date, the very few terminal oxo complexes having more than five valence d electrons are all stabilized by powerful electron accepting ligands: namely $\text{NaRe}^{(I)}(\text{O})(\text{PhCCPh})_2$, in which extensive back bonding to the alkyne ligands was noted¹⁴, and complexes stabilized by the encapsulating, highly effective π -accepting polytungstate ligand, including $\text{Pt}^{(IV)}$ (ref. 15), $\text{Pd}^{(IV)}$ (ref. 16) and Au (ref. 17). A d^5 Fe(III) oxo complex stabilized by a protective hydrogen bond cavity has been reported¹⁸. Isolation of a terminal d^6 metal-oxo complex not bearing strong electron withdrawing groups is desirable, as it may provide insight into the reactivity potential of the metal-oxo bond, in addition to information regarding spectroscopic and structural aspects. Particularly desirable are terminal oxo complexes of platinum, as this metal and its compounds are widely used by industry

in oxygen-based technologies. Towards this goal, we have used a pincer complex of platinum.

Pincer complexes, involving a meridional, tridentate ligand framework, are of considerable current interest, owing to the structural versatility of such systems, leading to a variety of bond activation and catalytic processes¹⁹. Reaction of the cationic pincer PCN Pt complex **1a** ($\text{PCN} = \text{C}_6\text{H}_3[\text{CH}_2\text{P}(\text{t-Bu})_2](\text{CH}_2)_2\text{N}(\text{CH}_3)_2$; ref. 20) with a freshly prepared acetone solution of dioxirane²¹ resulted in immediate formation of a new complex, formulated as the terminal oxo complex **2** (Fig. 1a). The $^3\text{1P}\{^1\text{H}\}$ NMR spectrum of **2** shows a singlet at 64.27 p.p.m. with Pt satellites (coupling constant $J_{\text{Pt-P}} = 2,686$ Hz) and the $^{195}\text{Pt}\{^1\text{H}\}$ NMR spectrum exhibits a signal at -645.88 p.p.m. (broad doublet, $J_{\text{P-Pt}} = 2,686$ Hz), definitely indicating a Pt(IV) oxidation state (for comparison, the chemical shift of the starting Pt(II) complex **1a** is $-4,015$ p.p.m.). (Here $\{^1\text{H}\}$ indicates proton-decoupled.) In the $^{13}\text{C}\{^1\text{H}\}$ NMR spectrum, the *ipso* carbon gives rise to a doublet at 147.25 p.p.m. ($J_{\text{P-C}} = 5$ Hz), and in the $^{19}\text{F}\{^1\text{H}\}$ NMR spectrum, the outer-sphere BF_4^- anion gives rise to a singlet at -149.87 p.p.m. The NMR data exclude the possibility of the corresponding (PCN)Pt(OH) complex, which has a completely different NMR pattern²⁰. Electrospray mass spectrometry analysis is in line with the structure of **2**, indicating two signals at mass/charge ratios m/z^+ 518.07 ($\text{M}+1$) and m/z^- 87.29 (BF_4^-). The infrared spectrum in acetone solution shows an absorption at 783 cm^{-1} , which is in the range expected for $\text{Pt}=\text{O}$ vibration (Supplementary Fig. 4)²².

To exclude a dimeric $[(\text{PCN})\text{Pt}(\mu\text{-O})]_2$ structure, PGSE (pulsed gradient spin echo) NMR studies were performed in acetone- d_6 . Diffusion coefficients (D) and hydrodynamic radius (r) of complex **2** and, for comparison, complex **3** (see below) were determined, giving $D = 1.078 \times 10^{-9}\text{ m}^2\text{ s}^{-1}$, $r = 6.1\text{ \AA}$ for **2**, and $D = 1.186 \times 10^{-9}\text{ m}^2\text{ s}^{-1}$, $r = 5.6\text{ \AA}$ for **3**. Both the absolute D and r values of

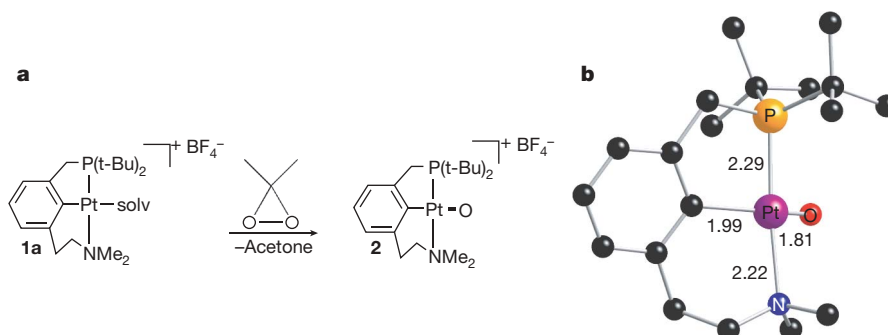


Figure 1 | Preparation and DFT structure of complex 2. **a**, Preparation of complex **2** by reaction of the Pt(II) complex **1a** with dioxirane. **b**, DFT

structure of complex **2** optimized at the PBE0/pc1 level of theory (hydrogen atoms are omitted for clarity).

¹Department of Organic Chemistry, ²Unit of Chemical Research Support, The Weizmann Institute of Science, Rehovot 76100, Israel. ³Department of Physics, Yeshiva University, New York, New York 10016, USA.

complex **2** and their good similarity to that of the unambiguously monomeric **3** clearly indicate the monomeric structure of **2** (ref. 23), as also strongly indicated by density functional theory (DFT) calculations, which show that it is impossible to obtain a Pt(IV) μ -oxo dimer, or a μ -hydroxo-dimer, starting from complex **2** because of severe steric constraints. The radius obtained by rotating the DFT structure of **2** (see below) about its geometric centre is 6.06 Å, in correlation with the experimental hydrodynamic radius. The diverse reactivity of complex **2** is commensurate with its monomeric structure (see later).

DFT studies performed on complex **2** show that the reaction **1a** \rightarrow **2** is thermodynamically favourable ($\Delta G_{298}^0 = -11.1$ kcal mol $^{-1}$ in acetone solution). According to the calculations, the optimized structure of **2** adopts a distorted square planar geometry with the oxygen atom being 35.3° out of the C–Pt–P plane (Fig. 1b). The calculated Pt–O bond length (1.811 Å) is unambiguously shorter than typical Pt(IV)–OH single bonds, which are in the range 1.943–2.079 Å (based on the Cambridge Structural Database), but it is longer than that reported¹⁵ for $K_7Na_2[O=Pt(H_2O)(PW_9O_{34})_2]$, 1.720 Å. Analysis of the covalent part of the Pt–O bonding in complex **2** shows that the low stability of electron-rich terminal oxo complexes can be attributed to occupation of strongly antibonding Pt–O π^* molecular orbitals. The non-planar geometry of the complex decreases the overlap between metal-ligand orbitals, reducing this unfavourable occupation. The phenyl group serves as an electron donor, and no backdonation to it takes place because of the high energy of the vacant phenyl orbitals (Supplementary Fig. 2 presents a simplified molecular orbital diagram), as supported also by a comparison of natural bond orbital charges in **2** and **1** (Supplementary Fig. 3). According to the DFT calculation, acetone coordination is unfavourable (see Supplementary Information).

The local atomic environment and charge state of Pt in complex **2** were investigated by two methods of X-ray absorption spectroscopy, namely, extended X-ray absorption fine structure (EXAFS) and X-ray absorption near edge structure (XANES).

XANES data (Fig. 2a) of **2** and other compounds used for calibration (complexes **1a** (solv = H₂O), **1c** and **4** (Fig. 3) as well as Pt foil) confirmed the nominal charge states of Pt in all the complexes. The observed differences in the d -hole density which is proportional to the absorption peak area are consistent with the difference in the formal valences of Pt in complexes **2** and **4** (4+), **1a** and **1c** (2+) and Pt foil (0).

Analysis of EXAFS data in the four complexes was performed consistently by imposing constraints dictated by our X-ray diffraction and DFT analyses: for example, we assumed that the lengths of Pt–P, Pt–N, Pt–C, Pt=O, Pt–OH and Pt–OH₂ bonds are unique and do not significantly depend on a particular complex. By using such a ‘fingerprinting’ approach, we obtained partial contributions χ_{Pt-OH_2}

and $\chi_{Pt=O}$ to EXAFS data of these complexes. These three types of platinum–oxygen bond were found to have very different strengths: Pt=O is the stiffest, Pt–OH₂ the weakest and Pt–OH the intermediate in strength between the two former bonds, as intuitively expected (Fig. 2b). Our results demonstrate that the Pt=O peak maximum is shifted to the left relative to the Pt–OH peak maximum (Fig. 2b, inset) by approximately 0.1 Å, in agreement with our DFT calculations described above, which indicate that the Pt=O in **2** differs from the Pt–OH in complex **4** (see below) by 0.14 Å (at the PBE/sdd level). FEFF6 calculations of the theoretical EXAFS signal for the DFT model of complex **2** are in qualitative agreement with the DFT calculations.

Complex **2**, which has no significant electron accepting framework that can stabilize the terminal oxo ligand, exhibits diverse reactivity (Fig. 3). Initially, we explored its oxygen transfer reactivity. Reaction of **2** with PPh₃ at room temperature resulted in quantitative formation of OPPh₃ with parallel quantitative formation of complex **1a**. Oxygen transfer activity was also observed upon reaction with CO. When **2** was treated with 4 equivalents of CO gas, it was quantitatively transformed into the cationic carbonyl complex **1b** with concomitant formation of CO₂ (83% yield) as determined by gas chromatography. Complex **2** also reacts with hydrogen. Stirring **2** under 5 atm of H₂ led to deoxygenation, forming complex **1a** in 52% yield, with complex **3** (see later) being a competitive product. Mechanistic studies of H₂ oxidation by MnO₄[−] and RuO₄ have been reported²⁴.

Complex **2** can also be attacked by nucleophiles. Addition of KH to a THF solution of **2** resulted in formation of the reported²⁰ Pt(II) hydroxo complex **1c**, probably by hydride attack at the metal centre, followed by its migration to the oxo ligand (Fig. 3). Complex **1c** constitutes 78% of the organometallic products (see Supplementary Information).

Complex **2** is only moderately thermally stable. After 7–10 h at room temperature, in the absence of an external oxygen acceptor, it undergoes intramolecular oxygen transfer, resulting in insertion of the oxo ligand into the Pt–P bond to give the new complex **3** (Fig. 3). Complex **3** was fully characterized by multinuclear NMR spectroscopy. The ³¹P{¹H} NMR spectrum of **3** exhibits a singlet at 76.57 p.p.m. with a very small Pt–P coupling constant (40 Hz) due to oxygen incorporation. The ¹⁹⁵Pt NMR spectrum exhibits a singlet at −2,842.87 p.p.m. Colourless needles of **3** suitable for a single-crystal X-ray diffraction study were obtained from an acetone/pyridine solution by slow vapour diffusion of ether at room temperature (Fig. 4a). Complex **3** (solv = pyridine) exhibits a slightly distorted square planar structure. The oxygen atom is bound to the Pt and P atoms, and the Pt–O length (2.031 Å) indicates a single-bond character, while the P–O bond length of 1.529 Å is short enough to be considered a double bond (based on the Cambridge Structural Database). Results of DFT calculations on the structure of complex **3** are in good agreement with the X-ray data. The geometries of

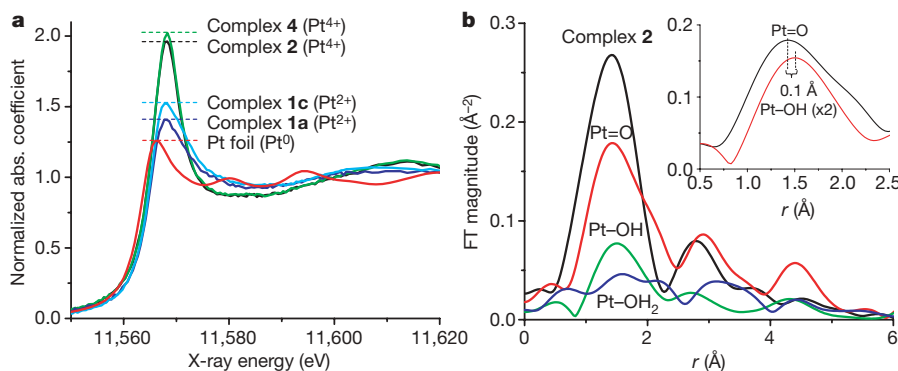


Figure 2 | XANES spectra of complexes and Fourier transform magnitudes of EXAFS data. **a**, XANES spectra for complex **2** and reference complexes **1a** (solv = H₂O), **1c**, **2** and **4**. **b**, Fourier transform (FT) magnitudes, uncorrected for photoelectron phase shifts, of k -weighted EXAFS data for

complex **2** and individual contributions Pt=O, Pt–OH and Pt–OH₂. Inset, the ~0.1 Å shift to lower distances of the Pt=O peak relative to Pt–OH (the latter peak is scaled up by a factor of 2 for clarity).

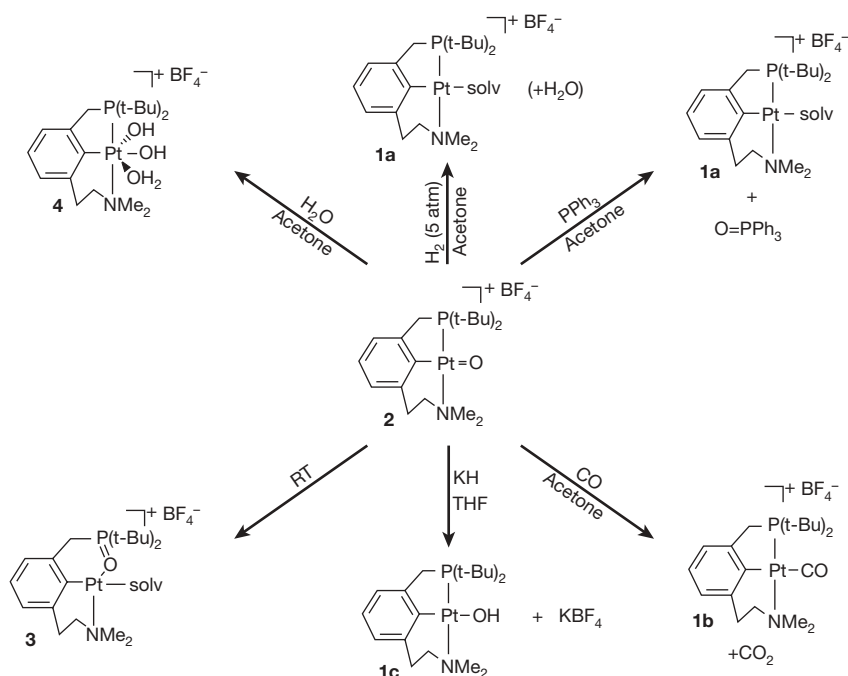


Figure 3 | Reactivity of complex 2. Oxygen transfer to H_2 and to PPh_3 with reduction to the Pt(II) complex **1a**; oxygen transfer to CO forming complex **1b** and CO_2 ; intramolecular oxo transfer to form complex **3**; nucleophilic

attack by a hydride, generating the Pt(II) hydroxo complex **1c**; and water activation to form the dihydroxo Pt(IV) complex **4**.

complexes **2**, **3** and **4** were optimized at the same level of theory. The observed good correlation between theoretical and X-ray single-crystal data for **3** and **4** (Supplementary Tables 2 and 3) lends credence to the calculated geometry of complex **2**.

Terminal oxo intermediates are implicated as key intermediates in the artificial catalytic water oxidation to O_2 , the mechanism of which is a subject of numerous theoretical and experimental studies^{25–28}, although the nature of the step leading to the generation of dioxygen is not clear^{9–13}. In this context, it is desirable to know how a late transition metal terminal oxo complex reacts with water. Interestingly, when excess water was added to **2**, the new dihydroxo Pt(IV) complex **4** was immediately formed (Fig. 3). Complex **4** was fully characterized by multinuclear NMR and mass spectroscopy (see Supplementary Information). Colourless crystals of **4** suitable for X-ray diffraction analysis were obtained from a CH_2Cl_2 solution at -30°C (Fig. 4b). Complex **4** has a classical octahedral structure, the Pt atom being coordinated to the PCN ligand and to three oxygen

atoms. The Pt–O bond lengths are 1.997(5), 2.017(5) and 2.171(5) Å for atoms O1, O2 and O3, respectively. Lacking the Pt=O functionality, and being significantly more stable than **2**, complex **4** does not exhibit oxygen transfer reactivity and remains unchanged for weeks upon addition of PPh_3 .

We are unaware of prior direct observations of water activation by a terminal oxo complex, and trapping of the product of such activation. It is noteworthy that oxidation of Pt(II) to Pt(IV) by O_2 in water to generate a Pt(IV) dihydroxo complex is proposed as a key step in a hypothetical catalytic cycle for alkane oxidation by O_2 to give alcohols^{29,30}. Our results suggest that such a process might involve O–H activation of water by a Pt(IV) oxo intermediate. DFT calculations show that in our system such activation is very favourable. Upon addition of two water molecules to the apical positions of the oxo complex **2**, geometry optimization gave the dihydroxo structure **4**. The calculated free energy change of this reaction is $\Delta G^\circ_{298} = -19.8$ (-20.6) kcal mol^{-1} in acetone (water) solution.

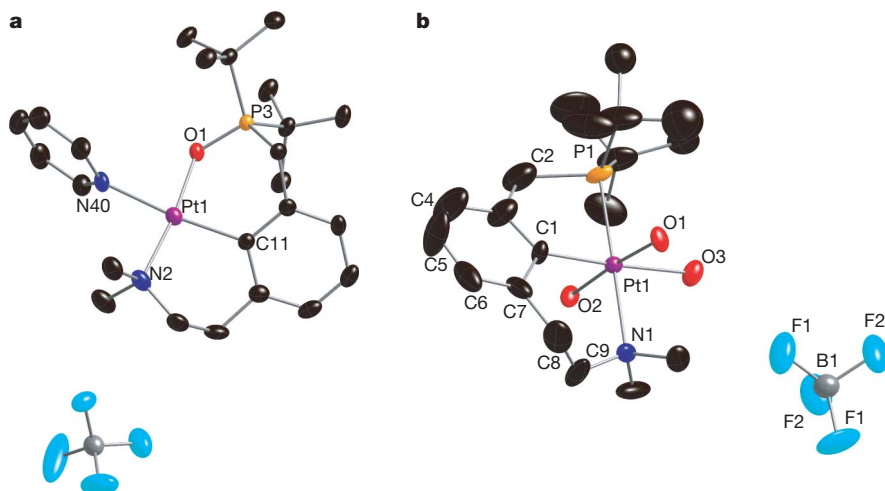


Figure 4 | ORTEP views of molecules of **3 and **4** with the thermal ellipsoids at 50% probability. a, **3**; b, **4**.** Hydrogen atoms were omitted for clarity (OH hydrogen atoms of complex **4** were not located).

Received 14 March; accepted 20 August 2008.

- Nugent, W. A. & Mayer, J. M. *Metal-Ligand Multiple Bonds* (Wiley, 1988).
- Holm, R. H. Metal-centered oxygen atom transfer reactions. *Chem. Rev.* **87**, 1401–1449 (1987).
- Sheldon, R. A. & Kochi, J. K. *Metal-Catalyzed Oxidations of Organic Compounds* (Academic, 1981).
- Meunier, B. (ed.) *Biomimetic Oxidations Catalyzed by Transition Metal Complexes* (Imperial College Press, 2000).
- Yoshizawa, K. Nonradical mechanism for methane hydroxylation by iron-oxo complexes. *Acc. Chem. Res.* **39**, 375–382 (2006).
- Rohde, J.-U. et al. Crystallographic and spectroscopic characterization of a nonheme Fe(IV)-O complex. *Science* **299**, 1037–1039 (2003).
- Green, M. T., Dawson, J. H. & Gray, H. B. Oxoiron(IV) in chloroperoxidase compound II is basic: Implications for P450 chemistry. *Science* **304**, 1653–1656 (2004).
- Somorjai, G. A. *Introduction to Surface Chemistry and Catalysis* (Wiley, 1994).
- Ruettinger, W. & Dismukes, G. C. Synthetic water-oxidation catalysts for artificial photosynthetic water oxidation. *Chem. Rev.* **97**, 1–24 (1997).
- Yagi, M. & Kaneko, M. Molecular catalysts for water oxidation. *Chem. Rev.* **101**, 21–35 (2001).
- Alstrum-Acevedo, J. H., Brennaman, M. K. & Meyer, T. J. Chemical approaches to artificial photosynthesis. 2. *Inorg. Chem.* **44**, 6802–6827 (2005).
- Dempsey, J. L. et al. Molecular chemistry of consequence to renewable energy. *Inorg. Chem.* **44**, 6879–6892 (2005).
- Lewis, N. S. & Nocera, D. G. Powering the planet: Chemical challenges in solar energy utilization. *Proc. Natl Acad. Sci. USA* **103**, 15729–15735 (2006).
- Spaltenstein, E., Conry, R. R., Critchlow, S. C. & Mayer, J. M. Low-valent rhenium-oxo complexes. 9. Synthesis, characterization, and reactivity of a formally rhenium(I) terminal oxo complex, $\text{NaRe}(\text{O})(\text{RC}\equiv\text{CR})_2$. *J. Am. Chem. Soc.* **111**, 8741–8742 (1989).
- Anderson, T. M. et al. Late-transition metal oxo complex: $\text{K}_7\text{Na}_9[\text{O}:\text{Pt}^{\text{IV}}(\text{H}_2\text{O})\text{L}_2]$, $\text{L} = [\text{PW}_9\text{O}_{34}]^{9-}$. *Science* **306**, 2074–2077 (2004).
- Anderson, T. M. et al. Palladium-oxo complex. Stabilization of this proposed catalytic intermediate by an encapsulating polytungstate ligand. *J. Am. Chem. Soc.* **127**, 11948–11949 (2005).
- Cao, R., Musaev, D. J., Morokuma, K., Takahashi, M. & Hill, C. L. Terminal gold-oxo complexes. *J. Am. Chem. Soc.* **129**, 11118–11133 (2007).
- MacBeth, C. E. et al. O_2 activation by nonheme iron complexes: A monomeric Fe(III)-oxo complex derived from O_2 . *Science* **289**, 938–941 (2000).
- Van der Boom, M. E. & Milstein, D. Cyclometalated phosphine-based pincer complexes: Mechanistic insight in catalysis, coordination, and bond activation. *Chem. Rev.* **103**, 1759–1792 (2003).
- Poverenov, E. et al. Pincer “hemilabile” effect. PCN platinum(II) complexes with different amine “arm length”. *Organometallics* **24**, 1082–1090 (2005).
- Murray, R. W. & Singh, M. Chemistry of dioxiranes. Reaction of dimethyldioxirane with alkynes. *J. Org. Chem.* **58**, 5076–5080 (1993).
- Sassenberg, U. & Scullman, R. The emission spectrum of PtO between 3800 Å and 8900 Å. *Phys. Scripta* **28**, 139–159 (1983).
- Schott, D., Pregosin, P. S., Albinati, A. & Rizatto, S. PGSE diffusion NMR studies on mononuclear and dinuclear cationic salts of (S)-MeO-Biphep and (R)-p-tolyl-BINAP. *Inorg. Chim. Acta* **360**, 3203–3212 (2007).
- Collman, J. P., Slaughter, L. M., Eberspacher, T. A., Strassner, T. & Brauman, J. I. Mechanism of dihydrogen cleavage by high-valent metal oxo compounds: Experimental and computational studies. *Inorg. Chem.* **40**, 6272–6280 (2001).
- Yang, X. & Baik, M.-H. *cis,cis*- $[(\text{bpy})_2\text{Ru}^{\text{V}}\text{O}]_2\text{O}^{4+}$ catalyzes water oxidation formally via in situ generation of radicaloid $\text{Ru}^{\text{IV}}\text{-O}^*$. *J. Am. Chem. Soc.* **128**, 7476–7485 (2006).
- Hurst, J. K. Water oxidation catalyzed by dimeric μ -oxo bridged ruthenium diimine complexes. *Coord. Chem. Rev.* **249**, 313–328 (2005).
- Elizarova, G. L., Zhidomirov, G. M. & Parmon, V. N. Hydroxides of transition metals as artificial catalysts for oxidation of water to dioxygen. *Catal. Today* **58**, 71–88 (2000).
- Binstead, R. A., Chronister, C. W., Ni, J., Hartshorn, C. M. & Meyer, T. J. Mechanism of water oxidation by the μ -oxo dimer $[(\text{bpy})_2(\text{H}_2\text{O})\text{Ru}^{\text{III}}\text{ORu}^{\text{III}}(\text{OH})_2(\text{bpy})_2]^{4+}$. *J. Am. Chem. Soc.* **122**, 8464–8473 (2000).
- Labinger, J. A. & Bercaw, J. E. Understanding and exploiting C–H bond activation. *Nature* **417**, 507–513 (2002).
- Rostovtsev, V. V., Labinger, J. A., Bercaw, J. E., Lasseter, T. L. & Goldberg, K. I. Oxidation of dimethylplatinum(II) complexes with dioxygen. *Organometallics* **17**, 4530–4531 (1998).

Supplementary Information is linked to the online version of the paper at www.nature.com/nature.

Acknowledgements This research was supported in part by the Israeli Science Foundation, by the German Federal Ministry of Education and Research (BMBF) under the framework of the German-Israeli Cooperation, by the Minerva Foundation, Munich, Germany, and by the Helen and Martin Kimmel Center for Molecular Design. A.I.F. acknowledges support from the US Department of Energy (DE-FG02-03ER15476). Beamline X18B is supported by the NSLS through the Divisions of Materials and Chemical Sciences of the US DOE, and the Synchrotron Catalysis Consortium through the US DOE (DE-FG02-05ER15688). We thank Q. Wang for help with the synchrotron measurements. D.M. holds the Israel Matz Professorial Chair.

Author Contributions E.P.: synthesis, characterization, reactivity studies of complexes and manuscript writing. I.E. and J.M.L.M.: DFT calculations and manuscript writing. A.I.F.: X-ray absorption spectroscopy studies. Y.B.-D.: synthesis of the PCN ligand and dioxirane. L.J.W.S. and G.L.: single-crystal X-ray diffraction analysis. L.K.: NMR studies. D.M.: design and direction of the project and manuscript writing.

Author Information Crystallographic data for complexes **3** and **4** have been deposited in the Cambridge Crystallographic Data Centre, under accession numbers 695884 and 695883, respectively. Reprints and permissions information is available at www.nature.com/reprints. Correspondence and requests for materials should be addressed to D.M. (david.milstein@weizmann.ac.il).

Fault-induced seismic anisotropy by hydration in subducting oceanic plates

Manuele Faccenda¹, Luigi Burlini², Taras V. Gerya¹ & David Mainprice³

The variation of elastic-wave velocities as a function of the direction of propagation through the Earth's interior is a widely documented phenomenon called seismic anisotropy. The geometry and amount of seismic anisotropy is generally estimated by measuring shear-wave splitting, which consists of determining the polarization direction of the fast shear-wave component and the time delay between the fast and slow, orthogonally polarized, waves. In subduction zones, the teleseismic fast shear-wave component is oriented generally parallel to the strike of the trench¹, although a few exceptions have been reported (Cascadia² and restricted areas of South America^{3,4}). The interpretation of shear-wave splitting above subduction zones has been controversial and none of the inferred models seems to be sufficiently complete to explain the entire range of anisotropic patterns registered worldwide¹. Here we show that the amount and the geometry of seismic anisotropies measured in the forearc regions of subduction zones strongly depend on the preferred orientation of hydrated faults in the subducting oceanic plate. The anisotropy originates from the crystallographic preferred orientation of highly anisotropic hydrous minerals (serpentine and talc) formed along steeply dipping faults and from the larger-scale vertical layering consisting of dry and hydrated crust–mantle sections whose spacing is several times smaller than teleseismic wavelengths. Fault orientations and estimated delay times are consistent with the observed shear-wave splitting patterns in most subduction zones.

Shear-wave splitting occurs when shear waves propagate in anisotropic elastic media. Strain-induced crystal preferred orientation (CPO) of anisotropic minerals is considered to be the main source of mantle anisotropy^{5,6}. CPO is produced locally in faults in the plastic part of the lithosphere or, more extensively, in the viscous upper mantle, where anisotropic olivine grains align by dislocation creep^{7,8}. Preferred orientation of faults, cracks, tabular intrusions and fine layering of two or more media with different elastic properties can produce an additional anisotropic mechanism (shape preferred orientation; SPO), provided that the spacing is smaller than the seismic wavelength to a sufficient degree^{9,10}.

Vertically travelling, long-period SKS waves, generated by the conversion of P waves at the core–mantle boundary, are often used to determine the anisotropy in subduction zones. Because the lower mantle is known to have no seismic anisotropy⁸, SKS anisotropy in forearcs is commonly interpreted as being produced by trench-parallel flow of a dry upper mantle (A-type olivine, flow parallel to fast axis), both below and above the subducting slab¹, or by two-dimensional trench-normal flow of a hydrated¹¹ mantle wedge (B-type olivine, flow normal to fast axis). Despite the fact that considerable slab trench-parallel anisotropy was detected in some subduction zones (see, for example, ref. 12), the slab-induced splitting is normally assumed to be low and related to the trench-normal fossilized anisotropy of the downgoing lithosphere¹.

However, these interpretations are in contrast with the experimental observations and with part of the local S-wave splitting patterns. For example, analogue and numerical modelling of slab retreat indicates that the toroidal component of the mantle flow is oriented perpendicular to the slab, not parallel to it^{13,14}. If we assume a dry mantle in which the A-type olivine fast axis is aligned parallel to the flow direction, it follows that the sub-slab-induced anisotropy must be oriented perpendicular to the trench and that the SKS anisotropic source(s) must lie within or above the slab. Mantle wedge-splitting measurements performed with local S waves show that the fast components can be oriented either parallel (constructive interference) or perpendicular (destructive interference) to that measured with SKS waves¹. In addition, low splitting delay times of the mantle wedge (little or no interference) measured at the South America and Sumatra subduction zones suggest that the anisotropy sited above the slab can contribute only occasionally to the SKS splitting.

Where is the main source for SKS anisotropy located? A close inspection of the slab fabric can help us in answering this question. The subducting oceanic plate is pervasively affected by localized serpentinization. Faulting of the oceanic plate along trenches and along active and fossil volcanic ridges may form a dense network of preferentially oriented faults, providing a pathway for water percolation in the crust and the mantle^{15–17}. Considerations about the triggering mechanism of earthquakes at intermediate depths nucleating in the lower plane of the Wadati–Benioff zone place the hydration depth several tens of kilometres below the upper boundary of the slab^{18,19}. Shallow seismicity and low heat flux measured at the trench slope also indicate that hydration continues at shallow depths^{16,17,20}.

To investigate how those sets of faults form and how their orientations change as the slab is subducted, we performed two-dimensional numerical experiments in which an oceanic plate bends spontaneously under the control of realistic visco-elasto-plastic rheologies (Supplementary Fig. 1; see Methods for details of the numerical model). The models show that when subduction is in a steady-state condition, faults dip at about 30° from the vertical at the trench, whereas below the forearc they attain a near-vertical orientation (Fig. 1). The results are consistent with the fault geometry of the outer rise and with focal-plane solutions of intermediate-depth earthquakes^{16,21}, as well as with the common 8–40-km thickness of double Benioff zones interpreted as sites of dehydration of subducted slabs^{18,22}. Therefore, in the forearc region, where dehydration reactions have not yet affected the cold core of the slab and faults are near the vertical, a large-scale texture composed of low-velocity hydrated zones, including the faults and the adjacent wall rocks, and high-velocity areas of dry peridotite may both be present within the upper part of the descending plate.

Large faults spaced about 2.5 km apart and average degrees of serpentinization of the plate ranging from 17% to 25% have been

¹Institute of Geophysics, ETH Zürich, Schafmattstrasse 30, 8093 Zürich, Switzerland. ²Institute of Geology, ETH Zürich, Leonhardstrasse 19, 8092 Zürich, Switzerland. ³Geosciences Montpellier, Université Montpellier II and CNRS, 34090 Montpellier, France.

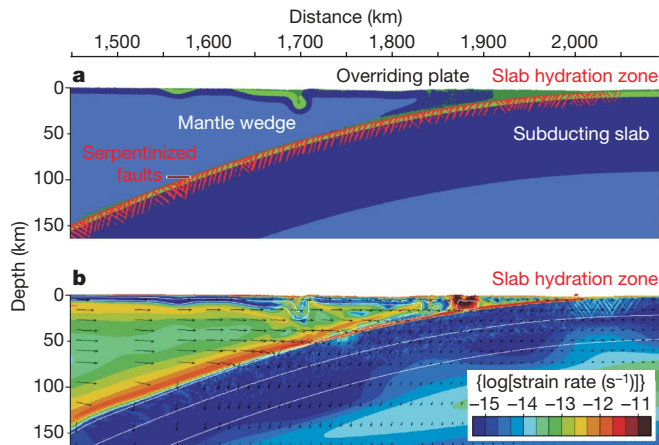


Figure 1 | Thermo-mechanical two-dimensional model of a spontaneously bending oceanic plate. **a**, Compositional map. Serpentinized faults are trenchward dipping but sets of antithetic and seaward-dipping faults are occasionally visible. Light green is gabbroic oceanic crust; basalt and sediments are shown in dark green. **b**, Strain rate map. Fault activation due to the bending of the plate occurs mainly at the trench in the upper layer of the slab. Arrows indicate the direction of material displacement. White lines are isotherms in °C (see Methods for details of the numerical model).

reported^{17,23}. If we assume that hydration occurs mainly close to large faults, an upper oceanic plate section would be then formed by layers 400–600 m thick interbedded with dry portions of the mantle 1,900–2,100 m wide. Shear-wave splitting generated by preferentially oriented layers one order of magnitude thicker than the spacing of large outer-rise faults has already been reported²⁴. Moreover, it has recently been shown that the long-wavelength SKS waves are indeed able to detect the anisotropy produced by bodies a few tens of kilometres thick (for example, the 10–20-km-thick shear zone of ref. 25; see also discussion in Supplementary Information). Hence, for vertically incident teleseismic waves, the slab can be considered to be a transverse isotropic body with a horizontal axis of symmetry.

Hydration of ultramafic rocks leads to the formation of sheet silicates such as lizardite, antigorite, talc and chlorite. Anisotropies of sheet silicates are highest for waves travelling in the (001) plane (up to 82% for lizardite), so that a near-vertical preferred orientation of hydrous minerals in the upper mantle will produce an important anisotropic source detectable by teleseismic waves. Microstructural analysis of serpentinized rocks deformed either naturally (see, for example, Supplementary Fig. 2) or in laboratory experiments indicate that the (001) plane of sheet silicates tends to align parallel to the shear zone during and after serpentinization^{26,27}, and that the CPO can be continuous along strike for as much as 50 km (ref. 28).

We propose a new model for the observed shear-wave splitting in the forearc, in which the resultant anisotropy is a combination of the SPO produced by near-vertical layers of rocks having different elastic properties and of the CPO of highly anisotropic hydrous minerals oriented parallel to the faults (Figs 2a, b and 3). The total amount and direction of the splitting would then be a function of the orientation, size, spacing and aspect ratio of the faults (Fig. 2c). The total delay time ($t_{d,\text{tot}}$) is

$$t_{d,\text{tot}} = t_{d,\text{SPO}} + t_{d,\text{CPO}_{\text{hyd}}} \pm t_{d,\text{CPO}_{\text{ol}}}$$

where $t_{d,\text{SPO}}$ and $t_{d,\text{CPO}_{\text{hyd}}}$ are the delay time contributions of the geometrical effect and the preferred alignment of hydrous minerals, respectively. Because the slab fossil anisotropy ($t_{d,\text{CPO}_{\text{ol}}}$) is perpendicular to magnetic lineations and spreading fabric trends that in most cases are oriented parallel to the trench at the outer rise (see, for example, ref. 15), the CPO of the olivine and enstatite grains will interfere destructively with that of the sheet silicates in faults parallel

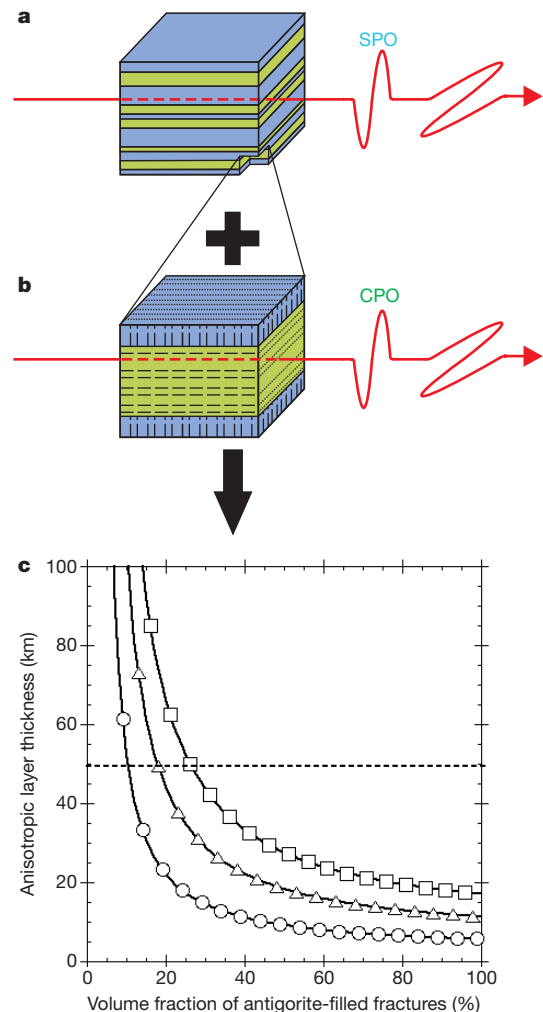


Figure 2 | Schematic diagram of the anisotropic components and estimates of the delay time. **a**, Thin layering of dry (blue) and hydrated (green) mantle portions results in an SPO-induced anisotropy for long-wavelength SKS waves. **b**, CPO_(hyd+ol) formed by hydrated minerals parallel to the layering in the hydrated mantle and by perpendicular olivine and enstatite grains in the dry mantle (destructive interference). **c**, Contours of delay time for an anisotropic plate dipping at 30° with strong transverse isotropic antigorite, as a function of the volume fraction of antigorite-filled fractures and fault length, with a fracture aspect ratio of 100:1 (see Methods for details of the anisotropy model). Delay times: circles, 0.5 s; triangles, 1.0 s; squares, 1.5 s. The horizontal dashed line indicates a 50-km-thick antigorite layer.

to the trench strike (CPO_{hyd+ol}; see Methods for details of the anisotropy model).

Calculated delay times can account for more than 50% of those measured in the forearc (Table 1), indicating that slab anisotropy can indeed constitute the main anisotropic source of the upper mantle, provided that the faults extend deeply in the slab and the orientation is parallel to the fast splitting direction.

In most subduction regions, where vertical distances between the upper and lower planes of the double Benioff zone range from 10 to 50 km (refs 18, 22), bending-related faults trend parallel to the trench and to the direction of the fast shear-wave (SKS) component of the forearc (Fig. 4). We also found that in forearc regions where the fast shear-wave component is subparallel to the convergence direction, faults are at a high angle to the trench.

One of these cases is South America, where the fast components are generally oriented parallel to the trench. However in Central Chile, between 30° and 32° S, fast splitting directions are trench-normal, trending ENE⁴, and seem to align roughly parallel with elongated clusters of intermediate-depth earthquakes coincident with the

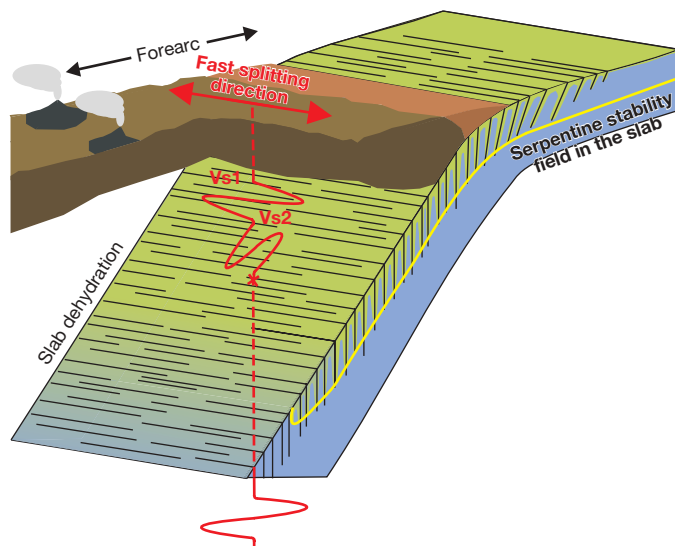


Figure 3 | Schematic diagram of the tectonic and compositional structure of the slab and the inferred splitting behaviour. Vs1 and Vs2 are the fast and slow, orthogonally polarized, shear waves, respectively. The polarization of Vs1 aligns parallel to the strike of the fault set. The colour scheme of the slab is as in Fig. 2a, b.

projected continuation of the subducted Juan Fernández Ridge¹⁶. The nodal planes of these clusters have azimuths similar to those of trench faults flanking the offshore volcanoes of the Juan Fernández Ridge and penetrating as deep as 30 km in the lithosphere¹⁶, suggesting that there might be a close relation between the orientation of the fault set, earthquake clusters and the anisotropic pattern. Further north, other ENE–NE-trending earthquake clusters that parallel trends in Cenozoic offshore volcanic chains have been identified (see Fig. 7 of ref. 29). These elongated clusters coincide with ENE–NE-trending, trench-normal splitting directions identified in ref. 3 in restricted areas of South America. Thus, subduction at a high angle from the trench of volcanic chains flanked by hydrated faults can explain occasional trench-normal splitting patterns such those observed in South America.

In Cascadia, although fractures trend NE–ENE³⁰, parallel to the SKS fast splitting directions², the fact that the Juan de Fuca plate is young and hot confines the slab hydration to shallow depths. Because anisotropies of the crust and of the mantle wedge are perpendicular to that measured with SKS waves, we believe that the main anisotropic source in Cascadia should lie in the below-slab mantle, an interpretation that is compatible with analogue and numerical models^{13,14}.

We note here that our anisotropy model and calculated time delays are intended as an upper-limit case in which sheet minerals are mostly aligned in the vertical direction parallel to fractures, whereas foliation at a high angle to the shear zone borders and isotropic microstructures have been recognized in serpentinites (see, for example, ref. 26). In addition, it has been shown³¹ that the magnitude of shear-wave splitting often (but not always) decreases for ray paths at high angles to the foliation. Despite the uncertainties regarding

Table 1 | Shear-wave-splitting delay times

Fracture aspect ratio	Fault length (km)				
	10	20	30	40	50
1:5	0.26	0.51	0.77	1.03	1.29
1:100	0.35	0.71	1.06	1.41	1.77

For the differential effective medium (DEM) model, delay times (in seconds) are shown for vertically propagating S waves in an anisotropic plate dipping at 30° containing 30% by volume of vertical fractures filled with oriented antigorite. The subvertical fractures have propagated to different depths into the plate from the plate's top surface. See Methods for details of the anisotropy model.

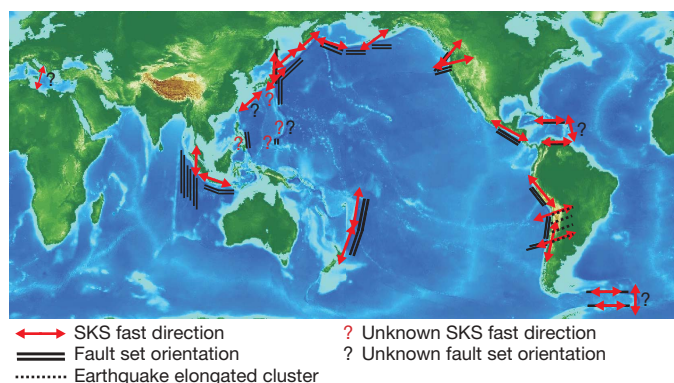


Figure 4 | Summary of SKS fast directions and fault set orientations. Question marks indicate that no data are available. See Methods for data sources.

the behaviour of serpentinite, hydrated portions of the slab with non-subvertical orientation of the foliation should contribute less to the CPO-induced anisotropy. In contrast, our calculations do not take into account the possibility that water could remain trapped inside fractures with sealing serpentinitized margins. A preferential orientation of subvertical water-filled cracks at a high pore pressure could constitute an additional anisotropic source (SPO¹⁰) and further increase the estimated shear-wave-splitting delay time (N.I. Christensen, personal communication; see Methods and Supplementary Fig. 4). Indeed, we believe that the slab anisotropy is a combination of CPO, SPO and fluid-filled cracks.

From our calculations of anisotropy, our numerical model of slab-bending-related faults and observations including trench bathymetry¹⁷, slab anisotropy measurements¹², SKS splitting patterns¹ and earthquake distributions^{16,29}, we conclude that in subduction zones SKS splitting seems to be related more to the spatial distribution of the slab faulting than to the flow in the upper mantle. The magnitude of the splitting produced by localized hydration of the oceanic plate (Fig. 2) depends mainly on the fault depth and on the degree of hydration of the slab. In a young and hot slab (that is, shallow faults), the calculated amount of delay time can be lower (Table 1) than those measured, indicating that further sources in the upper mantle are needed. As discussed above, analogue and numerical models show that the below-slab mantle can contribute to the observed anisotropy only when the splitting patterns are trench-normal (for example, Cascadia). In contrast, a hydrated mantle wedge dominated by two-dimensional corner flow and composed of B-type olivine and subvertical hydrous minerals³² would be a good candidate for this additional anisotropic layer. We suggest that the main anisotropic sources of SKS waves lie within the slab, with additional contributions coming from the mantle wedge if the local S-wave anisotropy is oriented parallel to that of SKS waves.

METHODS SUMMARY

The numerical technique used is based on a combination of a finite difference method, applied on a staggered irregular grid, and a marker-in-cell technique. The momentum, continuity and energy equations are solved on the Eulerian frame, and physical properties are transported by Lagrangian markers that move according to the velocity field interpolated from the fix grid. Realistic and non-Newtonian visco-elasto-plastic rheologies are used in the model (Supplementary Table 1). Subduction of oceanic plates is spontaneous and no velocity field is applied.

Splitting delay times were calculated with an averaged elastic tensor of dry peridotitic rocks and elastic properties of a serpentinitized and foliated sample. Calculations were made for a 30° dipping slab with subvertical fractures of different aspect ratios; they include the combined effect of the SPO and CPO. We also undertook an upper-bound calculation of water-filled cracks (no antigorite present) in our anisotropic elastic model with a plate dipping at 30° using the properties of water at *in situ* conditions at 50 km depth (see Methods).

Full Methods and any associated references are available in the online version of the paper at www.nature.com/nature.

Received 28 April; accepted 27 August 2008.

- Long, M. D. & Silver, P. The subduction zone flow field from seismic anisotropy: a global view. *Science* **319**, 315–318 (2008).
- Currie, C. A., Cassidy, J. F., Hyndman, R. D. & Bostock, M. G. Shear wave anisotropy beneath the Cascadia subduction zone and western North American craton. *Geophys. J. Int.* **157**, 341–353 (2004).
- Russo, R. M. & Silver, P. G. Trench-parallel flow beneath the Nazca plate from seismic anisotropy. *Science* **263**, 1105–1111 (1994).
- Anderson, M. L., Zandt, G., Triep, E., Fouch, M. & Beck, S. Anisotropy and mantle flow in the Chile–Argentina subduction zone. *Geophys. Res. Lett.* **31**, L23608, doi:10.1029/2004GL020906 (2004).
- Savage, M. K. Seismic anisotropy and mantle deformation: what have we learned from shear wave splitting? *Rev. Geophys.* **37**, 65–106 (1999).
- Park, J. & Levin, V. Seismic anisotropy: tracing plate dynamics in the mantle. *Science* **296**, 485–489 (2002).
- Nicolas, A. & Christensen, N. I. in *Composition, Structure and Dynamics of the Lithosphere–Asthenosphere System* (eds Fuchs, K. & Froidevaux, C.) 111–123 (Am. Geophys. Union, 1987).
- Visser, K., Trampert, J., Lebedev, S. & Kennett, B. L. N. Probability of radial anisotropy in the deep mantle. *Earth Planet. Sci. Lett.* **270**, 241–250 (2008).
- Backus, G. E. Long-wave elastic anisotropy produced by horizontal layering. *J. Geophys. Res.* **67**, 4427–4440 (1962).
- Crampin, S. The fracture criticality of crustal rocks. *Geophys. J. Int.* **118**, 428–438 (1994).
- Kneller, E. A., van Keken, E., Karato, S. & Park, J. B-type olivine fabric in the mantle wedge: insight from high-resolution non-Newtonian subduction zone models. *Earth Planet. Sci. Lett.* **237**, 781–797 (2005).
- Matcham, I., Savage, M. K. & Gledhill, K. R. Distribution of seismic anisotropy in the subduction zone beneath the Wellington region, New Zealand. *Geophys. J. Int.* **140**, 1–10 (2000).
- Kincaid, C. & Griffiths, R. W. Laboratory models of the thermal evolution of the mantle during rollback subduction. *Nature* **425**, 58–62 (2003).
- Piomallo, C., Becker, T. W., Funicello, F. & Faccenna, C. Three-dimensional instantaneous mantle flow induced by subduction. *Geophys. Res. Lett.* **33**, L08304, doi:10.1029/2005GL025390 (2006).
- Masson, D. G. Fault patterns at outer trench walls. *Mar. Geophys. Res.* **13**, 209–225 (1991).
- Ranero, C. R., Villaseñor, A., Phipps Morgan, J. & Weinrib, W. Relationship between bend-faulting at trenches and intermediate-depth seismicity. *Geochem. Geophys. Geosyst.* **6**, Q12002, doi:10.1029/2005GC000997 (2005).
- Ranero, C. R., Phipps Morgan, J. & Reichert, C. Bending-related faulting and mantle serpentinization at the Middle America trench. *Nature* **425**, 367–373 (2003).
- Peacock, S. M. Are the lower planes of double seismic zones caused by serpentine dehydration in subducting oceanic mantle? *Geology* **29**, 299–302 (2001).
- Omori, S., Komabayashi, T. & Maruyama, S. Dehydration and earthquakes in the subducting slab: empirical link in intermediate and deep seismic zones. *Phys. Earth Planet. Inter.* **146**, 297–311 (2004).
- MacDonald, H. & Fyfe, W. S. Rate of serpentinization in seafloor environments. *Tectonophysics* **116**, 123–135 (1985).
- Jiao, W., Silver, P. G., Fei, Y. & Prewitt, T. Do intermediate- and deep-focus earthquakes occur on preexisting weak zones? An examination of Tonga subduction zone. *J. Geophys. Res.* **105**, 28,125–28,138 (2000).
- Brudzinski, M. R., Thurber, C. H., Hacker, B. R. & Engdahl, E. R. Global prevalence of double Benioff zones. *Science* **316**, 1472–1474 (2007).
- Grevemeyer, I., Ranero, C. R., Flueh, E. R., Klaeschen, D. & Bialas, J. Passive and active seismological study of bending-related faulting and mantle serpentinization at the Middle America trench. *Earth Planet. Sci. Lett.* **258**, 528–542 (2007).
- Gee, L. S. & Jordan, T. H. Polarization anisotropy and fine-scale structure of the Eurasian upper mantle. *Geophys. Res. Lett.* **15**, 824–827 (1988).
- Babuska, V., Plomerova, J., Vecsey, L., Granet, M. & Achauer, U. Seismic anisotropy of the French Massif and predisposition of Cenozoic rifting and volcanism by Variscan suture hidden in the mantle lithosphere. *Tectonics* **21**, 1029, doi:10.1029/2001TC901035 (2002).
- Norrel, G. T., Teixell, A. & Harper, G. D. Microstructure of serpentine mylonites from the Josephine ophiolites and serpentinization in retrogressive shear zones, California. *Geol. Soc. Am. Bull.* **101**, 673–682 (1989).
- Escartin, J., Hirth, G. & Evans, B. Nondilatant brittle deformation of serpentinites: implications for Mohr–Coulomb theory and the strength of faults. *J. Geophys. Res.* **102**, 2897–2913 (1997).
- Hirauchi, K. Serpentinite textural evolution related to tectonically controlled solid-state intrusion along the Kurosegawa Belt, northwestern Kanto Mountains, central Japan. *J. Arc* **15**, 156–164 (2006).
- Kirby, S., Engdahl, R. & Denlinger, R. Intermediate-depth intraslab earthquakes and arc volcanism as physical expression of crustal and uppermost mantle metamorphism in subducting slabs. *Geophys. Monogr.* **96**, 195–214 (1996).
- Chaytor, J. D. & Goldfinger, C. Dziak, R. P. & Fox, C. G. Active deformation of the Gorda plate: constraining deformation models with new geophysical data. *Geology* **32**, 353–356 (2004).
- Okaya, D. A. & Christensen, N. I. Anisotropic effects of non-axial seismic wave propagation in foliated crustal rocks. *Geophys. Res. Lett.* **29**, 1507, doi:10.1029/2001GL014285 (2002).
- Kneller, E. A., Long, M. D. & van Keken, P. E. Olivine fabric transition and shear wave anisotropy in the Ryukyu subduction system. *Earth Planet. Sci. Lett.* **268**, 268–282 (2008).

Supplementary Information is linked to the online version of the paper at www.nature.com/nature.

Acknowledgements We thank M. Savage and N. I. Christensen for critical discussion, reading of the manuscript and English polishing, and Gabriele Morra and F. J. Simons helping to improve the manuscript. L.B. thanks W. Weder for his work. This work was supported by ETH Research Grant TH-12/05-3, SNF Research Grant 200021-113672/1 and 200021-116153.

Author Information Reprints and permissions information is available at www.nature.com/reprints. Correspondence and requests for materials should be addressed to M.F. (faccenda@erdw.ethz.ch).

METHODS

Numerical model. The numerical experiment was performed with I2ELVIS code developed by ref. 33. The computational domain is $3,000 \times 200$ km ($1,001 \times 141$ nodes, ~ 5 million markers). Horizontal resolution moves together with the retreating slab and is maximal (1 km) starting 400 km on the right of the trench to 300 km on its left; elsewhere, the resolution increases gradually from 1 km to 20 km. Vertical resolution is 1 km for the first 80 km and 2 km for the last 120 km. The initial setup is shown in Supplementary Fig. 1. Subduction starts spontaneously³⁴ as the result of the juxtaposition of two plates of different ages (1 and 70 Myr for the left and right plates, respectively) along a transform fault that is assumed to be weak due to water percolation and hydration of the boundary (low plastic strength of 1 MPa; refs 34, 35). The thermal structure of the initial plate setup is computed according to the cooling of a semi-infinite half-space equation³⁶:

$$T = T_1 + (T_0 - T_1)(1 - \operatorname{erf}(\eta))$$

$$\eta = d/2\sqrt{\kappa\tau}$$

where $T_0 = 0^\circ\text{C}$ for both plates, $T_1 = 1,270$ and $1,350^\circ\text{C}$ for the young and old plates, respectively, d is depth, κ is thermal diffusivity ($10^{-6}\text{ m}^2\text{ s}^{-1}$), τ is the age in seconds of the plates and η is the dimensionless similarity variable. The age of the older plate decreases linearly towards the right boundary corresponding to a mid-ocean ridge (0 Myr). Serpentinization (that is, weakening) of the oceanic slab is assumed along the faults having a finite plastic strain of more than 0.01. A low-viscosity lower boundary (10^{19} Pa s, from 180 to 200 km depth) is imposed to facilitate slab penetration.

Anisotropic model. The composition of the plate is 70% olivine and 30% enstatite, where the plate is elastically anisotropic, calculated with the CPO from a database (refs 37, 38) of 110 and 68 samples for olivine and enstatite, respectively. The elastic tensors for olivine and enstatite were calculated at 500°C and 1.5 GPa, corresponding to a depth of about 50 km on a warm slab geotherm³⁹. For olivine we used the single crystal elastic constants and pressure derivatives reported in ref. 40 and the temperature derivatives in ref. 41. For enstatite we used the elastic constants and pressure derivatives in ref. 42 and temperatures derivatives in ref. 43. For antigorite we used the single crystal elastic constants determined recently through atomic modelling in ref. 44 under ambient conditions.

For the CPO inside serpentinized fractures, we used seismic velocities of naturally deformed antigorite measured in ref. 45 (see more details in Supplementary Fig. 3). The velocity measurements⁴⁵ show a transverse isotropic symmetry with velocities in the x and y directions for P and S waves being equal within experimental uncertainty, pressure-independent S-wave anisotropy, volumetric compaction of 1.2% and ratio of compaction strains between z and x or y of about 4:1. The compaction data would, to first order, constrain the fracture porosity to be about 1% and the aspect ratio to 4:1.

To obtain the CPO for antigorite, we used the March strain model⁴⁶, often used for characterizing (001) pole figures of naturally deformed layered silicates (see, for example, ref. 47). To produce an axial (001) pole figure similar to that reported in ref. 45 for a naturally deformed antigorite sample, we applied a series of axial strains with the March model to an initially uniform pole figure. To obtain the complete CPO we assumed that the crystallographic axes normal to the c axes were randomly distributed, which results in transverse isotropic (TI) elastic symmetry when combined with the elastic constants of antigorite. We increased the axial strain until the calculated velocities matched the experimentally measured velocity anisotropy reported in ref. 45.

The 21 elastic constants for the anisotropic plate (70% olivine, 30% enstatite) and 5 independent transverse isotropic elastic constants of the antigorite fracture fill represent the two elastic tensors of the end-member compositions in our model (Supplementary Table 2). We used the differential effective medium (DEM) to represent a two-phase composite model of the fractured plate by incrementally adding three-dimensional ellipsoidal inclusions of serpentine fracture fill to the anisotropic plate and then recalculating the new effective background material at each increment. The tensorial equations for the DEM model were derived in ref. 48 as

$$\frac{dC_{\text{DEM}}}{dV} = \frac{1}{(1-V)}(C_i - C_{\text{DEM}})A_i$$

where the term $A_i = [I + G(C_i - C_{\text{DEM}})]^{-1}$ is the strain concentration factor coming from the Eshelby formulation of the inclusion problem, I being the unit elastic tensor, G the symmetrical tensor of Green's function, C_i the elastic constant of the serpentine fracture fill and C_{DEM} the elastic constant of the background material (that is, the plate) (see ref. 49 for more details and references). The ellipsoidal penny-shaped fractures had axial ratios along the x : y : z orthogonal directions of 1:5:5 to 1:100:100, where x is the horizontal axis normal to the subduction trench, y is parallel to the trench axis and z is the vertical axis. In our models, as a result of the very high anisotropy of TI antigorite, the fracture axial ratios of the fractures have little relative influence on shear-wave anisotropy (Supplementary Fig. 3).

To evaluate the possible contribution of penny-shaped cracks in the foliation inferred from the v_p velocity measurements of ref. 45, we have modelled the water-filled vertical fractures in the anisotropic plate. The calculated S-wave anisotropy is very high even for 5% of water-filled fractures (5–80%), depending very strongly on aspect ratio (Supplementary Fig. 4). Hence a small percentage of aligned water-filled cracks in the foliation plane will greatly enhance the anisotropy of a serpentine-filled fracture, even if the filling is isotropic. Because dry microcracks may be preserved and influence seismic properties to pressures as high as 1 GPa (ref. 50), fluid-filled cracks will be even more resistant to closure at high pressure.

Splitting and fault set pattern data. All the compiled data included in Fig. 4 regarding the worldwide orientations of SKS fast components and fault sets, and earthquake clusters located in South America were taken from the literature. SKS fast directions data are from refs 1–4, 51–53. Fault set orientation are from refs 15–17, 54–60. Earthquake elongated clusters are from ref. 29.

33. Gerya, T. V. & Yuen, D. A. Robust characteristic method for modeling multiphase visco-elasto-plastic thermo-mechanical problems. *Phys. Earth Planet. Inter.* **163**, 83–105 (2007).
34. Hall, C. E., Gurnis, M., Sdrolias, M., Lavie, L. L. & Muller, R. D. Catastrophic initiation of subduction following forced convergence across fractures zones. *Earth Planet. Sci. Lett.* **212**, 15–30 (2003).
35. Gerya, T. V., Connolly, J. A. D. & Yuen, D. A. Why is terrestrial subduction one-sided? *Geology* **36**, 43–46 (2008).
36. Turcotte, D. L. & Schubert, G. *Geodynamics* (Cambridge Univ. Press, 2002).
37. Ben Ismail, W. & Mainprice, D. A statistical view of the strength of seismic anisotropy in the upper mantle based on petrofabric studies of ophiolite and xenolith samples. *Tectonophysics* **296**, 145–157 (1998).
38. Ben Ismail, W. & Mainprice, D. An assessment of the contribution of enstatite to the upper mantle seismic anisotropy. *Tectonophysics* (submitted).
39. Wada, I., Wang, K., He, J. & Hyndman, R. D. Weakening of the subduction interface and its effects on surface heat flow, slab dehydration, and mantle wedge serpentinization. *J. Geophys. Res.* **113**, B04402, doi:10.1029/2007JB005190 (2008).
40. Abramson, E. H., Brown, J. M., Slutsky, L. J. & Zang, J. The elastic constants of San Carlos olivine to 17 GPa. *J. Geophys. Res.* **102**, 12253–12263 (1997).
41. Isaak, D. G. High-temperature elasticity of iron-bearing olivine. *J. Geophys. Res.* **97**, 1871–1885 (1992).
42. Chai, M., Brown, J. M. & Slutsky, L. J. The elastic constants of an aluminous orthopyroxene to 12.5 GPa. *J. Geophys. Res.* **102**, 14779–14785 (1997).
43. Jackson, J. M., Sinogeikin, S. V. & Bass, J. D. Sound velocities and single-crystal elasticity of orthoenstatite to 1073 K at ambient pressure. *Phys. Earth Planet. Inter.* **161**, 1–12 (2007).
44. Pellenq, R. J.-M. *et al.* Atomistic calculations of the elastic properties of antigorite at upper mantle conditions: application to the seismic properties in subduction zones. *Earth Planet. Sci. Lett.* (submitted).
45. Kern, H., Liu, B. & Popp, B. Relationship between anisotropy of P and S wave velocities and anisotropy of attenuation in serpentine and amphibolite. *J. Geophys. Res.* **102**, 3051–3065 (1997).
46. March, A. Mathematische Theorie der Regelung nach der Korngestalt bei affiner Deformation. *Z. Kristallogr.* **81**, 285–297 (1932).
47. Paterson, S. R., Yu, H. & Oertel, G. Primary and tectonic fabric intensities in mudrocks. *Tectonophysics* **247**, 105–119 (1995).
48. McLaughlin, R. A. A study of the differential scheme for composite materials. *Int. J. Eng. Sci.* **15**, 237–244 (1977).
49. Mainprice, D. Modelling the anisotropic seismic properties of partially molten rocks found at Mid-Ocean. *Tectonophysics* **279**, 161–179 (1997).
50. Christensen, N. I. Compressional wave velocities in possible mantle rocks to pressures of 30 kilobars. *J. Geophys. Res.* **79**, 407–412 (1974).
51. Müller, C. Upper mantle seismic anisotropy beneath Antarctica and the Scotia Sea region. *Geophys. J. Int.* **147**, 105–122 (2001).
52. Russo, R. M., Silver, P. G., Franke, M., Ambeg, W. B. & James, D. E. Shear-wave splitting in northeast Venezuela, Trinidad, and the eastern Caribbean. *Phys. Earth Planet. Inter.* **95**, 251–275 (1996).
53. Müller, C., Bayer, B., Eckstaller, A. & Miller, H. Mantle flow in the South Sandwich subduction environment from source-side shear wave splitting. *Geophys. Res. Lett.* **35**, L03301, doi:10.1029/2007GL032411 (2008).
54. Chaytor, J. D., Goldfinger, C., Dziak, R. P. & Fox, C. G. Active deformation of the Gorda plate: constraining deformation models with new geophysical data. *Geology* **32**, 353–356 (2004).
55. Deplus, C. *et al.* Direct evidence of active deformation in the eastern Indian oceanic plate. *Geology* **26**, 131–134 (1998).
56. Lallemand, S. E. *et al.* Genetic relations between the central and southern Philippine trench and Sangihe trench. *J. Geophys. Res.* **103**, 933–950 (1998).
57. Masson, D. G. *et al.* Subduction of seamounts at the Java trench: a view with long-range sidescan sonar. *Tectonophysics* **185**, 51–65 (1990).
58. Billen, M. I. Seafloor morphology of the Osborn Trough and Kermadec Trench. (<http://resolver.caltech.edu/CaltechETD:etd-11012001-142941>) (2001).
59. Fujiwara, T. *et al.* Morphology and tectonics of the Yap trench. *Mar. Geophys. Res.* **21**, 69–86 (2000).
60. Kobayashi, K., Nakanishi, M., Tamaki, K. & Ogawa, Y. Outer slope faulting associated with the western Kuril and Japan trenches. *Geophys. J. Int.* **134**, 356–372 (1998).

Reassessing the first appearance of eukaryotes and cyanobacteria

Birger Rasmussen¹, Ian R. Fletcher¹, Jochen J. Brocks^{2,3} & Matt R. Kilburn⁴

The evolution of oxygenic photosynthesis had a profound impact on the Earth's surface chemistry, leading to a sharp rise in atmospheric oxygen between 2.45 and 2.32 billion years (Gyr) ago^{1,2} and the onset of extreme ice ages³. The oldest widely accepted evidence for oxygenic photosynthesis has come from hydrocarbons extracted from ~2.7-Gyr-old shales in the Pilbara Craton, Australia, which contain traces of biomarkers (molecular fossils) indicative of eukaryotes and suggestive of oxygen-producing cyanobacteria^{4–7}. The soluble hydrocarbons were interpreted to be indigenous and syngenetic despite metamorphic alteration and extreme enrichment (10–20‰) of ¹³C relative to bulk sedimentary organic matter^{5,8}. Here we present micrometre-scale, *in situ* ¹³C/¹²C measurements of pyrobitumen (thermally altered petroleum) and kerogen from these metamorphosed shales, including samples that originally yielded biomarkers. Our results show that both kerogen and pyrobitumen are strongly depleted in ¹³C, indicating that indigenous petroleum is 10–20‰ lighter than the extracted hydrocarbons⁵. These results are inconsistent with an indigenous origin for the biomarkers. Whatever their origin, the biomarkers must have entered the rock after peak metamorphism ~2.2 Gyr ago⁹ and thus do not provide evidence for the existence of eukaryotes and cyanobacteria in the Archaean eon. The oldest fossil evidence for eukaryotes and cyanobacteria therefore reverts to 1.78–1.68 Gyr ago and ~2.15 Gyr ago^{10,11}, respectively. Our results eliminate the evidence for oxygenic photosynthesis ~2.7 Gyr ago and exclude previous biomarker evidence for a long delay (~300 million years) between the appearance of oxygen-producing cyanobacteria and the rise in atmospheric oxygen 2.45–2.32 Gyr ago¹.

Hydrocarbon biomarkers represent an important source of information about the diversity and evolution of life, but their application to metamorphosed Precambrian rocks has been plagued by contamination from non-indigenous hydrocarbons^{5,8,12}. Recent geochemical studies, using rigorous laboratory procedures designed to minimize this problem, recovered traces of hydrocarbon biomarkers⁴ from organic-rich shales as old as ~2.7 Gyr^{4–7}. The extracted bitumens mainly consisted of *n*-alkanes, methylalkanes and acyclic isoprenoids, but also included complex polycyclic biomarkers such as 2 α -methylhopanes and steranes, suggesting the presence of cyanobacteria and eukaryotes, respectively^{4–6}. The biomarker results set new minimum ages for fossil evidence of cyanobacteria (previously ~2.15 Gyr old)¹¹ and eukaryotes (previously between 1.78 Gyr ago and 1.68 Gyr ago)¹⁰. The presence of biomarkers linked to oxygen-producing cyanobacteria as well as steranes, the biosynthesis of which in extant eukaryotes requires molecular oxygen, also provides the most reliable minimum age for the onset of oxygenic photosynthesis^{4–6}. Although the weight of evidence pointed to a probable syngenetic origin for the biomarkers, the possibility of contamination was not entirely ruled out⁵. An ongoing problem for a syngenetic interpretation, acknowledged

in previous studies^{4–6}, is the extreme enrichment in ¹³C of the extracted hydrocarbons relative to the bulk kerogen.

Sedimentary rocks of Neoproterozoic age (2.8–2.5 Gyr old) typically contain strongly ¹³C-depleted kerogen ($\delta^{13}\text{C}_{\text{bulk}} < -39\text{‰}$)^{5,8}, which has been interpreted as evidence for the activity of aerobic¹³ or anaerobic¹⁴ methanotrophs, possibly fuelled by a methane-rich atmosphere. Hydrocarbons extracted from 2.7–2.6-Gyr-old shales in the Pilbara Craton, Australia, are enriched in ¹³C relative to bulk organic matter by 10‰ to 20‰ ($\delta^{13}\text{C}_{n\text{-alkanes}} = -29\text{‰}$ to -26‰)⁵. This contrasts with patterns in most Phanerozoic source rocks, in which oils tend to be depleted by 1‰ to 3‰ relative to associated kerogens¹⁵, although slightly enriched bitumen has been recorded in some Proterozoic shales⁶. There are two competing hypotheses that attempt to explain the large isotopic discrepancy in the Neoproterozoic shales^{5,6}. In the first hypothesis the kerogen is interpreted to have consisted of two isotopically distinct components. One fraction was strongly depleted in ¹³C and comprised highly refractory organic debris from methanotrophs ($\delta^{13}\text{C} = -80\text{‰}$), which yielded only minor volumes of petroleum on maturation. The other fraction was enriched in ¹³C and formed most of the extractable bitumen⁶, including lipids from phototrophic organisms ($\delta^{13}\text{C} = -26\text{‰}$). The alternative hypothesis is that ¹³C-enriched bitumens were introduced into the shales by post-Archaean fluids or through anthropogenic contamination⁵.

Until recently it had not been possible to distinguish between these two hypotheses. However, the development of ion microprobe techniques for micrometre-scale ¹³C/¹²C analysis¹⁶ now allows direct measurement of minute residues of solidified oil (pyrobitumen) and kerogen preserved in the matrix of the Neoproterozoic shales¹⁷, including samples that originally yielded molecular fossils. Specifically, *in situ* carbon isotopic analysis of the kerogen and pyrobitumen can test whether oil generated by means of thermal maturation was enriched in ¹³C by 10–20‰ relative to kerogen, as suggested from the isotopic composition of the solvent-extracted hydrocarbons^{4–6}.

In this study we have examined organic-rich shale from the ~2.63-Gyr-old Roy Hill Shale Member of the Jeerinah Formation, Fortescue Group, from three diamond-drill holes (WRL-1, DDH 186 and FVG-1) in the southern Pilbara Craton, Australia. In this region, mineral assemblages in basalts from the Fortescue Group suggest that the shales have undergone prehnite–pumpellyite facies metamorphism (200–300 °C)¹⁸, consistent with kerogen hydrogen:carbon ratios of 0.1 to 0.3 (refs 5, 8). Heating at these temperatures is estimated to produce a ~1–3‰ enrichment of ¹³C in the organic matter owing to preferential release of ¹³C-depleted mobile hydrocarbons during progressive maturation¹⁹.

Petrographic examination shows that most samples contain micrometre-sized residues of organic carbon dispersed in the shale matrix. The organic carbon may occur as bands (>0.1-mm thick) of near-continuous, anastomosed laminae (Fig. 1a–d), comprising

¹Department of Applied Geology, Curtin University of Technology, Kent Street, Bentley, Western Australia 6102, Australia. ²The Research School of Earth Sciences, ³Centre for Macroevolution and Macroecology, The Australian National University, Canberra, Australian Capital Territory 0200, Australia. ⁴Centre for Microscopy, Characterisation and Analysis, The University of Western Australia, 35 Stirling Highway, Crawley, Western Australia 6009, Australia.

>50% kerogen (Fig. 1c, d). However, more commonly it is present as lenticular streaks surrounded by a mineral matrix (Fig. 1e). The kerogen resembles sedimentary organic matter termed 'lamalginites' in shales from the Palaeoproterozoic Barney Creek Formation, McArthur Group, northern Australia²⁰. However, unlike the fluorescent kerogen in the mid-Proterozoic samples, which has yielded some of the oldest unambiguously syngenetic biomarkers^{12,21}, the Neoproterozoic kerogen is opaque, non-fluorescent and highly reflective, indicative of higher thermal maturity.

The shales also contain irregular-to-circular masses of pyrobitumen dispersed in the mineral matrix (Fig. 2a–e) and, locally, lining the walls of crosscutting hydrothermal veins (Fig. 2f, g). The solid spheres and circular outlines, which are encased in pyrite (Fig. 2a–c), represent former oil droplets that have been converted to pyrobitumen during thermal alteration that caused significant volume loss (Fig. 2a–c). Residual oil is a common constituent of younger source rocks^{20,22}. With increased burial and heating, oil is destroyed by means of cracking reactions, forming solid and insoluble pyrobitumen that becomes increasingly enriched in ¹³C owing to the loss of isotopically depleted methane²².

The preservation of solidified oil droplets and pore-filling pyrobitumen (Fig. 2a–e) deeply embedded within metamorphosed, organic-rich shale provides strong evidence for former *in situ* oil generation and primary migration. The intergrowth of pyrobitumen with authigenic pyrite that displays evidence of differential compaction suggests that oil may have formed before deep burial. The optical properties of the pyrobitumen, including high reflectivity and the absence of fluorescence, combined with ubiquitous shrinkage cracks (Fig. 2e), is typical of metamorphosed petroleum. These properties are shared with co-occurring kerogen ($R_{\max} > 4.5\%$; $n = 3$), and are consistent with the metamorphic grade of the samples (200–300 °C)¹⁸. The severe thermal alteration experienced by the organic matter in these shales is incompatible with the preservation of indigenous hydrocarbon biomarkers.

Carbon isotopic measurements on individual kerogen and pyrobitumen particles were carried out to test whether oil generated in the

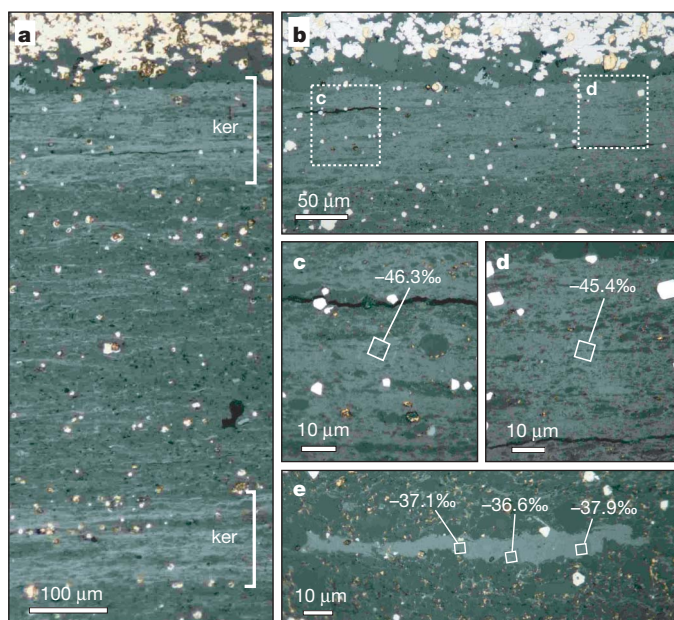


Figure 1 | Reflected light photomicrographs of kerogen. **a**, Two bands containing abundant kerogen laminae (ker). **b**, Close-up of the kerogen-rich layer (top) in **a**, located between pyrite-rich (white) and kerogen-poor (dark grey) matrix. **c**, **d**, Close-up of two areas in kerogen-rich band in **b** (two insets) showing areas of analysis (white box) and their $\delta^{13}\text{C}$ values. **e**, Isolated streak of kerogen with three analytical areas (white squares) and corresponding $\delta^{13}\text{C}$ values. $\delta^{13}\text{C} = 1000\{[(^{13}\text{C}/^{12}\text{C})_{\text{sample}}/(^{13}\text{C}/^{12}\text{C})_{\text{standard}}] - 1\}$.

Jeerinah shales is enriched in ¹³C relative to the associated kerogen⁴. Because of the minute size of most of the organic residues, a NanoSIMS 50 ion microprobe was used to carry out *in situ* ¹³C/¹²C measurements at high spatial resolution (typically 5 µm by 5 µm; see Methods Summary and ref. 16 for detailed analytical procedures). All $\delta^{13}\text{C}$ values are reported relative to the Pee Dee Belemnite standard, and full data tables are available in Supplementary Information.

In situ analysis of kerogen in streaks and laminae (Fig. 1a–e) yielded $\delta^{13}\text{C}$ values ranging between −47.2‰ and −36.6‰ ($n = 20$; Fig. 3, see Supplementary Table 2), which is similar to the carbon isotopic composition of bulk organic matter^{5,8} (Fig. 3). The $\delta^{13}\text{C}$ values for pyrobitumen in the shale matrix vary between −50.7‰ and −36‰ ($n = 69$; Fig. 3), and suggest that, on average, the indigenous oil is slightly more depleted in ¹³C than co-occurring kerogen (Fig. 3; see Supplementary Table 2). The carbon isotopic results show that the soluble hydrocarbons are enriched in ¹³C by 10–20‰ relative to matrix pyrobitumens and source kerogens (from which the biomarkers were reportedly extracted). On the basis of the carbon isotopic results and textural relationships, it is likely that the strongly ¹³C-depleted pyrobitumen was derived from co-occurring kerogen in

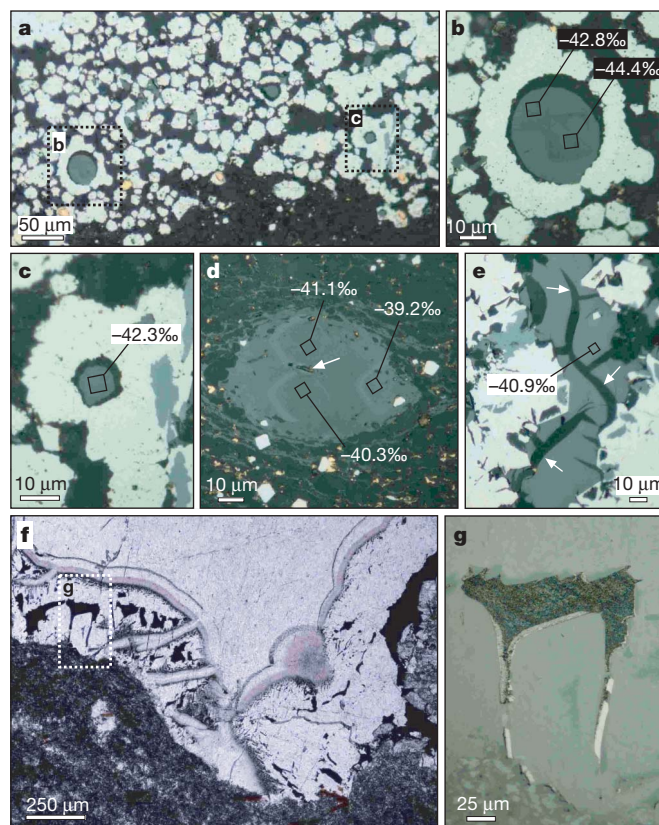


Figure 2 | Reflected light photomicrographs (a–e, g) and a plane-polarized light photomicrograph (f) of pyrobitumen. **a**, Band of authigenic pyrite (white) containing abundant pyrobitumen spheres and circular outlines (see insets). **b**, Close-up of solid pyrobitumen sphere (grey) surrounded by pyrite rim (white). Black squares represent analysis areas with corresponding $\delta^{13}\text{C}$ values. **c**, Minute pyrobitumen globule engulfed by pyrite (white) with a single analytical area and $\delta^{13}\text{C}$ value. The gap between the pyrobitumen and pyrite (in **b** and **c**) reflects shrinkage due to post-engulfment thermal cracking of former oil droplets. **d**, A nodule comprising a U-rich mineral core (see arrow) surrounded by pyrobitumen (grey). Three black outlines represent analytical areas with $\delta^{13}\text{C}$ values. Arrow, U-rich core. **e**, Irregular mass of pyrobitumen (grey) within authigenic pyrite (white). Sinuous shrinkage cracks (see arrows) indicate extensive thermal alteration of former oil. **f**, Opaque pyrobitumen (black) lining the margins of a hydrothermal vein. **g**, Close-up of pyrobitumen (inset in **f**) partly surrounding a vein-lining crystal that has been replaced by sparry carbonate.

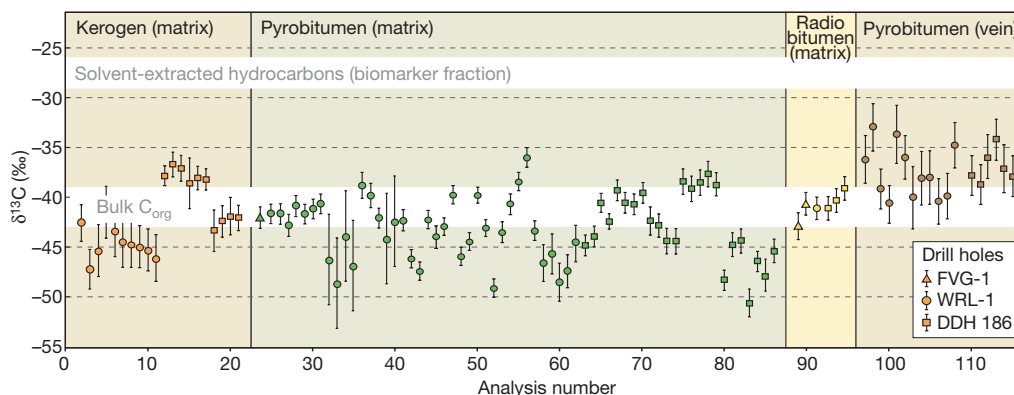


Figure 3 | Carbon isotopic composition of organic matter. The carbon isotopic fields for most of the solvent-extracted hydrocarbons⁵ (white) and bulk organic matter^{5,8} (white) from the Roy Hill Shale Member have been

included for comparison. The precision of individual data points is indicated by vertical lines (1σ). The data points are listed in the order of appearance in Supplementary Table 2.

the Jeerinah shales. The production of highly ^{13}C -depleted petroleum suggests that a methanotrophic biomass made a substantial contribution to the oil-producing lipids, supporting models for increased rates of methanogenesis in the Neoarchaeon¹³. Owing to the absence of n -alkanes and isoprenoids derived from ^{13}C -depleted membrane lipids of methanotrophs⁴, it is difficult to explain how the molecular fossils could have been derived from organic matter indigenous to the ~ 2.63 -Gyr-old shales. The extreme isotopic disparity between oil generated in the shale and hydrocarbons extracted from the shale is thus inconsistent with a syngenetic origin for the molecular fossils.

The pyrobitumen in younger veins in the shale (Fig. 2f, g) is ^{13}C -enriched relative to matrix pyrobitumen and kerogen (Fig. 3), suggesting that oil migrated through the shales from an isotopically distinct, external source. This ^{13}C -enriched pyrobitumen was not identified in the shale matrix, and, given its high thermal maturity, it also is unlikely to be the source of the n -alkanes and biomarkers extracted from the shales. Numerous episodes of post-Archaeon fluid flow have been recognized in the region, ranging in age from 2.4 Gyr ago to <1.0 Gyr ago^{9,23}. Each of these events may have transported non-indigenous organic molecules into the Neoarchaeon shales. However, the liquid, non-pyrolytic bitumens must have entered the rocks after peak thermal alteration, which occurred over a 50-million-year (Myr) interval between 2.2 and 2.15 Gyr ago, on the basis of U–Pb dating of low-grade metamorphic monazite in the shales⁹. These dates also provide a maximum age for biomarkers extracted from the ~ 2.5 -Gyr-old Mt McRae Shale^{5,7}, which was also heated to prehnite–pumpellyite facies by the same event⁹.

Biomarkers have also been extracted from Archaean rocks of similar metamorphic grade in South Africa²⁴; however, their origin and age remain uncertain¹². Quartz-pebble conglomerates from the 2.45- to 2.21-Gyr-old Huronian Supergroup, Canada, contain oil-bearing fluid inclusions and yielded biomarkers for cyanobacteria and eukaryotes²⁵. The inferred maximum age of the oil-bearing fluid inclusions is only constrained by the timing of peak metamorphism (upper prehnite–pumpellyite to lower greenschist facies; up to $\sim 350^\circ\text{C}$), which probably occurred during orogeny 1.89–1.8 Gyr ago. However, the low thermal maturity of the biomarkers and the presence of post-Devonian plant waxes²⁶ suggest a contribution from post-metamorphic molecular fossils. If the biomarkers detected in Archaean and early Palaeoproterozoic rocks are not indigenous, then a reassessment of the previously presented evidence for the first appearance of oxygenic photosynthesis, cyanobacteria⁷ and eukaryotes⁴ is required.

It has been proposed that oxygen-producing cyanobacteria evolved shortly before the Great Oxidation Event between 2.45 and 2.32 Gyr ago, triggering the collapse of a methane greenhouse and plunging the planet into a series of extreme glaciations³. However, the biomarker evidence for cyanobacteria and eukaryotes 2.7 Gyr ago^{4–6}

suggested a much earlier origin for oxygenic photosynthesis and a protracted interval (~ 300 Myr) of oxygenation, spawning several hypotheses for the long delay^{27,28}. Our results suggest that the evidence provided by molecular fossils for the advent of oxygenic photosynthesis in the Archaean is not valid. Although cyanobacteria may have evolved during the Archaean, there is currently no evidence that requires it. Our findings also negate the use of cyanobacterial and eukaryotic biomarkers from 2.7- to 2.5-Gyr-old rocks as calibration points for molecular clocks and the universal tree of life.

There is possible geochemical evidence from late Archaean shales for trace amounts of oxygen ~ 2.5 Gyr ago²⁹. However, the strongest indirect evidence for the appearance of oxygenic cyanobacteria is the rapid accumulation of atmospheric oxygen between 2.45 and 2.32 Gyr ago¹. The oldest morphological fossils of clearly cyanobacterial affinity are only ~ 2.15 Gyr old¹¹, and the oldest fossils that are probably eukaryotic are 1.78–1.68 Gyr old¹⁰. If the origin of oxygenic photosynthesis postdated most of the Archaean, then this would strengthen arguments that phylogenetically older anoxygenic phototrophic bacteria that oxidize ferrous iron were responsible for the deposition of Archaean banded iron formations³⁰. In addition, the production of extreme ^{13}C -depleted organic matter in a pre-oxic environment would favour the presence of anaerobic¹⁴ rather than aerobic¹³ methanotrophic microbes. Our results eliminate the prime source of evidence for oxygenic photosynthesis before 2.5 Gyr ago^{4–6} and the ~ 300 Myr delay in oxygen accumulation^{27,28}, rendering permissive models that link the emergence of cyanobacteria with an immediate rise of atmospheric oxygen and subsequent extreme glaciations³.

METHODS SUMMARY

Polished thin sections were prepared from drill core samples of the Roy Hill Shale Member (Fortescue Group) and examined by optical and scanning electron microscopes. Isotopic measurements were performed using the Cameca NanoSIMS 50 ion microprobe at the University of Western Australia. A ~ 1 pA Cs^+ primary ion beam was rastered across $5 \times 5 \mu\text{m}$ areas of the sample surface. The $^{12}\text{C}^-$ and $^{13}\text{C}^-$ secondary ions were recorded simultaneously on electron multipliers. Carbon isotope ratios were determined from the total number of $^{12}\text{C}^-$ and $^{13}\text{C}^-$ counts recorded during each analysis, with corrections for electron-multiplier dead-time and the effects of quasi-simultaneous secondary ion arrivals (QSA). Measurements of kerogen and pyrobitumen in the sample were bracketed between measurements of the K-1 carbon standard under identical analytical conditions, and converted to $\delta^{13}\text{C}$ values normalized to the K-1 standard ($\delta^{13}\text{C}_{\text{PDB}} = -29.1\text{‰}$).

Full Methods and any associated references are available in the online version of the paper at www.nature.com/nature.

Received 13 April; accepted 28 August 2008.

1. Bekker, A. *et al.* Dating the rise of atmospheric oxygen. *Nature* **427**, 117–120 (2004).
2. Canfield, D. E. The early history of atmospheric oxygen. *Annu. Rev. Earth Planet. Sci.* **33**, 1–36 (2005).

3. Kopp, R. E., Kirschvink, J. L., Hilburn, I. A. & Nash, C. Z. The Paleoproterozoic snowball Earth: a climate disaster triggered by the evolution of oxygenic photosynthesis. *Proc. Natl Acad. Sci. USA* **102**, 11131–11136 (2005).
4. Brocks, J. J., Logan, G. A., Buick, R. & Summons, R. E. Archean molecular fossils and the early rise of eukaryotes. *Science* **285**, 1033–1036 (1999).
5. Brocks, J. J., Buick, R., Logan, G. A. & Summons, R. E. Composition and syngeneity of molecular fossils from the 2.78 to 2.45 billion-year-old Mount Bruce Supergroup, Pilbara Craton, Western Australia. *Geochim. Cosmochim. Acta* **67**, 4289–4319 (2003).
6. Brocks, J. J., Buick, R., Summons, R. E. & Logan, G. A. A reconstruction of Archean biological diversity based on molecular fossils from the 2.78 to 2.45 billion-year-old Mount Bruce Supergroup, Hamersley Basin, Western Australia. *Geochim. Cosmochim. Acta* **67**, 4321–4335 (2003).
7. Summons, R. E., Jahnke, L. L., Hope, J. M. & Logan, G. A. 2-Methylhopanoids as biomarkers for cyanobacterial oxygenic photosynthesis. *Nature* **400**, 554–557 (1999).
8. Hayes, J. M., Kaplan, I. R. & Wedeking, K. W. in *Earth's Earliest Biosphere: Its Origin and Evolution* (ed. Schopf, J. W.) 93–134 (Princeton Univ. Press, 1983).
9. Rasmussen, B., Fletcher, I. R. & Sheppard, S. Isotopic dating of the migration of a low-grade metamorphic front during orogenesis. *Geology* **33**, 773–776 (2005).
10. Knoll, A. H., Javaux, E. J., Hewitt, D. & Cohen, P. Eukaryotic organisms in Proterozoic oceans. *Phil. Trans. R. Soc. B* **361**, 1023–1038 (2006).
11. Hofmann, H. J. Precambrian microflora, Belcher Islands, Canada: Significance and systematics. *J. Paleontol.* **50**, 1040–1073 (1976).
12. Brocks, J. J., Grosjean, E. & Logan, G. A. Assessing biomarker syngeneity using branched alkanes with quaternary carbon (BAQCs) and other plastic contaminants. *Geochim. Cosmochim. Acta* **72**, 871–888 (2008).
13. Hayes, J. M. in *Early Life on Earth* (ed. Bengtson, S.) 220–236 (Columbia Univ. Press, 1994).
14. Hinrichs, K.-U. Microbial fixation of methane carbon at 2.7 Ga: was an anaerobic mechanism possible? *Geochem. Geophys. Geosyst.* **3**, 1–10 (2002).
15. Hoefs, J. *Stable Isotope Geochemistry* 158 (Springer, 2004).
16. Fletcher, I. R., Kilburn, M. R. & Rasmussen, B. NanoSIMS μm -scale in situ measurement of $^{13}\text{C}/^{12}\text{C}$ in early Precambrian organic matter, with permil precision. *Int. J. Mass Spec.* (in the press).
17. Rasmussen, B. Evidence for pervasive petroleum generation and migration in 3.2 and 2.63 billion-year old shales. *Geology* **33**, 497–500 (2005).
18. Smith, R. E., Perdrix, J. L. & Parks, T. C. Burial metamorphism in the Hamersley Basin, Western Australia. *J. Petrol.* **23**, 75–102 (1982).
19. Des Marais, D. J. in *Stable Isotope Geochemistry* (eds Valley, J. W. & Cole, D. R.) 555–578 (Reviews in Mineralogy and Geochemistry, Vol. 43, Mineralogical Society of America, 2001).
20. Crick, I. H., Boreham, C. J., Cook, A. C. & Powell, T. G. Petroleum geology and geochemistry of middle Proterozoic McArthur Basin, northern Australia II: assessment of source rock potential. *Am. Assoc. Petrol. Geol. Bull.* **72**, 1495–1514 (1988).
21. Summons, R. E., Powell, T. G. & Boreham, C. J. Petroleum geology and geochemistry of the middle Proterozoic McArthur Basin, northern Australia: III. Composition of extractable hydrocarbons. *Geochim. Cosmochim. Acta* **52**, 1747–1763 (1988).
22. Hunt, J. M. *Petroleum Geochemistry and Geology* (Freeman, 1995).
23. Rasmussen, B., Fletcher, I. R., Muhling, J. R., Thorne, W. S. & Broadbent, G. C. Prolonged history of episodic fluid flow in giant hematite ore bodies: Evidence from in situ U-Pb geochronology of hydrothermal xenotime. *Earth Planet. Sci. Lett.* **258**, 249–259 (2007).
24. Sherman, L. S., Waldbauer, J. R. & Summons, R. E. Improved methods for isolating and validating indigenous biomarkers in Precambrian rocks. *Org. Geochem.* **38**, 1987–2000 (2007).
25. Dutkiewicz, A., Volk, H., George, S. C., Ridley, J. & Buick, R. Biomarkers from Huronian oil-bearing fluid inclusions: An uncontaminated record of life before the Great Oxidation Event. *Geology* **34**, 437–440 (2007).
26. George, S. C., Volk, H., Dutkiewicz, A., Ridley, J. & Buick, R. Preservation of hydrocarbons and biomarkers in oil trapped inside fluid inclusions for >2 billion years. *Geochim. Cosmochim. Acta* **72**, 844–870 (2008).
27. Kump, L. R. & Barley, M. E. Increased subaerial volcanism and the rise of atmospheric oxygen 2.5 billion years ago. *Nature* **448**, 1033–1036 (2007).
28. Goldblatt, C., Lenton, T. M. & Watson, A. J. Bistability of atmospheric oxygen and the Great Oxidation. *Nature* **443**, 683–686 (2006).
29. Anbar, A. D. *et al.* A whiff of oxygen before the Great Oxidation Event? *Science* **317**, 1903–1906 (2007).
30. Konhauser, K. O. *et al.* Could bacteria have formed the Precambrian banded iron formations? *Geology* **30**, 1079–1082 (2002).

Supplementary Information is linked to the online version of the paper at www.nature.com/nature.

Acknowledgements We thank S. Bengtson, G. A. Logan, J. R. Muhling, S. Revets and S. Sheppard for discussion and comments; and A. C. Cook for organic reflectivity measurements. We acknowledge the facilities of the Australian Microscopy and Microanalysis Research Facility at the Centre for Microscopy, Characterisation and Analysis, University of Western Australia, a facility funded by the University, State and Commonwealth Governments.

Author Information Reprints and permissions information is available at www.nature.com/reprints. Correspondence and requests for materials should be addressed to B.R. (B.Rasmussen@curtin.edu.au).

METHODS

Samples and sample preparation. Organic-rich shale from the Roy Hill Shale Member (Fortescue Group) was sampled from three drill cores—WRL-1 (22° 11.7' S, 118° 12.6' E), DDH 186 (22° 24' S, 117° 55' E) and FVG-1 (22° 33' S, 119° 30' E)—in the southern Pilbara Craton, Western Australia. Polished thin sections of the shale were prepared and examined by optical microscopy and scanning electron microscopy. Areas containing suitably large masses of organic matter were drilled out as 3-mm discs and set into 10-mm epoxy resin mounts with similar discs containing the K-1 standard. The mounts were coated with gold to provide electrical conductivity across non-conductive matrix minerals.

Analytical procedures. *In situ* isotopic measurements were performed using the Cameca NanoSIMS 50 ion microprobe at the University of Western Australia. Further information on the analytical procedures is given in ref. 16. All analyses were obtained by rastering a ~ 1 pA Cs^+ primary ion beam across 5×5 μm areas of the sample. The secondary ion species $^{12}\text{C}^-$, $^{13}\text{C}^-$, $^{16}\text{O}^-$ and $^{12}\text{C}^{14}\text{N}^-$ were recorded simultaneously by electron multipliers. The regions of interest were located using real-time secondary electron and $^{12}\text{C}^{14}\text{N}^-$ ion imaging. The instrument was tuned to achieve high mass resolution to separate the isobaric interference of $^{12}\text{C}^{14}\text{H}^-$ from $^{13}\text{C}^-$. For most analyses, a $^{12}\text{C}^-$ ion image acquired after the analysis was used to determine coverage (p of ref. 16) of the analyte in the rastered area. However, for analytical sessions 4 and 5, p was determined (with poorer precision) from subsequent $^{12}\text{C}^-$ images of a small selection of the original analysis areas, scanning electron microscope images and count rates. This is a major contributor to the overall uncertainties in some of the data from session 4. The $^{16}\text{O}^-$ signal was used to record supplementary images of the sample/matrix distribution. Taking images after analyses also allowed a check for local (that is, within the analysis raster area) sample charging. One analysis was rejected on this basis.

Interspersed analyses of the in-house K-1 carbon standard ($\delta^{13}\text{C}_{\text{PDB}} = -29.1\text{‰}$; ref. 16) were used to correct for drift in recorded ratios and to determine absolute $\delta^{13}\text{C}_{\text{PDB}}$ values. Data were collected in ten analytical sessions (Supplementary Table 1) over four months. Raw $^{13}\text{C}/^{12}\text{C}$ ratios were corrected for electron multiplier dead-time, and corrected for QSA by determining the primary-to-secondary ion ratio for each measurement and applying the first-order equation of ref. 31. Where necessary, the dead-time and QSA corrections were modified to account for incomplete coverage (ref. 16). Because there is some question concerning the general validity of the QSA model^{32,33}, we have recalculated the data using the empirical QSA factors for carbon from ref. 33 (data not shown). This increases the final $\delta^{13}\text{C}_{\text{PDB}}$ values for low-count-rate analyses, but only several of the vein analyses with low count rates increase by $>5\text{‰}$. For the pyrobitumen and kerogen data, the average shift is $<2\text{‰}$ and there is no significant change in the data distributions.

All the data are plotted session-by-session in Supplementary Fig. 1, and are listed in Supplementary Table 2. The uncertainties shown for sample $\delta^{13}\text{C}$ include the 1σ random statistical components from internal precision (the greater of Gaussian counting precision and block-to-block reproducibility), scatter around the K-1 standard regression in excess of the reproducibility expected from internal precision, and the estimated uncertainty in p . A notional systematic uncertainty in the QSA model ($\pm 10\%$ of the QSA correction) has been added linearly to the statistical uncertainty. Uncertainties in the mean values and slopes of the K-1 regressions (generally $<1\text{‰}$ total) and the absolute value (0.24‰) have not been added.

31. Slodzian, G., Chaintreau, M., Dennebouy, R. & Rousse, G. Precise *in situ* measurements of isotopic abundances with pulse counting of sputtered ions. *Eur. Physical J. Appl. Physics* **14**, 199–232 (2001).
32. Slodzian, G., Hillion, F., Stadermann, F. J. & Zinner, E. QSA influences on isotopic ratio measurements. *Appl. Surf. Sci.* **231–232**, 874–877 (2004).
33. Hillion, F., Kilburn, M. R., Hoppe, P., Messenger, S. & Weber, P. K. The effect of QSA on S, C, O and Si isotopic ratio measurements. *Geochim. Cosmochim. Acta* **72**, A377 (2008).

A bizarre Jurassic maniraptoran from China with elongate ribbon-like feathers

Fucheng Zhang¹, Zhonghe Zhou¹, Xing Xu¹, Xiaolin Wang¹ & Corwin Sullivan¹

Recent coelurosaurian discoveries have greatly enriched our knowledge of the transition from dinosaurs to birds, but all reported taxa close to this transition are from relatively well known coelurosaurian groups^{1–3}. Here we report a new basal avialan, *Epidexipteryx hui* gen. et sp. nov., from the Middle to Late Jurassic of Inner Mongolia, China. This new species is characterized by an unexpected combination of characters seen in several different theropod groups, particularly the Oviraptorosauria. Phylogenetic analysis shows it to be the sister taxon to *Epidendrosaurus*^{4,5}, forming a new clade at the base of Avialae⁶. *Epidexipteryx* also possesses two pairs of elongate ribbon-like tail feathers, and its limbs lack contour feathers for flight. This finding shows that a member of the avialan lineage experimented with

integumentary ornamentation as early as the Middle to Late Jurassic, and provides further evidence relating to this aspect of the transition from non-avian theropods to birds.

Theropoda Marsh 1881

Coelurosauria Huene 1914

Maniraptora Gauthier 1986

Avialae Gauthier 1986 (Padian, 2004)

Scansoriopterygidae Czerkas et Yuan 2002

Epidexipteryx hui gen. et sp. nov.

Etymology. *Epidexi* (Greek): display; *pteryx* (Greek): wing, feather; *hui*, in honour of the late young palaeontologist Yaoming Hu, who

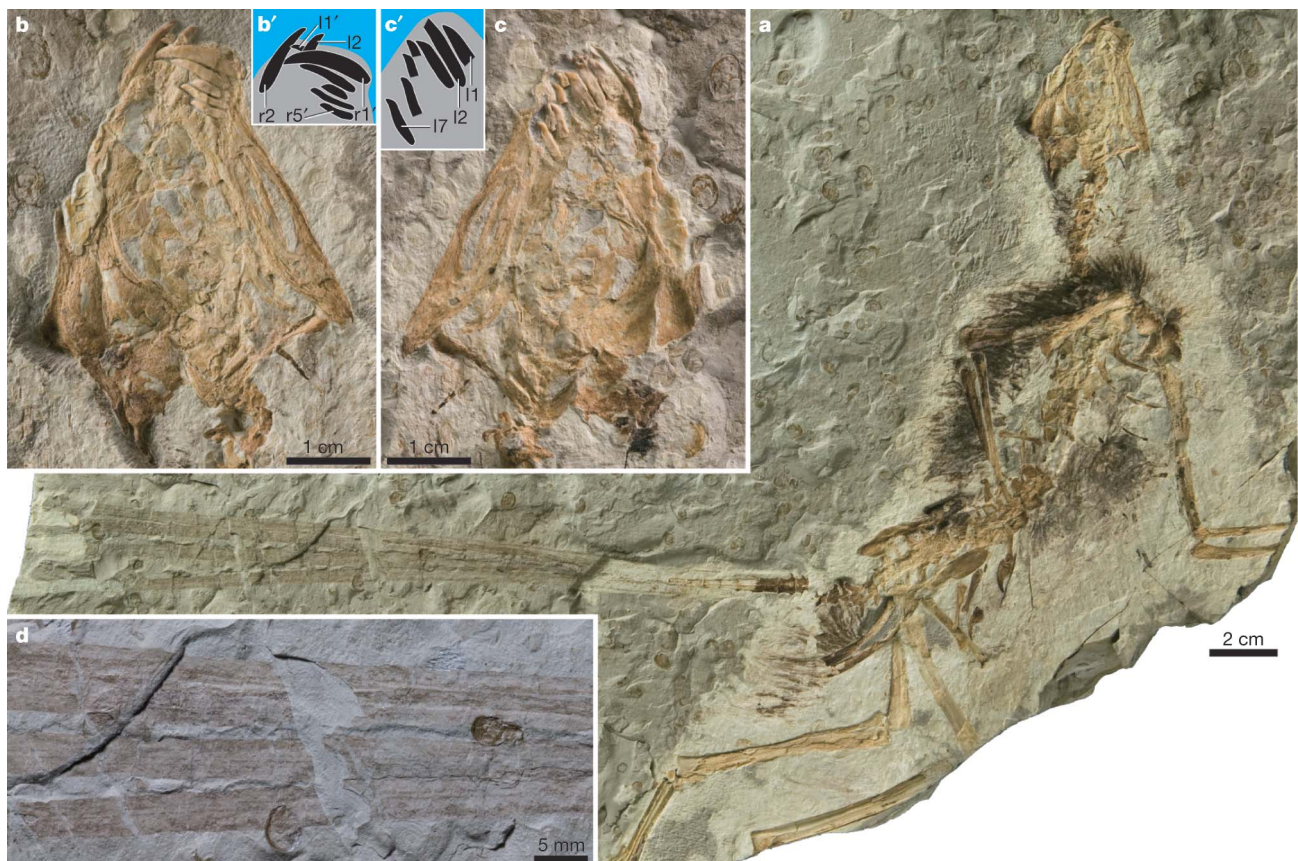


Figure 1 | *Epidexipteryx hui* gen. et sp. nov., IVPP V15471, main slab and close-up photos. **a**, Main slab; **b**, **c**, skull in main slab (**b**) and counterslab (**c**); **d**, four elongate ribbon-like tail feathers; **b'**, **c'**, line drawings of **b** and

c, respectively. Abbreviations: l1, l2 and l7, 1st, 2nd and 7th left teeth of upper jaw; l1', r1' and r5', 1st left, 1st right and 5th right teeth of lower jaw; l2 and r2, 2nd left and right teeth of upper jaw.

¹Laboratory of Evolutionary Systematics of Vertebrates, Institute of Vertebrate Paleontology and Paleoanthropology, Chinese Academy of Sciences, PO Box 643, Beijing 100044, China.

contributed significantly to the study of Mesozoic mammals from China. Generic name pronounced 'ep-id-ecks-IP-ter-icks'.

Holotype. A feathered pigeon-sized skeleton, preserved on part and counterpart slabs, and housed at the Institute of Vertebrate Paleontology and Paleoanthropology, Chinese Academy of Sciences, collection number IVPP V15471 (Fig. 1; see Supplementary Information).

Locality and horizon. Daohugou, Ningcheng County, Inner Mongolia, north China. The age of the Daohugou sediments is contentious, with possible dates ranging from Middle Jurassic⁷ to Early Cretaceous. However, published radioisotopic dating results span a narrower range from 152 to 168 Myr (Middle to Late Jurassic)^{8–10}.

Diagnosis. Medium-sized avialan with four elongate ribbon-like tail feathers (ETFs), highly procumbent and significantly enlarged anterior teeth, and a distally tapering pygostyle-like structure formed by ten unfused caudals at the end of the tail (Figs 1 and 2; see Supplementary Information). Differs significantly from *Epidendrosaurus*, the only other known scansoriopterygid, in caudal morphology (tail 70% of trunk length in *Epidexipteryx*, compared with more than 300% in *Epidendrosaurus*; 16 caudal vertebrae in *Epidexipteryx*, compared with

more than 40 in *Epidendrosaurus*; caudal prezygapophyses reduced in *Epidexipteryx* but significantly elongated in *Epidendrosaurus*).

Description and comparisons. *Epidexipteryx* is estimated to be 164 g in body mass (see Supplementary Information), smaller than most other basal avialans^{3,11}. The holotype probably represents a subadult individual, because the ends of some of the long bones seem imperfectly ossified.

As in oviraptorosaurs¹², the skull is high in lateral view (height about 60% of length), the external naris is positioned high on the snout, and the parietal is proportionally long. The teeth of both the upper and lower jaws are highly procumbent, a feature previously known only in the ceratosaurian *Masiakasaurus* among theropods¹³. Furthermore, the anterior teeth are much larger than the posterior ones, as in basal oviraptorosaurs¹², basal therizinosaur¹⁴ and probably *Epidendrosaurus*^{4,5}. There are probably 9 cervicals and 14 thoracic vertebrae, and the synsacrum is composed of 7 vertebrae. The caudal series is much shorter than in non-avian theropods or in other basal avialans. The anterior six caudal vertebrae are proportionally short and wide. The posterior ten caudals bear no transverse

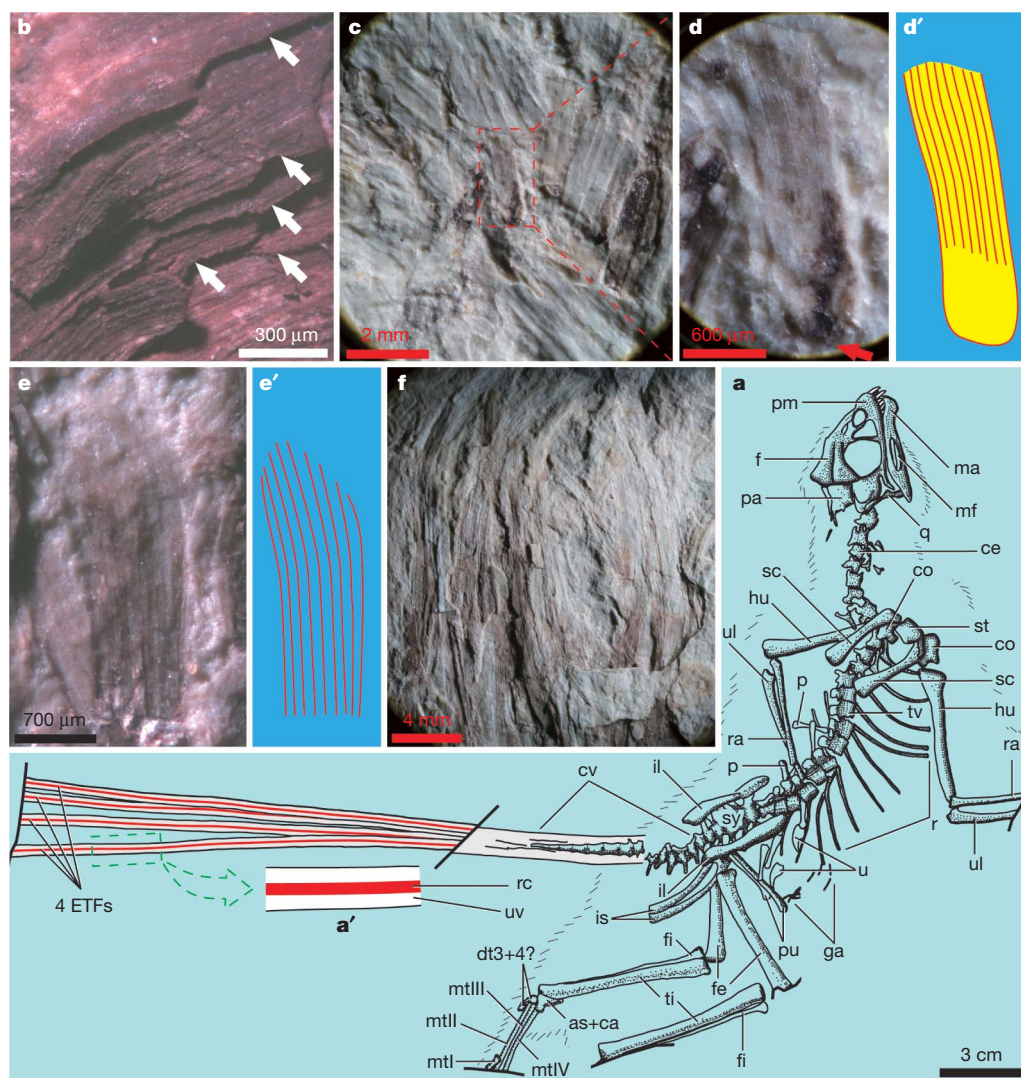


Figure 2 | Line drawings and close-up photographs of *Epidexipteryx hui* gen. et sp. nov. **a**, Skeleton and feather outline, based on both main slab and counterslab, showing that each shafted feather is formed by central rachis and two unbranched vanes (**a'**). **b**, **d**, **d'**, Proximal regions of non-shafted feathers; barbs are parallel and closely united as an unbranched membranous structure (**d**, **d'**), vanes are either layered, indicated by white arrows (**b**), or arranged irregularly (**c**). The red arrow indicates the proximal end of the feather (**d**). **e**, **e'**, **f**, Distal regions of non-shafted feathers, in which

barbs appear loosely parallel. Abbreviations: as+ca, astragalus and calcaneum; ce, cervical vertebrae; co, coracoid; cv, caudal vertebrae; dt3+4, distal tarsals 3 and 4; f, frontal; fe, femur; fi, fibula; ga, gastalia; hu, humerus; il, ilium; is, ischium; ma, mandible; mtlI–IV, metatarsals I–IV; p, phalanges or metacarpals; pa, parietal; pm, premaxilla; pu, pubis; q, quadrate; r, ribs; ra, radius; rc, rachis; sc, scapula; st, sternum; ti, tibia; tv, thoracic vertebrae; u, ungual phalanges; ul, ulna; uv, unbranched vane.

processes. They form a structure similar to the elongated, incipient pygostyle in some basal birds^{15,16} but are not fused to each other (Figs 1a and 2a; see Supplementary Information).

The partly preserved sternum is small and convex anteriorly, and seems to comprise two incompletely fused sternal plates, as in the primitive bird *Jeholornis*¹⁷. The scapula is significantly shorter than the humerus, as in some derived maniraptorans, and the coracoid is sub-rectangular. The pelvis has an unexpected combination of features among theropods, as in *Epidendrosaurus*^{4,5}. The ilium is bird-like in having a long preacetabular process with a strongly convex anterior margin, but differs from the ilia of most non-avian theropods in having a small pubic peduncle. Unusually among theropods, the straight pubis is shorter than the ischium and is significantly shorter than the femur. It is anteroventrally oriented and lacks a pubic boot. The posteriorly curved ischium is laterally compressed, gradually widens towards the distal end, and lacks an obturator process. The humerus is about same length as the femur, proportionally longer than in most other basal avialans. The ulna is posteriorly bowed and the manus is significantly elongated (see Supplementary Information) as in birds and other derived theropods^{18–22}. The curvature of the manual claws falls within the range known for the pedal claws of ground-based foraging birds (see Supplementary Information). The femur is about 160% the length of the metatarsus, and 80% the length of the tibia (Figs 1a and 2a; see Supplementary Information).

Phylogeny and affinity. Phylogenetic analysis indicates that *Epidexipteryx* and *Epidendrosaurus* form a monophyletic Scansoriopterygidae (see Supplementary Information), representing a bizarre lineage at the base of the Avialae (Fig. 3; see Supplementary Information).

Although possessing many derived features seen in birds, including a humerus as long as the femur, a long preacetabular process of the ilium with a strongly convex margin, and many other features, *Epidexipteryx* and *Epidendrosaurus* also show some striking similarities to oviraptorosaurs¹² and to a lesser degree therizinosauroids^{14,21}, including a short and high skull, an external naris positioned high on the snout, an anteriorly downturned and strongly dorsally convex mandible, a large external mandibular fenestra, and enlarged anterior

teeth. Furthermore, some pelvic features, such as a proportionally very short pubis and a distally widening ischium, are not known in any other theropod. The bizarre appearance of scansoriopterygids indicates that morphological disparity among maniraptorans close to the origin of birds is higher than has previously been assumed, and underscores the importance of Jurassic theropods for understanding avian origins.

Integument. The integument bears feather-like structures of two types, ETFs and non-ETFs, which are roughly comparable to shafted and non-shafted feathers, respectively²³. The distal part of each non-ETF is composed of filamentous parallel barbs (Fig. 2e, e', f), similar to the condition seen in the non-shafted feathers of other feathered dinosaurs and primitive birds^{18,22–25}. However, the free distal barbs of *Epidexipteryx* arise from the edge of a membranous structure (Fig. 2b, c, d, d'), an arrangement that has never previously been reported.

The four ETFs are tightly attached to the last ten caudal segments (Figs 1a and 2a). These feathers are incomplete distally, but the preserved part of each ETF is identical to the corresponding structure in some primitive birds^{16,26–28}, for example in having a similar central rachis and unbranched vanes (Fig. 1a, d and 2a, a'; see Supplementary Information). Elongate tail feathers are a normal component of the ornamental plumage in extant birds. In contrast to other feather types, ornamental plumage is used to send visual signals that are essential to a wide range of avian behaviour patterns, particularly relating to courtship²⁹. For example, experiments have shown that, in some species, males with long tail plumage attract more mates than their short-tailed counterparts³⁰. It is highly probable that the ETFs of *Epidexipteryx* similarly had display as their primary function, rather than serving other purposes such as flight or insulation²⁹. Indeed, pennaceous feathers suitable for flight are not present in *Epidexipteryx*, even though the bones and integument are well preserved. Because pennaceous feathers are commonly encountered in other feathered maniraptorans^{2,21,22,25}, their absence constitutes another highly unusual feature of *Epidexipteryx*, as well as strongly implying that this taxon was non-volant. *Epidexipteryx* is the oldest and most phylogenetically basal theropod known to possess display feathers, indicating that basal avialans experimented with integumentary ornament as early as the Middle to Late Jurassic. Unless *Epidexipteryx* is interpreted as secondarily flightless, the absence of pennaceous limb feathers in this taxon suggests that display feathers appeared before airfoil feathers and flight ability in basal avialan evolution.

Received 14 June; accepted 19 September 2008.

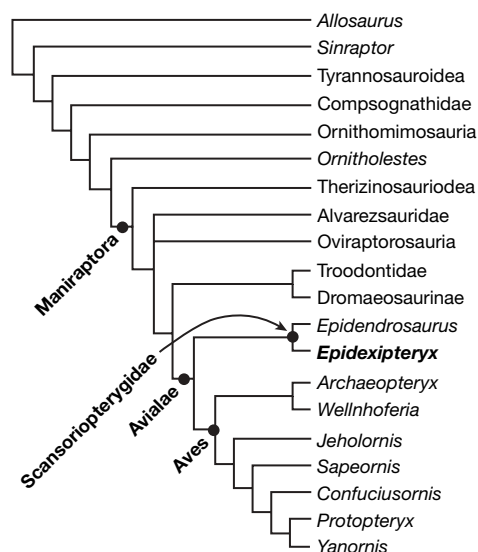


Figure 3 | Phylogenetic relationships of *Epidexipteryx hui* gen. et sp. nov. The cladogram is simplified from the strict consensus of nine most parsimonious trees (tree length 1,255; consistency index 0.35; retention index 0.75; see Supplementary Information). Scansoriopterygidae is defined as the least inclusive clade including *Epidendrosaurus* and *Epidexipteryx*, Avialae as the most inclusive clade including *Vultur gryphus* but not *Deinonychus antirrhopus*, and Aves as the least inclusive clade including *Archaeopteryx* and *Vultur gryphus*.

1. Makovicky, P. J. et al. The earliest dromaeosaurid theropod from South America. *Nature* **437**, 1007–1011 (2005).
2. Xu, X. & Norell, M. A. Non-avian dinosaur fossils from the Lower Cretaceous Jehol Group of western Liaoning, China. *Geol. J.* **41**, 419–438 (2006).
3. Turner, A. H. et al. A basal dromaeosaurid and size evolution preceding avian flight. *Science* **317**, 1378–1381 (2007).
4. Zhang, F.-C. et al. A juvenile coelurosaurian theropod from China indicates arboreal habits. *Naturwissenschaften* **89**, 394–398 (2002).
5. Czerkas, S. A. & Yuan, C. in *Feathered Dinosaurs and the Origin of Flight* (ed. Czerkas, S. J.) 63–95 (The Dinosaur Museum, Blanding, 2002).
6. Padian, K. in *The Dinosauria* 2nd edn (eds Weishampel, D. B., Dodson, P., Osmolska, H.) 210–231 (Univ. of California Press, Berkeley, 2004).
7. Gao, K.-Q. & Ren, D. Radiometric dating of ignimbrite from Inner Mongolia provides no indication of a post-Middle Jurassic age for the Daohugou Beds. *Acta Geol. Sin.* **80**, 42–45 (2006).
8. Chen, W. et al. Isotope geochronology of the fossil-bearing beds in the Daohugou area, Ningcheng, Inner Mongolia. *Geol. Bull. Chin.* **23**, 1165–1169 (2004).
9. He, H.-Y. et al. ⁴⁰Ar/³⁹Ar dating of ignimbrite from Inner Mongolia, northeastern China, indicates a post-Middle Jurassic age for the overlying Daohugou Bed. *Geophys. Res. Lett.* **31**, L20609, doi:10.1029/2004GL020792 (2004).
10. Liu, Y.-X., Liu, Y.-Q. & Zhang, H. LA-ICPMS zircon U-Pb dating in the Jurassic Daohugou Beds and correlative strata in Ningcheng of Inner Mongolia. *Acta Geol. Sin.* **80**, 733–742 (2006).
11. Christiansen, P. & Fariña, R. A. Mass prediction in theropod dinosaurs. *Hist. Biol.* **16**, 85–92 (2004).
12. Xu, X. et al. An unusual oviraptorosaurian dinosaur from China. *Nature* **419**, 291–293 (2002).

13. Sampson, S. D., Carrano, M. T. & Forster, C. A. A bizarre predatory dinosaur from Madagascar: implications for the evolution of Gondwanan theropods. *Nature* **409**, 504–505 (2001).
14. Kirkland, J. I. *et al.* A primitive therizinosauroid dinosaur from the Early Cretaceous of Utah. *Nature* **435**, 84–87 (2005).
15. Hou, L.-H. & Chen, P.-J. *Liaoxiornis delicatus* gen. et sp. nov., the smallest Mesozoic bird. *Chin. Sci. Bull.* **44**, 834–838 (1999).
16. Zhang, F.-C., Zhou, Z.-H. & Benton, M. J. A primitive confuciusornithid bird from China and its implications for early avian flight. *Sci. China D* **51**, 625–639 (2008).
17. Zhou, Z. & Zhang, F. A long-tailed, seed-eating bird from the Early Cretaceous of China. *Nature* **418**, 405–409 (2002).
18. Zhang, F.-C., Zhou, Z.-H. & Hou, L.-H. in *The Jehol Biota* (eds Chang, M.-M., Chen, P.-J., Wang, Y.-Q. & Wang, Y.) 129–149 (Shanghai Sci. Technol. Publ., 2003).
19. Zhou, Z., Barrett, P. M. & Hilton, J. An exceptionally preserved Lower Cretaceous ecosystem. *Nature* **421**, 807–814 (2003).
20. Zhou, Z.-H. & Zhang, F.-C. Anatomy of the primitive bird *Sapeornis chaoyangensis* from the Early Cretaceous of Liaoning, China. *Can. J. Earth Sci.* **40**, 731–737 (2003).
21. Weishampel, D. B., Dodson, P. & Osmólska, H. *The Dinosauria* 2nd edn (Univ. of California Press, Berkeley, 2004).
22. Xu, X. in *Originations, Radiations and Biodiversity Changes* (eds Rong, J.-Y. *et al.*) 627–642; 927–930 (Sci. Press, Beijing, 2006).
23. Zhang, F.-C. & Zhou, Z.-H. in *Originations, Radiations and Biodiversity Changes* (eds Rong, J.-Y. *et al.*) 611–625; 923–925 (Sci. Press, Beijing, 2006).
24. Prum, R. O. & Brush, A. H. The evolutionary origin and diversification of feathers. *Q. Rev. Biol.* **77**, 261–295 (2002).
25. Xu, X. Scales, feathers and dinosaurs. *Nature* **440**, 287–288 (2006).
26. Chiappe, L. M. *et al.* Anatomy and systematics of the Confuciusornithidae (Theropoda: Aves) from the Late Mesozoic of Northeastern China. *Bull. Am. Mus. Nat. Hist.* **242**, 1–89 (1999).
27. Zhang, F.-C. & Zhou, Z.-H. A primitive enantiornithine bird and the origin of feathers. *Science* **290**, 1955–1959 (2000).
28. Zheng, X.-T., Zhang, Z.-H. & Hou, L.-H. A new enantiornithine bird with four long rectrices from the Early Cretaceous of northern Hebei, China. *Acta Geol. Sin.* **81**, 703–708 (2007).
29. Gill, F. B. *Ornithology* 2nd edn (Freeman, 1995).
30. Andersson, M. Female choice selects for extreme tail length in a widowbird. *Nature* **299**, 818–820 (1982).

Supplementary Information is linked to the online version of the paper at www.nature.com/nature.

Acknowledgements We thank F. Jin for discussion, Y. Li for specimen preparation, W. Gao for photography, and J. Choiniere for the use of his laptop computer. This research was funded by the National Natural Science Foundation of China, the Chinese Academy of Sciences, and Major Basic Research Projects of the Ministry of Science and Technology, China.

Author Information Reprints and permissions information is available at www.nature.com/reprints. Correspondence and requests for materials should be addressed to F.Z. (zhangfucheng@ivpp.ac.cn).

Innate immunity and intestinal microbiota in the development of Type 1 diabetes

Li Wen^{1*}, Ruth E. Ley^{2*†}, Pavel Yu. Volchkov^{3*}, Peter B. Stranges^{3,4}, Lia Avanesyan^{3,4}, Austin C. Stonebraker⁴, Changyun Hu¹, F. Susan Wong⁵, Gregory L. Szot⁶, Jeffrey A. Bluestone⁶, Jeffrey I. Gordon² & Alexander V. Chervonsky^{3,4}

Type 1 diabetes (T1D) is a debilitating autoimmune disease that results from T-cell-mediated destruction of insulin-producing β -cells. Its incidence has increased during the past several decades in developed countries^{1,2}, suggesting that changes in the environment (including the human microbial environment) may influence disease pathogenesis. The incidence of spontaneous T1D in non-obese diabetic (NOD) mice can be affected by the microbial environment in the animal housing facility³ or by exposure to microbial stimuli, such as injection with mycobacteria or various microbial products^{4,5}. Here we show that specific pathogen-free NOD mice lacking MyD88 protein (an adaptor for multiple innate immune receptors that recognize microbial stimuli) do not develop T1D. The effect is dependent on commensal microbes because germ-free MyD88-negative NOD mice develop robust diabetes, whereas colonization of these germ-free MyD88-negative NOD mice with a defined microbial consortium (representing bacterial phyla normally present in human gut) attenuates T1D. We also find that MyD88 deficiency changes the composition of the distal gut microbiota, and that exposure to the microbiota of specific pathogen-free MyD88-negative NOD donors attenuates T1D in germ-free NOD recipients. Together, these findings indicate that interaction of the intestinal microbes with the innate immune system is a critical epigenetic factor modifying T1D predisposition.

Toll-like receptors (TLRs) are innate pattern-recognition receptors⁶ involved in host defence⁷, control over commensal bacteria and the maintenance of tissue integrity^{8,9}. The role of the involvement of TLRs in organ-specific autoimmunity is not clear. The MyD88 adaptor protein is used by multiple TLRs (except TLR4 and TLR3, which can or must signal by means of TRIF (Toll/IL-1 receptor (TIR)-domain-containing adapter-inducing interferon- β), respectively) and other receptors (for example, interleukin-1 receptor, IL-1R). To test the contributions of these receptors to development of T1D in NOD mice, we examined the effect of *Myd88* gene disruption on disease incidence and progression. Two MyD88 knockout (KO) NOD strains were independently derived at the Jackson Laboratory and at Yale University. Both showed a loss of diabetes development during 30-week observation periods when housed under normal specific pathogen-free (SPF) conditions with continuous monitoring for the presence of mouse pathogens (Fig. 1). Because multiple TLRs signal through the MyD88 adaptor, follow-up studies were conducted in NOD mice lacking individual TLRs (TLR^{KO}). We found that TLR2 and TLR4 (as well as TLR3, data not shown) were dispensable for development of T1D (or protection from it by complete Freund's adjuvant; Supplementary Fig. 1) when

deleted individually, in contrast to the effect of complete protection from diabetes associated with loss of MyD88 (Fig. 1).

These findings suggested that signalling through receptors that use the MyD88 adaptor is critical for T1D development, and that the autoimmune T cells would probably be affected systemically in MyD88^{KO} NOD mice. Two types of experiments were performed to examine this hypothesis. First, splenocytes from pre-diabetic MyD88-sufficient and MyD88^{KO} NOD mice were transferred into immunodeficient NOD/SCID (severe combined immunodeficient) animals. All recipients of control MyD88-sufficient splenocytes ($n = 5$), and four out of five recipients of MyD88^{KO} NOD splenocytes, became diabetic, arguing against profound systemic tolerance of T cells in MyD88^{KO} NOD mice. Second, an enzyme-linked immunospot (ELISPOT) analysis of interferon- γ (IFN- γ) production by T cells in response to four peptides known to be recognized by diabetogenic T cells^{10–13} was performed (Fig. 2). T cells from spleens, mesenteric lymph nodes and pancreatic lymph nodes (MLNs and PLNs, respectively) were analysed. Spleens and MLNs of MyD88^{KO} NOD mice contained activated precursors of the diabetogenic T cells, whereas their numbers were clearly reduced in PLNs (Fig. 2a). Because individual mice vary in their responses to different peptides¹⁴, the overall reactivity to all four peptides is shown in Fig. 2a (see Supplementary Fig. 2 for primary data). The responses to a prevalent diabetes-associated peptide recognized by the 8.3-CD8⁺ T cell clone^{12,15} were found to be attenuated in the PLN of MyD88^{KO} NOD mice in a statistically significant manner (Fig. 2b). In addition, adoptively transferred carboxy-fluorescein succinimidyl

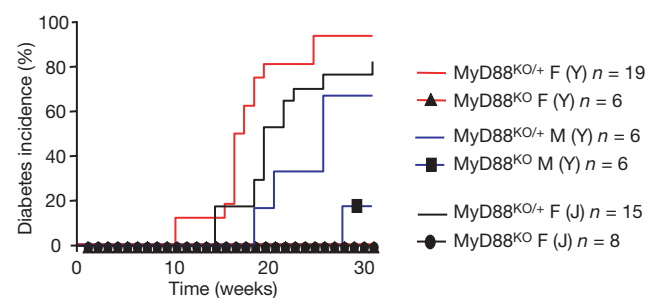


Figure 1 | MyD88-negative (MyD88^{KO}) mice are completely protected from development of type 1 diabetes. Incidence of diabetes in two independently derived MyD88^{KO} NOD and heterozygous MyD88^{KO/+} NOD stocks (J, Jackson Laboratory; Y, Yale University; 12 backcrosses to NOD). F, females; M, males; n , number of animals per group.

¹Section of Endocrinology, Yale University School of Medicine, New Haven, Connecticut 06520, USA. ²Center for Genome Sciences, Washington University School of Medicine, St Louis, Missouri 63108, USA. ³Department of Pathology, University of Chicago, Chicago, Illinois 60637, USA. ⁴The Jackson Laboratory, Bar Harbor, Maine 04609, USA. ⁵Department of Cellular and Molecular Medicine, School of Medical Science, Bristol University, Bristol, BS8 1TD, UK. ⁶Diabetes Center at the University of California San Francisco, San Francisco, California 94143, USA. [†]Present address: Department of Microbiology, Cornell University, Ithaca, New York 14850, USA.

*These authors contributed equally to this work.

ester (CFSE)-labelled naive CD4⁺ T cells from mice carrying the diabetogenic T-cell receptor BDC2.5 proliferated in the PLN but not in other (mesenteric or skin-draining) lymph nodes of the NOD mice; however, their proliferation was clearly attenuated in the PLN of MyD88^{KO} mice (Fig. 2c).

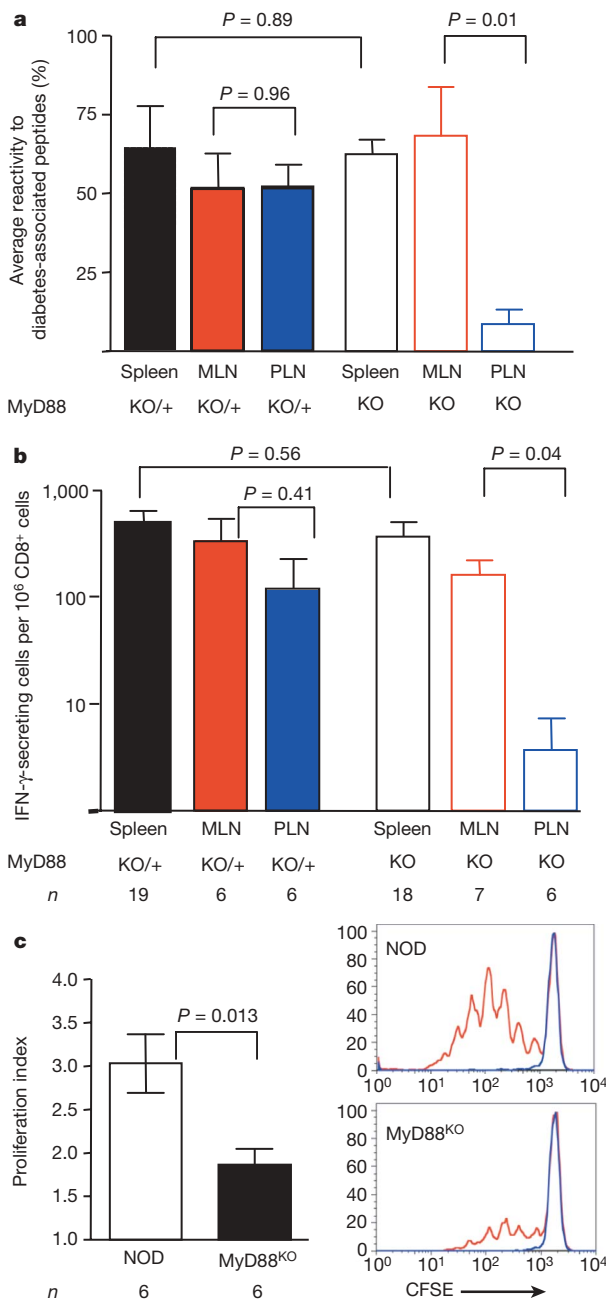


Figure 2 | MyD88 deficiency leads to local tolerance to pancreatic antigens. **a**, The overall reactivity of T cells from secondary lymphoid organs of MyD88-sufficient (filled bars) and MyD88-negative (open bars) NOD mice was calculated as a mean of the percentages of mice in the given group reacting to individual diabetes-associated peptides (see Supplementary Fig. 2c). Error bars, s.e.m. **b**, The frequency of CD8⁺ T cells producing IFN-γ in response to peptide recognized by diabetogenic clone 8.3 was determined in the spleens, MLNs and PLNs of MyD88-sufficient (filled bars) and MyD88-negative (open bars) NOD mice. Error bars, s.e.m. **c**, Proliferation of CFSE-labelled BDC2.5 CD4⁺ T cells, depleted of CD25⁺ T cells, in the PLNs of SPF NOD and MyD88^{KO} NOD mice assayed on day 3 after intravenous injection. Representative CFSE dilution profiles are shown for BDC2.5⁺-gated cells in PLNs (red) and control skin-draining lymph nodes (blue). *P* values in all experiments were determined using unpaired Student's *t* test. Error bars, s.e.m.; *n*, number of animals per group.

Because the anti-diabetogenic effect of MyD88 deficiency was localized to PLNs, it became clear that there was no systemic suppression of immune activation in SPF MyD88^{KO} NOD mice, making our initial conclusions about the requirement of MyD88 signalling for initiation of T1D an oversimplification.

PLNs drain both the pancreas and the intestine, and they are an important compartment in which islet-specific T cells are activated^{16,17}. Because MyD88 signalling could be critical for the interactions of the host with the gut microbiota, we explored the hypothesis that the T1D resistance of MyD88^{KO} NOD mice could be driven by their intestinal microbiota. First, we treated SPF MyD88^{KO} NOD mice with a broad-spectrum antibiotic (Sulfatrim) throughout their lifetime. Antibiotic-treated MyD88^{KO} NOD animals developed T1D at higher rates than untreated MyD88^{KO} NOD mice (Fig. 3a versus Fig. 1), although they did not quite reach the incidence observed in control MyD88^{KO/+} NOD mice. Thus, to fully eliminate any residual microbes, we re-derived NOD and MyD88^{KO} NOD animals as germ-free. T1D development in our germ-free MyD88-sufficient NOD mice was similar to that previously reported¹⁸ and was not notably different from that in mice raised in our SPF facilities (Fig. 3b and Supplementary Figs 3 and 4). Thus, initiation of autoimmunity is genetically programmed and not affected by the presence of microbiota in immunocompetent SPF NOD animals in high-health-standard facilities.

Most importantly, in contrast to our finding that MyD88^{KO} NOD mice raised under SPF conditions did not develop T1D, germ-free MyD88^{KO} NOD mice robustly developed diabetes (Fig. 3b and Supplementary Fig. 3). This finding clearly shows that neither IL-1R nor MyD88-dependent TLRs are required for activation of an anti-islet T-cell response (similar to MyD88^{KO}, autoimmune regulator (AIRE)-deficient mice¹⁹). The efficient T-cell priming observed in germ-free MyD88^{KO} NOD mice does not confirm a previous report

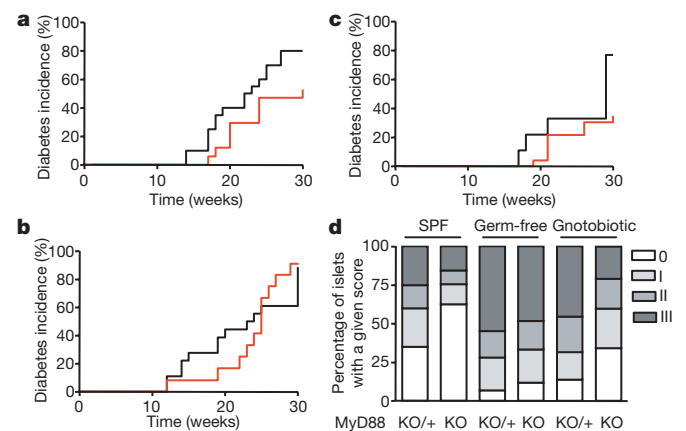


Figure 3 | MyD88-negative NOD mice are protected from diabetes by the gut microbiota. **a**, Diabetes incidence in SPF MyD88^{KO} NOD (J) females (red trace, *n* = 16) and control heterozygous MyD88^{KO/+} NOD littermates (black trace, *n* = 24) treated with a broad-spectrum antibiotic from birth. **b**, Diabetes incidence in germ-free MyD88^{KO} NOD (red trace, *n* = 12) and control MyD88^{KO/+} (black trace, *n* = 18) mice. Incidence is shown for male mice; 100% of female MyD88^{KO} NOD and MyD88^{KO/+} NOD female germ-free mice became diabetic (Supplementary Fig. 1). **c**, Diabetes incidence in gnotobiotic male MyD88^{KO} NOD (red trace, *n* = 23) and control MyD88^{KO/+} NOD (black trace, *n* = 9) mice colonized with a consortium of six bacterial strains (ASF 361, 519, 356, 492, 502 and 500; see Supplementary Information for descriptions). The incidence of diabetes in gnotobiotic MyD88^{KO} NOD mice was significantly different from the incidence in germ-free MyD88^{KO} NOD animals (*P* < 0.001) and in gnotobiotic MyD88^{KO/+} NOD mice (*P* < 0.05; Kaplan–Meier test). **d**, Histological scores of islet destruction in SPF, germ-free and ASF-colonized MyD88^{KO/+} NOD and MyD88^{KO} NOD mice. Mice in all groups were males, except for the SPF MyD88^{KO} NOD group, which included both genders.

that suggested that TLR2 signalling, which is MyD88-dependent, is required for T-cell priming in NOD mice²⁰.

To show directly that T1D development in germ-free MyD88^{KO} NOD mice was indeed a consequence of the lack of a microbiota, adult germ-free MyD88^{KO/+} NOD mice were colonized with a consortium of bacterial species contained in the altered Schaedler flora (ASF)²¹ and intercrossed. After introducing the ASF cocktail, polymerase chain reaction (PCR) assays revealed that six of the eight species colonized the animals (based on sampling of caecal contents; Supplementary Information and Supplementary Fig. 5). The ASF-colonized MyD88^{KO} NOD mice exhibited a significant reduction in the incidence of diabetes (Fig. 3c): only 34% of males became diabetic at 30 weeks of age, compared to >80% of germ-free MyD88^{KO} NOD males (Fig. 3b), whereas 70% of ASF-colonized MyD88^{KO/+} NOD males developed diabetes with kinetics similar to disease development in SPF MyD88^{KO/+} NOD mice (Fig. 3c versus Fig. 1).

A histological analysis of pancreata from SPF, germ-free and ASF-colonized MyD88^{KO} NOD mice was performed to compare the effects of the microbiota on T-cell-mediated destruction of the islets of Langerhans. The islets of SPF MyD88^{KO} NOD mice were less infiltrated compared to islets of SPF MyD88^{KO/+} NOD mice.

Moreover, germ-free MyD88^{KO} NOD mice had considerably increased islet infiltration, which was moderated by the introduction of the ASF (Fig. 3d, histological grading shown in Supplementary Fig. 6). Although, the overall effect of ASF on diabetes development was not fully penetrant, these results suggest that bacterial lineages normally present in the gut can modify T1D progression.

We found that MyD88 signalling is critical for development of T1D, and postulated that it is needed for control over component(s) of the microbiota that otherwise (in MyD88^{KO} mice) can protect against development of T1D. To test how MyD88-dependent innate immunity shapes the composition of the gut microbiota, we used a culture-independent, 16S ribosomal RNA gene-sequence-based approach to characterize the microbial communities of SPF MyD88^{KO/+} NOD and MyD88^{KO} NOD littermates. Because MyD88 deficiency affects T1D development at the early stages (Supplementary Fig. 7), experimental female mice were housed individually and killed at 8 weeks of age. DNA was isolated from their caecal contents, bacterial 16S rRNA genes were amplified by PCR, and the resulting full-length amplicons were sequenced ($n = 36$ mice; total of 7,223 16S rRNA gene sequences; average of 201 sequences per animal; average sequence length of 1,310 nucleotides).

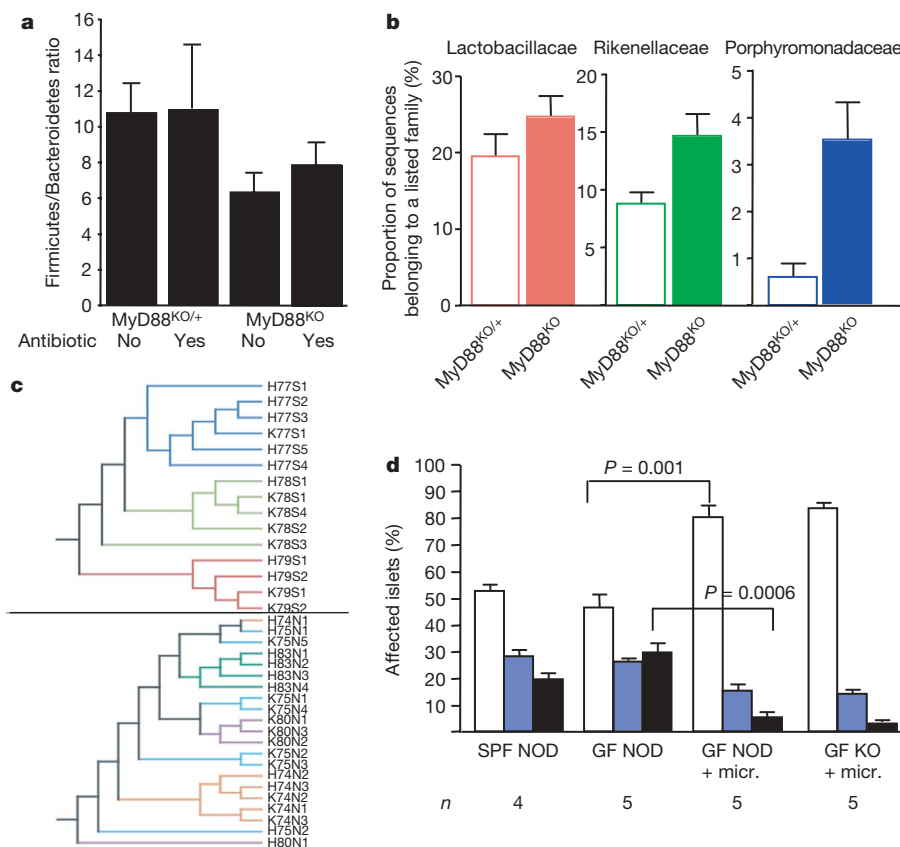


Figure 4 | MyD88 deficiency leads to specific changes in the composition of intestinal microbiota. **a**, Ratio of Firmicutes to Bacteroidetes in the caecal microbiota of MyD88^{KO/+} NOD and MyD88^{KO} NOD mice who were or were not treated with the antibiotic Sulfatrim. Mean and s.e.m. is shown. Untreated MyD88^{KO} NOD mice had, on average, a significantly lower Firmicutes/Bacteroidetes ratio than all other mice combined (one-tailed t -test, $t = -2.31$, $P = 0.013$). When comparing post-hoc the effect of Sulfatrim in MyD88^{KO} NOD mice only, no significant difference in Firmicutes/Bacteroidetes ratios was observed ($t = 0.85$, $P = 0.20$). **b**, Abundance of members of three different bacterial families in the caecal contents of MyD88^{KO/+} NOD and MyD88^{KO} NOD mice (not treated with Sulfatrim). Mean and s.e.m. Each of the three families is enriched in MyD88^{KO} NOD mice (Lactobacillaceae $t = -1.54$, $P = 0.07$; Rikenellaceae $t = 2.74$, $P = 0.007$; Porphyromonadaceae $t = 2.1$, $P = 0.03$; one-tailed

t -test). **c**, Clustering of mouse caecal bacterial communities using the unweighted UniFrac metric; $n = 7,223$ sequences. Diversity, not abundance, of bacteria was taken into consideration. Top panel, Sulfatrim-treated litters; bottom panel, untreated litters. Line colours indicate families. Each label is a mouse: H stands for MyD88^{KO/+} NOD, K stands for MyD88^{KO} NOD. The number is the common mother; S and N designate exposure to Sulfatrim or no Sulfatrim, respectively. The final number represents an individual animal. **d**, Histological examination of the pancreata of 8-week-old males from SPF NOD, germ-free (GF) NOD, as well as germ-free NOD and germ-free MyD88^{KO} NOD (KO) strains exposed from birth to microbiota (micr.) of an SPF MyD88^{KO} NOD female. The percentages (mean and s.e.m.) of affected islets with no infiltration (open bars), periinsulitis (blue bars) and true infiltration (combined grades II and III) are shown. P values were obtained using unpaired Student's t test. n , number of animals per group.

In concordance with previous findings in mice and humans^{22–24}, two bacterial divisions (phyla)—the Firmicutes and the Bacteroidetes—dominated the distal gut (caecal) microbiota of mice from all groups (80.7% and 16.9% of all sequences, respectively). The remainder of the microbiota was composed of divisions commonly encountered at lower abundance in the mouse and human gut: Verrucomicrobia, Proteobacteria, Actinobacteria and the candidate phylum TM7 (ref. 25). Furthermore, close relatives of ASF strains were detected in SPF NOD mice.

Analysis of the caecal microbiota of MyD88^{KO/+} NOD versus MyD88^{KO} NOD mice showed significant differences. Antibiotic-free MyD88^{KO} NOD mice had, on average, a significantly lower Firmicutes/Bacteroidetes ratio compared to all other groups (one-tailed *t*-test *t* = −2.31, *P* = 0.013; Fig. 4a). Antibiotic treatment of animals eliminated the statistically significant difference in Firmicutes/Bacteroidetes ratio (Fig. 4a). A change of Firmicutes/Bacteroidetes ratio may be important by itself because it can influence the efficiency of processing of otherwise indigestible complex polysaccharides in the diet^{26,27}. Diet-related changes in diabetes in germ-free NOD mice have been observed²⁸; these effects could be related to the components of the diet *per se* or attributed to the presence of microbial products in the feed.

To characterize further the changes in the gut microbiota imposed by MyD88 deficiency, 16S rRNA genes were classified taxonomically to the family level (using the Ribosomal Database Project Classifier²⁹). The proportion of sequences in each family was determined for individual mice, averaged and compared across treatments. The representation of three bacterial families was increased significantly in the microbiota of antibiotic-free SPF MyD88^{KO} NOD mice compared to the SPF NOD animals: the Lactobacillaceae (Firmicutes), Rikenellaceae and Porphyromonadaceae (both Bacteroidetes; Fig. 4b). Interestingly, the VSL3 probiotic mix, containing four species of Lactobacillaceae, affects diabetes³⁰ in NOD mice.

Gut microbial communities are known to be inherited from the mother²²; this was also the case in these experiments, where clustering of 16S rRNA genes was strongly influenced by shared mothers (Fig. 4c).

To show that the changes in the intestinal microbiota of MyD88^{KO} NOD animals were responsible for attenuation of T1D development, the newborn progeny of germ-free NOD mice were exposed to SPF MyD88^{KO} NOD females and allowed to mature to 8 weeks of age, after which time their pancreata were removed and analysed histologically (Fig. 4d). Islet infiltration was significantly reduced in germ-free NOD animals exposed to microbiota from SPF MyD88^{KO} mouse compared to germ-free NOD mice (increased percentage of intact islets (*P* = 0.001) and reduced percentage of infiltrated islets (*P* = 0.0006)).

Although the precise mechanism of induction of local tolerance by the microbiota remains to be elucidated (see Supplementary Fig. 8), the finding that the normal intestinal microbiota can alleviate progression of autoimmune diabetes in a MyD88-independent manner provides a different perspective about disease pathogenesis. Moreover, knowledge-based use of live microbial lineages or microbial products could present new therapeutic options for T1D in the future.

METHODS SUMMARY

Mice. B6 mice carrying MyD88 and TLR mutations were backcrossed 10–12 times to NOD/LtJ (at The Jackson Laboratory) or to NOD/Caj (at Yale University) mice and intercrossed to produce KO and heterozygous animals. Germ-free animals were re-derived from NOD/LtJ females impregnated by MyD88^{KO} NOD males and kept germ-free at Taconic Farms, the University of Chicago and Washington University in St Louis. ASF was introduced to germ-free MyD88^{KO} NOD mice by adding caecal contents from donor mice to sterile drinking water. Wild-type germ-free mice were colonized with microbiota from SPF MyD88^{KO} NOD animals by co-housing germ-free NOD females and newborn progeny with SPF MyD88^{KO} NOD females.

Histopathology of diabetes. Damage to the islets was scored in a blinded fashion, and graded as follows: 0, no visible infiltration; I, periinsulitis; II, insulitis with <50%; and III, insulitis with >50% islet infiltration (Supplementary Fig. 6). At least 100 islets in each group of 5 to 12 animals were scored. In microbiota transfer experiments, 20 sections per pancreas cut at 40-μm intervals (≥10 islets per section) were examined and scored (combining grades II and III).

ELISPOT analysis. 6 × 10⁵ splenocytes alone, or 2 × 10⁵ lymph node cells mixed with 4 × 10⁵ irradiated splenocytes from B6.NOD-(D17Mit21-D17Mit10)/LtJ (B6.g7) mice, per well of 96-well plates pretreated with anti-IFN-γ antibodies were incubated overnight (16–18 h) with corresponding peptides. Lymphocytes were stained with antibodies against CD4 and CD8 to calculate the frequency of peptide-specific cells per 10⁶ CD4⁺ or CD8⁺ T cells.

Sequence and phylogenetic analysis. 16S rRNA gene sequences were edited and assembled into consensus sequences using PHRED and PHRAP, aided by XplorSeq²³, and bases with a PHRAP quality score of <20 were trimmed. Sequences were aligned using the NAST online alignment tool (http://greengenes.lbl.gov/cgi-bin/nph-NAST_align.cgi), and checked for chimaeras using the online Greengenes server (http://greengenes.lbl.gov/cgi-bin/nph-bel3_interface.cgi) with a window size of 300 and using the NAST-aligned sequences³¹.

Full Methods and any associated references are available in the online version of the paper at www.nature.com/nature.

Received 18 July; accepted 8 August 2008.

Published online 21 September 2008.

- Karvonen, M., Tuomilehto, J., Libman, I. & LaPorte, R. A review of the recent epidemiological data on the worldwide incidence of type 1 (insulin-dependent) diabetes mellitus. World Health Organization DIAMOND Project Group. *Diabetologia* **36**, 883–892 (1993).
- Patterson, C. C., Dahlquist, G., Soltesz, G. & Green, A. Is childhood-onset type 1 diabetes a wealth-related disease? An ecological analysis of European incidence rates. *Diabetologia* **44** (suppl. 3), B9–B16 (2001).
- Pozzilli, P., Signore, A., Williams, A. J. & Beales, P. E. NOD mouse colonies around the world—recent facts and figures. *Immunol. Today* **14**, 193–196 (1993).
- McInerney, M. F., Pek, S. B. & Thomas, D. W. Prevention of insulinitis and diabetes onset by treatment with complete Freund's adjuvant in NOD mice. *Diabetes* **40**, 715–725 (1991).
- Sadelain, M. W., Qin, H. Y., Lauzon, J. & Singh, B. Prevention of type 1 diabetes in NOD mice by adjuvant immunotherapy. *Diabetes* **39**, 583–589 (1990).
- Janeway, C. A. Jr. Approaching the asymptote? Evolution and revolution in immunology. *Cold Spring Harb. Symp. Quant. Biol.* **54**, 1–13 (1989).
- Akira, S., Uematsu, S. & Takeuchi, O. Pathogen recognition and innate immunity. *Cell* **124**, 783–801 (2006).
- Rakoff-Nahoum, S., Paglino, J., Eslami-Varzaneh, F., Edberg, S. & Medzhitov, R. Recognition of commensal microflora by Toll-like receptors is required for intestinal homeostasis. *Cell* **118**, 229–241 (2004).
- Strober, W. Epithelial cells pay a Toll for protection. *Nature Med.* **10**, 898–900 (2004).
- Wong, F. S. et al. Identification of an MHC class I-restricted autoantigen in type 1 diabetes by screening an organ-specific cDNA library. *Nature Med.* **5**, 1026–1031 (1999).
- Graser, R. T. et al. Identification of a CD8 T cell that can independently mediate autoimmune diabetes development in the complete absence of CD4 T cell helper functions. *J. Immunol.* **164**, 3913–3918 (2000).
- Amrani, A. et al. Perforin-independent beta-cell destruction by diabetogenic CD8⁺ T lymphocytes in transgenic nonobese diabetic mice. *J. Clin. Invest.* **103**, 1201–1209 (1999).
- Haskins, K. & McDuffie, M. Acceleration of diabetes in young NOD mice with a CD4⁺ islet-specific T cell clone. *Science* **249**, 1433–1436 (1990).
- Lieberman, S. M. et al. Individual nonobese diabetic mice exhibit unique patterns of CD8⁺ T cell reactivity to three islet antigens, including the newly identified widely expressed dystrophin myotonic kinase. *J. Immunol.* **173**, 6727–6734 (2004).
- Lieberman, S. M. et al. Identification of the beta cell antigen targeted by a prevalent population of pathogenic CD8⁺ T cells in autoimmune diabetes. *Proc. Natl Acad. Sci. USA* **100**, 8384–8388 (2003).
- Hoglund, P. et al. Initiation of autoimmune diabetes by developmentally regulated presentation of islet cell antigens in the pancreatic lymph nodes. *J. Exp. Med.* **189**, 331–339 (1999).
- Turley, S. J., Lee, J. W., Dutton-Swain, N., Mathis, D. & Benoist, C. Endocrine self and gut non-self intersect in the pancreatic lymph nodes. *Proc. Natl Acad. Sci. USA* **102**, 17729–17733 (2005).
- Suzuki, T. et al. in *Immune-deficient Animals in Biomedical Research* (eds Rygaard, J. B. N., Graem, N. & Spang-Thomsen, M.) 112–116 (Karger, 1985).
- Gray, D. H., Gavanescu, I., Benoist, C. & Mathis, D. Danger-free autoimmune disease in Aire-deficient mice. *Proc. Natl Acad. Sci. USA* **104**, 18193–18198 (2007).
- Kim, H. S. et al. Toll-like receptor 2 senses beta-cell death and contributes to the initiation of autoimmune diabetes. *Immunity* **27**, 321–333 (2007).
- Dewhirst, F. E. et al. Phylogeny of the defined murine microbiota: altered Schaedler flora. *Appl. Environ. Microbiol.* **65**, 3287–3292 (1999).

22. Ley, R. E. *et al.* Obesity alters gut microbial ecology. *Proc. Natl Acad. Sci. USA* **102**, 11070–11075 (2005).
23. Ley, R. E., Turnbaugh, P. J., Klein, S. & Gordon, J. I. Microbial ecology: human gut microbes associated with obesity. *Nature* **444**, 1022–1023 (2006).
24. Rawls, J. F., Mahowald, M. A., Ley, R. E. & Gordon, J. I. Reciprocal gut microbiota transplants from zebrafish and mice to germ-free recipients reveal host habitat selection. *Cell* **127**, 423–433 (2006).
25. Ley, R. E., Peterson, D. A. & Gordon, J. I. Ecological and evolutionary forces shaping microbial diversity in the human intestine. *Cell* **124**, 837–848 (2006).
26. Turnbaugh, P. J. *et al.* An obesity-associated gut microbiome with increased capacity for energy harvest. *Nature* **444**, 1027–1031 (2006).
27. Turnbaugh, P. J., Backhed, F., Fulton, L. & Gordon, J. I. Diet-induced obesity is linked to marked but reversible alterations in the mouse distal gut microbiome. *Cell Host Microbe* **3**, 213–223 (2008).
28. Funda, D. P., Fundova, P. & Harrison, L. C. Microflora-dependency of selected diabetes-preventive diets: germ-free and ex-germ-free monocolonized NOD mice as models for studying environmental factors in type 1 diabetes. *Proc. 13th Int. Congr. Immunol.* MS-11.4 16 (Brazilian Society for Immunology, Rio de Janeiro, 2007).
29. Wang, Q., Garrity, G. M., Tiedje, J. M. & Cole, J. R. Naive Bayesian classifier for rapid assignment of rRNA sequences into the new bacterial taxonomy. *Appl. Environ. Microbiol.* **73**, 5261–5267 (2007).
30. Calcinaro, F. *et al.* Oral probiotic administration induces interleukin-10 production and prevents spontaneous autoimmune diabetes in the non-obese diabetic mouse. *Diabetologia* **48**, 1565–1575 (2005).
31. Huber, T., Faulkner, G. & Hugenholtz, P. Bellerophon: a program to detect chimeric sequences in multiple sequence alignments. *Bioinformatics* **20**, 2317–2319 (2004).

Supplementary Information is linked to the online version of the paper at www.nature.com/nature.

Acknowledgements The authors are thankful to A. Putnam, T. Park, D. Schumann, M. Prokhorovich, W. Du, D. O'Donnell, M. Karlsson and S. Wagoner for help with experiments, and S. Dryden Perkins and M. Garcia for assistance with sequence analysis. This work was supported by the ADA grant 1-05-RA-142 to L.W.; JDRF grant 19-2006-1075 to L.W. and F.S.W.; Animal Genetic Core of Diabetes Endocrinology Research Center (NIH grant DK45735) to L.W.; NIH grants R37 AI46643 and P30 DK63720 as well as the JDRF 4-2005-1168 grant to J.A.B.; NIH grants DK30292 and DK70977, and a W. M. Keck Foundation award to J.I.G.; NIH grant DK063452 to A.V.C.; JDRF grants 2005-204 and 2007-353 to A.V.C.; and the NIH/NIDDK Digestive Disease Research Core Center grant DK42086.

Author Contributions L.W. designed and supervised experiments at Yale University; R.E.L. performed analysis of 16S rRNA sequences of the gut microbiota; P.Yu.V. analysed T1D development in germ-free and microbiota-colonized mice; P.B.S. performed ELISPOT analysis; L.A. and A.C.S. established and characterized mutant mouse strains at The Jackson Laboratory and at The University of Chicago; C.H., F.S.W. and L.W. characterized mutant mouse strains at Yale University; G.L.S. was involved in performance of regulatory-T-cell-based assays; J.A.B. designed and supervised the T cell assays; J.I.G. helped with design and interpretation of gut microbial ecology studies and oversaw the microbiota transfer experiments; A.V.C. conceived and designed the project, and wrote the manuscript with substantial critical contributions from L.W., R.E.L., F.S.W., J.A.B. and J.I.G.

Author Information 16S rRNA sequences obtained from microbiota of SPF NOD and MyD88^{KO} NOD mice treated and not-treated with antibiotic were deposited in GenBank under accession numbers EU450891–EU458113. Reprints and permissions information is available at www.nature.com/reprints. Correspondence and requests for materials should be addressed to A.V.C. (achervon@bsd.uchicago.edu).

METHODS

Mice. TLR4-negative C57BL/10ScN mice were purchased from the NIH. TLR2 and MyD88^{KO} B6 mice were a gift from S. Akira. TLR2^{KO}-carrying animals at Yale were obtained as an early backcross to NOD/LtJ through the generosity of M. O. Li. KO/+ and KO animals used for diabetes experiments were F₂ of extensively backcrossed KO/+ mice; this strategy was designed to reduce the impact of non-NOD genetic loci possibly present elsewhere in the genomes of these mice.

SPF mice were fed with autoclaved NIH 5K52 diet (see <http://www.labdiet.com>) or Harlan Teklad 7012 diet (see <http://www.teklad.com/standardrodentdiet/r7012.asp>), whereas germ-free mice received an autoclaved NIH 31 chow (see <http://www.teklad.com/pdf/7017.pdf>).

DNA isolated from NOD animals carrying the targeted mutations was subjected to genome-wide screening using the Illumina Sentrix Universal BeadChips. The analysis was performed at University of Texas Southwestern Medical Center in Dallas (for details see http://microarray.swmed.edu/s_illumina.html and <http://www.illumina.com>). In addition, we used the PCR-based Amplifluor SNP analysis platform³² at Kbiosciences with primers distinguishing NOD and 129 alleles in the regions flanking the targeted genes (*Tlr2*, *Tlr4* and *Myd88*) on chromosomes 3, 4 and 9, respectively³². The combined data from these two approaches showed that the genetic boundaries for the 129 or B6 sequences still present in the flanking regions between positions for telomeric (t) and centromeric (c) ends were as follows: TLR2^{KO} NOD (J): t, 46624359/48004616; c, 91071226/93995376. TLR2^{KO} NOD(Y): t, 70607621/74327277; c, 121126022/122002332. TLR4 NOD (J): t, 47358427/51035410; c, 70467819/74403260. MyD88 NOD (J): t, 108690630/109861337; c, 117891342/123174839. MyD88 NOD (Y): t, 115090216/117891342; c, 122337931/123174839.

In addition TLR2^{KO} NOD (Y) mice had a non-NOD segment on chromosome 11 (32946888–43847855). However, TLR2^{KO} NOD (J) mice carried the NOD sequence in the same segment.

Positions of *Idd* (insulin dependent diabetes susceptibility) loci were determined according to the T1D database (<https://dil.t1dbase.org/page/Welcome/display/species/Mouse>). Accordingly, in TLR2^{KO} NOD (J) mice the 129 sequences flanking *Tlr2* gene could not be segregated from *Idd17*, whereas in NOD TLR2^{KO} (Y) mice these sequences also included *Idd10* and *Idd18*. These loci were found to affect T1D development in NOD × (NOD × 129/SvJ.H2^{E7})_{F1} backcrosses (E. Leiter, personal communication). In the same cross, no T1D-affecting genes were found on chromosome 9 harbouring the *Myd88* gene.

Antibiotic treatment. Sulfatrim (JA Webster) was delivered through drinking water according to the manufacturer's instructions. Breeding mice were kept on Sulfatrim through mating and nursing, and the progeny were kept on the drug until the end of the observation period.

Complete Freund's adjuvant injections. Three-week-old female mice were injected with 25–30 µl of a 1:1 mixture of complete Freund's adjuvant (Difco Laboratories) and saline into the hind footpads. Diabetes development was monitored up to 30 weeks of age.

Diabetes monitoring. Mice were tested for diabetes weekly, starting at 10 weeks of age, by measuring urine glucose with Diastix strips (Bayer); this was confirmed by testing for blood glucose >2.5 g l⁻¹ (13.9 mmol l⁻¹).

FACS analysis. Lymph node and splenic cells were stained with antibodies directly coupled to fluorochromes against CD4, CD25 and FOXP3 (all from e-Biosciences) according to the manufacturer's protocols. For transfer experiments, T cells were treated with 0.5 µM CFSE (Invitrogen). Lymph node cells containing CFSE⁺ cells were counterstained with anti-CD4 and anti-BDC2.5 clone type³³ followed by rat anti-mouse IgG2b–biotin (Becton-Dickinson) and streptavidin–PE (Becton-Dickinson). Data were acquired using FACSCalibur or LSR II (Becton-Dickinson) flow cytometers. Data analysis was performed using FlowJo (Tree Star Inc.) and ModFit LT (Verity Software House) software. Proliferation of CFSE⁺ cells was measured by using ModFit and expressed as a 'proliferation index' (defined as the sum of the cells in all generations divided by the computed number of original parent cells theoretically present at the start of the experiment).

ELISPOT analysis. An IFN-γ ELISPOT antibody pair was purchased from Pharmingen. MultiScreen plates (96 wells) were from Millipore. Peptides used were from the insulin B chain (InsB amino acids 15–23) (ref. 10), or mimic peptides recognized by islet-specific TCRs AI-4 (ref. 34), 8.3 (ref. 15) and BDC2.5 (ref. 35). Plates were treated and spots revealed according to the manufacturer's protocol. Background dots in the wells with the same T cells incubated without peptides were subtracted.

Transfer of T cells. CD4⁺ T cells were isolated from spleens and lymph nodes of BDC2.5 transgenic NOD mice using anti-CD4⁺ magnetic beads and MACs technology (Miltenyi Biotech). CD25⁺ T cells were removed either by treating with anti-CD25 antibodies and rabbit complement (Pel-Freezer) or by treatment with anti-CD25 biotinylated antibodies followed by anti-biotin magnetic beads. Recipient mice were injected intravenously with 1–2 × 10⁶ CFSE-labelled cells. PLNs, MLNs and skin-draining nodes were collected on day 3 and analysed by flow cytometry. No proliferation was observed in either mesenteric or skin-draining lymph nodes.

16S-rRNA-sequence-based studies of the caecal microbiota. SPF MyD88^{KO} NOD grandmothers of experimental animals were bred to SPF MyD88^{KO} NOD males without exposure to Sulfatrim. Their daughters were separated into two groups and harem-mated with SPF MyD88^{KO/+} NOD males with or without antibiotic. The female progeny were weaned, housed individually to prevent exchange of their gut microbiota, and maintained either with or without Sulfatrim treatment until they were 8 weeks of age. Caecal contents from experimental mice (8–11 mice per group) were quickly removed, snap-frozen in liquid nitrogen and stored at –80 °C.

DNA was extracted from frozen caecal contents using a bead-beating/phenol–chloroform extraction protocol³⁶. 16S rRNA amplicons were obtained as described²³ using bacteria-specific forward (5'-AGAGTTTGATCC TGGCTCAG-3') and a universal reverse (5'-GACGGGCGGTGTGTRCA-3') primer³⁷. Amplicons were gel-purified (Qiagen), cloned into TOPO TA pCR4.0, and transformed into *Escherichia coli* TOP10 cells (Invitrogen). For each sample, 384 colonies were selected; inserts were sequenced using vector-specific primers and the internal 16S rRNA primer 907R (5'-CCGTCAATTCCTTTAGTTT-3'), and an ABI 3730xl capillary DNA sequencer.

Putative non-chimaeric sequences (not flagged as chimaeric using the on-line tool Bellerophon (http://greengenes.lbl.gov/cgi-bin/nph-bel3_interface.cgi) with parameters setting that included a 'parent to fragment threshold' of 90; and a 'divergence threshold' ratio of 1.1) >800 bp in length were named according to the mouse genotype, antibiotic treatment and the mother's identity: sequences derived from mice that were heterozygous (KO/+) for the MyD88 gene have prefixes beginning in 'H', in contrast to 'K' for sequences derived from MyD88^{KO} mice; the middle two digits of the prefix refer to the mother's identity; antibiotic treatment is denoted as 'S' and no treatment as 'N'; and the last digit of the prefix refers to a specific mouse sibling.

Sequences were added to an existing Arb alignment (http://greengenes.lbl.gov/Download/Sequence_Data/Arb_databases/prokMSA_old.arb) using the parsimony insertion tool³⁸ and tree (tree_1250_nochimera), which was used for clustering mouse communities using the online version of UniFrac (<http://bmf.colorado.edu/unifrac/>)^{39,40}.

Statistical analyses. Statistical significance for sequence classification results was determined by one-tailed *t*-test implemented in Excel (version 11.0, Microsoft).

Statistical significance of ELISPOT and regulatory T cell staining results was determined by unpaired Student's *t*-test. Diabetes incidence curves were compared by Kaplan–Meier survival curve statistics using GraphPad Prism version 4.00c for OS X, GraphPad Software.

- Petkov, P. M. *et al.* An efficient SNP system for mouse genome scanning and elucidating strain relationships. *Genome Res.* **14**, 1806–1811 (2004).
- Kanagawa, O., Militech, A. & Vaupel, B. A. Regulation of diabetes development by regulatory T cells in pancreatic islet antigen-specific TCR transgenic nonobese diabetic mice. *J. Immunol.* **168**, 6159–6164 (2002).
- Takaki, T. *et al.* Requirement for both H-2Db and H-2Kd for the induction of diabetes by the promiscuous CD8⁺ T cell clone type AI4. *J. Immunol.* **173**, 2530–2541 (2004).
- Stratmann, T. *et al.* Susceptible MHC alleles, not background genes, select an autoimmune T cell reactivity. *J. Clin. Invest.* **112**, 902–914 (2003).
- Dojka, M. A., Hugenholtz, P., Haack, S. K. & Pace, N. R. Microbial diversity in a hydrocarbon- and chlorinated-solvent-contaminated aquifer undergoing intrinsic bioremediation. *Appl. Environ. Microbiol.* **64**, 3869–3877 (1998).
- Weisburg, W. G., Barns, S. M., Pelletier, D. A. & Lane, D. J. 16S ribosomal DNA amplification for phylogenetic study. *J. Bacteriol.* **173**, 697–703 (1991).
- Ludwig, W. *et al.* ARB: a software environment for sequence data. *Nucleic Acids Res.* **32**, 1363–1371 (2004).
- Lozupone, C. & Knight, R. UniFrac: a new phylogenetic method for comparing microbial communities. *Appl. Environ. Microbiol.* **71**, 8228–8235 (2005).
- Lozupone, C., Hamady, M. & Knight, R. UniFrac—an online tool for comparing microbial community diversity in a phylogenetic context. *BMC Bioinformatics* **7**, 371 (2006).

LETTERS

Conjugated action of two species-specific invasion proteins for fetoplacental listeriosis

Olivier Disson^{1,2,*}, Solène Grayo^{1,2,3,*}, Eugénie Huillet^{4,5,6,*}, Georgios Nikitas^{1,2}, Francina Langa-Vives⁷, Olivier Dussurget^{4,5,6}, Marie Ragon³, Alban Le Monnier³, Charles Babinet^{8,†}, Pascale Cossart^{4,5,6} & Marc Lecuit^{1,2,3,9}

The ability to cross host barriers is an essential virulence determinant of invasive microbial pathogens. *Listeria monocytogenes* is a model microorganism that crosses human intestinal and placental barriers, and causes severe maternofetal infections by an unknown mechanism¹. Several studies have helped to characterize the bacterial invasion proteins InlA and InlB². However, their respective species specificity has complicated investigations on their *in vivo* role^{3,4}. Here we describe two novel and complementary animal models for human listeriosis: the gerbil, a natural host for *L. monocytogenes*, and a knock-in mouse line ubiquitously expressing humanized E-cadherin. Using these two models, we uncover the essential and interdependent roles of InlA and InlB in fetoplacental listeriosis, and thereby decipher the molecular mechanism underlying the ability of a microbe to target and cross the placental barrier.

Several microorganisms that cross the intestinal barrier also cross the placental barrier. Yet little is known about the mechanisms underlying their fetoplacental tropism. As for most vertically transmitted infections, maternofetal listeriosis is associated with high neonatal mortality, even when adequate antimicrobial therapy is administered^{1,5}. Pregnancy-associated immunosuppression is thought to favour systemic microbial dissemination⁶, but an elective microbial targeting and crossing of the placental barrier relying on specific interactions of microbial ligands with placental receptors, although attractive, has never been demonstrated *in vivo*.

Listeria monocytogenes is a model microorganism for *in vitro* and *in vivo* studies². Two bacterial proteins, InlA and InlB, mediate its internalization into human cultured non-phagocytic cells^{2,7,8}. The receptor for InlA is E-cadherin (Ecad), whereas the receptor for InlB is Met, together with gC1qR and proteoglycans^{9–12}. InlA and InlB interactions with their respective receptors are species-specific: InlA interacts with human and guinea-pig Ecad, but not mouse and rat Ecad³; whereas InlB interacts with human and mouse Met, but not guinea-pig Met⁴. In transgenic mice expressing human Ecad in enterocytes (iFABP-hEcad mice), InlA has a critical role in *L. monocytogenes* crossing of the intestinal barrier¹³, whereas InlB has no role⁴.

Epidemiological investigations also support a role for InlA in human listeriosis¹⁴, as clinical strains express a functional InlA far more frequently (96%) than strains recovered from food products (65%) ($P < 0.001$)¹⁴. To specifically address the contribution of InlA in pregnancy-related cases, we performed a larger epidemiological survey (Supplementary Methods). This demonstrated that expression

of full-length InlA is significantly associated with *L. monocytogenes* isolates from pregnancy-related cases, if compared with those of bacteraemia origin ($P = 0.01$, Supplementary Table 1), a result in favour of a role for InlA in human fetoplacental infection. Results of *ex vivo* infections of human placental explants also suggest a role for InlA, as well as InlB, in placental infection¹⁵. In line with these results, the human trophoblastic cell line JAR is permissive to both InlA and InlB pathways (Supplementary Fig. 1). Yet, in contradiction with these epidemiological, *ex vivo* and *in vitro* results, InlA has no role in *L. monocytogenes* fetoplacental infection in the guinea-pig, despite its permissiveness to the InlA pathway¹⁶. Similarly, InlB has no role in *L. monocytogenes* fetoplacental infection in the mouse, despite its permissiveness to the InlB pathway¹⁷.

Given our observations in human placental explants that InlA exerts a role in placental tissue invasion in the presence of InlB, we hypothesized that both InlA and InlB might be critical for fetoplacental invasion *in vivo*. Accordingly, only an animal model in which both pathways are functional would constitute an appropriate system to study fetoplacental listeriosis and its molecular determinants. Here we characterize two novel and complementary animal models for human listeriosis: a natural host for *L. monocytogenes*, the gerbil, and a novel knock-in mouse line, and we reveal the critical and interdependent roles of InlA and InlB in fetoplacental listeriosis. Ligand–receptor interactions mediating microbial targeting and crossing of the placental barrier have not been documented previously.

In 1927, J. H. Harvey Pirie discovered a novel Gram-positive bacillus, which he named *Listerella hepatolytica* (later renamed *L. monocytogenes*), as a cause of lethality in wild gerbils, indicating their natural susceptibility to this bacterial species¹⁸. From this seminal observation and the fact that gerbils are closely related to rodents permissive to either InlA or InlB pathway (Supplementary Fig. 2), we tested the hypothesis that the gerbil might be permissive to both pathways and therefore constitute a suitable model to test the respective contributions of InlA and InlB *in vivo*, notably in the context of fetoplacental listeriosis. First, we isolated primary gerbil intestinal epithelial cells and showed that they co-express the InlA and InlB receptors Ecad and Met (Fig. 1a–c). We next conducted a gentamicin survival assay and demonstrated that, in contrast to what is observed in the rat and guinea-pig, respectively, both InlA and InlB pathways are functional in the gerbil, as in humans (Fig. 1d, Supplementary Fig. 3). We determined the amino-acid sequence of gerbil Ecad first extracellular domain (EC1): it harbours a proline at

¹Institut Pasteur, Groupe Microorganismes et Barrières de l'Hôte, Unité des Interactions Bactéries-Cellules, F-75015 Paris, France. ²Inserm U604, F-75015 Paris, France.

³Institut Pasteur, Centre National de Référence des *Listeria*, F-75015 Paris, France. ⁴Institut Pasteur, Unité des Interactions Bactéries-Cellules, F-75015 Paris, France. ⁵Inserm U604, F-75015 Paris, France. ⁶INRA USC2020, F-75015 Paris, France. ⁷Institut Pasteur, Centre d'Ingénierie Génétique Murine, F-75015 Paris, France. ⁸Institut Pasteur, Unité de Biologie du Développement, F-75015 Paris, France. ⁹Centre d'Infectiologie Necker-Pasteur, Service des Maladies Infectieuses et Tropicales, Hôpital Necker-Enfants malades, Assistance Publique-Hôpitaux de Paris, Université Paris Descartes, F-75015 Paris, France.

*These authors contributed equally to this work.

†Deceased.

position 16, as for other Ecads able to interact with InlA^{3,19} (Supplementary Fig. 2a,b). We also determined the amino-acid sequence of the gerbil Met region orthologous to the human one interacting with InlB²⁰: it clusters with species permissive to InlB pathway, whereas species non-permissive to InlB (guinea-pig and rabbit) harbour key amino-acid differences in the InlB recognition domain of Met (Supplementary Fig. 2c,d). Together, these *in vitro* results demonstrate that the gerbil is naturally permissive to both InlA and InlB pathways, and thus constitutes an appropriate model to address the roles of these two invasion proteins in the successive steps of listeriosis.

We next performed oral inoculation of gerbils and showed that InlA plays a critical role in the crossing of the intestinal barrier (Supplementary Fig. 4), as in guinea-pig and iFABP-hEcad mice¹³. Interestingly, we demonstrated that InlA-dependent invasion by *L. monocytogenes* is not restricted to the small intestine, but also occurs in the caecum and colon. This is in contrast to what is observed in iFABP-hEcad mice, in which hEcad expression is restricted to enterocytes of the small intestine. We also showed that InlB is not involved in the crossing of the intestinal barrier, as in iFABP-hEcad mice^{13,21}. These results in orally inoculated gerbils prompted us to investigate maternofetal listeriosis in pregnant gerbils.

We first tested gerbil permissiveness to listerial fetoplacental infection after oral inoculation, the natural route for human infection. By using bioluminescent *L. monocytogenes*, we showed that fetoplacental listeriosis develops in orally inoculated gerbils, and leads to 100% fetal lethality with wild-type (WT) *L. monocytogenes*. In contrast, the *inlAB* isogenic mutant led to a weaker fetoplacental infection and no fetal lethality (Supplementary Fig. 5). To assess directly the role of InlA and InlB in fetoplacental infection, and bypass the filter effect of the intestinal barrier, we intravenously inoculated pregnant gerbils. Real-time imaging of fetoplacental listeriosis in these gerbils clearly revealed the contribution of the *inlAB* operon in fetoplacental infection (Fig. 2a–c). Histological analysis of the placentas showed the

co-expression of Ecad and Met at the syncytiotrophoblast level, which is the epithelial tissue that constitutes the maternal blood–fetal interface (Fig. 2d–f). At 24 h after infection, WT *L. monocytogenes* were detected at the syncytiotrophoblast–fetal vessel interface, whereas none were observed with the *inlAB* mutant. At 42 h after infection, we detected small abscesses with WT *L. monocytogenes*, whereas no abscess was detectable with the *inlAB* mutant (12 vibratome sections examined, four abscesses with 20–200 bacteria per abscess for *L. monocytogenes*, none for the *inlAB* mutant; $P = 0.02$) (Fig. 2g–i and Supplementary Movies 1–3).

To evaluate and quantify the contribution of InlA and InlB in fetoplacental infection, we used the competition index method, and co-infected pregnant gerbils intravenously with a chloramphenicol-resistant *L. monocytogenes* strain and its parental WT strain, or each isogenic *inlA*, *inlB* or *inlAB* deletion mutant (see Methods). Using this technique, a competition index equal to 1 indicates a similar virulence of the two strains, a competition index significantly greater than 1 indicates a defect in virulence of the co-administered *Listeria* strain and a competition index significantly less than 1 indicates the contrary. Fetoplacental infection was steadily observed for inocula greater than 2×10^5 (Supplementary Fig. 6). In contrast to what was observed with WT *L. monocytogenes*, the *inlA*, *inlB* and *inlAB* mutants all showed a significant defect in placental invasion (Fig. 3a and Supplementary Fig. 7a) and fetal infection (Fig. 3b and Supplementary Fig. 7b), with a competition index very significantly different from 1 ($P < 0.001$) at the placental level 72 h after infection and at the fetal level 96 h after infection, whereas no significant difference was observed in maternal liver (Supplementary Fig. 7c). These results sharply contrast with those observed in pregnant mice and guinea-pigs, for which, as previously reported^{16,17}, neither InlA nor InlB played any role in fetoplacental invasion (Supplementary Fig. 8). Together, these results establish that in species in which either the InlA or the InlB internalization pathway is non-functional, neither InlB nor InlA, respectively, can mediate invasion at the placental level. In contrast, in a species in which both pathways are functional, both InlA and InlB are critical for placental invasion and fetal infection. These *in vivo* results obtained in a naturally permissive model, the gerbil, are in full agreement with human epidemiological and *ex vivo* data (refs 14 and 15, and Supplementary Table 1).

To assess the causal relation between permissiveness to InlA and InlB pathways and InlA- and InlB-dependent placental invasion and fetal dissemination, we followed a gain-of-function approach and generated a humanized E16P knock-in mouse line in which the endogenous mouse Ecad is punctually modified ('humanized') so that it harbours a proline at position 16 in place of a glutamic acid (see Methods and Supplementary Fig. 9). This single amino-acid substitution is sufficient to convert mouse Ecad into an InlA receptor³. We first infected primary enterocytes isolated from homozygote E16P^{+/+} mice: bacteria expressing InlA specifically adhered to and entered these cells, and recruited E16PmEcad, in contrast to what was observed with primary enterocytes of WT mice (Fig. 4a). This demonstrated that mutated E16P mEcad acts as an InlA receptor, in contrast to WT mEcad, as previously reported³. The functionality of the InlA and InlB pathways in homozygote E16P^{+/+} mice was also demonstrated by gentamicin protection assay (Fig. 4b). We next inoculated knock-in mice orally, and showed, as in iFABP-hEcad mice, guinea-pigs¹³ and gerbils, that InlA mediates the crossing of the intestinal barrier (Fig. 4c). As observed in gerbils, but in contrast to what was observed in iFABP-hEcad mice in which hEcad expression is restricted to the small intestine¹³, InlA-dependent translocation was observed at the caecum and colon level, that is in tissues in which Ecad is physiologically expressed (Fig. 4c).

We next assessed competition indexes in pregnant E16P^{+/+} mice inoculated intravenously. In sharp contrast to WT mice (ref. 17 and Supplementary Fig. 8), knock-in mice exhibit striking InlA- and

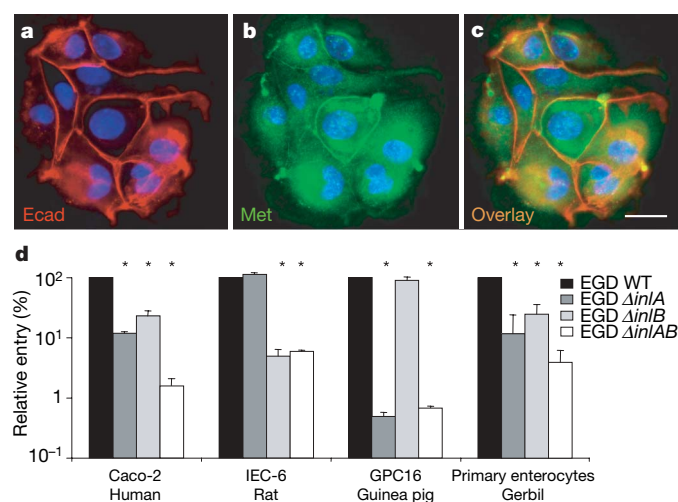


Figure 1 | InlA and InlB internalization pathways in gerbils. Primary gerbil enterocytes were labelled with Dapi (blue), an anti-Ecad (red, **a**) and an anti-Met (green, **b**) antibody, (**c**: overlay). **d**, Entry of *L. monocytogenes* (EGD WT) and isogenic mutants $\Delta inlA$, $\Delta inlB$ and $\Delta inlAB$ in human (Caco-2), rat (IEC-6), guinea-pig (GPC16) and gerbil primary enterocytes. Cells were incubated for 1 h with bacteria, 1 h with gentamicin and lysed. CFUs of gentamicin-resistant bacteria were enumerated. Values for mutants are expressed as the percentage of recovered bacteria relative to EGD WT, for which the value is normalized to 100. Asterisks indicate a significant difference ($P < 0.05$) relative to EGD WT. Scale bar, 10 μ m. Error bars, s.d.

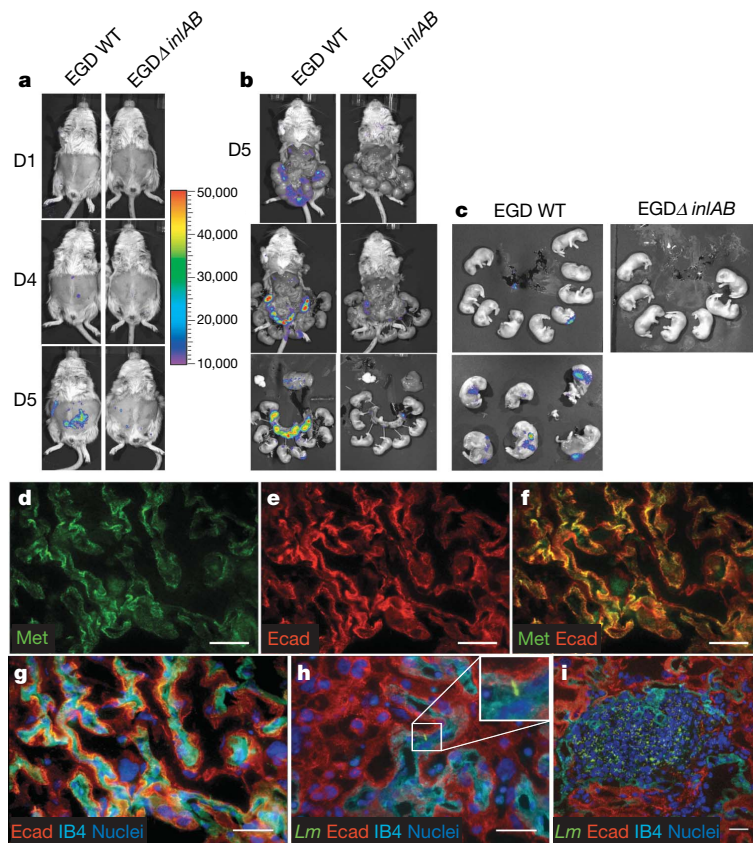


Figure 2 | *In vivo* real-time imaging of fetoplacental listeriosis in gerbils. **a**, Time course of infection of pregnant gerbils inoculated intravenously with 2×10^6 bioluminescent EGD WT or EGD Δ inlAB mutant. **b**, Dissection at day 5 after infection of the same animals, showing a far greater placental bioluminescence with EGD WT than Δ inlAB. **c**, Fetuses retrieved from two EGD WT or one EGD Δ inlAB-inoculated pregnant gerbil at day 5 after infection. **d–i**, Immunolabelling of gerbil placentas. **d–f**, Expression of Ecad (red) and Met (green) by the syncytiotrophoblast barrier bathed in maternal blood and surrounding fetal capillaries (isolectin B4, cyan) (**g**). Nuclei are labelled with Dapi (blue) (**g–i**). **h, i**, Sections of placentas 24 and 72 h after intravenous infection with EGD WT: **h**, a bacterium located at the syncytiotrophoblast–fetoplacental capillary interface; **i**, a placental abscess 72 h after infection with EGD WT. Scale bar, 10 μ m.

InlB-dependent fetoplacental invasion phenotypes ($P < 0.001$) revealed by the acquisition of a functional InlA pathway, in the presence of a pre-existing InlB pathway (Fig. 4d). In agreement with these results, when comparing the barrier function of the placenta—ratio of bacterial counts between placentas and fetuses—of non-permissive models (guinea-pig, mouse) with a permissive model (E16P mEcad), a difference of more than one order of magnitude is observed (Supplementary Fig. 10).

Our study demonstrates the concordance of epidemiological, *in vitro*, *ex vivo* and *in vivo* data and establishes that *L. monocytogenes* specifically targets the placenta *in vivo*, if and only if both InlA and InlB pathways are functional. These data shed light on previous reports using the mouse or guinea-pig as models that found no role for InlA or InlB in placental invasion^{16,17}: these studies had not taken into account the double species specificity of *L. monocytogenes* and the possibility that both InlA and InlB pathways had to be functional to unveil specific invasion of the placental tissue by *L. monocytogenes*. To our knowledge, this is the first report demonstrating the species- and tissue-specific recognition of the placenta by a microbial pathogen enabling it to breach the placental barrier.

The *inlAB* operon is located in the *L. monocytogenes* genome away from the 'virulence locus', which harbours the genes critical for *L. monocytogenes* intracellular life^{22,23}. The precise roles of InlA and InlB *in vivo* have long remained elusive. We had shown the role of InlA at the intestinal barrier level¹³, but found no role for InlB at this early step of the infection⁴. Here we demonstrate a role for InlB, in combination with InlA, in fetoplacental invasion, a key step of listeriosis in its natural hosts. This demonstrates that fetoplacental-specific tropism of *L. monocytogenes* correlates with host permissiveness to both InlA and InlB. Accordingly, cattle and sheep, which are natural hosts for *L. monocytogenes* and develop fetoplacental listeriosis *in natura*, are both permissive to InlA and InlB (unpublished data).

Some questions remain about the mechanism of *L. monocytogenes* targeting and crossing the placental barrier. Indeed, *in vitro*, both InlA and InlB are sufficient to mediate entry into cells expressing their respective receptors^{24,25}. In addition, at the intestinal barrier level, InlA does not require InlB to exert its function⁴. This suggests that InlA could be sufficient for placental targeting and crossing. Here we show that this is not the case. To our knowledge, the placenta is the only tissue—with brain microvessels, although this is controversial²⁶—for which Ecad is accessible from the blood systemic circulation. This suggests that InlA could mediate adherence of maternal blood-borne bacteria to the syncytiotrophoblast maternal–fetal interface. However, InlA seems insufficient to mediate invasion in the absence of InlB, possibly because of the non-functionality, at the syncytiotrophoblast level, of the downstream effectors needed for InlA-mediated internalization². On the other hand, InlB, in the absence of a functional InlA pathway, also appears unable to fulfil its function *in vivo*, contrary to what is observed *in vitro*²⁵. This suggests that InlA-mediated bacterial adhesion is a prerequisite for InlB-mediated placental tissue invasion. In line with this hypothesis, InlB is a weak adhesin loosely attached to the bacterial surface²⁷, and InlB-mediated adherence of *L. monocytogenes* to the placenta could thus be insufficient *in vivo* because of the shear stress at the maternal blood–placenta interface. Understanding how InlA and InlB act in concert to mediate placental invasion and why this contrasts with the InlA-dependent, albeit InlB-independent, intestinal invasion will be critical to our complete understanding of the behaviour of *L. monocytogenes* *in vivo*.

Other microbial pathogens share with *L. monocytogenes* the ability to breach host barriers. Identification of the ligand–receptor interactions mediating microbial crossing of host barriers may help in developing inhibitors to these interactions. Conversely, these interactions may also be exploited to target therapeutic molecules across host barriers.

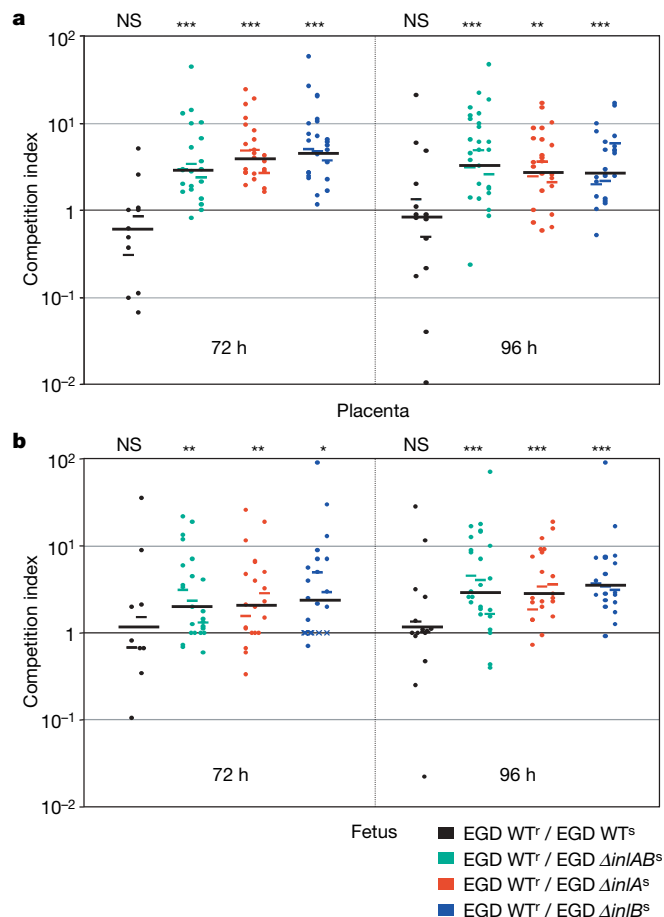


Figure 3 | Interdependent roles of InlA and InlB in placental invasion and fetal infection in gerbils. Competition index of EGD WT and Δ inlA, Δ inlB and Δ inlAB mutants tested against chloramphenicol-resistant EGD WT^r. Pregnant gerbils were inoculated intravenously with a 1:1 mixture of the two strains (total dose 2×10^6 CFUs). Bacteria were enumerated at 72 and 96 h after infection and competition indexes calculated for placenta (a) and fetuses (b). Each dot represents one placenta or fetus, a cross an uninfected organ. Each vertical dot alignment originates from one mother. Small, coloured bars represent mean competition indexes for placentas or fetuses of one animal. Large, black bars represent mean competition indexes for three animals. Asterisks indicate that the competition index is significantly greater than one (* $P < 0.05$; ** $P < 0.01$; *** $P < 0.001$), NS a non-significant difference.

METHODS SUMMARY

Bacteria and cell culture conditions. The *Listeria* strains and cell lines used are listed in the Supplementary Methods. Primary enterocytes were prepared as previously described²⁸.

Cell and tissue immunolabelling. Cell and tissue immunolabelling was performed as previously described¹⁵. Mouse and gerbil E-cadherins were stained with the ECCD2 antibody (Takara). Met was stained with the SP-260 antibody (Santa Cruz). Endothelial cells were stained with isolectin B4, and bacteria with R11 (*L. monocytogenes*) and R6 (*Listeria innocua*) antibodies²⁹.

Animal experiments: infection. Animal experiments were performed according to the Institut Pasteur guidelines for the husbandry of laboratory animals. Pregnant gerbils were infected at day 18/26 of gestation, pregnant mice at day 14/21 and pregnant guinea-pigs at day 36/60. Oral infections were performed as previously described¹³. In gerbils, intravenous infections were performed surgically in the femoral vein as described³⁰.

Animal experiments: bacterial enumeration. At indicated times, animals were killed and their organs harvested. The intestine, colon and caecum were rinsed, incubated in DMEM medium containing gentamicin and rinsed again. All organs were then homogenized in PBS buffer and colony-forming units (CFUs) enumerated.

Animal experiments: bioluminescence real-time imaging. Animals were infected with the luminescent EGD WT (BUG2473) and EGD Δ inlAB

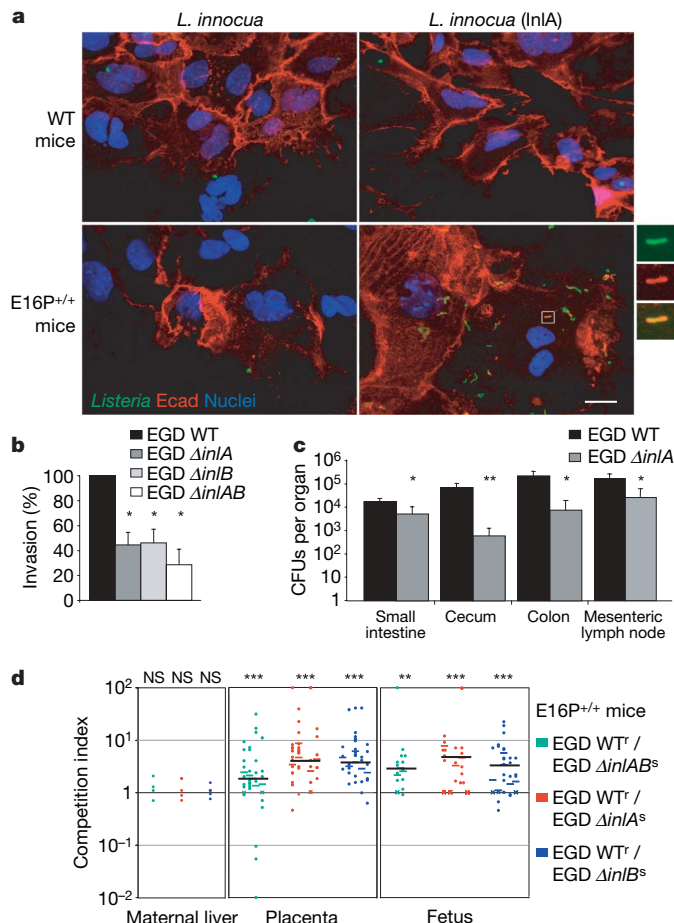


Figure 4 | Infection of primary epithelial cells and mice expressing a humanized mEcad able to interact with InlA. a, InlA-mediated adhesion on cells expressing E16P mEcad, but not on those expressing WT mEcad. *L. innocua* (InlA) recruits E16P mEcad (boxed area and inset). Scale bar, 10 μ m. b, Entry of *L. monocytogenes* (EGD WT) and Δ inlA, Δ inlB and Δ inlAB mutants in enterocytes of E16P^{+/+} mice. c, InlA-dependent intestinal invasion in E16P^{+/+} mice infected orally with 10^9 CFUs and dissected 48 h after infection. In a, b, asterisks indicate significant differences relative to EGD WT (* $P < 0.05$; ** $P < 0.01$). Error bars, s.d. (b, c). d, Competition indexes of Δ inlA, Δ inlB and Δ inlAB deletion mutants against EGD WT^r at 72 h after infection. E16P^{+/+} pregnant mice were inoculated intravenously, inoculum 2×10^5 CFUs. Each dot represents an infected organ, a cross an uninfected one. Refer to Fig. 3 for details.

(BUG2474) strains. Bioluminescence, measured in relative light units (photons per second), was monitored each day in a Xenogen IVIS 100 system. At indicated times, animals were killed and the bioluminescence of the internal organs measured.

Animal experiments: competition index assay. Both CmR reference EGD WT (BUG2472) and chloramphenicol-sensitive (CmS) test strains were mixed in a 1:1 ratio to perform infection. At indicated times, animals were killed and their organs homogenized in PBS. Serial dilutions of the homogenates were plated onto brain–heart infusion (BHI) agar plates with or without chloramphenicol. Competition indexes were calculated by dividing the number of CmR CFUs by the number of CmS CFUs.

Received 19 March; accepted 30 July 2008.

Published online 17 September 2008.

1. Mylonakis, E., Paliou, M., Hohmann, E. L., Calderwood, S. B. & Wing, E. J. Listeriosis during pregnancy: a case series and review of 222 cases. *Medicine (Baltimore)* **81**, 260–269 (2002).
2. Hamon, M., Bienne, H. & Cossart, P. *Listeria monocytogenes*: a multifaceted model. *Nature Rev. Microbiol.* **4**, 423–434 (2006).
3. Lecuit, M. et al. A single amino acid in E-cadherin responsible for host specificity towards the human pathogen *Listeria monocytogenes*. *EMBO J.* **18**, 3956–3963 (1999).
4. Khelif, N., Lecuit, M., Bienne, H. & Cossart, P. Species specificity of the *Listeria monocytogenes* InlB protein. *Cell. Microbiol.* **8**, 457–470 (2006).

5. Lecuit, M. Human listeriosis and animal models. *Microbes Infect.* **9**, 1216–1225 (2007).
6. Abram, M. *et al.* Murine model of pregnancy-associated *Listeria monocytogenes* infection. *FEMS Immunol. Med. Microbiol.* **35**, 177–182 (2003).
7. Cossart, P., Pizarro-Cerda, J. & Lecuit, M. Invasion of mammalian cells by *Listeria monocytogenes*: functional mimicry to subvert cellular functions. *Trends Cell Biol.* **13**, 23–31 (2003).
8. Pizarro-Cerda, J. & Cossart, P. Bacterial adhesion and entry into host cells. *Cell* **124**, 715–727 (2006).
9. Mengaud, J., Ohayon, H., Gounon, P., Mege, R. M. & Cossart, P. E-cadherin is the receptor for internalin, a surface protein required for entry of *L. monocytogenes* into epithelial cells. *Cell* **84**, 923–932 (1996).
10. Shen, Y., Naujokas, M., Park, M. & Ireton, K. InlB-dependent internalization of *Listeria* is mediated by the Met receptor tyrosine kinase. *Cell* **103**, 501–510 (2000).
11. Braun, L., Ghebrehiwet, B. & Cossart, P. gC1q-R/p32, a C1q-binding protein, is a receptor for the InlB invasion protein of *Listeria monocytogenes*. *EMBO J.* **19**, 1458–1466 (2000).
12. Jonquieres, R., Pizarro-Cerda, J. & Cossart, P. Synergy between the N- and C-terminal domains of InlB for efficient invasion of non-phagocytic cells by *Listeria monocytogenes*. *Mol. Microbiol.* **42**, 955–965 (2001).
13. Lecuit, M. *et al.* A transgenic model for listeriosis: role of internalin in crossing the intestinal barrier. *Science* **292**, 1722–1725 (2001).
14. Jacquet, C. *et al.* A molecular marker for evaluating the pathogenic potential of foodborne *Listeria monocytogenes*. *J. Infect. Dis.* **189**, 2094–2100 (2004).
15. Lecuit, M. *et al.* Targeting and crossing of the human maternofetal barrier by *Listeria monocytogenes*: role of internalin interaction with trophoblast E-cadherin. *Proc. Natl Acad. Sci. USA* **101**, 6152–6157 (2004).
16. Bakardjiev, A. I., Stacy, B. A., Fisher, S. J. & Portnoy, D. A. Listeriosis in the pregnant guinea pig: a model of vertical transmission. *Infect. Immun.* **72**, 489–497 (2004).
17. Le Monnier, A. *et al.* ActA is required for crossing of the fetoplacental barrier by *Listeria monocytogenes*. *Infect. Immun.* **75**, 950–957 (2007).
18. Pirie, J. H. H. A new disease of veld rodents. 'Tiger river disease'. *Publ. S. Afr. Inst. Med. Res.* **3**, 163–186 (1927).
19. Schubert, W. D. *et al.* Structure of internalin, a major invasion protein of *Listeria monocytogenes*, in complex with its human receptor E-cadherin. *Cell* **111**, 825–836 (2002).
20. Niemann, H. H. *et al.* Structure of the human receptor tyrosine kinase met in complex with the *Listeria* invasion protein InlB. *Cell* **130**, 235–246 (2007).
21. Lecuit, M. & Cossart, P. Genetically-modified-animal models for human infections: the *Listeria* paradigm. *Trends Mol. Med.* **8**, 537–542 (2002).
22. Glaser, P. *et al.* Comparative genomics of *Listeria* species. *Science* **294**, 849–852 (2001).
23. Vazquez-Boland, J. A. *et al.* *Listeria* pathogenesis and molecular virulence determinants. *Clin. Microbiol. Rev.* **14**, 584–640 (2001).
24. Lecuit, M., Ohayon, H., Braun, L., Mengaud, J. & Cossart, P. Internalin of *Listeria monocytogenes* with an intact leucine-rich repeat region is sufficient to promote internalization. *Infect. Immun.* **65**, 5309–5319 (1997).
25. Braun, L., Ohayon, H. & Cossart, P. The InlB protein of *Listeria monocytogenes* is sufficient to promote entry into mammalian cells. *Mol. Microbiol.* **27**, 1077–1087 (1998).
26. Rubin, L. L. *et al.* A cell culture model of the blood–brain barrier. *J. Cell Biol.* **115**, 1725–1735 (1991).
27. Bierne, H. & Cossart, P. InlB, a surface protein of *Listeria monocytogenes* that behaves as an invasin and a growth factor. *J. Cell Sci.* **115**, 3357–3367 (2002).
28. Athman, R. *et al.* *Shigella flexneri* infection is dependent on villin in the mouse intestine and in primary cultures of intestinal epithelial cells. *Cell. Microbiol.* **7**, 1109–1116 (2005).
29. Dramsi, S., Levi, S., Triller, A. & Cossart, P. Entry of *Listeria monocytogenes* into neurons occurs by cell-to-cell spread: an *in vitro* study. *Infect. Immun.* **66**, 4461–4468 (1998).
30. Perez-Garcia, C. C. *et al.* A simple procedure to perform intravenous injections in the Mongolian gerbil (*Meriones unguiculatus*). *Lab. Anim.* **37**, 68–71 (2003).

Supplementary Information is linked to the online version of the paper at www.nature.com/nature.

Acknowledgements This paper is dedicated to the memory of Charles Babinet, our friend and colleague, who died a few days before the submission of this manuscript. We thank his collaborators S. Vandormael-Pournin, C. Kress and M. Cohen-Tannoudji, as well as L. Larue and S. Tajbakhsh for help in generating the knock-in mice. We thank C. Hill for the gift of the pPL2lux-P_{hlyA} plasmid, M.-A. Nahori for help with animal experiments, P. Roux for help with confocal imaging, P.-M. Lledo and M. Gabellec for help with vibratome sectioning, V. Masse for help with statistical analysis and O. Lortholary for his support. We also thank S. Mostowy for reading the paper. This work received financial support from the Institut Pasteur, Inserm and INRA. O. Disson received financial support from the Fondation pour la Recherche Médicale (FRM) and Inserm, P.C. is an Howard Hughes Medical Institute international research scholar and M.L. is a recipient of an Inserm interface contract.

Author Contributions M.L. planned the project and analysed the experiments, together with P.C., as well as O. Disson, S.G., E.H. and G.N. O. Disson, S.G., E.H. and G.N. performed the experiments. Engineering of knock-in mice was done with F.L.-V. and C.B. O. Dussurget was involved in bioluminescence imaging; M.R. and A.L.M. were involved in the epidemiological study. M.L. wrote the manuscript and all co-authors commented on it.

Author Information The Gerbil Ecad and Gerbil Met nucleotide sequences are deposited in GenBank under accession numbers EU878370 and EU878371, respectively. Reprints and permissions information is available at www.nature.com/reprints. Correspondence and requests for materials should be addressed to M.L. (mlecu@pasteur.fr).

Paracrine Wingless signalling controls self-renewal of *Drosophila* intestinal stem cells

Guonan Lin^{1,2}, Na Xu² & Rongwen Xi²

In the *Drosophila* midgut, multipotent intestinal stem cells (ISCs) that are scattered along the epithelial basement membrane maintain tissue homeostasis by their ability to steadily produce daughters that differentiate into either enterocytes or enteroendocrine cells, depending on the levels of Notch activity^{1–3}. However, the mechanisms controlling ISC self-renewal remain elusive. Here we show that a canonical Wnt signalling pathway controls ISC self-renewal. The ligand Wingless (Wg) is specifically expressed in the circular muscles next to ISCs, separated by a thin layer of basement membrane. Reduced function of *wg* causes ISC quiescence and differentiation, whereas *wg* overexpression produces excessive ISC-like cells that express high levels of the Notch ligand, Delta. Clonal analysis shows that the main downstream components of the Wg pathway, including Frizzled, Dishevelled and Armadillo, are autonomously required for ISC self-renewal. Furthermore, epistatic analysis suggests that Notch acts downstream of the Wg pathway and a hierarchy of Wg/Notch signalling pathways controls the balance between self-renewal and differentiation of ISCs. These data suggest that the underlying circular muscle constitutes the ISC niche, which produce Wg signals that act directly on ISCs to promote ISC self-renewal. This study demonstrates markedly conserved mechanisms regulating ISCs from *Drosophila* to mammals. The identification of the *Drosophila* ISC niche and the principal self-renewal signal will facilitate further understanding of intestinal homeostasis control and tumorigenesis.

Previous studies demonstrate the presence of ISCs in the *Drosophila* midgut, which has structural and functional similarities to the mammalian counterpart, although the cell lineage is much simpler. ISCs are located at the basement membrane of intestinal epithelia. Each of them steadily generates two daughters: one which undergoes self-renewal to become a new ISC, and another which undergoes a rapid transition stage as an enteroblast before terminally differentiating into either an enterocyte as the absorptive cell type or an enteroendocrine as the secretory cell type (Fig. 1a)^{1,2}. ISCs can be distinguished by their enriched expression of a Notch ligand, Delta (Dl), through which ISCs control Notch activity of their differentiating daughters. In both *Drosophila* and mammals, Notch activation favours absorptive cell differentiation from the progenitors at the expense of secretory cells^{3,4}, suggesting that there is an evolutionarily conserved role of Notch in intestinal lineage specification. However, the mechanisms controlling *Drosophila* ISC self-renewal remain unknown. Furthermore, although adult stem cells are commonly associated with a specialized micro-environment or niche composed of fixed stromal cells, ISCs are scattered along the basement membrane of the epithelia, and thus do not seem to have specialized physical niches.

Similarities in cell lineage specification and Notch pathway function from *Drosophila* ISCs to that in mammals suggest that self-renewal signalling may also be similar. In mammals, the Wnt/ β -catenin

signalling pathway is required for the maintenance of a proliferative state of the crypt, where ISCs and transit amplifying cells reside⁴. However, because of the lack of a transit amplifying population in the *Drosophila* intestine, the involvement of Wnt signalling becomes obscure. To test its possible role in *Drosophila* intestinal function, we first examined midgut expression of *wg*, which encodes a ligand for the Wnt pathway in *Drosophila*. *In situ* hybridization experiments showed that *wg* transcripts were specifically detected in the circular muscles that envelop gut epithelia (Fig. 1b, c). A *lacZ* enhancer trap⁵ of *wg* also demonstrated specific nuclear β -galactosidase expression in the muscle cells (Fig. 1d, e). Moreover, Wg protein, revealed by staining with a monoclonal antibody, was specifically accumulated between the luminal surface of the circular muscles and the basement membrane of the gut epithelia (Fig. 1f). Weak Wg accumulation in ISCs was also detected (Fig. 1f), suggesting that Wg secreted from the muscle is able to migrate through the basement membrane and reach ISCs. The specific expression pattern indicates a possible role of *wg* in regulating ISCs. To test this hypothesis, we examined ISC behaviour in *wg* mutants. *wg* is an essential gene and homozygous null mutants cannot survive to adulthood. We thus used *wg^{ts}*, a temperature sensitive allele. The *wg^{ts}* homozygous flies can survive to adulthood at permissive temperature (18 °C)⁶, which allows us to examine *wg* function in the adult intestine. The newly enclosed *wg^{ts}* females were cultured at restrictive temperature (29 °C) for two weeks. By examining the expression of the ISC marker Dl, we found that the percentage of ISCs in the epithelia was reduced in *wg^{ts}* intestines (10.5% ($n = 10$) in homozygous versus 14.2% ($n = 8$) in heterozygous intestines; Fig. 2a–c). Using bromodeoxyuridine (BrdU) to label cycling ISCs, we found that 21.1% of ISCs were labelled in *wg^{ts}* intestines ($n = 10$), compared to 31.8% in the heterozygous intestines ($n = 12$; Fig. 2c). These data suggest that in the *wg^{ts}* mutant intestine, the number of ISCs is decreased and their division rate has also declined. TUNEL labelling for apoptotic cells showed that there was no obvious increase in ISC death in *wg^{ts}* animals (0 out of 66). We conclude that *wg* is required for the maintenance and proliferation of ISCs, but is not necessary for their survival.

To determine whether *wg* function is sufficient for ISC self-renewal, we used a binary GAL4/UAS system⁷ to forcibly express *wg* in the ISC compartment using the *esg-Gal4* driver. *esg-Gal4,UAS-GFP* is expressed specifically in ISCs and enteroblast cells (Fig. 2d)¹. In the wild type, there is usually one ISC in a diploid cell nest (of common stem cell origin) that is marked by high Dl expression (Fig. 2d)³. However, overexpression of *wg* caused expansion of Dl- and green fluorescent protein (GFP)-positive cells (Fig. 2e, f). Taken together, our loss- and gain-of-functional analyses suggest that *wg* is both necessary and sufficient for maintaining ISC fate and promoting their self-renewal.

Because ISCs and the circular muscles are only separated by a thin layer of basement membrane composed of extracellular matrix², and

¹Graduate program, Peking Union Medical College and Chinese Academy of Medical Sciences, Beijing 100730, China. ²National Institute of Biological Sciences, No. 7 Science Park Road, Zhongguancun Life Science Park, Beijing 102206, China.

weak Wg accumulation is detected in ISCs, Wg secreted from the muscle could migrate through the extracellular matrix and act directly on ISCs. In *Drosophila*, the Wg signal is transduced by Frizzled receptors, including Frizzled (Fz) and Frizzled 2 (Fz2), followed by phosphorylation of the cytoplasmic protein Dishevelled (Dsh), inhibition of Shaggy (Sgg), Axin and adenomatous polyposis coli (Apc) complex activity, and stabilization of Arm (the *Drosophila* β -catenin). Arm then translocates to the nucleus and cooperates with the transcription factor dTCF (also known as Pan) to regulate transcription of their target genes⁸. To determine whether Wg signals act directly on ISCs, we generated positively marked ISC clones that were homozygous mutant for *fz* and *fz2*, *dsh* or *arm* using the MARCM (mosaic analysis with a repressible cell marker) technique⁹. The initially GFP-marked normal or mutant ISCs were generated by

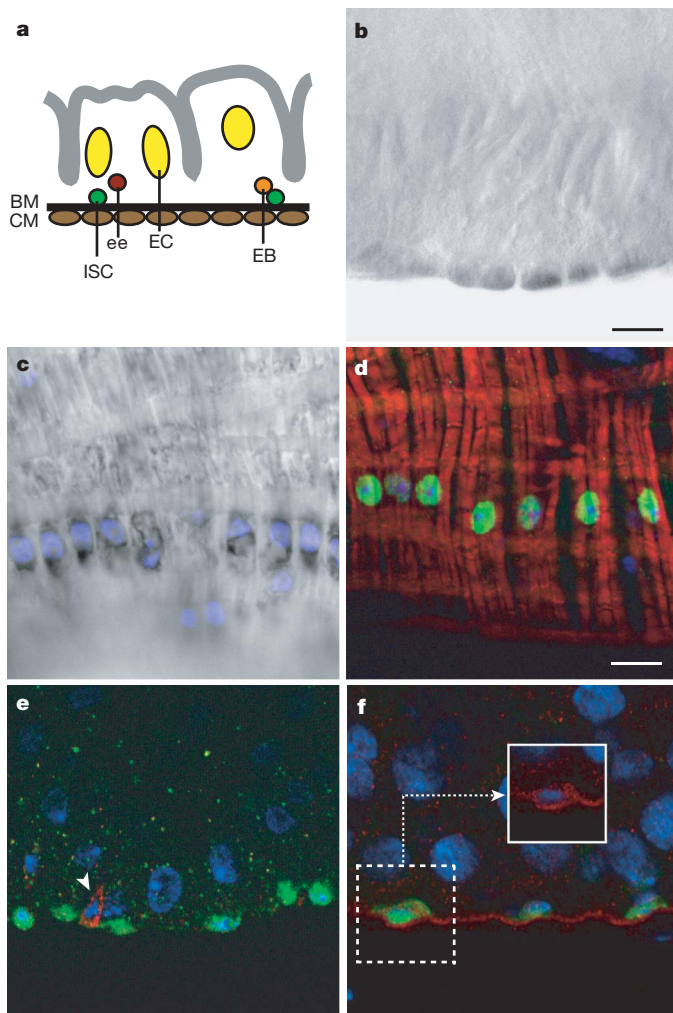


Figure 1 | *wg* is specifically expressed in the circular muscles. **a**, A cartoon of a cross-section of the *Drosophila* midgut. BM, basement membrane; CM, circular muscle; EB, enteroblast; EC, enterocyte; ee, enteroendocrine. **b**, **c**, A cross-section (**b**) and a superficial section (**c**) through the muscle layer showing *wg* messenger RNA by *in situ* hybridization. *wg* transcripts are specifically detected in the circular muscle and are enriched in the perinuclear regions. **d**, A section through the muscle layer showing *wg-lacZ* (green) and phalloidin (red) staining. The circular muscle nuclei show linear alignment along the gut longitudinal axis. **e**, A cross-section stained with *wg-lacZ* (green) and anti-Dl antibody (red, arrow). **f**, Wg protein (red, anti-Wg antibody) accumulates at the basement membrane. Weak Wg accumulation is also detected in ISCs (inset). ISCs are identified by *esgGal4,UAS-GFP* (green) and by their direct contact with the basement membrane. Note that the circular muscle nuclei are out of the focal plane in this image. DAPI (4',6'-diamidino-2-phenylindole) nuclear staining is shown in blue. Scale bars, 10 μ m.

heat-shock treatment to induce mitotic recombination in females of appropriate genotypes. As a control, the marked wild-type ISCs were able to generate and maintain clusters of GFP-labelled ISC clones over time, with 75.8% of ISC clones maintained 30 days after clone induction (Fig. 3a, k), consistent with previous observations². The *wg*^{CX4} (a null allele) mutant ISCs behaved very similarly to the wild-type cells, further suggesting that Wg does not act as an auto-crine signal for ISC self-renewal (Fig. 3b, k). The *fz* and *fz2* double mutant ISCs, but not the *fz2* single mutant, showed reduced maintenance rate, with only 30.5% of ISC clones maintained in double mutants, whereas as many as 72.1% were maintained in *fz2* single mutants (Fig. 3c, k). This is consistent with a redundant role of *fz* and *fz2* in transducing Wg signals^{10,11}. Similarly, ISCs that were homozygous for *dsh*^{v26}, *arm*³ or *arm*⁸—all representing loss of function alleles^{12–14}—showed stem cell loss phenotype over time, with about 53.3%, 32.5% and 41.8% of ISC clones maintained at day 30 after clone induction, respectively, for each allele (Fig. 3e, f, k). The ability to produce enteroendocrine cells (data not shown) and enterocytes

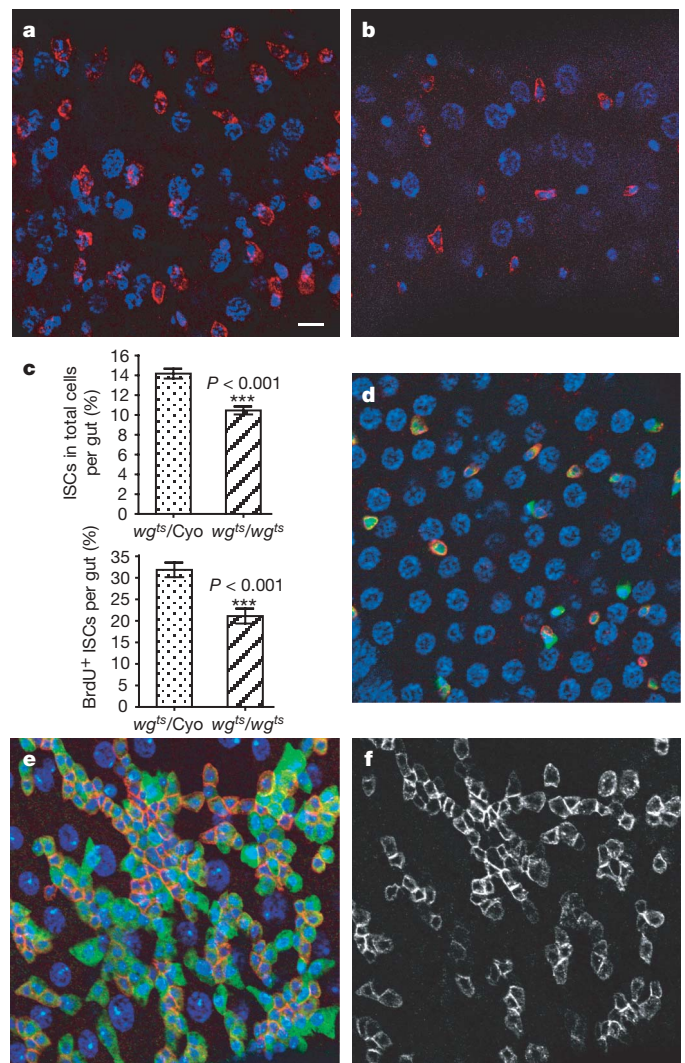


Figure 2 | *wg* is necessary and sufficient for ISC self-renewal.

a, **b**, Examination of ISCs (anti-Dl antibody, red; DAPI staining, blue) in *wg*^{ts} heterozygous (**a**) and homozygous (**b**) flies. **c**, Quantitative analysis of ISC number and division per midgut (dotted columns, *wg*^{ts}/Cyo; hatched columns, *wg*^{ts}/wg^{ts}). Error bars indicate s.e.m.; *n* = 8–12. **d–f**, *wg* is sufficient for ISC self-renewal. Flies of the genotype *esg-Gal4,UAS-GFP, tub-Gal80^{ts}* were used as a control (**d**). Experimental flies were of the genotype *UAS-wg;esg-Gal4,UAS-GFP, tub-Gal80^{ts}* (**e**) and were cultured at 29 °C for 3 weeks. GFP (green), anti-Dl antibody (red) and DAPI (blue) staining is shown. **f**, The red channel of **e** is shown (anti-Dl antibody). Scale bar, 10 μ m.

from these mutant ISCs indicates that Wg signalling is not essential for downstream lineage differentiation. We noticed that many mutant ISC-derived clones contained fewer numbers of cells, even when ISCs were still present in the clone (Fig. 3d). We thus performed pulsed BrdU labelling to test whether this was due to reduced proliferation of the mutant ISCs. As a control, the wild-type ISCs had 21.4% BrdU-positive ISCs 2 weeks after clone induction. In contrast, the *dsh* and *arm* mutant ISCs had only about half the amount of BrdU labelling (Fig. 3l), suggesting that the mutant ISCs are less proliferative. *Sgg* is a negative regulator of Wg signalling that regulates Arm degradation. *sgg* mutant ISC clones typically showed larger clone size than the wild-type ones (data not shown), but they did not accumulate extra ISCs. By staining with the mitotic marker phosphohistone H3 (PH3), we found that there were 3- to 4-fold more PH3-positive ISCs in the *sgg* mutant ISC population (Fig. 3m), suggesting that *sgg* mutant ISCs are more proliferative, presumably caused by increased activity of Wg signalling. Thus, the canonical Wg signalling downstream components are autonomously required for ISC maintenance and proliferation. These data also show that a fraction of the mutant ISC clones is still maintained at day 30 after clone induction. Perdurance of leftover gene products could be a possibility. Alternatively, there could be extra pathways that have compensatory or partially redundant functions with Wg signalling in regulating ISC maintenance.

To evaluate further a cell-autonomous role of Wg pathway activity in ISCs, we tested the effect of overexpression of *Arm*^{S10}, an active

form of Arm, within ISCs¹⁵. Forced expression of *arm*^{S10} by the *esg-Gal4* driver produced extra ISC-like cells and early progenitors (Fig. 3g, h). We also used a Flp-out cassette¹⁶ to generate GFP-marked ISC clones with all GFP-labelled cells continuously expressing *sgg*, or dTCFΔN, a dominant-negative form of dTCF¹⁷, both known to be able to attenuate or disrupt Wg signalling activity¹⁸. Both mutants produced clones that frequently contained only one or two cells at one week after clone induction, with none expressing DI (Fig. 3i, j), suggesting that the initially marked ISCs could not be maintained and rapidly differentiate. Thus, Wg pathway activation in ISCs is both necessary and sufficient for ISC self-renewal, and the Wg produced from the muscle functions as a paracrine signal that directly acts on ISCs.

The anatomical niche structure of ISC compartment and reciprocal *wg* and DI expression patterns suggest that Wg signalling could function upstream of the Notch pathway to prevent ISC differentiation. To test this hypothesis, we determined whether Notch activation is able to overcome the *wg*-induced ISC-like tumour phenotype. *N*^{intra} is a constitutively active form of Notch. Forced expression of *N*^{intra} was able to promote differentiation of *wg*-induced ISC-like cells into enterocyte cells and inhibit tumour formation (Fig. 4a, b). We further determined the epistatic relationship between Notch and Wg signalling by generating ISCs that lacked functional copies of both *dsh* and *N* genes. The *dsh* and *N* double-mutant ISCs behaved similarly to single *N* mutant ISCs, as both ISC-like (Fig. 4c) and enteroendocrine-like tumours (Fig. 4d) were observed,

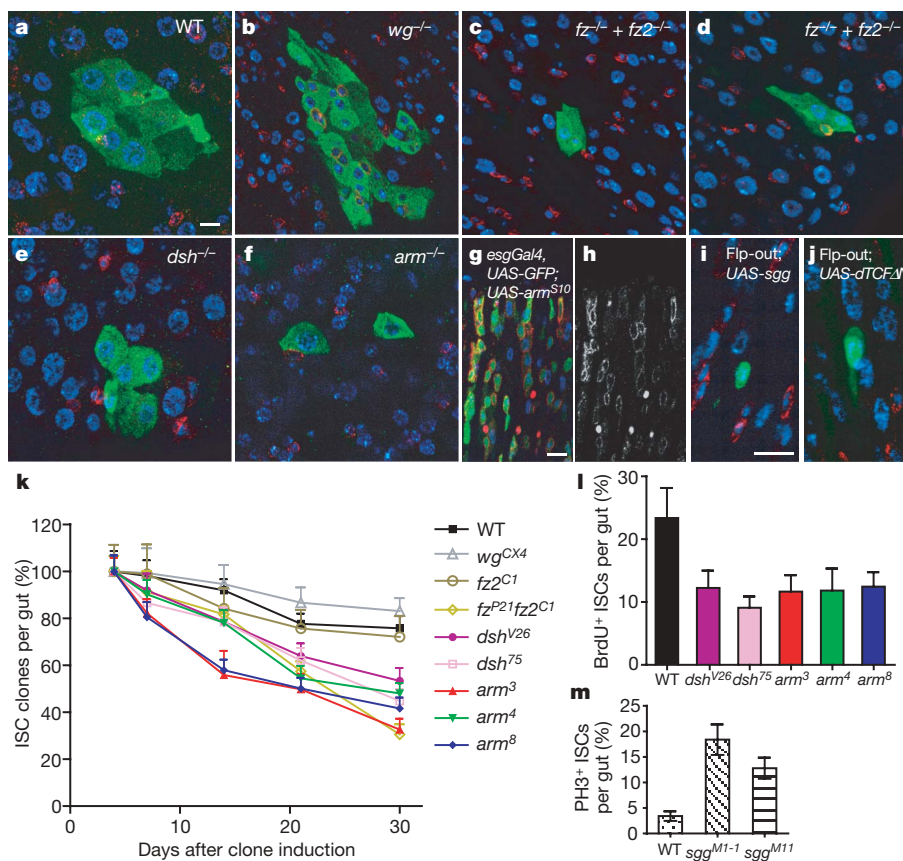


Figure 3 | Canonical *wg* signalling pathway components function cell-autonomously for ISC self-renewal. **a–f**, GFP clones (green) of given genotypes at 30 days after clone induction (anti-DI antibody, red). **g**, *arm*^{S10} expression causes extra ISC-like cells (DI⁺) and progenitors (GFP⁺, Pros⁺). Anti-DI (membrane, red) and anti-Pros (nucleus, red) antibody staining is shown. **h**, The red channel of **g** is shown. **i, j**, *sgg* (**i**) or *dTCFΔN* (**j**) expression promotes ISC loss (anti-DI antibody, red; anti-GFP antibody, green). **k**, A plot showing time course analysis of wild-type and mutant ISC clones. The percentage of ISC clones at a given time point is calculated as the average

number of clones carrying DI⁺ cells in each midgut divided by the average number of DI⁺ clones in each midgut at day 4. **l**, A graph showing percentages of BrdU-positive wild-type, *dsh* and *arm* mutant ISCs per midgut at 2 weeks. **m**, A graph showing the percentages of PH3-positive wild-type and *sgg* mutant ISCs per midgut at 2 weeks. Error bars in all graphs indicate s.e.m. *n* = 10–22 (intestines examined for each genotype at each time point). DAPI staining is shown in blue. WT, wild type; scale bars, 10 μm.

which are presumably caused by mutations in ISCs and enteroblasts, respectively³. These data further support the idea that Notch signalling functions downstream of Wg signalling in regulating ISCs. These results also indicate that Wg pathway activation is not absolutely required for DI expression in ISCs when Notch activity is disrupted. We suggest that DI expression in ISCs is controlled by a balanced outcome of opposite activities between Wg signalling from the niche and Notch signalling from their immediate daughters. We propose that the antagonistic activities of Wg and Notch signalling pathways control the balance between self-renewal and differentiation of ISCs (Fig. 4e).

Our results indicate that the underlying circular muscle is an important constitution of the ISC niche, which produces Wg as an important niche signal. Thus, *Drosophila* ISC self-renewal is also controlled, at least in part, by paracrine signals from a regulatory niche, a common theme found for many adult stem cells¹⁹. Notably, ISCs do not have specialized stromal cells for their localization, similar to the follicle stem cells in the *Drosophila* ovary²⁰. It is intriguing how stem cell location is controlled along the basement membrane. There could be unidentified substances in the extracellular matrix that restrict or facilitate ISC anchorage. It is also possible that other environmental cues contribute to niche establishment. For example, vascular or hypoxic niches have been found to support specific adult stem cells or progenitors in mammals²¹. Nevertheless, further investigation of ISC distribution mechanisms should provide insights into our understanding of niche structure and function.

In the mammalian intestine, Wnt ligands and receptors are expressed at the crypt base²², where ISCs and transient amplifying cells reside^{4,23}; Wnt signalling is crucial for maintaining the proliferative

state of the crypt and initiating colorectal cancer in APC mutations in humans²⁴. Thus, our study also shows Wnt signalling as an evolutionarily conserved mechanism regulating ISCs from *Drosophila* to mammals. Moreover, this study provides an important insight into the relationships between Wnt and Notch in regulating ISC self-renewal. Notch in mammals seems to function cooperatively with Wnt signalling to maintain the proliferative and undifferentiated state of intestinal progenitors⁴, although the exact role of Notch in ISCs and in transiently amplifying cells is not clear. Owing to the similarities in structure and regulatory mechanisms, our study further supports *Drosophila* as a powerful genetic model to dissect intestinal function. Further genetic analysis on *Drosophila* ISCs should help to understand better the stem cell niche, cell lineage specification and homeostasis control in intestine, and may lead to important insights into the underlying mechanisms of intestinal dysfunction and tumorigenesis.

METHODS SUMMARY

For clonal analysis, clones were generated either by the MARCM technique or by the Flp-out cassette. In both cases, mitotic clones were conditionally induced on heat-shock treatments for flipase expression, and clones were marked by GFP. Statistical analysis in Fig. 2c was done using the Student's *t*-test. For standard immunostaining, intestines were dissected in Grace's media, and fixed in a 1:1 (v/v) mixture of 4% formaldehyde and *n*-heptane for 15 min at room temperature. Samples were washed with 100% methanol and were gradually rehydrated in PBT (10 mM NaH₂PO₄/Na₂HPO₄, 175 mM NaCl, pH 7.4, 0.1% Triton X-100). For anti-Wg staining, samples were fixed in PEM-FA (0.1 M PIPES, 2 mM EGTA, 1.0 mM MgSO₄, 3.7% formaldehyde, pH 7.0) for 20 min and then washed with PBT. Appropriate primary antibodies were added to the samples and incubated at 4 °C overnight. Secondary antibodies were incubated either for 2 h at room temperature or overnight at 4 °C. For *in situ* hybridization, intestines were dissected in PBS and fixed as described above. After washing with PBT, samples were pre-hybridized at 55 °C for 1 h in hybridization buffer. RNA probes were added to hybridization buffer and incubated at 55 °C with shaking at 125 r.p.m. overnight; subsequently, standard labelling procedures were followed. An *in situ* cell death detection kit (Roche) was used for TUNEL labelling. For BrdU labelling, intestines were dissected in PBS, and incubated in 100 µg ml⁻¹ BrdU (Sigma) in PBS for 1 h at 25 °C. Samples were fixed in 4% formaldehyde for 30 min and followed by DNase I treatment for 1 h at 37 °C. The reaction was stopped by washing with PBT. All graphs were made using windows Prism 4 software, and all images were captured by a Zeiss Imager Z1 equipped with an ApoTome system, and were processed in Adobe Photoshop and Illustrator.

Full Methods and any associated references are available in the online version of the paper at www.nature.com/nature.

Received 27 April; accepted 8 August 2008.

Published online 21 September 2008.

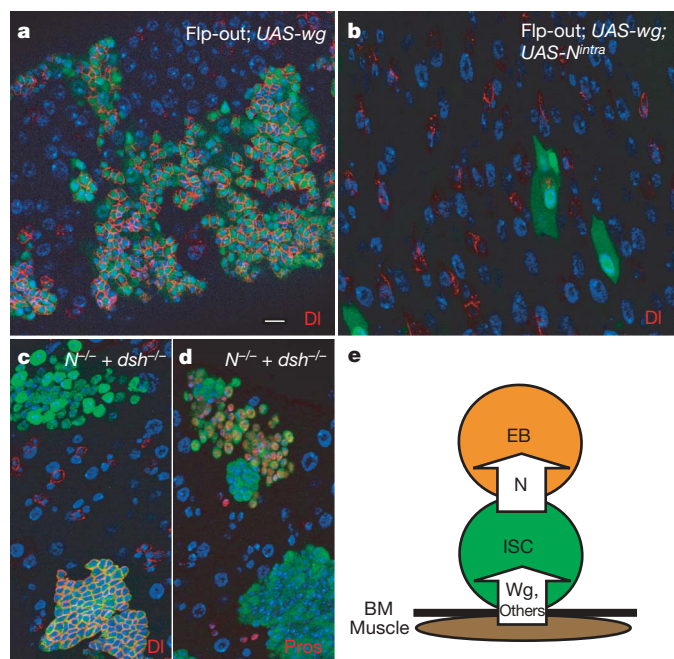


Figure 4 | Functional relationships between Wg and Notch signalling in regulating ISCs. **a**, wg overexpression results in an ISC-like tumour. **b**, wg and *N^{intra}* co-expression suppresses wg-induced tumour development and promotes ISC differentiation towards an enterocyte lineage (anti-DI antibody, red; anti-GFP antibody, green). **c**, **d**, *N²⁶⁴⁻⁴⁰*; *dsh²⁶* double mutant clones exhibit tumour phenotypes. ISC-like tumours (**c**; anti-DI antibody, red) and enteroendocrine-like tumours (**d**; anti-Pros antibody, red) are observed. **e**, A proposed model for controlling ISC self-renewal and differentiation. Wg (and possibly other signals from the underlying muscle) directly promotes ISC self-renewal by antagonizing Notch activation. Notch activation, through interactions between ISCs and their immediate daughters, promotes ISC differentiation. DAPI staining is shown in blue. BM, basement membrane; EB, enteroblast; N, Notch. Scale bar, 10 µm.

1. Micchelli, C. A. & Perrimon, N. Evidence that stem cells reside in the adult *Drosophila* midgut epithelium. *Nature* **439**, 475–479 (2006).
2. Ohlstein, B. & Spradling, A. The adult *Drosophila* posterior midgut is maintained by pluripotent stem cells. *Nature* **439**, 470–474 (2006).
3. Ohlstein, B. & Spradling, A. Multipotent *Drosophila* intestinal stem cells specify daughter cell fates by differential notch signaling. *Science* **315**, 988–992 (2007).
4. Crosnier, C., Stamatakis, D. & Lewis, J. Organizing cell renewal in the intestine: stem cells, signals and combinatorial control. *Nature Rev. Genet.* **7**, 349–359 (2006).
5. Kassis, J. A., Noll, E., VanSickle, E. P., Odenwald, W. F. & Perrimon, N. Altering the insertional specificity of a *Drosophila* transposable element. *Proc. Natl Acad. Sci. USA* **89**, 1919–1923 (1992).
6. Bejsovec, A. & Martinez Arias, A. Roles of *wingless* in patterning the larval epidermis of *Drosophila*. *Development* **113**, 471–485 (1991).
7. Brand, A. H. & Perrimon, N. Targeted gene expression as a means of altering cell fates and generating dominant phenotypes. *Development* **118**, 401–415 (1993).
8. Moon, R. T., Bowerman, B., Boutros, M. & Perrimon, N. The promise and perils of Wnt signaling through β -catenin. *Science* **296**, 1644–1646 (2002).
9. Lee, T., Winter, C., Marticke, S. S., Lee, A. & Luo, L. Essential roles of *Drosophila* RhoA in the regulation of neuroblast proliferation and dendritic but not axonal morphogenesis. *Neuron* **25**, 307–316 (2000).
10. Chen, C. M. & Struhl, G. Wingless transduction by the Frizzled and Frizzled2 proteins of *Drosophila*. *Development* **126**, 5441–5452 (1999).
11. Bhanot, P. et al. Frizzled and Dfrizzled-2 function as redundant receptors for Wingless during *Drosophila* embryonic development. *Development* **126**, 4175–4186 (1999).

12. Heslip, T. R., Theisen, H., Walker, H. & Marsh, J. L. Shaggy and dishevelled exert opposite effects on *Wingless* and *Decapentaplegic* expression and on positional identity in imaginal discs. *Development* **124**, 1069–1078 (1997).
13. Peifer, M. & Wieschaus, E. The segment polarity gene *armadillo* encodes a functionally modular protein that is the *Drosophila* homolog of human plakoglobin. *Cell* **63**, 1167–1176 (1990).
14. Song, X. & Xie, T. *wingless* signaling regulates the maintenance of ovarian somatic stem cells in *Drosophila*. *Development* **130**, 3259–3268 (2003).
15. Pai, L. M., Orsulic, S., Bejsovec, A. & Peifer, M. Negative regulation of Armadillo, a *Wingless* effector in *Drosophila*. *Development* **124**, 2255–2266 (1997).
16. Struhl, G. & Basler, K. Organizing activity of wingless protein in *Drosophila*. *Cell* **72**, 527–540 (1993).
17. van de Wetering, M. et al. Armadillo coactivates transcription driven by the product of the *Drosophila* segment polarity gene *dTCF*. *Cell* **88**, 789–799 (1997).
18. Bourouis, M. Targeted increase in shaggy activity levels blocks wingless signaling. *Genesis* **34**, 99–102 (2002).
19. Ohlstein, B., Kai, T., Decotto, E. & Spradling, A. The stem cell niche: theme and variations. *Curr. Opin. Cell Biol.* **16**, 693–699 (2004).
20. Nystul, T. & Spradling, A. An epithelial niche in the *Drosophila* ovary undergoes long-range stem cell replacement. *Cell Stem Cell* **1**, 277–285 (2007).
21. Nikolova, G., Strilic, B. & Lammert, E. The vascular niche and its basement membrane. *Trends Cell Biol.* **17**, 19–25 (2007).
22. Gregorieff, A. et al. Expression pattern of Wnt signaling components in the adult intestine. *Gastroenterology* **129**, 626–638 (2005).
23. Barker, N. et al. Identification of stem cells in small intestine and colon by marker gene *Lgr5*. *Nature* **449**, 1003–1007 (2007).
24. Radtke, F. & Clevers, H. Self-renewal and cancer of the gut: two sides of a coin. *Science* **307**, 1904–1909 (2005).

Acknowledgements We thank G. Struhl, L. Cooley, S. Hayashi, T. Xie, the Bloomington Stock Center for fly stocks, and members of the Xi laboratory for comments and discussions. This work was supported by an '863' grant 2007AA02Z1A2 to R.X. from the Chinese Ministry of Science and Technology.

Author Contributions G.L. and R.X. designed the research; N.X. performed the *in situ* hybridization experiments and G.L. performed all other experiments; G.L., N.X. and R.X. analysed the data and R.X. wrote the paper.

Author Information Reprints and permissions information is available at www.nature.com/reprints. Correspondence and requests for materials should be addressed to R.X. (xirongwen@nibs.ac.cn).

METHODS

Fly stocks. Flies were cultured on standard media with fresh yeast paste added to the food surface. Crosses were performed at 25 °C in humidity controlled incubators, or as otherwise noted. In all experiments, only female posterior midgut was analysed. Information for alleles and transgenes used in this study can be found either in FlyBase or as noted: *wg*^{ts}; *wg*^{CX4}; *wg-lacZ*; *esg-Gal4,UAS-GFP* (gift from S. Hayashi); *UAS-wg*; *fz*^{P21}; *fz2*^{C1}; *dsh*^{V26}; *dsh*⁷⁵; *arm*³; *arm*⁴; *arm*⁸; *UAS-sgg*; *UAS-dTCFΔN*; *N*²⁶⁴⁻⁴⁰; *UAS-N^{inttra}*.

Mosaic analysis. For MARCM clones, fly crosses were made to generate the following adults of genotypes: *hsflp122, tub-gal80 FRT19A/FRT19A; Act-Gal4, UAS-GFP/+*; *hsflp122, tub-gal80 FRT19A/arm⁺ FRT19A; Act-Gal4, UAS-GFP/+*; *hsflp122, tub-gal80 FRT19A/dsh⁺ FRT19A; Act-Gal4, UAS-GFP/+*; *hsflp122/+*; *tub-gal80 FRT40A/wg^{CX4} FRT40A; Act-Gal4, UAS-GFP/+*; *hsflp122/+*; *Act-Gal4, UAS-GFP/+*; *Tub-Gal80 FRT2A/fz⁺ FRT2A; hsflp122, tub-gal80 FRT19A/N²⁶⁴⁻⁴⁰dsh^{V26} FRT19A; Act-Gal4, UAS-GFP/+*. These adult females of 2–5 days old were subjected to heat-shock treatments for 1 h in a 37 °C running water bath. Flies were maintained at 25 °C after the treatment. Control flies that did not receive heat-shock treatment were also cultured at 25 °C. We found that there was a low incidence of leaky MARCM clones in the control intestines without heat-shock treatment, with about one ISC clone per midgut at several different time points examined (day 4, 14 and 30), which should not significantly affect the results of time course clonal analysis. For clones made by the Flp-out cassette, the following adults of genotypes were generated: *hsflp122/+*; *Act5C > y > Gal4, UAS-GFP/UAS-wg*; *hsflp122/+*; *Act5C > y > Gal4, UAS-GFP/UAS-N^{inttra}*; *UAS-wg*; *hsflp122/+*; *Act5C > y > Gal4, UAS-GFP/+*; *UAS-dTCFΔN/+*; *hsflp122/+*; *Act5C > y > Gal4, UAS-GFP/+*; *UAS-sgg/+*. Flies were heat-shocked at 37 °C for 1 h and were dissected and stained 2 weeks after clone induction.

Immunostaining and fluorescence microscopy. Intestines were dissected in Grace's media, and fixed in a 1:1 (v/v) mixture of 4% formaldehyde and *n*-heptane for 15 min at room temperature. The lower phase of the mixture was then removed and replaced by an equal volume of methanol. Samples were gradually rehydrated in PBT. For anti-Wg staining, samples were fixed in PEM-FA (0.1 M PIPES, 2 mM EGTA, 1.0 mM MgSO₄, 3.7% formaldehyde, pH 7.0) for 20 min and washed by PBT. Samples were then incubated in 5% normal goat serum in PBT for 1 h. Appropriate primary antibodies were added to the samples and incubated at 4 °C overnight. Secondary antibodies were incubated for either 2 h at room temperature or overnight at 4 °C. Samples were mounted in 70% glycerol. The following antibodies or dyes were used: mouse anti-Delta antibody (Developmental Studies Hybridoma Bank (DSHB); 1:100); mouse anti-Wg antibody (DSHB, 1:200); mouse anti-Pros antibody (DSHB, 1:100); rabbit anti-BrdU antibody (1:300); rabbit anti-phosphor-Histone H3 antibody (Upstate, 1:1,000); rabbit polyclonal anti-β-gal antibodies (Cappel, 1:6,000); Alexa-568-conjugated goat anti-mouse/rabbit and Alexa-488-conjugated goat anti-rabbit/

mouse secondary antibodies (Molecular Probes, 1:300); rhodamine-conjugated phalloidin (Molecular Probes, 1:200); and DAPI (Sigma; 0.1 μg ml⁻¹, 6 min incubation). All images were captured by a Zeiss Imager Z1 equipped with an ApoTome system, and were processed in Adobe Photoshop and Illustrator.

In situ hybridization. Intestines were dissected in PBS and fixed as described above. After washing with PBT, samples were pre-hybridized at 55 °C for 1 h in hybridization buffer (50% formamide, 4× SSC, 5% dextran sulphate and 0.01% Tween 20). RNA probes were added to hybridization buffer and incubated at 55 °C with shaking at 125 r.p.m. overnight. Samples were then washed with wash buffer (50% formamide, 2× SSC and 0.01% Tween 20) at 55 °C with shaking, and blocked in 5% normal goat serum in PBS, and then incubated with alkaline phosphatase-conjugated anti-digoxigenin Fab fragments (Roche, 1:1,000) at 4 °C overnight, then washed with PBT and AP buffer (0.1 M NaCl, 0.05 M MgCl₂, 0.1 M Tris, pH 9.5, 0.1% Tween 20). Bound antibody was detected by incubating samples in developing solution (45 μl NBT (nitroblue tetrazolium) and 35 μl BCIP (5-bromo-4-chloro-3-indolylphosphate-p-toluidine salt) per 10 ml of AP buffer). The colour reaction was stopped by washing samples with PBT.

TUNEL staining. An *in situ* cell death detection kit (Roche) was used to detect apoptosis. Intestines were dissected and fixed as described above. After washing with PBT, samples were blocked in 5% normal goat serum for 30 min, and then incubated in TUNEL reaction mixture at 37 °C for 1 h. The reaction was stopped by washing samples with PBT three times.

BrdU labelling. Intestines were dissected in PBS, and incubated in 100 μg ml⁻¹ BrdU (Sigma) in PBS for 1 h at 25 °C. After washing with PBS, samples were fixed in 4% formaldehyde for 30 min and subsequently washed with PBT three times. The fixed guts were treated with DNase I for 1 h at 37 °C. The reaction was stopped by washing samples with PBT three times. Subsequent immunostaining procedures were as described above.

Data analysis. In Fig. 2c, the percentage of ISCs is calculated as the total number of ISCs divided by the total number of epithelial cells per midgut; the percentage of BrdU-positive ISCs is calculated as the number of BrdU positive ISCs divided by the total number of ISCs per midgut. Statistical analysis was done using the Student's *t*-test. For time course clonal analysis shown in Fig. 3k, we quantified the average number of ISC-containing clones per midgut at day 4, 7, 14, 21 and 30 after clone induction, respectively, and the percentage of ISC clones at different time points is calculated as the average number of ISC-containing clones per midgut in a given time point divided by the average number of ISC-containing clones per midgut at day 4; the value at each time point reflects the percentage of clones that still retain ISCs. The percentage of BrdU- or PH3-positive ISCs of a given genotype shown in Fig. 3l, m is calculated as the number of BrdU- or PH3-positive ISCs divided by the total number of ISCs per midgut. For all graphs in Fig. 3, 10–22 intestines (which contain 150–350 clones) were examined for each genotype at each time point. The graphs were made using windows Prism 4 software.

LETTERS

MicroRNAs to *Nanog*, *Oct4* and *Sox2* coding regions modulate embryonic stem cell differentiation

Yvonne Tay^{1†}, Jinqiu Zhang¹, Andrew M. Thomson^{1*}, Bing Lim^{1,2*} & Isidore Rigoutsos^{3*}

MicroRNAs (miRNAs) are short RNAs that direct messenger RNA degradation or disrupt mRNA translation in a sequence-dependent manner^{1–7}. For more than a decade, attempts to study the interaction of miRNAs with their targets were confined to the 3' untranslated regions of mRNAs¹, fuelling an underlying assumption that these regions are the principal recipients of miRNA activity. Here we focus on the mouse *Nanog*, *Oct4* (also known as *Pou5f1*) and *Sox2* genes^{8–11} and demonstrate the existence of many naturally occurring miRNA targets in their amino acid coding sequence (CDS). Some of the mouse targets analysed do not contain the miRNA seed, whereas others span exon–exon junctions or are not conserved in the human and rhesus genomes. miR-134, miR-296 and miR-470, upregulated on retinoic-acid-induced differentiation of mouse embryonic stem cells, target the CDS of each transcription factor in various combinations, leading to transcriptional and morphological changes characteristic of differentiating mouse embryonic stem cells, and resulting in a new phenotype. Silent mutations at the predicted targets abolish miRNA activity, prevent the downregulation of the corresponding genes and delay the induced phenotype. Our findings demonstrate the abundance of CDS-located miRNA targets, some of which can be species-specific, and support an augmented model whereby animal miRNAs exercise their control on mRNAs through targets that can reside beyond the 3' untranslated region.

The founding members of the miRNA class were shown to act on the 3' untranslated regions (UTRs) of transcripts^{12,13} and, with a few exceptions^{14,15}, subsequent efforts focused almost uniquely on the interaction of miRNAs with 3' UTRs^{16,17}. Our earlier computational analyses predicted an abundance of miRNA targets beyond the confines of a 3' UTR¹⁸. We investigate this conjecture below focusing on targets that exist naturally within the CDS of a gene, an exploration that differs from earlier work with artificial constructs¹⁹. We selected the *Nanog*, *Oct4* and *Sox2* transcription factors given their importance in maintaining the pluripotency of mouse embryonic stem cells (ESCs) and determining the initiation of differentiation^{8–11,20–23}.

After retinoic acid treatment of mouse ESC line E14, we profiled the expression of miRNAs using quantitative polymerase chain reaction (PCR). miR-296, miR-470 and miR-134 were all significantly upregulated relative to their expression at day 0 in undifferentiated mouse ESCs (see Supplementary Information), and were also predicted computationally by rna22 (ref. 18) to target the CDSs of *Nanog*, *Oct4* and *Sox2* in various combinations. Because rna22 does not need validated targets for training, and neither requires nor relies on cross-species conservation, it is an ideal tool for determining miRNA targets in CDSs.

Rna22 predicts two miR-296 targets (also known as miRNA-response elements or MREs) and six miR-470 targets in the CDS of

Nanog, three miR-470 targets in the CDS of *Oct4*, and five miR-134 targets in the CDS of *Sox2*. We denote these sites as X-Yp-Z, in which X is the targeted gene, Y is the distance (in bases) of the 5' end of the predicted target from the transcription initiation site, Z represents the targeting miRNA (that is, one of miR-296, miR-470 or miR-134), and p stands for predicted. These predicted targets are: *Nanog*-425p-296, *Nanog*-683p-296, *Nanog*-271p-470, *Nanog*-290p-470, *Nanog*-363p-470, *Nanog*-457p-470, *Nanog*-615p-470, *Nanog*-727p-470, *Oct4*-380p-470, *Oct4*-401p-470, *Oct4*-410p-470, *Sox2*-910p-134, *Sox2*-974p-134, *Sox2*-980p-134, *Sox2*-1037p-134 and *Sox2*-1224p-134.

We transfected mouse ESCs with precursor miRNA (pre-miRNA) oligomers (see Methods) separately for each miRNA and measured the effect on the predicted corresponding endogenous target using quantitative PCR and western blotting. Each miRNA had only a limited effect on the mRNA of the endogenous target but affected the corresponding protein more substantially (Fig. 1a). Transfection with the scrambled control oligomer *Scr* (negative control) or pre-miR-181a (non-targeting miRNA) resulted in no significant decrease in mRNA or protein expression. These results indicate that each miRNA induces post-transcriptional downregulation of its predicted endogenous target in mouse ESCs, predominantly by inhibiting translation.

To ensure that our findings were not the consequence of a complex interplay among the numerous interacting proteins present in mouse ESCs²¹, we used 293T cells as a control environment devoid of such interactions. Indeed, western blotting did not detect any *Nanog*, *Oct4* or *Sox2* proteins therein (data not shown).

We created wild-type CDS constructs for *Nanog*, *Oct4* and *Sox2* (see Methods) and used each in turn with its matching pre-miRNA to co-transfect 293T cells. Figure 1b shows quantitative PCR measurements and western blotting for the four pre-miRNA plus CDS-construct combinations. The results in 293T cells mirrored those we obtained with mouse ESCs in that the effect of the pre-miRNA on the selected mRNA was minimal, but protein expression decreased substantially. Neither *Scr* nor pre-miR-181a controls induced significant changes.

We subsequently screened the predicted MREs using luciferase assays (see Supplementary Information) and then selected five (*Nanog*-425p-296, *Nanog*-683p-296, *Nanog*-457p-470, *Oct4*-410p-470 and *Sox2*-1037p-134) that substantially suppressed luciferase expression in the presence of the matching miRNA. For each of the five MREs, we generated and tested several variants by introducing silent mutations designed to disrupt the putative base pairings between the miRNA and the corresponding predicted target. We generated five mutants of the *Nanog*-425p-296 MRE, eight of the *Nanog*-683p-296 MRE, five of the *Nanog*-457p-470 MRE, three of

¹Stem Cell and Developmental Biology, Genome Institute of Singapore, Agency for Science Technology and Research (A*STAR), #08-01, Genome, 60 Biopolis Street, Singapore 138672, Singapore. ²Beth-Israel Medical Center, Harvard Medical School, 77 Avenue Louis Pasteur, Boston, Massachusetts 02215, USA. ³Bioinformatics and Pattern Discovery Group, IBM Thomas J. Watson Research Center, Yorktown Heights, PO Box 218, New York 10598, USA. [†]Present address: Experimental Therapeutics Center, Agency for Science Technology and Research (A*STAR), Nanos Level 3, 31 Biopolis Way, Singapore 138669, Singapore.

*These authors contributed equally to this work.

the *Oct4*-410p-470 MRE and four of the *Sox2*-1037p-134 MRE. All of the mutants affected luciferase expression (see Supplementary Information). On the basis of their observed effect on the reporter, the *Nanog*-425p-296-m4, *Nanog*-683p-296-m2, *Nanog*-683p-296-m4, *Nanog*-457p-470-m5, *Oct4*-410p-470-m3 and *Sox2*-1037p-134-m4 mutants were then selected for the remaining experiments.

In addition to the wild-type *Nanog*-, *Oct4*- and *Sox2*-CDS constructs, we generated the following mutants: (1) *Nanog*-425p-296 was replaced with *Nanog*-425p-296-m4, but *Nanog*-683p-296 was kept intact; (2) *Nanog*-425p-296 was kept intact, but *Nanog*-683p-296 was replaced with *Nanog*-683p-296-m2; (3) *Nanog*-425p-296 was kept intact but *Nanog*-683p was replaced with *Nanog*-683p-296-m4; (4) *Nanog*-425p-296 and *Nanog*-683p-296 were replaced with *Nanog*-425p-296-m4 and *Nanog*-683p-296-m2, respectively; (5) *Nanog*-457p-470 was replaced with *Nanog*-457p-470-m5; (6) *Oct4*-410p-470 was replaced with *Oct4*-410p-470-m3; and (7) *Sox2*-1037p-134 was replaced with *Sox2*-1037p-134-m4.

We co-transfected 293T cells with each CDS construct and the matching pre-miRNA and measured the effect using quantitative PCR and western blotting. *Scr* was again used as a negative control. Silent mutations introduced into either one of the two predicted targets disrupted the ability of miR-296 to repress translation of the mutant *Nanog*-CDS (Fig. 2a). However, simultaneous introduction of silent mutations at both the *Nanog*-425p-296 and the *Nanog*-683p-296 sites successfully abolished the downregulation of *Nanog* by pre-miR-296. Thus, miR-296 independently targets these two sites. Similar results were obtained using the other two miRNAs as the introduced silent mutations rescued the corresponding *Nanog*-, *Oct4*- and *Sox2*-CDS constructs from downregulation by pre-miR-470 and pre-miR-134 (Fig. 2b, c).

We next examined whether the miRNAs could modulate ESC differentiation and elicit phenotypic effects. We focused on miR-296 and

miR-470 only because we have shown previously²³ that miR-134 targets the 3' UTR of wild-type *Nanog* while participating in a rather complex network potentially comprising several thousand targets including other transcription factors upstream of *Sox2* (refs 18 and 23).

Quantitative PCR measurements of total RNA samples taken from E14 ESCs three days after transfection with pre-miR-296 were compared to samples obtained after transfection with *Scr*. Transfection of pre-miR-296 into undifferentiated E14 ESCs led to increased expression of the differentiation markers *Fgf5*, *Sox1*, *Mixl1* and *Kdr*. In relation to the retinoic-acid-treated E14 ESCs that were transfected with the *Scr* control oligomer, transfection of pre-miR-296 resulted in accelerated acquisition of the ectoderm markers *Fgf5*, *Sox1* and *Otx2* (see Supplementary Information). The presence of pre-miR-296 also enhanced the retinoic-acid-induced decrease in *Nanog* but elicited only minimal changes in *Oct4* or *Sox2* mRNA levels (see Supplementary Information).

Transfection of mouse ESCs with pre-miR-296 led to morphological changes within three days as the cells acquired a flattened epithelial-like morphology typical of differentiating ESCs. The levels of alkaline phosphatase, a marker of ESC pluripotency²⁴, were reduced after pre-miR-296 transfection, whereas no changes were induced after transfection with either *Scr* or *Scr* plus the empty vector control (Fig. 3a). The visible phenotypic changes of differentiating ESCs (as well as the reduced alkaline phosphatase activity) induced by pre-miR-296 were partially rescued by the double mutant *Nanog*-CDS construct (*Nanog*-425-296-m4 + *Nanog*-683p-296-m2), whereas rescue by the wild-type *Nanog*-CDS was marginal (Fig. 3a). Pre-miR-296 also significantly decreased the ability of mouse ESCs to form colonies (see Supplementary Information). Consistent with this, co-transfection of pre-miR-296 with the double mutant *Nanog*-CDS construct into undifferentiated E14 ESCs rescued

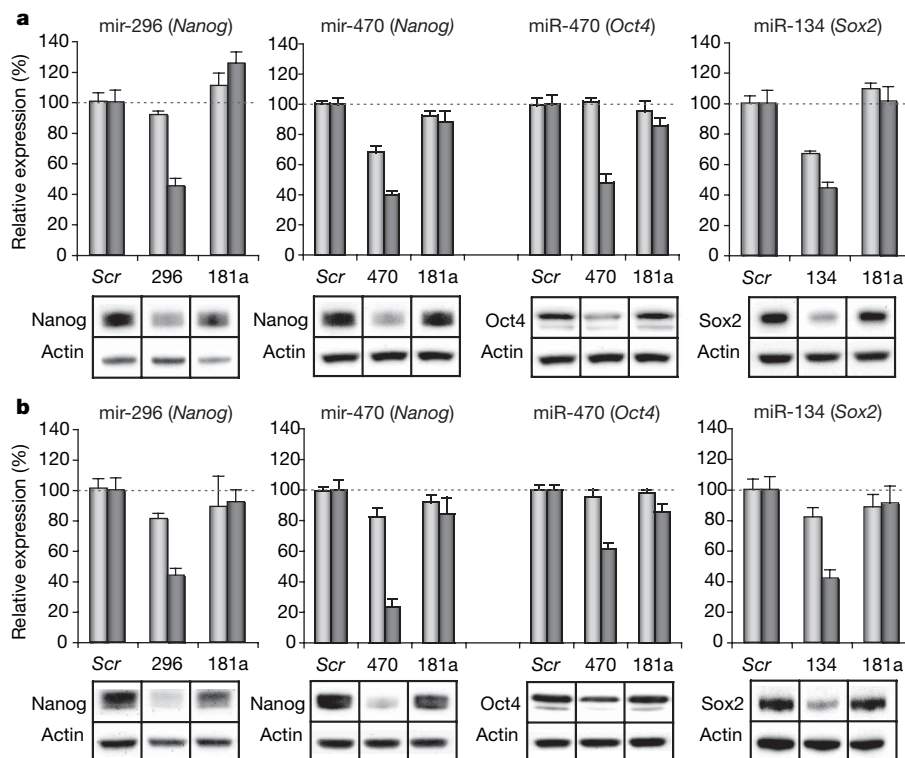


Figure 1 | MicroRNA effect on the amount of the mRNA and protein of the corresponding predicted target. a, b, Transfection of mouse ESCs with pre-miR-296, pre-miR-470 and pre-miR-134, respectively (**a**); and co-transfection of 293T cells with pre-miR-296 and *Nanog*-CDS, pre-miR-470 and *Oct4*-CDS, or pre-miR-134 and *Sox2*-CDS (**b**). Also shown are the results obtained using the control *Scr* oligomer

and the non-targeting pre-miR-181a. Each of the six panels shows mRNA (light grey) and protein (dark grey) measurements and the corresponding western blots. β -actin antibody was used as a loading control. All experiments were performed in triplicate, thrice ($n = 9$); error bars denote the standard deviation.

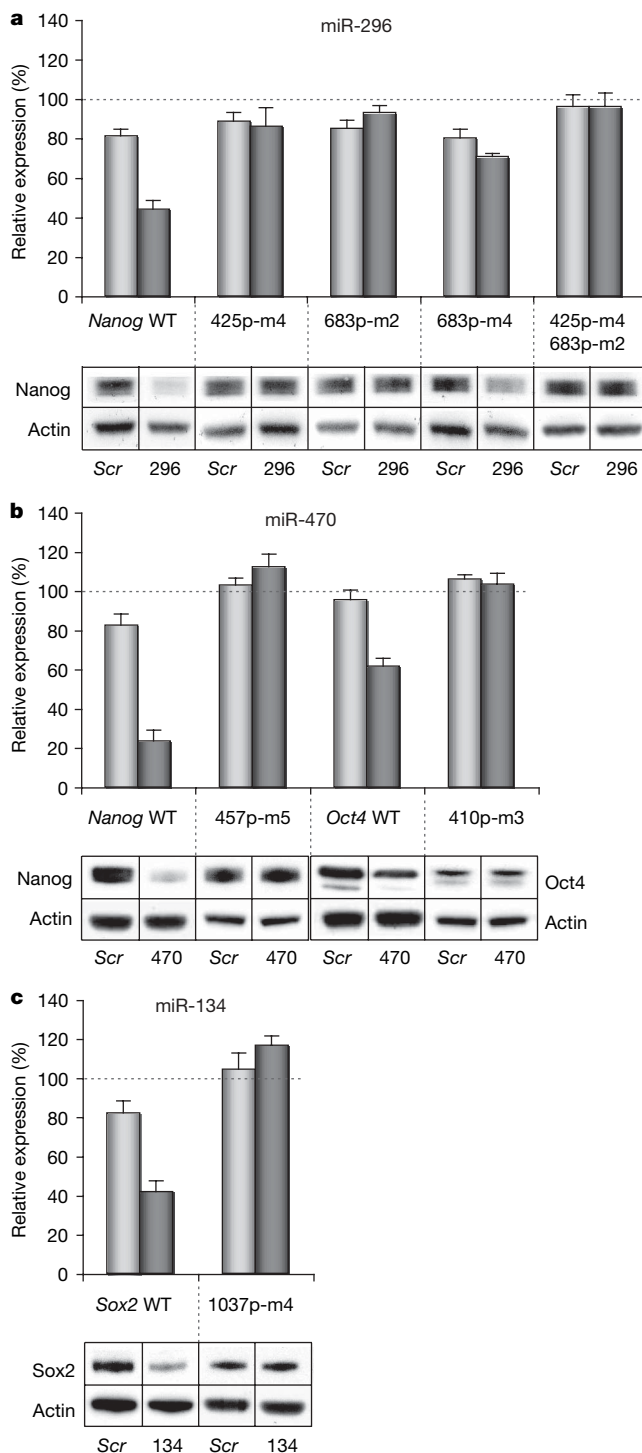


Figure 2 | MicroRNA effect on the amount of mRNA and protein of a CDS construct. **a–c**, Co-transfection of 293T cells with pre-miR-296 (**a**), pre-miR-470 (**b**) or pre-miR-134 (**c**). The top panels show quantitative PCR measurements (light grey) and quantification of the western blots (dark grey); the bottom panels show the western blots. The cells were co-transfected with control *Scr* or the pre-miRNA with wild-type (WT) or mutant-CDS construct. *Nanog*-425p-296-m4, *Nanog*-683p-296-m2, *Nanog*-683p-296-m4, *Nanog*-457p-470-m5, *Oct4*-410p-470-m3 and *Sox2*-1037p-134-m4 are abbreviated as 425p-m4, 683p-m2, 683p-m4, 457p-m5, 410p-m3 and 1037p-m4, respectively. All experiments were performed in triplicate, thrice ($n = 9$); error bars denote the standard deviation.

the pre-miR-296-induced upregulation of *Fgf5*, *Sox1*, *Mixl1* and *Couptf*, but not of *Kdr* (Fig. 3b). Western blotting showed that the double mutant was able to rescue the pre-miR-296-induced downregulation of Nanog protein (Fig. 3c). Overexpression of the wild-type *Nanog*-CDS construct increased Nanog protein expression in the presence of *Scr* or pre-miR-296 to a higher amount than that which was observed when *Scr* or pre-miR-296 alone was transfected. However, Nanog protein levels were lower in ESCs co-transfected with pre-miR-296 (Fig. 3c and Supplementary Information).

Transfecting pre-miR-470 into E14 ESCs led, by the third day, to visible morphological changes (Fig. 4a) compared to control. Relative to the empty vector, co-transfection of the mutant CDS constructs *Nanog*-457p-470-m5 and *Oct4*-410p-470-m3 into undifferentiated E14 ESCs partially rescued the morphological changes and alkaline phosphatase activity, whereas co-transfection of pre-miR-470 and wild-type *Nanog*- and *Oct4*-CDS constructs resulted in a phenotype between that of the empty vector co-transfection and the mutant CDS construct co-transfection, with little rescue at the morphological level. Transcript analysis showed increased expression of the markers *Fgf5*, *Nes* and *Otx2* in relation to control transfection; co-transfection of the CDS constructs *Nanog*-457p-470-m5 and *Oct4*-410p-470-m3 partially rescued this upregulation (Fig. 4b). Western blot analyses corroborated these findings (Fig. 4c and Supplementary Information).

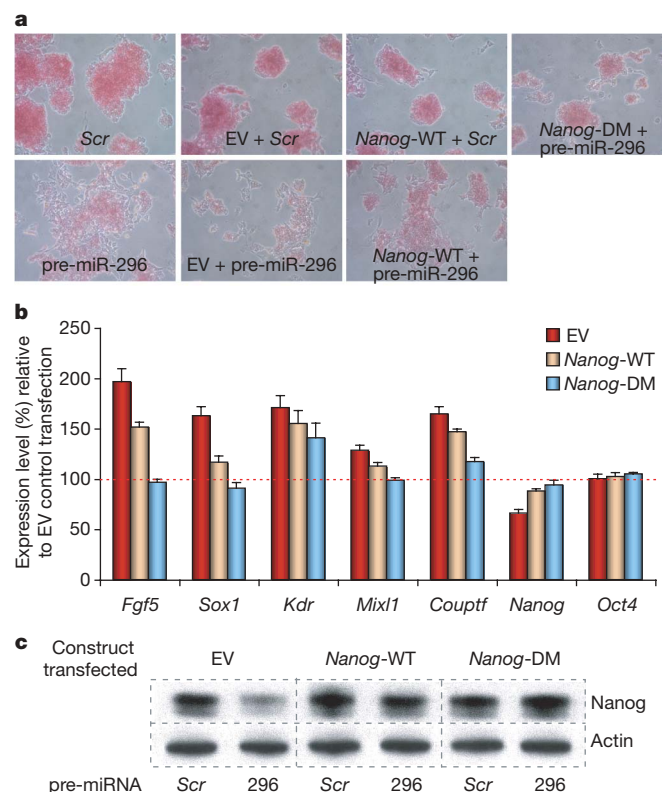


Figure 3 | The mutant *Nanog*-CDS construct partially rescues miR-296 modulated mouse ESC differentiation. **a**, Alkaline phosphatase staining of E14 ESCs three days after transfection. The *Nanog* double mutant (*Nanog*-DM) partially rescues the pre-miR-296-induced phenotypic changes and reduced alkaline phosphatase activity. EV, empty vector. Original magnifications for all images was $\times 400$. **b**, Relative to the empty vector control, transfection of *Nanog*-DM into undifferentiated E14 ESCs rescues the pre-miR-296-induced upregulation of *Fgf5*, *Sox1*, *Mixl1* and *Couptf*. All experiments were done in triplicate, thrice ($n = 9$); error bars denote the standard deviation. **c**, Western blots showing that transfection of the *Nanog*-DM into mouse ESCs rescues the pre-miR-296-induced downregulation of Nanog protein. See also Supplementary Information.

Treatment of mouse ESCs with anti-miRNA combinations reduced the retinoic-acid-induced changes to Nanog, Oct4 and Sox2 protein and biomarker transcript levels while delaying differentiation (see Supplementary Information). This supports the participation of these miRNAs in the differentiation process and is consistent with our earlier report that retinoic-acid-induced differentiation of ESCs affects the expression of many miRNAs²³.

Our findings posit a realm of miRNA activity that extends well beyond the very recent reporting of a single, evolutionary-conserved CDS target^{25,26}. We show that one miRNA can simultaneously target several sites in the CDS of one mRNA or the CDSs of different mRNAs. Furthermore, we show that several miRNAs can simultaneously target the same mRNA through its CDS and 3' UTR (miR-296 or miR-470 plus *Nanog*-CDS, and miR-134 plus *Nanog*-3' UTR). These miRNA properties parallel transcription factor activity²⁷. We note that the target of miR-134 in the 3' UTR of *Nanog*²³ is within a mouse B2 SINE element, suggesting that miRNAs can regulate gene expression by targeting repeat elements embedded in gene transcripts. In most of the heteroduplexes we studied, the degree of complementarity is not pronounced (unlike in plants²⁸) suggesting

that short interfering RNAs can modulate gene expression through CDS sites with only partial complementarity to the siRNA. Four of the five validated targets do not contain the miRNA seed due to G:U pairs or bulges; thus, enforcing the seed constraint will underestimate the number of true miRNA targets (see also related work²⁹). Furthermore, four of the five validated mouse targets are not conserved in human and rhesus, and therefore enforcing the cross-species conservation constraint will also underestimate the number of true miRNA targets. Finally, two of the five validated targets stride exon-exon junctions, a potentially powerful finding that suggests that a miRNA can selectively target splice variants.

METHODS SUMMARY

Rna22 (ref. 18) was used to predict target sites for the miRNAs of interest; these sites are full-length, that is, each predicted heteroduplex extends beyond the span of the seed of the corresponding miRNA. HEK293T/17 (CRL-11268, American Tissue Culture Collection) cells and mouse embryonic stem cell line E14 (CRL-1821, ATCC) were maintained as described previously²³. The scrambled RNA oligomer (*Scr*, AGACUAGCGUAUCUUUAUCC) and the pre-miRNAs and anti-miRNAs (Ambion) were transfected into mouse ESCs at a final concentration of 100 nM using Lipofectamine 2000 (Invitrogen). Co-transfection of pre-miRNAs or the *Scr* RNA oligomer with CDS constructs into 293T cells or mouse ESCs was performed in 12-well plates; 0.2 µg of each CDS construct was transfected per well, together with pre-miRNAs or *Scr* RNA oligomer at a final concentration of 100 nM using Lipofectamine 2000 according to the manufacturer's instructions. RNA extraction, purification and quantitative PCR were as described previously²³ with *Gapdh* expression used as an internal control. All amplicons analysed using Prism 7900HT sequence detection system 2.2 software (Applied Biosystems). Primer sequences are available on request. Cell lysis, protein concentrations and western blot analyses were performed as described previously²³, in which membranes were probed with specific primary antibodies (Nanog, AB5731; β-actin, MAB1501; Chemicon; Oct4, sc-8629; Sox2, sc-17320; Santa Cruz Biotechnology) and secondary horseradish-peroxidase-conjugated antibodies (anti-goat-HRP, sc2768; anti-rabbit-HRP, sc2030; anti-mouse-HRP, sc2005; Santa Cruz Biotechnology). Antibody-protein complexes were detected using ECL-plus (GE Healthcare) on a Bio-Rad Versadoc 5000 and images were quantified using QuantityOne software. The wild-type *Nanog*-, *Oct4*- and *Sox2*-CDSs, and respective CDS mutants were each cloned into pcDNA3.1 (Invitrogen) at restriction sites BamHI and XhoI. To generate each CDS mutant construct, PCR directed mutagenesis was performed with a pair of primers containing the mutant MRE sequence. The primer sequences used for mutagenesis are given in the Methods section. Alkaline phosphatase activity was measured as described previously²³.

Full Methods and any associated references are available in the online version of the paper at www.nature.com/nature.

Received 10 April; accepted 30 July 2008.

Published online 17 September 2008.

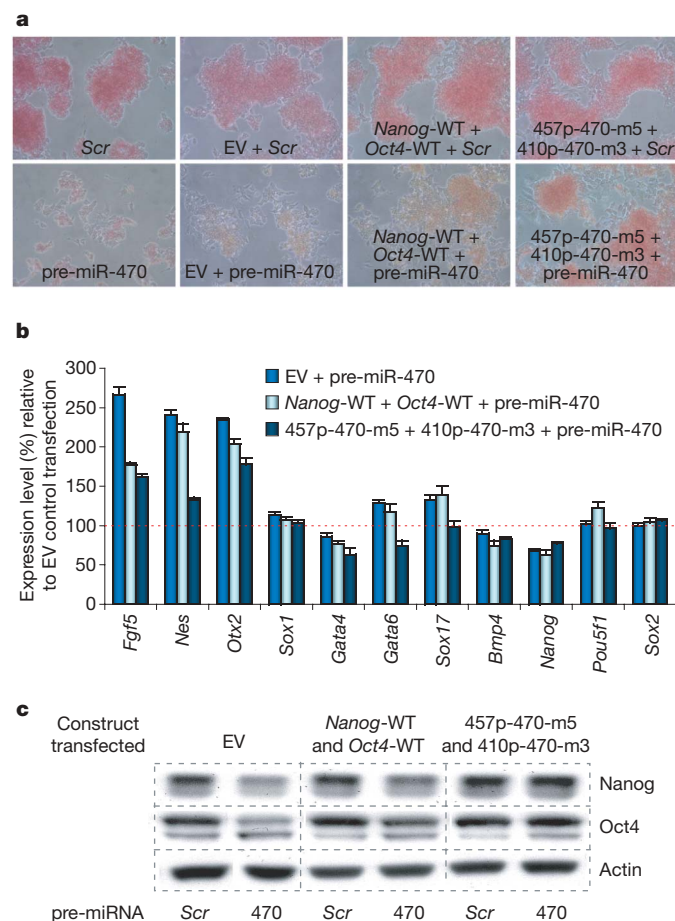


Figure 4 | Mutant *Nanog*- and *Oct4*-CDS constructs partially rescue miR-470 modulated mouse ESC differentiation. **a**, Alkaline phosphatase staining of E14 ESCs three days after transfection. *Nanog*-457p-470-m5 and *Oct4*-410p-470-m3 partially rescue the pre-miR-470-induced phenotypic changes and reduced alkaline phosphatase activity. EV, empty vector; WT, wild type. Original magnifications for all images was $\times 400$. **b**, Relative to the empty vector control, co-transfection of the *Nanog*-457p-470-m5 and *Oct4*-410p-470-m3 CDS mutants into undifferentiated E14 ESCs rescues the pre-miR-470-induced upregulation of several markers. All experiments were carried out in triplicate, thrice ($n = 9$); error bars denote the standard deviation. **c**, Western blots showing that simultaneous transfection of these two mutants into mouse ESCs rescues the pre-miR-470-induced downregulation of Nanog and Oct4. See also Supplementary Information.

1. Bartel, D. P. MicroRNAs: genomics, biogenesis, mechanism, and function. *Cell* **116**, 281–297 (2004).
2. Elbashir, S. M., Lendeckel, W. & Tuschl, T. RNA interference is mediated by 21- and 22-nucleotide RNAs. *Genes Dev.* **15**, 188–200 (2001).
3. Hammond, S. M. Dicing and slicing: the core machinery of the RNA interference pathway. *FEBS Lett.* **579**, 5822–5829 (2005).
4. Hannon, G. J. RNA interference. *Nature* **418**, 244–251 (2002).
5. Lagos-Quintana, M., Rauhut, R., Lendeckel, W. & Tuschl, T. Identification of novel genes coding for small expressed RNAs. *Science* **294**, 853–858 (2001).
6. Pillai, R. S., Bhattacharyya, S. N. & Filipowicz, W. Repression of protein synthesis by miRNAs: how many mechanisms? *Trends Cell Biol.* **17**, 118–126 (2007).
7. Pillai, R. S. MicroRNA function: multiple mechanisms for a tiny RNA? *RNA* **11**, 1753–1761 (2005).
8. Niwa, H., Miyazaki, J. & Smith, A. G. Quantitative expression of Oct-3/4 defines differentiation, dedifferentiation or self-renewal of ES cells. *Nature Genet.* **24**, 372–376 (2000).
9. Okumura-Nakanishi, S., Saito, M., Niwa, H. & Ishikawa, F. Oct-3/4 and Sox2 regulate Oct-3/4 gene in embryonic stem cells. *J. Biol. Chem.* **280**, 5307–5317 (2005).
10. Pan, G. & Thomson, J. A. Nanog and transcriptional networks in embryonic stem cell pluripotency. *Cell Res.* **17**, 42–49 (2007).
11. Mitsui, K. *et al.* The homeoprotein Nanog is required for maintenance of pluripotency in mouse epiblast and ES cells. *Cell* **113**, 631–642 (2003).
12. Slack, F. J. *et al.* The *lin-41* RBCC gene acts in the *C. elegans* heterochronic pathway between the *let-7* regulatory RNA and the LIN-29 transcription factor. *Mol. Cell* **5**, 659–669 (2000).

13. Lee, R. C., Feinbaum, R. L. & Ambros, V. The *C. elegans* heterochronic gene *lin-4* encodes small RNAs with antisense complementarity to *lin-14*. *Cell* **75**, 843–854 (1993).
14. Easow, G., Teleman, A. A. & Cohen, S. M. Isolation of microRNA targets by miRNP immunopurification. *RNA* **13**, 1198–1204 (2007).
15. Lytle, J. R., Yario, T. A. & Steitz, J. A. Target mRNAs are repressed as efficiently by microRNA-binding sites in the 5' UTR as in the 3' UTR. *Proc. Natl Acad. Sci. USA* **104**, 9667–9672 (2007).
16. Bentwich, I. Prediction and validation of microRNAs and their targets. *FEBS Lett.* **579**, 5904–5910 (2005).
17. Rajewsky, N. microRNA target predictions in animals. *Nature Genet.* **38**, S8–S13 (2006).
18. Miranda, K. C. *et al.* A pattern-based method for the identification of microRNA binding sites and their corresponding heteroduplexes. *Cell* **126**, 1203–1217 (2006).
19. Kloosterman, W. P., Wienholds, E., Ketting, R. F. & Plasterk, R. H. Substrate requirements for *let-7* function in the developing zebrafish embryo. *Nucleic Acids Res.* **32**, 6284–6291 (2004).
20. Silva, J., Chambers, I., Pollard, S. & Smith, A. Nanog promotes transfer of pluripotency after cell fusion. *Nature* **441**, 997–1001 (2006).
21. Loh, Y. H. *et al.* The Oct4 and Nanog transcription network regulates pluripotency in mouse embryonic stem cells. *Nature Genet.* **38**, 431–440 (2006).
22. Chambers, I. *et al.* Functional expression cloning of Nanog, a pluripotency sustaining factor in embryonic stem cells. *Cell* **113**, 643–655 (2003).
23. Tay, Y. M. *et al.* MicroRNA-134 modulates the differentiation of mouse embryonic stem cells, where it causes post-transcriptional attenuation of Nanog and LRH1. *Stem Cells* **26**, 17–29 (2008).
24. Palmqvist, L. *et al.* Correlation of murine embryonic stem cell gene expression profiles with functional measures of pluripotency. *Stem Cells* **23**, 663–680 (2005).
25. Duursma, A. M., Kedde, M., Schrier, M., le Sage, C. & Agami, R. miR-148 targets human DNMT3b protein coding region. *RNA* **14**, 872–877 (2008).
26. Lal, A. *et al.* p16^{INK4a} translation suppressed by miR-24. *PLoS ONE* **3**, e1864 (2008).
27. Hobert, O. Gene regulation by transcription factors and microRNAs. *Science* **319**, 1785–1786 (2008).
28. Floyd, S. K. & Bowman, J. L. Gene regulation: ancient microRNA target sequences in plants. *Nature* **428**, 485–486 (2004).
29. Didiano, D. & Hobert, O. Perfect seed pairing is not a generally reliable predictor for miRNA-target interactions. *Nat. Struct. Mol. Biol.* **13**, 849–851 (2006).

Supplementary Information is linked to the online version of the paper at www.nature.com/nature.

Acknowledgements We thank T. Huynh for assistance with building the rna22 pipeline that was used to make the miRNA target predictions, and H. Zhang and Y. L. Lee for their help with some of the constructs. The work of Y.T., J.Z., A.M.T. and B.L. was supported by the Agency for Science, Technology and Research of Singapore. Y.T. was the recipient of an A*STAR graduate scholarship. B.L. was also partially supported by National Institutes of Health grants DK47636 and AI54973.

Author Contributions Y.T. carried out the experiments and assisted with writing the paper. J.Z. assisted with the experiments. A.M.T. assisted with and supervised the experiments, and assisted with writing the paper. B.L. supervised the experiments and supported the experimental aspects of the research. I.R. designed the research and experiments, carried out the computational analyses and wrote the paper.

Author Information Reprints and permissions information is available at www.nature.com/reprints. Correspondence and requests for materials should be addressed to I.R. (rigoutso@us.ibm.com).

METHODS

Prediction of miRNA targets. We used rna22 (ref. 18) to compute putative target sites for miR-296, miR-470 and miR-134 in the CDS regions of the *Nanog*, *Sox2* and *Oct4* mRNAs. These putative target sites are full-length, that is, each predicted heteroduplex extends beyond the span of the corresponding miRNA's seed. Access to the rna22 method is available through a graphical user interface or a batch utility at <http://cbcsrv.watson.ibm.com/rna22.html>.

Cell culture, synthetic miRNA oligomers and transfection. All cell culture reagents and culture plasticware were from Invitrogen/Gibco and BD Biosciences, respectively, unless otherwise specified. Cell cultures were maintained at 37 °C with 5% CO₂. The mouse ESC line E14 (CRL-1821, ATCC) was cultured feeder-free on 0.1% gelatin-coated plates (Sigma) in ESC-medium (DMEM, 15% heat-inactivated fetal bovine serum ESC-qualified, 100 µM non-essential amino acids, 2 mM L-glutamine, 55 nM β-mercaptoethanol, 1% (v/v) penicillin/streptomycin, and mouse leukaemia inhibitory factor (10³ U ml⁻¹, Chemicon). HEK 293T/17 cells (CRL-11268, ATCC) were maintained in DMEM plus 10% heat-inactivated FBS and penicillin/streptomycin. The scrambled RNA oligomer (*Scr*, AGACUAGCGGUAUCUUUAUCCC), the pre-miRNAs (referred to as pre-miR-X throughout the text, in which X denotes a number) and the anti-miRNA inhibitors were purchased from Ambion.

Luciferase assays. MicroRNA target validation assays were performed as described previously¹⁸. 293T cells were seeded 24 h before transfection at a density of 5 × 10⁴ cells/well in 96-well plates. Pre-miRNAs or the scrambled RNA oligomer were co-transfected at a final concentration of 12.5 nM with 2 ng of the pLuc-MRE or pLuc-UTR vector. In all cases, a constitutively expressed firefly luciferase gene in psiCHECK-2 was used as a normalization control for transfection efficiency. Forty-eight hours after transfection, firefly and *Renilla* luciferase activities were measured consecutively with the dual-luciferase reporter system (Promega) using a luminometer (Centro LB960; Berthold Technologies). All luciferase assays were repeated a minimum of three times with four culture replicates each.

RNA extraction and quantitative PCR. For quantitative PCR analyses, total RNA was extracted from cells using Trizol reagent as per the manufacturer's instructions and subsequently column-purified with RNeasy kits (Qiagen). cDNA synthesis was performed with 1 µg of total RNA at 37 °C for 2 h according to the manufacturer's instructions (Applied Biosystems). The amounts of mRNA were measured using SYBR Green PCR Master Mix with *Gapdh* as an internal control. Primer sequences are available on request. All amplicons were analysed using Prism 7900HT sequence detection system 2.2 software (Applied Biosystems).

Protein extraction and western blot analysis. Cell pellets were washed in chilled PBS and incubated for 20 min in ice-cold lysis buffer containing freshly added protease inhibitors³⁰. Lysates were cleared by centrifugation at 4 °C for 10 min at

12,100g, and protein concentrations were determined using Bradford dye (Bio-Rad). For western blot analysis, 10 µg of total protein was size fractionated by SDS-PAGE on 10% Bis-Tris acrylamide NuPAGE gels in MES-SDS running buffer (Invitrogen), transferred to Hybond-P PVDF membranes (GE Healthcare) in NuPage transfer buffer (Invitrogen) containing 10% methanol³⁰. The membrane was probed with specific primary antibodies (see Methods Summary).

Vector construction. For pLuc-MRE constructs, the sequences corresponding to the rna22-predicted miRNA-MREs were synthesized as sense and antisense oligomers, annealed and cloned into psiCHECK-2 (Promega) at restriction sites XhoI and NotI, directly 3' downstream of *Renilla* luciferase. The wild-type *Nanog*, *Oct4* and *Sox2*-CDSs were cloned into pcDNA3.1 (Invitrogen) at restriction sites BamHI and XhoI. To generate each CDS mutant construct, PCR-directed mutagenesis was performed using a pair of primers containing the mutant MRE sequence. The PCR products were subsequently used as a template for full-length PCR. The CDS mutants were also cloned into pcDNA3.1 (Invitrogen) at restriction sites BamHI and XhoI. The primer sequences used for mutagenesis were 425-4mutmNanogF1, 5'-AGCTCTCAAGTCCCGAAGCTGACAAAGGACCGGAGGAGGAGGA-3'; 425-4mutmNanogR1, 5'-TCCTCCTCCTCCGGTCTTTGTACGCTTCGGGACTTGAGAGCT-3'; 683-2mutmNanogF1, 5'-ACTAGCAATGGTCTGATTGAGAAAGGAAGCGCACCAGTGA-3'; 683-2mutmNanogR1, 5'-TCCACTGGTGGCGCTTCCTTTCTGAATCAGACCATTCGTAGT-3'; 683-4mutmNanogF2, 5'-ACTAGCAATGGTCTGATCCAAAAGGGAAGCGCACCAGTGA-3'; 683-4mutmNanogR2, 5'-TCCACTGGTGGCGCTTCCTTTTGGATCAGACCATTCGTAGT-3'; 457-5mutmNanogF, 5'-GGAGGAGGAGACAAGGTCCTTGCTCGTAAGCAGAAGATGCGG-3'; 457-5mutmNanogR, 5'-CCGCATCTTCTGCTTACGACGAAGGACCTTGTTCTCCTCCTCC-3'; 410-3mutmOct4F, 5'-TGGAACCAACTCCCAGGAAAGTCAAGACATGAAAGCCCTGCAGA-3'; 410-3mutmOct4R, 5'-TCTGCAGGGCTTTCATGTCTTGACTTTCCCTCGGGAGTTGGTTCCA-3'; 1037-4mutmSox2F, 5'-GTCAGCGCCCTGCAGTACAACAGCATGACGTCCAGTCAGACCTACATGAACGGCT-3'; 1037-4mutmSox2R, 5'-AGCCGTTTCATGTAGGTCTGACTGGACGTCTGCTGTTGTACTGCAGGGCGCTGAC-3'.

Colony formation assay. The ability of ESCs to form colonies was gauged using the methodology that we have described previously²³.

Alkaline phosphatase detection. The alkaline phosphatase detection kit (Chemicon) was used to determine alkaline phosphatase activity, according to manufacturer's instruction, see also earlier discussion²³.

30. Thomson, A. M. *et al.* The acute box *cis*-element in human heavy ferritin mRNA 5'-untranslated region is a unique translation enhancer that binds poly(C)-binding proteins. *J. Biol. Chem.* **280**, 30032–30045 (2005).

CORRIGENDUM

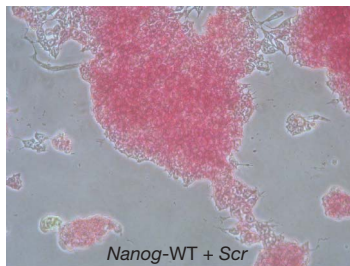
doi:10.1038/nature07880

MicroRNAs to *Nanog*, *Oct4* and *Sox2* coding regions modulate embryonic stem cell differentiation

Yvonne Tay, Jinqiu Zhang, Andrew M. Thomson, Bing Lim & Isidore Rigoutsos

Nature 455, 1124–1128 (2008)

In this Letter, an incorrect micrograph was inadvertently used in the panel entitled '*Nanog*-WT + *Scr*' in row 1 of Fig. 3a: the used micrograph was from a different field of view from the '*EV* + *Scr*' experiment. A representative micrograph from the '*Nanog*-WT + *Scr*' experiment is presented below. This oversight affects neither the data nor the conclusions of the work presented in the manuscript.



p53 and Pten control neural and glioma stem/progenitor cell renewal and differentiation

Hongwu Zheng^{1*}, Haoqiang Ying^{1*}, Haiyan Yan¹, Alec C. Kimmelman^{1,4}, David J. Hiller⁸, An-Jou Chen¹, Samuel R. Perry^{1,2}, Giovanni Tonon¹, Gerald C. Chu^{1,2,5}, Zhihu Ding¹, Jayne M. Stommel¹, Katherine L. Dunn¹, Ruprecht Wiedemeyer¹, Mingjian J. You¹, Cameron Brennan^{9,10}, Y. Alan Wang^{1,2}, Keith L. Ligon^{1,3,5,6}, Wing H. Wong⁸, Lynda Chin^{1,2,7} & Ronald A. DePinho^{1,2,11}

Glioblastoma (GBM) is a highly lethal brain tumour presenting as one of two subtypes with distinct clinical histories and molecular profiles. The primary GBM subtype presents acutely as a high-grade disease that typically harbours mutations in *EGFR*, *PTEN* and *INK4A/ARF* (also known as *CDKN2A*), and the secondary GBM subtype evolves from the slow progression of a low-grade disease that classically possesses *PDGF* and *TP53* events^{1–3}. Here we show that concomitant central nervous system (CNS)-specific deletion of *p53* and *Pten* in the mouse CNS generates a penetrant acute-onset high-grade malignant glioma phenotype with notable clinical, pathological and molecular resemblance to primary GBM in humans. This genetic observation prompted *TP53* and *PTEN* mutational analysis in human primary GBM, demonstrating unexpectedly frequent inactivating mutations of *TP53* as well as the expected *PTEN* mutations. Integrated transcriptomic profiling, *in silico* promoter analysis and functional studies of murine neural stem cells (NSCs) established that dual, but not singular, inactivation of *p53* and *Pten* promotes an undifferentiated state with high renewal potential and drives increased Myc protein levels and its associated signature. Functional studies validated increased Myc activity as a potent contributor to the impaired differentiation and enhanced renewal of NSCs doubly null for *p53* and *Pten* (*p53*^{−/−} *Pten*^{−/−}) as well as tumour neurospheres (TNSs) derived from this model. Myc also serves to maintain robust tumorigenic potential of *p53*^{−/−} *Pten*^{−/−} TNSs. These murine modelling studies, together with confirmatory transcriptomic/promoter studies in human primary GBM, validate a pathogenetic role of a common tumour suppressor mutation profile in human primary GBM and establish Myc as an important target for cooperative actions of *p53* and *Pten* in the regulation of normal and malignant stem/progenitor cell differentiation, self-renewal and tumorigenic potential.

High-grade malignant glioma, the most common intrinsic brain tumour, is uniformly fatal despite maximum treatment³. A wealth of molecular genetic studies has established central roles of the RTK-PI3K-PTEN, ARF-MDM2-p53 and INK4a-RB pathways in gliomagenesis^{3,4}. To explore the role of *p53* and *Pten* in glioma, we used the *hGFAP-Cre* transgene^{5,6} to delete *p53* alone or in combination with *Pten* in all CNS lineages using conditional *p53* (ref. 7) and *Pten* alleles (Supplementary Figs 1 and 2a–c). Because broad CNS deletion of *Pten* results in lethal hydrocephalus in early postnatal life (data not shown), modelling efforts henceforth emphasized the *Pten*^{lox/+} genotype.

Clinically, between 15 to 40 weeks of ages, 42 out of 57 (73%) of the *hGFAP-Cre*⁺; *p53*^{lox/lox}; *Pten*^{lox/+} mice presented with acute-onset neurological symptoms—seizure, ataxia and/or paralysis (Fig. 1a). Histopathologically, all 42 neurologically symptomatic mice harboured malignant gliomas that were classified on the basis of WHO (World Health Organization) criteria⁸ as anaplastic astrocytomas (WHO III, *n* = 28, 66%) or GBM (WHO IV, *n* = 14, 34%; Fig. 1b). These GBMs had classical features of pseudopalisading necrosis, marked cellular pleomorphism, and highly infiltrative spread including perineuronal and perivascular satellitosis as well as subpial spread in the cerebral cortex (Supplementary Fig. 3a). Occasionally tumours had abnormal vessels suggestive of microvascular proliferation. All tumours showed increased mitoses (Ki67 staining) and expression of the classical human glioma markers Gfap and Nestin (Fig. 1c). Necropsy of 15 neurologically asymptomatic mice showed no cases of incipient low-grade glioma disease but 8 had high-grade pathology including very small lesions with anaplastic features of nuclear atypia, multinucleated tumour cells and/or high cellularity (Supplementary Fig. 3b). For the remaining genotypes, 4 out of 23 *hGFAP-Cre*⁺; *p53*^{lox/lox} mice developed anaplastic astrocytoma (WHO III); conversely 19 out of 23 *hGFAP-Cre*⁺; *p53*^{lox/lox} mice, 12 out of 12 *hGFAP-Cre*⁺; *p53*^{lox/+}; *Pten*^{lox/+} mice and 10 out of 10 *hGFAP-Cre*⁺; *p53*^{lox/+} mice had no CNS pathology and developed only non-CNS tumours (data not shown).

Historically, *TP53* inactivation has been considered a classical lesion in low-grade astrocytomas and secondary GBM but infrequently in primary GBM^{1,9}. The remarkable clinical and histological resemblance of this model to the primary GBM subtype in humans prompted *TP53* and *PTEN* resequencing in human primary GBM. Of the 35 clinically annotated human primary GBM samples, 10 (29%) tumours registered prototypical *TP53* mutations and 14 (40%) tumours had *PTEN* missense mutations, insertions, deletions or splicing mutations (Supplementary Table 1). Moreover, six out of ten tumours with *TP53* mutations harboured concomitant *PTEN* mutations or homozygous deletion. Encouragingly, our mutational data agrees with The Cancer Genome Atlas data reporting *TP53* and *PTEN* as the two most commonly mutated tumour suppressor genes (<http://tcga-data.nci.nih.gov/tcga/findArchives.htm>). These results, together with recent population-based studies^{10,11}, indicate that *TP53* is a key tumour suppressor for both GBM subtypes.

Consistent with frequent *PTEN* loss of heterozygosity (LOH; 60–70%) in human high-grade glioma³, 16 out of 16 mouse high-grade

¹Department of Medical Oncology, ²Center for Applied Cancer Science, Belfer Foundation Institute for Innovative Cancer Science, ³Center for Molecular Oncologic Pathology, Dana-Farber Cancer Institute and Harvard Medical School, Boston, Massachusetts 02115, USA. ⁴Harvard Radiation Oncology Program, ⁵Department of Pathology, ⁶Division of Neuropathology, ⁷Department of Dermatology, Brigham and Women's Hospital, Harvard Medical School, Boston, Massachusetts 02115, USA. ⁸Department of Statistics, Stanford University, Stanford, California 94305, USA. ⁹Department of Neurosurgery, Memorial Sloan-Kettering Cancer Center, New York, New York 10065, USA. ¹⁰Department of Neurosurgery, Weill-Cornell Medical College, New York, New York 10065, USA. ¹¹Departments of Medicine and Genetics, Harvard Medical School, Boston, Massachusetts 02115, USA. *These authors contributed equally to this work.

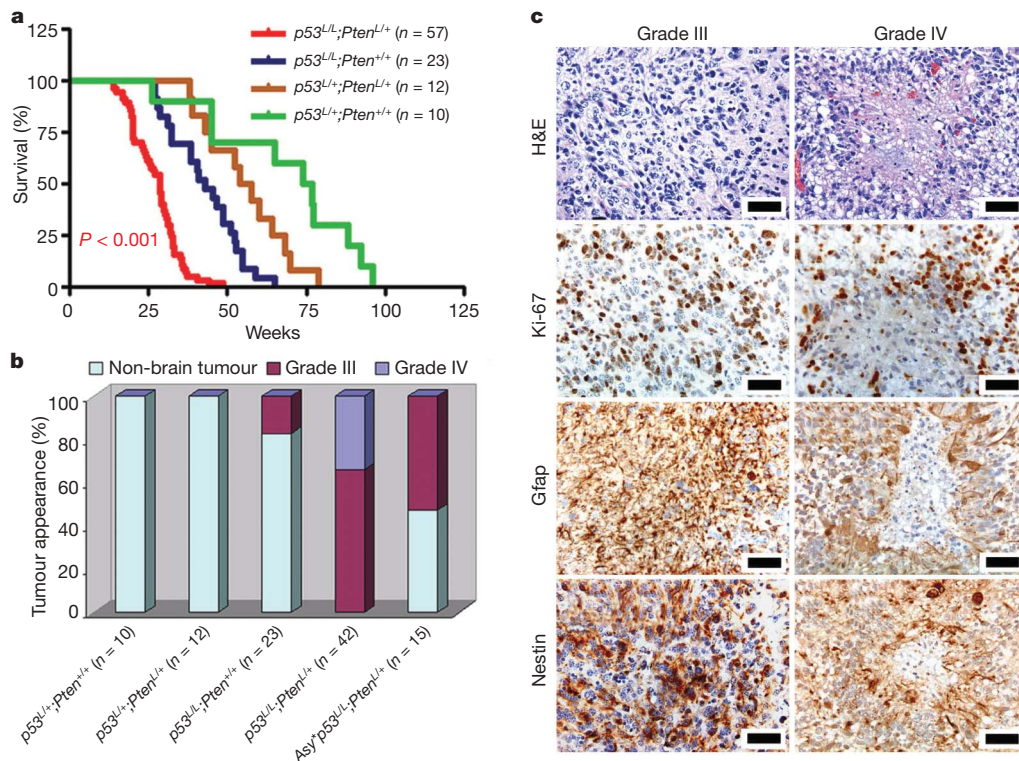


Figure 1 | *p53* and *Pten* inactivation cooperate to induce high-grade malignant gliomas. **a**, Kaplan–Meier tumour-free survival curves for mice of indicated genotypes as a function of weeks. ‘+’ designates the wild-type allele, ‘L’ denotes the conditional allele. **b**, Graph shows frequency and grade of gliomas versus non-CNS malignancies observed in end-stage of indicated mice from **a**. *Asy** indicates neurological asymptomatic *hGFAP*-

Cre⁺; *p53*^{lox/lox}; *Pten*^{lox/+} mice (*n* = 15) killed for non-CNS malignancies. **c**, Haematoxylin and eosin (H&E) histology and immunohistochemical staining of sections of WHO grade III and IV malignant gliomas from *hGFAP-Cre*⁺; *p53*^{lox/lox}; *Pten*^{lox/+} mice with antibodies against Ki67, Gfap and Nestin. Scale bars, 50 μ m.

gliomas showed no *Pten* expression in tumour cells but a robust signal in surrounding non-malignant cells and intratumoral vessels (Fig. 2a). Polymerase chain reaction (PCR) genotyping indicated that six out of seven tested tumours sustained loss of the wild-type *Pten* allele (Fig. 2b). The *Pten* reduction to homozygosity and the documented Cre-mediated deletion of both *p53* floxed alleles indicate that the inactivation of both genes is required for gliomagenesis. Loss of *Pten* expression correlated with activation of key PI3K signalling surrogates: Akt and ribosomal protein S6 kinase (Fig. 2c). In accordance with human high-grade disease, eight out of eight malignant murine gliomas expressed high *Vegf* levels relative to normal brain tissue (Fig. 2c). Co-activation of multiple receptor tyrosine kinases in human primary GBM¹² was also evident in the murine tumours with robust *Pdgfr* expression overlapping with strong regional activation of *Egfr* (Supplementary Fig. 4a–d).

A classical feature of human high-grade malignant glioma is a significant degree of intertumoral and intratumoral morphological and lineage heterogeneity, hence the moniker glioblastoma ‘multiforme’. This characteristic plasticity was evident in the *hGFAP-Cre*⁺; *p53*^{lox/lox}; *Pten*^{lox/+} gliomas in which occasional tumours (5 out of 50) presented with both astrocytic and oligodendroglial histopathological features (Supplementary Fig. 5). The basis for morphological variability is not known and may relate, among many possibilities, to the acquisition of an immature developmental state with multipotency and/or differentiative plasticity. Consistent with this notion, all murine tumours express stem or lineage progenitor markers (including Nestin, Gfap and Olig2) similar to human glioma profiles¹³ but are negative for mature neuronal and oligodendrocyte markers (NeuN and Mbp; Supplementary Fig. 6a, b). This stem/progenitor marker profile is in accord with the ability of all murine

tumours tested to readily generate TNSs with (i) strong tumour-initiating potential with secondary tumours faithfully retaining the primary tumour’s histological features (Supplementary Fig. 7); (ii) robust NSC marker Nestin expression; and (iii) limited capacity to differentiate into astrocytic and neuronal lineages after exposure to differentiation agents (Fig. 2d). As NSC/progenitor cells have been proposed to be the preferred cell-of-origin for GBM⁶, the immature marker profile and varied morphological presentation of our murine tumours prompted us to posit that *Pten* and *p53* deficiencies might contribute to gliomagenesis by affecting NSC self-renewal and differentiation potential.

To explore this hypothesis, we characterized primary murine embryonic day (E)13.5 NSC cultures singly or doubly null for *p53* and *Pten*. Compared to NSCs null for either *Pten* or *p53*, which show only modestly increased proliferation and self-renewal reflected by neurosphere formation capacity^{14–16}, NSCs null for both *p53* and *Pten* showed significant proliferation and self-renewal activity (Fig. 3a and Supplementary Fig. 8a). This effect on NSC renewal, coupled with the aforementioned varied tumour histology, suggests that combined *p53* and *Pten* loss might cooperate in tumorigenesis by impairing NSC differentiation potential. When NSCs were continuously cultured in NSC medium, all genotypes showed a similar robust expression of NSC/progenitor markers (for example Nestin) and minimal expression of differentiated lineage markers (Supplementary Fig. 8b). After exposure to differentiation-inducing medium, wild-type and single-null NSC cultures differentiated into Gfap-positive astrocytes, Tuj1-positive neurons, or O4-positive oligodendrocytes. In contrast, *p53*^{−/−} *Pten*^{−/−} NSCs failed to respond to these differentiation cues and retained stem-cell-like morphology and lineage marker (Nestin) expression (Fig. 3b and Supplementary Fig. 9a). Similar

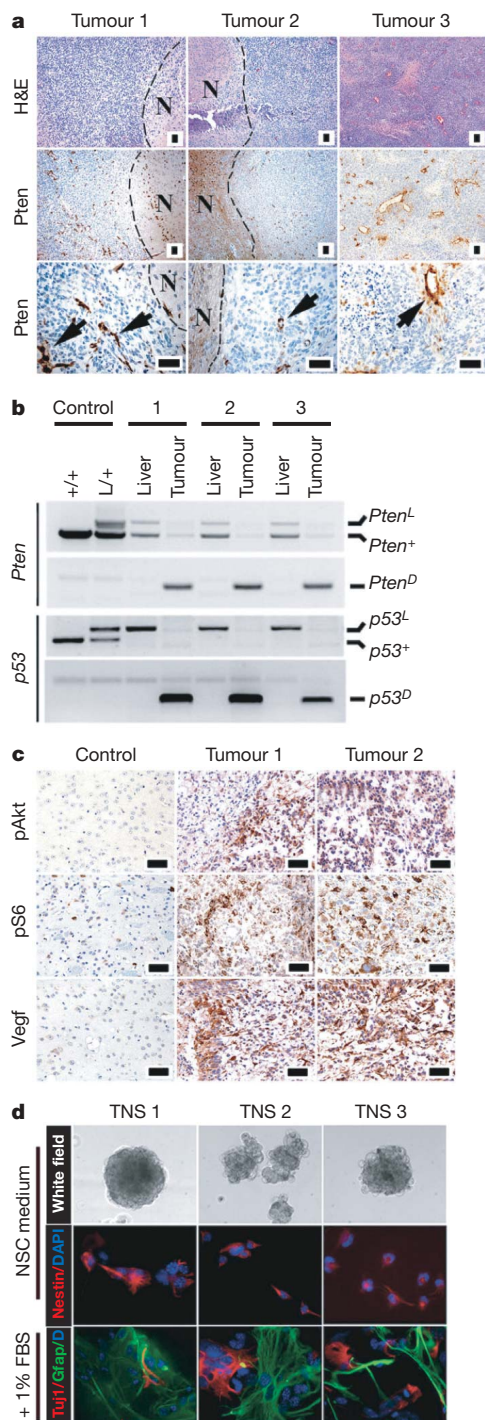


Figure 2 | *hGFAP-Cre⁺;p53^{lox/lox};Pten^{lox/+}* gliomas mirror key features of human malignant gliomas. **a**, Pten expression is completely extinguished in tumour cells. Sections of three independent malignant gliomas were stained with haematoxylin and eosin (H&E) and an anti-Pten antibody. 'N' indicates the adjacent normal regions of the tumour cells; the arrows point to Pten-positive vascular cells embedded in the tumour. **b**, The wild-type *Pten* allele is lost in glioma cells. Genomic DNA isolated from liver tissues and brain tumour cells was subjected to PCR-based assays for genotyping *Pten* and *p53* alleles. '+' designates the *Pten* wild-type allele, 'L' denotes the conditional allele, and 'D' denotes the inactivated form of the conditional allele after Cre-mediated recombination. **c**, Immunohistochemical staining of mouse normal brain or glioma sections with antibodies against activated phosphorylated Akt (pAkt), phosphorylated ribosomal protein S6 kinase (pS6) and Vegf. **d**, TNS lines isolated from independent malignant gliomas were cultured in NSC medium or differentiation medium (1% fetal bovine serum (FBS)) and immunostained for Nestin, Gfap and Tuj1 as indicated. Scale bars, 50 μ m (**a**, **c**); original magnification in **d** \times 400.

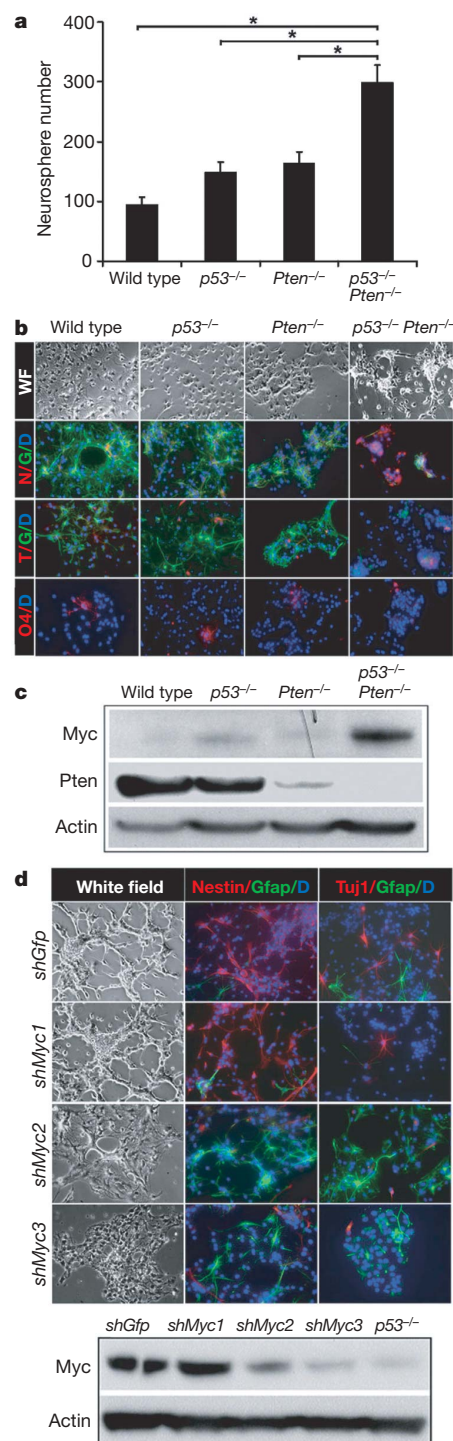


Figure 3 | *p53* and *Pten* coordinately regulate Myc protein level as well as NSC self-renewal and differentiation. **a**, The number of neurospheres formed by *p53*^{-/-} *Pten*^{-/-} NSCs in culture is significantly increased as compared to wild-type or singly null NSCs; asterisk, $P < 0.001$; $n = 3$. Values represent mean \pm s.d. from three experiments. **b**, The multilineage differentiation potential was impaired in *p53*^{-/-} *Pten*^{-/-} NSCs. **d**, DAPI (blue); G, Gfap (green); N, Nestin (red); O4 (red); WF, white field; T, Tuj-1 (red). **c**, Combined inactivation of *p53* and *Pten* in NSCs stimulates Myc protein expression. **d**, Knockdown of Myc expression restores *p53*^{-/-} *Pten*^{-/-} NSC differentiation capacity. Lower panel, western blot of double-null NSC Myc protein expression after infected with indicated lentiviral shRNA. Note Myc expression in *shMyc2*- and *shMyc3*-infected *p53*^{-/-} *Pten*^{-/-} cells is comparable to that in *p53*^{-/-} cells, and *shMyc1* as a control shows no knockdown. Original magnification used for **b** and **d**: \times 200.

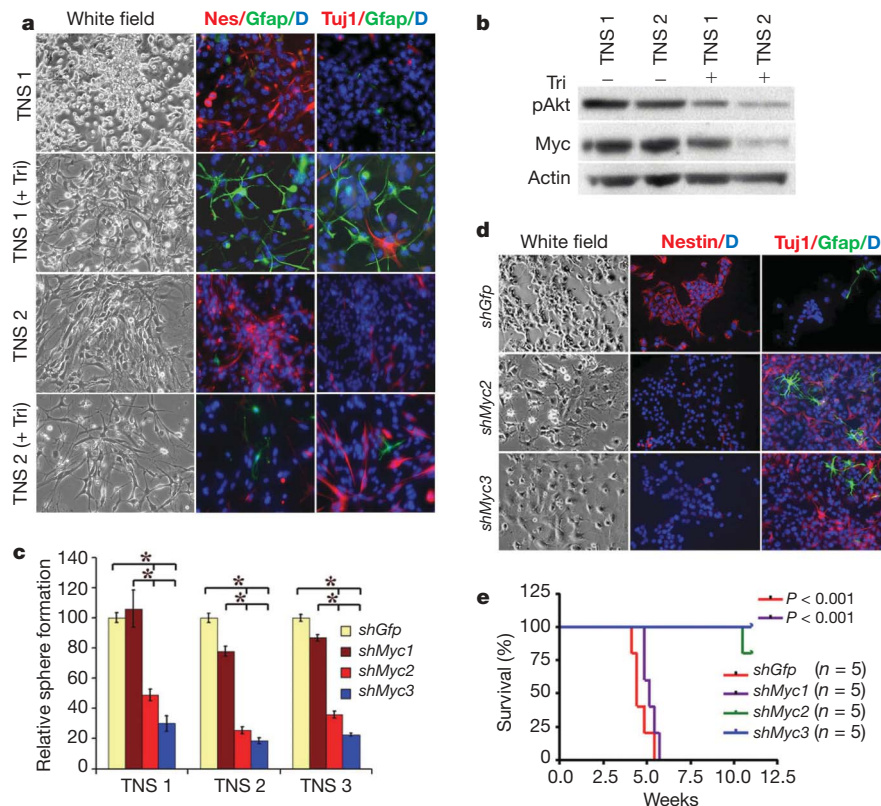


Figure 4 | Attenuated Myc expression restores *hGFAP-Cre⁺p53^{lox/lox};Pten^{lox/+}* TNS differentiation potential and reduces tumorigenic potential. **a**, Inhibition of the Akt pathway by triciribine induces TNS cell differentiation. Two independent TNS lines were cultured in 1% FBS in the absence or presence of triciribine (Tri, 5 μ M) for 7 days before being subjected to immunostaining with antibodies against Nestin (Nes, red), Gfap (Green) and Tuj1 (red). D, DAPI (blue). **b**, Inhibition of the Akt pathway in TNS cells with triciribine attenuates their cellular Myc expression. **c**, Knockdown of Myc expression in TNS cells reduces their

self-renewal potential assessed by sphere formation; asterisk, $P < 0.001$; $n = 3$. Values represent mean \pm s.d. from three experiments. **d**, shRNA-mediated reduction of Myc expression in TNS cells sensitizes cells to differentiation stimuli. Cells infected with control (*shGfp*) and the indicated shRNA were incubated with differentiation medium before being subjected to lineage marker analysis. **e**, shRNA-mediated reduction of Myc expression represses TNS tumorigenic potency in orthotopically transplanted SCID mice. Original magnification for **a** and **d**: $\times 200$.

differentiation defect and abnormal self-renewal potential were also observed in adult NSCs that were deleted for *Pten* and *p53* postnatally (Supplementary Fig. 9b, c). The contribution of *Pten* deficiency in maintaining impaired differentiation was further verified by the ability of the Akt inhibitor triciribine¹⁷ to enable differentiation of NSCs null for both *Pten* and *p53* (Supplementary Fig. 10a, b).

To understand the molecular basis of impaired differentiation capacity, we performed transcriptome comparisons of murine *p53*^{-/-} NSCs with *p53*^{-/-} *Pten*^{-/-} NSCs at 1 day after exposure to the differentiation inducer. Among the 410 genes showing significant differential expression (Supplementary Table 2) promoter analysis identified E2F and Myc motifs as two of the most enriched promoter binding elements (1.7 \times and 1.4 \times , respectively; $P < 10^{-4}$). Notably, promoter analysis using 69 pretreatment human primary GBM cases in the TCGA database showed strong enrichment of MYC binding elements: 10 *p53*^{-/-} *Pten*^{-/-} double-mutant tumours versus the 59 remaining tumours (1.40 \times , $P = 2.20 \times 10^{-3}$) or versus the 12 *p53*^{-/-} single-mutant tumours (1.46 \times , $P = 1.54 \times 10^{-3}$).

MYC is well-known for its roles in cell cycle progression and apoptosis¹⁸ as well as in stem cell self-renewal and differentiation during development and oncogenic processes^{19–22}. It is also notable that both *p53* and *Pten*/PI3K pathways can directly regulate MYC with *p53* repressing MYC transcription by directly binding to the MYC promoter²³, whereas downstream PI3K pathway arms can modulate MYC translation and protein degradation^{24,25}. In agreement, Myc protein levels were substantially increased in the murine double-null NSCs, but only marginally elevated in *p53*^{-/-} or *Pten*^{-/-} NSCs when compared to wild-type controls (Fig. 3c), raising the

possibility that *p53* and *Pten* cooperate to regulate Myc levels which in turn could control NSC self-renewal and differentiation.

To test this hypothesis, we examined the effect of Myc knockdown on murine *p53*^{-/-} *Pten*^{-/-} NSC differentiation potential and observed that Myc short hairpin RNA (shRNA; *shcMyc2* and *shcMyc3*), which reduced Myc levels to those in *p53*^{-/-} NSCs, largely restored their differentiation capacity (Fig. 3d and Supplementary Fig. 11a). Conversely, enforced Myc expression in *p53*^{-/-} NSCs repressed their differentiation and enabled retention of stem/progenitor marker expression (Nestin and Sox2; Supplementary Fig. 11b), indicating that the concomitant loss of *p53* and *Pten* elevates Myc activity to impede NSC differentiation capacity.

The strong pleiotropic activities attributed to MYC demands tight control of its expression to avoid development of diverse human malignancies, including gliomas^{21,26}. Our finding that the concomitant loss of *p53* and *Pten* compromises NSC differentiation capacity by means of elevated Myc levels prompted further assessment of its relevance in the so-called 'brain cancer stem cells' in our model. Using murine TNSs which are enriched for such tumour initiating cells (TICs), Akt inhibitor treatment strongly reduced Myc protein and promoted differentiation (Fig. 4a, b and Supplementary Fig. 12a). Correspondingly, Myc knockdown in TNS cells not only markedly reduced their proliferation and self-renewal capacity (Fig. 4c and Supplementary Fig. 12b, c) but also strongly sensitized them to differentiation induction (Fig. 4d and Supplementary Fig. 12d). Notably, although ten out of ten intracranial injections of vector-transduced murine TNSs resulted in lethal infiltrating gliomas within 1 month, nine out of ten mice injected with Myc knockdown TNSs

survived for more than 3 months (Fig. 4e). Thus, Myc has a crucial involvement in maintaining the impaired differentiation and potent tumorigenic potential of *p53*- and *Pten*-inactive TNSs (Supplementary Fig. 13).

The identification of TICs with stem-like properties in diverse human cancers including GBM represents an important conceptual advance in cancer biology with therapeutic implications^{27,28}. These TICs seem to constitute a reservoir of self-sustaining cells with potent tumorigenic potential. However, unlike normal NSCs which readily differentiate along a developmental hierarchy into lineage-restricted differentiated progenies, TNSs derived from *p53*^{-/-} *Pten*^{-/-} malignant gliomas show resistance towards differentiation cues. The diminished tumorigenicity of these TICs on restoration of differentiation potential, along with recent reports supporting pro-differentiation as a potential strategy to inhibit GBM-derived TICs^{29,30}, encourages the identification and testing of agents targeting these differentiation pathways including MYC in the treatment of primary GBM in humans.

METHODS SUMMARY

Standard gene targeting and chimera formation methods were used to generate the conditional *Pten*^f allele in the mouse germ line in which *Pten* exon 5 is flanked by loxP sites; the conditional *p53*^f mouse was generated by A. Berns; *hGFAP-Cre* mice were purchased from the Jackson Laboratory. All mice were maintained in pathogen-free facilities and followed for development of neurological deficits. After culling, tissues were collected and processed for histological, immunohistochemical, immunofluorescence or western blot analyses, as detailed in the Methods. For *p53* and *Pten* mutation analysis, surgically resected human primary glioblastoma were flash-frozen and genomic DNA was prepared from frozen tumour samples. For microarray analysis, total RNAs from indicated early passage NSCs were amplified and labelled by standard methods and hybridized to Affymetrix 430 2.0 chips. For tumorigenic analysis, TNS cells isolated from *hGFAP-Cre*⁺;*p53*^{lox/lox};*Pten*^{lox/+} murine malignant gliomas were infected with indicated lentivirus shRNA and orthotopically injected into the forebrain of SCID mice. Animals were observed daily for the development of neurological deficits and subjected to histological analysis once killed.

Full Methods and any associated references are available in the online version of the paper at www.nature.com/nature.

Received 2 May; accepted 10 September 2008.

- Kleihues, P. & Ohgaki, H. Primary and secondary glioblastomas: from concept to clinical diagnosis. *Neuro-oncol.* **1**, 44–51 (1999).
- Zhu, Y. & Parada, L. F. The molecular and genetic basis of neurological tumours. *Nature Rev. Cancer* **2**, 616–626 (2002).
- Furnari, F. B. *et al.* Malignant astrocytic glioma: genetics, biology, and paths to treatment. *Genes Dev.* **21**, 2683–2710 (2007).
- Wiedemeyer, R. *et al.* Feedback circuit among INK4 tumor suppressors constrains human glioblastoma development. *Cancer Cell* **13**, 355–364 (2008).
- Zhuo, L. *et al.* hGFAP-cre transgenic mice for manipulation of glial and neuronal function *in vivo*. *Genesis* **31**, 85–94 (2001).
- Zhu, Y. *et al.* Early inactivation of p53 tumor suppressor gene cooperating with NF1 loss induces malignant astrocytoma. *Cancer Cell* **8**, 119–130 (2005).
- Jonkers, J. *et al.* Synergistic tumor suppressor activity of BRCA2 and p53 in a conditional mouse model for breast cancer. *Nature Genet.* **29**, 418–425 (2001).
- Louis, D. N., Ohgaki, H., Wiestler, O. D. & Cavenee, W. K. *WHO Classification of Tumours of the Central Nervous System* 4th edn (eds Louis, D. N., Ohgaki, H., Wiestler, O. D. & Cavenee, W. K.) (World Health Organization, 2007).
- Watanabe, K. *et al.* Overexpression of the EGF receptor and p53 mutations are mutually exclusive in the evolution of primary and secondary glioblastomas. *Brain Pathol.* **6**, 217–223 (1996).
- Ohgaki, H. *et al.* Genetic pathways to glioblastoma: a population-based study. *Cancer Res.* **64**, 6892–6899 (2004).
- Fukushima, T. *et al.* Genetic alterations in primary glioblastomas in Japan. *J. Neuropathol. Exp. Neurol.* **65**, 12–18 (2006).
- Stommel, J. M. *et al.* Coactivation of receptor tyrosine kinases affects the response of tumor cells to targeted therapies. *Science* **318**, 287–290 (2007).
- Ligon, K. L. *et al.* Olig2-regulated lineage-restricted pathway controls replication competence in neural stem cells and malignant glioma. *Neuron* **53**, 503–517 (2007).

- Groszer, M. *et al.* PTEN negatively regulates neural stem cell self-renewal by modulating G₀–G₁ cell cycle entry. *Proc. Natl Acad. Sci. USA* **103**, 111–116 (2006).
- Gil-Perotin, S. *et al.* Loss of p53 induces changes in the behavior of subventricular zone cells: implication for the genesis of glial tumors. *J. Neurosci.* **26**, 1107–1116 (2006).
- Meletis, K. *et al.* p53 suppresses the self-renewal of adult neural stem cells. *Development* **133**, 363–369 (2006).
- Yang, L. *et al.* Akt/protein kinase B signaling inhibitor-2, a selective small molecule inhibitor of Akt signaling with antitumor activity in cancer cells overexpressing Akt. *Cancer Res.* **64**, 4394–4399 (2004).
- Patel, J. H., Loboda, A. P., Showe, M. K., Showe, L. C. & McMahon, S. B. Analysis of genomic targets reveals complex functions of MYC. *Nature Rev. Cancer* **4**, 562–568 (2004).
- Cartwright, P. *et al.* LIF/STAT3 controls ES cell self-renewal and pluripotency by a Myc-dependent mechanism. *Development* **132**, 885–896 (2005).
- Takahashi, K. & Yamanaka, S. Induction of pluripotent stem cells from mouse embryonic and adult fibroblast cultures by defined factors. *Cell* **126**, 663–676 (2006).
- Ben-Porath, I. *et al.* An embryonic stem cell-like gene expression signature in poorly differentiated aggressive human tumors. *Nature Genet.* **40**, 499–507 (2008).
- Wong, D. J. *et al.* Module map of stem cell genes guides creation of epithelial cancer stem cells. *Cell Stem Cell* **2**, 333–344 (2008).
- Ho, J. S., Ma, W., Mao, D. Y. & Benichou, S. p53-Dependent transcriptional repression of c-myc is required for G₁ cell cycle arrest. *Mol. Cell. Biol.* **25**, 7423–7431 (2005).
- Gera, J. F. *et al.* AKT activity determines sensitivity to mammalian target of rapamycin (mTOR) inhibitors by regulating cyclin D1 and c-myc expression. *J. Biol. Chem.* **279**, 2737–2746 (2004).
- Sears, R. *et al.* Multiple Ras-dependent phosphorylation pathways regulate Myc protein stability. *Genes Dev.* **14**, 2501–2514 (2000).
- Bredel, M. *et al.* Functional network analysis reveals extended gliomagenesis pathway maps and three novel MYC-interacting genes in human gliomas. *Cancer Res.* **65**, 8679–8689 (2005).
- Clarke, M. F. *et al.* Cancer stem cells—perspectives on current status and future directions: AACR Workshop on cancer stem cells. *Cancer Res.* **66**, 9339–9344 (2006).
- Lobo, N. A., Shimono, Y., Qian, D. & Clarke, M. F. The biology of cancer stem cells. *Annu. Rev. Cell Dev. Biol.* **23**, 675–699 (2007).
- Piccirillo, S. G. *et al.* Bone morphogenetic proteins inhibit the tumorigenic potential of human brain tumour-initiating cells. *Nature* **444**, 761–765 (2006).
- Lee, J. *et al.* Epigenetic-mediated dysfunction of the bone morphogenetic protein pathway inhibits differentiation of glioblastoma-initiating cells. *Cancer Cell* **13**, 69–80 (2008).

Supplementary Information is linked to the online version of the paper at www.nature.com/nature.

Acknowledgements We thank A. Berns for providing *p53*^f mice; S. Zhou and S. Jiang for mouse husbandry and care; R. T. Bronson for discussion on pathology analysis; K. Montgomery for discussion on sequencing; and Y.-H. Xiao, B. Feng and J. Zhang for bioinformatic help. H.Z. was supported by Helen Hay Whitney Foundation. H. Ying is a recipient of the Marsha Mae Moeslein Fellowship from the American Brain Tumor Association. A.C.K. is a recipient of the Leonard B. Holman Research Pathway Fellowship. Z.D. is supported by the Damon Runyon Cancer Research Foundation. J.M.S. is supported by a Ruth L. Kirschstein National Research Service Award Fellowship. R.W. is supported by a Mildred Scheel Fellowship (Deutsche Krebshilfe). Grant support comes from the Goldhirsh Foundation (R.A.D.), and NIH grants U01 CA84313 (R.A.D.), RO1CA99041 (L.C.) and 5P01CA95616 (R.A.D., L.C., W.H.W., C.B. and K.L.L.). R.A.D. is an American Cancer Society Research Professor supported by the Robert A. and Renee E. Belfer Foundation Institute for Innovative Cancer Science.

Author Contributions H.Z. and H. Ying performed the experiments and contributed equally as first authors. R.A.D. supervised experiments and contributed as senior author. M.J.Y. generated the *Pten*^f mouse allele. D.J.H., W.H.W. and G.T. conducted the microarray and promoter analyses. K.L.L., H.Z. and G.C.C. provided the pathology analyses. H. Yan, A.C.K., A.-J.C., S.R.P., Z.D., J.M.S., K.L.D. and R.W. performed the experiments. C.B. contributed patient samples and pathologic information. L.C. and Y.A.W. contributed to the writing of the manuscript.

Author Information Reprints and permissions information is available at www.nature.com/reprints. Correspondence and requests for materials should be addressed to R.A.D. (ron_depinho@dfci.harvard.edu).

METHODS

Mice. *p53^L* and *hGFAP-Cre* mice have been described previously^{5,7}. *Pten^L* mice were generated using a standard knock-in approach in which *Pten* exon 5 is flanked by loxP sites (details on targeting construct and procedures are available on request). Mice were interbred and maintained on a FvB/C57Bl6 hybrid background in pathogen-free conditions at the Dana-Farber Cancer Institute, monitored for signs of ill-health every other day, and euthanized and necropsied when moribund. All manipulations were performed with Institutional Animal Care and Use Committee (IACUC) approval.

Histology and immunohistochemistry. Once killed, mice were perfused with 4% paraformaldehyde (PFA) and brains were dissected, followed by overnight post-fixation in 4% PFA at 4 °C. Serial sections were prepared at 5 µm for paraffin sections or 10 µm for cryostat sections with every tenth slide stained by haematoxylin and eosin (DF/HCC Research Pathology Cores). Tumour grading was determined by K.L.L. and H.Z. on the basis of the WHO grading system for malignant astrocytoma⁸. Immunohistochemical and immunofluorescence analyses were performed as described³¹. The Pdgfrα and pEgfr double immunohistochemical staining was performed using DakoCytomation EnVision doublestain system (K1395, Dako) following manufacturer's instructions. The primary antibodies used were: Ki67 (VP-RM04, Vector), Gfap (Z0334, DAKO), Gfap (556330, BD Pharmingen), Nestin (MAB5353, Chemicon; specifically for mouse), Nestin (MAB5326, Chemicon; specifically for human), Pten (9559, Cell Signaling), phospho-Akt^{Ser473} (3787, Cell Signaling), phospho-ribosomal protein S6 kinase (2215, Cell Signaling), Cyclin D1 (18-0220, ZYMED), Vegf (sc-152, Santa Cruz), Pdgfrα (3174, Cell Signaling), phospho-Pdgfrα^{Y754} (sc-12911, Santa Cruz), Egfr (IHC-00005, Bethyl), phospho-Egfr^{Y1068} (ab40815, Abcam), phospho-Egfr^{Y1173} (sc-12351, Santa Cruz), Olig-2 (AB9610, Chemicon), Tuj-1 (MMS-435P, Covance), O4 (MAB1326, R&D), NeuN (MAB377, Millipore), Mbp (ab7349, Abcam), Myc (ab39688, Abcam), and Cre (69050-3, Novagen). Images were captured using a Leica DM1400B microscope and Leica FW4000 version 1.2.1.

Cell culture. Primary NSCs were isolated from the brain subventricular zone (SVZ) of E13.5 embryos or 1-month-old mice with the indicated genotype as previously described^{31,32}. NSCs were maintained in NSC proliferation media (05702, StemCell) supplemented with 20 ng ml⁻¹ EGF (E4127, Sigma) and 10 ng ml⁻¹ bFGF (F0291, Sigma). To generate primary TNS cells, tumour samples from freshly dissected mouse brains were subjected to mechanical and enzymatic dissociation. Single-cell suspensions were cultured in NSC proliferation media. Tumour spheres formed were then disaggregated and used for indicated assays. NSC differentiation assays were carried out by plating the indicated cells in culture wells on coverslips precoated with 15 µg ml⁻¹ poly-L-ornithine (P3655, Sigma) and 1 µg ml⁻¹ fibronectin (F1141, Sigma); the cells were incubated in neurobasal medium supplemented with 1% FBS for 7–10 days, and the differentiation capacities were examined under either a light or fluorescence microscope (Nikon). For TNS cell differentiation, cells were incubated in differentiation media with varying doses of trichiribine (BioMol) or vehicle (dimethylsulphoxide, Sigma). Knockdown of mouse Myc was performed by infecting the indicated cells with lentivirus containing *shMyc* constructs (provided by W. Hahn). The shRNA constructs *shMyc1*, *shMyc2* and *shMyc3* correspond to clone IDs TRCN000000 54856, 42517 and 42513, respectively (The DFCI-Broad RNAi Consortium, commercially available from Sigma-Aldrich).

Western, cell growth and self-renewal assays. Western blot assays were performed as previously described³¹ with antibodies against Myc (sc-42, Santa Cruz), phospho-Akt^{Ser473} (9271, Cell Signaling), Pten (9569, Cell Signaling) and Actin (sc-1615, Santa Cruz). For *in vitro* cell growth assays, NSCs or TNS cells (10,000) were plated in triplicate in 96-well format and incubated in NSC proliferation media for 5 days, and growth was quantified using Luminescence

ATP detection assay system (PerkinElmer). Self-renewal capacity was measured by plating 1,000 cells per well (6-well plate) in NSC proliferation media containing EGF and bFGF with 0.3% agarose (A9049, Sigma). The number of neurospheres or tumour neurospheres that formed subsequently per well was quantified after 10–14 days and relative sphere formation was plotted versus indicated control. Three replicates were performed for each. All experiments were conducted at cell passage <5.

Orthotopic transplants. Female SCID mice (Charles River) aged 6–8 weeks were anesthetized and placed into stereotactic apparatus equipped with a Z axis (Stoelting). A small hole was bored in the skull 0.5 mm anterior and 3.0 mm lateral to the bregma using a dental drill. Twenty thousand cells in Hanks Buffered Salt Solution was injected into the right caudate nucleus 3 mm below the surface of the brain using a 10-µl Hamilton syringe with an unbeveled 30 gauge needle. The scalp was closed using a 9-mm Autoclip Applier. Animals were followed daily for the development of neurological deficits.

Mutation screening. Frozen tumour specimens were obtained from the Memorial Sloan Kettering Cancer Center tumour bank. Genomic DNA was prepared from frozen primary GBM tumour samples using the Qiagen genomic purification kit. Coding exons were PCR amplified and sequenced using standard protocols at the Harvard Partners Center for Genetics and Genomics as previously described³³. All known single nucleotide polymorphisms and synonymous mutations were removed from the analysis in the current study. This study was approved by the Institutional Review Board of the hospital.

Microarray analysis. Early passage wild-type and indicated mutant NSCs were incubated with NSC proliferation media or differentiation media for 18 h. RNA was isolated using Trizol (Invitrogen) and the RNeasy mini kit (Qiagen). Gene expression profiling was performed using the Affymetrix 430 2.0 chips at DFCI Microarray core facility.

Promoter analysis. Gene expressions were modelled using dChip software³⁴. Sets of genes differentially expressed pre- and post-differentiation induction were generated using the SAM statistic³⁵, with a cutoff of ± 2.0 . Promoter analysis on both these gene sets used the CisGenome software (<http://biogibbs.stanford.edu/~jihk/CisGenome/index.htm>) to scan the 8 kb upstream to 2 kb downstream regions of these genes for the ~550 motifs in the TRANSFAC 12.1 database. Enrichment was measured against control regions at a comparable distance from the transcription start sites of random genes.

Statistical analysis. Tumour-free survivals were analysed using Graphpad Prism4. Statistical analyses were performed using the non-parametric Mann–Whitney test. Significance of enrichment in the promoter analysis was computed based on Poisson distribution with Bonferroni correction. Comparisons of cell growth, self-renewal and differentiation were performed using the unpaired Student's *t*-test. For all experiments with error bars, standard deviation was calculated to indicate the variation within each experiment and data, and values represent mean \pm s.d.

- Bachoo, R. M. *et al.* Epidermal growth factor receptor and Ink4a/Arf: convergent mechanisms governing terminal differentiation and transformation along the neural stem cell to astrocyte axis. *Cancer Cell* **1**, 269–277 (2002).
- Rietze, R. L. & Reynolds, B. A. Neural stem cell isolation and characterization. *Methods Enzymol.* **419**, 3–23 (2006).
- Maser, R. S. *et al.* Chromosomally unstable mouse tumours have genomic alterations similar to diverse human cancers. *Nature* **447**, 966–971 (2007).
- Li, C. & Wong, W. H. Model-based analysis of oligonucleotide arrays: expression index computation and outlier detection. *Proc. Natl Acad. Sci. USA* **98**, 31–36 (2001).
- Tusher, V. G., Tibshirani, R. & Chu, G. Significance analysis of microarrays applied to the ionizing radiation response. *Proc. Natl Acad. Sci. USA* **98**, 5116–5121 (2001).

LETTERS

Control of plant germline proliferation by SCF^{FBL17} degradation of cell cycle inhibitors

Hyo Jung Kim¹, Sung Aeong Oh^{3†}, Lynette Brownfield³, Sung Hyun Hong¹, Hojin Ryu¹, Ildoo Hwang¹, David Twell³ & Hong Gil Nam^{1,2}

Flowering plants possess a unique reproductive strategy, involving double fertilization by twin sperm cells¹. Unlike animal germ lines, the male germ cell lineage in plants only forms after meiosis and involves asymmetric division of haploid microspores, to produce a large, non-germline vegetative cell and a germ cell that undergoes one further division to produce the twin sperm cells². Although this switch in cell cycle control is critical for sperm cell production and delivery, the underlying molecular mechanisms are unknown. Here we identify a novel F-box protein of *Arabidopsis thaliana*, designated FBL17 (F-box-like 17), that enables this switch by targeting the degradation of cyclin-dependent kinase A1 inhibitors specifically in male germ cells. We show that FBL17 is transiently expressed in the male germ line after asymmetric division and forms an SKP1–Cullin1–F-box protein (SCF) E3 ubiquitin ligase complex (SCF^{FBL17}) that targets the cyclin-dependent kinase inhibitors KRP6 and KRP7 for proteasome-dependent degradation. Accordingly, the loss of FBL17 function leads to the stabilization of KRP6 and inhibition of germ cell cycle progression. Our results identify SCF^{FBL17} as an essential male germ cell proliferation complex that promotes twin sperm cell production and double fertilization in flowering plants.

The differential control of cell cycle progression is paramount in patterning development and in the establishment of germ cell populations in animals³. This is also apparent in the highly reduced plant male germ cell lineage, in which cell division is promoted or suppressed in unequal daughter cells² (Supplementary Fig. 1a). The key mechanism underlying cell cycle control is achieved by regulating the activity of cyclin-dependent kinases (CDKs)^{4,5} and male germ cell division requires the conserved CDKA1 in *Arabidopsis*^{6,7}. Although *cdka1* mutants show specific arrest of male germ cell proliferation, CDKA1 is expressed in germ and non-germ cells formed after asymmetric division⁷. Thus, cell-specific modulation of CDKA1 activity may distinguish germ and non-germ cell cycles.

CDKs are controlled by the ubiquitin-mediated proteolysis of key regulators such as cyclins and cyclin-dependent kinase inhibitors (CKIs)⁸. SCF complexes are the largest family of E3 ubiquitin protein ligases that facilitate the ubiquitination of proteins targeted for proteasome-dependent degradation^{9,10}, and are critically involved in cell cycle control and diverse developmental processes with various substrate-specific F-box proteins^{11,12}. The *Arabidopsis* genome contains hundreds of F-box proteins¹³, indicating the existence of a large array of SCF complexes. Yet, the functions of only a few F-box proteins have been identified^{12,14–16}.

We identified a T-DNA mutant in the *F-BOX-LIKE17* (*FBL17*) gene that encodes a protein with an amino terminus F-box motif and 12 leucine-rich repeats (LRRs) in the carboxy terminus

(Supplementary Fig. 2). Subsequent analysis revealed that *fbl17* mutants displayed remarkably similar phenotypes to *cdka1* mutants^{6,7}. We could not obtain homozygous progeny ($n = 1,999$), and heterozygous *fbl17/+* plants showed no noticeable phenotypic defects. In *cdka1* mutants, the single male germ cell preferentially fertilizes the egg cell to initiate embryo development, leading to endosperm failure and embryo abortion^{6,7}. Similar to *cdka1* mutants, the male transmission of *fbl17* was almost completely blocked (Table 1) and heterozygous *fbl17/+* plants produced 42% of seeds ($n = 278$) that contained arrested embryos with no or limited endosperm development (Fig. 1a–d, Supplementary Fig. 3, Supplementary Table 1). The pollen phenotype in *fbl17* mutants also closely resembled that observed in *cdka1* mutants. Early pollen development in *fbl17/+* plants was normal (Fig. 1e–i), but 47.2% of pollen ($n = 720$) failed to undergo germ cell division and contained a single male germ cell (Fig. 1j–o). Moreover, the *fbl17* mutant pollen phenotype was rescued by introduction of the wild-type *FBL17* gene (Fig. 1m), demonstrating the requirement for FBL17 in male germ cell division.

To determine when during the cell cycle *fbl17* germ cells arrest, we measured nuclear DNA content in mature pollen from *fbl17/+* plants. *fbl17* germ cells have an average DNA content of 1.52C (where 1C is the DNA content of a haploid cell), similar to the average DNA content of mature sperm cells^{6,17} (Fig. 1p). The incomplete S phase in *fbl17* germ cells is similar to that observed in *cdka1* germ cells⁶. Moreover, the germline-specific nuclear marker DUO1::H2B-mRFP1 that is expressed in twin sperm cells in wild-type pollen¹⁸ is expressed in *fbl17* germ cells (Fig. 1q, r). Thus, arrested *fbl17* germ cells have male germ cell characteristics and are functionally differentiated in a similar fashion to *cdka1* germ cells^{6,7}.

The remarkably similar phenotypes of *fbl17* and loss-of-function *cdka1* mutants^{6,7} suggested a possible connection between FBL17 and CDKA1 activity in germ cells. In yeast and animals, the SCF complex is a critical component of a canonical mechanism controlling cell division by targeting CKIs for proteasome-dependent degradation^{9,19,20}. We showed that the F-box domain of FBL17 was both necessary and sufficient for binding to the Skp1 homologue ASK1 in yeast (Supplementary Fig. 4); and using plant cell extracts we showed that both FBL17 and Cullin1 were pulled down with green fluorescent protein (GFP)-tagged ASK1 (Fig. 2a). These results suggest that FBL17 forms an SCF complex in plant cells, consisting of ASK1, Cullin1 and FBL17. The *Arabidopsis* genome contains seven CKIs designated Kip-related proteins (KRPs), which can bind to CDKA1 and inhibit its activity at least *in vitro*^{21,22}. Among these only KRP4, KRP6 and KRP7 showed clear binding to FBL17 in yeast (Supplementary Fig. 5a) that was mediated through the LRR domain

¹Division of Molecular Life Sciences, ²School of Interdisciplinary Bioscience and Bioengineering, Pohang University of Science and Technology, Pohang 790-784, South Korea.

³Department of Biology, University of Leicester, University Road, Leicester LE1 7RH, UK. †Present address: School of Life Sciences, Kyungpook National University, Daegu 702-701, South Korea.

(Fig. 2b, c). In contrast to KRP4, which was not expressed in developing pollen, KRP6 and KRP7 showed enhanced expression in bicellular pollen similarly to FBL17 (Supplementary Fig. 5b) and were further investigated as candidate targets of FBL17.

Further support for the hypothesis that KRP6 and KRP7 may be *in vivo* substrates of FBL17 is provided by binding of N-terminal yellow fluorescent protein (YFP)–FBL17 to C-terminal YFP–KRP6 and KRP7 in bimolecular fluorescence complementation (BiFC) assays in transfected protoplasts (Fig. 2d). In addition, in co-immunoprecipitation assays haemagglutinin (HA)-tagged FBL17 was pulled down in extracts of transfected protoplasts by GFP-tagged KRP6 and KRP7, demonstrating *in vivo* interaction of FBL17 and these KRPs (Fig. 2e). We also examined whether KRP6 and KRP7 are degraded through a proteasome-dependent pathway. When recombinant glutathione S-transferase (GST) fusion proteins GST–KRP6 or GST–KRP7 were incubated with crude extracts from floral buds of wild-type plants, their abundance decreased during incubation. However, the rate of decrease was reduced by treatment with the proteasome inhibitor, MG132, indicating that degradation of KRP6 and KRP7 is dependent on 26S proteasome activity (Fig. 2f). In other studies on F-box proteins, a reduced degradation rate of target proteins has been shown using F-box knockout lines^{14,23}. Unfortunately, homozygous plants that are null for *fbl17* cannot be made because of the lack of male transmission. Therefore, we

examined degradation of KRP6 and KRP7 in assays in which GST–KRP fusion proteins were added to extracts from transgenic plants where expression of *FBL17* was under the control of the inducer methoxy fenozide (MOF). Even though FBL17 was rapidly degraded in plant extracts, recombinant GST–KRP6 and GST–KRP7 showed relatively modest, but consistent, increases in the rate of degradation when incubated with extracts of MOF-induced transgenic plants (Supplementary Fig. 6). Collectively, these results strongly support the conclusion that FBL17 exists in an SCF complex and provides evidence that this is causally required for degradation of KRP6 and KRP7.

FBL17 transcripts are widely expressed in different plant organs²⁴ and could therefore have other roles in addition to that in male germ cell division. In pollen, however, *FBL17* transcripts are present throughout development (Supplementary Fig. 5b), but peak in bicellular pollen, consistent with its role in male germ cell division. To monitor the expression of FBL17 protein during pollen development, we constructed a fusion of full-length *FBL17* and GFP under the control of the *FBL17* promoter. The fusion protein FBL17–GFP was able to complement the *fbl17* mutation and we could observe GFP signal only in the male germ cell nucleus of early to mid bicellular pollen (Fig. 3a). The GFP signal was not detected in uninucleate microspores, or in tricellular or mature pollen; nor was it observed in

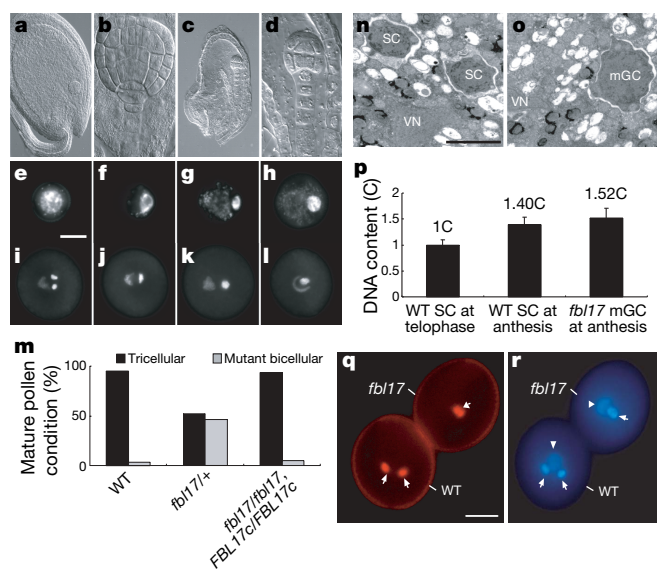


Figure 1 | FBL17 is required for the single male germline division.

a–d, Embryogenesis in *fbl17/+* plants. Cleared whole mount seeds were viewed by DIC optics. **a**, **c**, Embryos at globular stage in wild-type (**a**) and *fbl17* mutant (**c**) seeds; endosperm is underdeveloped in *fbl17* mutant seeds. **b**, **d**, Close-up images of wild-type (**b**) and arrested mutant (**d**) embryos. **e–l**, DAPI staining of wild-type and *fbl17* pollen during male gametophyte development. **e**, Early microspore. **f**, Late microspore. **g**, Early bicellular pollen. **h**, Mid bicellular pollen. **i**, Mature wild-type pollen. **j–l**, Multiple examples of mature *fbl17* mutant pollen. Scale bar, 10 μ m. **m**, Tricellular (black bars) and bicellular (grey bars) pollen grains were counted for complementation analysis in wild type (WT; $n = 709$), *fbl17/+* ($n = 720$) and *fbl17/fbl17;FBL17c/FBL17c* ($n = 657$). *FBL17c* represents a 5.0 kb genomic fragment including the *FBL17* locus. **n**, **o**, Electron micrographs of mature pollen at tricellular stage. **n**, Wild-type pollen contains two sperm cells (SC), whereas *fbl17* mutant pollen (**o**) contains a single mutant germ cell (mGC). VN, vegetative nucleus. Scale bar, 2 μ m. **p**, DNA content of wild-type sperm-cells (WT SC) at telophase ($n = 9$) and at anthesis ($n = 43$) and *fbl17* mutant germ cells (*fbl17* mGC) at anthesis ($n = 67$) from wild-type and *fbl17/+* plants. Error bars, s.e.m. **q**, **r**, Expression of DUO1::H2B-mRFP1 protein (**q**) and DAPI staining (**r**) of mature pollen from heterozygous *fbl17/+* plants. Arrowheads indicate the vegetative nucleus. Arrows indicate the single germ cell nucleus in *fbl17* pollen and sperm-cell nuclei of wild-type pollen. Scale bar, 10 μ m.

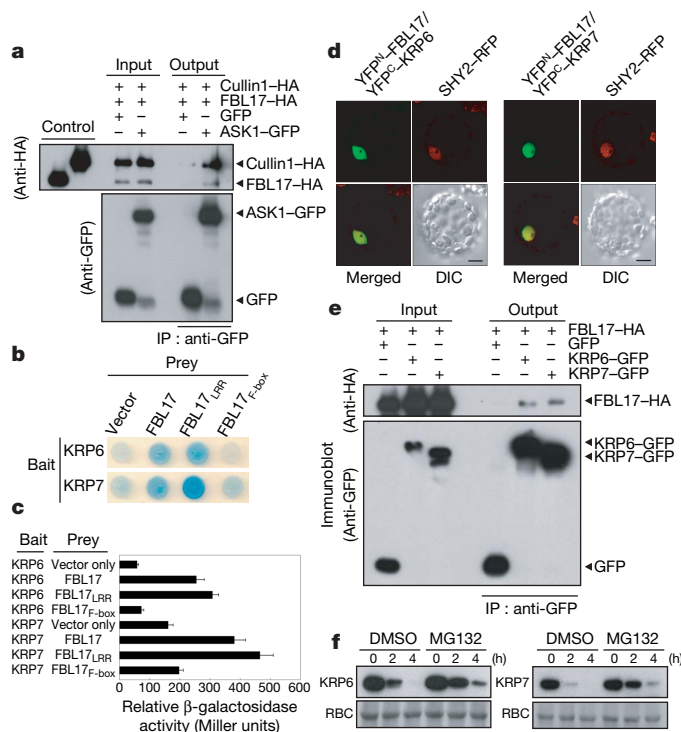


Figure 2 | FBL17 is part of an SCF complex and binds to KRP6 and KRP7 that show proteasome-dependent degradation. **a**, Co-immunoprecipitation of FBL17, Cullin1 and ASK1 with monoclonal anti-GFP antibody in total protein extracts from *Arabidopsis* protoplasts transfected with *Cullin1*–HA, *FBL17*–HA and *ASK1*–GFP. **b**, Yeast two-hybrid analysis of the binding of FBL17 to KRP6 and KRP7. The full-length FBL17, the LRR domain (FBL17_{LRR}), or the F-box domain of FBL17 (FBL17_{F-box}) were used as ‘prey’ (see Methods). **c**, The mean β -galactosidase activity is expressed as Miller units (error bars, s.d.; $n = 3$). **d**, BiFC analysis of FBL17–KRP6 and FBL17–KRP7 interaction. SHY2–RFP was used as a control nuclear marker protein. Scale bar, 10 μ m. **e**, Co-immunoprecipitation of FBL17 and KRP6 or KRP7, with anti-GFP antibody in total protein extracts from *Arabidopsis* protoplasts transfected with *FBL17*–HA and *KRP6*–GFP or *KRP7*–GFP. **f**, Proteasome-dependent degradation of KRP6 and KRP7. Extracts from wild-type floral buds were treated with a control (DMSO) or the proteasome inhibitor (MG132). The Coomassie stained RbcS (RBC) serves as a protein loading control.

vegetative cells (Fig. 3a). These results suggest that FBL17 protein transiently accumulates in male germ cells and is degraded before division into the twin sperm cells.

We investigated the expression of the candidate FBL17 target proteins, KRP6 and KRP7, in wild-type pollen. We constructed full-length KRP6–GFP and KRP7–GFP fusion proteins under control of their native promoters, and examined their expression in stably transformed plants. KRP6–GFP expression was detectable in microspores and increased strongly in vegetative cell nuclei immediately after asymmetric division (Fig. 3b). KRP7–GFP showed a similar nuclear localization and expression profile, but the GFP signal was significantly weaker and not detectable in microspores or in mature pollen (Supplementary Fig. 7). Both fusion proteins were present in newly formed male germ cells after asymmetric division, but the GFP signal was rapidly turned over and was absent from sperm cells. The degradation of KRP6 and KRP7 in wild-type early male germ cells therefore coincides with the transient expression of FBL17–GFP.

In contrast to KRP7–GFP, the highly expressed KRP6–GFP fusion allowed us to monitor KRP6 degradation in the absence of FBL17. When KRP6–GFP fluorescence was examined in pollen from heterozygous *fbl17* plants, persistent GFP was detected in the single germ cell in *fbl17* pollen (Fig. 3b panel 6). When KRP6–GFP expression was monitored in pollen stained with DAPI to allow direct detection of mutant pollen, persistent GFP was observed in 86% (44/51) of *fbl17* mutant germ cells but not in any sperm cells (0/63) in wild-type pollen grains. Thus, KRP6–GFP showed persistent expression in mutant *fbl17* germ cell nuclei, while vegetative cell expression was unaffected, consistent with a germ-cell-specific role for FBL17 in the proteasome-dependent turnover of KRP6 (Fig. 3b).

The data presented here leads to the following model for the differential control of male germ cell proliferation in flowering plants (Supplementary Fig. 1b); in this model, the canonical SCF-mediated mechanism of cell cycle regulation is being used in unique cellular contexts in different kingdoms^{9,13}. Inhibitors of CDKA;1 activity KRP6 and KRP7 are present in vegetative and germ cells following asymmetric microspore division. Vegetative cell cycle progression is inhibited by persistent KRP expression. However, the transient expression of FBL17 in germ cells promotes germ cell cycle progression through an SCF^{FBL17} complex that targets the proteolysis of KRP6 and KRP7, enabling CDKA;1 activation and germ cell S-phase progression. But completion of germ cell division at G2/M to form twin sperm cells requires the germline-specific Myb protein DUO1 during G2/M transition^{17,18}. Thus, flowering plants have developed parallel regulatory mechanisms to control the differential

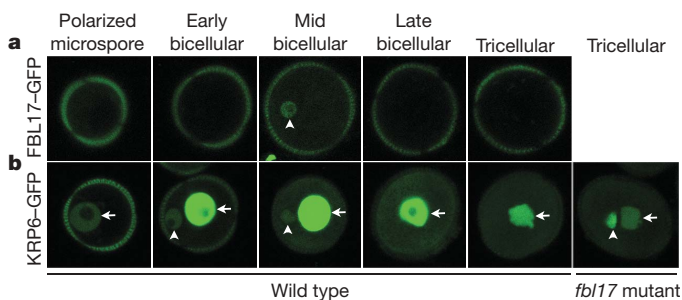


Figure 3 | FBL17 is required for KRP6 turnover in the male germ line. **a, b**, Expression of FBL17–GFP (**a**) and KRP6–GFP (**b**) during pollen development. Buds from a single inflorescence were dissected and pollen teased from anthers, mounted in 0.3 M mannitol and viewed by confocal laser scanning microscopy. The stage of development was determined by pollen morphology. Panels 1 to 5 (left to right) show GFP at stages of development in a wild-type background, while panel 6 shows *fbl17* mutant pollen from the *fbl17*/+ background. Arrows indicate GFP in the microspore nucleus (panel 1) and vegetative cell nucleus (panels 2–6), and arrowheads indicate germ cell GFP signal when present. Scale bar, 10 μ m.

Table 1 | Genetic transmission of the *fbl17* mutation

Parental genotypes	Genotype of F ₁ plants		n	TE (%)
(female \times male)	<i>fbl17</i> /+	Wild type		
<i>fbl17</i> /+ \times <i>fbl17</i> /+	1,004	995	1,999	NA
<i>fbl17</i> /+ \times +/+	73	75	148	97.3
+/+ \times <i>fbl17</i> /+	3	141	144	2.1

+/, Col-0, parental ecotype; n, number of F₁ plants scored; NA, not applicable; TE, transmission efficiency²⁵.

proliferation of germ and non-germ cells and the production of the twin sperm cells that are essential for double fertilization.

METHODS SUMMARY

Plant materials and growth conditions. *Arabidopsis thaliana* Columbia (Col-0) ecotype was the parent strain for mutants and transgenic lines. The *fbl17* mutant allele (GABI_170E02) was screened from the GABI-Kat T-DNA population. The genotype at the *FBL17* locus and its transmission efficiency (TE)²⁵ in reciprocal crosses was determined by PCR. Segregation of T-DNA antibiotic resistance markers was assayed by growing seedlings in 0.5 \times B5 medium containing 5.25 μ g ml^{−1} sulphadiazine (4-amino-N-[2-pyrimidinyl]benzene-sulphonamide-Na). Plants were grown in an environmentally controlled growth room at 22 °C with a 16-h-light/8-h-dark cycle.

Microscopy. Nuclei in pollen grains were visualized by DAPI (4',6'-diamidino-2-phenylindole) staining and fluorescence microscopy as previously described²⁶. Transmission electron microscopy was carried out as described²⁷. To monitor the expression of FBL17–GFP, KRP6–GFP and KRP7–GFP, pollen at different stages was teased out of the anther with a needle and mounted in 0.3 M mannitol; mature pollen was released directly into 0.3 M mannitol. Confocal laser scanning microscopy was conducted with a Nikon TE2000E inverted microscope and C1 confocal system using a Melles Griot argon ion laser (emission 488 nm), detection filter for GFP, and EZ-C1 control and imaging software. For phenotypic characterization of mutant embryos, cleared whole mount seeds were prepared as described²⁸ and viewed with differential interference contrast microscopy (DIC) on a Nikon TE2000E inverted microscope. Images were captured and processed as described²⁶.

Full Methods and any associated references are available in the online version of the paper at www.nature.com/nature.

Received 22 May; accepted 24 July 2008.

- Yadegari, R. & Drews, G. N. Female gametophyte development. *Plant Cell* **16** (Suppl), S133–S141 (2004).
- McCormick, S. Control of male gametophyte development. *Plant Cell* **16** (Suppl), S142–S153 (2004).
- Strome, S. & Lehmann, R. Germ versus soma decisions: Lessons from flies and worms. *Science* **316**, 392–393 (2007).
- Inze, D. & Veylder, L. D. Cell cycle regulation in plant development. *Annu. Rev. Genet.* **40**, 77–105 (2006).
- Sánchez, I. & Dynlacht, B. D. New insights into cyclins, CDKs, and cell cycle control. *Semin. Cell Dev. Biol.* **16**, 311–321 (2005).
- Nowack, M. K. et al. A positive signal from the fertilization of the egg cell sets off endosperm proliferation in angiosperm embryogenesis. *Nature Genet.* **38**, 63–67 (2006).
- Iwakawa, H., Shinmyo, A. & Sekine, M. *Arabidopsis* CDKA;1, a cdc2 homologue, controls proliferation of generative cells in male gametogenesis. *Plant J.* **45**, 819–831 (2006).
- Nakayama, K. I. & Nakayama, K. Regulation of the cell cycle by SCF-type ubiquitin ligases. *Semin. Cell Dev. Biol.* **16**, 323–333 (2005).
- Smalle, J. & Vierstra, R. D. The ubiquitin 26S proteasome proteolytic pathway. *Annu. Rev. Plant Physiol. Plant Mol. Biol.* **55**, 555–590 (2004).
- Petroski, M. D. & Deshaies, R. J. Function and regulation of cullin-RING ubiquitin ligases. *Nature Rev. Mol. Cell Biol.* **6**, 9–20 (2005).
- Cardozo, T. & Pagano, M. The SCF ubiquitin ligase: Insights into a molecular machine. *Nature Rev. Mol. Cell Biol.* **5**, 739–751 (2004).
- Lechner, E., Achard, P., Vansiri, A., Potuschak, T. & Genschik, P. F-box proteins everywhere. *Curr. Opin. Plant Biol.* **9**, 631–638 (2006).
- Xiao, W. & Jang, J. F-box proteins in *Arabidopsis*. *Trends Plant Sci.* **5**, 454–457 (2000).
- Kiba, T., Henriques, R., Sakakibara, H. & Chua, N. H. Targeted degradation of PSEUDO-RESPONSE REGULATOR5 by an SCF^{ZTL} complex regulates clock function and photomorphogenesis in *Arabidopsis thaliana*. *Plant Cell* **19**, 2516–2530 (2007).
- Chini, A. et al. The JAZ family of repressors is the missing link in jasmonate signalling. *Nature* **448**, 666–671 (2007).
- Thines, B. et al. JAZ repressor proteins are targets of the SCF^{CO1} complex during jasmonate signalling. *Nature* **448**, 661–665 (2007).

17. Durbarry, A., Vizir, I. & Twell, D. Male germ line development in *Arabidopsis duo* pollen mutants reveal gametophytic regulators of generative cell cycle progression. *Plant Physiol.* **137**, 297–307 (2005).
18. Rotman, N. *et al.* A novel class of MYB factors controls sperm-cell formation in plants. *Curr. Biol.* **15**, 244–248 (2005).
19. Toda, T., Ochotorena, I. & Kominami, K. Two distinct ubiquitin-proteolysis pathways in the fission yeast cell cycle. *Phil. Trans. R. Soc. Lond. B* **354**, 1551–1557 (1999).
20. Nakayama, K. I. & Nakayama, K. Ubiquitin ligases: Cell-cycle control and cancer. *Nature Rev. Cancer* **6**, 369–381 (2006).
21. De Veylder, L. *et al.* Functional analysis of cyclin-dependent kinase inhibitors of *Arabidopsis*. *Plant Cell* **13**, 1653–1668 (2001).
22. Verkest, A., Weinl, C., Inze, D., De Veylder, L. & Schnittger, A. Switching the cell cycle. Kip-related proteins in plant cell cycle control. *Plant Physiol.* **139**, 1099–1106 (2005).
23. Grey, W. M., Kepinski, S., Rouse, D., Leyser, O. & Estelle, M. Auxin regulates SCF^{TIR1}-dependent degradation of AUX/IAA proteins. *Nature* **414**, 271–276 (2001).
24. Dupl'akova, N. *et al.* *Arabidopsis* Gene Family Profiler (aGFP)—user-oriented transcriptomic database with easy-to-use graphic interface. *BMC Plant Biol.* **7**, 39 (2007).
25. Howden, R. *et al.* Selection of T-DNA-tagged male and female gametophytic mutants by segregation distortion in *Arabidopsis*. *Genetics* **149**, 621–631 (1998).
26. Park, S. K., Howden, R. & Twell, D. The *Arabidopsis thaliana* gametophytic mutation *geminipollen1* disrupts microspore polarity, division asymmetry and pollen cell fate. *Development* **125**, 3789–3799 (1998).
27. Park, S. K. & Twell, D. Novel patterns of ectopic cell plate growth and lipid body distribution in the *Arabidopsis geminipollen1* mutant. *Plant Physiol.* **126**, 899–909 (2001).
28. Park, S. K., Rahman, D., Oh, S. A. & Twell, D. *geminipollen2*, a male and female gametophytic cytokinesis defective mutation. *Sex. Plant Reprod.* **17**, 63–70 (2004).

Supplementary Information is linked to the online version of the paper at www.nature.com/nature.

Acknowledgements We thank K. H. Suh, Y. S. Park and B. H. Kim for technical assistance. This work was supported by MOST (KOSEF) through the National Core Research Center for Systems Bio-Dynamics (to H.G.N.) and the Crop Functional Genomics Research Program (to H.G.N.), by the Biotechnology and Biological Sciences Research Council (to D.T.), by the BK21 research fellowship for Life Science, Kyungpook National University (to S.A.O.), and by a KRF grant from MOHERD (to I.H.).

Author Contributions H.J.K. carried out Y2H analysis, FBL17 protein and molecular analysis, construction of FBL17 and KRP transgenic lines, *in vitro* degradation assays and wrote the manuscript. S.A.O. characterized *fbl17* mutant phenotype and nuclear DNA content analysis. L.B. analysed *in vivo* expression of FBL17 and KRP by confocal laser scanning microscopy and contributed to manuscript writing. S.H.H. carried out co-immunoprecipitation assay of FBL17. H.R., I.H. and H.J.K. initially isolated *fbl17* T-DNA mutant. D.T. and H.G.N. contributed to planning, interpretation and manuscript writing and are considered co-senior authors. All authors discussed the results and commented on the manuscript.

Author Information Reprints and permissions information is available at www.nature.com/reprints. Correspondence and requests for materials should be addressed to D.T. (twe@le.ac.uk) or H.G.N. (nam@postech.ac.kr).

METHODS

Generation of transgenic plants. For complementation analysis, the 5.0 kb DNA fragment containing 1.4 kb of the promoter region, the predicted ORF and 0.7 kb of downstream sequence of *FBL17* was amplified by PCR using primers FBL17c-F and FBL17c-R (Supplementary Table 2). The fragment was cloned into the KpnI and SalI sites of the pCAMBIA1300 vector (MRC). Transformed plants were selected on 0.5× B5 medium containing 20 µg ml⁻¹ hygromycin and 5.25 µg ml⁻¹ sulphadiazine. For conditional expression of *FBL17*, the *C. fumiferana* EcR-based inducible system was used^{29,30}. For expression of FBL17, KRP6 and KRP7 during pollen development, the full-length DNA fragments were generated by PCR with primer pairs FBL17-F/FBL17-R, KRP6-F/KRP6-R and KRP7-F/KRP7-R, and inserted into a vector containing a GFP-tag with their own promoters, which were amplified with primer pairs promFBL17-F/promFBL17-R, promKRP6-F/promKRP6-R and promKRP7-F/promKRP7-R (Supplementary Table 2). *Agrobacterium* strain AGL1 harbouring these binary vectors was used for transformation of wild-type or *fbl17*/+ plants using the floral dip method³¹.

Yeast two-hybrid assay. The DupLEX-A system (OriGene Technologies) was used. The full-length *FBL17* and *FBL17* cDNA fragments encoding FBL17_{F-box} (1–175) and FBL17_{LRR} (176–593) were obtained by PCR amplification with primer pairs FBL17-F/FBL17-R, FBL17-F/FBL17_{F-box}-R and FBL17_{LRR}-F/FBL17-R (Supplementary Table 2), and cloned into the both pGilda bait vector and pJG4-5 prey vector, which produce an in-frame fusion with the LexA DNA-binding domain and B42 activation domain, respectively. The full-length *ASK1* and *KRP* coding sequences were amplified with primer pairs ASK1-F/ASK1-R and KRP1~7-F/KRP1~7-R (Supplementary Table 2), and fused to the pJG4-5 prey vector and pGilda bait vector, respectively. The yeast strain EGY48 (*MATa*, *trp1*, *his3*, *ura3*, *leu2::6 LexAop-LEU2*) that contains the *lacZ* reporter plasmid pSH18-34 was transformed with the appropriate 'bait' and 'prey' plasmids. Interactions were tested on 5-bromo-4-chloro-3-indolyl-β-D-galactopyranoside (X-gal) media. A β-galactosidase activity assay of the transformants was performed as described³².

Co-immunoprecipitation assay. The full-length *FBL17* and *Cullin1* were generated by PCR amplification with primer pairs FBL17_{ha}-F/FBL17_{ha}-R and Cullin1_{ha}-F/Cullin1_{ha}-R (Supplementary Table 2), and inserted into a plant expression vector that containing two copies of HA tag driven by the 35S4PPDK promoter³³. DNA fragments encoding *ASK1*, *KRP6* and *KRP7* were obtained by PCR amplification with primer pairs ASK1_{gfp}-F/ASK1_{gfp}-R, KRP6-F/KRP6-R and KRP7-F/KRP7-R (Supplementary Table 2), and fused to GFP coding sequences controlled by the cassava vein mosaic virus promoter³⁴. *Arabidopsis* mesophyll protoplasts were isolated from mature leaves of the wild-type plants and transfected with various constructs expressing HA- or GFP-tagged proteins as described³⁵. Protoplasts were further incubated overnight at 22 °C under dim light. Cells (0.4 × 10⁵ per sample) were harvested and solubilized with 100 µl 1× immunoprecipitation (IP) buffer containing 50 mM Tris-HCl pH 7.5, 150 mM NaCl, 0.1% SDS, 0.1% Nonidet P-40, 50 µM MG132, 1 mM PMSF and protease inhibitor cocktail (Roche). The extracts were centrifuged at 12,000g for 15 min at 4 °C. The supernatant was incubated with 3 µg of agarose-conjugated anti-GFP monoclonal antibody (Santacruz) for 6 h at 4 °C and the pellet fraction was washed four times with washing buffer containing 50 mM Tris-HCl pH 7.5, 150 mM NaCl, 0.1% Nonidet P-40 and protease inhibitor cocktail (Roche). The protein extracts and immunoprecipitated samples were separated on 10% SDS-PAGE gels, transferred to PVDF membranes, and detected with HRP-conjugated anti-GFP (Santacruz) and anti-HA (Roche) monoclonal antibodies.

Bimolecular fluorescence complementation assay. DNA fragments encoding *FBL17*, *KRP6* and *KRP7* were obtained by PCR amplification with primer pairs FBL17_{yfp}^N-F/FBL17_{yfp}^N-R, KRP6_{yfp}^C-F/KRP6_{yfp}^C-R and KRP7_{yfp}^C-F/KRP7_{yfp}^C-R (Supplementary Table 2), and fused to plant expression vector containing either N- or C-terminal fragments of the YFP fluorescent (YFP^N and

YFP^C). Transfected protoplasts were examined with a confocal laser scanning microscope (Olympus FluoView FV1000).

RNA extractions and RT-PCR analysis. For expression analysis of *FBL17* and *KRP* genes during pollen development, total RNA was extracted from 50 mg of isolated spores at each developmental stage using the RNeasy Plant Kit (Qiagen) as described³⁶. Samples of 750 ng of total RNA were reverse transcribed using Superscript III RNase H reverse transcriptase (Invitrogen). For PCR amplification, 1 µl of a 20× diluted RT mix was used in a 25 µl reaction using Biotaq DNA polymerase (Bioline). The histone H3 gene (At4g40040) was used as a control.

Expression and purification of recombinant proteins. The full-length *KRP6* and *KRP7* cDNAs were amplified by PCR with primer pairs KRP6-F/KRP6-R and KRP7-F/KRP7-R (Supplementary Table 2), respectively, to introduce EcoRI and XhoI restriction enzyme sites. This fragment was inserted into corresponding sites of the pGEX4T-1 vector (Amersham Pharmacia Biotech) to generate an in-frame fusion with GST. The plasmid was introduced into *Escherichia coli* strain BL21-Codon Plus (DE3)-RIL (Stratagene) and *E. coli* cells were grown to an OD₆₀₀ of approximately 0.6. Fusion protein expression was then induced with 0.5 mM isopropyl-β-D-thiogalactopyranoside (IPTG) for 16 h at 18 °C. After centrifugation, the pellets were lysed in 1/10 culture volume of lysis buffer (50 mM sodium phosphate pH 7.2, 150 mM NaCl, 2 mM EDTA, 1% Triton X-100 and protease inhibitor cocktail) and cleared by centrifugation. The GST fusion protein was purified by glutathione sepharose 4B beads (Amersham Pharmacia Biotech). All purification steps were performed at 4 °C. The recombinant proteins were then eluted with a buffer containing 50 mM Tris-HCl pH 8.0, 120 mM NaCl and 10 mM glutathione overnight at 4 °C.

In vitro degradation assays. To test the effect of the proteasome inhibitor on KRP stability, MG132 (100 µM) or DMSO (1%) was added directly to protein extracts of wild-type floral buds for 2 h before mixing with recombinant GST-KRP proteins. For induction of FBL17-HA protein, *VGE::FBL17-HA* seedlings were grown on 0.5× B5 medium for 10 days before treatment with 50 µM MOF for 3 days. Seedlings were ground to a fine powder and homogenized at 4 °C in extraction buffer (50 mM Tris-HCl pH 7.5, 150 mM NaCl, 0.1% Nonidet P-40, 1 mM PMSF and protease inhibitor cocktail). Crude extracts (~400 µg) were pretreated with 10 µM MG132 to slow down FBL17 degradation, and mixed with 0.8 µg purified GST-KRP proteins in a total volume of 400 µl and incubated at 4 °C. At each time point 16 µl was removed, heated at 95 °C for 5 min in 4 µl of 5× SDS-PAGE sample buffer and subjected to 10% SDS-PAGE. GST-tagged KRP proteins were detected using peroxidase-conjugated (HRP) anti-GST antibody (Santacruz). The same membrane was stripped and re-probed with anti-HA antibody to detect the induced level of FBL17.

29. Koo, J. C., Asurmendi, S., Bick, J., Woodford-Thomas, T. & Beachy, R. N. Ecdysone agonist-inducible expression of a coat protein gene from tobacco mosaic virus confers viral resistance in transgenic *Arabidopsis*. *Plant J.* **37**, 439–448 (2004).
30. Padidam, M., Gore, M., Lu, D. L. & Smirnova, O. Chemical-inducible, ecdysone receptor-based gene expression system for plants. *Transgenic Res.* **12**, 101–109 (2003).
31. Clough, S. J. & Bent, A. F. Floral dip: A simplified method for *Agrobacterium*-mediated transformation of *Arabidopsis thaliana*. *Plant J.* **16**, 735–743 (1998).
32. Ryu, J. S. et al. Phytochrome-specific type 5 phosphatase controls light signal flux by enhancing phytochrome stability and affinity for a signal transducer. *Cell* **120**, 395–406 (2005).
33. Sheen, J. Ca²⁺-dependent protein kinases and stress signal transduction in plants. *Science* **274**, 1900–1902 (1996).
34. Verdaguier, B., de Kochko, A., Beachy, R. N. & Fauquet, C. Isolation and expression in transgenic tobacco and rice plants, of the cassava vein mosaic virus (CVMV) promoter. *Plant Mol. Biol.* **31**, 1129–1139 (1996).
35. Kovtun, Y., Chiu, W. L., Tena, G. & Sheen, J. Functional analysis of oxidative stress-activated mitogen-activated protein kinase cascade in plants. *Proc. Natl Acad. Sci. USA* **97**, 2940–2945 (2000).
36. Honys, D. & Twell, D. Transcriptome analysis of haploid male gametophyte development in *Arabidopsis*. *Genome Biol.* **5**, R85 (2004).

LETTERS

Protein-folding location can regulate manganese-binding versus copper- or zinc-binding

Steve Tottey¹, Kevin J. Waldron¹, Susan J. Firbank¹, Brian Reale¹, Conrad Bessant², Katsuko Sato¹, Timothy R. Cheek¹, Joe Gray¹, Mark J. Banfield¹, Christopher Dennison¹ & Nigel J. Robinson¹

Metals are needed by at least one-quarter of all proteins^{1,2}. Although metallochaperones^{3–8} insert the correct metal into some proteins, they have not been found for the vast majority, and the view is that most metalloproteins acquire their metals directly from cellular pools. However, some metals form more stable complexes with proteins than do others. For instance, as described in the Irving–Williams series⁹, Cu^{2+} and Zn^{2+} typically form more stable complexes than Mn^{2+} . Thus it is unclear what cellular mechanisms manage metal acquisition by most nascent proteins. To investigate this question, we identified the most abundant Cu^{2+} -protein, CucA (Cu^{2+} -cupin A), and the most abundant Mn^{2+} -protein, MncA (Mn^{2+} -cupin A), in the periplasm of the cyanobacterium *Synechocystis* PCC 6803. Each of these newly identified proteins binds its respective metal via identical ligands within a cupin fold. Consistent with the Irving–Williams series, MncA only binds Mn^{2+} after folding in solutions containing at least a 10^4 times molar excess of Mn^{2+} over Cu^{2+} or Zn^{2+} . However once MncA has bound Mn^{2+} , the metal does not exchange with Cu^{2+} . MncA and CucA have signal peptides for different export pathways into the periplasm, Tat and Sec respectively. Export by the Tat pathway allows MncA to fold in the cytoplasm, which contains only tightly bound copper or Zn^{2+} (refs 10–12) but micromolar Mn^{2+} (ref. 13). In contrast, CucA folds in the periplasm to acquire Cu^{2+} . These results reveal a mechanism whereby the compartment in which a protein folds overrides its binding preference to control its metal content. They explain why the cytoplasm must contain only tightly bound and buffered copper and Zn^{2+} .

Proteins can selectively bind different metals on the basis of factors that include the nature, number and geometric arrangement of the binding residues and also the size and charge of the metal-binding pocket. However, this selection is imperfect because proteins are flexible, and this is especially true of newly synthesized unfolded proteins. The affinities of proteins for the different trace metals are substantially determined by universal series, which for divalent metals is the Irving–Williams series ($\text{Mn}^{2+} < \text{Fe}^{2+} < \text{Co}^{2+} < \text{Ni}^{2+} < \text{Cu}^{2+} > \text{Zn}^{2+}$), and Cu^+ is also highly competitive⁹. How can cells contain proteins requiring weak-binding metals while simultaneously containing proteins requiring tight-binding ones? In a simple model, all metalloproteins would bind the most competitive metals. Cyanobacteria such as *Synechocystis* PCC 6803 have a high demand for metals at opposite extremes of the affinity series (Mn^{2+} and copper are both required for enzymes of photosynthesis¹⁴), and so this bacterium was selected for these studies.

The initial objective was to discover which soluble proteins bind most Mn^{2+} and most Cu^{2+} in the periplasm. Cold osmotic shock was used to liberate periplasm contents, which were resolved by native two-dimensional liquid chromatography; eluant was analysed for metals by inductively coupled plasma mass spectrometry (ICP-MS;

Fig. 1a) and for proteins by denaturing sodium dodecyl sulphate polyacrylamide gel-electrophoresis (SDS-PAGE; Fig. 1b). The predominant copper-complex (p1) contains $\sim 2.5 \times 10^3$ atoms of copper per cyanobacterial cell and the predominant Mn^{2+} -complex (p2) contains $\sim 1.5 \times 10^3$ atoms of Mn^{2+} per cell. To characterize the protein binding the copper in complex p1, the abundance of individual proteins in the p1 region was first estimated by integrating peak areas from scanned SDS-PAGE gels. Principal component analysis was then used to compare the rise and fall of p1 copper with the rise and fall of each protein by their proximity on scatter plots (Fig. 1c and Supplementary Fig. 1). We used an algorithm designed to compare profile shape and not amplitude. More than one protein clustered with p1 copper (Fig. 1c), so the second dimension separation was repeated with greater resolution (Supplementary Fig. 2), now obtaining only one candidate, C_{p1} (Fig. 1d), closely matching the p1 copper profile (Fig. 1e). C_{p1} was excised from a gel and identified via mass fingerprinting as the product of open reading frame *sll1785* (Fig. 1e), which is a predicted (InterPro e-score, 8.7×10^{-6}) cupin (which possess a β -barrel structural fold). One cupin that contains Cu^{2+} within the barrel is known, namely quercetin 2,3 dioxygenase (Supplementary Fig. 3)¹⁵, as are Fe^{2+} , Mn^{2+} and Zn^{2+} cupins^{16,17}.

To check that *sll1785* was the correct gene, we generated a mutant with inactive *sll1785*, confirmed that the p1 copper peak was missing (Fig. 1f) and designated the *sll1785* product CucA. The approach used to discover CucA was then used to characterize the predominant Mn^{2+} -complex (Fig. 2a, b and Supplementary Fig. 4); we identified the product of open reading frame *sll1358*, which has strong sequence similarity (InterPro e-score, 4×10^{-70}) to a Mn^{2+} -protein from other organisms, oxalate decarboxylase¹⁶ (Supplementary Fig. 5). A cupin fold is also predicted (InterPro e-score, 3.9×10^{-26}) for the *sll1358* product, which was thus designated MncA. Finally, to unequivocally confirm that CucA and MncA can bind Cu^{2+} and Mn^{2+} , both were expressed in *Escherichia coli* and purified after exposure to surplus Cu^{2+} or Mn^{2+} , respectively (Fig. 2c). Recovery of soluble MncA required metal to be present during refolding *in vitro*. Each isolated protein did indeed co-migrate with the respective metal during gel filtration, and $10 \mu\text{M}$ CucA was also shown to withhold $10 \mu\text{M}$ Cu^{2+} from the metallochromic indicator 4-(2-pyridylazo)-resorcinol, establishing that one copper atom binds to each CucA molecule (Fig. 2c). Thus CucA is the principal copper-protein and MncA the principal Mn^{2+} -protein in the cyanobacterial periplasm.

Although similarity between the principal proteins for Mn^{2+} and copper had not been anticipated, bioinformatics predicted that MncA and CucA are both cupins that coordinate their respective metals via three histidines and a glutamate (Supplementary Figs 3 and 5). Electron paramagnetic resonance spectroscopy was used to compare the coordination environments in CucA and MncA (Fig. 3a and Supplementary Fig. 6). The electron paramagnetic resonance spectra

¹Cell and Molecular Biosciences, Medical School, Newcastle University, Newcastle NE2 4HH, UK. ²Cranfield Bioinformatics Group, Cranfield University, Bedfordshire, MK43 0AL, UK.

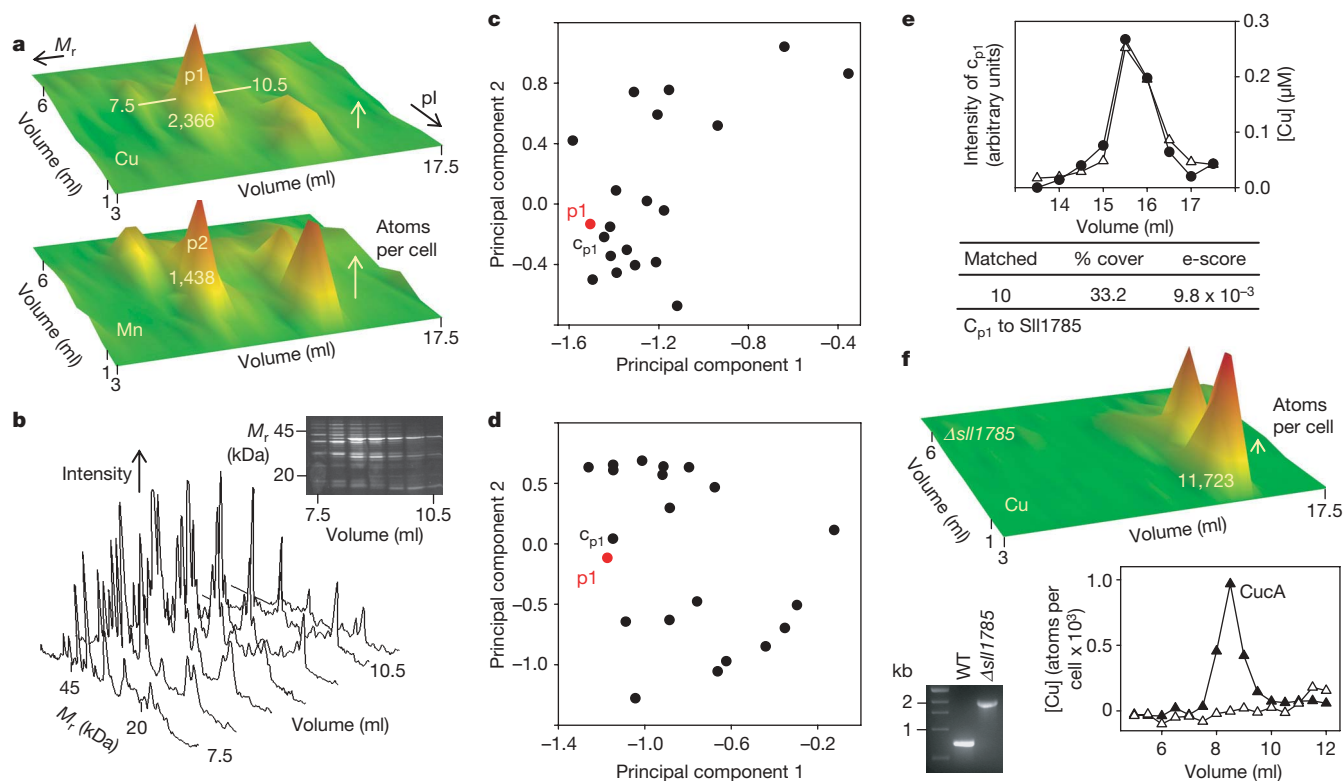


Figure 1 | Cuca is the principal periplasmic Cu^{2+} -protein. **a**, Profile showing two-dimensional liquid chromatography based on relative molecular mass (M_r) and charge (pI) of periplasm copper (top) p1 and Mn^{2+} (bottom) p2 complexes. Data are means of three replicates with atoms per cell in p1 and p2 shown. **b**, SDS-PAGE (inset) of fractions from **a**, with proteins visualized using SYPRO Ruby, scanned for fluorescence intensity and plotted as a function of relative molecular mass (main panel). **c**, The profile distribution of p1- Cu^{2+} (red) compared with protein peaks in

b (black) by principal component analysis (C_{p1} is the candidate for p1). **d**, As **c** but from a separation (Supplementary Fig. 2) with enhanced resolution. **e**, [Cu^{2+}] (triangles) and C_{p1} (circles), in part of a profile used in **d** plus identification of C_{p1} as Sll1785 by mass-fingerprinting. **f**, Profile of Δ sll1785 (top), and PCR products of sll1785 region confirming kanamycin gene insertion in Δ sll1785 (bottom left). Bottom right, [Cu^{2+}] in a part of the Δ sll1785 profile (open triangles) and in wild type (filled triangles).

of Cu^{2+} -CucA, and of MncA folded in Cu^{2+} as opposed to Mn^{2+} , are similar to each other (Fig. 3a), while Mn^{2+} -MncA and Cu^{2+} -CucA spectra are also similar to those of related proteins from other organisms^{18,19}, consistent with the predicted metal ligands. We produced diffraction quality crystals and generated a structure of MncA at 2.95 Å resolution (Supplementary Figs 7 and 8, and Supplementary Table 1).

MncA adopts a bicupin fold, and the crystal form contains metal coordinated to three histidine residues and a glutamate, with one metal in each cupin domain (Fig. 3b). Because the metal ligands of MncA and CucA have not diverged, these two proteins provide an especially valuable system for understanding the cellular mechanism which ensures that the correct metal is bound by a protein.

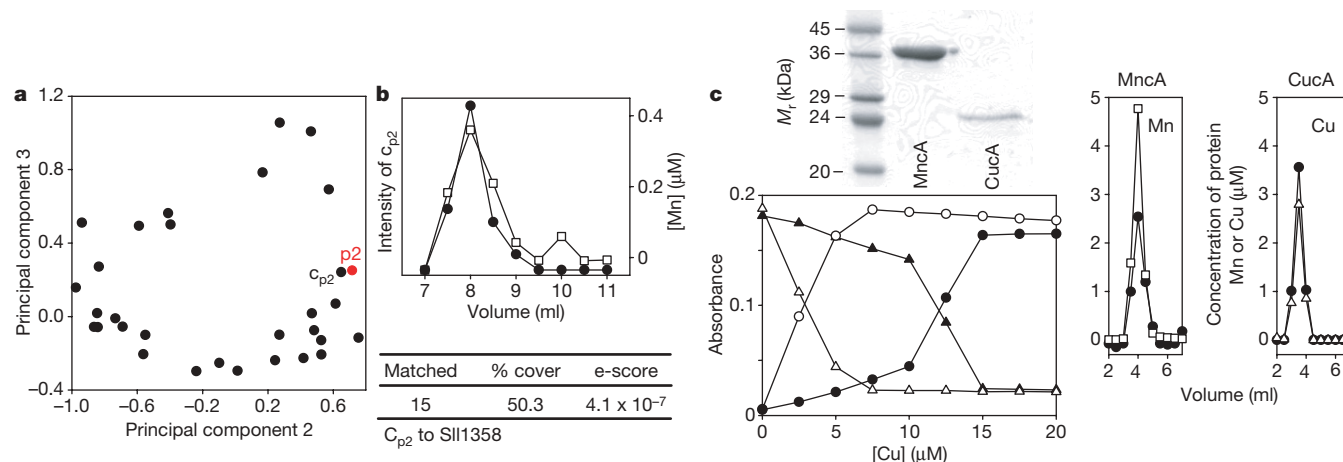


Figure 2 | MncA is the principal periplasmic Mn^{2+} -protein. **a**, The distribution of p2- Mn^{2+} (red) compared with protein (black), from Supplementary Fig. 4, by principal component analysis. **b**, [Mn^{2+}] (squares) and candidate for p2, C_{p2} (circles), in part of a profile used in Fig. 1a (lower) plus mass-fingerprinting identification of C_{p2} as Sll1358. **c**, SDS-PAGE of purified MncA and CucA (top left) and co-migration of the respective

proteins (filled circles) with Mn^{2+} (open squares) or Cu^{2+} (open triangles) by gel filtration (right). Bottom left, titration of apo-4-(2-pyridylazo)-resorcinol, which absorbs at 410 nm (triangles), to its copper-form absorbing at 510 nm (circles), in the absence (open symbols) and presence (filled symbols) of 10 μ M CucA.

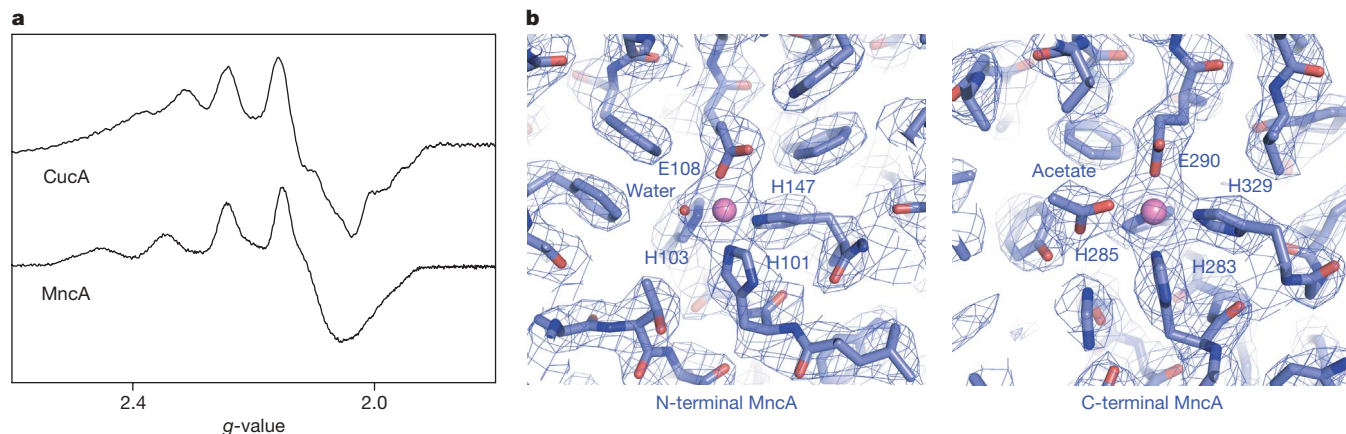


Figure 3 | MncA and CucA have similar metal-sites. **a**, X-band electron paramagnetic resonance spectra of Cu^{2+} -CucA and Cu^{2+} -MncA. **b**, Residues (blue) surrounding the metal ions (pink) within each MncA cupin fold

(amino-terminal, left panel; carboxy-terminal, right panel), with corresponding final $2F_o - F_c$ electron density maps contoured at 1.1σ .

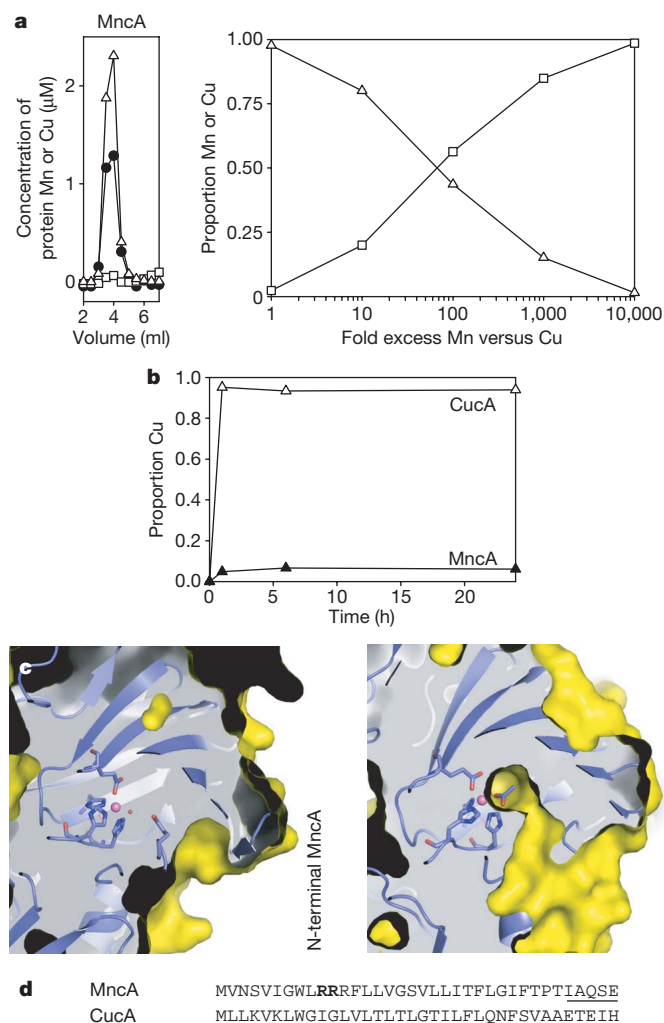
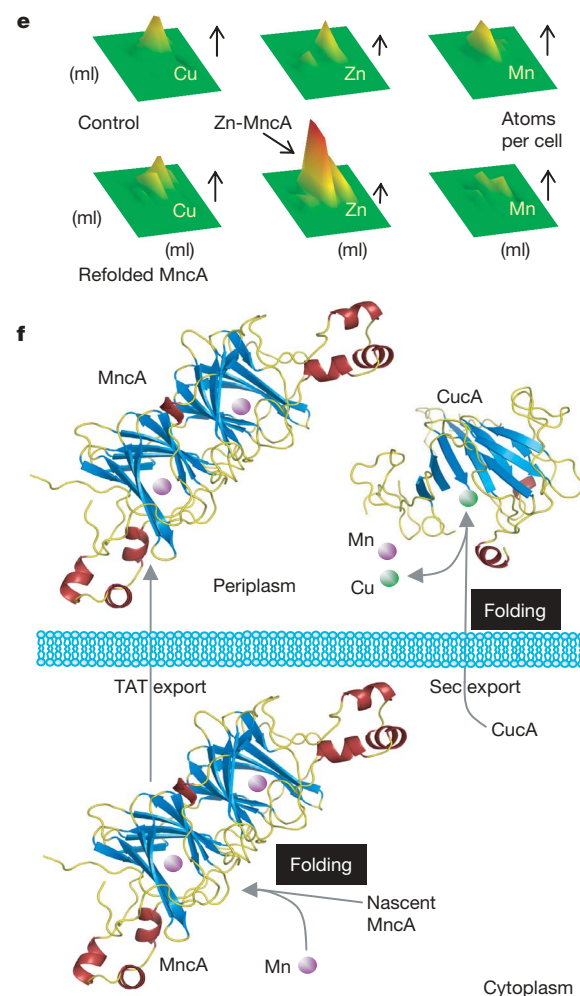


Figure 4 | MncA prefers Cu^{2+} but entraps Mn^{2+} . **a**, Co-migration by gel-filtration of Cu^{2+} (triangles) but not Mn^{2+} (squares) after folding MncA (circles) in an excess of equimolar metals (left), and metals bound at increasing $[\text{Mn}^{2+}]$ (right). **b**, Substitution of Mn^{2+} -MncA (filled triangles) or Mn^{2+} -CucA (open triangles) with Cu^{2+} . **c**, MncA metal-sites are buried with a channel to the surface only apparent in the C-terminal domain. Protein surfaces (yellow) are shown surrounding the MncA metal-sites



(metals in pink, protein interior shaded grey). Chelating residues are those shown in Fig. 3. **d**, Signal peptides (not underlined), and twin arginines (bold). **e**, Regions of profiles containing MncA before (top) and after (bottom) addition of unfolded MncA to a periplasm extract. **f**, Bi-cupin MncA folds and entraps uncompetitive Mn^{2+} in the cytoplasm, without competition from copper or Zn^{2+} , before Tat-export. Mono-cupin CucA (modelled) is exported unfolded via Sec and acquires competitive Cu^{2+} .

When MncA folds in equimolar Cu^{2+} and Mn^{2+} , the protein acquires exclusively the wrong metal, Cu^{2+} , as predicted from the Irving–Williams series and the rationale behind this work (Fig. 4a). Folding MncA in the presence of increasing amounts of Mn^{2+} relative to Cu^{2+} , and determining the proportions of protein-associated metal, establishes that a 10^4 -fold molar excess of Mn^{2+} is required to fully populate MncA with the correct element (Fig. 4a). A similar experiment establishes that MncA acquires Zn^{2+} unless folding occurs in a 10^5 -fold excess of Mn^{2+} relative to Zn^{2+} (Supplementary Fig. 9). Nascent MncA must have negligible access to either copper or Zn^{2+} , but this seems incompatible with its co-existence with Cu^{2+} -CucA. CucA will also bind Mn^{2+} (Supplementary Fig. 10). Crucially, Cu^{2+} rapidly exchanges with Mn^{2+} -CucA but not with Mn^{2+} -MncA (Fig. 4b). The MncA crystal structure confirms that its metal-binding sites are buried (Fig. 4c) thereby preventing exchange of hydrated metals. Thus, provided MncA is protected from Cu^{2+} or Zn^{2+} during folding in the presence of Mn^{2+} , it can subsequently be exposed to Cu^{2+} or Zn^{2+} because Mn^{2+} becomes kinetically restrained inside the folded protein.

The amino-terminal signal peptides of CucA and MncA (Fig. 4d) imply different export pathways: Sec for CucA and Tat for MncA. MncA (sll1358) was one of 10 designated Tat-substrates found among 57 salt-induced periplasm proteins in *Synechocystis* PCC 6803 (ref. 20). Export of MncA is impaired in a ΔtatABC strain of *E. coli*, and while the MncA signal sequence can drive a Tat-only substrate into the periplasm the CucA signal sequence can not (Supplementary Fig. 11). Tat-substrates fold within the cytoplasm before export²¹. Crucially, when recombinant MncA refolds in *Synechocystis* PCC 6803 periplasm extracts, it does acquire a more competitive metal, Zn^{2+} (Fig. 4e and Supplementary Fig. 12), inactivating the enzyme (Supplementary Fig. 13). Several lines of evidence have previously indicated that the cytosol contains only bound Zn^{2+} or copper^{10–12}. By folding in the cytosol, nascent MncA is protected from copper and Zn^{2+} when in a vulnerable form, allowing it to entrap less competitive Mn^{2+} . Oxalate decarboxylase has no signal sequence in bacteria such as *Bacillus subtilis* (Supplementary Fig. 5), and is a cytosolic protein which acquires Mn^{2+} . MncA retains the same folding location to overcome a challenge of coordination chemistry (Fig. 4f).

We show that compartmentalization can be used to keep competitive metals out of the wrong nascent proteins. Copper can catalyse the production of reactive oxygen species, but it is also vital to bind and buffer any cytoplasmic copper in order to keep it out of sites for less competitive metals. Copper ions are handed to cytoplasmic destinations by metallochaperones^{3–8}. Cyanobacteria have compartments, thylakoids, containing plastocyanin and cytochrome *c*-oxidase that require copper which is indeed delivered by a metallochaperone²². In eukaryotes, including humans, copper-proteins similarly obtain their copper inside compartments, namely the *trans*-Golgi network and mitochondria, or in the case of superoxide dismutase, from a dedicated metallochaperone¹¹. By passing copper to these destinations via ligand-exchange reactions, metallochaperones protect other metal-binding sites from the competitive ions^{4–8}. Metallochaperones are not known for Zn^{2+} , and there is interest in understanding how Zn^{2+} is specifically acquired by ~10% of proteins.

It was already known that Tat-substrates can acquire cofactors before export^{23–25}, but exploitation of Tat-export to overcome a protein's metal-binding preference is a newly discovered mechanism. Intriguingly, it has emerged that Co^{2+} toxicity in *E. coli* is mediated by the replacement of Fe^{2+} in iron-sulphur clusters with Co^{2+} (ref. 26). The clusters are protected once inside the holoproteins²⁶. As these clusters are common in Tat-substrates, cofactor insertion before export affords protection from a metal higher up the stability series when the clusters are in a vulnerable state. One crucial consequence of nascent proteins having tight affinities for the wrong metals is a risk of metal associations with aberrant binding sites. Imperfect metal homeostasis, due to environmental or genetic factors, may allow accumulation of

competitive metals in the wrong proteins, which could be pathological. There is a need to test whether this is one factor underlying links between copper and degenerative disorders, including Alzheimer's disease and Creutzfeldt–Jakob disease^{27–29}.

METHODS SUMMARY

Analysis of *Synechocystis* PCC 6803 extracts. Osmotic shock extracts were separated by anion exchange chromatography. Aliquots of the eluant were resolved by size exclusion chromatography followed by metal quantification via ICP-MS³⁰ and protein quantification using SYPRO Ruby stained SDS–PAGE. Metal abundance was plotted as a surface representation, with the z-axis showing atoms per cell and colour thresholds set to arbitrary values. Principal component analysis used a custom algorithm written within MatLab. Mass fingerprinting used a Voyager DE-STR MALDI-TOF mass spectrometer.

Mutants. A *Synechocystis* PCC 6803 strain lacking CucA was generated via transformation with a kanamycin resistance cassette flanked with *sll1785* regions and segregation confirmed by PCR. To characterize the MncA Tat signal peptide, carboxyl-terminal His-tagged MncA was generated via PCR, as were fusions of the CucA and MncA signal sequences to GFP–SsrA.

Recombinant protein analyses. The *sll1358* and *sll1785* genes were expressed in *E. coli* BL21 (DE3) and protein recovered from inclusion bodies. Urea-solubilized CucA was refolded by rapid dilution into 20 mM Tris, pH 7.5, and MncA by dilution in the same buffer containing excess metal. For metal-competition experiments, urea-solubilized MncA (70 nM) was refolded in 50 ml buffer containing 400 nM CuSO_4 and increasing concentrations of MnCl_2 . Protein was concentrated by anion exchange chromatography, then resolved by gel filtration with eluant analysed for metals by ICP-MS and protein by Coomassie assay.

Electron paramagnetic resonance spectroscopy and crystallography. MncA (~0.7 mM) and CucA (~1.0 mM) were analysed at -196°C using a Bruker EMX EPR spectrometer. MncA crystals were generated at pH 4.2 and metal remains bound at this pH (Supplementary Fig. 14). Diffraction data were collected at the European Synchrotron Radiation Facility, Grenoble, France. Protein estimations used theoretical and determined $\epsilon_{280\text{nm}}$ for CucA and MncA, respectively (Supplementary Fig. 15). Cu^+ -MncA was analysed under anaerobic conditions (Supplementary Fig. 16).

Full Methods and any associated references are available in the online version of the paper at www.nature.com/nature.

Received 23 October 2007; accepted 13 August 2008.

- Rosenzweig, A. C. Metallochaperones: Bind and deliver. *Chem. Biol.* **9**, 673–677 (2002).
- Ferrer, M., Golyshina, O. V., Beloqui, A., Golyshin, P. N. & Timmis, K. N. The cellular machinery of *Ferroplasma acidiphilum* is iron-protein-dominated. *Nature* **445**, 91–94 (2007).
- Odermatt, A. & Solioz, M. Two trans-acting metalloregulatory proteins controlling expression of the copper-ATPases of *Enterococcus hirae*. *J. Biol. Chem.* **270**, 4349–4354 (1995).
- Beers, J., Glerum, D. M. & Tzagoloff, A. Purification, characterisation, and localisation of yeast Cox17p, a mitochondrial copper shuttle. *J. Biol. Chem.* **272**, 33191–33196 (1997).
- Carr, S. & Winge, D. R. Assembly of cytochrome c oxidase within the mitochondrion. *Acc. Chem. Res.* **36**, 309–316 (2003).
- Pufahl, R. A. et al. Metal ion chaperone function of the soluble Cu^I receptor Atx1. *Science* **278**, 853–856 (1997).
- Valentine, J. S. & Gralla, E. B. Delivering copper inside yeast and human cells. *Science* **278**, 817–818 (1997).
- Banci, L. et al. The Atx1–Ccc2 complex is a metal-mediated protein–protein interaction. *Nature Chem. Biol.* **2**, 367–368 (2006).
- Frausto da Silva, J. J. R. & Williams, R. J. P. *The Biological Chemistry of the Elements: The Inorganic Chemistry of Life* 2nd edn (Clarendon, 2001).
- Changela, A. et al. Molecular basis of metal-ion selectivity and zeptomolar sensitivity by CueR. *Science* **301**, 1383–1387 (2003).
- Rae, T. D., Schmidt, P. J., Pufahl, R. A., Culotta, V. C. & O'Halloran, T. V. Undetectable intracellular free copper: The requirement of a copper chaperone for superoxide dismutase. *Science* **284**, 805–808 (1999).
- Outten, C. E. & O'Halloran, T. V. Femtomolar sensitivity of metalloregulatory proteins controlling zinc homeostasis. *Science* **292**, 2488–2492 (2001).
- Helmann, J. D. Measuring metals with RNA. *Mol. Cell* **27**, 859–860 (2007).
- Totter, S., Harvie, D. R. & Robinson, N. J. in *Molecular Microbiology of Heavy Metals* (eds Nies, D. H. & Silver, S.) 1–35 (Microbiology Monographs Vol. 6, Springer, 2007).
- Fuseti, F. et al. Crystal structure of the copper-containing quercetin dioxygenase from *Aspergillus japonicus*. *Structure* **10**, 259–268 (2002).
- Tanner, A., Bowater, L., Fairhurst, S. A. & Bornemann, S. Oxalate decarboxylase requires manganese and dioxygen for activity. *J. Biol. Chem.* **276**, 43627–43634 (2001).

17. Dunwell, J. M., Khuri, S. & Gane, P. J. Microbial relatives of the seed storage proteins of higher plants: Conservation of structure and diversification of function during evolution of the cupin superfamily. *Microbiol. Mol. Biol. Rev.* **64**, 153–179 (2000).
 18. Kooter, I. M. *et al.* EPR characterization of the mononuclear Cu-containing *Aspergillus japonicus* quercetin 2,3-dioxygenase reveals dramatic changes upon anaerobic binding of substrates. *Eur. J. Biochem.* **269**, 2971–2979 (2002).
 19. Angerhofer, A. *et al.* Multifrequency EPR studies on the Mn(II) centers of oxalate decarboxylase. *J. Phys. Chem. B* **111**, 5043–5046 (2007).
 20. Fulda, S., Huang, F., Nilsson, F., Hagemann, M. & Norling, B. Proteomics of *Synechocystis* PCC 6803: Identification of periplasm proteins in cells grown at low and high salt concentrations. *Eur. J. Biochem.* **267**, 5900–5907 (2000).
 21. Robinson, C. & Bolhuis, A. Tat-dependent protein targeting in prokaryotes and chloroplasts. *Biochim. Biophys. Acta* **1694**, 135–147 (2004).
 22. Tottey, S. *et al.* A copper metallochaperone for photosynthesis and respiration reveals metal-specific targets, interaction with an importer, and alternative sites for copper acquisition. *J. Biol. Chem.* **277**, 5490–5497 (2002).
 23. Santini, C. L. *et al.* A novel sec-independent periplasmic protein translocation pathway in *Escherichia coli*. *EMBO J.* **17**, 101–112 (1998).
 24. Palmer, T. & Berks, B. C. Moving folded proteins across the bacterial cell membrane. *Microbiology* **149**, 547–556 (2003).
 25. Keegstra, K. & Cline, K. Protein import and routing systems of chloroplasts. *Plant Cell* **11**, 557–570 (1999).
 26. Ranquet, C., Ollagnier-de-Choudens, S., Loiseau, L., Barras, L. & Fontecave, M. Cobalt stress in *E. coli*: The effect on the iron-sulfur proteins. *J. Biol. Chem.* **282**, 30442–30451 (2007).
 27. Brown, D. R. *et al.* The cellular prion protein binds copper *in vivo*. *Nature* **390**, 684–687 (1997).
 28. Bellingham, S. A. *et al.* Copper depletion down-regulates expression of the Alzheimer's disease amyloid-beta precursor protein gene. *J. Biol. Chem.* **279**, 20378–20386 (2004).
 29. Bush, A. I. The metallobiology of Alzheimer's disease. *Trends Neurosci.* **26**, 207–214 (2003).
 30. Waldron, K. J., Tottey, S., Yanagisawa, S., Dennison, C. & Robinson, N. J. A periplasmic ironbinding protein contributes toward inward copper supply. *J. Biol. Chem.* **282**, 3837–3846 (2007).
- Supplementary Information** is linked to the online version of the paper at www.nature.com/nature.
- Acknowledgements** This work was supported by the BBSRC PMS committee (BBS/B/02576 and BB/E001688/1). B.R. was supported by J. Gitlin and the Children's Discovery Institute. M.J.B. is a Royal Society University Research Fellow. J. Kotz provided advice on the draft manuscript. We thank T. Palmer, B. Ize and G. Buchanan for donating *E. coli* BL21 *tat* deletion strains and for advice.
- Author Contributions** S.T. and K.J.W. contributed equally, doing most of the laboratory work and playing a part in planning and data interpretation. S.J.F. and M.J.B. collected and interpreted the X-ray diffraction data. C.D. and K.S. collected and interpreted the EPR data. B.R. did the metal exchange experiment. J.G. did the mass fingerprinting. C.B. generated the algorithm for principal component analysis and T.R.C. did the confocal microscopy. N.J.R. managed the programme, and had overall responsibility for data interpretation and writing the manuscript.
- Author Information** The crystallographic coordinates of MncA have been deposited in the Protein Data Bank under accession number 2VQA. Reprints and permissions information is available at www.nature.com/reprints. Correspondence and requests for materials should be addressed to N.J.R. (n.j.robinson@ncl.ac.uk).

METHODS

Synechocystis PCC 6803 periplasmic extraction and analysis. We previously used the early steps in this procedure to identify iron as the metal associated with a periplasmic component (FutA2) of a metal importer³⁰. Initial misidentification of FutA2 as a copper-protein (unpublished) exposed the need to improve the methodology for protein assignment and hence the use of principal component analysis for this purpose as reported here. *Synechocystis* PCC 6803 was cultured at 28 °C under constant light set to 100 $\mu\text{mol photon m}^{-2} \text{s}^{-1}$ photosynthetically active radiation, in Rippka's standard BG-11 medium without any modifications, as used in previous studies with this organism³⁰. For osmotic shock extraction of $(2-3) \times 10^{11}$ cells (Casy TT cell counter), 2-l cultures were harvested by centrifugation (6,000g, 20 min, 4 °C), washed in 500 ml 50 mM Tris, pH 7.5, before resuspension in 500 ml 50 mM Tris, pH 7.5, 0.5 M sorbitol. EDTA was added to a final concentration of 10 μM , and the cell suspension incubated at room temperature for 20 min. Cells were pelleted by centrifugation (11,000g, 20 min, 4 °C) and washed in a further 200 ml 50 mM Tris, pH 7.5, 0.5 M sorbitol to remove residual traces of EDTA. After further centrifugation (11,000g, 20 min, 4 °C), the cells were resuspended in 500 ml ice-cold de-ionized H₂O to release periplasmic components. Cells were removed from the shock fluid by two centrifugation steps (16,000g, 30 min, 4 °C).

Cell-free shock fluid was adjusted to 50 mM Tris, pH 8.8, and loaded onto a 1 ml HiTrap Q HP anion exchange column (GE Healthcare) over 16 h at 4 °C, before washing with 10 ml 50 mM Tris, pH 8.8 buffer and eluting with 1 ml each of the same buffer containing 100 mM, 200 mM, 300 mM, 400 mM, 500 mM and 1 M NaCl. Aliquots (200 μl) of each fraction of anion exchange eluant were then subjected to HPLC size exclusion chromatography on a TSK-SW3000 column (Tosoh Biosciences) in 10 mM Tris, pH 7.5, 50 mM NaCl at 0.5 ml min⁻¹ collecting 30 \times 0.5 ml fractions.

Aliquots (300 μl) of each fraction of eluant were diluted into 1.2 ml 2.5% v/v Suprapur HNO₃ (Merck) and analysed by ICP-MS (Thermo Electron Corp., X-Series). Mass ions (⁵⁵Mn and ⁶³Cu) were measured 100 times using the peak-jump method, in triplicate for each fraction, and counts compared with standard metal concentrations prepared in the same solution. Data were converted to atoms per cell, and plotted as surface representations in SigmaPlot 9 with the z-axis representing metal concentration with colour thresholds set at arbitrary values. Figure 1a and f show averages of the results obtained from assays of three independently grown cultures.

Aliquots (100 μl) of eluant were boiled for 10 min in 1% (w/v) SDS, 100 mM DTT, and analysed by SDS-PAGE on 15% (w/v) acrylamide gels. Gels were stained with SYPRO Ruby (Molecular Probes) according to manufacturer's instructions. Gels were scanned for fluorescence and relative protein abundances estimated using the ImageJ application (NIH).

Relative protein abundances were compared with the profile of the predominant copper (p1) or manganese (p2) complex, using two complementary data analysis techniques implemented in custom scripts in Matlab (The MathWorks). First, simple pairwise correlation coefficients were calculated between the vectors representing the metal profile and the profiles of the proteins present in those fractions. The resulting list of correlation coefficients provides an objective quantitative measure of the similarity of each protein profile to the metal profile. The more similar the protein and metal profile, the closer the coefficient is to unity. The protein and metal profiles were also inter-compared using principal component analysis (PCA). PCA is a data reduction technique that can combine the multiple values associated with a given sample to a much smaller number of composite variables, called the principal component scores, without losing a significant amount of the variance in the data³¹. Using this approach, each profile can be represented by a point on a scatter plot, with the position of that point specified by the PC scores derived from that profile. In this way, all profiles can be plotted together on a single 2D or 3D plot, with their proximity indicating how similar they are. To ensure that the analysis focused on the shapes of the profiles, rather than their amplitude, the profiles were all scaled to a common range before performing PCA and correlation analysis. Figures 1b, c, 2a, b and Supplementary Figs 1 and 4 utilize a single replicate taken from the triplicate data sets used to generate Fig. 1a, while Fig. 1d, e and Supplementary Fig. 2 are generated from a single fractionation of protein on two TSK-SW3000 columns to provide greater resolution.

Proteins correlating with p1 and p2 were excised from gels and digested with trypsin (25 ng) in 20 ml 50 mM NH₄HCO₃ buffer, pH 8.0. Peptide digests were analysed using a Voyager DE-STR MALDI-TOF mass spectrometer (Applied Biosystems). The instrument was equipped with a delayed extraction ion source, used a nitrogen laser at 337 nm and was operated in reflector mode at accelerating voltages of 20–25 kV. Mass spectra were obtained over a mass range of 900–4,000 Da and monoisotopic peptide mass fingerprints were assigned and used for database searches. Identifications were performed using the peptide mass

fingerprint data and the Mascot search engine program (Matrix Science Ltd) where the peptide mass tolerance was limited to 50 p.p.m. and searched against the latest NCBI non-redundant protein sequence database.

Insertional inactivation of *CucA*. *Synechocystis* PCC 6803 genomic DNA was used as template for PCR with primers 1 and 2 which anneal to *slI1785* (*cucA*) flanking sequences (Supplementary Table 2). The amplification product (1.5 kb) was ligated to pGEM-T (Promega) before a 1.3 kb BamHI fragment of pUK4K (GE Healthcare), containing a kanamycin resistance gene, was ligated to a unique BamHI site within *slI1785*. Cells were transformed to kanamycin resistance following incubation with this plasmid. Transformants were selected on solid medium containing 25 $\mu\text{g ml}^{-1}$ kanamycin before growth in liquid medium containing 50 $\mu\text{g ml}^{-1}$ kanamycin. Interruption of *slI1785* by insertion of the kanamycin resistance gene into the *Synechocystis* PCC 6803 chromosome was confirmed by PCR (Fig. 1f, lower panel) using primers 3 and 4 (Supplementary Table 2), generating a 0.8 kb wild-type DNA product and a 2.1 kb *slI1785* DNA product additionally containing the 1.3 kb kanamycin resistance gene.

Characterization of *MncA* Tat signal sequence. PCR with primers 5 and 6 (Supplementary Table 2) was used to generate a DNA fragment which was cloned into pET29a (Novagen) to express His-tagged *MncA* with signal sequence. *MncA* was expressed in *E. coli* BL21 (DE3) and in BL21 (DE3) ΔtatABC^{32} . All cultures were grown in 100 ml selective LB medium, at 37 °C with 180 r.p.m. orbital shaking. Gene expression was induced by addition of IPTG to 0.25 mM followed by further incubation for 2 h. Periplasmic protein was liberated from a standard cell number (5×10^{10} cells, Casy-TT cell counter) via osmotic shock or using lysozyme and EDTA³³. Proteins (50 μl aliquot) were resolved on 12% (w/v) acrylamide SDS-PAGE. Spheroplasts were collected after periplasm extraction by centrifugation, resuspended in 500 μl of 10 mM Tris pH 7.5, 200 mM NaCl, lysed by sonication and aliquots (5 μl) resolved by SDS-PAGE. Proteins were transferred to PVDF membrane for 1 h at 20 V in 40 mM glycine, 50 mM Tris, pH 8.3, 0.37% (w/v) SDS and 20% (v/v) methanol. Immunoblot was performed with a commercial rabbit polyclonal HRP conjugated His-tag antibody (Abcam) and rabbit polyclonal HRP conjugated GroEL antibody (Sigma), both at 1:10,000 dilution and signal detected via chemiluminescence.

PCR with primers 7 and 8, plus 9 and 10 was used to amplify the signal sequences of *MncA* and *CucA*, respectively. Reaction products were digested with EcoRI and XbaI (restriction endonuclease sites included within the primer sequences), fragments recovered from an agarose gel and ligated to pBAD24-ssTorA-GFP-SsrA³³, previously digested with the same enzymes to release the TorA signal sequence and treated with calf intestinal phosphatase, to create plasmids pBAD24-ssMncA-GFP-SsrA and pBAD24-ssCucA-GFP-SsrA. Constructs were verified by diagnostic restriction digests and transformed into *E. coli* MC4100³³. Fusion constructs were expressed under the control of an arabinose (0.2%; w/v) inducible promoter for 4 h and periplasm extracts from standard numbers of cells were prepared according to the standard protocol³³, resolved by SDS-PAGE and GFP detected with a commercial goat polyclonal HRP-conjugated GFP antibody (Abcam) at 1:10,000 dilution and signal detected via chemiluminescence. It is noted that DADE cells ($\Delta\text{tatABCDE}$ in the MC4100 background) containing pBAD24-ssMncA-GFP-SsrA, but not pBAD24-ssCucA-GFP-SsrA, ceased to grow upon addition of arabinose. Cells were washed and suspended in PBS and equivalent numbers (in 20 μl) were applied to a poly-lysine coated slide and visualized with a Zeiss laser scanning LMS510 confocal with Axiovert 200M microscope, using a 63 \times (1.4 NA) oil immersion objective. An argon ion laser was used with λ_{Ex} 488 nm and GFP emission detected at λ_{Em} 505–550 nm. Optical differential interference contrast (DIC) images were overlaid with GFP fluorescence and all images captured using identical laser intensity, amplifier gain, detector gain, amplifier offset, resolution, scan rate and a pinhole of 0.93 Airy Unit.

Recombinant protein production. The *slI1358* (*mncA*) and *slI1785* (*cucA*) genes, lacking their respective signal peptides (residues 2–34 and 2–30, respectively), were amplified by PCR from *Synechocystis* PCC 6803 genomic DNA using primer pairs 11 and 12 (for *slI1358*) and 3 and 4 (for *slI1785*) and cloned into pGEM-T (Promega). After sequencing of the inserts, the genes were liberated from pGEM-T using NdeI/BamHI, the fragments purified by agarose gel electrophoresis and ligated into pET29a to create pET29a-*mncA* and pET29a-*cucA* plasmids.

E. coli BL21 (DE3) cells were transformed to kanamycin resistance with the respective expression plasmids, then used to inoculate 500 ml selective LB medium, cultured at 37 °C with 180 r.p.m. orbital shaking until OD_{595nm} \approx 0.6. Gene expression was induced by addition of IPTG to 1.0 mM followed by further incubation for 4 h. Cells were harvested by centrifugation (6,000g, 10 min, 4 °C) and stored at –20 °C. Both *MncA* and *CucA* were recovered from inclusion bodies.

BL21 (DE3) pET29a-*mncA* cells were resuspended in 100 mM Tris, pH 7.5, 100 mM NaCl, 1 mM EDTA, 1 mM phenylmethylsulphonyl fluoride and lysed by sonication (4 \times 10 s, with 1 min intervals on ice), and lysate cleared by centrifugation (27,000g, 20 min, 4 °C). The pellet was resuspended in 10 ml

100 mM Tris, pH 7.5, 1% v/v Triton X-100 and the sonication and centrifugation steps repeated. The resulting pellet was washed in 100 mM Tris, pH 7.5, 100 mM NaCl to remove Triton, then sequentially in 50 mM Tris, pH 7.5 buffer containing 0.1 M, 1 M, 2 M and 8 M urea. The MncA protein was efficiently resolubilized in 8 M urea. Urea-solubilized MncA was refolded by rapid 400-fold dilution into 50 mM Tris, pH 7.5 in the presence of excess metal (1 mM MnCl_2) and collected by binding to Q-Sepharose HP matrix (GE Healthcare) and eluted with increasing [NaCl].

BL21 (DE3) pET29a-*cucA* cells were lysed and inclusion bodies recovered in the same way except that the 2 M urea wash was omitted. Refolding of urea-solubilized CucA was performed in the same way except that no metal ions were added to the refolding solution. Once eluted from the Q Sepharose matrix with 500 mM NaCl, CucA was further purified by size exclusion chromatography (Sephadex G-75), and CucA-containing fractions concentrated by anion exchange chromatography. Purity of MncA (682 ng) and CucA (668 ng) was examined via SDS-PAGE (Fig. 2c, top).

Recombinant protein metal binding analysis. For analysis of MncA Mn^{2+} -binding (Fig. 2b bottom, left), unfolded MncA (~ 0.7 mM) in 8 M urea was refolded by rapid dilution (400-fold) in 50 mM Tris pH 7.5, 1 mM MnCl_2 , before further purification and concentration using Q Sepharose HP matrix. Bound protein was washed in buffer (10 mM Tris, pH 7.5, 50 mM NaCl), and eluted with buffer containing 500 mM NaCl. An aliquot of protein (5 μM , 500 μl) was resolved by gel filtration on Sephadex G-25 (GE Healthcare) and 500 μl fractions collected. Eluant was analysed for protein by Coomassie assay calibrated with MncA standards. Bound metal was quantified by ICP-MS as described above. For competitive metal-binding experiments, unfolded MncA was refolded to a final protein concentration of 70 nM, in 50 mM Tris, pH 7.5 containing 1:1 MnCl_2 to CuSO_4 (both at 400 nM) (Fig. 4a, left). Refolding was similarly carried out in the presence of increasing equivalents of MnCl_2 relative to CuSO_4 (Fig. 4a, right) or ZnSO_4 (Supplementary Fig. 9). Protein was concentrated by anion exchange chromatography, washed and eluted in 1 ml of buffer containing elevated NaCl, then resolved by gel filtration as above. Metal in protein-containing fractions was summed to yield total metal content.

For analysis of CucA Cu^{2+} -binding (Fig. 2c middle, right), apo-CucA (5 μM) was metallated with addition of a twofold excess of copper and incubated for at least 5 min before fractionation. Protein and metal were resolved and analysed as above. Additional analysis of CucA Cu^{2+} -binding was obtained via colorimetric titration (Fig. 2c, lower). Apo-4-(2-pyridylazo)-resorcinol (10 μM) in buffer (10 mM Tris, pH 7.5, 50 mM NaCl) was titrated against copper (0–20 μM) in a 1 ml, 1 cm path length cuvette, measuring absorbance in the 800–200 nm range. Absorbance of apo-4-(2-pyridylazo)-resorcinol (410 nm) and Cu^{2+} -4-(2-pyridylazo)-resorcinol (510 nm) were plotted against $[\text{Cu}^{2+}]$. Titrations were repeated in the same way but with the addition of 10 μM apo-CucA. For analyses of weak Mn^{2+} -binding to CucA, apo-CucA (500 μl , 5 μM) was resolved on a Sephadex G-25 gel filtration column equilibrated and run with buffer containing 10 μM MnCl_2 (Supplementary Fig. 10). Protein and metal were analysed as above.

The exchangeability of Mn^{2+} -CucA to Cu^{2+} -CucA (Fig. 4b) was analysed via incubation of 5 μM Mn^{2+} -CucA with 5 μM Cu^{2+} for 0, 1, 6 and 24 h before fractionation and quantification of bound and unbound metals, performed as above. Metal in protein-containing fractions was summed to yield total protein-associated metal. Figure 4b shows the proportion of copper as a fraction of total metal associated with CucA. Analysis of exchangeability of Mn^{2+} -MncA to Cu^{2+} -MncA was performed in the same way except that 3.5 μM Mn^{2+} -MncA was incubated with 10 μM Cu^{2+} before fractionation.

Re-folding of apo-MncA in periplasm extracts. Periplasm extract (500 ml) was prepared from 2 l of *Synechocystis* PCC 6803 culture ($\sim 2 \times 10^{11}$ cells) grown in standard BG-11 as before and adjusted to 20 mM Tris pH 7.5 (with 10 ml of stock buffer). The extract was split into 2×255 ml, and 1 ml of ~ 0.7 μM MncA in 8 M urea was added to one of the samples while 1 ml of 8 M urea alone was added to the other as a control. Each extract was applied to a 1 ml Q HP column and fractionated as described in a previous section. Aliquots (50 μl) were resolved using 15% (w/v) SDS PAGE, protein visualized with SYPRO Ruby and further aliquots (200 μl) resolved by gel filtration on a TSK SW3000 column and analysed for Cu^{2+} , Mn^{2+} and Zn^{2+} by ICP-MS.

EPR spectroscopy. MncA and CucA were purified as described above after exposure to Cu^{2+} (Fig. 3a) or Mn^{2+} (Supplementary Fig. 6), and concentrated to ~ 0.7 and 1.0 mM respectively using Centricon YM-10 centrifugal concentrators (Amicon). EDTA washed MncA (100 μl in 10 mM HEPES, pH 7.5, 50 mM NaCl) was placed in a quartz EPR tube and X-band EPR spectra were recorded at -196°C on a Bruker EMX spectrometer. Diphenylpicrylhydrazyl was used as an external reference and the program SIMFONIA (Bruker) was used for spectral simulations. EPR spectra of CucA were obtained in the same way but over a range of pH conditions; pH 7.0 (10 mM Tris, 50 mM NaCl), pH 9.0 (10 mM CHES, 50 mM NaCl) and pH 10.0 (10 mM CHES, 50 mM NaCl).

Crystallography. MncA, refolded in excess Mn^{2+} , was concentrated to 10 mg ml^{-1} using a YM-10 centrifugal concentrator and exchanged into 10 mM Tris, pH 7.5, 50 mM NaCl. Initial crystallization trials were set up as sitting drops using a Mosquito robot (TTP Labtech) and commercially available precipitant screens. Two drop sizes were sampled, (1) 100 nl protein:100 nl precipitant solution and (2) 200 nl protein:100 nl precipitant. Conditions yielding crystals were scaled up and optimized in standard 24 well plates using the hanging drop method of vapour diffusion. All crystallization experiments were maintained at 20°C . Diffraction quality crystals were produced from conditions containing 0.1 M sodium acetate, pH 3.25, 8% (w/v) PEG 8000, at a protein to precipitant solution ratio of 2 μl protein solution:1 μl precipitant solution. The crystallization solution pH is 4.2 and Mn^{2+} remains protein-associated under these conditions (Supplementary Fig. 14). Prior to data collection, crystals were flash frozen in liquid nitrogen using the precipitant solution supplemented with 25% (v/v) glycerol as a cryoprotectant. Data were collected on station BM14 at 0.931 Å at the European Synchrotron Radiation Facility (ESRF), Grenoble, France. Data were processed using MOSFLM³⁴ then scaled and merged with SCALA³⁵. The diffraction data were weak, probably a result of the small crystal (rod with a cross-sectional diameter of 50 μm that was exposed to the X-ray beam) with a high solvent content and large unit cell dimensions (see Supplementary Table 1). The weak data are also presumably responsible for the relatively high value for the merging statistics (R_{merge}). In the first instance, a data set that only included fully recorded reflections was generated (Supplementary Table 1). Analysis of this data set suggested three molecules of MncA were present in the asymmetric unit. The structure was solved by molecular replacement using AMoRe³⁶. The search model comprised a monomer of *B. subtilis* OxdC (PDB entry used: 1L3J)³⁷, which shares $\sim 37\%$ sequence identity with MncA. This structure was edited to truncate all residues not conserved with MncA to C_γ positions using CHAINSAW³⁸. Three unique molecules were placed in the unit cell, and the resulting electron density maps allowed manual building of the majority of the model. COOT³⁹ and REFMAC5⁴⁰ were used for manual building and refinement respectively to produce a complete model. Medium non-crystallographic symmetry restraints (as described in the REFMAC5 documentation) were maintained for residues 39–390 throughout refinement (residues 1–34 are the signal sequence which is absent from the mature MncA molecule); no σ cut-off was applied to the data. A single overall value for the B-factor was refined due to the resolution. The completed model comprises residues 39–394 of the native MncA sequence in chains A and B. In chain C, the electron density maps did not permit the positioning of the two C-terminal residues and these are not included in the model. Two Mn^{2+} ions were associated with each protein chain and a total of 32 water molecules are included. This structure was then refined against a data set including all data (including partially recorded reflections) to generate the final model, which has the same composition as above. It is worth noting that the quality of the electron density maps generated from the two data sets (using the respective final models) is equivalent (they are essentially superimposable). The atomic positions of the models are virtually identical. Statistics for the final refinement/model analysis are summarized in Supplementary Table 1, and the structure determined with all reflections was 95.9% Ramachandran favoured with zero Ramachandran outliers. Figures were prepared using PyMOL⁴¹.

Assays of oxalate decarboxylase and quercetin dioxygenase activities. Quercetin dioxygenase activity of CucA (0.5 μM , containing one equivalent of Cu^{2+} , Zn^{2+} , Mn^{2+} or apo-protein) was quantified in reactions containing quercetin (50 μM in 50 mM Tris, pH 7.5, 100 mM NaCl, 5% (v/v) DMSO). The 20 min reactions were initiated by the addition of CucA (or an equivalent volume of buffer in the control reactions) and monitored for loss of absorbance at 414 nm using a 96 well-plate reader. Oxalate decarboxylase activity of MncA was measured in a modified coupled assay⁴², using ~ 0.7 μM Mn^{2+} , Cu^{2+} , or Zn^{2+} -MncA in 5 mM potassium acetate buffer pH 4.2 overnight. Reaction products were incubated with formate dehydrogenase (5 units) for 1 h and NADH measured at 340 nm.

Alternative methods of protein quantification. Proteins were routinely quantified based upon their absorbance at 280 nm or using Coomassie R250 assays calibrated against the respective purified proteins, previously quantified from a theoretical extinction coefficient of 32,890 $\text{M}^{-1} \text{cm}^{-1}$ for CucA and an experimentally determined extinction coefficient for MncA which was established to be 1.43 times greater than the theoretical value of 83,880 $\text{M}^{-1} \text{cm}^{-1}$ (ProtParam). To determine the extinction coefficient of MncA, an aliquot (~ 20 μg) was subjected to acid hydrolysis followed by quantitative amino acid analysis (Alta Biosciences) (Supplementary Fig. 15). Additional aliquots of the same sample were also quantified using Coomassie R250 (Pierce) and bicinchoninic acid (ThermoFisher) assays, both calibrated (in this experiment alone) against bovine serum albumin. Mn^{2+} was quantified by ICP-MS to generate multiple estimates of the Mn^{2+} :MncA stoichiometry (Supplementary Fig. 15).

Analysis of monovalent copper binding to MncA. A Cu^+ stock was prepared within a N_2 atmosphere chamber by mixing Cu(I) chloride with HCl followed by neutralization via the addition of concentrated buffer. The anaerobic copper stock was analysed for total copper by ICP-MS and determined to be $\sim 100\%$ cuprous by titration against $100\ \mu\text{M}$ of the chromogenic cuprous indicator bathocuproine disulphonate monitored at $483\ \text{nm}$ using an ϵ value of $13,300\ \text{M}^{-1}\text{cm}^{-1}$ for $\text{Cu}^+(\text{BCS})_2$. Anaerobic MncA was refolded to a 0.7:2:2 mix of protein: Mn^{2+} : Cu^+ , concentrated by anion exchange chromatography and fractionated on Sephadex G-25 equilibrated in, and eluted with, $10\ \text{mM}$ Tris, $\text{pH}\ 7.5$, $50\ \text{mM}$ NaCl . Eluant was analysed for copper and manganese by ICP-MS and for protein by Coomassie assay normalized against MncA standards (Supplementary Fig. 16).

31. Wold, S., Esbensen, K. & Geladi, P. Principal component analysis. *Chemom. Intell. Lab. Syst.* **2**, 37–52 (1987).
32. Orriss, G. L. et al. TatBC, TatB and TatC form structurally autonomous units within the twin arginine transport system of *Escherichia coli*. *FEBS Lett.* **581**, 4091–4097 (2007).
33. DeLisa, M. P., Samuelson, P., Palmer, T. & Georgiou, G. Genetic analysis of the twin arginine translocator secretion pathway in bacteria. *J. Biol. Chem.* **277**, 29825–29831 (2002).
34. Leslie, A. G. W. *Recent Changes to the MOSFLM Package for Processing Film and Image Plate Data* (Joint CCP4 + ESF-EAMCB Newsletter on Protein Crystallography, Number 26, Daresbury Laboratory, Warrington, UK, 1992).
35. Kabsch, W. J. Evaluation of single-crystal X-ray diffraction data from a position-sensitive detector. *J. Appl. Crystallogr.* **21**, 916–924 (1988).
36. Navaza, J. AMoRe: An automated package for molecular replacement. *Acta Crystallogr.* **A50**, 157–163 (1994).
37. Anand, R., Dorrestein, P. C., Kinsland, C., Begley, T. P. & Ealick, S. E. Structure of oxalate decarboxylase from *Bacillus subtilis* at $1.75\ \text{\AA}$ resolution. *Biochemistry* **41**, 7659–7669 (2002).
38. Schwarzenbacher, R., Godzik, A., Grzechnik, S. K. & Jaroszewski, L. The importance of alignment accuracy for molecular replacement. *Acta Crystallogr. D* **60**, 1229–1236 (2004).
39. Emsley, P. & Cowtan, K. Coot: Model-building tools for molecular graphics. *Acta Crystallogr.* **60**, 2126–2132 (2004).
40. Murshudov, G. N., Vagin, A. A. & Dodson, E. J. Refinement of macromolecular structures by the maximum-likelihood method. *Acta Crystallogr.* **53**, 240–255 (1997).
41. DeLano, W. *The PyMOL Molecular Graphics System* (DeLano Scientific, 2002).
42. Svedružić, D. et al. Investigating the roles of putative active site residues in the oxalate decarboxylase from *Bacillus subtilis*. *Arch. Biochem. Biophys.* **464**, 36–47 (2007).

naturejobs

**THE CAREERS
MAGAZINE FOR
SCIENTISTS**

Singapore's national science administration resembles a Hollywood studio during the golden age of motion pictures: it has the money to launch big projects and the centralized authority to see them through. It also expects big returns on its investment and sometimes keeps its stars on a short lead.

As such, the Singapore science studio is once again unrolling the red carpet. Five years after debuting Biopolis, a life-sciences blockbuster cluster, the Singapore government is unveiling Fusionopolis, its physical-sciences sequel (see page 1144). The Biopolis box office results have been mixed; the S\$500-million (US\$340-million), seven-building complex signed star scientists, produced an avalanche of publications and attracted satellites from several multinational companies and world-class universities. But it has yet to generate sufficiently impressive technology-transfer returns. The twin-tower sequel — with its emphasis on microelectronics, materials, communications and computing research — is perhaps a safer bet. Basic life-science research often takes decades and hundreds of millions of dollars to yield a result, whereas materials and information technology tends to need just a few years and a few million dollars.

There are signs that the heads of the science studios are growing impatient with Biopolis' emphasis on basic research — or, at least, its relative lack of patents and products. The Biopolis advisory board recently increased investments in translational and clinical sciences. Fusionopolis seems intended to bypass basic research — or, at least, fast track research into the applied sciences. Some Fusionopolis projects will work well with those at Biopolis, such as cheaper, faster genome-sequencing technologies.

Contemporary Hollywood suggests that it is possible for big-budget and independent cinema to coexist. The neighbouring Biopolis and Fusionopolis complexes will test how well physics and biology, basic and applied science, and big and small budgets can work together. For now, hundreds of candidates are lining up for what should be a very exciting test screening.

Paul Smaglik moderates the *Naturejobs* Nature Network career-advice forum.

CONTACTS

Editor: Gene Russo

European Head Office, London
The Macmillan Building,
4 Crinan Street, London N1 9XW, UK
Tel: +44 (0) 20 7843 4961
Fax: +44 (0) 20 7843 4996
e-mail: naturejobs@nature.com

European Sales Manager:
Andy Douglas (4975)
e-mail: a.douglas@nature.com

Natureevents:
Ghizlaine Ababou (+44 (0) 20 7014 4015)
e-mail: g.ababou@nature.com

UK Corporate:
Nils Moeller (4953)

Southwest UK/RoW:
Alexander Ranken (4944)

Northeast UK/Ireland:
Matthew Ward (+44 (0) 20 7014 4059)

France/Switzerland/Belgium:
Muriel Lestringuez (4994)

Scandinavia/Spain/Portugal/Italy:
Evelina Rubio-Hakansson (4973)

North Germany/The Netherlands/Eastern Europe: Reya Silao (4970)

South Germany/Austria:
Hildi Rowland (+44 (0) 20 7014 4084)

Advertising Production Manager:

Stephen Russell
To send materials use London address above.
Tel: +44 (0) 20 7843 4816
Fax: +44 (0) 20 7843 4996
e-mail: naturejobs@nature.com

Naturejobs web development: Tom Hancock
Naturejobs online production: Dennis Chu

US Head Office, New York
75 Varick Street, 9th Floor,
New York, NY 10013-1917
Tel: +1 800 989 7718

Fax: +1 800 989 7103
e-mail: naturejobs@natureny.com

US Sales Manager: Peter Bless

India
Vikas Chawla (+91 1242881057)
e-mail: v.chawla@nature.com

Japan Head Office, Tokyo
Chiyoda Building, 2-37 Ichigayatamachi,
Shinjuku-ku, Tokyo 162-0843
Tel: +81 3 3267 8751
Fax: +81 3 3267 8746

Asia-Pacific Sales Manager:
Ayako Watanabe (+81 3 3267 8765)
e-mail: a.watanabe@natureasia.com
Business Development Manager, Greater China/Singapore:
Gloria To (+852 2811 7191)
e-mail: g.to@natureasia.com



A*STAR

Singapore surges upwards

Part laboratory, part resort and part architectural gem, Fusionopolis is Singapore's newest mega-science facility. Visitors who walk through its theatre, shops and cafes, up past the gym and the bar to the 24th-floor swimming pool, may not realize that this is the biggest piston of Singapore's roaring science-based economic engine. It is a futuristic, twin-towered laboratory cluster for communications, materials and electronics research, and it's opening this month. Fusionopolis looks down on Singapore's flagship biological sciences conglomerate, Biopolis, just 600 metres away (see *Nature* **425**, 746–747; 2003), as well as the National University of Singapore (NUS) and the National University Hospital. The area is becoming a city unto itself, a commune of scientists and engineers. "By 2010, there will be 10,000 here," says Chuan Poh Lim, chairman of A*STAR, Singapore's central agency for encouraging science and technology.

Launched in February 2003, Fusionopolis is the physical-sciences sequel to Biopolis. Housing six institutes and some 3,000 PhDs, it will capitalize on the city-state's strengths in microelectronics, materials, communications and computing research. The buildings are meant to spur interdisciplinary research not only among its own institutes but also with those of Biopolis. Industry initiatives will occupy 60% of the space, and collaborations between the private and

The Fusionopolis towers are the latest signs of Singapore's determination to build its future on science. But can the city-state meet the expectations it has raised? **David Cyranoski** reports.

India and other regional competitors move into generic drugs and low-cost electronics, Singapore has fewer lucrative alternatives. "In terms of 'cheaper and faster', we will lose out," says Lim. "We need a framework for innovation."

It is a sentiment common at many a research hub. But nowhere else are such plans so generously funded on a per capita basis or so quickly executed. Singapore's science budget more than doubled to S\$13.5 billion (US\$880 million) in the current five-year plan compared with the previous one.

The city-state's achievements are already impressive. Thanks to researchers at A*STAR institutes, some university labs and other standouts such as the Temasek Life Sciences Laboratory, Singapore's scientific output (in terms of the number of published papers) increased 79% between 2000 and 2006 to 6,226 papers. That figure is only 0.6% of the world's total, but it places Singapore at the top per capita. Their impact, however, is low; in 2006, Singaporean papers were cited only 80% as often as the world average.

By 2010, Singapore plans to increase scientific funding from an already impressive 2.6% of gross domestic product in 2007 to 3%, which would put it ahead of most of the big players, including Britain and the United States. But as Singapore continues its scientific spending spree, observers are asking what economic gains these high-profile projects will achieve.

University overhaul

A key government objective is to improve not only the country's institutes but also its universities. Despite their standing as two of the top universities in Asia, Nanyang Technological University (NTU) and the NUS have long

been considered teaching rather than research institutions. When Philip Yeo, the former A*STAR head mainly responsible for Biopolis, sought to train the next generation of Singaporean scientists, he sent the most promising students abroad on full scholarships for their university studies. He also hired from overseas. With a few exceptions, Singapore's universities did not have the infrastructure to support top-class research.

This is changing rapidly, thanks in large part to a new funding scheme — the National Research Foundation (NRF). For the 2006–10 period, Singapore's research budget is slated to rise from S\$6 billion in the previous period to S\$13.55 billion — although slow economic times could have an effect. So far, S\$5 billion has been used to establish the NRF, which has helped to revitalize the universities with high-powered recruitment.

Like A*STAR's institutes, the first three NRF-supported 'research centres of excellence' all have foreign directors: Artur Ekert, a professor of quantum physics at the University of Oxford, UK, for the NUS Centre for Quantum Technologies; Daniel Tenen, who will keep his laboratory at Harvard, at the NUS Cancer Research Centre of Excellence; and Kerry Sieh, of the California Institute of Technology, for NTU's Earth Observatory of Singapore.

Funded with S\$150 million each over 5 years, all aim to become world leaders. The cancer institute will carve out five cancer-related areas, including cancer stem cells, led by Tenen, and cancer biology. Ekert, who started last December, says his centre already has good interdisciplinary teams in theory and experimental quantum optics. The goal, he writes, is "to boldly go where no man has gone before, into the quantum world (or worlds)".

But it isn't just those with centres of excellence that are benefiting. "It was the best thing that ever happened to me as a scientist," says Wun Jern Ng, director of the Nanyang Environment and Water Resources Institute, about the NRF funding. The money enabled Ng to pull together the NTU's water-related research into a new institute. Membrane technology, water reclamation, desalination and biofilms — all of which are already Singaporean strong points — are among its projects. The institute is recruiting 50 to 100 people, and Ng hopes to link up with a proposed 'clean tech hub' next door. The NTU's Swedish provost Bertil Andersson calls it the "Greenopolis" and says it will lure companies developing water, photovoltaics and wind technologies.

The NRF also offers grants for fledgling researchers. Its Competitive Research Programme gives S\$10 million over 3–5 years for projects expected to benefit Singapore's economy. Young Singaporean researchers can apply for NRF research fellowships, which provide US\$1.5 million on top of salary for three years.

Facing criticism

A central focus of Singapore's latest round of spending is to expand its pharmaceutical and biotechnology industry. Facing criticism from its advisory council over the lack of clinical applications likely to come from its basic-research investment in Biopolis, A*STAR teamed up with the NRF and the health ministry and put together a S\$1.55-billion 5-year 'integrated biomedical sciences initiative'. They quickly funded, among others, a translational clinical research flagship programme (S\$125 million, the first S\$25 million of which will go to the Singapore Gastric

Cancer Consortium), the Singapore Institute for Clinical Sciences (S\$116 million) and the Experimental Therapeutics Centre (S\$100 million), an incubator for Biopolis technologies. Biopolis, which has assembled seven biological-science institutes since it opened in 2003, is adding two new buildings dedicated to translational and industry research.

A promising sign for future biomedical success is the Duke–NUS Graduate Medical School. Established in 2005 with staff from Duke University in Durham, North Carolina, and the promise of hundreds of millions of dollars from the Singapore government, the school offers a joint MD and PhD. New buildings with 24,000 square metres of space will be ready in late 2009. The school already has 108 faculty members, mostly from the United States.

Good quality-control and patent protection have lured industry, for both research and manufacturing. In less than two years, Genentech, GlaxoSmithKline, Lonza and Novartis all decided to build biologics manufacturing facilities in Singapore. In 2007, GlaxoSmithKline added a US\$13-million laboratory to its Singapore facility to develop therapies for Alzheimer's disease and schizophrenia. At about the same time, Eli Lilly decided to triple the number of researchers at its Singapore base with a US\$150-million boost over 5 years to focus on cancer and type 2 diabetes therapies. Just this August, AstraZeneca teamed up with the National Cancer Centre Singapore and the National University Hospital to carry out research on liver-cancer drugs.

Fuelled by Fusionopolis

Given the difficulties facing the global pharmaceutical industry, Singapore's hopes of making money are likely to be fulfilled sooner by Fusionopolis. This month, some 500 researchers will arrive from the Institute for High Performance Computing, the Institute for Infocomm Research and the Data Storage Institute. In 2010, another 1,000 will come from the Institute of Microelectronics (IME), the Institute of Materials Research and Engineering (IMRE) and the Singapore Institute of Manufacturing Technology (SIMTech).

The IME's director, Dim-Lee Kwong, says it was partly "R&D for the sake of commercialization" that enticed him from the University of Texas three years ago. "In the United States, that is not explicit," says Kwong, whose institute's work on silicon nanowires — aiming to keep semiconductors improving their capacity — won the 2007 George E. Smith technology award.

The IME already has 26 projects with industry, from which it receives 25% of its operating budget. In 2007, the institutes that will comprise Fusionopolis had 202 R&D projects with 339 companies. Industrial spin-offs have made some wealthy: researchers from the IMRE, for example, sold the company owning its magnetic fingerprint-tagging technology for S\$19.6 million.

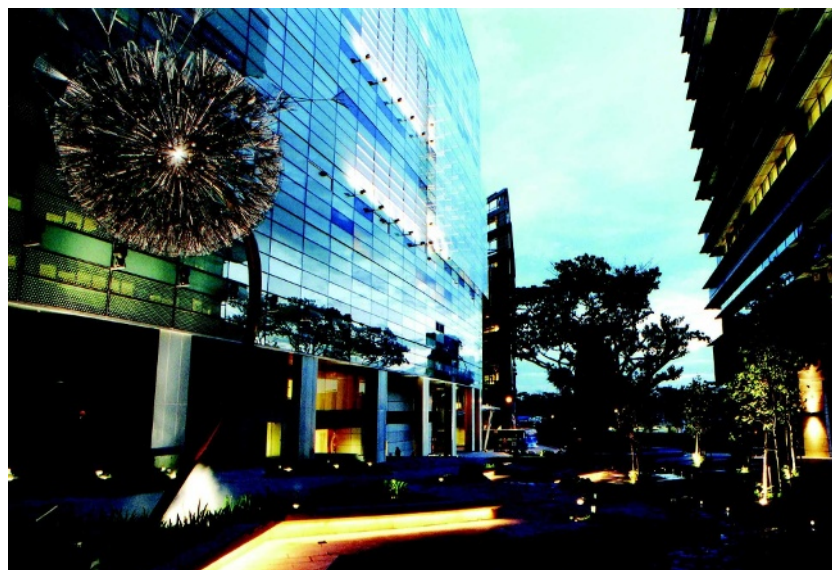
Its cutting-edge facilities could arouse further industry interest. Fusionopolis will have an anechoic chamber and supercomputing, nanofabrication, characterization and test-bedding facilities. Fourteen corporate labs, including wind-turbine maker Vestas and Second Life creator Linden Lab, have signed up for Fusionopolis.

Collaborations between Fusionopolis and Biopolis could reap rewards as well. An 'e-health' initiative, for instance, will draw expertise from both to provide remote diagnoses based on urine or stool samples,

"It was the best thing that ever happened to me as a scientist."
— Wun Jern Ng



Artur Ekert (top) and Dim-Lee Kwong are both heading for Fusionopolis.



wound image analysis, diabetic retinal imaging and delivery of drugs. And A*STAR is offering grants to encourage such links. Photochemist Jonathan Hobley of the IMRE, for example, is leading a project with scientists at A*STAR's Institute of Molecular and Cell Biology (IMCB) to use the reflectivity and emission of light at interfaces to assess what surface properties guide axonal growth. "There's something the cell does or doesn't like about a surface, and that guides it along. It's really a surface chemistry problem," he says. The project will get S\$750,000 for 3 years for postdocs and equipment.

Edison Liu, head of the Biopolis's Genome Institute of Singapore, is leading two crossover projects. One, with the IME and SIMTech, aims to develop a DNA preparation device to sequence the human genome for less than US\$10,000 and claim the US\$10-million Archon X Prize. "Many people talk about doing interdisciplinary research, but here we're doing it," says Liu.

Research challenges

Despite ample investment and impressive progress, Singapore's science programme does face stumbling blocks. Controls meant to stem corruption make the day-to-day use of funds a tedious affair. "There are too many well-meaning bureaucrats," says Tenen. "They question every little purchase, without understanding the science or the way science works. You buy a paper clip and they want to know why." Stem-cell biologist Davor Solter, who recently joined the A*STAR Institute of Medical Biology from the Max Planck Institute of Immunobiology in Freiburg, Germany, says he had to get the rubber stamps of some 16 people to get a computer. "It can take a month or more," he says.

Some worry about Singapore's reputation for heavy-handed government. In 2005, the University of

Biopolis is expanding, and will also feature in crossover projects with Fusionopolis.

"In terms of 'cheaper and faster', we will lose out. We need a framework for innovation."

— Chuan Poh Lim

Warwick, UK, dropped plans to open a Singapore campus for fear that academic freedom would not be protected. That, and the closure within 6 months of opening of the University of New South Wales's Singapore campus last year for financial reasons, set back efforts to internationalize university education.

Concerns about how Singapore's government deals with recruited international scientists were raised by a case involving UK neuroscientist Simon Shorvon. Brought in to run the National Neuroscience Institute in 2000, Shorvon, an authority on epilepsy, was ousted in 2003 after being accused of failing to secure proper informed consent from study patients. Shorvon denied any impropriety. He returned to Britain, where the General Medical Council cleared him of any wrongdoing. But in an unprecedented move, Singapore officials challenged that decision in London. The UK High Court subsequently dismissed this claim. Adding to the controversy, Shorvon's initial critic was Lee Wei Ling, daughter of Singapore's long-time ruler Lee Kuan Yew (see *Nature* doi:10.1038/news061218-15; 2006).

"It takes time to explain to some of our colleagues and potential hires that one can speak English here, that one can jaywalk and chew gum without being caned on the spot," says Ekert. Still, the combination of funding and research freedom will probably continue to be a draw as budgets get slashed elsewhere.

But as expectations rise, some fear that research independence might get curtailed. Government officials are "feeling insecure as to whether it is useful for the economy," says Jean Paul Thiery of the IMCB, who also heads the Experimental Therapeutics Centre. "Will the pharmaceutical companies stay? It is a very fragile structure," he says.

Questions of researcher priorities and independence will take centre stage as Singapore prepares its next five-year plan, in 2010. Failure to secure patents and technology transfer could cost funding. "When we first started at the high-growth phase, the runway was big and you couldn't see the guy next to you," says Lim. "In the next two years when we have full recruitment, we have to move into the high-productivity phase. There will be more competition for resources — and that's a good thing."

David Cyranoski is Nature's Asia-Pacific correspondent.



ADVERTISEMENT FEATURE

Biopolis, Fusionopolis, and the bridge in-between—the place for multidisciplinary science

Small in size, Singapore packs a powerful research punch. Is it too small to compete against the United States, Japan, and other scientific powerhouses? “These days, you don’t see countries competing, you see centres competing,” says LIM Chuan Poh, Chairman of the Agency for Science, Technology and Research (A*STAR), Singapore’s leading public research agency. And in that multi-centred world, Singapore is fast becoming one of the elite players, led in large part by A*STAR and its constellation of 22 research institutes, consortia and centres. Indeed as research becomes increasingly multidisciplinary to reflect the needs of industry and society, A*STAR is exploiting its unique advantages.

The booming biological research centre, Biopolis, which houses A*STAR’s biomedical research institutes and consortia, was put together over the past 8 years. It has become a symbol of Singapore’s ability to move quickly into cutting edge fields and attract top international talent.

Now A*STAR has other tricks up its sleeves. Biopolis gazes out to Fusionopolis, the nation’s second R&D hub that officially opened its doors on 17 October 2008. It will host pre-existing strengths in materials, high performance computing, microelectronics, data storage, info-communications and manufacturing technologies that reside in A*STAR’s physical

sciences and engineering research institutes located in various parts of the island. The aim is to draw together the diverse expertise into a unique interdisciplinary arrangement to tackle large-scale, complex challenges including sustainable development and ageing populations.

But the barriers are expected to fall even further. The close proximity between Biopolis and Fusionopolis—less than a kilometer apart—will enhance collaboration between engineers and biomedical and physical scientists for innovative research. A*STAR is backing this up with financial incentives and an environment, which is conducive to fruitful scientific interaction.

All these developments have attracted international talent, ranging from the young and upcoming to the experienced and renowned, who continue to flood in. They are joined by a growing pool of Singaporean researchers that includes young Singaporean scientists cultivated in A*STAR programs.

Biopolis today, the clinic tomorrow

The launch of Singapore’s biomedical initiative in 2000 saw the rapid creation of new research institutes under A*STAR to add to the pre-existing Institute of Molecular and Cell Biology (IMCB) and the Bioprocessing Technology Institute (BTI). The Genome Institute of Singapore (GIS) was set up in 2000, the Bioinformatics Institute (BII) in 2001, the Institute of Bioengineering and Nanotechnology (IBN) in 2003, and the Centre for Molecular Medicine (since renamed the Institute of Medical Biology (IMB)) in 2004. The institutes form the core of Biopolis – they are fundamental pieces of a bigger plan to grow Singapore’s biomedical industry sector.

However, buildings and institutions alone, no matter how impressive, are not enough – it is talent that matters. Thus, A*STAR recruited Edison Liu, from the US National Cancer Institute (NCI), to head the GIS. A stream of big names followed. Sir David Lane, former director of Cancer Research UK’s Cell Transformation Research Group at the University of Dundee, came to lead the IMCB in 2004. In 2007, Lane handed over the reins to another internationally renowned scientist, Neal Copeland, who has been ranked among 50 of the most-cited biomedical scientists in the world. Copeland had moved to Singapore with his



Neal and Nancy Copeland moved to A*STAR after spending 20 years at the NIH National Cancer Institute.

Advertiser retains sole responsibility for content.

JP171376R

1 | NATUREJOBS | 23 October 2008

SPOTLIGHT ON SINGAPORE

ADVERTISEMENT FEATURE

wife, Nancy Jenkins, a well-established cancer researcher in her own right. Lane continues as Chairman of the A*STAR Biomedical Research Council (BMRC) that oversees the research institutes. Most recently, A*STAR recruited cloning and epigenetics pioneer Davor Solter to the IMB, which now focuses on stem cells and regenerative medicine.

Having internationally renowned researchers at the top has made it easier to do what other countries in the region have struggled to do—recruit a diverse group of top-notch younger scientists that will form the core of the laboratory. For example, when Japan's Yoshiaki Ito, famous for his work on the tumor suppressor RUNX3, moved to IMCB in 2002, nine members of his laboratory followed him.

Singapore is attractive because of the infrastructure and investment. But scientists are also drawn by the rare vision of the policymakers, such as A*STAR's first Chairman, Philip Yeo, and Lim, who engage them and their research while allowing them to follow their instincts. The close connection has led to a type of trust that allows for the government to take chances on its scientists. "A*STAR is basically like the [US] National Institute of Health," says Copeland, who spent 20 years at the NIH NCI before coming to Singapore. "It carries out high risk, high pay off science."

Less than a decade after getting started, the Biopolis complex is showing early signs of success. Publications in biomedical journals shot up from 111 in 2001 to 392 in 2007. The number of biomedical researchers jumped from 540 to 1000.

Academic breakthroughs at the Biopolis carry potential clinical applications. In 2007, a team led by IMCB's Dmitry Bulavin announced results of experiments showing how to induce self-destruction in stem cells that would otherwise cause intestinal cancer. More recently, in February 2008, researchers led by GIS' NG Huck Hui made a breakthrough in understanding the reprogramming of bodily cells to an embryonic state—one of the hottest fields in biology. Ng's team showed that one of factors thought necessary for the reprogramming of bodily cells is not necessary in embryonic stem cells.

The spillover to the economy is evident. From a base of almost zero in 2000, there are now over 30 biotech companies that have set up research centres in Singapore. These include corporate R&D laboratories by global pharmaceutical companies GlaxoSmithKline, Novartis and Eli Lilly that are located at Biopolis. The contribution of the biomedical sciences sector to the overall economy grew, from 2.5 percent of GDP in 2000 to 6 percent in 2007. The manufacturing output in the sector increased almost fourfold, from S\$6.3 billion in 2000 to S\$24.0 billion in 2007. Employment in the sector almost doubled, from 5,880 jobs in 2000 to about 11,500 jobs in 2007.

Singapore and A*STAR are now ready to move to the next stage—taking research findings and moving them to the clinic. "We want to move up the value chain," says Andre Wan, deputy executive director of A*STAR's BMRC. To do so, A*STAR combined forces with the Ministry of Health (MOH) and the National Research Foundation to create the S\$1.5 billion translational and clinical research initiative.

The decisions on how to distribute such money are made quickly in Singapore, earning the country its reputation for fast action. "We locked ourselves up in a building to determine how to spend the 1.5 billion. We can make decisions in one meeting," says Lim.

Edward Holmes moved from the University of California, San Diego (UCSD), where he was vice-chancellor for health

sciences and the dean of the school of medicine, to Singapore to lead in the translational and clinical research initiative. He holds a strategic dual appointment as BMRC's Deputy Chairman for Translational and Clinical Sciences and the Executive Chairman of the MOH's National Medical Research Council.

He is joined by his wife, Judith Swain, who also left UCSD to become the founding Executive Director of the Singapore Institute for Clinical Sciences, one of A*STAR's new units that have been set up to focus on translational research.

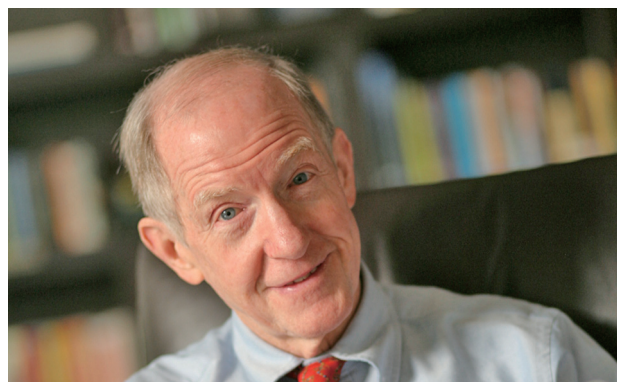
Together with MOH, A*STAR launched the Translational & Clinical Research Flagship Program, which aims to put Singapore at the very cutting edge of a number of niche areas within cancer, cardiovascular and metabolic disorders, neuroscience, infectious disease, and ophthalmology. The first, Singapore Gastric Cancer Consortium, was allocated \$25 million over 5 years in 2007 so that industrial scientists, principal investigators from the four public hospitals, the National University of Singapore, the Nanyang Technological University, and A*STAR research institutes, can work together to "improve the early detection and treatment of gastric cancer with significant clinical benefits to patients." This year, \$100 million has been awarded over 5 years to four more flagship programs in glaucoma, severe psychotic disorders, metabolic diseases and dengue.

The initiative will also put tens of millions of Singapore dollars into scientist awards and training programs in an effort to develop human capital, as well as the setting up of an Experimental Therapeutics Centre (ETC), which will translate A*STAR discoveries into commercial opportunities.

Jean Paul Thiery, deputy director of the IMCB and chief scientific officer of ETC, describes the centre as an educational training ground that uses recruits from both the public and private sectors. "Most basic researchers don't want to take the time to show that a discovery is useful. At ETC we train people to think differently." Experiments there started within days of its August 2007 opening, and ETC researchers already have a few promising drug targets.

Building Fusionopolis on a solid foundation

The Fusionopolis has been launched with similar goals: to carry out cutting-edge research, especially multi-disciplinary science, leading to commercial applications. It officially opened its doors just this month, but it will be building its interdisciplinary



Edward Holmes leads the translational and clinical research initiative in Singapore, with a strategic dual appointment at A*STAR and the Ministry of Health.



Charles Zukoski heads the A*STAR Science and Engineering Research Council at Fusionopolis.

platform out of the institutes of A*STAR's Science and Engineering Research Council which already have a prominent international presence. SERC's institutes have 1500 researchers, 55% of which are from foreign countries like UK, Germany, China, and India—820 hold doctorates. The synergy created by housing these researchers together in the Fusionopolis will quickly make it one of the greatest centres of its kind.

The Institute of High Performance Computing (IHPC), the Institute for Infocomm Research (I²R), and part of the Data Storage Institute (DSI) have moved into Fusionopolis. In 2011, these will be joined by the remainder of DSI, the Institute of Microelectronics (IME), the Institute of Materials Research and Engineering (IMRE), and the Singapore Institute of Manufacturing Technology (SIMTech). A seventh institute, the Institute of Chemical and Engineering Sciences, will remain in its existing location that is just a 30-minute drive away from Fusionopolis.

The SERC institutes have proven themselves in various fields. In 2005, DSI won the Information Storage Industry Consortium Technical Achievement Award—the first institution outside the United States to do so—with an ultra-low flying femto slider for extremely high density magnetic data storage. The scientists describe it as “flying a jet one millimetre over the runway without touching the ground.” In 2007, LO Guo-Qiang and his team at IME produced silicon nanowires in diameter of 3-4 nanometers that could scale the gate length of transistors to 2-3 nanometres. The technology, which will have applications in fields like biosensing, could enable the doubling of the density of transistors on silicon chips every two years—in accordance with “Moore's Law”—well beyond the predicted end of the law's reign around 2020. The excitement in the field landed Lo's team the coveted IEEE George E. Smith award.

Overall, in 2007 alone, SERC researchers filed 130 patents and published 1536 papers.

It is the focus on fundamental research with applications that attracts many of SERC's researchers. “It's goal-oriented fundamental research with industry as a target. It's unique,” says Charles Zukoski, who has served as SERC chairman since 2004 and move to Singapore this past summer after relinquishing his vice-chancellor post at the University of Illinois.

Indeed IME, which gets 25% of its budget from industry, has 26 industrial contracts, mainly for helping Japanese or US companies develop and demonstrate their prototypes. “We develop IP and bring in new business with it,” says IME executive director

KWONG Dim-Lee, who moved from University of Texas at Austin three years ago.

Fusionopolis will give the talent at SERC an opportunity to explore new dimensions by linking scientists in different fields. The IME, for example, will be collaborating with I²R to design high-frequency circuits that are combined with micro-electro-mechanical systems for terahertz applications. “We have expertise in circuit design, processing, packaging and work with people focused on materials, system, and manufacturing. It will expand integration significantly,” says Kwong.

The range of skills in SERC means that experimental, theoretical and computational projects can all be conducted under one roof at Fusionopolis. “If you look across the globe, there is no place that integrates so many diverse areas of physical science expertise under one roof,” adds Kwong.

The hub's work-live-play-learn environment that includes pubs, cafes, a theatre and a roof-top swimming pool is aimed at encouraging scientists to get together. They also double up as testbedding sites.

Companies are already lining up for the chance to take advantage of the opportunities at Fusionopolis—but space is limited. “We have had to turn away clients,” says Lim. Thirteen corporate laboratories are already in the first phase of Fusionopolis. Construction continues rapidly to meet the demand from companies.

But SERC and Fusionopolis also give opportunities to scientists whose research work may not have specific applications on the horizon. Northwestern University's Andrew Ortony has recently started a multidisciplinary project called Cognitive Computing for Social Systems at the IHPC. Ortony, famous for his work on metaphors and emotion in artificial intelligence, describes the project's goal as “trying to develop agent-based models of plausible, contextually appropriate, social interaction.” He expects the research by his team to contribute to the next generation of work in social robotics. Whether or not robots look like humans, they will need social skills. “For example, they will have to recognize suffering,” he says. The research will require investigation of human intentions and emotions. For the task, Ortony is pulling together an international team covering social and cognitive psychology, computational linguistics, decision theory, cognitive architectures and multi-agent systems, and social robotics.

Robots are expected to become big business, especially as ageing populations worldwide make greater demands on



Rooftop swimming pool at Fusionopolis: the complex's work-live-play-learn environment aims to encourage scientists to collaborate.

automization, so there is a practical element to the Ortony's work. But these applications are far off—something A*STAR policymakers understood. Ortony says his main goal is “to raise consciousness, excite people.” Of his team he only requires hard work and “that they think this is the coolest thing in the world.”

Building bridges

Future demands of industry and society will require work at the interface of different fields. So Lim acted to maximise the opportunity of having biomedical scientists and engineers in close proximity by setting up the A*STAR Cross Council Office (CCO) last November to tear down the walls between disciplines.

“Rarely around the world do you get the scientists in biomedicine, basic human biology sciences and engineers to come together. There are cultural differences in the way they approach science and the way they want to solve problems,” adds Zukoski.

CCO provides funding support for research and workshops to seed bottom-up collaborative research ideas. It will also invite research proposals for specific themes. It also organises activities that connect A*STAR's researchers with one another.

“We want to get people to really talk about how they can collaborate,” says Lim.

Five groups were selected from 13 applications to receive the first round of grants, and they are already at work. GIS director Edison Liu has teamed up with Kwong of IME and SIMTech to compete for the coveted Archon X prize by developing the fastest and least expensive sequencer that is able to sequence a human genome for under US\$1000. Horst Flotow is leading ETC and DSI scientists in micro-fabricating chips that can be used for imaging-based molecular diagnostics. In a collaborative project with IMCB, IMRE's Jonathan Hobley will lead a group to use optical microscopy and scanning probe microscopy to understand how axons are guided by surface properties.

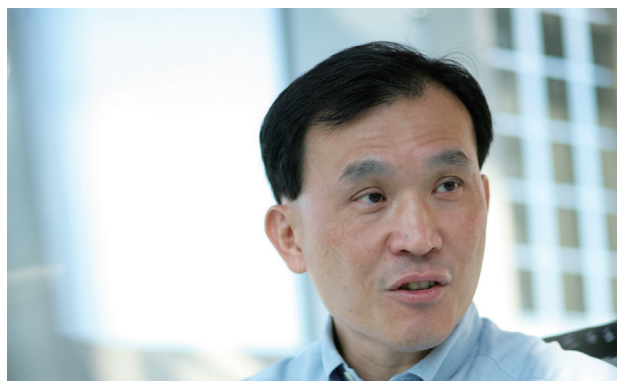
“We had been discussing how we could work together in an informal way,” says Hobley. “The Cross Council grant provided a way to really pursue it.”

The next generation

The greatest imperative for Singapore is to keep the flow of talent coming in.

Recruitment of experienced leaders continues. Colin Blakemore, former President of the British Neuroscience Association and former chief Executive of the UK Medical Research Council, was appointed by A*STAR and Duke-NUS Graduate Medical School to be chairman of the Neuroscience Research Partnership in 2007. In the same year, renowned cell and developmental biologist, Dr Colin Stewart, moved from the NCI at Frederick, US, to join IMB as a principal investigator.

For established scientists who want to retain their post, SERC offers the Visiting Investigatorship Programme (VIP). The opportunity to run a 3-year project, like Ortony's cognitive computing program, has drawn eminent scientists from all over the globe. Since 2005, Christian Joachim has been coming to IMRE from France's Centre for Material Elaboration & Structural Studies at least three months a year to run his laboratory in atomic and molecular devices. Ortony says the chance to come and start something new is “like a rebirth.”



LIM Chuan Poh, Chairman of A*STAR.

Younger scientists have also been drawn to Singapore by the A*STAR Investigatorship scheme. It targets outstanding promising talent and helps them get ahead in their career early. Thirty-three-year-old developmental biologist, Bruno Reversade, came from France to take up the appointment that comes with a US\$500,000 per year grant. “It's abundant funding, and I get to start my career as a principal investigator,” says Reversade, who is working on the biology of identical twinning. But he is getting the best of both worlds—independence and guidance. A week after he arrived at the IMB, he was joined by Solter, providing an experienced mentor. “It will be a great stepping stone,” he says.

From last year, A*STAR is also attracting young foreign scientists to do graduate studies in Singapore with the Singapore International Graduate Award (SINGA). France's Franck Courtes, one of 20 SINGA recipients at A*STAR, says the grant was too good to turn down, especially after looking into the research of Niki Wong, the Bioprocessing Technology Institute scientist that will be his mentor. “I went back and read her articles. It was exactly what I wanted to do,” says Courtes, who will study what factors make monoclonal antibodies such good producers.

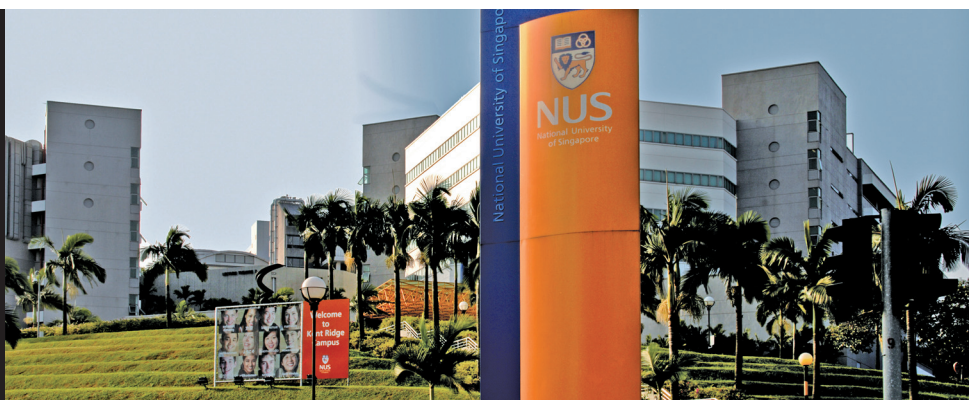
A*STAR continues to cultivate the next generation of local young scientists and is on track to train 1000 PhDs by 2010. Its graduate academy offers scholarships for undergraduate, graduate, MD-PhD, and postdoctoral studies in Singapore or at any of A*STAR's overseas partners, which include Imperial College London and the University of Illinois at Urbana-Champaign. Currently 800 students have been supported, and more than 90 are back at A*STAR.

“We welcome talent at all levels,” says Lim.



Agency for
Science, Technology
and Research

A*STAR
1 Fusionopolis Way
#20-10 Connexis North Tower, Singapore 138632
Tel: (65) 6826 6111
Email: a-star_contact@a-star.edu.sg
Website: www.a-star.edu.sg



A Global University in Asia

The National University of Singapore (NUS) is poised to become a major player in science and technology. As a leading global university based in Asia, NUS offers education and research of the highest international standards, yet with unique Asian expertise and perspectives.

Over the last decade, with significant government investment and recruitment in strategic areas, NUS has strengthened its research capacity and honed its focus, resulting in exciting developments in several fields. Symbolic of this transformation are two Research Centres of Excellence specialising in quantum technologies and cancer, which were awarded to NUS in 2007 and 2008 respectively, following stringent external review.

Some of the world's top universities have welcomed NUS into the research elite through strategic partnerships. In 2005, in collaboration with Duke University, it established the Duke-NUS Graduate Medical School Singapore, which delivers a pioneering M.D. (Doctor of Medicine) programme in Singapore. Massachusetts Institute of Technology has set up its first research unit outside of Cambridge—the Singapore-MIT Alliance for Research and Technology—on the NUS campus, and is collaborating with researchers on infectious diseases and environmental modeling. The recognition of the commercial significance of NUS research has paved the way for links with multinational companies. Siemens Medical Solutions, NUS and the Agency for Science, Technology and Research (A*STAR) are jointly building a Clinical Imaging Research Centre. US industrial giant, General Electric has established a GE Water and Process Technologies Global R&D Centre at NUS.

From a teaching university to an internationally ranked research institution

"Many factors have been at work here, including a conscious decision by the university to strengthen graduate education and cross-disciplinary research, and a growth in the funding sources in Singapore," says Professor Barry Halliwell, Tan Chin Tuan Centennial Professor and NUS Deputy President (Research and Technology). NUS has successfully competed for the new funding and put in place scientific infrastructure that enables research at internationally competitive levels. It is now brimming with new talent, either cultivated at home or welcomed from abroad.

Cutting-edge research, cutting across disciplines

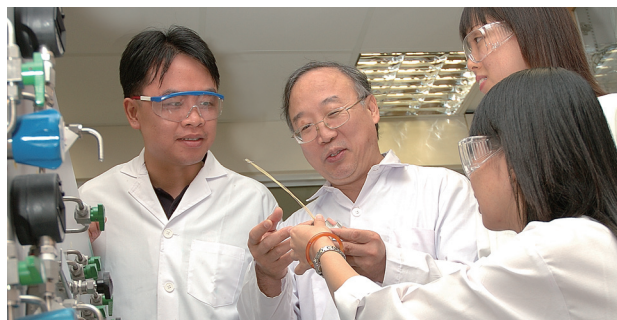
NUS researchers excel in a wide variety of fields and are constantly proving themselves with diverse applications. Theoretical physicist Professor Li Baowen won the 2005 National Science Award for his work on heat conduction and control of heat flow at the microscopic level. Professor Seeram Ramakrishna and his colleagues have patented a nanofibre membrane adorned with

catalysts that degrade chemical warfare agents, for use in garments and face masks. Professor Thirumalai Venky Venkatesan, a pioneer in epitaxial metal oxide thin films and superconductors and one of the most highly cited physicists in the world, came from the University of Maryland last year and has already assembled a powerful team of international researchers to study nanostructured materials and devices.

NUS biologists are also producing exciting results. Professor Manjunatha Kini has established himself as one of the world's leaders in snake toxins. Professor Peter Ng's research on crustaceans has carried him to world prominence in ecology circles. Associate Professor Yu Hao's work on genetic engineering of plants produced techniques for manipulating orchids—a discovery with great potential for this commercial crop. "Especially in the last 7 or 8 years, we have made the transition to a research university," says Kini. "Now there are many strong laboratories, some of them the best in the world."

To stay at the forefront of research, NUS emphasises multidisciplinary initiatives. In the biomedical sciences, for example, the Life Sciences Institute, the National University Health System and the Centre for Translational Medicine give scientists a broad range of areas to pursue their ideas. The Centre for Optoelectronics, the Centre for Remote Imaging, Sensing and Processing, and various nanoscience initiatives offer physical scientists the same flexibility. The NUS Environmental Research Institute (NERI) likewise pulls together the university's programmes related to water, air, environmental health, and energy.

Basic research is ever relevant at NUS. The Solar Energy Research Institute of Singapore (SERIS), established with S\$130 million this February, will build on NUS' strengths in areas such as novel materials, silicon thin film technology and solar-thermal energy systems, nanoscience and self-assembly of microstructures to



Researchers at NUS are given broad latitude to pursue their ideas, and they are proving themselves in a wide variety of fields – from engineering to life sciences.

build novel solar energy applications. Professor Joachim Luther, formerly the director of the world-renowned Fraunhofer Institute for Solar Energy Systems, leads the institute. SERIS is strongly supported by the Economic Development Board (EDB).

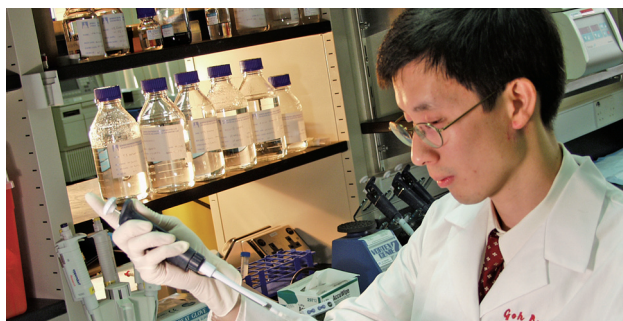
Biomedical scientists at NUS focus on health issues of special concern within Asia with the goal of bringing medical solutions to the world. Strategic initiatives at the Life Sciences Institute and the Yong Loo Lin School of Medicine include cancer, cardiovascular medicine, ageing, infectious diseases, neurobiology, and metabolic diseases. To support these priorities, NUS has developed expertise in bioengineering, bioinformatics, tissue engineering, imaging and clinical trials infrastructure, among other “platform technologies”.

Barry Halliwell is now coordinating a new university-wide programme on ageing, which encompasses some 300 ageing-related projects at NUS. The initiative brings together researchers in fields ranging from molecular biology to social policy, from nursing to architectural design to environment studies. “Ageing is a serious problem facing Singapore,” he says. “We are going to look at it from various angles—ageing cell, ageing body, ageing society,” he adds. Other such programmes, for example on “food security”, are in the works.

Centres of Excellence: Taking a leadership role

The Singapore government has dramatically increased its support for universities through competitive research programmes, especially those administered by the National Research Foundation (NRF). One of NRF’s major projects was the creation of Research Centres of Excellence in Singapore, “aimed at developing a virtuous cycle of research excellence in our universities.” Two of the first three are hosted at NUS.

Professor Daniel Tenen, Saw Swee Hock Centennial Professor in Medical Sciences and a Harvard Medical School expert on transcription regulation and differentiation into leukemic cells, leads the NUS Cancer Research Centre of Excellence (RCE). Many of NUS’ top scientists will be involved, including Professor Yoshiaki Ito, Yong Loo Lin Professor in Medical Oncology and famous for his studies of the role of Runx 3 as a tumor suppressor of gastric cancer. Professor John Wong, a practicing medical oncologist, brings his interest in drug development and the differences between Asian and Caucasian cancers to the centre. Associate Professor Yeoh Khay Guan, a native Singaporean like Professor Wong, leads a translational clinical research project on gastric cancer—a critical health issue for Asian populations. Together the diverse mix of scientists will extend their studies “from basic cancer studies all the way to experimental therapeutics”.



Strategic biomedical initiatives at NUS include cancer, neurobiology, cardiovascular medicine, ageing, infectious diseases and metabolic diseases.



While NUS has built a formidable research programme, it retains its commitment to nurturing the next generation of scientists and leaders.

NUS’ other research centre of excellence—the NUS Centre for Quantum Technologies—aims to overcome the fundamental limits to information processing by harnessing the power of individual atoms, photons and other quantum phenomena to store information in new ways. The centre was launched in December 2007, but its director Lee Kong Chian Centennial Professor Artur Ekert, who holds a joint position at Oxford University, says that it already has “international visibility, a good interdisciplinary team of theorists, good experimental quantum optics and microtrap groups, and a new cold atoms group.” Success builds on success. “Recruiting is getting easier and easier—the community already knows that something good is brewing up in Singapore,” says Professor Ekert.

Nurturing the next generation of scientists

As seen by the presence of Tenen, Ekert, Luther and other leading scientists, NUS seeks to attract top minds from around the world to lead its scientific initiatives and to train scientists and engineers at the graduate level. Singapore offers generous grants for promising junior scientists and established scholars. For example, Professor David Virshup, director of the Cancer and Stem Cell Biology programme at the Duke-NUS Graduate Medical School, won the prestigious Singapore Translational Research Investigator Award (STaR) to expand his cancer stem cell research programme. Other recipients of STaR awards have been Professor Daniel Tenen of the NUS Cancer RCE, Professor Wong Tien Yin, who studies retinal vascular imaging, and Professor Michael Chee, who works on cognitive neuroscience at the Duke-NUS Graduate Medical School.

While NUS has built a formidable research programme, it retains its commitment to training students—though now with a mission to nurture the next generation of great scientists and leaders. The NUS Graduate School for Integrative Sciences and Engineering (NGS), established in 2003, offers scholarships and a multidisciplinary environment for top students. As Professor Virshup puts it, “One of my major goals here is to train our replacements. The acid test will be, in 15 years, where are they?”



National University of Singapore
21 Lower Kent Ridge Road, Singapore 119077
Tel: (65) 6516 6666
Email: dprsec@nus.edu.sg
www.nus.edu.sg



NTU@one-north—NTU's second campus in Singapore



ADVERTISEMENT FEATURE

A collegiate quantum leap: Nanyang Technological University moves forward with bold vision

The excitement of change is palpable at Nanyang Technological University (NTU).

Until recently it was known mainly for its strength in electronics and engineering. The accumulation of expertise since its establishment in 1955 has placed it in the world's top 100 universities (2008 Times Higher Education Supplement) and also led to it being the preferred partner in a host of international collaborations.

NTU is now enhancing its strengths to adapt to new challenges requiring more and new interdisciplinary research. It is also reinventing itself as a broad-spectrum, research university. "It's an engineering-based university which includes one of the best Business Schools in the region, with the addition of an art and design school, humanities, chemistry, physics and mathematics, and the range of biological sciences," says Bertil Andersson, NTU's Provost. "We are now becoming even more research-intensive and competitive, winning new sources of government support, including support for two new large-scale initiatives in earth science and water resources. These are giving momentum to the transformation."

These initiatives demonstrate NTU's continuing leadership in engineering while transforming itself into a more broad-based institution. "We're making a quantum leap both in quality of the research and in the promotion of interdisciplinary and new areas of scholarship," says Andersson. A former member of the committee that determines Nobel Prizes in Chemistry, Andersson speaks with the authority about what makes scientific breakthroughs possible.

Proven ability, new directions

As Singapore's science and technology university, NTU has a solid base upon which to build this vision. Its 28,000 students and 2,500 international faculty have accumulated an impressive list of world firsts. The School of Electrical and Electronic Engineering developed the world's smallest integrated circuit transformer for electronic devices while the School of Mechanical and Aerospace Engineering developed a wristwatch that takes its place as the world's smallest non-intrusive blood pressure measurement device. The School of Materials Science and Engineering developed the world's smallest piezoelectric heart pump. Freddy Boey, Chair of the School of Materials Science and Engineering, also developed the first biodegradable multiple drug-releasing stents that deliver drugs for vascular disorders.

Such achievements allow NTU to take advantage of new opportunities provided by a government intent on establishing a knowledge and innovation-based economy. For example, the National Research Foundation (NRF) recently began the Competitive Research Programme, a fund for "research comprising multiple related projects under a unifying theme" that will bridge gaps with industry. In the latest round of funding, NTU captured three of the four grants—with Boey receiving support to further develop his stents. The other two, each totalling S\$10 million for 3–5 years, went to projects in cryptography and carbon nanotube-based printed electronics.

NTU's reputation attracts leading academics from around the world. One example is Jitendra Singh, who was appointed Dean of Nanyang Business School (NBS) in 2007. Singh came from the Wharton School, University of Pennsylvania, where he was Vice Dean of International Academic Affairs charged with shaping and implementing the global strategy of Wharton. Now, he is doing the same for NBS (which recently broke into the top 50 MBA programmes in the 2008 Financial Times rankings.)

NTU has attracted a broadening network of academic partnerships, including those with the United States Air Force Academy and Stanford University, Germany's Fraunhofer-Gesellschaft, and France's Centre National de la Recherche



NTU's research innovations includes the world's first multiple drug-eluting biodegradable stent.

Scientifique. Its research reputation has also led to a growing list of industrial collaborations with companies such as the European Aeronautic Defence and Space Company, Siemens and Thales. In February 2008, Rolls-Royce launched a Fuel Cell Systems Process Engineering and Verification Facility at NTU.

"These collaborations continue to come because of the quality of the students and the research," says Tony Mayer, NTU's Senior Science Officer. Mayer explains how NTU capitalized on an opportunity to team up with Robert Bosch. "Bosch wanted laboratory space at NTU to work on organic photovoltaics. I offered a collaborative approach and now we have an excellent relationship with research students being jointly supervised by Bosch and NTU professors," says Mayer.

NTU has now embarked on a quest to build a world-class research-intensive environment. The School of Biological Sciences—established in 2001—has already developed strengths in structural biology, proteomics and infectious diseases research. This will be further enhanced when it opens a satellite campus to develop structural genomics as a new area of focus in Singapore.

The School of Physical and Mathematical Sciences is rapidly building expertise in synthesis & catalysis, condensed matter physics & optoelectronics, and coding theory & cryptography. The school won the highest concentration of NRF Research Fellows with scholars including Steve Zhou, a chemist in organic synthesis and asymmetric catalysis and Christos Panagopoulos, a physicist in magnetic materials and superconducting materials.

Panagopoulos moved from Cambridge, where he had been for 14 years, because of NTU's growing research profile and excellent facilities; it provides the opportunity to work with industry, and also attracts excellent research students. "It's a well planned approach. And it is very well networked," he says.

Panagopoulos sees part of his job as trying to make the School into one of the world's top in the next 10 years. "Considering how quickly NTU became a top engineering school it shouldn't take long to the do the same for science."

Scaling new heights: Two bold missions

Two new flagship projects underscore the significant role that NTU plays in fuelling Singapore's drive for research and innovation.

The Earth Observatory of Singapore, which was awarded S\$150 million by the NRF and the Singapore Ministry of Education, will be dedicated to understanding the basic processes that produce natural hazards such as earthquakes, tsunamis, volcanic eruptions and climate change. Geologist Kerry Sieh left the California Institute of Technology to head the Observatory. He drew on his experience in studying Southeast Asian earthquakes and ties he had developed in Singapore to conceive the project. Sieh says the Singapore government has demonstrated great vision in supporting an establishment aimed at understanding dynamic earth processes relevant to human welfare. "Our work will help the country and the region address nature's 21st century challenges."

Sieh also experienced the benefits of being part of NTU's transformation into a more comprehensive university. During his recent trip to Sumatra, a team of faculty and students from the School of Art, Design and Media accompanied him to make a documentary. "This is one of our first interdisciplinary efforts to get science into the public eye. There are many exciting scientific stories and explorations about and in Southeast Asia. Why not work with film-makers to tell them?" says Sieh.



Kerry Sieh, Head of Earth Observatory of Singapore, surveying a newly dead coral reef on Mego Island, offshore western Sumatra, uplifted 1.5 meters during the great magnitude 8.4 earthquake of September 2007.

The Nanyang Environmental and Water Research Institute (NEWRI) is also making Singapore a global hub of environmental science and technology. The institute pulls together NTU's water and environment-related institutes under one body. "It is like an ecosystem in itself," says NEWRI director, Wun Jern Ng. NEWRI's five centres and two research groups will examine processes of desalination, reduction of energy consumption and recovery in treatment, biofilms and bioprocesses, resource reclamation, and residues and wastewater treatment. Over the next five years, NEWRI plans to produce 400 Masters and 120 PhDs, and also create technologies that can be transferred to industry. "We want to apply our research to the benefit of Singapore," says Ng.

Opportunities abound

Sieh has made a good start in recruiting top names to his observatory, including former United States Geological Survey volcanologist Chris Newhall and neotectonicist Paul Tapponnier from the Institut de Physique du Globe de Paris. But he worries about the challenge of ramping up quickly—he plans to have some 20 faculty members and 70 graduate students, and he will only take the best people.

But with new grant opportunities available at NTU and in Singapore, NTU might have an easier time recruiting talent than Sieh imagines. The Nanyang Assistant Professorship, launched in 2007 to attract the best young talent, offers generous salary and start-up grants to scholars. The scheme received more than 300 applicants for only 10 positions. The Nanyang President's Graduate Scholarship offers grants for Singaporean students to pursue PhD programmes at NTU. Furthermore, NTU also benefits from national grant programmes like the NRF Fellowship and the Singapore International Graduate Award. It now has research students from all over the world, including Middle East and Eastern Europe.

"It's easy to recruit good researchers. Singapore doesn't have a language barrier, and these really are golden opportunities in a country that is making a great leap forward in research and in a university which shares the same ambition," says Andersson.



50 Nanyang Avenue, Singapore 639798
www.ntu.edu.sg



WIND - NO LONGER AN ALTERNATE ENERGY

Vestas is the world's largest manufacturer of wind turbines. One in three of the world's wind turbines has been installed by the company. This translates to more than 35,500 wind turbines across 62 countries. In fact, Vestas turbines generate more than 50 million MW a year, enough power to a country the size of Spain with its population of 45 million.

It is undeniable that the potential of wind energy is enormous. Not only is it an inexhaustible and non-polluting source, it also contributes to ensure energy independence and - in contrast to other forms of energy - does not draw on precious water resources

Despite this, wind energy currently makes up only one per cent of global electricity consumption. However, this figure is increasing at an exponential rate. According to the Global Wind Energy Council, the installed capacity of wind power increased by 27% just in 2007 alone. Vestas believes that by 2020, this figure could reach 10 % of global electricity consumption - even taking into account that the demand for energy is set to rise significantly over the same period.

With a 23 per cent accumulated market share in 2007, Vestas is the world leader in delivering wind energy. Significantly, the company installs one wind turbine every four hours, 24 hours a day, somewhere in the world.

WIND POWER IN ASIA

Wind is a well-established energy source in Europe and the United States, but its potential is only just being realized in the Asia-Pacific region. Vestas currently has an installed base of 5,000 wind turbines in wind farms across China, Taiwan, South Korea, Japan, India, Australia and New Zealand.

President of Vestas Technology R&D Finn Strøm Madsen believes Asia is the new hotbed for the adoption of wind technology: "Asia's electricity demand is growing rapidly and wind energy will be an important part of covering the demand. We expect high growth in Asia".



JP171378R



"The message is not that wind will replace other energy resources, but that wind energy will be an important part of the energy mix going forward," stressed Madsen.

Until 2004, wind power was an insignificant form of energy in Asia. With countries like China and India accelerated economic growth, the need for energy had these countries seriously developing wind as a viable source of energy to coal and gas. And last year, China alone installed no less than 3000 MW, overtaking the traditional "big hitters" of Spain and Germany, and coming second only to the United States in newly installed capacity.

Faced with such overwhelming demand in Asia, the challenge for Vestas is to maintain a strong long-term position. To this end, Vestas relocated its Asia Pacific Business Unit Headquarters to Singapore in 2006, to further expand its existing business offices in China, India and Australia.

"Wind Energy is a global business and we need a global presence to get closer to our markets and customers in order to develop a deep understanding their needs," said Dr Ian Chatting, Vestas' Vice President Global Research. "Our business continues to grow at an incredible rate."

Today, the Vestas has expanded its Technology R&D facilities from Europe in Denmark and United Kingdom, to Asia Pacific in Singapore and India, and has recently announced a new

VESTAS TECHNOLOGY R&D IN ASIA

As wind technology was primarily developed in Northern Europe and America, Vestas understood the pressing need to attract, develop and train a competent and highly skilled talent pool for wind technology in this region.

"One of the challenges is the global war for talents," said Madsen. "The demand for people and best brains is very high."

So Vestas embarked on a mission to establish a research and development center in Asia. The company already had three regional sales and service centers, as well as manufacturing plants in India and China. Deciding where to locate this R&D hub was not a straightforward one. Vestas's plans to invest S\$500 million here over the next 10 years had many countries calling.

"In the final round were also China and India, but we found that Singapore has the best match to the four criteria: access to world-class talent, IPR environment, competitive costs and ease of doing business," said Madsen. "After comprehensive due diligence in Asia and we found that Singapore best matched our drivers."

R&D TALENT POOL IN SINGAPORE

Since it started operation in mid-2007, the company's regional R&D hub has already outgrown two offices. It is now located at Fusionopolis, a newly launched 120,000 sqm science and technology test-bedding center in Singapore.

Management, Engineers and Researchers work to increase product reliability by improving on sub-system performance, evaluating new ways to maximize turbine performance efficiency, leveraging on cross-industries best practices, and by creating a vibrant environment for creativity and product innovation.

"What we have experience over the last few years that in order to make wind energy ever more cost effective we have to deal with some fundamental science in many areas such as new materials and sensor and actuator concepts, this is also a strength in Singapore," said Chatting.

The setup also works on technology research and development projects with regional and worldwide partners, universities and research institutions.

Matthew Low, Managing Director, who heads the R&D Hub attested. "By August '08, we have already established three local research collaboration agreements with Singapore varsities, namely NTU, NUS and A*Star. In addition, we have also established two regional Master collaboration agreements with Tsinghua University in Beijing, China, and the Collaborative Research Council in Advanced Composite based in Melbourne, Australia."

In the search of manpower resources to conduct research and development for the No.1 Wind Energy Company, Low has this to say, "Even though there is not much wind in Singapore, and therefore, there is no wind industry, does not mean we cannot find talents here. Since a Wind Turbine Generator is a multi-disciplined engineering machine, we need different caliber of talents from all fields of science and engineering, such as power electronics, electrical engineering, material science, structural mechanics, fluid dynamics, hydraulics, signal processing etc. to work together in a very efficient and reliable manner."

"So far, we are able to find such talents from a rich and broad engineering-based cluster in Singapore and the surrounding countries, such as semiconductor & electronics sector, industrial automation, aerospace and automotive industries," said Low.



Vestas Technology R&D Singapore will be over 100 R&D engineers in 2008, and Low is certain that the target of 150 engineers will be exceeded before end 2009, and even growing beyond 300 headcount is within expectation of the near future.

OPEN INNOVATION

Working with partners outside the company flies in the face of the conventional business innovation model where research is kept strictly in-house. Vestas promotes an "open innovation" approach that actively seeks out external partners with special expertise in a particular field.

"To reach our goals we need to reach out to the best talent that is available. Part of this is to work with the world's top universities and research institutions. Through this network, our engineers can get early and sometimes unique access to new materials, techniques and developments that would otherwise not be commercially available," explained Chatting.

"It also provides the opportunity for Vestas Engineers to develop technologies with world leading scientists and this can be a very exciting environment to be in."



Setting up operations in Singapore has also allowed Vestas easy access to a highly qualified and international workforce. Over the years, the island state has built up a robust ecosystem of enterprises of 115,000 local SMEs and 28,000 international companies. The country's open and welcoming environment attracts global talents that companies like Vestas needs.

There is no doubt that the wind power is hot. While it is not yet replacing the conventional fossil fuels in the immediate future, in today's carbon constrained economy, wind is emerging as a key player in shifting global energy supply for domestic and national power grids.

VESTAS Global University Programme

In our experience, the independent research being conducted at universities inspires and contributes significantly to the creation of innovative wind power solutions. We believe in the value of contributing to this knowledge development so we jointly can take on the challenge of setting the agenda for the next generation wind turbine solutions.

We want to attract and collaborate with the best wind power students and researchers at universities around the world. Thus, outstanding students can apply for scholarships to write their Master's thesis or PhD with Vestas, while well-established researchers can apply for sponsorship of a five-year position as a professor.

We invite you to send declarations of interest in the following technical research programmes:

- Aerodynamics
- Materials science
- Composites
- Advanced control systems
- Structural design & analysis
- Gear & drive train
- Power electronics
- Electromagnetic design
- Advanced loads modelling
- Wind power plant



VESTAS TECHNOLOGY R&D SINGAPORE PTE LTD

Connexis North Tower, 1 Fusionopolis Way #06-10
Singapore 138632

For more information, please visit www.vestas.com

Vestas[®]
No. 1 in Modern Energy

Trail Blazer Lighting Up Research Path in Singapore



Physician-scientist Dr David M Virshup's research on cancer treatment targeting the proliferation of cancer stem cells spells new hope for cancer patients.

Dr Virshup who is from the US, came to Singapore a year ago to join the newly opened Duke-NUS Graduate Medical School Singapore where he is Director of the Cancer and Stem Cell Biology programme.

Prior to his arrival here, Dr Virshup was involved in research targeting the proliferation of cancer stem cells as a potential treatment for many common cancers such as colon, liver, breast cancers and leukaemia. Research in this area is still very new and there is much more that needs to be done before the drugs make it to the patients.

Given his expertise and experience, Dr Virshup is one of the awardees of the newly introduced **Singapore Translational Research Investigator award (STaR)**. For this award, he will receive a generous S\$5 million grant over five years for his research on cancer treatment. Dr. Virshup feels that stable multi-year funding is key to encouraging the strongest research, by allowing higher risk and higher yield projects to be undertaken.

For his research under STaR, Dr Virshup will be working on developing small molecule inhibitors of Wnt signalling - which is a complex network of proteins well known for their role in cancer. Wnt signalling is also important in cell proliferation and stem cell maintenance.

Dr Virshup completed his clinical training in Paediatrics and Paediatric Haematology/Oncology at Johns Hopkins. He was most recently an Investigator at the Huntsman Cancer Institute at the University of Utah before moving to Singapore.

On his decision to come to Singapore, Dr. Virshup said: "I was very attracted by the opportunity to help establish a pioneering graduate medical school in Asia." And, he is looking forward to helping train physician-scientists like himself.

Reach for the 
STaRs

The Singapore Translational Research Investigator Award (STaR) is a programme under the Singapore's Biomedical Sciences Initiative Phase II to boost the pool of clinician scientists and translational researchers in Singapore.

This prestigious award aims to recruit and nurture world-class clinician scientists to undertake cutting edge translational and clinical research (TCR) in Singapore. Some will also lead or contribute to the development of national flagship research programmes which are oriented around strategic disease areas.

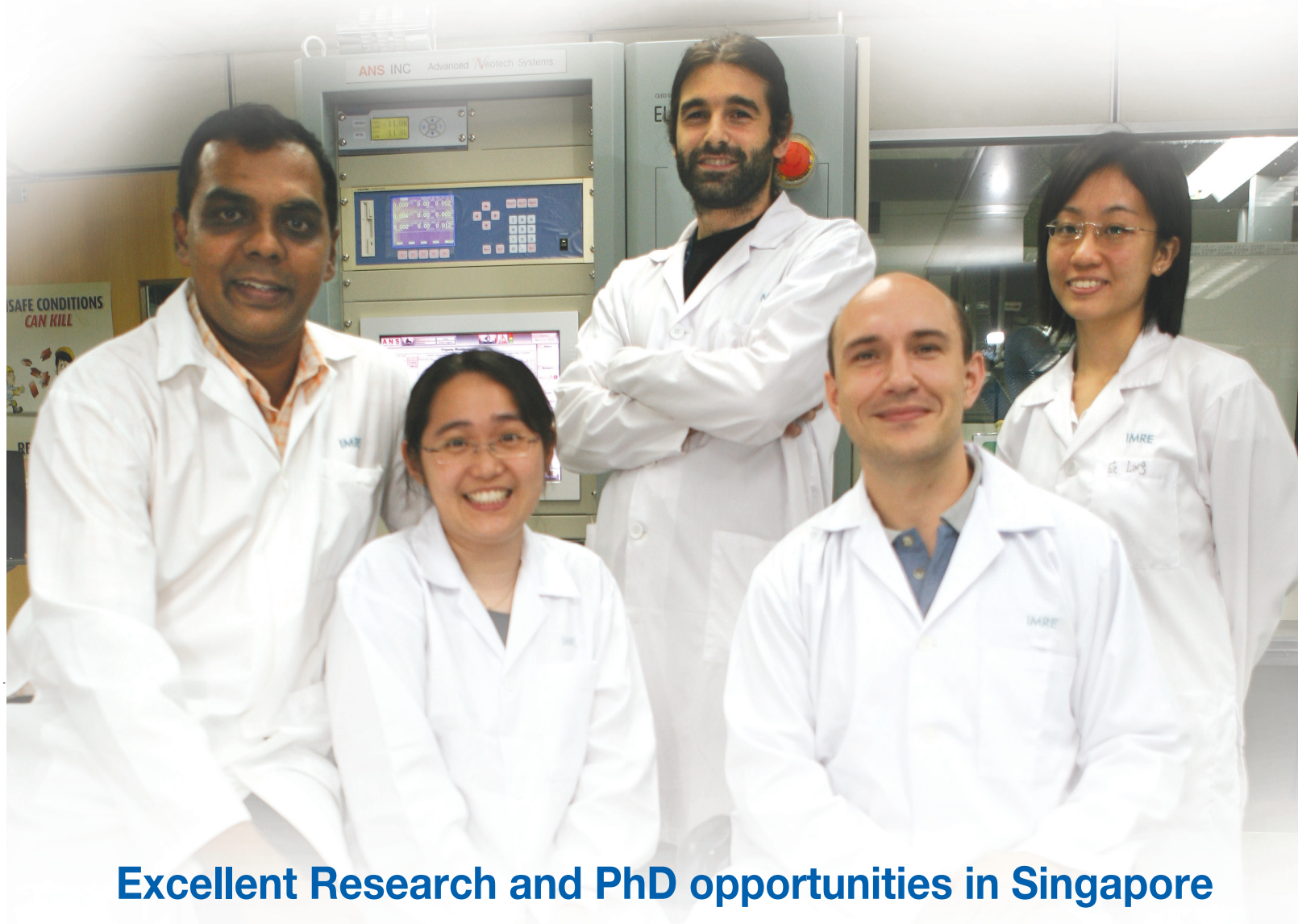
Bringing along their research experience, STaR investigators will serve as catalysts to foster strong collaborations between research groups and institutions locally and internationally. They will also act as mentors for younger researchers.

The award is for a period of up to five years and includes funding for salary, an annual budget for research support and a one-time start up grant. The amount varies according to the proposals submitted by the Investigators. Four renowned translational and clinical researchers, including Dr Virshup, formed the inaugural batch of STaR. They were awarded in May 2008 in Singapore.

Call for STaR is now open
Visit www.nmrc.gov.sg

NMRC *National Medical Research Council*
Singapore

JP171377R



Excellent Research and PhD opportunities in Singapore

Earn a prestigious PhD degree from Singapore while working with top researchers in the laboratory of your choice. You can do that, with the Singapore International Graduate Award (SINGA).

The SINGA programme is a collaboration between the Agency for Science, Technology & Research (A*STAR), Nanyang Technological University (NTU) and the National University of Singapore. It aims to bring together top talents from all over the world to work in Singapore's research-intensive environment.

SINGA offers full tuition support, generous monthly stipends and grants.
To find out more, visit www.singa.a-star.edu.sg

Research Categories: -
Biomedical Sciences | Physical Sciences & Engineering

JP171428R

APPLY ONLINE NOW AT WWW.SINGA.A-STAR.EDU.SG

ASSAY DEVELOPMENT & VALIDATION



- > A QIAGEN and Bio*One Capital joint venture
- > Development & Validation of client-provided content in:
 - Molecular diagnostics**
 - Infectious disease testing
 - Genetic predisposition
 - Oncology
 - Pre-clinical drug development**
 - Robust assays for decision making
- > Equipped with state-of-the-art technology
- > GLP compliance

Is your assay as good as you want it to be?

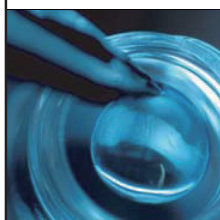
Address: Unit #02-01/02, Blk 35 Marsiling Ind Estate Road 3, Woodlands Central Industrial Estate, Singapore 739257
Telephone: +65 6499 0720 **Fax:** +65 6499 0721 **Email:** enquiries@dxassays.com

Developed by  nocodeconsultant

JP171321R

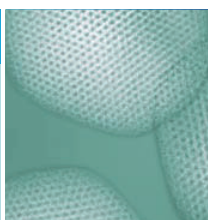
CAREERS IN BIOENGINEERING AND NANOTECHNOLOGY

The Institute of Bioengineering and Nanotechnology in Singapore is seeking highly motivated individuals who are interested in making an impact in advancing research and development in the following areas:



Drug and Gene Delivery

where the controlled release of various therapeutics involve the use of functionalized polymers and hydrogels for targeting diseased cells and organs, or for responding to specific biological stimuli.



Pharmaceuticals Synthesis and Nanobiotechnology

which encompasses the efficient catalytic synthesis of chiral pharmaceuticals, and new materials for sustainable technology and alternative energy generation.



Cell and Tissue Engineering

where biomimicking materials, stem cell technology and bioimaging are combined to develop novel approaches to regenerative medicine and artificial organs.



Biosensors and Biodevices

which involve nanotechnology and microfabricated platforms for the detection and treatment of diseases, and the synthesis and screening of biologics.

Positions are available for **Senior Group Leader, Group Leader, Principal Research Scientist, Senior Research Scientist, Research Scientist, Postdoctoral Fellow, Research Officer and Lab Officer** in IBN's four research areas.

We provide competitive salaries as well as attractive benefits. Remuneration will commensurate with qualification and experience.

If you are interested in joining a multi-disciplinary research institute at the cutting edge of bioengineering and nanotechnology, please forward a cover letter, your curriculum vitae, and a list of three references to:

Prof. Jackie Y. Ying, Executive Director
Institute of Bioengineering and Nanotechnology
31 Biopolis Way, The Nanos, #04-01, Singapore 138669
Email: recruit@ibn.a-star.edu.sg Website: www.ibn.a-star.edu.sg



Local Address. Global Perspective.



National University of Singapore Graduate School for Integrative Sciences and Engineering (NGS)

The home of cutting-edge, cross-disciplinary PhD Research and Graduate Education

Research-Intensive PhD at NGS

NGS offers generous, full PhD scholarships to talented students with strong research potential in science, engineering, computing and related aspects of medicine. All students have access to ample resources, a world-class infrastructure, and receive supervision from top flight academics. Coursework is tailored to individual student needs and interests.

What We Offer

- Four-Year PhD programme
- Full Fees, Monthly Stipend of S\$3,200 (approximately USD 2,500)
- Allowances for ITware, books and International Conferences
- No bond
- Cross-disciplinary research at the forefront of science, engineering, computing, and related aspects of medicine
- Opportunities for PhD research projects based both in Singapore, and the USA/Europe/Japan/China

Examples of Research Areas

(Please refer to our website for the complete list)

Engineering

Biomolecular, Chemical, Computer, Electrical, Environmental, Manufacturing, Mechanical, Materials, Nanotechnology, Robotics

Information Technology

Bioinformatics, Computational Science, Info-communications, Interactive Digital Media

Life Sciences

Biochemistry, Cell and Molecular Biology, Developmental Biology, Genetics, Genomics, Lipidomics, Proteomics, Immunology, Pharmacology, Physiology, Regenerative Medicine, Stem-Cell Research

Physical Sciences

Biophysics, Chemistry, Physics (Atomic, Computational, Experimental, Fluid Dynamics, Nano, Particle, Quantum Mechanics, Solid State), Structural Sciences

Seize the opportunity, challenge yourself, and achieve research excellence among the world's best. Apply through our website today at <http://www.ngs.nus.edu.sg>.

APPLICATIONS OPEN YEAR ROUND

NUS Graduate School for Integrative Sciences and Engineering

Tel: +65 6516 1480

Email: ngsenquiry@nus.edu.sg

Website: <http://www.ngs.nus.edu.sg>



NUS
National University
of Singapore

JP171324R



Lead the next generation of pharmaceutical science.

Discover the Answers that Matter.

Eli Lilly and Company is a leading, innovation-driven pharmaceutical corporation with approximately 42,000 employees worldwide. Lilly is developing a growing portfolio of best-in-class, first-in-class pharmaceutical products. We achieve this by applying the latest research from our own worldwide laboratories, by collaborating with eminent scientific organizations and by making use of the most up-to-date technological tools.

Established in 2002, Lilly Singapore Centre for Drug Discovery (LSCDD) is now expanding its capabilities to discover and develop new medicines more productively, in the areas of cancer and metabolic disorders. We form a network of drug development partners, and through innovative data integration approaches, discover and apply biomarker and patient-tailoring solutions.

Located in the exciting Singapore Biopolis, LSCDD's multi-disciplinary and multi-cultural team is working to redefine the leading edge. We are looking for outstanding individuals with demonstrated industry experience in Biotech/Pharmaceutical/Drug Discovery to fill the following positions:

- Group Leader, Diabetes Pharmacology
- Senior Scientist, Diabetes Pharmacology
- Group Leader, Diabetes Biology
- Senior Scientist, Diabetes Biology
- Senior Scientist, Diabetes (in vitro) Biology
- Research Associate, Diabetes (in vivo) Pharmacology
- Research Associate, Diabetes (in vitro) Biology
- Research Associate, Oncology (in vivo) Pharmacology
- Research Associate, Oncology (in vitro) Biology
- Group Leader, Cancer Biology
- Senior Scientist, Cancer Biology
- Senior Scientist, Cancer Biomarker Discovery
- Senior Biosafety Officer
- Staff Scientist, Assay Development
- Senior Systems Analyst
- Software Architect
- Group Leader, Epigenetics
- Senior Scientist, Systems Biology (Computational)
- Senior Scientist, Systems Biology (Experimental)
- Associate Bioinformatics Scientist, Systems Biology
- Associate Director, Bioinformatics (ICS)
- Senior Software Engineer (ICS)
- Senior Bioinformatics Scientist (ICS)
- Manager, Software Engineering (ICS)
- Associate Scientist, Biomarkers

Log on to **www.lscdd.lilly.com.sg** to find out more about these positions and what a career at Eli Lilly and Company can offer you. Eli Lilly is an equal opportunity employer.

www.lscdd.lilly.com.sg

Lilly

Answers That Matter.



Singapore's Science & Technology University

Top-ranked university

- Among the world's top 100 universities today*
- First Singapore business school to break into the top 50** in the world

Culture of innovation

- Strong innovation ethos with a well-developed ecosystem for technology transfer and commercialization
- Attracts substantial worldwide funding due to its research investments and high-impact research

Nobel boost

- 10 Nobel Laureates and a Fields medallist on NTU Institute of Advanced Studies' panel of International Advisors
- Promotes regular high-level meetings with Nobel Laureates

First-class infrastructure

- Home to some of the best facilities, including a US\$17.8 million Research TechnoPlaza and more than 70 research centres

Globally-relevant

- Cosmopolitan hub for 30,000 students and 4,000 faculty and staff from over 40 countries
- Partner of choice for many leading academic and research institutions

Industry-academic partnership

- Extensive research collaborations with industry, including technology-based partners such as EADS, Thales, Rolls-Royce, Robert-Bosch and Infineon

Interdisciplinary approach

- Strong emphasis on interdisciplinary approach to research and education
- Combines science and technology with business, arts, humanities, and social sciences

Preferred choice of international graduate students

- 85% of PhD students from Asia, Europe and the United States
- Offers generous scholarships

Research excellence

- Earth Observatory of Singapore, the region's flagship institute for earth sciences research and innovation
- Nanyang Environment and Water Research Institute, a one-stop centre for industry and research partners to access NTU's capabilities in environment and water technologies

Best of Asian culture and modern technology

- Brings together culture and technology, bridging the best of East and West

* The Times Higher Education Supplement 2008

** Financial Times 2008

JP171375R

• College of Engineering
• Nanyang Business School
• National Institute of Education

• College of Science
• College of Humanities, Arts, & Social Sciences
• S. Rajaratnam School of International Studies

www.ntu.edu.sg



Earthquakes, tsunamis, volcanic eruptions, sea-level rise, tropical storms, changes in patterns of precipitation and temperature and other natural hazards are increasingly challenging human aspirations and well-being. Research at the Earth Observatory of Singapore (EOS) will focus on understanding Southeast Asia's dynamic oceans, atmosphere and tectonic plates and characterizing the tectonic, volcanic and climatic processes responsible for these hazards. These scientific characterizations will promote forecasts of natural processes that will aid governments, communities and businesses to anticipate and adapt creatively to these environmental challenges, as well as develop and implement visionary policies.

The EOS was recently funded by Singapore's National Research Foundation (NRF) and Ministry of Education (MOE) as a Research Centre of Excellence and an autonomous institute at Nanyang Technological University (NTU). Through a new School of Earth Science (SES) at NTU, EOS scientists will also work to integrate research and teaching into education of future generations.



We plan to make about 15 tenure-track appointments over the next few years. Most will be at the assistant-professor level, but a few will be more senior.

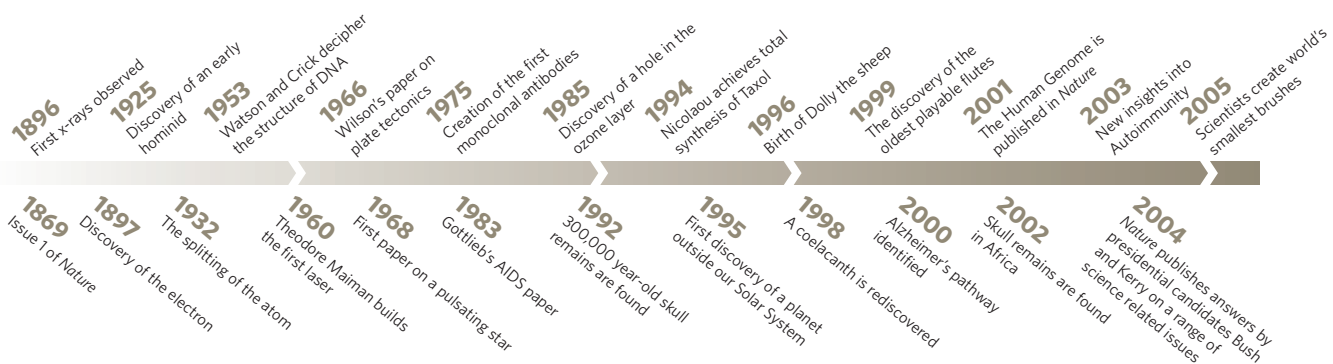
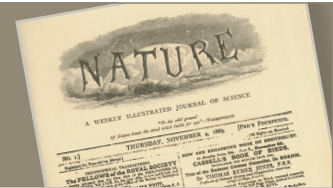
If being part of a new earth-science research team in tropical Asia intrigues you, please email your application package (consisting of a curriculum vitae, list of publications, statement of research and teaching interest, and the names of 3 references) to EOS@ntu.edu.sg by **1st December 2008**.

For further information about the Earth Observatory of Singapore, please refer to <http://www.ntu.edu.sg/EarthObservatory>



JP171527R

The complete *Nature* archive is now available online



Nature's archive is the history of science. Since launch in November 1869, *Nature* has published many of the most significant and influential papers in modern science. Articles are published in PDF with HTML abstracts.

You can search by author, affiliation or citation, or simply browse by issue. All articles can be searched from www.nature.com.

Full text access to the article is available with a site license. Ask your Librarian or information manager about site license access. Individual articles can also be purchased online.

Are you interested in *Nature's* history?

For video interviews, articles, and timelines, visit www.nature.com/nature/history.

www.nature.com/nature/archive

nature publishing group



A major center of excellence for tropical disease research.

A research institute hiring only the best scientists.

A global center with outstanding training opportunities.

Think what's possible.

Novartis Institute for Tropical Diseases (NITD) Singapore

Backed by one of the largest pharmaceutical companies in the world and major foundations, the Novartis Institute for Tropical Diseases is an established organization that intends to become a major force in fighting the spread of tropical diseases. In developing countries where these diseases are endemic, the Novartis Group intends to make treatments available to poor patients without profit. With over 100 researchers and support staff, the focus of the Institute's research activities is on Dengue, Tuberculosis and Malaria. The discovery technology is state-of-the art and the scope of activities ranges from target discovery, screen development and compound optimization, up to readiness for clinical testing, or Proof of Concept in man.

Director of Institute

We are seeking a renowned scientist to join us as Director of Institute, in succession of the present Director who will retire in mid 2009. Reporting to the Head of Corporate Research of Novartis and the Chairman of the Board of NITD, the Director will promote the discovery of drugs with significant medical advantage and economic viability in the developing world, making the most efficient use of available resources.

Based in Singapore, one of the fastest-growing bioclusters in Asia, the Director will lead the organization to the next stage of its development and guide a motivated team of best-in-class researchers to accomplish the Institute's mission.

You will promote resource-sharing within Novartis' research organizations and manage a complex network of collaborations with internal and external Institutes/organizations. You will also be responsible for implementing the Institute's research strategy and be the key decision maker for our pipeline of programs, with the goal of maintaining an innovative and competitive program portfolio. In addition, you will represent the Institute within the international scientific community.

Ideally, you will be a senior scientist with a genuine passion for the advancement and application of medical science for the benefit of the society. You must have an M.D. or Ph.D. in Biology or a related discipline, with at least 10 to 15 years' relevant research experience in industry drug discovery, early stage drug development and academia. You must possess working knowledge of infectious diseases/anti-infectives, and be familiar with drug discovery concepts. Additionally, you should have proven leadership capabilities with excellent implementation skills, along with a strong command of the English Language. Experience in collaborating with multicultural teams across multiple functions will be a distinct advantage. An attractive remuneration will be offered to the right candidate, and relocation assistance will be provided as necessary.

Interested candidates should email their CV and cover letter, stating details of current remuneration, to Berit Bretthauer or Charles Moore at Novartis-ITD@heidrick.com. Closing date for applications is 21 November 2008.



www.novartis.com

JP171373R



Master of Science Degree in Infectious Diseases, Vaccinology and Drug Discovery

The National University of Singapore (NUS), the Novartis Institute for Tropical Diseases (NITD), the Biozentrum of the University of Basel (UoB) and the Swiss Tropical Institute (STI) are jointly recruiting candidates for a research-based joint M.Sc. program on the approaches to control communicable diseases, particularly in vaccinology and drug discovery.

M.Sc. Programme

This program comprises 18 months of formal teaching and research work, of which students will spend the first 5 months (September 2009 to January 2010) in Basel, Switzerland, attached to the STI and the UoB-Biozentrum, before moving to Singapore for research work and their selected course modules. As the vacancies for this program are limited to a maximum of 20, candidates will be admitted based on the selection criteria of the Admission Committee of the National University of Singapore and the Teaching Committee for Biology of the University of Basel.

Degree

Upon completion of the program, graduates will receive a joint M.Sc. Degree from NUS and UoB.

Funding

Selected students will be offered a stipend which covers the 18 months of studies, including tuition fees, research and travel expenses. The number of stipends is limited, and students may opt for self-funding.

What Will You Learn?

Students will obtain a comprehensive insight into the basics of infectious diseases, as well as the strategies of vaccine designing and drug discovery. Lectures will complement a research project undertaken within the leading laboratories at NUS and NITD.

Application

Please refer to the document "Applications and FAQs" posted on the following websites: www.nitd.novartis.com, www.sti.ch/teaching-and-training/msc-in-infectious-diseases.html and medicine.nus.edu.sg/corporate/joint_msc.shtml. Graduates who have obtained a Bachelor's Degree in Biology or a related subject, (e.g Microbiology, Immunology) or successfully completed a degree course in Medicine, may apply for this program.

Closing Date

Applications should reach us by 30 November 2008. The M.Sc. program will commence on 14 September 2009 in Basel, Switzerland.



JP171433R



nature publishing group
language editing

Premium science and medical editing

NPG Language Editing is a high-quality English language editing service for researchers preparing papers for publication in scientific and medical journals. Our focus is on improving the clarity and sense of the written manuscript, so that **your research results stand out.**

Visit languageediting.nature.com for your 10% welcome discount.

Dewey Smith and the meaning of All

Physics in action.

Robert Reed

A man named Dewey can't be taken seriously. Dewey should be a cartoon character or a scruffy little kid or a simple-minded giant who loves puppy dogs.

Dewey Smith wasn't much to look at in his own right — smallish, profoundly bald at 20, with bad skin and bad clothes and a big belly. If it weren't for the asymmetries in his very plain face, nothing about the man would strike the eye. And his voice was as unappealing as it was soft — sharp mumbles laced with long silences that pushed audiences into comas.

By rights, the preeminent mind of our times should be six foot three, blond and respectably handsome. And he would have a voice that could fill any room, proudly telling the world how it was that he and he alone had discerned the rules of the Universe. And he would have a worthy name too, like Vincent Starr.

Which is my name, as it happens.

I met Dewey at Stanford, and I was as close to him as any tall, good-looking 19-year-old could be with an introverted 15-year-old savant. The kid graduated before me, then lingered another two years. He was the strongest horse in a Nobel laureate's stable, which made it all the more spectacular when that squeaky little voice announced that string theory was a religion; M-theory was ridiculous; and modern physics was an embarrassing mess. Then he left campus, and for the next 20 years he existed as a sequence of rumours ranging from the peculiar to the out-and-out absurd.

Meanwhile, the old masters of our field died off, taking their obscure and unworkable ideas with them.

The Modified Brane Theory lasted long enough to destroy a few careers. Then the Inspiration Theory retrieved order from chaos, sustaining half-a-thousand professors for several lucrative years. The trick was to stop thinking about the Universe as our private possession, but see it as somebody else's. We didn't bring back the Grand Deity, but accepting the idea that a single creative force had shaped the Big Bang allowed ripe new predictions, plus easy tests that didn't laugh at us when we set them up in the lab.

Then I turned 45, and the lunar cyclotron went online, throwing dust into our clever machinations.

Despite a rich career and a new wife — a beautiful girl half my age — I suddenly faced the clawing, suffocating sense that my final two or three decades would bring nothing but a rain of manageable disappointments.

There are worse fates, I'll grant you.

And better.

Then one day, I unlocked my office door, and discovered a pudgy little bald man sitting behind my desk.

"Dewey?"



His voice was unchanged. "Vince," he rasped. "Hope you don't mind the intrusion, and how are you?"

"I'm well," I managed, staring at the doorknob. "How are you, Dewey?"

He just smiled.

"You picked this lock?"

"I made the most of my jail time," he replied.

"In Oklahoma," I said. "Stolen funds of some kind, wasn't it?"

"Oh, you heard?" His smile hadn't changed with the years. Earnest, but perched on the brink of imbecilic. "Really, that prison in Nepal was much more productive."

"Why were you there?"

"To speak to a certain political prisoner."

I sat on the chair my students used — a symbolic moment, I might point out — and Dewey gave me a brief but thorough outline of his past 20-some years.

I'd heard about Oklahoma and the Brazilian commune and Cape Town. But not about living with wolves in Alaska or

his lucrative stint as a carbon-broker. Then came Siberia and the Russian mathematician-nationalist. I knew about that incident and heard how he slipped back into California, hired and then fired by a prominent AI firm, and soon rehired again, all of which happened before a long stint inside a quality mental-health facility.

"Except I wasn't crazy," he concluded.

"Of course not."

He heard the doubt in my voice. "I needed to confer with a patient."

"Which patient?"

He preferred not to say. Instead he told me: "You and your colleagues made good progress, Vince. That Inspiration Theory, I mean. Except of course there's more than one hand behind the Universe."

"Oh yeah?" I said smugly. "How many hands?"

"Three very big ones, and countless little ones. But the point is that each hand had its own purpose, and our physical laws and constants are nothing more, or less, than a set of compromises. The residue of competing geniuses, if you will. And no amount of cleverness will ever reveal the underlying order in this magnificent chaos."

"That's what the madhouse taught you?"

He hesitated. "What I came to understand is that when there are no true rules governing every aspect of our lives, much is possible. Much more than we'd find in any strict law-abiding Universe."

"And that means?"

"Ask yourself, Vince. What if you were me? Ugly, creepy Dewey. And what if you found the means to manipulate the All?"

I gave that question a moment of honest consideration. Then I tried to stand.

Behind my eyes, a fire blossomed.

"One more god shaping a very messy pile," said a confident, booming voice.

And I found myself sitting behind my desk, and the man wearing my face and body rose from the students' chair. "You'll find keys in your pocket," he told me, "and two million in the Lexus beside the student union."

"This isn't fair," I complained with a soft, grating voice.

"What is?" he replied. "When does 'fair' show its head in any of our pretty equations?"

Robert Reed is the author of nearly 200 stories and a dozen novels. He won a Hugo in 2007 for his novella *A Billion Eves*.

JACEY